UNIL | Université de Lausanne

Unicentre
CH-1015 Lausanne
http://serval.unil.ch

Year : 2014

Budgeting rockfall and modeling sediment delivery in torrent systems

Loye Alexandre

Loye Alexandre, 2014, Budgeting rockfall and modeling sediment delivery in torrent systems

Originally published at : Thesis, University of Lausanne

Posted at the University of Lausanne Open Archive http://serval.unil.ch
Document URN : urn:nbn:ch:serval-BIB_A7FE10712EB80

Droits d'auteur
L'Université de Lausanne attire expressément l'attention des utilisateurs sur le fait que tous les documents publiés dans l'Archive SERVAL sont protégés par le droit d'auteur, conformément à la loi fédérale sur le droit d'auteur et les droits voisins (LDA). A ce titre, il est indispensable d'obtenir le consentement préalable de l'auteur et/ou de l'éditeur avant toute utilisation d'une oeuvre ou d'une partie d'une oeuvre ne relevant pas d'une utilisation à des fins personnelles au sens de la LDA (art. 19, al. 1 lettre a). A défaut, tout contrevenant s'expose aux sanctions prévues par cette loi. Nous déclinons toute responsabilité en la matière.

Copyright
The University of Lausanne expressly draws the attention of users to the fact that all documents published in the SERVAL Archive are protected by copyright in accordance with federal law on copyright and similar rights (LDA). Accordingly it is indispensable to obtain prior consent from the author and/or publisher before any use of a work or part of a work for purposes other than personal use within the meaning of LDA (art. 19, para. 1 letter a). Failure to do so will expose offenders to the sanctions laid down by this law. We accept no liability in this respect.

UNIL | Université de Lausanne

UNIL | Université de Lausanne
Institut de géomatique
et d'analyse du risque

Budgeting rockfall and modeling sediment delivery in torrent systems

Thèse de doctorat

présentée à la Faculté des Géosciences et de l'Environnement de l'Université de Lausanne par

M. Alexandre Loye

diplomé en Sciences de la Terre de l'Ecole Polytechnique Fédérale de Zürich

Devant le Jury composé des:

Prof. Klaus Holliger, Président du jury, Université de Lausanne
Prof. Michel Jaboyedoff, Directeur de la thèse, Université de Lausanne
Dr. Marc-Henri Derron, Expert interne, Université de Lausanne
Dr. Frédéric Liébault, Expert externe, IRSTEA Grenoble
Dr. Francesco Brardinoni, Expert externe, University of Milano-Bicocca
Prof. Oldrich Hungr, Expert externe, University of British Columbia

Unil
UNIL | Université de Lausanne
Décanat Géosciences et de l'Environnement
bâtiment Géopolis
CH-1015 Lausanne

IMPRIMATUR

Vu le rapport présenté par le jury d'examen, composé de

Président de la séance publique :	M. le Professeur Klaus Holliger
Président du colloque :	M. le Professeur Klaus Holliger
Directeur de thèse :	M. le Professeur Michel Jaboyedoff
Expert externe :	M. le Professeur Oldrich Hungr
Expert externe :	M. le Docteur Francesco Brardinoni
Expert externe :	M. le Docteur Frédéric Liebault
Expert interne :	M. le Docteur Marc-Henri Derron

Le Doyen de la Faculté des géosciences et de l'environnement autorise l'impression de la thèse de

Monsieur Alexandre LOYE

Titulaire d'un
Diplôme en Sciences naturelles
Ecole Polytechnique Fédérale, Zürich

intitulée

BUDGETING ROCKFALL AND MODELING SEDIMENT DELIVERY IN TORRENT SYSTEMS

Lausanne, le 13 décembre 2013

Pour le Doyen de la Faculté des géosciences et de l'environnement

K. Holliger

Professeur Klaus Holliger

Contents

Contents i
List of Figures vii
List of Tables xi
Abstract xiii
Résumé xv
Zusammenfassung xvii
Quotation xix

1 Introduction **1**
- 1.1 Topic overview 3
- 1.2 Research projects and related study site 5
  - 1.2.1 Torrential hazard contend 5
  - 1.2.2 Landscape evolution 5
  - 1.2.3 Sediment yield magnitude prediction and managment 7
- 1.3 Research focus and objectives 7
- 1.4 Techniques of investigations 10
  - 1.4.1 Experimental investigations 10
  - 1.4.2 Methods of analysis 13
  - 1.4.3 Sediment discharge prediction 13
- 1.5 Structure of the thesis 14

I Laser scanning sediment dynamics in torrent catchment 17

2 Debris supply and torrent response inducing debris flows: the case of the Manival catchment 19

2.1 Introduction 20

2.2 Study site 21

2.2.1 General setting 21

2.2.2 Characteristics of the headwater sediment dynamic 22

2.3 Methods and data processing 26

2.3.1 Topographic monitoring using ground-based laser scanning . . . 26

2.3.2 Topographic change identification and characterization 27

2.3.3 Volume computation 31

2.3.4 Point cloud accuracy and limits of detection of the geomorphic features 33

2.3.5 Sediment budgets of the Manival torrent 35

2.3.6 Estimation of debris production rate 35

2.4 Observation: Hillslope process activity monitoring 36

2.4.1 1st monitoring period (April 2009 – August 2009) 36

2.4.2 2nd monitoring period (September 2009 – November 2010) 36

2.4.3 3rd monitoring period (November 2009 – July 2010) 40

2.4.4 Rock slope production inventory 41

2.4.5 Torrent in-channel storage changes 42

2.5 Summary: Manival headwater sediment budgets 43

2.6 Discussion 50

2.6.1 Debris supply through rock slope production 50

2.6.2 Debris supply through hillslope activity 54

2.6.3 Sediment recharge of the torrent 54

2.6.4 Possible causes of seasonal fluctuations in debris supply 55

2.6.5 The role of sediment source stability 56

2.7 Conclusions 57

II Morphological implications and structural control of geomorphic process activity 61

3 Morphological and structural analyses of a torrent catchment: implications for debris supply at channel heads 63

3.1 Introduction 64
3.2 Study site 65
3.3 Methods 70
  3.3.1 General approach 70
  3.3.2 Morphological study 71
  3.3.3 Structural study 71
3.4 Data processing 74
  3.4.1 Classified map of slope steepness 74
  3.4.2 Morphostructural analysis 75
  3.4.3 Areas of potential rock slope failure (using kinematic tests) 75
  3.4.4 Susceptibility assessment to rock slope failure 77
3.5 Results 80
  3.5.1 Identification of the morphological units 80
  3.5.2 Structural analysis performed in the field 81
  3.5.3 Structural analyses using COLTOP 3D: 83
  3.5.4 Zones of susceptibility to rock instability 90
3.6 Analysis and discussion 97
  3.6.1 Hillslope process activity derived from morphological units . . . 97
  3.6.2 Stage of erosion development in lithologies 98
  3.6.3 Structural investigation based on DEM of different resolution . . 99
  3.6.4 Interpretation of the discontinuity sets 101
  3.6.5 Areas potentially exposed to rock slope instability 102
  3.6.6 Susceptibility assessment 102
  3.6.7 Implication for debris supply 105
3.7 Conclusions 107

4 Influence of bedrock structures on the spatial pattern of erosional landforms in small alpine catchments 111

4.1 Introduction 112
4.2 Study sites 113
4.2.1 The Saxé and Métin catchment 113
4.2.2 The Manival catchment 116
4.3 Data sources, methods and statistical analysis 116
4.3.1 Morphostructural analysis using DEM 116
4.3.2 Relevance of the discontinuity pattern for the catchment morphology 118
4.3.3 Correspondence between gully network and potential slope failure geometry 118
4.3.4 Orientation of the maximum joints frequency 119
4.3.5 Data processing 120
4.3.6 Structural data validation 121
4.4 Results 121
4.4.1 Morphostructural analysis of the Saxé and Métin catchment . . . 121
4.4.2 Morphostructural analysis of the upper Manival catchment 124
4.4.3 Geomorphic feature orientation analysis of the Saxé and Métin catchment 127
4.4.4 Geomorphic feature orientation analysis of the upper Manival catchment 132
4.5 Discussion 135
4.5.1 Saxé and Métin catchment 136
4.5.2 Manival catchment 137
4.6 Structural control of erosion 140
4.7 Conclusions 140

III Modeling sediment budgets of torrent systems 143

5 Alpine catchment sediment budget modeling through a quantitative sediment cascade procedure 145

5.1 Introduction 146

5.2 Study site 146

5.3 The quantitative and dynamic sediment cascade 146

5.3.1 The sediment budget approach 146

5.3.2 The torrent system dynamics 148

5.3.3 The sediment flow routine 151

5.4 Model application and data processing 151

5.4.1 Field data 151

5.4.2 In-channel storage (direct debris sources) 152

5.4.3 Recharge from hillslope (indirect debris sources) 152

5.4.4 Sediment cascade structure and in-torrent sediment flow dynamics 155

5.4.5 Volume flux and rates of sediment transfer 155

5.4.6 Frequency and magnitude of stochastic events 160

5.4.7 MATEROSION model application 161

5.5 Sediment budget projections 162

5.6 Conclusive comments 163

Conclusion **167**

Bibliography **173**

Aknowledgments **195**

Appendix **197**

A The MatErosion project **197**

B Watershed sediment balance and local denudation rate based on hydropower reservoir sedimentation data **285**

C Erosion process monitoring in the Roubine elementary gully of the ERS Draix using TLS devices **327**

D Identification of potential rockfall source areas at a regional scale using a DEM-based geomorphometric analysis **345**

E Preliminary regional rockfall hazard mapping using LiDAR-based slope frequency distribution and Conefall modelling 359

F DEM-based detection of potential rockfall source areas at regional scale using the software COLTOP 3D and susceptibility hazard mapping assessment 371

G Earth flow in a complex geological environment: the example of Pont Bourquin, Les Diablerets (Western Switzerland) 377

H Debris flows and Avalanches Susceptibility Hazard Mapping for Pakistan 387

I Monitoring rock glacier with terrestrial laser scanning 413

List of Figures

1.1 A debris flow event 2

1.2 In-channel storage as function of debris flow events 4

1.3 The Manival torrent catchment 6

1.4 The Saxé and Métin torrent catchment 8

1.5 The small hillside torrents of Zinal 9

1.6 The terrestrial laser scanner device 12

2.1 Basin location and aerial view 22

2.2 Geological map of the Manival upper catchment 23

2.3 Geomorphic process map 24

2.4 3-D shaded view of the Manival headwaters and subdivision in subcatchments 25

2.5 Topographic change identification: visual approach 28

2.6 Topographic change identification: automatic approach 30

2.7 Geomorphic feature identification and volume computation 32

2.8 Point distance distribution after co-registration procedure 33

2.9 Hillslope process activity: 1st monitoring period 37

2.10 Hillslope process activity: 2nd monitoring period 38

2.11 Hillslope process activity: 3rd monitoring period 39

2.12 Volume distribution of the rockfall inventory 41

2.13 Torrent in-channel storage changes and cumulative sediment budgets . . . 44

2.14 Storage changes from debris sources to fan apex 45

2.15 Headwater sediment budget: 1st monitoring period 47

2.16 Headwater sediment budget: 2nd monitoring period 48

2.17 Headwater sediment budget: 3^{rd} monitoring period 49
2.18 Erosion rate as function of the size of events 52
2.19 Volume esimation of an old rock avalanche using the SLBL procedure . . 53
2.20 Maximum rainfall intensity 56

3.1 Location of the study site 66
3.2 Tectonic features of the Chartreuse Massif 67
3.3 Tectonic features of the Manival catchment 68
3.4 Geological cross-sections 69
3.5 Strahler's law of constancy of slope 72
3.6 Illustration of the morphostructural hypothesis 73
3.7 Illustration of the susceptibility assessment 74
3.8 Illustration of the software Coltop 3D 76
3.9 Illustration of the software Matterocking 77
3.10 Susceptibility assessment after Matterocking 78
3.11 Slope angle frequency distribution analysis 81
3.12 Classified map of slope steepness 82
3.13 Slope angle frequency distribution of scree slopes and lithology 83
3.14 Structural setting from field data 84
3.15 Structural setting from TLS data 85
3.16 Illustration of the structural setting on TLS data 86
3.17 Structural setting from LiDAR DEM 88
3.18 Structural analysis illustrations on photographs 89
3.19 Structural setting from standard DEM 90
3.20 Map of density of potential failure with a uniform joint spacing 91
3.21 Map of density of potential failure with relative joint spacings 92
3.22 Map of density of potential failure weighted with geotechnical parameters 93
3.23 Map of density of potential plane failures with uniform joint spacing . . . 94
3.24 Map of density of potential wedges with uniform joint spacing 95
3.25 Map of density of potential toppling with uniform joint spacing 96
3.26 Map of the rockfall inventory comparison 99

3.27 Rockfall volume inventory expressed as function of the density of potential failure . . . 104
3.28 Cumulative frequency distribution of susceptibility in regards to the rockfall inventory . . . 105
3.29 Rock slope production and susceptibility to slope failure . . . 106
3.30 Rock slope erosion rate and susceptibility to slope failure . . . 107
3.31 Net sediment balances and susceptibility to slope failure . . . 108

4.1 Study sites: locations and tectonic maps . . . 113
4.2 Saxé and Métin catchment: study site and geological context . . . 114
4.3 Manival catchment: study site and geological context . . . 115
4.4 The Coltop 3D hypothesis . . . 117
4.5 The sampling window approach . . . 119
4.6 Saxé and Métin: morphostructural analysis . . . 122
4.7 Saxé and Métin: joint spacing distribution . . . 123
4.8 Saxé and Métin: influence of joint orientations . . . 124
4.9 Saxé and Métin: orientations of geomorphic features and the maximum joint frequency . . . 125
4.10 Saxé and Métin: topography oriented in the direction of the maximum joint frequency . . . 126
4.11 Manival: morphostructural analysis . . . 128
4.12 Manival: joint spacing distribution . . . 129
4.13 Manival: influence of joint orientations . . . 130
4.14 Manival: orientations of geomorphic features and the maximum joint frequency . . . 130
4.15 Manival: topography oriented in the direction of the maximum joint frequency . . . 131
4.16 Saxé and Métin: associations of potential wedges and gullies . . . 132
4.17 Manival: associations of potential wedges and gullies . . . 133
4.18 Conceptual model of development of geomorphic features . . . 139

5.1 Study side . . . 147
5.2 Hillslope and channel sediment stocks . . . 149

5.3 Illustration of the sediment cascade 150
5.4 Illustration of a time series of events 152
5.5 Flow chart of sediment flow routine 153
5.6 Maximum sediment supply assessment 154
5.7 Process map and indirect sediment stocks 156
5.8 Sediment cascade reservoirs, links and flow dynamics 157
5.9 Length profile analysis 158
5.10 Index of sediment transfer rates and examples 159
5.11 Boxplot statistics for event frequency simulation 161
5.12 Sediment budget projection for the Perrec torrent 164
5.13 Sediment budget projection for the Lirec torrent 165
5.14 Debris supply and torrential activity 168

List of Tables

2.1 TLS dates of acquisitions. 26

2.2 TLS data and surface coverage characteristics 27

2.3 Minimum limits of detection (LoD) 34

2.4 1th monitoring sediment budget 37

2.5 2nd monitoring sediment budget 38

2.6 3rd monitoring sediment budget 39

2.7 Estimation of rock slope production rate 42

2.8 Morphological sediment budgets of the torrent 43

2.9 Overall headwater sediment budget 46

2.10 Monthly average overall sediment budget 50

2.11 Overall sediment budgets per catchment subsystem 59

3.1 Susceptibility assessment: joint spacings. 79

3.2 Susceptibility assessment: factor of safety (FS) 80

3.3 Morphological unit: threshold slope angles 83

4.1 Saxé and Métin catchment: potential wedges and correspondences with geomorphic features 134

4.2 Manival catchment: potential wedges and correspondences with geomorphic features 135

5.1 Sediment stocks detected in the torrent catchments 162

5.2 Torrent debris flow magnitude and intensity 162

Abstract

This thesis is a compilation of projects to study sediment processes recharging debris flow channels. These works, conducted during my stay at the University of Lausanne, focus in the geological and morphological implications of torrent catchments to characterize debris supply, a fundamental element to predict debris flows. Other aspects of sediment dynamics are considered, e.g. the coupling headwaters – torrent, as well as the development of a modeling software that simulates sediment transfer in torrent systems.

The sediment activity at Manival, an active torrent system of the northern French Alps, was investigated using terrestrial laser scanning and supplemented with geostructural investigations and a survey of sediment transferred in the main torrent. A full year of sediment flux could be observed, which coincided with two debris flows and several bedload transport events. This study revealed that both debris flows generated in the torrent and were preceded in time by recharge of material from the headwaters. Debris production occurred mostly during winter-early spring and was caused by large slope failures. Sediment transfers were more puzzling, occurring almost exclusively in early spring, subordinated to runoff conditions, and in autumn during long rainfall events. Intense rainstorms in summer did not affect debris storage that seems to rely on the stability of debris deposits.

The morpho-geological implication in debris supply was evaluated using DEM and field surveys. A slope angle-based classification of topography could characterize the mode of debris production and transfer. A slope stability analysis derived from the structures in rock mass could assess susceptibility to failure. The modeled rockfall source areas included more than 97% of the recorded events and the sediment budgets appeared to be correlated to the density of potential plane failure. This work showed that the analysis of process-related terrain morphology and of susceptibility to slope failure document the sediment dynamics to quantitatively assess erosion zones leading to debris flow activity.

The development of erosional landforms was evaluated by analyzing their geometry with the orientations of potential rock slope failure and with the direction of the maximum joint frequency. Structure in rock mass, but in particular wedge failure and the dominant discontinuities, appear as a first-order control of erosional mechanisms affecting bedrock-dominated catchments. They represent some weaknesses that are exploited primarily by mass wasting processes and erosion, promoting not only the initiation of rock couloirs and gullies, but also their propagation. Incorporating the geological control in geomorphic processes contributes to better understand the landscape evolution of active catchments.

A sediment flux algorithm was implemented in a sediment cascade model that discretizes the torrent catchment in channel reaches and individual process-response systems. Each conceptual element includes in a simple manner geomorphological and sediment flux information derived from GIS complemented with field mapping. This tool enables to simulate sediment transfers in channels, considering evolving debris supply and conveyance, and helps reducing uncertainty inherent to sediment budget prediction in torrent systems.

This thesis aims in a modest way to shine light on some aspects of sediment dynamics of torrent systems.

Résumé

Cette thèse est un recueil de projets d'études des processus de recharges sédimentaires des chenaux torrentiels. Ces travaux, réalisés lorsque j'étais employé à l'Université de Lausanne, se concentrent sur les implications géologiques et morphologiques des bassins dans l'apport de sédiments, élément fondamental dans la prédiction de laves torrentielles. D'autres aspects de dynamique sédimentaire ont été abordés, p. ex. le couplage torrent – bassin, ainsi qu'un modèle de simulation du transfert sédimentaire en milieu torrentiel.

L'activité sédimentaire du Manival, un système torrentiel actif des Alpes françaises, a été étudiée par relevés au laser scanner terrestre et complétée par une étude géostructurale ainsi qu'un suivi du transfert en sédiments du torrent. Une année de flux sédimentaire a pu être observée, coincidant avec deux laves torrentielles et plusieurs phénomènes de charriage. Cette étude a révélé que les laves s'étaient générées dans le torrent et étaient précédées par une recharge de débris depuis les versants. La production de débris s'est passée principalement en l'hiver – début du printemps, causée par de grandes ruptures de pentes. Le transfert était plus étrange, se produisant presque exclusivement au début du printemps subordonné aux conditions d'écoulement et en automne lors de longues pluies. Les orages d'été n'affectèrent guère les dépôts, qui semblent dépendre de leur stabilité.

Les implications morpho-géologiques dans l'apport sédimentaire ont été évaluées à l'aide de MNT et études de terrain. Une classification de la topographie basée sur la pente a permis de caractériser le mode de production et transfert. Une analyse de stabilité de pente à partir des structures de roches a permis d'estimer la susceptibilité à la rupture. Les zones sources modélisées comprennent plus de 97% des chutes de blocs observées et les bilans sédimentaires sont corrélés à la densité de ruptures potentielles. Ce travail d'analyses des morphologies du terrain et de susceptibilité à la rupture documente la dynamique sédimentaire pour l'estimation quantitative des zones érosives induisant l'activité torrentielle.

Le développement des formes d'érosion a été évalué par l'analyse de leur géométrie avec celle des ruptures potentielles et avec la direction de la fréquence maximale des joints. Les structures de roches, mais en particulier les dièdres et les discontinuités dominantes, semblent être très influents dans les mécanismes d'érosion affectant les bassins rocheux. Ils représentent des zones de faiblesse exploitées en priorité par les processus de démantèlement et d'érosion, encourageant l'initiation de ravines et couloirs, mais aussi leur propagation. L'incorporation du control géologique dans les processus de surface contribue à une meilleure compréhension de l'évolution topographique de bassins actifs.

Un algorithme de flux sédimentaire a été implémenté dans un modèle en cascade, lequel divise le bassin en biefs et en systèmes individuels répondant aux processus. Chaque unité inclut de façon simple les informations géomorpologiques et celles du flux sédimentaire dérivées à partir de SIG et de cartographie de terrain. Cet outil permet la simulation des transferts de masse dans les chenaux, considérants la variabilité de l'apport et son transport, et aide à réduire l'incertitude liée à la prédiction de bilans sédimentaires torrentiels.

Ce travail vise très humblement d'éclairer quelques aspects de la dynamique sédimentaire en milieu torrentiel.

Zusammenfassung

Diese Doktorarbeit ist eine Sammlung verschiedener Forschungsprojekte über Geschiebeanreicherung in Wildbachsystemen. Der Schwerpunkt dieser Arbeiten, die während meiner Anstellung an der Universität Lausanne zu Stande gekommen sind, liegt bei geologischen und morphologischen Auswirkungen von Einzugsgebieten auf Geschiebe-lieferungen. Diese sind entscheidend, um Murgänge vorherzusagen. Es wurden auch andere Aspekte der Geschiebeprozesse erhörtet, wie z. B. die Verknüpfung Wildbach – Hangsystem wie auch die Erarbeitung eines Simulationsmodells von Geschiebefrachten in Wildbachsystemen.

Anhand des terrestrischen Laserscannings wurden Geschiebeprozesse im Manival, ein aktives Wildbachsystem in den französischen Alpen, untersucht und durch eine strukturgeologische Analyse wie auch ereignisbasierte Beobachtungen von Geschiebetrieben im Wildbach, ergänzt. Während eines Jahres konnten Geschiebeprozesse beobachtet werden, die mit zwei Murgängen und mehreren Geschiebefrachten zusammen fielen. Die Studie hat gezeigt, dass die Murgänge sich im Wildbach bilden, dem eine Geschiebeanreicherung vom Hang vorausgegangen war. Die Produktion von Lockermaterial welches aus Felssturzmassen stammt, fand hauptsächlich im Winter – anfangs Frühling statt. Die Geschiebelieferung war seltsamer. Sie trat fast ausschliesslich anfangs Frühling auf, abhängig von den Abflussbedingungen und im Herbst während langen Niederschlägen. Die Gewitter im Sommer hatten sehr wenig Einfluss auf die Schuttverlagerungen. Es scheint, als seien diese von ihrer Festigkeit abhängig.

Die Entwicklung der Erosionsformen wurden einerseits anhand einer Analyse der Ausrichtung der potentiellen Sturzereignisse und anderseits durch die maximale Ausrichtung der Klüftungsdichte bewertet. Die Struktur der Felsen, insbesondere die Keile und die vorherrschenden Diskontinuitäten, scheint ein wichtiger Faktor für die erosiven Mechanismen eines mit Felsen dominierten Wildbaches zu sein. Es sind Schwachzonen, in denen die Verwitterung und Erosion einen wichtigen Einfluss haben. Diese Gegebenheit fördert die Entstehung von Felsrinnen und Runsen wie auch deren Ausbreitung. Mit Hilfe der geologischen Strukturen in den Hangprozessen kann ein vertieftes Verständnis der topographischen Entwicklung der aktiven Wildbachsysteme entwickelt werden.

Ein Sedimentflussalgorithmus wurde in einem Sedimentkaskadenmodell implementiert, das den Wildbach in Gerinneabschnitte und einzelne Systeme aufteilt, die die Prozesse widerspiegelt. Jeder Bestandteil beinhaltet auf einfache Weise die geomorphologischen Informationen und die der Sedimentfracht. Diese Informationen stammen aus dem GIS und der erstellten Kartographie des Geländes. Dieses Werkzeug ermöglicht eine Geschiebefrachtsimulation eines Wildbaches unter Berücksichtigung der Variabilität der Geschiebelieferung und seines Transports. Zudem kann man anhand dieses Werkzeugs die Unsicherheit bei der Prognose des Geschiebehaushalts im Wildbachsystem einschränken.

Diese Doktorarbeit will in aller Bescheidenheit einige Aspekte von Geschiebeprozessen in Wildbachsystemen erläutern.

"Ce n'est pas de l'eau pure, mais une espèce de boue liquide, mêlée d'ardoise décomposée et de fragments de rochers; la force impulsive de cette bouillie dense et visqueuse est incompréhensible; elle entraîne des rochers, renverse les édifices qui se trouvent sur son passage, déracine les plus grands arbres et désole les campagnes, en creusant de profondes ravines, et couvrant les terres d'une épaisseur considérable de limon, de gravier et de fragments de rochers..."

"Voyages dans les Alpes" – Horace-Bénédict de Saussure, 1781.

Chapter 1

Introduction

Torrential process activity is integrally linked to particular hydrometeorological events, such as rainstorms or prolonged periods of rainfall, and often associated with rapid snowmelt (Johnson and Rodine, 1984; Zimmermann et al., 1997b). In mountain environments, the interactions between the hydrologic network and debris derived from mass wasting and weathering processes pose one of the greatest and far reaching mass movement related hazard: debris surges. A surge of debris torrent involves an *en-masse* entrainment of significant amounts of poorly-sorted coarse material associated with a fast-moving flow of water (Varnes, 1978). The high potential of destruction reposes in sediment transfer dynamics, which tends to proceed by pulses (slugs) and to occur with little warnings. This mode of sediment transport is called *debris flow* (Fig. 1.1), a common term referring to various types of unsorted flow-like mass movement related phenomena operating in an established gully or confined channel (Rickenmann, 1990). Debris flow encompasses usually several processes of mass flux such as bedload transport, torrential floods and mud flows, this latter being considered as cohesive debris flow (Hungr et al., 2001). The development of debris flow can be attributed to two distinct characteristics inherent to the nature of mountain basins (Barsch and Caine, 1984): First, the high local relief and the steep gradient of topography provide much potential energy for slope erosion and sediment delivery processes. Second, the climatic conditions cause intensive precipitation associated geomorphic effects, large temperature fluctuation (e.g. frost-shattering) and lower-coverage vegetation. Many mountain areas include also seismic disturbance associated with tectonic activity (Eisbacher and Clague, 1984; Lin et al., 2003). This combination of factors ensures these terrain types to be highly dynamic in terms of sediment production and transfer rate, inducing rapid changes in the contemporary morphodynamic settings of drainage basins and fans. The mountain system gives debris flows considerable momentum once an initial sediment deposit turns into a mobile mass flow. They are able to travel over long distance across gentle slope gradients and can incorporate important volumes of material with disastrous consequences for the nearby channels and the debris fan. The challenge in terms of quantitative risk assessment has currently increased by the runaway extension of settlements in potentially hazardous locations as well as the pressing economic and social need for mobility and leisure infrastructures in mountain regions.

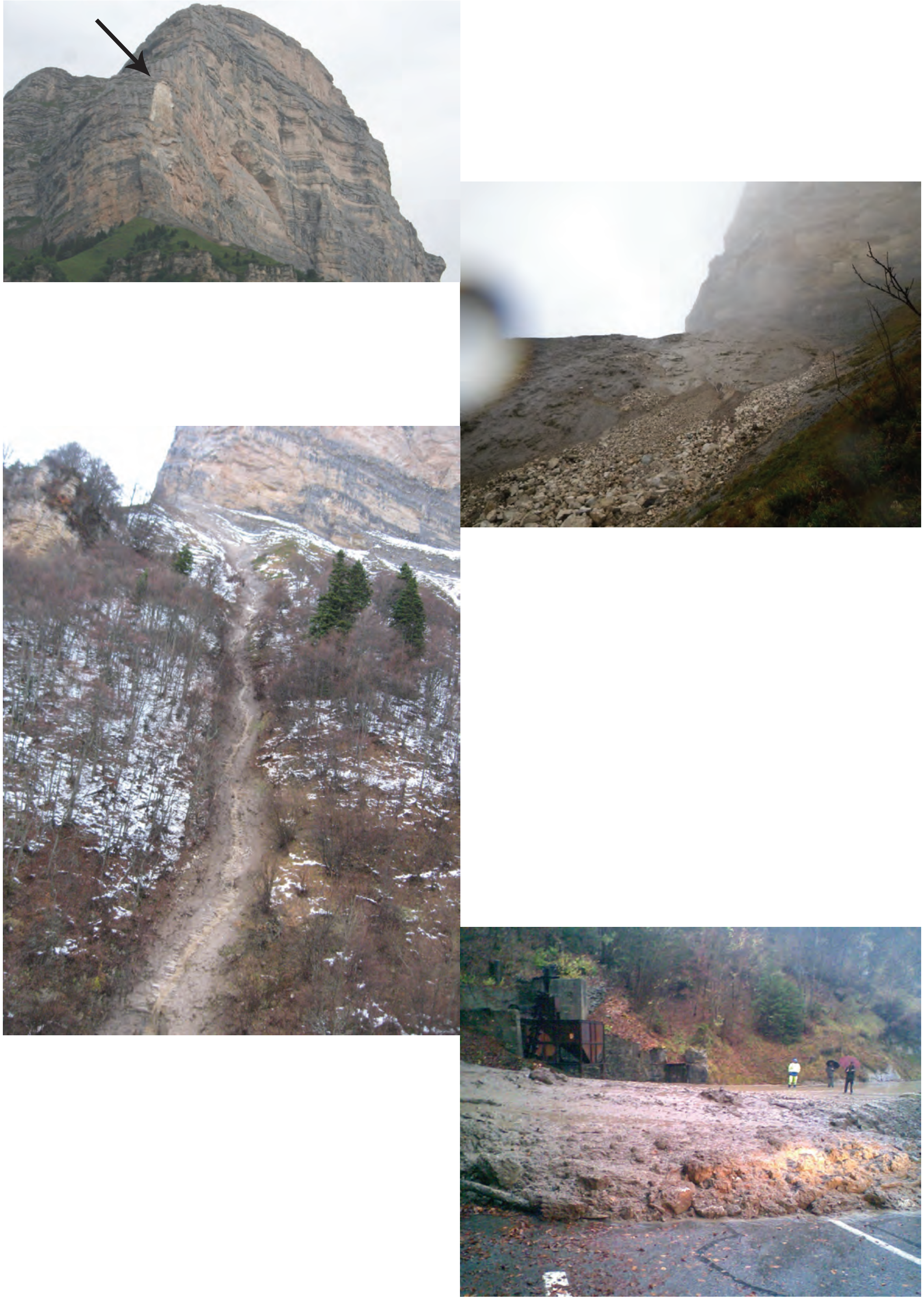

Figure 1.1: *Debris flow of a few 100* m^3 *that occurred in october 2010 below the south face of the Dent de Crolles near Grenoble (France) and reached the road that goes up to the top of the Manival Catchment. The event was triggered about two weeks after that a rock collapse (cf. arrow) deposited a substantial amount of debris at the channel head (Photographs from L. Dorren).*

1.1 Topic overview

Although debris flow regime depends on runoff, rainstorm intensity or duration (including snow melt) turn out to be poorly correlated in terms of frequency and magnitude in alpine catchments (VanSteijn, 1996; Bovis and Jakob, 1999; Pelfini and Santilli, 2008). The establishment of rainfall thresholds remains mainly indicative and is used for susceptibility assessment only. The main reason arises from the fact that most gullies and channels must be (re)charged with material before a debris flow can initiate (Fig. 1.2). Studies devoted to correlate torrential process activity with degrees of sediment load in channels could demonstrate that the character of an event is closely associated to the conditions of sediment supply prevailing in the torrent system (Veyrat-Charvillon and Mémier, 2006; Coe et al., 2008; Gertsch and Kienholz, 2008). Hence, the emphasis should be placed on the geomorphic effectiveness (in the sense of Wolman and Gerson, 1978) of the hillslope process activity. However, debris flow investigations have been mostly carried out on channel processes, without referring much to the hillslope. A large number of studies focuses heavily on debris flow rheology (see Iverson et al., 1997) and runout (see Rickenmann, 2005). In contrast, contributions dedicated to the role of sediment delivery and channel recharge rate is less prodigious. Little attention has been paid to the torrent response to hillslope sediment dynamics (Gabbet and Mudd, 2006; Bardou and Jaboyedoff, 2008; Fuller and Marden, 2009). Only few studies have focused on the connectivity (coupling) between the hilllslope and the channel network (Hooke, 2003; Johnson and Warburton, 2006; Schlunegger et al., 2009), despite being a key element for debris supply. As well, knowledge about slope degradation within permafrost (Davies et al., 2001; Harris, 2005) and about stability of rock glaciers or till-moraine deposits as sediment sources initiating debris flows (Haeberli et al., 1997; Arenson, 2002) remain limited. Consequently, relative little progress has been made in predicting debris flow activity, and both frequency – magnitude relationship and triggering processes need better understanding.

Perhaps, the multiplicity of geomorphic processes governing the torrent systems appeared too complex. There exists a great variability in sediment dynamics, most obviously between torrents fed by distinct landslides and torrents in which mass wasting behaves gradually with moderate proportion (Jakob et al., 2005; Brayshaw and Hassan, 2009). Several studies attempted to accommodate this physical complexity with terrain parameters taken for having the greatest influences on sediment dynamics. Many empirical relationships were developed based on the physical and morphological characteristics of the catchment (see Brochot et al., 1998, 2002), such as contributing area (Hungr et al., 1984; Takahashi, 1991), morphometric variables (Melton, 1965; Johnson et al., 1990), slope gradient (Kronfellner-Kraus, 1984; D'Agostino, 1996), or a combination of these factors (Hampel, 1980; DallaFontana and Marchi, 2003). Others tried to apply rule-based models using several relevant geological and morphological observation controlling debris supply and transfer processes (Lehmann, 1993; Zimmermann et al., 1997a). All these models deserve credit for considering the overall range of processes contributing to sediment discharge in torrent. Their predictive application remains in fact of limited scope. They only incorporate global and permanent predisposing factors that characterize catchment sediment dynamics, but miss the rapid geomorphic changes occurring over seasons. They may still represent significant volume estimates over historical and geological time scale.

On the other hand, spatially distributed modeling approaches attempt to simulate the sediment cascade interaction by combining digital elevation model (DEM) with physically-based sediment routing algorithms and hydrometeorological forcing mechanisms (Wicks and Bathurst, 1996; Benporad et al., 1997; Downs and Priestnall, 2003). However, the complexity induced by sediment transport models and mass-wasting processes of stochastic nature requires simplifying the deterministic physical laws with (semi-)empirical approaches (Barthurst et al., 1997; VanRompaey et al., 2001). Many models exists (see Merritt et al., 2003), but the ones dedicated to torrent systems, e.g. ETC (Mathys et al., 2003), SEDAG (Wichmann and Becht, 2005), TOPKAPI (Konz et al., 2011), are still in an early stage of development. The delineation of sediment sources, as well as the contrasting topography affecting the distribution of precipitation, strongly influence sediment generation and thus, debris transfer within the catchment. These elements remain challenging for real volumes estimates.

So far, direct measurements of sediment flux provide the best capabilities to predict the torrent response to catchment sediment dynamics. In the past, direct measurements of hillslope sediment delivery by traditional techniques, such as painted surface debris, lines of stakes and sediment traps on slopes or at channel junctions, were very often limited to provide information of the most disturbed areas only (Coe et al., 1997). The setup of sediment budgets was restricted to accessible perimeters and the volume information required labor-intensive fieldwork. Recent development in multitemporal digital stereopho-

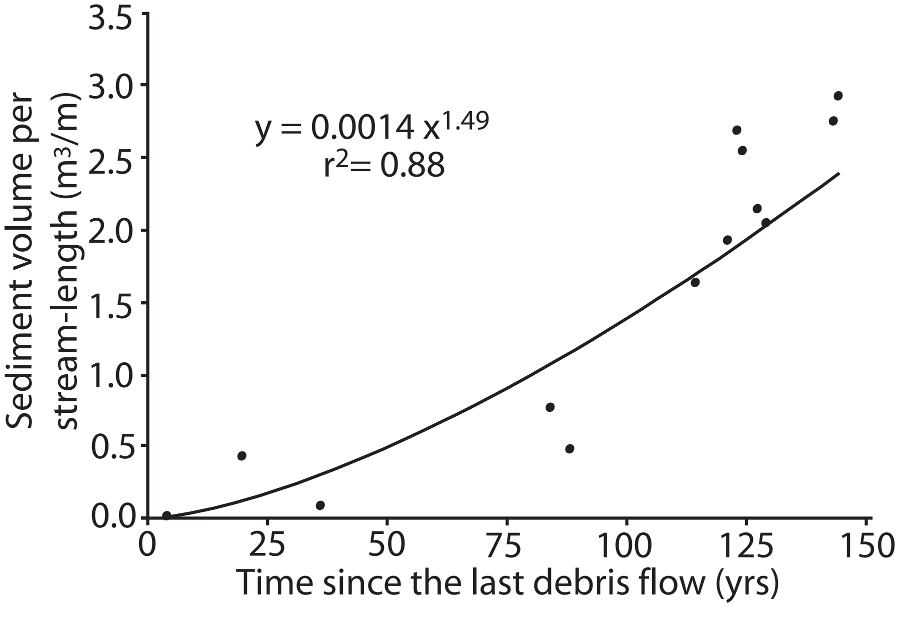

Figure 1.2: *Relation between the volumes of material stored in channels and the time since the last debris flow events, showing that rates of material delivery recharging the channel with material influence debris flow processes and triggering rates. Data collected in channels from the Oregon Coast Range and estimated from dendrochronology (modified from May and Gresswell, 2003, 2004).*

togrammetry (Lane et al., 2000; Veyrat-Charvillon and Mémier, 2006), laser scanning (see Jaboyedoff et al., 2012) and other remote-sensing techniques, e.g. differential SAR (Squarzoni et al., 2003; Bozzano et al., 2010) has become the basis for recording topographic changes over the entire hillslope extent. Derived digital terrain model (DTM) differencing is used to map modern hillslope process activity and quantify the volumetric changes of surface features (Scheidl et al., 2008; Prokop and Panholzer, 2009; Fuller and Marden, 2009). Additionally, DTM is widely used for geomorphological and geological application within GIS technologies (Günther, 2003; Derron et al., 2004; Jaboyedoff et al., 2006; Trevisani et al., 2012). A quantitative geomorphic process monitoring enables a reliable identification of hillslope and channel material erosion, transport and deposition as well as the assessment of their rates and controls. They also provide the necessary high quality field data at different time-scales to adjust sediment cascade numerical simulation and adequately calibrate model parameters.

1.2 Research projects and related study site

During this PhD, several small alpine catchments were investigated according to the specific aspects of the research projects; each study site displaying particular debris flow related geomorphic dynamics inherited from distinct geological and morphological aspect.

1.2.1 Torrential hazard contend

The Manival (Fig. 1.3), located in the Chartreuse Massif (northern French Alps), has been one of the most contemporary active torrents of the Alps. Historical records reveal that debris flows were generated with some consistent occurrence during the last centuries, including several extreme debris floods reaching up to 60’000 m^3 of material deposited down the fan area (Desplanches, 1999). The damages caused on the constantly growing farming and urbanization had required the French National Agency in charge of natural hazard mitigation already in the middle of the 18th century to protect people and infrastructures against torrential hazard. A large panel of mitigation works (reforestation, hydraulic adjustment, slope and channel bed stabilization, sediment trap construction) was taken on to reduce sediment supply and constrain substantially the risk of torrent overflow affecting the fan (see the online movie RisquesTV (2012)). Despite all mitigation works, the Manival catchment provides highly favorable natural conditions to study hillslope process activity and geomorphic work inducing run-off generated debris flows in mountain environment.

1.2.2 Landscape evolution

Besides their geological hazard, debris flows are geomorphologically an important characteristic of the mountain system. They have for many years captured the attention of

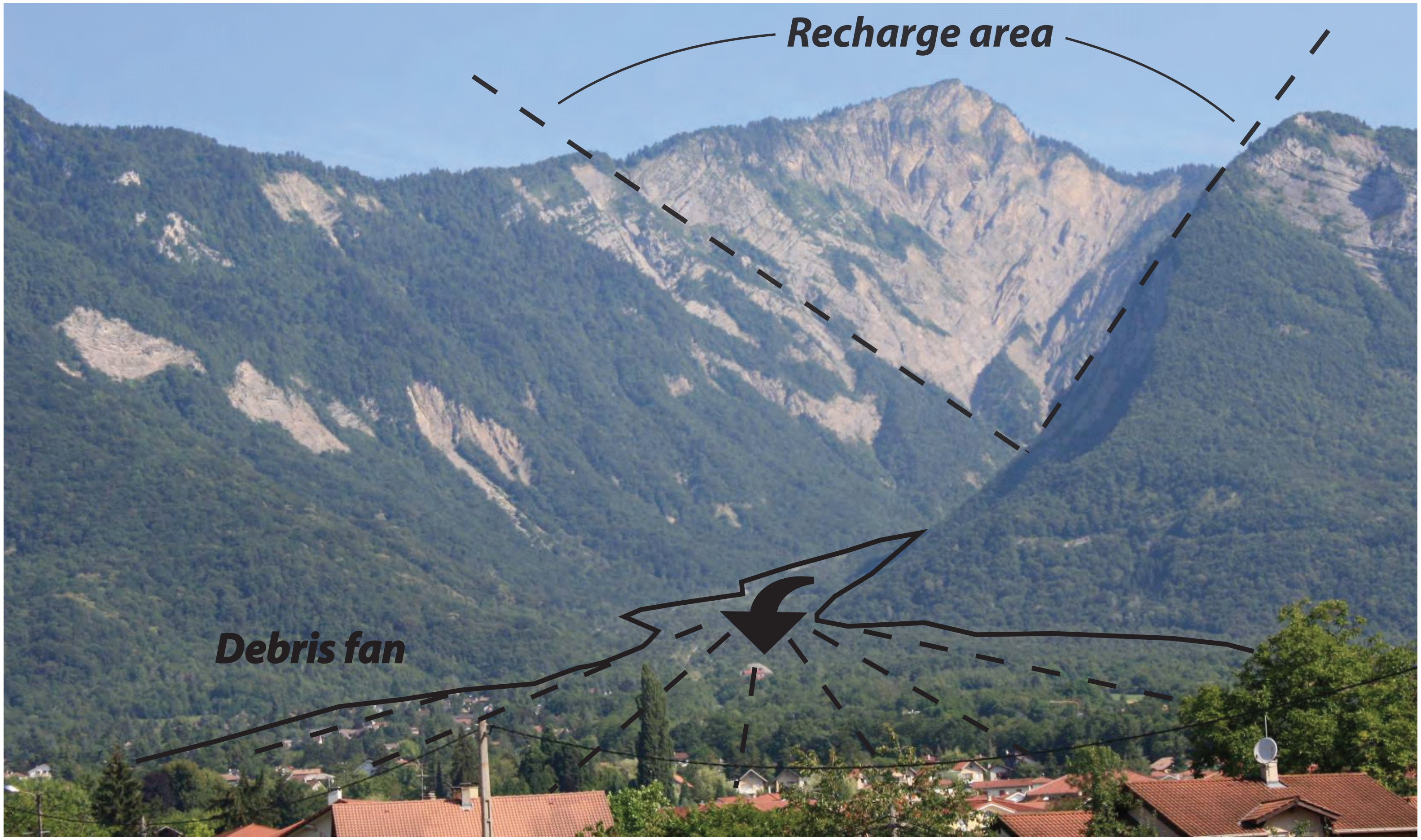

Figure 1.3: *Photograph of the Manival torrent catchment and the extent of settlement on its debris fan. Note the impressive headwater entrenchment providing a large amount of coarse material to the torrent.*

researchers concerned with catchment denudation rates, geomorphic-transport laws and long-term landscape evolution (Eaton et al., 2003; Stock and Dietrich, 2006; Griffiths and Stokes, 2008). Debris flows illustrate the intermittent removal of coarse detritus from the source areas (rock walls and their associated talus slope deposits) to the depositional sink (the downstream valley). They are one of the most dynamic components of the Caine's (1974) cascade of sediment flux, the sediment routing system operating in mountain catchment, and are now understood as a means of connecting hillslope with the stream network (Hovius, 2000), representing a first-order control on the morphological development of mountain topography. Although regional factors such as climate and tectonics may give a conceptual framework for the present landscape morphology, catchments prone to debris flow display traditionally a great contrast in the spatial pattern of their geomorphic features derived from hillslope processes . This suggests the influence of intrasic parameters related to the bedrock structures and the lithology. The Saxé and the Métin catchments (Fig. 1.4), in the northwestern margin of the Rhone Valley (Switzerland), display in their headwater a geometrically-ordered network of gullies and torrent channels incised in the bedrock. This style of geomorphic features enables to examine the control exerted by geological structures on the development of erosional landforms.

1.2.3 Sediment yield magnitude prediction and managment

Preventing approaches in quantitative risk assessment do not usually consider extreme events other than the ones already known. In torrent systems, an important volume of loose material derived from potential rock slope failures or permafrost degradation can have catastrophic consequences that cannot be usually anticipated in the absence of clear geomorphic evidence. The small hillside torrents situated upon the village of Zinal in the upper Anniviers Valley (southwestern Walliser Alps – Switzerland) have their drainage headwater located in glacial and periglacial terrain (Fig. 1.5). Historical testimonies attest of the existence of several intense torrent floods (Ayer, 2003). Quantitative data about the magnitude and frequency of the events remain however largely uncertain since only few noticeable debris flows were observed during the last decades. Such environment is particularly sensitive to the occurrence of large magnitude debris flows resulting from the availability of large amounts of unconsolided sediment associated to the possibility of significant water flow derived from rapid snowmelt or the sudden release of ice or morainic-dammed lake (Loye, 2006). In these high mountain torrents, there exists a pressing need for methodology that can predict, at the scale of individual stream, the effects of different levels of landslide incidence and hillslope erosion upon the catchment sediment yield, especially in the form of bedload and debris flows.

1.3 Research focus and objectives

Quantitative torrential risk assessment in mountain catchment requires a better understanding of processes of debris generation, storage and transfer contributing to load the

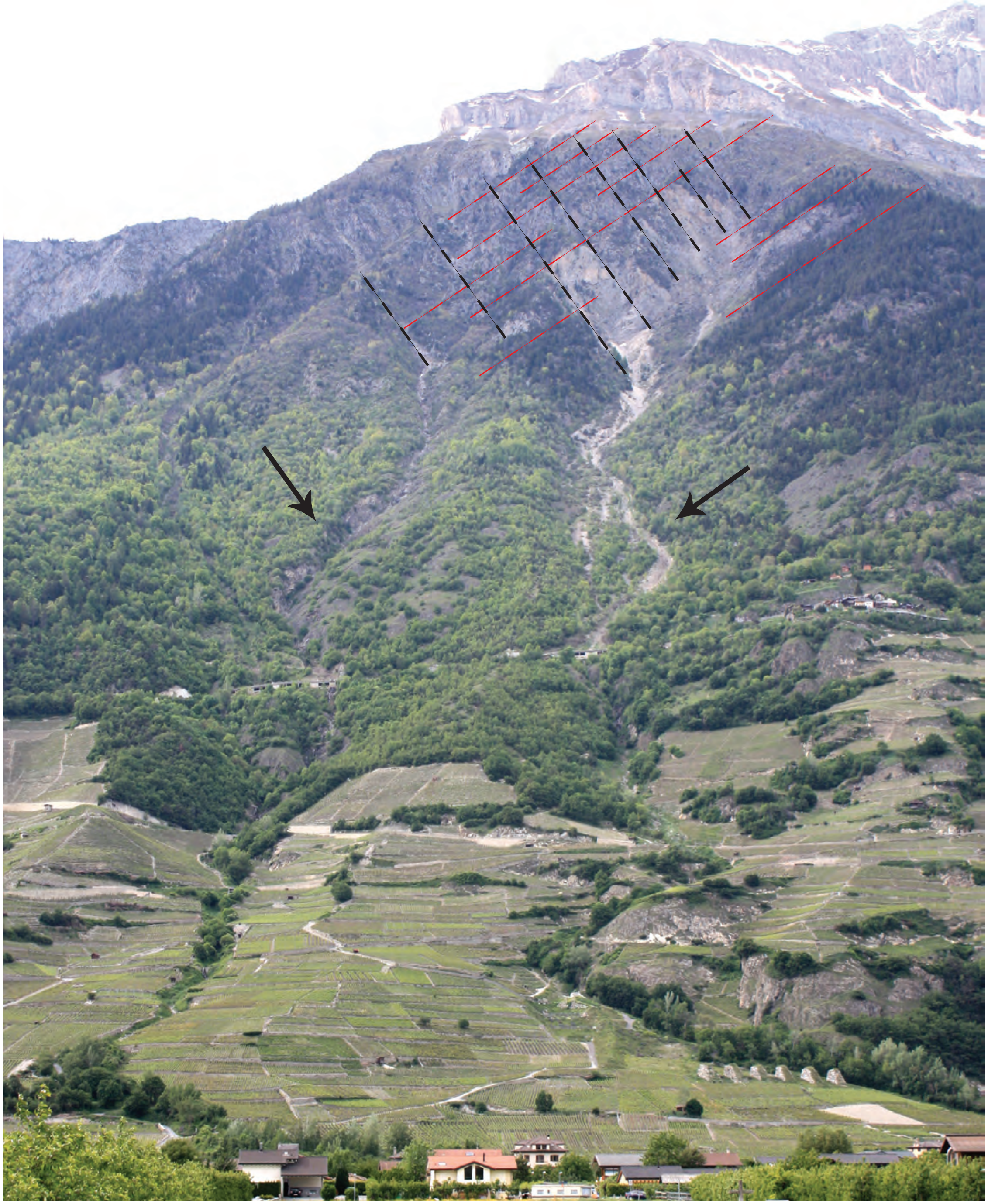

Figure 1.4: *View of the Métin (left arrow) and Saxé (right arrow) torrent catchment. The headwater is dominantly rock gullies (couloirs) and channels embedded in bedrock structures (dashed lines).*

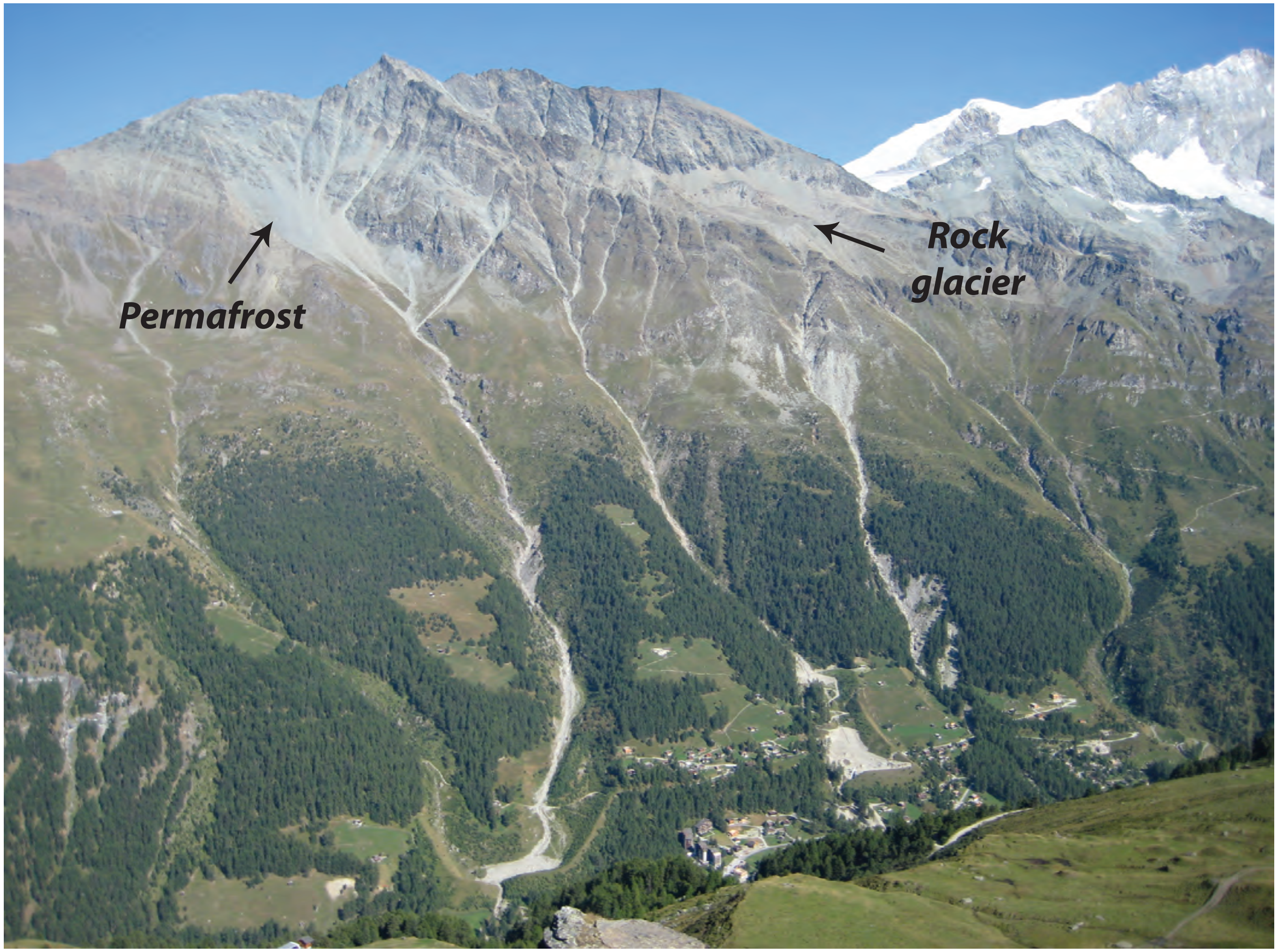

Figure 1.5: *View of the periglacial torrents located above the village of Zinal. Note the large sediment traps at their outlet.*

drainage network with sediment. The project researches herein intent to develop several investigation procedures to document sediment recharge and delivery upstream from channel reaches, i.e. on the hillslope. The purposes were more exactly:

- to develop monitoring procedures from terrestrial laser scanner (TLS) survey to experimentally study hillslope sediment process activity. This implies the development of data processing tools that enable to provide fine-scale sediment budgets.
- to investigate the role played by bedrock structures in the process of debris supply for developing sediment production hazard mapping. This implies innovative morphological and structural approaches to document the geological implication on debris production and contemporary erosional landforms, and to study the relationship between susceptibility to slope failure according to the general structural setting and their rate of magnitude of debris generation particularly.
- to model quantitatively the sediment dynamics for sediment discharge hazard management. This implies the development of computer algorithms that simulate the flows of sediment, and thus enable to assess projected sediment yield throughout the catchment over the short, middle or long term.

1.4 Techniques of investigations

1.4.1 Experimental investigations

The Manival hillslope and low-order channels sediment activity were monitored periodically by TLS (Fig. 1.6), which provides a three dimensional representation of the topography with high spatial resolution and accuracy. Over 250 TLS measurements were performed during 5 field campaigns conducted from spring 2009 to summer 2010 in order to observe the seasonal geomorphic evolution in the headwater torrent. TLS, also known as ground-based LiDAR (for **Li**ght **D**etection **A**nd **R**anging) consists of a portable transmitter/receiver integrated device that emits series of laser pulses (beams of light) and records the returning signal back-scattered by the target object. The three dimensional position of the reflected object is computed using the distance (range) measured from the time of flight of the laser beams and their predefined orientation (the line of sight). LiDAR (laser scanning) technology outperforms traditional position acquiring techniques by the fact that the signal doesn't require any supplementary reflector to acquire a measurement point, but holds on the intensity of the surface reflectivity of the scanned object. The point position accuracy depends on the conditions encountered by the beam during the flight (e.g. atmospheric disturbance), the size of the beam, which increases with range, and the beam spot elongation derived from the laser incidence angle hitting the object. The latest developments of devices provide an instrumental accuracy of ±1.5 cm up to 1 km of range in typical field application (e.g. ILRIS© – LR Laser Scanner). TLS is an easily-handing and flexible remote sensing mean of acquiring large amounts of measurement points (point clouds of 50 to 10'000 pts/m^2) with fast recording speed. This generates three dimensional topographic models of the visible terrain surface with decametric to centric information resolution over an acquiring range of a few kilometers. The main difficulties rely upon the ground-based status of the scanner platform. This requires efficient, labor-intensive procedures (but very often cost-effective) to achieve an homogeneous fully three dimensional cover of large area without data gaps induced by shadowing effect. Though in some terrain, this aspect is just impossible. In recent years, LiDAR techniques have been successfully applied to monitor and characterize a wide pattern of mass movement, from highly active small shallow landslides and rock faces (Rosser et al., 2007; Oppikofer et al., 2008; Dunning et al., 2009; Jaboyedoff et al., 2009b) to slow-motion large scale deep-seated gravitational slope deformations (Agliardi et al., 2009). This has been also widely used to generate reliable high resolution DEM for the detection of geomorphological features and the quantification of topographic changes by comparing multi-temporal sequences. TLS application has been particularly successful in improving rock slope instability monitoring and characterization (Jaboyedoff et al., 2007; Sturzenegger et al., 2007b; Kemeny and Turner, 2008; Lato et al., 2008) due to the high rendering of the modeled slope for the study of structures and shapes in local detachment. Airborne laser scanner (ALS) is very limited in acquiring terrain approaching verticallity and not adapted for overhanging topography. More information on LiDAR techniques and LiDAR-derived high resolution DEM application can be found in Jaboyedoff et al. (2012).

The TLS measurements that I carried out, complemented with a geomorphic process mapping, a structural field study, rainfall data and event-based observation of sediment transfer performed in the downstream torrent (Theule et al., 2012; Theule, 2012), were used:

- to provide seasonally a point cloud surface model representing the headwater topography. The changes in terrain morphology enable to identify mass movement expressing erosion, transfer and deposition of debris.
- to compute the volume of each active feature in order to deduce fine-scale sediment budgets at specific locations of the catchment sediment system.
- to analyze the frequency – magnitude relationship of rock slope instabilities and estimate a rate of debris production.
- to examine the seasonal variability in hillslope sediment delivery and the influence on the low-order gullies and channels.
- to study hillslope sediment yield and low-order channel sediment activity and their interactions (principally discharge) with the downstream torrent.
- to observe a whole cycle of debris supply and channel recharge rate in the headwater evolving into a debris flow in the torrent.
- to generate a 3-D high resolution DEM of the headwater to investigate the morphological aspect of the erosional landforms as well as the structural characteristics of the headwalls and their implications for debris supply.

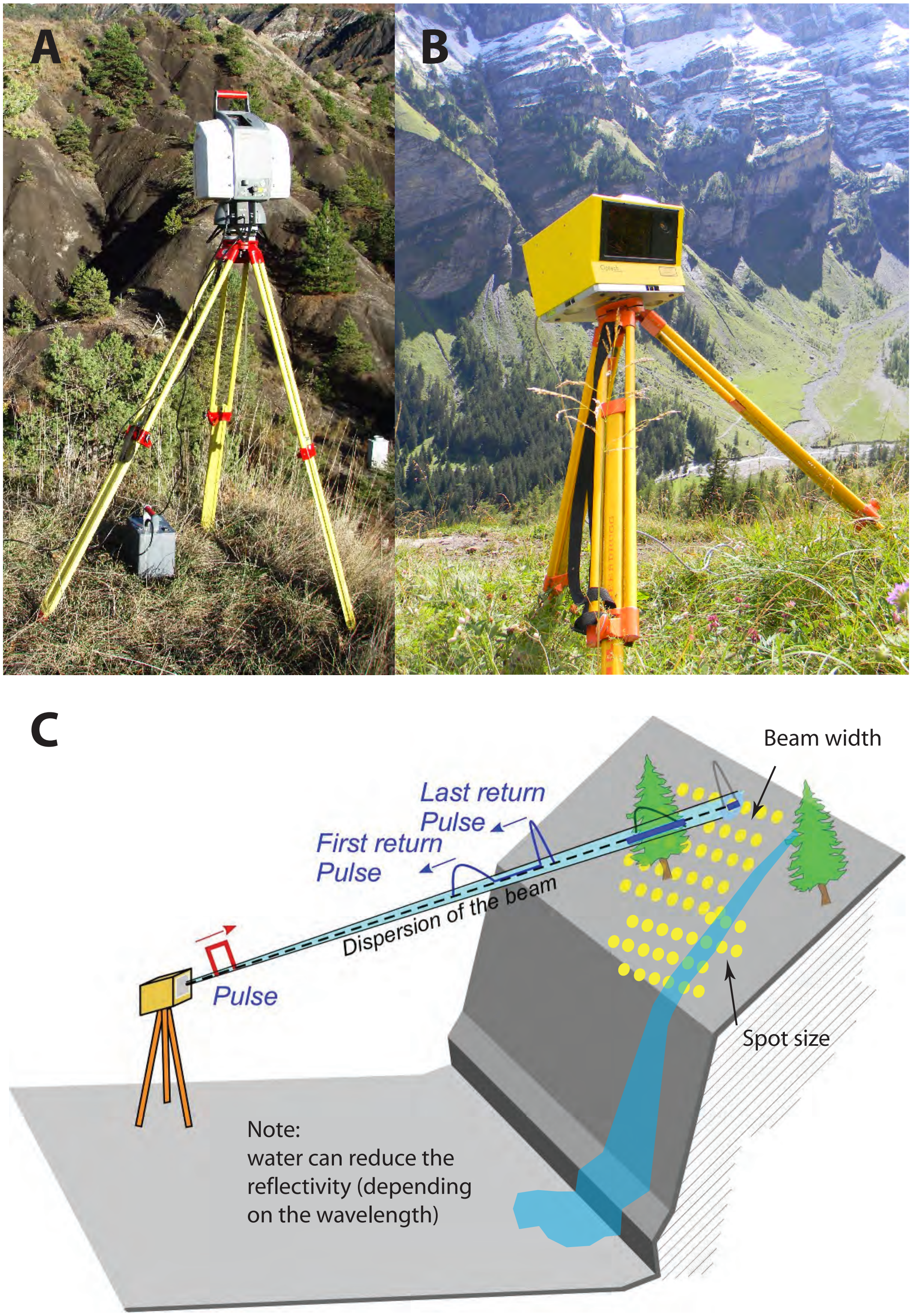

Note:
water can reduce the
reflectivity (depending
on the wavelength)

Figure 1.6: *Terrestrial Laser Scanner devices: (A) Leica Scan Station II, (B) Optech ILRIS-3D and (C) schematic illustration of their application (from Jaboyedoff et al., 2012).*

1.4.2 Methods of analysis

The morphological and geological implications in the mechanisms of sediment production and transfer leading to the recharge of low-order channels were evaluated with the help of several tools developed at the institute. They enable to interpret terrain information from point clouds and high resolution DEM derived from TLS data:

- The spatial extend of predominant geomorphic processes, such as zones of potential debris production and deposition, were extracted by classifying the slope angle distribution according to the Strahler's law of constancy of slope (1950) implemented in the software HISTOFIT 1.0 (Histofit, 2009). The identification of hillslope process characteristic shapes reflected in the catchment morphology, assisted with shaded-relief maps, orthophotos and geological information provides a systematic approach to inform about the mode of sediment cascade.
- A local-scale structural analysis of the slopes supplying the tributary gullies and the low-order channels was performed with the software COLTOP 3D (Jaboyedoff et al., 2007), which enables to visualize the geometry of the discontinuities shaping the topography in a similar way as in the front of an outcrop. This enables to characterize the rock mass (e.g. joint sets, bedding plane orientation, joint spacing and trace length) and to determine the spatial variability in structures (structural domains) of the headwalls compared to the recorded geomorphic activity. The influence of the geological and structural setting is further assessed by studying:
  - the significance of the discontinuity pattern as morphostructures in the expression of the catchment morphology and erosional landforms.
  - the correspondence between the orientations of the active gullies and channel reaches and the orientation of potential failure mechanisms.
  - the joint density according to the rock slope orientation.
- Kinematic tests according to the spatial distribution of the major joint sets were performed to identify potential slope failure mechanisms using the software Matterocking (Jaboyedoff, 2002). This enables to develop susceptibility indexes to debris production in terms of number of potential instabilities per surface unit that can be combined with geomechanic slope stability parameters. The correspondances of these indexes with the effective debris production and the spatial distribution of this latter were analyzed.

1.4.3 Sediment discharge prediction

The quantitative prediction of sediment discharge magnitude over short, middle and long time-scale was achieved with the concept of sediment cascade (Chorley and Kennedy, 1971; Schrott et al., 2003), which enables to model the catchment sediment dynamics as a succession of sediment reservoirs reflecting the hillslope and torrent processes under mass balance conservation. The sediment production, the erosion and the rates of mass transfer are activated by a series of stochastic processes representing the hydrometeorological effects on hillslope process activity, the occurrence of landslides, and the onsets of debris flows, and implemented in a semi-distributed sediment flux routing system. Each element of the conceptual sediment cascade forms an individual geomorphic unit that includes proper geological and morphological aspect and sediment dynamics. The sediment budget modeling was used:

- to estimate the most likely sediment yield at the catchment outlet according to the contemporary conditions prevailing in the catchment.
- in the perspective of climate change, to simulate the sediment cascade with exaggerated model parameters in order to observe hillslope process reactions in terms of sediment discharge and average sediment budgets.

1.5 Structure of the thesis

All chapters of the thesis are set up to be self-contained. Chapter 2 is in preparation to be submitted (Loye et al., submitted) for publication. Chapter 3 is derived from two peer-reviewed publications (Loye et al., 2009a, see Appendix D, and Loye et al., 2011) and supplemented with new findings performed later on. Chapter 4 originates from another article (Loye et al., 2012). Chapter 5 is a short version of a technical report written (in french) in the framework of the MATEROSION project, which is added in Appendix A. In Appendix can be found other works and proceedings accomplished beside the PhD thesis.

Part I: Laser scanning sediment dynamics in torrent catchment

Chapter 2: Debris supply and torrent response inducing debris flows: the case of the Manival catchment.

The seasonal evolution of debris supply and channel recharge of the low-order channels of the Manival upper catchment is investigated using TLS-derived sediment budgets and complementary observations performed in the torrent channels. I attempted to interpret the observed bedload and debris flow torrent activity with the sediment delivery recorded from the headwater debris sources.

Part II: Morphological implications and structural control of geomorphic process activity

Chapter 3: Morphological and structural analyses of a torrent catchment: implications for debris supply at channel heads

The debris supply derived from rock slope activity of the rock walls of the Manival headwaters is investigated according to the terrain morphology and rock mass structures derived from topographic information contained in DEM. I attempted to characterize the major modes of geomorphic process activity and to evaluate the implication of catchment-scale geological structures in the production of debris through rockfalls.

Chapter 4: Influence of bedrock structures on the spatial pattern of erosional landforms in small alpine catchments
I analysed the topographic orientations of geomorphic features such as gullies and debris flow channels to see whether their geometry is controlled by the bedrock structures. This was evaluated by comparing the correspondence with the geometry of the potential slope failure mechanisms and the direction in which the maximum number of joint is encountered according to the slope face geometry and the most dominant sets of discontinuity. This work was performed in both Manival and Saxé and Métin catchment, providing different tectonic and lithologic setting to investigate.

Part III: Modeling sediment budgets of torrent systems

Chapter 5: Alpine catchment sediment budget modeling through a quantitative sediment cascade procedure

In the framework of more sustainable management of sediment trap deposits, a quantitative method for sediment yield assessment that could potentially accumulated at the outlet of alpine torrent at short, middle and long term was developped using geomorphic, geological and topographic information contained in GIS data and complemented with field mapping. A sediment cascade routine that enables to model the evolution of the torrent system in terms of sediment budgets was created with the philosophy to include in the most convenient manner the geological, morphological and sediment flow knowledge at the scale of the channel reach to simulate the individual process-response. Field surveys and data production were performed by B. Mazotti (Mazotti et al., 2010) during its stay at IGAR. I conducted essentially the development of the methodology and programmed the software MATEROSION 1.0 .

Part I

Laser scanning sediment dynamics in torrent catchment

Chapter 2

Debris supply and torrent response inducing debris flows: the case of the Manival catchment.

Abstract Debris flows have been recognized to be linked to amounts of material temporary stored in torrent channels. This first chapter addresses in-channel debris storage and sediment supply from hillslopes to study the coupling between catchment-scale sediment dynamics and torrent responses in terms of debris flows. This is illustrated in the active Manival catchment (French Alps). Rock slope sediment production and storage changes from low-order channels were surveyed periodically during 16 months using terrestrial laser scanning (TLS), a period including two debris flow events. Sediment transfer in the main torrent was monitored with event-based cross-section surveys. Hillslope sediment budgets were generated seasonally based on a semi-automatic identification of active geomorphic features using sequential TLS data differencing and adaptive point cloud gridding for volume computation. In the torrent, they were calculated from multi-date morphological extrapolations and volumes accumulated in a sediment trap. Field mapping provided properties of geomorphic process activity. Debris production (rockfall) follows power law distribution for volumes above 0.1 m^3 and is strongly dependent on winter – early spring season, while hillslope sediment reworking dominates debris recharge from spring to autumn. Both debris flows originate in the torrent exclusively, but their occurrence is linked to recharge from previous debris pulses from the hillside and from bedload transport. Headwater debris sources displays an equivocal behaviour in sediment transfer: despite of high storms inducing debris flows in the torrent, low geomorphic activity occurred; but a general reactivation of sediment transport in low-order channels was observed in autumn without new debris supply, suggesting no exhaustion of debris storages. The seasonal cycle of sediment yield seems therefore to depend not only on debris supply and runoff (flow capacity), but also on geomorphic conditions that destabilize remnant debris stocks. A monitoring of in-channel storage changes coupled to debris supply can readily improve knowledge on recharge threshold leading to debris flow activity, so their prediction.

2.1 Introduction

In steep mountain catchments, individual or sequences of rainfall intensity and duration (incl. snowmelt) are insufficient to predict debris flow occurrence, despite that condition of initiation for runoff-generated debris flow require a significant water inflow (VanDine, 1985; Decaulne and Saemundsson, 2007; Guzzetti et al., 2008). In many cases, the main reason arises from the fact that the amount of debris that can be entrained in a channel reach is very often more significant than the mechanism of initiation (Hungr, 2011). The frequency and magnitude of debris flow have been recognized to be linked to the amount of material temporary stored in channel reaches (VanSteijn, 1996; Cannon et al., 2003; Hungr et al., 2005), such that hillside sediment delivery recharging the channel represents a key factor for the occurrence of debris flow (e.g. Benda and Dunne, 1997; Bovis and Jacob, 1999; Berti et al., 2000). This implies efficient hillslope – channel coupling(Hooke, 2003; Johnson et al., 2010; Schlunegger et al., 2009). The rate of sediment supply recharging the channel network needs therefore to be considered for predicting debris flow hazard (Rickenmann, 1999; Jakob et al., 2005). The difficulty results however in quantifying sediment process activity from hillslopes and in-channel debris storage (Peiry, 1990; Zimmermann et al., 1997b).

Recording of the sediment production and transfer rate over the entire hillslope extent has increasingly relied upon multi-temporal digital stereophotogrammetry (Coe et al., 1997; Chandler and Brunsden, 1995; Veyrat-Charvillon, 2005) and elevation difference from High Resolution Digital Elevation Models (HRDEM) derived from various remote-sensing techniques, e.g. dGPS (Wu and Cheng, 2005), InSAR (Smith et al., 2000; Roering et al., 2009) and LiDAR (Oppikofer, 2009; Prokop and Panholzer, 2009). For large-scale catchment study, airborne laser scanner (ALS) has become to date the suitable survey technique to efficiently acquire vegetation-free DEM with high spatial resolution of topography with complex morphological structures (Oppikofer, 2009). In terrain dominated by slopes of high steepness, traditional aerial-derived DEM remain typically inappropriate to study geomorphic processes. Their application is very often not only limited by a too low rendering of the modelled surface to represent the small individual topographic changes related to the geomorphic activity and landforms (Perroy et al., 2010). This can be technically improved. The limitations concern also the poor surface representation of steep terrain with small curvature radii and data gaps in vertically oriented and overhanging topography. Even on gentler slopes, the sharp break of slopes encountered in erosion scars for instance was demonstrated to be insufficiently modelled by airborne-derived HRDEM, leading to erroneous volume estimations (Bremer and Sass, 2011). These elements represent a serious drawback in budgeting steep terrain, where sediment production comes mostly from rock walls and rugged gullies. Because of these issues, many hill and rock slope process studies have been investigated with terrestrial laser scanner (TLS) (Jaboyedoff et al., 2012). The recent development of long range TLS devices provides an effective mean of acquiring high resolution topographic information that adequately reflect the morphology of steep bedrock-dominated areas. The practical disadvantage in data acquisition related to ground survey can be compensated by flexibility in use and transport, ensuring a full coverage with minimum shadow zones. Using TLS to generate reliable digital terrain model (DTM) can only improve the three-dimensional monitoring, quantification and analysis of sediment transfers in very steep land prone to debris flow.

This chapter presents a quantitative study of sediment recharge and channel response leading to debris flow, using 3-D DTMs provided by TLS. TLS data enable to monitor the coupling between the sediment delivery from the hillslope and the transfer of material in torrent to generate fine-scale sediment budget. This is illustrated on the Manival, a torrent of the northern French Alps that experiments runoff-generated debris flow almost every year (Péteuil et al., 2008). The Manival torrent is quasi isolated from hillslope activity coming from the valley sides situated below the headwater confluence. Sediment delivery induced by mass-wasting processes can reach the valley-bottom from the hillside, but not the torrent. Only one tributary gully with old levees was observed, such that lateral contribution in terms of debris supply can be considered as marginal even by large rainstorms. The main torrent is therefore a zone of transfer exclusively (Gruffaz, 1997). Monitoring the catchment headwaters provides thus an ideal study site to investigate the pattern of sediment delivery from the hillslope that recharges the debris flow torrent. The entire hillslope processes and sediment dynamics from tributary channels connected to the torrent was survey periodically over 16 months using TLS techniques. In parallel, an event-based monitoring of the torrent was performed by the CEMAGREF of Grenoble (Theule, 2012) using cross-section morphological survey. The spatio-temporal variability of debris production and subsequent transport and storage of sediment are analysed on a seasonal time scale to discuss the debris supply dynamics and the implications in debris flow initiation.

2.2 Study site

2.2.1 General setting

The 3.9 km^2 Manival catchment is located in the edge of the Chartreuse Massif (France) (Fig. 2.1) and displays a rugged, 1200 m relief watershed resulting from a deep headward entrenchment developed in an anticline and comprising several thrust faults (Gidon, 1991). The topography consists of a steep-sided colluvium-filled valley, and displays a dissected morphology made of series of rock walls and slopes mantled with scree deposits. The lithology ranges in age from late Jurassic to early cretaceous (Fig. 2.2) and corresponds to the Mesosoic cover of the external crystalline belt (subalpine domain) (Charollais et al., 1986). In the heart of the basin, thick sequences of calcareous marl interbedded with layers of marl predominate. Towards the ridge, the bedrock evolves progressively from more stratified to massive limestone . The valley sides correspond to the fold limbs where secondary folding and minor faults induce local variations in structures (Gidon, 1991). This tectonic setting and the varying stratigraphic competency have strongly influenced the topographic development, providing a dynamic geomorphic environment supported by enhanced slope instabilities. Besides, the vegetation cover is low and forested areas are sparse. Steep slope gradient coupled with low vegetation cover induce an important runoff as a response to heavy rainstorms that occur regularly.

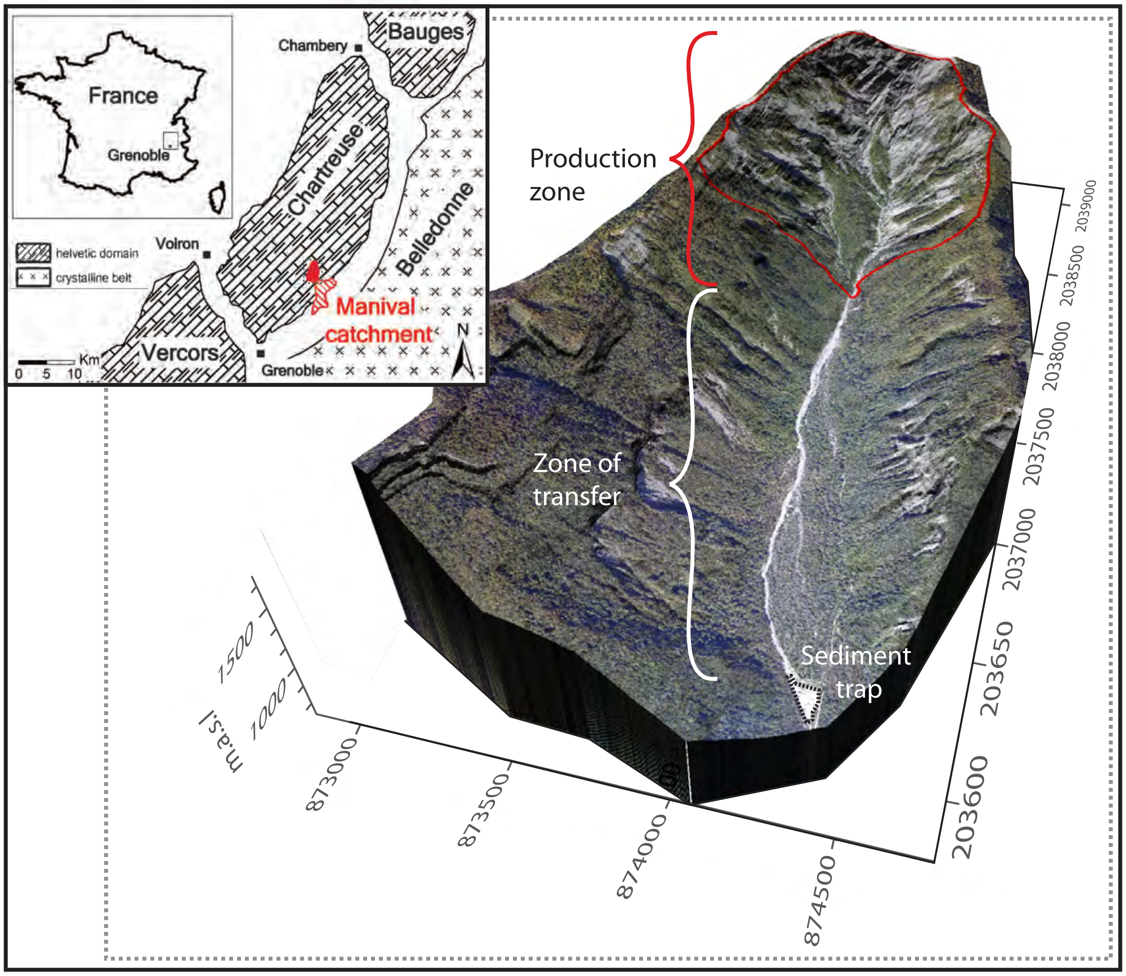

Figure 2.1: *(Inset) Map of the study area; the Manival catchment is displayed in full red and the impressive debris fan is streaked. (Outset) Aerial view of the Manival catchment; sediment supply concentrates exclusively in the headwater (production zone) as erosion activity from the middle and lower catchment is not connected to the main torrent (zone of transfer).*

2.2.2 Characteristics of the headwater sediment dynamic

Contemporary geomorphic activity contributing to recharge the torrent with debris concentrates exclusively in the headwaters, where any remnant glacial deposits are found (Gruffaz, 1997). In the upper catchment, a large old rock avalanche deposit flooring the hillslope side west (Fig. 2.3) have dramatically influenced the bottom topography and thus, the channel network, resulting to a conjunction of four first-order debris flow channels deeply incised in the deposit down to the bedrock in several reaches. The upper catchment can be therefore subdivided in 5 subcatchments in terms of sediment recharge (Fig. 2.4). The entrenchment of the channel beds is now much constrained by check dams. However, lateral erosion still occurs episodically by flooding and debris flow scouring.

The style of sediment production and delivery is somehow different throughout the headwater, according to the local morphology and the lithologic and structural setting. The major geomorphic processes, identified in details from aerial photographs observations

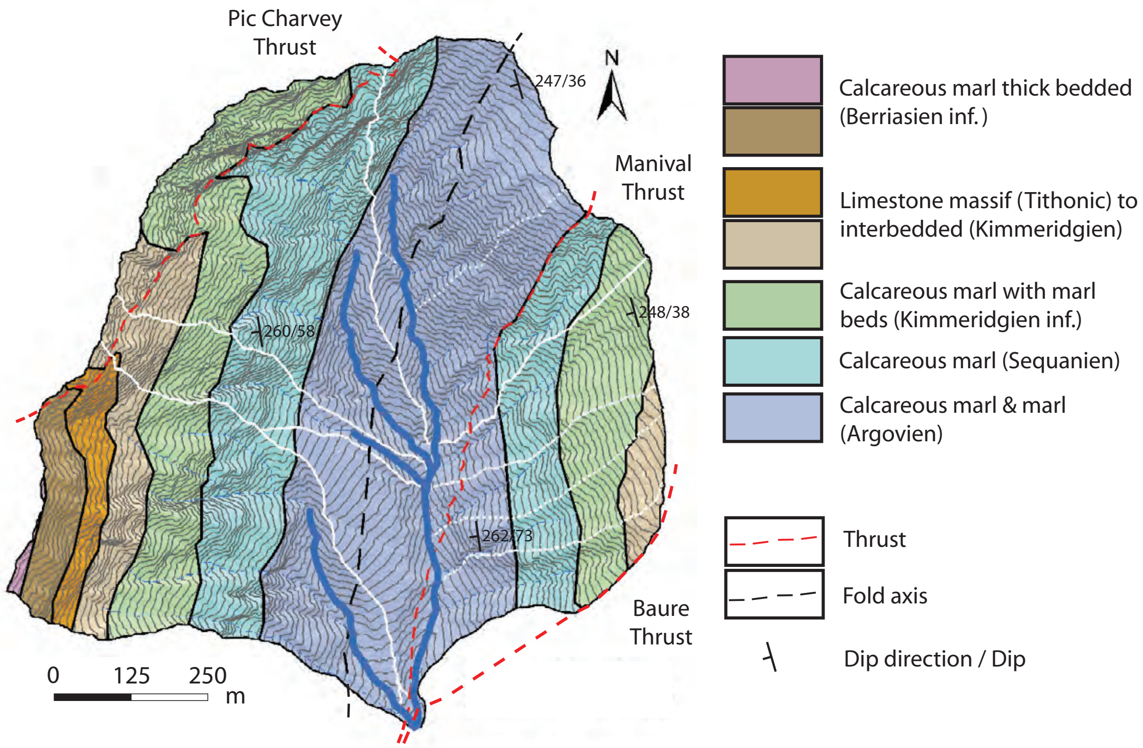

Figure 2.2: *Geological map of the upper catchment (adapted from Charollais et al., 1986). See in chapter 3 the geological map of the entire catchment (Fig. 3.3) and the cross-sections (Fig. 3.4).*

and field investigations, were characterized in a geomorphic process map (Fig. 2.3) that describes the spatial distribution of geomorphic features and sediment transfer processes contributing to recharge the low-order channels with debris. The west and upper sides are dominated by rockfall. Large rock collapses delimited by persistent joints occur due to the progressive erosion of the slope underneath (see Chapter 4). Where the slope gradient allows scree or talus slope deposits with soil development, erosion scars can be observed; sediment sources are remobilized from discrete shallow landslides and hillslope debris flows. Depending on the location and size, rockfall reach the channels directly or accumulate on slopes or in hollows and rock couloirs befor being subsequently routed to high-order segments by a combination of gravitational and hydrological processes. At their outlet, the scree-mantled slope deposits are scoured. Towards east, erosion seems to be more progressive through the formation of gullies along preferential paths following wedge configurations formed by distinct discontinuity sets (see Chapter 4). The slopes near the ridge display mostly talus and scree deposits lightly covered with vegetation, whereas the hillside below exposes steepened rock slopes with barely any soil development. Many active erosion scars can be observed. They contribute to accumulate debris into gullies and talus slope deposits that are subsequently entrained in channels downslope.

Debris flow intensity transported by the Manival torrent over the past is attested in the impressive flood-plain accumulation of material and the fan area ($\sim$4 km^2) is one of the largest of the Alps (Besson, 1996). Historical records of debris flow since the 18th

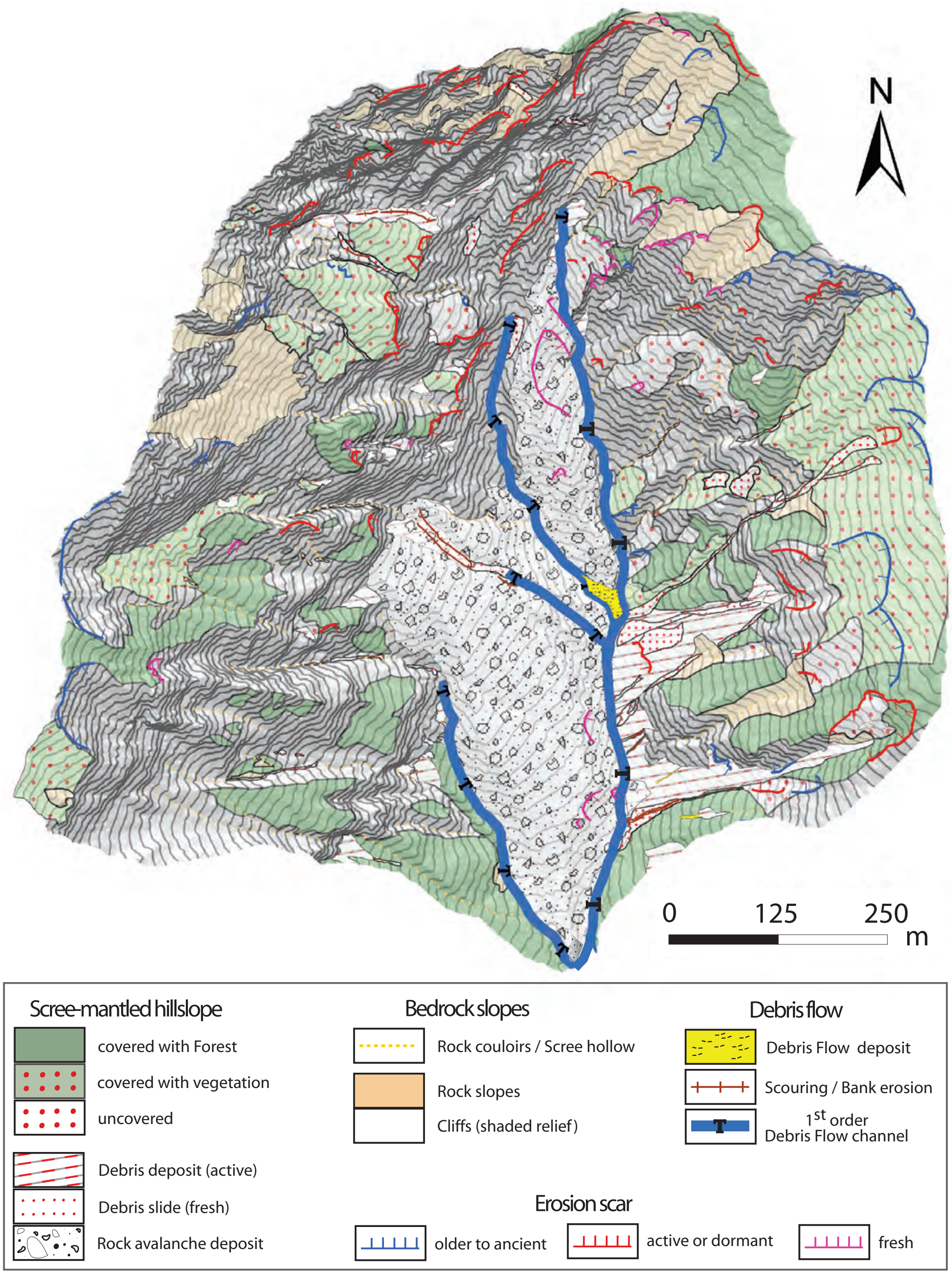

Figure 2.3: *Geomorphic process map (contour interval: 20 m) illustrating the spatial pattern of sediment sources and transfer in the debris flow channel complex. Note the impressive rock avalanche deposit now crossed by four first-order debris channels. Their bed incision is strongly constrained by series of check dams, but erosion scars all along the deposit suggest that reaches are still subject to lateral erosion.*

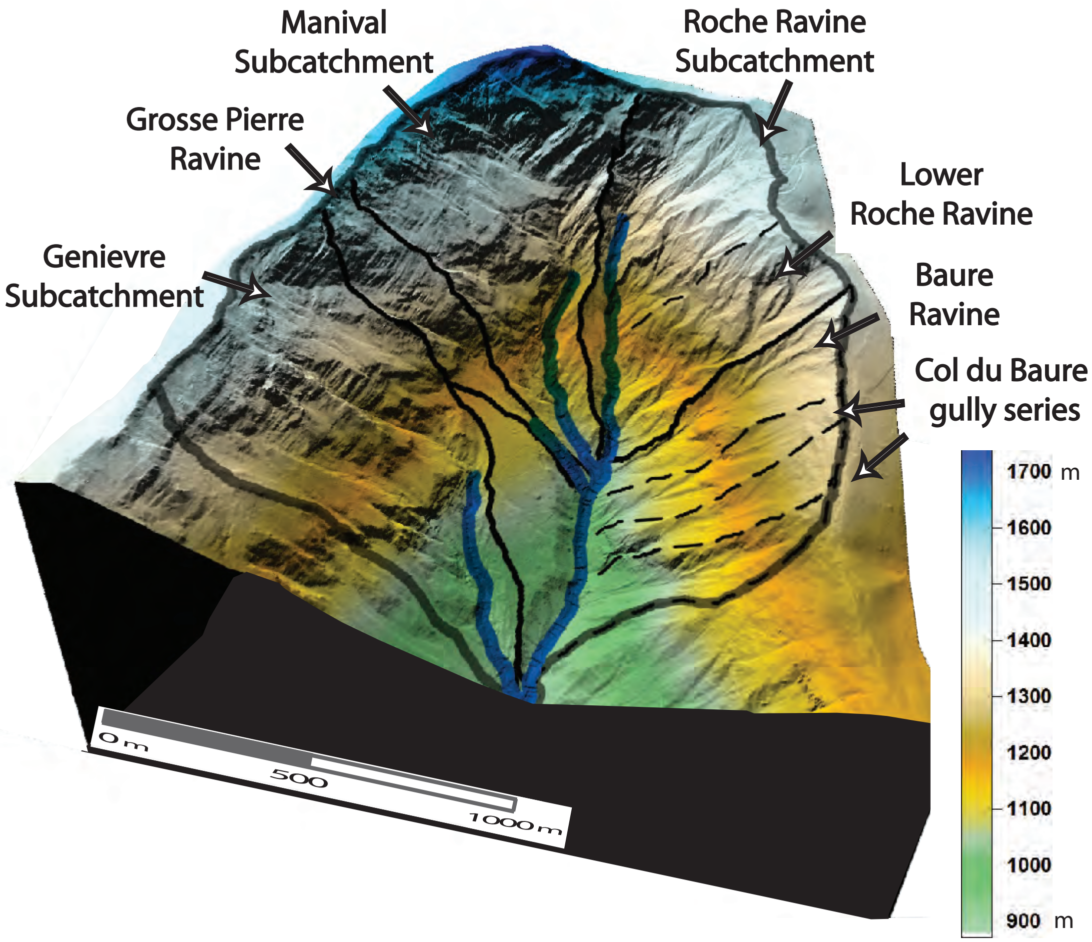

Figure 2.4: *3-D shaded view of the Manival headwaters (production zones), showing the first-order debris flow channels and their respective contributing area. For the ease of analysis, the Roche Ravine and Col du Baure subcatchments in the east side were further subdivided according to their gully complex. The topography of production zones consists of a narrowly confined valley head, delimited side west by series of rock walls and scree-mantled deposits separated by couloirs, and side east by steep rock and talus slopes divided by gullies.*

century show a frequency of 0.3 event per year that reached the apex of the fan (Brochot et al., 2000). The largest event recorded since volume estimation exists deposited about 60’000 m^3. However, the torrent experiences smaller flux of debris that are usually not recorded and thus, not reported in archives. Such small events can occur 2 to 3 times per year, when initiated by intense runoff (Veyrat-Charvillon, 2005). This progressive flow of sediment is not only bedload, remobilizing gravel wedges for instance, but has characteristic morphology, such as levees, boulders front and typical grain-size distribution (coarse lag). They can be associated to micro debris flow (<1000 m^3) routing the channel in pulses over short distance and re-deposited temporary (Theule et al., 2012). Volume of debris deposited in the sediment trap for the last 25 years represents 2200 m^3/yr, reaching a maximum of 7000 m^3/yr in 2008 (RTM, 2010).

Table 2.1: *TLS dates of acquisitions.*

Monitoring period	Survey date	Period ID
1st	01/04/2009 – 12/07/2009	MP1
2nd	12/07/2009 – 30/08/2009	merged with MP1
3rd	30/08/2009 – 11/11/2009	MP2
4th	11/11/2009 – 08/07/2010	MP3

2.3 Methods and data processing

2.3.1 Topographic monitoring using ground-based laser scanning

The terrain was surveyed with a long-range ILRIS-3D laser scanner (Optech Inc.). This device provides a distance of acquiring (range) up to 1.2 km for 80% reflectivity surface with a minimum laser beam diameter of 22 mm at a range of 100 m, giving an instrumental precision of about 7 mm/100 m range for both distance and position (Optech, 2008). The entire coverage of the upper catchment with TLS point clouds required 50 scans considering a 20 % surface overlapping. They were collected over a 5 days survey from 9 individual viewpoints to ensure a 3-D rendering of the topography. A particular attention was carried in irregular regions and major break of slopes, such as rock couloirs and deep-cut gullies. Using multiple scanning locations allow to limit shadow zones and increase the point cloud density of the scanned area. A series of 4 surveys was performed on a seasonal basis during 2009 and one extra survey was performed in July 2010 to analyse the effect of the winter period (Tab. 2.1). The monitoring setup remained similar for all surveys. Post-processing of TLS raw data was done using Polyworks® (InnovMetric Software Inc., 2009). Erroneous points and set of points modeling the vegetation were filtered manually, ensuring a total control of the removed data to preserve a high density of points in topographic features with small radii curvature. Although this manner is time consuming, (semi-)automatic approaches to filter vegetation accurately still remain in a stage of development for dissected mountain morphology (Brodu and Lague, 2012). Each multiple scans of a survey were merged to one another using common tie points of permanent topographic features and set in 12 local subsets. Given the size of the monitored area, dividing the point cloud in smaller datasets allows to avoid propagation of inaccuracy through large co-registered scans series. ICP (iterative closest point) algorithms (Besl and McKay, 1992) enable to minimize the distance between two sets of points. This procedure was used to determine the best alignment of a multiple scans subset in order to obtain the best co-registration within a time series. The same procedure was applied between the generated subset point cloud and a commercial airborne laser scanner-derived point cloud (mean density: 6.9 pts/m^2) acquired in June 2009 to get the TLS data georeferenced in the Lambert conformal conic projection coordinate system. The initial survey point cloud data was set as the surface model of reference. Each successive survey was best georeferenced on this reference using the ICP processing steps herein. The topographic change occurring between two successive surveys are too localized to influence

Table 2.2: *TLS data and surface coverage characteristics of the 5 subcatchments from MP1. As the view points and parameters of acquiring remained similar, the values are essentially the same within all surveys.*

Sub-catchment name	Surface[1]		LiDAR Data Survey				Scanned area[1]	
	Total [km^2]	Vegetated area [%]	Nbre of pts	Mean spacing [m]	Mean range [m]	Mean density [pts/m^2]	Total [km^2]	non vegetated [%]
Baure Gullies	0.29	43.0	37’625’236	0.05	131	340	0.11	84
Roche Ravine	0.30	20.5	43’736’412	0.07	278	251	0.17	79
Manival	0.35	9.1	40’192’976	0.10	349	141	0.28	90
Grosse Pierre	0.08	9.0	9’703’449	0.11	447	145	0.07	97
Genièvre	0.35	26.6	19’886’472	0.11	311	109	0.18	79
Production zone	1.36	22.7	151’144’545	0.08	275	219	0.82	84

[1] topographic surface area

the global co-registration within two survey data subsets consisting of millions of data points, therefore the alignment accuracy. More details about multiple scans registration techniques and point cloud time series comparison can be found in Oppikofer (2009). The generated surface produced by a survey possesses a point spacing ranging from 2.5 to 18 cm according to the distance of acquisition. A maximum range of about 800 m was reached on the top peak of the catchment with a point cloud density of 25 pts/m^2. The surface coverage represents 84 % of the deforested area under investigation (Tab. 2.2).

2.3.2 Topographic change identification and characterization

Manual approach

The identification of rockfall or areas of erosion and deposition between sequences of TLS datasets can be difficult due to the heterogeneity of the point clouds, its 3-D nature and the complexity of the modeled topography (Brodu and Lague, 2012). Data segmentation using global parameter classification, such as applying threshold values to the difference of positions of successive 3-D point clouds, includes lots of noise that affect feature identification and their spatial extraction. As well, a higher threshold would ignore features of low activity. This operation was therefore performed manually using visual techniques, ensuring a total control of detected objects. The active geomorphic features within two successive datasets were identified on a point to point approach using the short distance neighboring point search algorithm (Bitelli et al., 2004) that computes in 3-D the shortest vectors of difference between points of two datasets (Fig. 2.5). The vector sign indicates

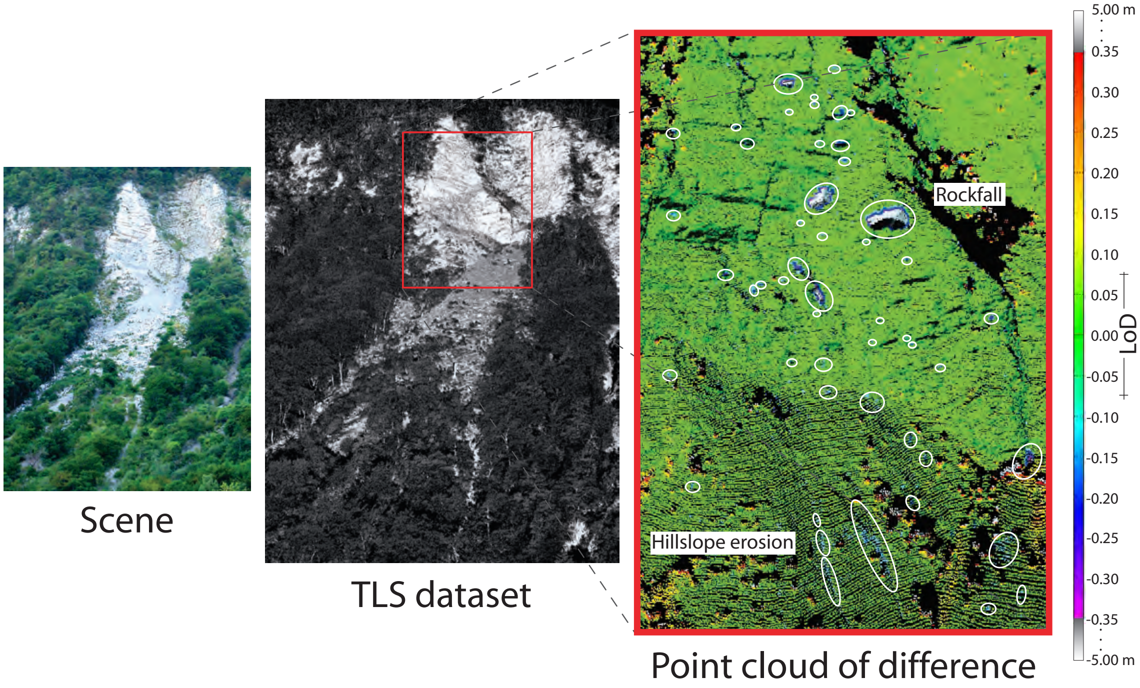

Figure 2.5: *Example of the identification procedure for geomorphic process activity using visual analysis of the point cloud of difference. Deposition (positive difference) is displayed with warm colors, whereas negative changes of topography (cold colors) characterize rockfall and hillslope erosion. Difference below the limit of detection (LoD) are denoted in green. Point subsets belonging to active features were extracted using the spatial extent coordinates of the line of delimitation (white lines) and assigned separately for volume computation.*

the net change direction of topography, i.e. surface of erosion or deposition. A subset of points was considered as active if at least 8 adjacent points of similar sign displayed an absolute difference above the limit of detection (LoD). Each active feature was outlined visually using the point cloud of difference and both point subsets, i.e. the pre- and post-topography of the features, were extracted individually according to their spatial extent coordinates. A label was attributed for each detected geomorphic feature: (1) *Rock slope erosion* characterises rockfall/rockslide; (2) *Hillslope erosion* concerns the reworking of loose/compacted debris on slopes, respectively in the torrent; (3) *Deposition* delineates material aggradation initiated by both rock slope failure (new production) and remobilisation of debris. Using the images captured by the TLS integrated camera, subsets of points not corresponding to geomorphic process activity, such as snow melt, were ignored. Sediment budgets presented in this chapter were generated using this procedure.

Automatic approach

The detection of topographic changes was also attempted to be integrated in an automated extraction procedure. After removing all points lying below the LoD, which are considered as "unchanged", the remnant subsets of the point cloud of difference were isolated from the noise using the Nearest-Neighbor Clutter Removal (NNCR) algorithm (Byers and Raftery, 1998). This is achieved using the distances of points to the K^th nearest neighbor (KNN). Intuitively, active features should have higher point density and hence, an average KNN distance smaller than points belonging to noise. Considering that both feature and clutter points are distributed as a homogeneous Poisson process, the distribution of the distance D_K to their KNN from a set of random points is given by (after Byers and Raftery, 1998):

$$p(D_k \geq x) = \sum_{k=0}^{K-1} \frac{e^{-\lambda \alpha x^3}(\lambda \alpha x^3)^k}{k!} = 1 - F_{D_K}(x) \tag{2.1}$$

where $x \,\epsilon\, [0, \infty]$ defines the radius of a hypersphere of volume αx^3, with:

$$\alpha = \frac{2\pi^{3/2}}{3\Gamma(3/2)} \tag{2.2}$$

This means that for $D_K \geq x$, there must be one of $0, 1, ..., K-1$ points in this hypersphere. The probability density function is expressed as:

$$f_{D_K}(x) = \frac{dF_{D_K}(x)}{dx} = \frac{e^{-\lambda \alpha x^3} 2(\lambda \alpha)^K x^{2K-1}}{(K-1)!} \tag{2.3}$$

and corresponds to a tranformed gamma random variable, $Y \sim \Gamma(K, \lambda\alpha)$, where $Y = (D_K)^3$. Therefore, assuming that both feature and clutter point distribution are superimposed Poisson processes, the KNN distance of the point cloud of difference can be modeled as a mixture of two Γ distributions composed of the distribution of the feature points and the one of the clutter, such as:

$$D_K \sim p\Gamma^{1/3}(K, \lambda_1 \alpha) + (1-p)\Gamma^{1/3}(K, \lambda_2 \alpha). \tag{2.4}$$

The parameters λ_1, λ_2 and p are estimated using the Expectation-Maximization (EM) algorithm (Dempster et al., 1977). This enables to calculate for each point the expected value of density δ_i from $f_{D_K}(x)$ according to the distribution of the observed KNN distances d_i for the n data points. The M – step consists of:

$$\lambda_1^{t+1} = \frac{K \sum\limits_{i=1}^{n} \delta_i^{t+1}}{\alpha \sum\limits_{i=1}^{n} d_i^3 \delta_i^{t+1}}; \quad \lambda_2^{t+1} = \frac{K \sum\limits_{i=1}^{n} (1 - \delta_i^{t+1})}{\alpha \sum\limits_{i=1}^{n} d_i^3 (1 - \delta_i^{t+1})}; \quad p^{t+1} = \frac{\sum\limits_{i=1}^{n} \delta_i^{t+1}}{n} \tag{2.5}$$

and maximizes a likelihood function that is refined in each iteration t by the E – step:

$$E(\delta_i^{t+1}) = \frac{p^t \delta(d_i; \lambda_1^t)}{p^t \delta(d_i; \lambda_1^t) + (1 - p^t)\delta(d_i; \lambda_2^t)} \tag{2.6}$$

Using these estimates, D_K becomes highly bimodal, displaying a strong separation between points that belong to features and the ones belonging to clutters (Fig. 2.6 A). Features of less than 8 points with similar sign were removed as for visual detection. The entire point classification procedure using NNCR algorithm was implemented in Matlab®.

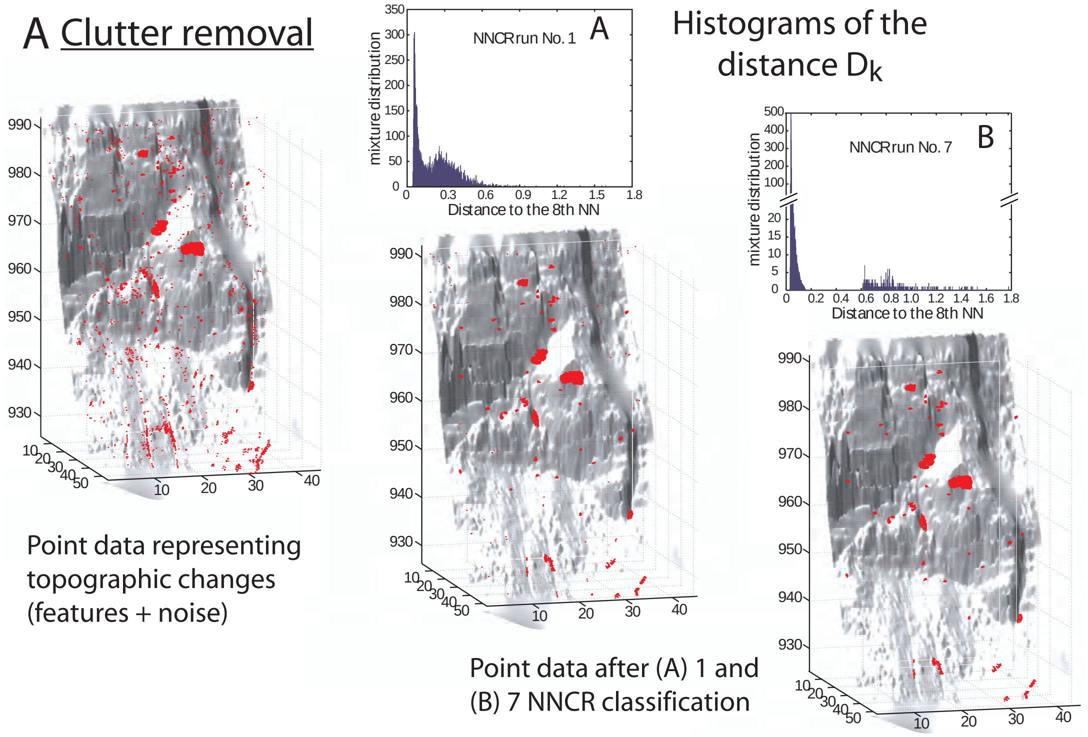

Point data representing topographic changes (features + noise)

Point data after (A) 1 and (B) 7 NNCR classification

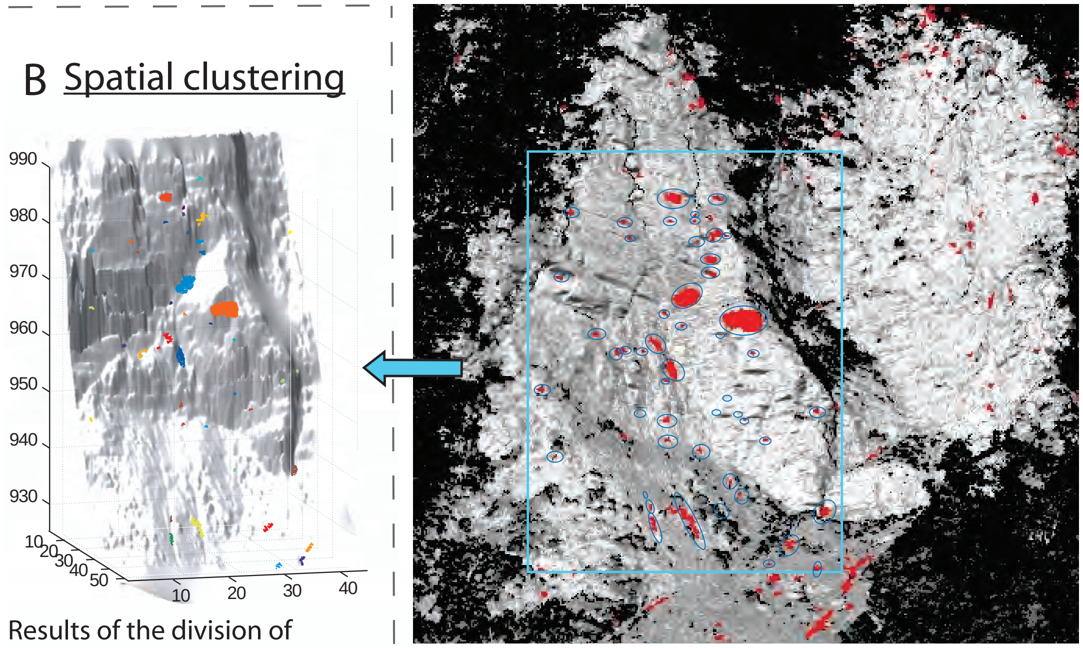

Results of the division of point data in subsets using the hierarchical clustering procedure for a cut-off = 5.

Results of the active features identification after 7 NNCR applications with a K = 8th NN and comparison with the visual approach (blue circles = lines of delimitation).

Figure 2.6: *Example of geomorphic process activity identification from TLS datasets using a classification of the point cloud of difference according to (A) the nearest-neighbor clutter removal algorithm (NNCR) and (B) a hierarchical clustering procedure. Noisy points are removed from feature data points according to the bimodal distribution of the distance of the KNN (Histogram A and B). Comparison between automatic and visual approach reveals a total correspondance for features that can be clearly identified on the point cloud of difference. A discrepancy occurs for small features having either very low number of points or a difference in position close to the LoD.*

The clean clusters of points representing active geomorphic features were grouped into single subsets using a hierarchical clustering procedure (Trauth, 2007). Data points are joined in binary clusters (clusters made of two data points) according to the distance to each others using the function *linkage* of the Matlab® statistic toolbox. This involves binary clusters that are in close proximity to be grouped successively into larger clusters until all data are assigned. This function creates also a hierarchical tree between clusters, such that the ones in close proximity to the anothers are linked together at a lower level than the ones located further away. Clusters having a certain level of hierarchy can be gathered into a single cluster. This can be defined by the user.

This automatic method of detection was tested in several parts of the Manival catchment (Fig. 2.6). The NNCR was treated with $K = 8^{th}$ nearest neighbor (NN), which represents the size of the smallest features that can be possibly detected. This low degree of NN included residual clutters of sufficiently low 8^{th} NN distances that could be removed after applying the procedure several times. Cutting off the hierarchical tree at a height of 5 could separated well the data points into clusters. Sometimes, point subsets of very large extent remained divided in several individual clusters. The solution is to treat those features separately and to increase the cutt-off value. Globally, the tests indicates that this procedure removes almost the totality of the clutters, making the topographic changes very distinct for visual identification and therefore facilitates spatial clustering. Comparison of both approaches shows that all features detected distinctly with the visual approach could also be extracted with the automatic procedure. A difference occurs for very small features subjected to visual interpretation. The automatic procedure may be more suited to finding features of very low extent that are likely to be omitted due to their small number of point data. These very small volumes were however insignificant for the sediment budgets presented in this study as demonstrated further in this chapter.

2.3.3 Volume computation

As the volume of the active features cannot be directly computed from TLS datasets differencing, the active features of two successive points cloud datasets must be interpolated into continuous surfaces (DEM). Gridded model (raster) is regarded as being most effective from irregularly distributed datasets containing in some parts only few or no data point (El-Sheimy et al., 2005), as this can be the case with points cloud-derived rockfalls and erosion scar. The algorithm of interpolation has however minor impacts, as TLS data provide an extremely dense coverage of the detected objects (Anderson et al., 2005). So, the point clouds of active features were interpolated using linear inverse distance weighting (Burrough and McDonnel, 1998) and generated in a regular grid separately. However, grid spacing and direction of interpolation were designed in a specific way for the generation of DEM of each active feature: the coordinate system of reference was replaced by a local orthogonal system where the x-y axes represent the average plane of topography surrounding the considered feature (Fig. 2.7). This new reference frame was defined using eigen-values decomposition of the covariance matrix of the point cloud of reference (Shaw, 2003). Interpolating the surface elevation in the direction of local topography allows to generate a highly realistic DEM independently of slope steepness and thus, a

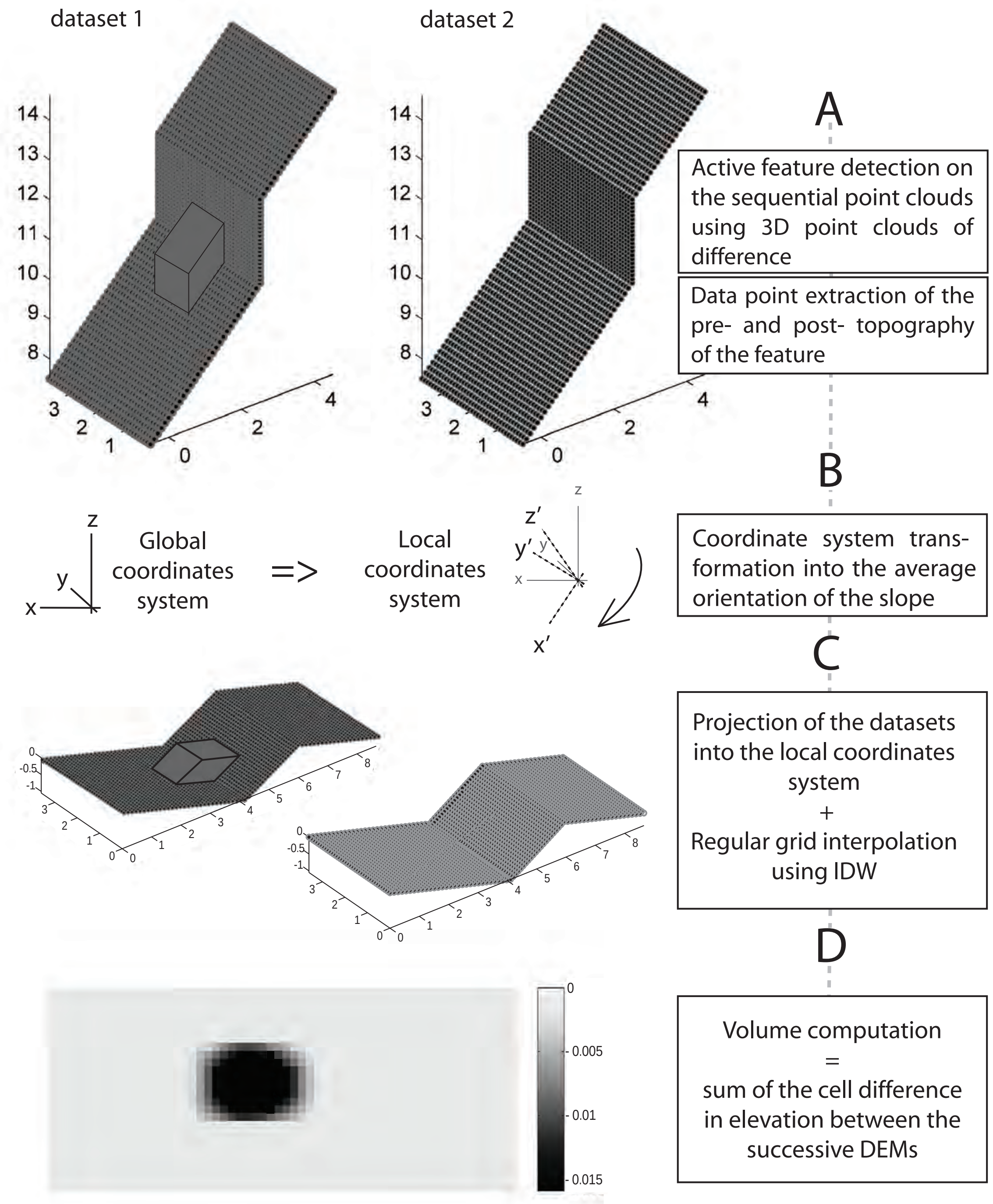

Figure 2.7: *3-D detection, extraction and volume computation method of an individual active feature provided by two successive point cloud datasets.*

close realistic representation of topography in case of overhanging features. The cell size was defined according to the point spacing distribution of both datasets. A series of tests revealed that setting the grid spacing at 68% of the cumulative frequency distribution of point spacing provides a continuous surface reconstruction while keeping a high degree of detail from the point cloud. This ensures an accurate volume computation. The volume of a geomorphic feature was computed as the sum of the cell difference in elevation between the successive DEM. Absolute cell difference lying below a given uncertainty was not considered. The processing of volume computation using local deterministic method of interpolation adopting the adaptive gridding approach were developed in Matlab®.

2.3.4 Point cloud accuracy and limits of detection of the geomorphic features

A reliable identification of erosion and deposition features requires the setting of a minimum LoD, where the elevation change between the successive point clouds can be considered as real in opposition to noise associated with each dataset. Each TLS data point has theoretically a unique precision depending on the range and laser incidence angle (Buckley et al., 2008). In practice, the individual point precision of a scan can be assumed to model a surface with a global uniform uncertainty, considering the very high point density (Abellán et al., 2009a). Given the homogeneity of surface error and considering that the distance between sequential points at a position (x, y) should tend to zero, the accuracy of TLS data can be estimated by substituting the precision of each data point by a singular

Histogram Statistics ICP : **Georeferencing Point Cloud April 2009 - July 2010**

Subcatch. name	Manival
Mean (μ)	0.000104
Std Dev. (σ)	0.060718
Minimum (min)	-0.212658
Maximum (max)	0.212658
Peak	48593
Number of Points	3526850

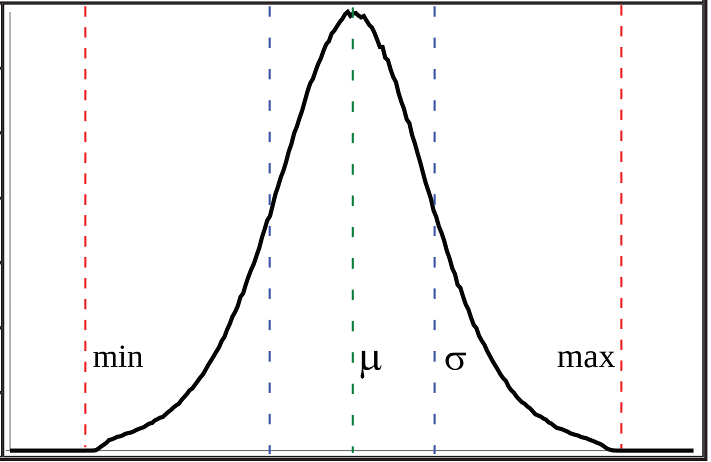

Figure 2.8: *Distribution of the distance between two survey point clouds after the process of georeferencing using ICP procedure. The distance approaches normal distribution with a zero mean, showing that errors generated by multiple scan registration and point cloud survey georeferencing are Gaussian, random and independent. Data are given in meters.*

Table 2.3: *Registration and georeferencing standard deviation (in cm) of the position uncertainty on a point to point basis period that were used to derive the LoD at 95% confidence interval.*

Sub-catchment name	2σ co-registered [cm]				2σ co-georeferencing (LoD) [cm]			2σ Taylor uncertainty[1] $\sigma_{d_{reg}} = \sqrt{\sigma^2_{d_{PC_1}} + \sigma^2_{d_{PC_2}}}$		
	Survey				Monitoring period			Monitoring period		
	1st	2nd	3rd	4th	1st	2nd	3rd	1st	2nd	3rd
Baure Gullies	1.9	1.7	1.5	1.5	5.9	6.9	6.9	5.1	4.5	4.2
Roche Ravine	3.2	2.9	2.6	2.7	8.4	9.4	9.0	8.6	7.7	7.5
Manival	4.6	4.1	3.0	3.4	9.6	10.2	12.2	12.3	10.2	9.1
Grosse Pierre	4.1	3.0	3.3	3.3	10.6	10.6	12.2	10.2	8.9	9.3
Genièvre	3.7	3.6	3.2	3.6	6.7	7.6	8.3	10.3	9.6	9.6

[1] pc = point cloud used to generate the map (point cloud) of difference in 3-D

measurement of the error associated with the entire point distribution across the surface (Lane et al., 2003). Hence, the uncertainty related to both scans registration ($_{reg}$) and point cloud georeferencing ($_{geo}$) was defined by the standard deviation of the distance (σ_d) between the points (Fig. 2.8). This includes the instrumental error of measurement, which increases with the point spacing. The LoD was therefore set at $2\sigma_{d_{geo}}$ and corresponds to the 95% confidence limit (Tab. 2.3). Comparison with the approach considering the error propagation for all uncertainties associated with each point cloud and assuming a normal distribution of the error in distance (Taylor, 1997) shows that the uncertainties considered here are reliable.

In the case of volume computation, information on elevation uncertainty associated with each point cloud survey needs to be extended on a DEM cell by cell basis. For any grid cell (i, j) generated by the interpolation of adjacent points p with independent elevation, the uncertainty of a cell elevation can be considered as the standard deviation (σ_e) of the data point elevation, where $\sigma_{\bar{e}_{i,j}} = \frac{\sigma_{e_p}}{\sqrt{n}}$ according to the equation of standard error of the mean, n being the number of points to define the cell elevation. The elevation uncertainty for each cell in a DEM of difference is then expressed by:

$$\sigma_{\Delta\tilde{e}_{i,j}} = \sqrt{\sigma^2_{1_{\bar{e}_{i,j}}} + \sigma^2_{2_{\bar{e}_{i,j}}}} \tag{2.7}$$

The volume uncertainty $\Delta\bar{V}$ is then calculated by summing up the derived volume uncertainty of each cell of the feature as follow:

$$\Delta\bar{V}_{feature} = a\sqrt{\sum_{i=1}^{n}\sum_{j=1}^{n}(\sigma_{\Delta\bar{e}_{i,j}})^2} \qquad \text{with}\, a \,=\, \text{cell area} \tag{2.8}$$

The smallest detectable volume is about 10^{-3} m^3 (10 x 10 x 10 cm^3) (Tab. 2.3), but can reach up to 0.006 m^3 (25 x 25 x 10 cm^3) depending on point spacing at maximum range.

Topographic change detection and volume computation hang however not only on the quality of TLS data, such as point density and post-processing related inaccuracy. The complexity in surface geometry must be considered, like here by integrating the range in position of all data point defining each grid cell value of a feature. The monitoring of hillslope activity is also limited by the ability of the process to create a distinct topographic change. Consequently, the deposition of individual small rockfall was not always detected, as detached rock mass fragments into pieces of sizes that are below the LoD. A similar issue was observed for erosion process on debris. Nevertheless, most of material accumulation could be related to landslides or scouring. Sediment budgets were therefore kept in volumetric units as they are commensurate for a consistent analysis. They were not converted to mass, although this would make more sense for comparing hillslope processes and rock slope yields. Such conversion requires an accurate density value of each surface process, whose approximations would bring unknown inaccuracies. Deposition related to rock failures may be slightly over significant in the sediment balance, although parts of the volumetric amplification are compensated by a limited detection of small features.

2.3.5 Sediment budgets of the Manival torrent

The monitoring of the coarse sediment transfer was performed all along the main torrent channel to the sediment trap located downstream from the apex of the alluvial fan. The in-storage change was established after every noticeable flow event using the morphological approach based on cross-section survey techniques (Ashmore and Church, 1998) and the volume of sediment deposited in the sediment trap was measured by TLS or total station survey differencing. The sequential volumes of recharge enable to study delivery rate and the influence of debris supply from the production zone through seasons. The characteristics and observational analysis of this event-based monitoring was documented in details in Theule et al. (2012) and is therefore only shortly reported here.

2.3.6 Estimation of debris production rate

A rate of debris production for the study period is obtained from the total volume of rock slope erosion. A more objective estimation can be deduced by characterising the cumulative distribution of rockfall volumes with a power law as follows (Gardner, 1970):

$$N(v > V) = aV^{-b} \tag{2.9}$$

N is the rockfall frequency for a volume v greater than V, a and b are constants. a depends on the study size and on rock slope properties, whereas b tends to be rather site independent (Dussauge et al., 2002; Dewez and Rohmer, 2011). Considering that rock slope process activity causing rockfall does not fluctuate much over time, the inventory analysis can be used to infer the frequency of occurrence of larger events. This is done by integrating the rockfall frequency derivative $n(v) = \frac{dN}{dV}$ over the range of potential volumes. Estimation of the total volume V_t per unit time that can be expected in average over a longer period of observation is therefore expressed by (modified from Hantz et al., 2002):

$$\begin{aligned} V_t &= \int_{n(V_{min})}^{n(V_{max})} V \; dn = -ab \int_{V_{min}}^{V_{max}} V \times V^{-b-1} \, dV \\ &= -ab \int_{V_{min}}^{V_{max}} V^{-b} \, dV = \frac{-ab}{(1-b)} V^{1-b} \Big|_{V_{max}}^{V_{min}} \end{aligned} \tag{2.10}$$

The goodness of fit of the power law was evaluated with the χ^2 test (Taylor, 1997) and the standard deviation of value a and b were determined with the maximum likelihood estimate (Aki, 1965). The erosion rates are assessed by dividing V_t with the surface prone to rockfall.

2.4 Observation: Hillslope process activity monitoring

2.4.1 1st monitoring period (April 2009 – August 2009)

The topographic changes recorded from July to August 2009 showed only few small rockfall but any relevant geomorphic activity. This is therefore not detailed explicitly and the results were merged with the preceding survey. Rock slope activity is dominated by individual small rockfall disseminated throughout the upper catchment. Only few events exceed 1 m^3, such that contributions in terms of debris production are marginal in most parts of the catchment (Fig. 2.9). The significant geomorphic activity was located almost exclusively in the major gullies of Baure and Grosse Pierre ravines, and consists of debris scouring of few 100 m^3 re-deposited further down essentially. Material re-entrainment was also observed in several other smaller gullies, but their volumes are not relevant. The rock couloirs of the Genievre subcatchment and the rock avalanche scar showed barely any geomorphic activity. The low-order channels displayed a net incision (-636 m^3 ± 43) in the upper reaches. Bed aggradation remains very low (+90 m^3 ± 6). Below the upper confluence, the channel trunk exhibits a mixed pattern of zones of erosion (-60 m^3 ± 2) and deposition (+80 m^3 ± 4) induced by bedload transport. The flow path scours in-channel gravel-wedges and creates new depositions further.

2.4.2 2nd monitoring period (September 2009 – November 2010)

Rock slope activity remains similar in spatial extend and volumes to the previous survey period, but rockfall frequency is higher (Fig. 2.10). Hillslope process activity was more widespread side east, but still particularly local on the western valley walls, while the rock couloirs showed any geomorphic activity. In the upper headwater, material reworking concentrated almost exclusively in steep tributary gullies. They displayed scouring of significant volume (-357 m^3 ± 12). Deposition features along the thalweg were quasi inexistent (+18 m^3 ± 1.3). In the south east, not only the Baure Ravine (net erosion:

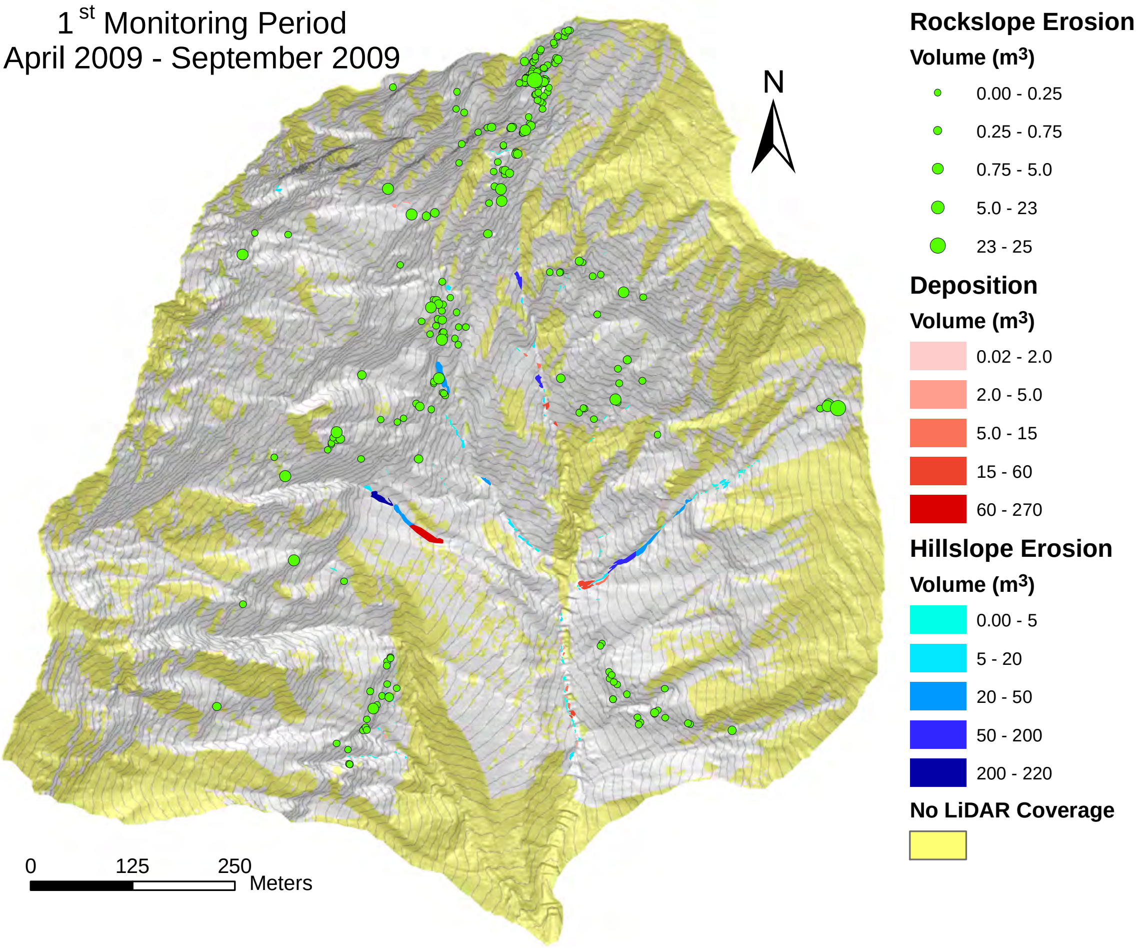

Figure 2.9: *Geomorphic activity revealed by comparing the topographic differences of the two successive TLS surveys operated in April and August 2009. The volumes are related to the sediment budgets in Tab. 2.4*

Table 2.4: *Overall headwater sediment budget recorded during the first monitoring period (Spring – Summer 2009).*

1st monitoring period	Volume total [m^3]		
	Hillside	Channel	Headwater
Rockfall	99.4 ± 5.9		99.4 ± 5.9
Deposition	408.2 ± 35.4	149.2 ± 10.9	557.4 ± 46.3
Erosion	547.2 ± 49.5	636.4 ± 43.3	1183.5 ± 92.8
Subtotal	-238.3 ± 61.2	-487.2 ± 44.7	-725.6 ± 103.9

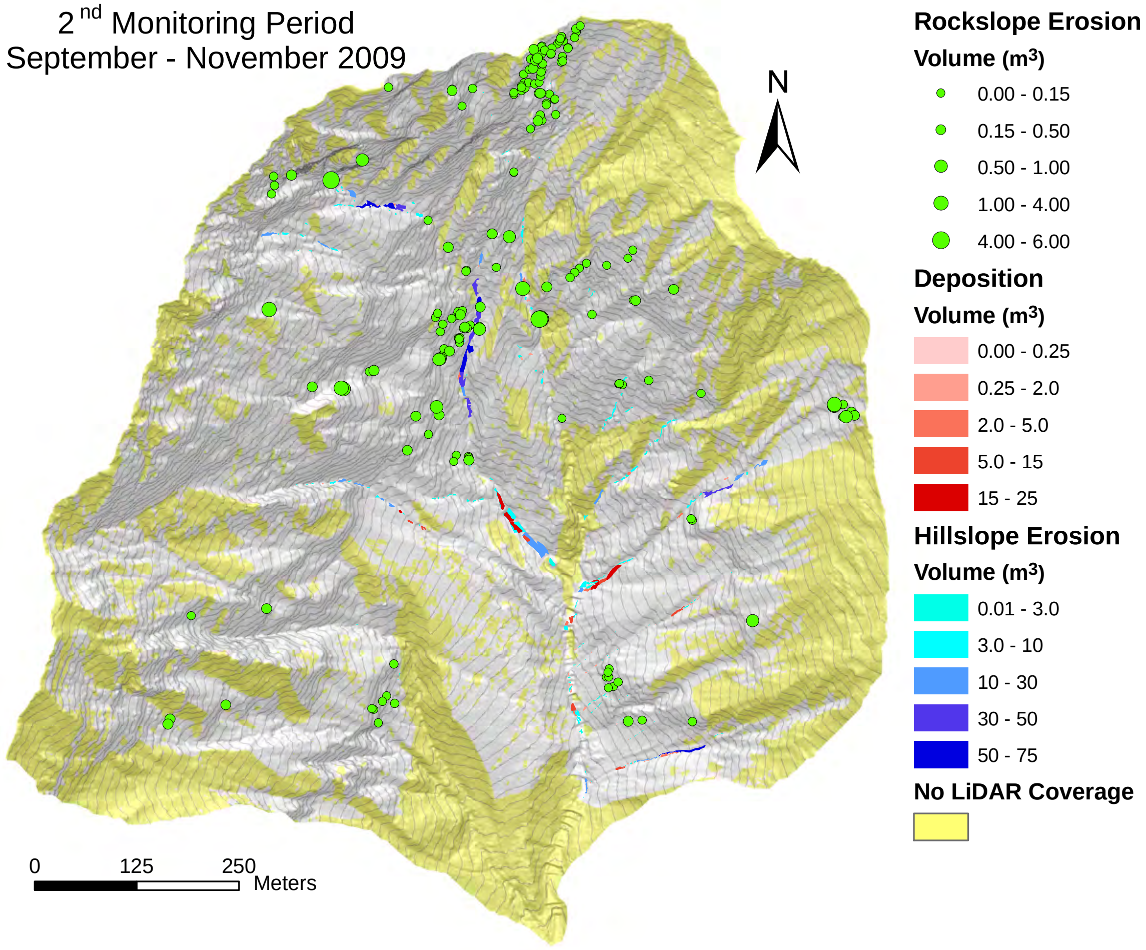

Figure 2.10: *Geomorphic activity revealed by comparing the topographic differences of the two successive TLS surveys operated in August and November 2009. The volumes are related to the sediment budgets in Tab. 2.5*

Table 2.5: *Overall headwater sediment budget recorded during the second monitoring period (Autumn 2009).*

2^{nd} monitoring period	Volume total [m^3]					
	Hillside		Channel		Headwater	
Rockfall	50.5	± 3.0			50.5	± 3.0
Deposition	181.8	±12.2	127.2	± 8.0	309.0	±20.5
Erosion	639.8	±27.1	522.5	±19.4	1162.3	±46.4
Subtotal	-508.5	±29.9	-395.3	±23.4	-903.7	±50.9

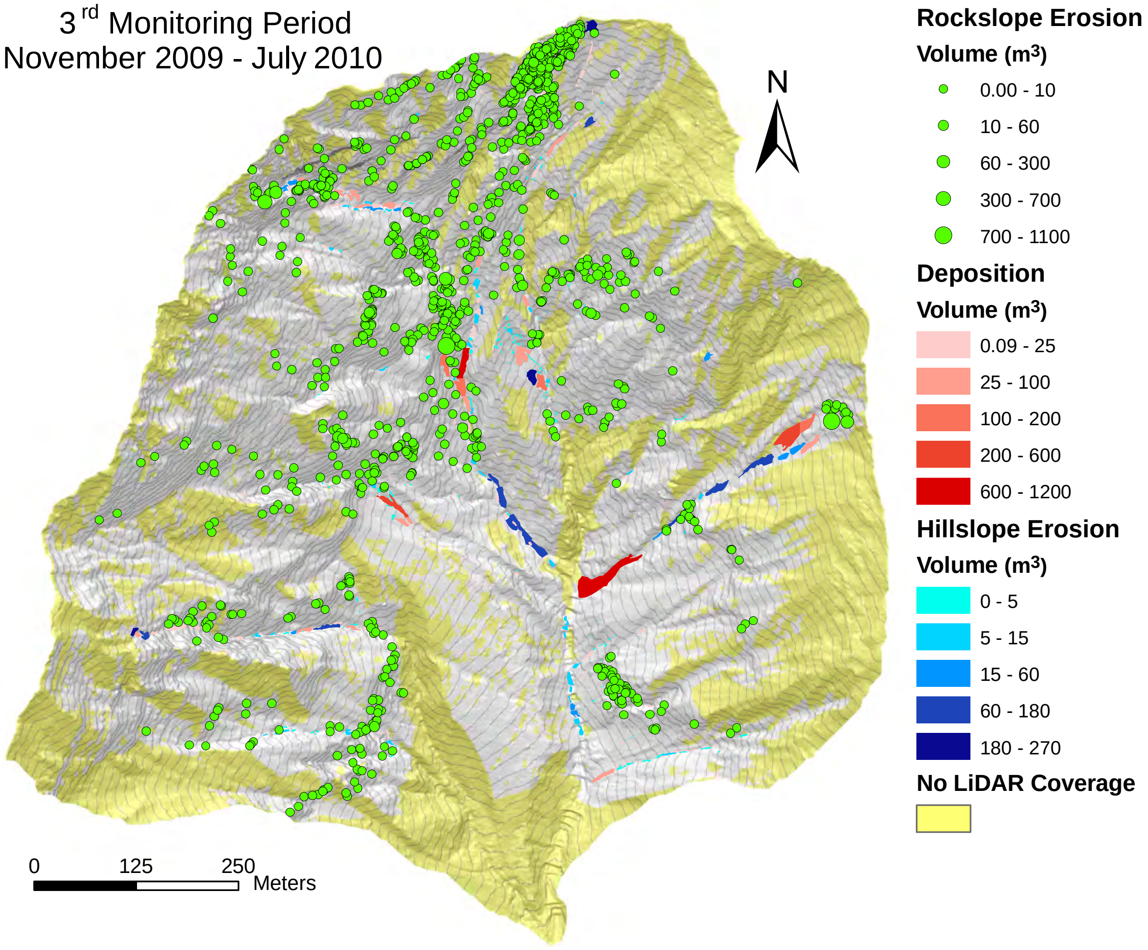

Figure 2.11: *Geomorphic activity revealed by comparing the topographic differences of the two successive TLS surveys operated in November 2009 and July 2010. The volumes are related to the sediment budgets in Tab. 2.6*

Table 2.6: *Overall headwater sediment budget recorded during the third monitoring period (Winter – Spring 2010).*

3rd monitoring period	Volume total [m^3]					
	Hillside		Channel		Headwater	
Rockfall	3424.9	± 89.1			3424.9	± 89.1
Deposition	3163.5	±147.9	1105.5	±36.4	4269.0	±175.6
Erosion	1941.6	± 72.8	650.8	±28.8	2592.4	± 91.6
Subtotal	-2203.0	±187.4	454.7	±46.5	-1748.3	±199.2

-61 m^3 ± 8), but the whole series of hillside gullies exhibited sign of activity, such as erosional segments alternate with deposition. On scree slopes, several minor rilling and their associated debris deposits were observed, some of them reached the channel trunk (+42 m^3 ± 2). Such small hillside debris flows were probably triggered by sediment entrainments in rills themselves as no evidence of sliding at their head was observed. The low-order channels show a net erosional character upstream (-482 m^3 ± 18), whereas continuous incisions were more pronounced in the Manival channel (-443 m^3 ± 16) as in the Roche Ravine (-40 m^3 ± 3). Deposition zones were almost completely absent (15 m^3 ± 1.3). Towards the confluence, the lower segments of Manival channel exhibited continuous zones of aggradation (97 m^3 ± 6) that were scoured on one side. This morphology is characteristic of close-process debris flow levees and run-up zones beside the incised channel bed. Below the upper confluence, channel bed cut (-40 m^3 ± 2) and fill (+16 m^3 ± 1) was sparse and concentrated at the junction with hillside gullies. Such pattern of bed reworking evidences the connectivity of the Baure gully series with the channel trunk.

2.4.3 3rd monitoring period (November 2009 – July 2010)

This period showed an important increase of rock slope production, both in frequency and magnitude, resulting from the occurrence of large slope failures and enhanced rockfall activity locally, for instance in rock walls made of calcareous marl situated directly above the Manival (2035 m^3 ± 39) and the Roche Ravine (256 m^3 ± 17) channels (Fig. 2.11). Most of debris collapses supplied the channel directly; the rest was temporary deposited in breaks of slopes. The lower headwater part showed a great fluctuation as well (Genievre: 116 m^3; Grosse Pierre: 145 m^3). At the top of the Baure Ravine, 816 m^3 (± 25) of rock fragments contributed substantially to recharge the gully head. Below, debris infilling was continuously scoured. An 1170 m^3 (± 18) rockslide is responsible for the large channel infilling of the Manival subcatchment. Several other smaller rockfall contributed to the recharge of tributary gullies and scree hollows. In the Roche Ravine, debris deposits were sparse, because rockfall remained of low magnitude in average (571 events < 1 m^3), although frequency was high (578 events). The large debris infilling of the channel head was caused by two erosion scars in side gullies (270 m^3 ± 14 and 65 m^3 ± 4). In the rock couloirs of the Genièvre subcatchment, a significant accumulation of material through landslides and rockfalls was observed (remnant volume: 204 m^3 ± 13), regarding that hillslope erosion represent 450 m^3 (± 14). In the Grosse Pierre Ravine, 343 m^3 (± 17) of debris were accumulated at the rock couloir outlet, recharging the scree slope above the channel head. In the Col du Baure, an important aggradation of the lower part of tributary gullies was observed (remnant volume: +142 m^3 ± 2), resulting from material entrainment. Several debris slides were also detected on scree slopes, without any contact with the channel trunk. The upper low-order reaches were clearly depositional, related to large slope failures. The Manival channel showed a continuous zone of remnant accumulation of 948 m^3 (± 18) that was reworked downstream as bedload. Towards the confluence, erosion dominated clearly (-487 m^3 ± 19) against deposition (+25 m^3 ± 3). In the Roche Ravine, a sustained erosion of the rock avalanche scar produced deposits mostly on slope. But a landslide of 190 m^3 (± 9) reached the channel. Globally, aggradation was observed all along the channel head (+148 $m^3 \pm 18$) and scouring was sparse (-65 $m^3 \pm 4$). From the upper confluence downstream, the channel behaviour is dominantly erosional (-97 $m^3 \pm 4$) with almost any aggradation (+3 $\pm$ 0.3 m^3).

2.4.4 Rock slope production inventory

Over the 16 months, 1’866 rockfalls of volumes ranging from 10^{-4} to 10^3 were recorded. This yields a total of 3’575 m^3 ($\pm$ 98) and an average erosion rate of 3.1 mm/yr given the topographic surface area. The inventory (Fig. 2.12) follows a power law with a 99% confidence level for events larger than 3 m^3 (χ^2 value = 17.3). For events larger than 1 m^3, the power law is accepted at the 95% confidence level (χ^2 value = 5.89). Both threshold volumes provide a b – value close to 0.81 $\pm$ 0.06. Considering volumes above 10 m^3 only (25 events) gives a b – value of 0.76. Below 0.1 m^3, the observed frequency

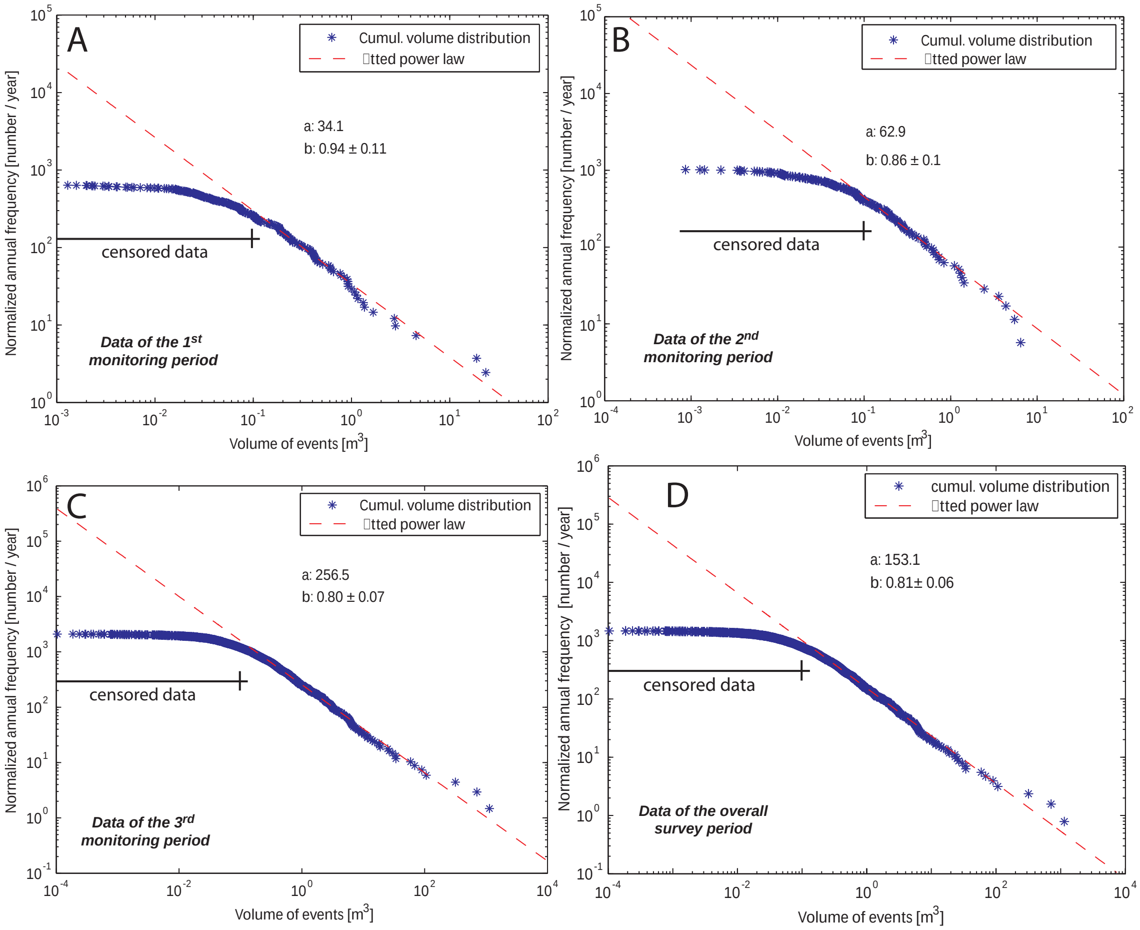

Figure 2.12: *Cumulative volume distribution of rockfall observed during the first (A), the second (B), the third monitoring period (C) and over the entire study time of 16 months (D). For each dataset, the power law is fitted for volumes larger than 0.1 m^3. Below this threshold volume, the distribution exhibits a roll-over that progressively reaches a quasi-constant frequency for the smallest detected volumes.*

Table 2.7: *Rock slope debris production rate estimated from the inventory analysis using power law distribution of volume for potential rockfall (Fig. 2.12).*

Class of volume in m^3	10^{-3} 10^{-2}	10^{-2} 10^{-1}	10^{-1} 1	1 10	10^{1} 10^{2}	10^{2} 10^{3}	10^{3} 10^{4}	10^{4} 10^{5}	10^{5} 10^{6}	10^{6} 10^{7}
Measured frequency (per year)	143 (113)	742 (584)	789 (621)	168 (132)	19 (15)	3 (2.4)	1 (0.8)			
Calculated frequency	36’990 ±4’366	5’621 ±581	854 ±86	130 ±9.6	19.7 ±1.2	3.0 ±0.14	0.46 ±0.02	0.069 $\pm 10^{-3}$	0.011 $\pm 10^{-4}$	0.0016 $\pm 10^{-5}$
Cumulative measured frequency (per year)	1’467	1’355	772	152	19	3.1	0.79			
Cumulative calculated frequency	43’619 ±5’043	6’629 ±677	1’007 ±97	153 ±11	23 ±1.6	3.5 ±0.2	0.54 ±0.02	0.08 $\pm 10^{-3}$	0.01 $\pm 10^{-4}$	0.0016 $\pm 10^{-5}$
Fallen volume per year [m^3]	102 ±12	155 ±16	236 ±19	358 ±26	544 ±32	827 ±37	1’257 ±39	1’911 ±32	2’904 ±8	4’413 ±51
Total fallen volume per year [m^3]	298 ±43	454 ±59	689 ±79	1’047 ±105	1’592 ±136	2’419 ±172	3’676 ±210	5’587 ±241	8’491 ±249	12’903 ±305
Cliff area	826’804 m^2 (only the topographic rock slope surface area)									
Erosion rate [mm]	0.36 ±0.05	0.54 ±0.07	0.83 ±0.1	1.3 ±0.1	1.9 ±0.2	2.9 ±0.2	4 ±0.3	6.8 ±0.3	10.2 ±0.3	15.6 ±0.4

deviated clearly from power law regime until the roll-over reaches a quasi-constant rate for the smallest volumes. The rockfall distribution of each monitoring period follows also a power law regime with b – values ranging from 0.8 to 0.94 for volumes above 0.1 m^3, although there is a great variability of frequency between the datasets. According to the inventory, rockfall of more than 1 m^3 are expected 153 ± 11 times per year in average. The largest event (1’170 m^3) occurs every two years and the one year return period rockfall is about 465 m^3. Considering only class of volumes of the inventory, the rock slope production reaches a rate of 3’676 m^3/yr ± 210 (4 mm/yr ± 0.3).

2.4.5 Torrent in-channel storage changes

Two debris flows of probably multiple surges and several remarkable bedload transport events were observed in the main torrent during the survey period. A debris flow occurred on the 25th August 2009 caused by a short duration rainstorm. The volume of sediment eroded in torrent (5232 m^3 ± 136) coincides that re-deposited in both the torrent itself and the sediment trap (5072 m^3 ± 125), suggesting that the induced material entrainment involved what was stored in the torrent in great majority (Tab. 2.8). Sediment input from the headwater can be considered as marginal, as suspended material was not accounted and depleted the true volume of deposition. Before that, no significant torrent activity was observed, despite series of rainfall of low to moderate intensity. In September 2009, a long period of moderate rainfall intensity caused material reworking induced by bedload transport all along the torrent. However, no sediment went supplying the sediment trap. A net gain of storage supplied by the headwater could be monitored. In October, a succession of low intensity rainfall induced some major sediment transport in the torrent that aggraded the sediment trap with at least 302 m^3 (± 36). The sediment budget indicates clearly a recharge of 229 m^3 (± 31), a transfer of debris that were stored mostly in the distal part of the torrent. Throughout the winter 2010, a gradual incision was observed all along the torrent resulting from frequent period of low intensity rainfall conjugated to snowmelt. Due to maintenance (dredging), the sediment trap was disturbed and any reliable data was available. Any sign of competent activity was detected anyway. A new debris flow on June 6^{th} deposited 3320 m^3 (± 176) in the sediment trap. This time, a certain supply from the headwater was observed (∼270 m^3). This event was followed by series of intense rainfall without much reworking in the distal part, suggesting that no competent transfer occurred anymore towards the torrent. The in-torrent storage changes and estimated recharge budgets are shown for each monitoring period in Fig. 2.13.

Table 2.8: *Sediment budgets (in m^3) of the Manival torrent established after noticeable events using the morphological approach (Theule et al., 2012). The torrent recharge (sediment input) is estimated from in-storage changes in channels and volumes deposited in the sediment trap (output).*

MP	Torrent Survey dates	Sediment output	Storage change	Channel erosion	Channel deposition	Sediment input	
						survey	Total
1^{st}	06/07/09 - 28/08/09	1873 ±62	-2034 ±559	5232±136	3199±63	0-63	0 - 63
2^{nd}	30/08/09 - 07/10/09	0	789±84	1409±31	2197±53	736-842	934-1102
	08/10/09 - 12/11/09	266-338	-73±66	1546±36	1473±31	198-260	
3^{rd}	13/11/09 - 01/06/10	580±45	-580 ±81	1961±45	1372±36	0-36	174-844[1]
	02/06/10 - 08/06/10	3320±176	-3052 ±272	7658±178	4606±93	0-537	
	09/06/10 - 08/10/10	773-865	-608 ±82	2246±46	1637±36	174-246	

[1] The 3^{rd} TLS survey lasted until 08/07/2010

2.5 Summary: Manival headwater sediment budgets

According to volumes detected during the 16 months study period, the headwater sediment budget reveals a net export of some 3378 m^3 (± 361) of material to the torrent (Tab. 2.9). The overall rock slope yield is about 3575 m^3 (± 30), for a volume of erosion reaching 3129 m^3 (± 150) on the hillside and 1809 m^3 (± 92) in the channel complex. Volume of deposition, induced from both debris production and material reworking, yields a total volume of 5135 m^3 (± 251), whereas only 1382 m^3 ± 56 (27%) concern the channel complex. The in-torrent sediment transfer is important (∼20'000 m^3) and essentially

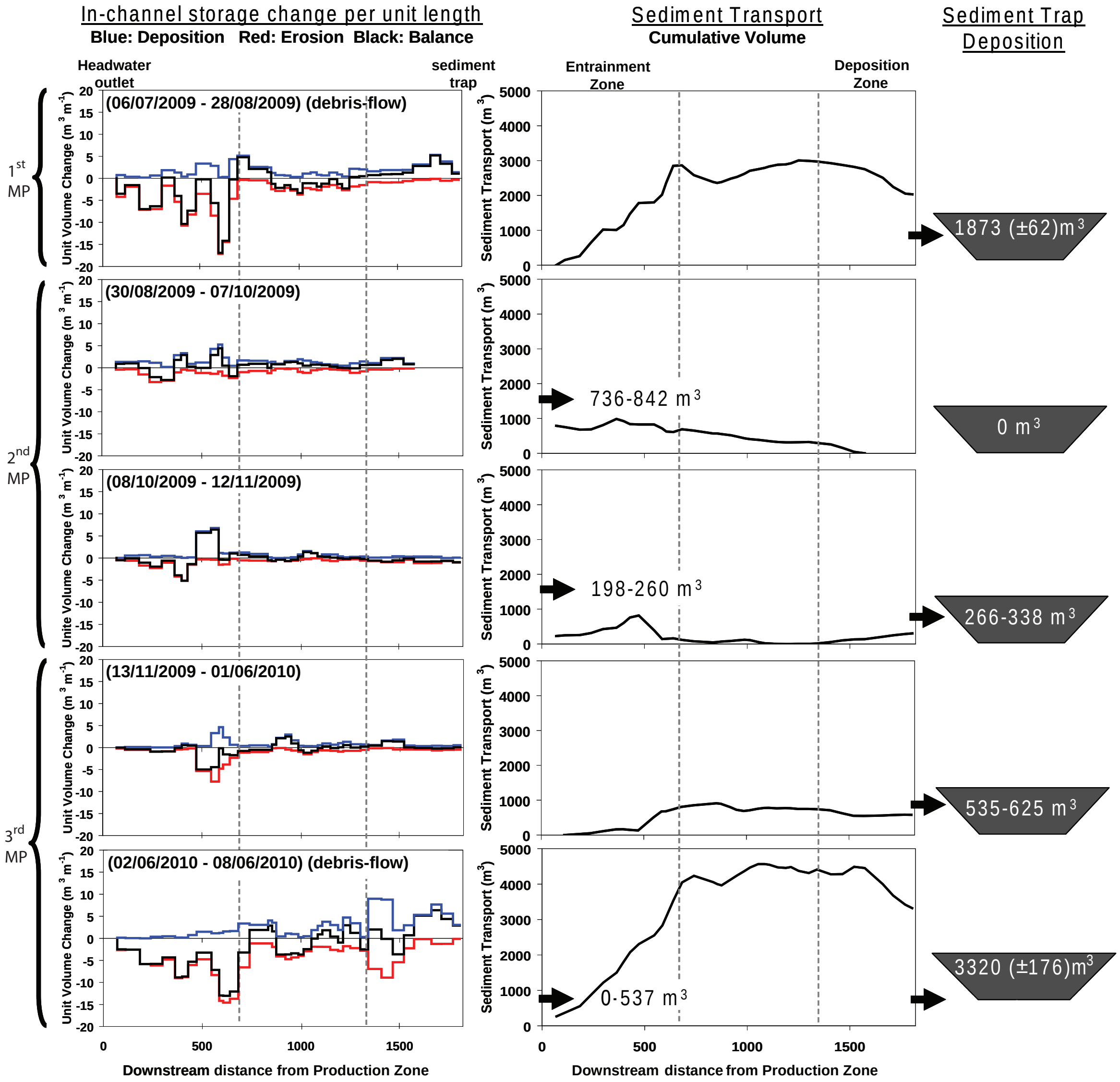

Figure 2.13: *Torrent in-channel storage changes per unit length and sediment budgets of cumulative volumes transported in the torrent from the headwater outlet to the sediment trap downstream for each monitoring period (MP) (Tab. 2.8). The torrent recharge (sediment input) was estimated given the in-storage change and the volume deposited in the sediment trap (modified from Theule et al., 2012).*

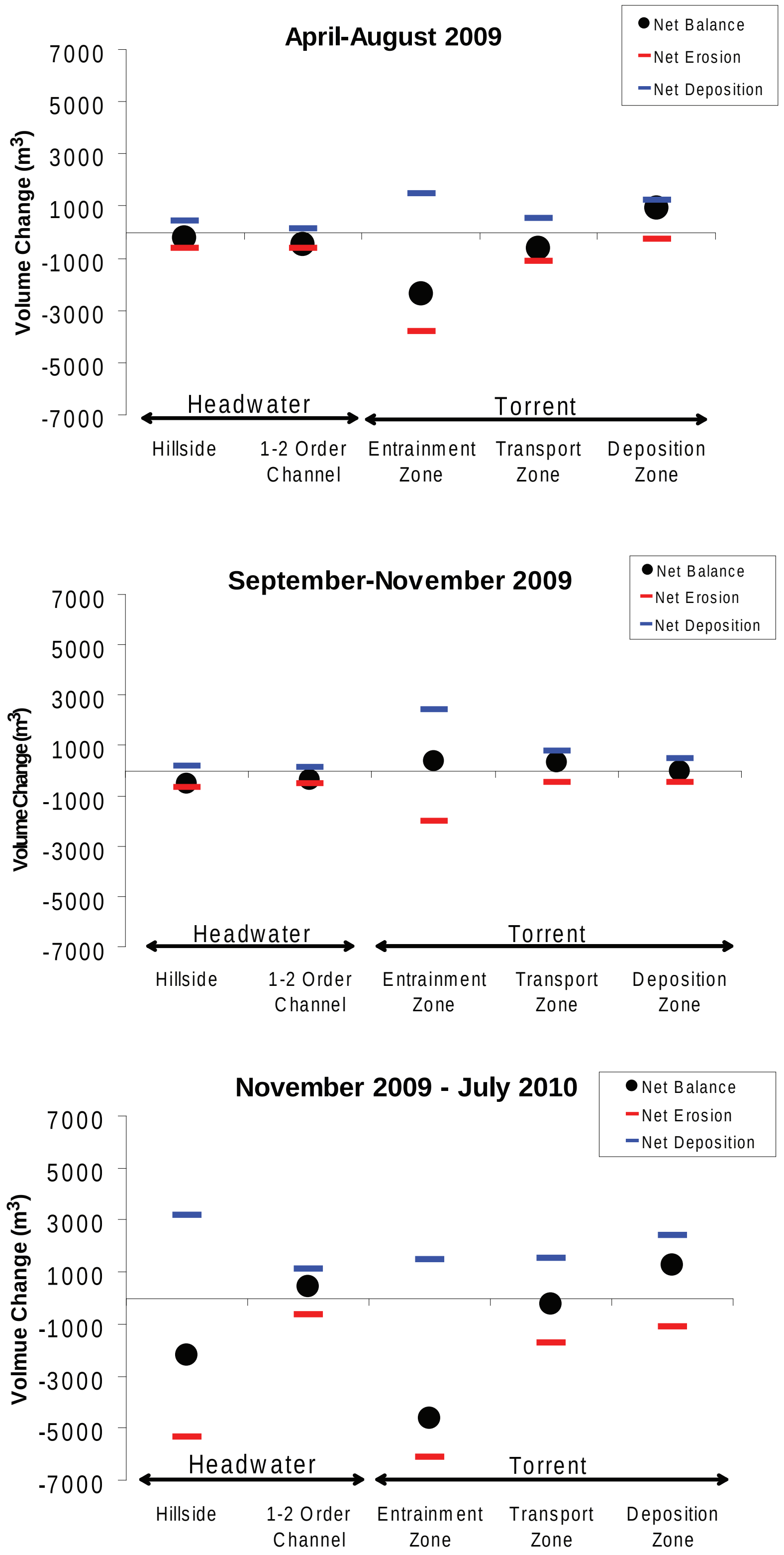

Figure 2.14: *Overall transfer dynamic from debris source zone in the headwater to the apex of the fan through the torrent observed during the period of investigation.*

Table 2.9: *Overall headwater sediment budget recorded during the three survey periods and net sediment balance of the 16 months of monitoring.*

Total monitoring	Volume total [m^3]					
	Hillside		Channel		Headwater	
Rockfall	3574.7	± 97.9			3574.7	± 97.9
Deposition	3753.5	±195.6	1381.9	± 55.6	5135.4	±251.3
Erosion	3128.5	±149.4	1809.7	± 91.3	4938.2	±240.8
Total	-2949.8	±264.9	-427.8	±106.9	-3377.6	±361.4

related to the occurrence of two debris flows (Theule et al., 2012), depleting significantly the storage of distal parts (entrainment zone). During the autumn, bedload transport of several hundreds of m^3 acts as recharging the torrent all along. Material deposited in the sediment trap for the survey period yields 6075 m^3 ± 45. The overall transfer dynamic from debris source zone to the apex of the fan is illustrated in Fig. 2.14. In the spring – midsummer period, the hillside sediment budget yields a total rock slope production of 99 m^3 ± 6 for a volume of erosion of -547 m^3 ± 50 and deposition of 408 m^3 ± 35 (Tab. 2.4 and 2.10). This suggests that about 238 m^3 ± 61 of material supplied the channel complex, coming almost exclusively from material re-entrainment in gullies (Fig. 2.15). The sediment budget of low-order channels indicate a significant degradation in storage (-487 m^3 ± 44), comprising large and continuous incision (-636 m^3 ± 43) in the upper reaches and material aggradation (+149 m^3 ± 11) in the lower reaches resulting mostly from zones of transient re-deposition. This results a recharge of the torrent of +726 m^3 ± 103 for this survey period.

During the late summer – autumn season, the headwater was characterized by a general increase of the hillside process activity. The total volume of erosion (-640 m^3 ± 27) doubled on average, resulting particularly from a widespread scouring of tributary gullies located east and south-east of the headwater (Fig. 2.16). Elsewhere, the geomorphic activity remained very local, but gain in intensity. The total volume of deposition of rock slope production (50 m^3 ± 3) and deposition (+182 m^3 ± 12) remained low. Globally, the sediment budget indicates that the hillslope contributed at recharging the channel reaches with sediment for about 510 m^3 (± 30) (Tab. 2.5 and 2.10). The low-order channels sediment budget yields -522 m^3 (± 20) of erosion for +127 m^3 (± 13) of deposition. This is characterized by bedload reworking in both low-order and trunk channels, and a progressive transfer of 904 m^3 (± 51) of material in the torrent.

During winter – spring 2010, a total volume of deposition of +3163 m^3 (± 147) is recorded on the hillside for a volume eroded of -3129 m^3 (± 150). An important production of debris (3424 m^3 (± 89)) is observed (Tab. 2.6 and 2.10). The net sediment balance on the hillside yields to a supply in the of 2203 m^3 (± 187) of sediment in low-order channels and the one for the channel complex indicate an increase of in-storage of 455 m^3 (± 47), according to a total volume of deposition of 1105 m^3 (± 36) and erosion of 651 m^3 (± 29) due to large portions of bed scouring in the downstream reaches. Sediment transfer to the torrent is 1749 m^3 (± 199) (Fig. 2.17).

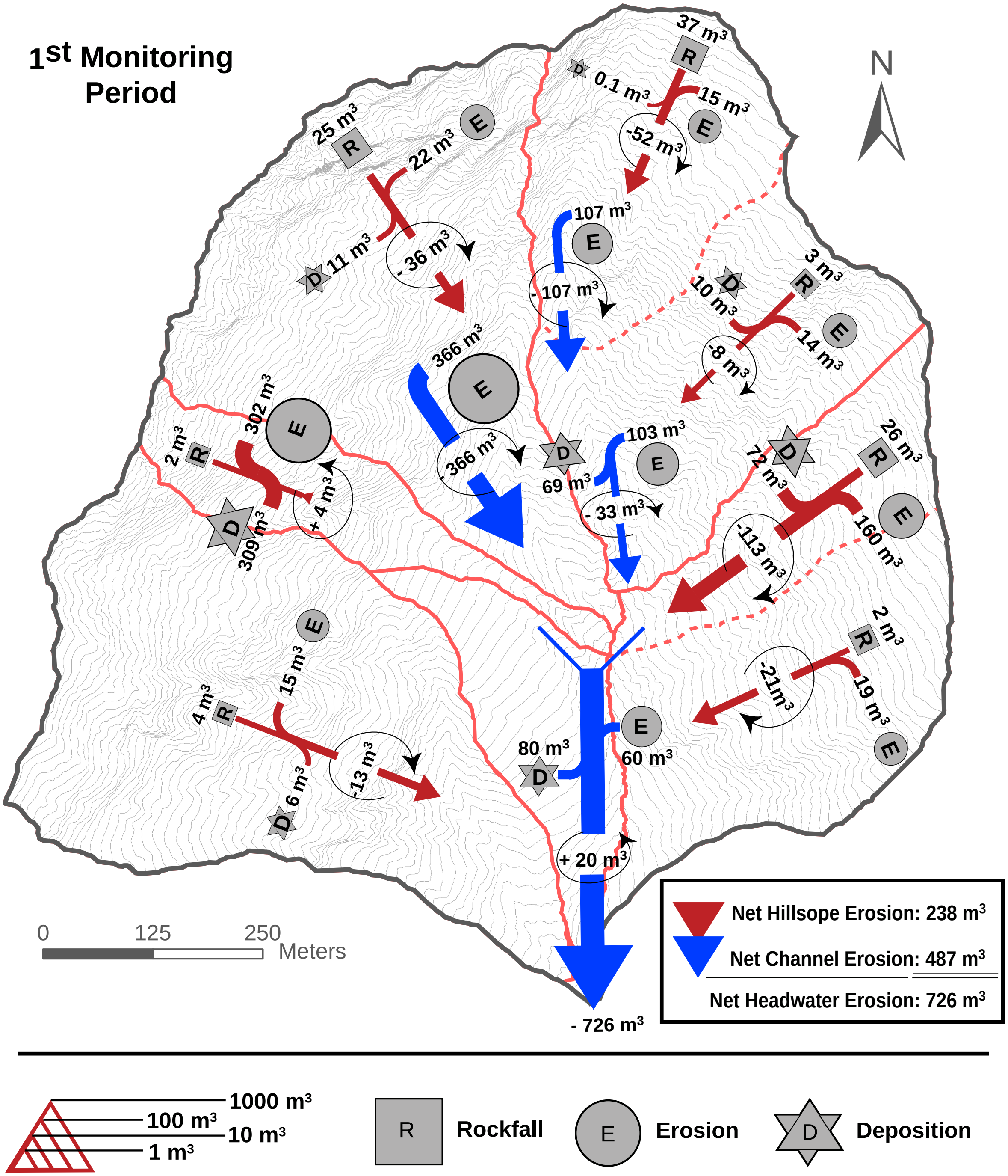

Figure 2.15: *Overall headwater sediment budget observed during the 1st monitoring period revealing the sediment dynamic through the spring – summer season and the net balance of sediment recharge in the downstream torrent for the several months preceding the August 2009 debris flow.*

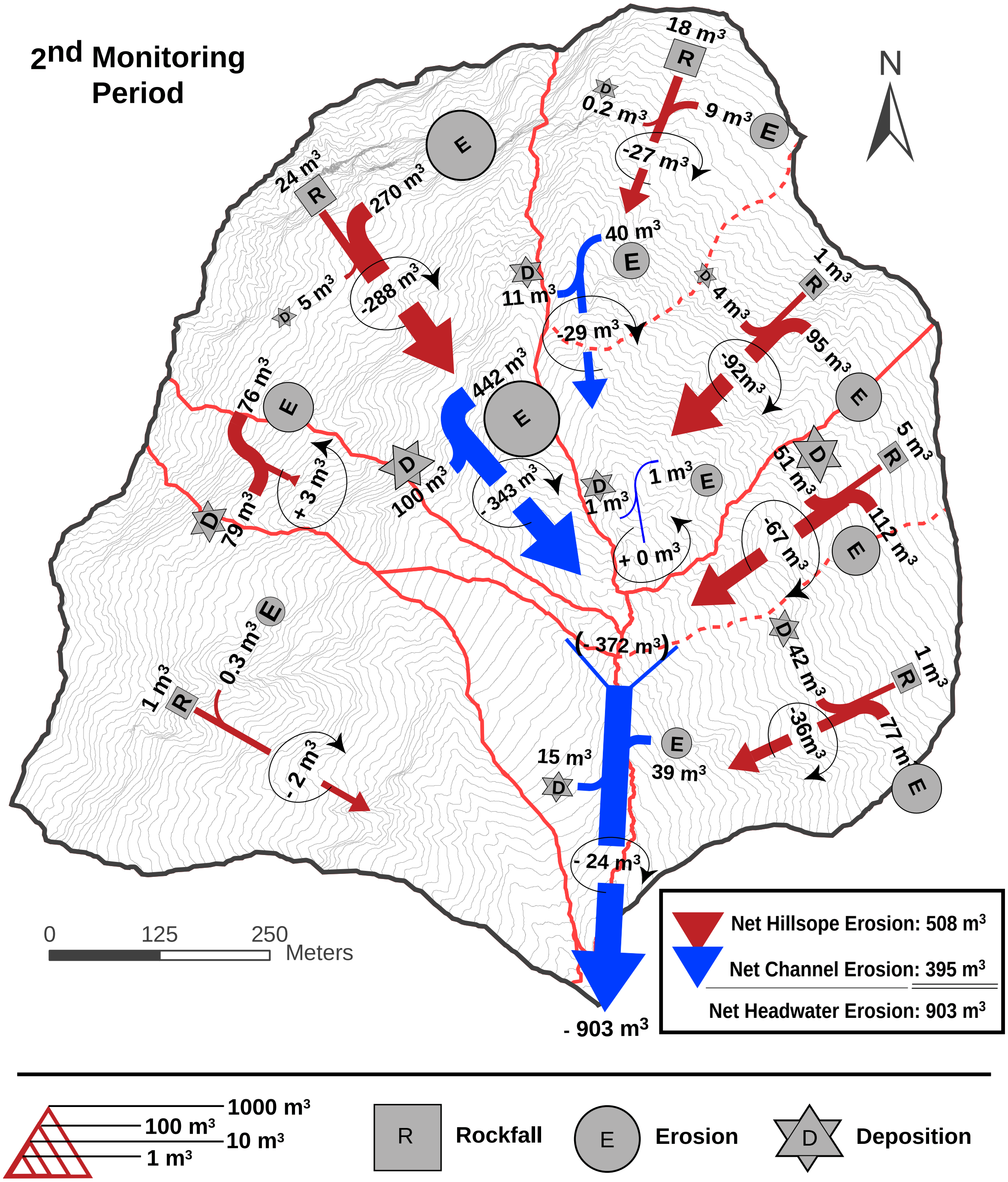

Figure 2.16: *Overall headwater sediment budget observed during the 2nd monitoring period revealing the sediment dynamic and the net balance of sediment recharge in the downstream torrent during the autumn.*

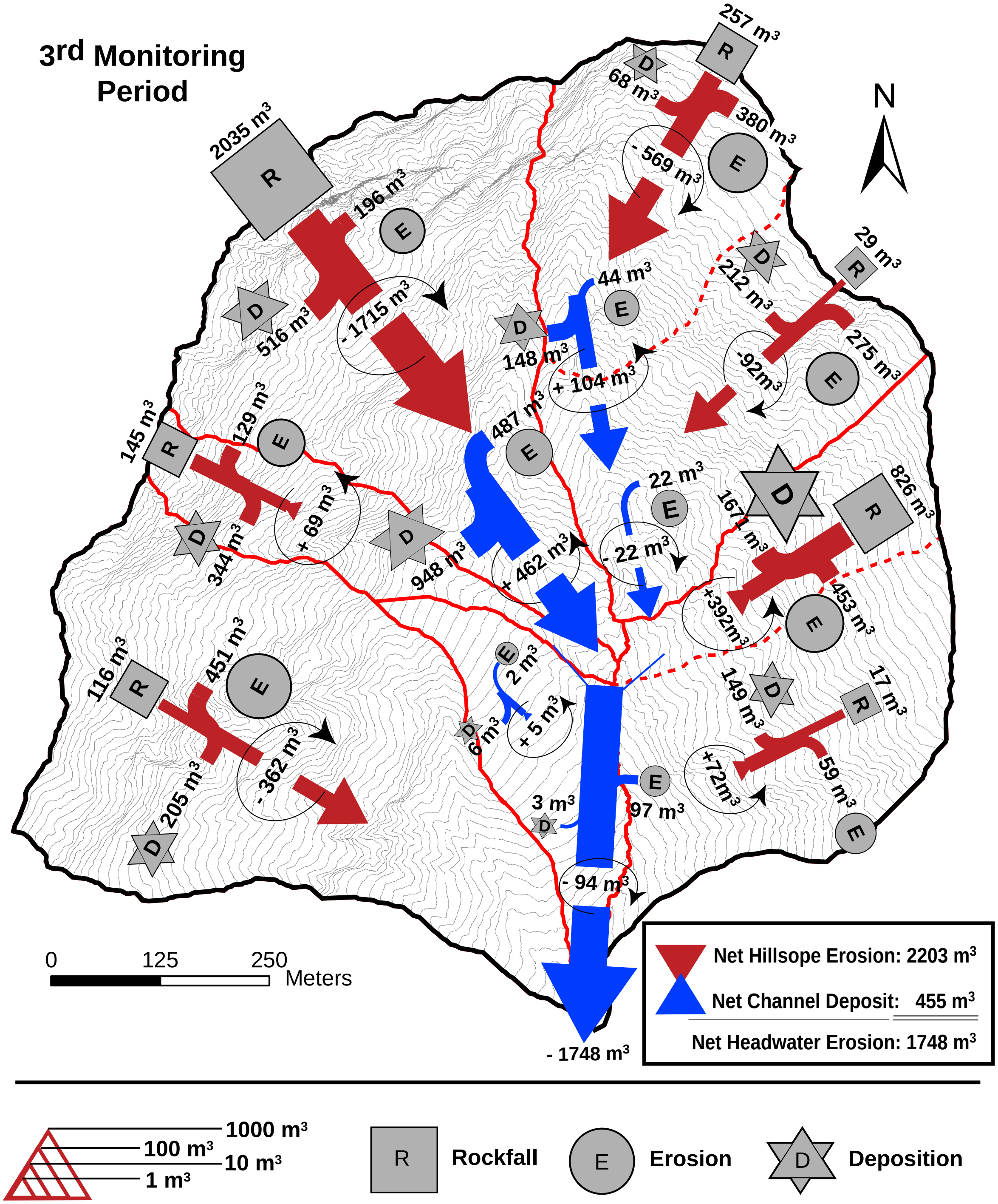

Figure 2.17: *Overall headwater sediment budget observed during the 3rd monitoring period revealing the sediment dynamic through the winter – spring and the net balance of sediment recharge in the downstream torrent for the period preceding the June 2010 debris flow.*

Table 2.10: *Overall headwater sediment budget given in volumes per month for the three monitoring periods (MP).*

1st monitoring period.

1st MP	Volume total per month [m^3]		
	Hillside	Channel	Headwater
Rockfall	19.6 ± 1.2		19.6 ± 1.2
Deposition	80.6 ± 7.0	29.4 ±2.2	110.0 ± 9.2
Erosion	108.0 ± 9.8	125.6 ±8.6	233.6 ±18.3
Subtotal	-47.0 ±12.1	-96.2 ±8.8	-143.2 ±20.5

2nd monitoring period.

2nd MP	Volume total per month [m^3]		
	Hillside	Channel	Headwater
Rockfall	23.7 ± 1.4		23.7 ± 1.4
Deposition	85.2 ± 5.7	59.6 ± 3.9	144.7 ± 9.6
Erosion	299.9 ±12.7	244.9 ± 9.1	544.8 ±21.8
Subtotal	-238.3 ±14.0	-185.3 ±11.0	-423.6 ±24.8

3rd monitoring period.

3rd MP	Volume total per month [m^3]		
	Hillside	Channel	Headwater
Rockfall	414.3 ±10.8		414.3 ±10.8
Deposition	382.7 ±18.0	133.7 ±4.4	516.4 ±22.3
Erosion	234.9 ± 8.8	78.73 ±3.5	313.6 ±12.3
Subtotal	-266.5 ±22.7	55.0 ±5.6	-211.5 ±27.6

2.6 Discussion

2.6.1 Debris supply through rock slope production

Debris production from rock walls degradation shows a strong seasonal pattern. The great majority of recorded rock instabilities in both magnitude (95%) and frequency (75%) occurred during the 3rd monitoring period, hence the cold season. Previous studies of the calcareous cliffs near Grenoble, which represent a similar morphotectonic context, revealed that freeze-thaw cycles are the main triggering factor of rockfall (Frayssines and Hantz, 2006). Ice jacking can cause microcracks propagation leading to failure (Matsuoka and Sakai, 1999). Along the eastern ridge, the bedrock surface is often highly fractured, suggesting frost shattering. The spatial pattern of rockfall strongly suggests also a lithologic influence that can be explained by differential erosion between the successive limestone and marl beds. In the rock walls series side west, the monoclinal configuration of the bedding combined with a strong difference of competency between stratigraphic sequences give rise to overhanging formation highly susceptible to slope failure. Side east, the bedding is mostly cataclinal and approaches dip slope depending on the topographic orientation of the slope. Rock slope failures initiated by planar sliding on bedding planes were observed.

The observed debris production follows a power law distribution in a range covering at least 3 orders of magnitude [10^0 m^3 - 10^3 m^3]. The exponent b is slightly higher than the average value reported for the Grenoble cliffs [0.4 - 0.7] (Hantz, 2011), but is in agreement with short inventories covering a lower range of volume [10^{-2} m^3 - 10^2 m^3] (Hungr et al., 1999; Dussauge et al., 2002). Inventories dominated by small volumes tend to increase the b – value compared to the ones covering rather large volumes (Stark and Hovius, 2001). Above 100 m^3, the deviation from the power law may be attributed to the short period of sampling for events of such large magnitude. The roll-over encountered towards small volumes (< 0.15 m^3) results most likely in the under-detection of the number of events. This sampling bias being far above the minimum volume of detection (0.006 m^3), another behaviour characterizing the failure of small volumes cannot be excluded. This may presuppose a physical erosion process that differs from the one influencing larger instabilities, which are controlled primarily by local predisposing factors such as the geometrical and geomechanical properties of the rock mass (Selby, 1993; Sauchyn et al., 1998) and the local condition of tectonic weakening (Cruden, 2003; Coe and Harp, 2007). Low magnitude rockfall represent anyway little contribution in terms of debris supply, even though they vary locally from 1 or 2 orders of magnitude over the time, as observed here. The amount of sediment available is only significantly influenced by instabilities of high magnitude (Fig. 2.18).

Previous sediment budgets derived from topographic measurement using stereophotogrammetry estimated the highest erosion rates over an average of 40 years to range from 10.8 mm/yr to 17.8 mm/yr in the headwater (Veyrat-Charvillon, 2005). Although the large uncertainty of the approach and the fact that they measured the hillslope and thalweg geomorphic activity, these values are compatible with the erosion rate revealed here from the short period rockfall inventory by supposing the possible occurrence of rockslides of magnitude [10^6 m^3 - 10^7 m^3]. Considering that the power law is valid for larger slope failures, a 7'500 m^3 event can be expected every 10, respectively 100 years for 120'000 m^3. The average debris production ranges between 5'587 ± 241 to 12'903 ± 305 m^3/yr according to a maximum potential erosion of 10^5 m^3, respectively 10^7 m^3 over several centuries (Tab. 2.7). Any historical Manival rockslide exists to support this estimation. The old rock avalanche deposit ($\sim$6.1 Mm^3) of the upper catchment is the largest detected event, but it may have formed from several collapses (Fig. 2.19). Rockfall inventory of the Grenoble cliffs reports volume smaller than 10^5 m^3 for the last century, respectively 10^7 m^3 since the 17th century (Hantz et al., 2003). Such a magnitude is also likely at Manival. A mean rate of rock slope erosion of about 1 cm/yr (10'000 m^3/yr) can be therefore expected in the upper catchment over the century.

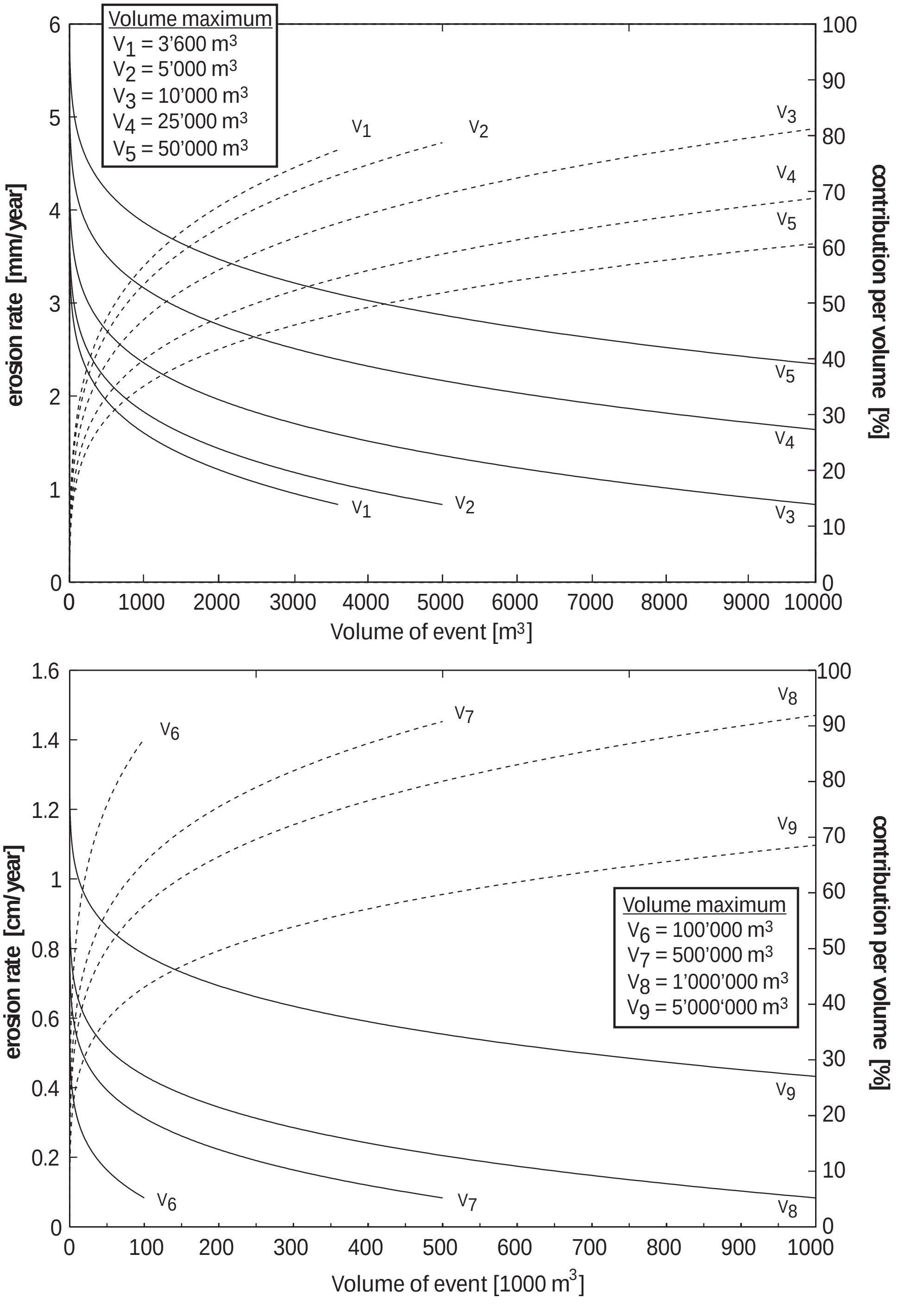

Figure 2.18: *(straight line) Erosion rate as function of size of events for a certain volume of production (potential maximum volume $V_{1...9}$), considering that rockfall volume distribution observed at Manival follows power law behaviour (Tab. 2.7). (dash line) Contribution of each class of volumes to the erosion rate, showing the significant effect of large slope failures. For a maximum volume eroded of 3'600 m^3/yr (V_1), the 1'000 m^3 rockfall event contributes for 60%, while events less than 100 m^3 induce less that 20% of erosion, although of much higher frequency; a 100'000 m^3 rockslide would generate 70% of a total of material eroded of 500'000 m^3 (V_7) over a century.*

Upstream from the Manival channel, scouring of debris slopes and scree hollows induced from rock slope production contributed for instance for about 40% of the net erosion recorded during the autumn period, respectively 25% for the Baure Ravine over the entire study period. The dominant mode of debris supply in the Manival headwater is therefore highly episodic (vs. chronical), implying a great spatial heterogeneity in recharge rate.

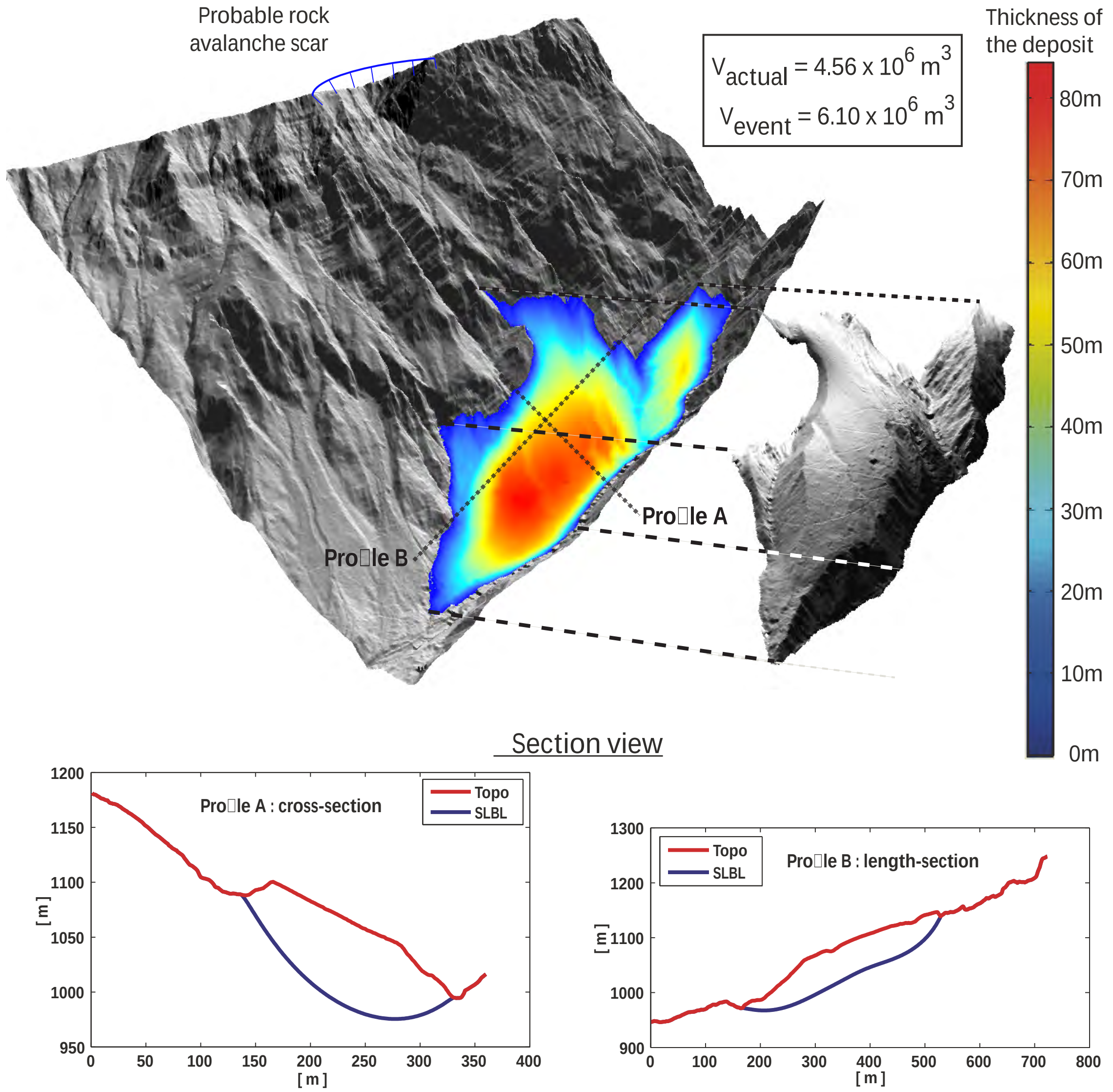

Figure 2.19: *Volume estimation of the old rock avalanche of the Manival upper catchment using the Sloping Local Based Level (SLBL) algorithm (Jaboyedoff and Derron, 2005). The basal surface (blue line) of the remnant rock avalanche deposit is determined by replacing in an iterative way the elevation of each DEM cell with a mean value ± a tolerance derived from the surrounding highest and lowest cell elevation. This progressive erosion procedure is applied until a curvature that may correspond to the topography before the event is obtained. The actual volume of deposited material reaches about 4.6 Mm*^{3}*. Given the full reconstruction of the top surface of the deposit, this event is estimated to be of 6.1 Mm*^{3}.

2.6.2 Debris supply through hillslope activity

Rock slope activity was very little from spring to autumn, such as hillslope geomorphic activity dominated the process of sediment recharge. Until the end of August, the geomorphic activity of both hillside and low-order channels recorded the lowest transfer of material on average and debris supplying the downstream torrent had mostly a low-order channel origin. The hillside monitoring reveals that debris supply to low-order channels was very local. Ephemeral debris-filled tributary streams and major hillside gullies remained quasi inactive in terms of sediment delivery.

The autumn period is characterized by a general increase in intensity of geomorphic activity. The negative sediment balances in all sediment cascade components suggests a very high degree of connectivity between hillside and low-order channels. Continuous scouring and the quasi inexistence of deposition features from hillside gullies indicate that mobilized material is integrally entrained downstream by runoff. In the channel reaches, competent incision and micro debris flow indicate a competent transfer of material. Globally, the hillside contribution represents on average a volume 5 times bigger than what was observed during the spring – summer period. Channel bed reworking was of much larger magnitude as well.

During winter – spring 2010, the huge increase of debris production can be attributed to the winter, according to observations carried out in the preceding spring. Consequently, the total volume of deposition recorded on the hillside increased readily (on average 382 m^3 ± 18 per month), which overcomes significantly the rate of deposition recorded so far. Hillslope and gully erosion remain in average comparable to the volumetric transfer of sediment observed in the preceding autumn, implying however a clear connectivity. Hillside fan deposits generated by small tributary gullies were observed along low-order channel banks. They imply thus an effective hillslope-channel coupling, whereas local sediment budgets are dominated by a recharge of material.

2.6.3 Sediment recharge of the torrent

The sediment input back-calculated from the in-torrent storage changes coincides with the net sediment output recorded from the headwater for the first two survey periods. In the torrent, the morphological monitoring that started in July revealed quasi no recharge ($< 70\ m^3$) and is coherent with the observations made in summer in the upper catchment. The headwater sediment output must have accumulated before, probably mobilized as bedload by common runoff events in spring. In autumn, both budgets coincide (1018 $m^3 \pm 84$ against 904 $m^3 \pm 51$), considering that few segments between both entities are missing and that both budgets were in volumetric units, although different process density. The morphological budget indicates that the torrent experienced a net recharge in the distal part, suggesting that the upper reaches acted as an effective buffer to the transfer of sediment from the headwater. This enhanced debris supply in torrent results from the efficient transport of material from sediment sources areas and all along the sediment network components and emphasized the high linkage from the source zones to the torrent.

In the 3rd survey period, the headwater sediment balance indicates a net export of debris (1749 m^3 ± 199), whereas the morphological monitoring detected any significant volume of debris entering the torrent. Even the recharge measured during the June 2010 debris flow events remains far below the sediment input recorded upstream (< 600 m^3). This discrepancy may result from material deposition right in the non-monitored segments at the headwater outlet. But field study did not confirm any of such trace. The analysis of past series of sediment budgets performed in the upper Manival catchment (Veyrat-Charvillon, 2005) reveals that the spring – early summer time exhibits currently a period of recharge following a phase of purge within a short time lapse depending on the hydrometeorological and snow melt conditions. The most reasonable explanation results therefore in the long time interval between measurements, such as the successive reworking of bedload transport must have inhibited the cut and fill pattern, and masked the true sediment transfer operated in the torrent. This is a well-known issue when working with channelized hillslope processes (Fuller and Marden, 2009). Although this monitoring aspect concerns the topographic changes recorded by TLS in the headwater as well, geomorphic activity such as micro debris flows and continuous channel bed degradation strongly suggest a net sediment delivery toward the torrent that must have occurred before the debris flow event.

2.6.4 Possible causes of seasonal fluctuations in debris supply

Headwaters are currently underlined as being more sensitive to intense rainfall in terms of geomorphic activity (Veyrat-Charvillon, 2005; Brayshaw and Hassan, 2009) and therefore should be more sediment delivery responsive than higher-order channels. However, the Manival headwater experienced low geomorphic activity through the summer, and consequently low recharge of the torrent, although the occurrence of high intensity rainstorms competent enough to trigger debris flow of significant magnitude in torrent. Considerations of the temporal pattern of sediment transfer and the analysis of erosion features, like alternating areas of scouring and infilling in gullies, suggest that runoff still exerts an important role on the headwater sediment dynamics. A clear relation between sediment transfer magnitude and precipitation remains however complex (Fig. 2.20). The enhanced hillside geomorphic activity observed in several headwater subsystems, for instance during the autumn period, induced simultaneously a highly heterogeneous response in their channel reaches: a significant increase of bed incision and debris flow similar geomorphic reworking was observed in the upper reaches of the Manival subcatchment, implying an important sediment transfer. In contrast, the activity of other channel reaches, for instance in the Roche Ravine, was reduced by half. Considering that meteorological conditions were similar, this opposite behaviour can only be explained by a certain starvation of debris availability. During the entire preceding study period, the Roche Ravine stayed geomorphically much inactive. Only little sediment recharge was observed. In the consequence, the channel segments underwent sediment exhaustion at some point, implying a reduced sediment yield. Exhaustion comes not only within a supply-limited regime of the contributing area, but also from the fact that check dams, like bedrock dominated reaches, inhibit channel bed incision. Hence, the sediment storage has to be refilled either from the contributing hillside or from upstream mass movement. A similar observation can be drawn from the Grosse Pierre Ravine sediment budget, whose gully downslope remained completely disconnected from the head over the whole study period at least. Although this ravine is very steep and incises the rock avalanche deposits, no geomorphic work was observed, resulting most likely from the absence of debris supply from upstream. Hillside sediment delivery seems therefore to be clearly a limiting factor to sediment yield from low to high-order channels, and thus to the recharge rate of the debris flow torrent downstream. The Genièvre subsystem, which showed to be mostly inactive during the survey periods of 2009, displayed a large sediment transfer in spring 2010 until exhaustion. As the occurrence of bedload transport and micro debris flow is controlled predominantly by the availability of mobilizable sediment, numerous suitable meteorological conditions do not conduct systematically to a significant transfer of sediment from the hillside to low-order channels.

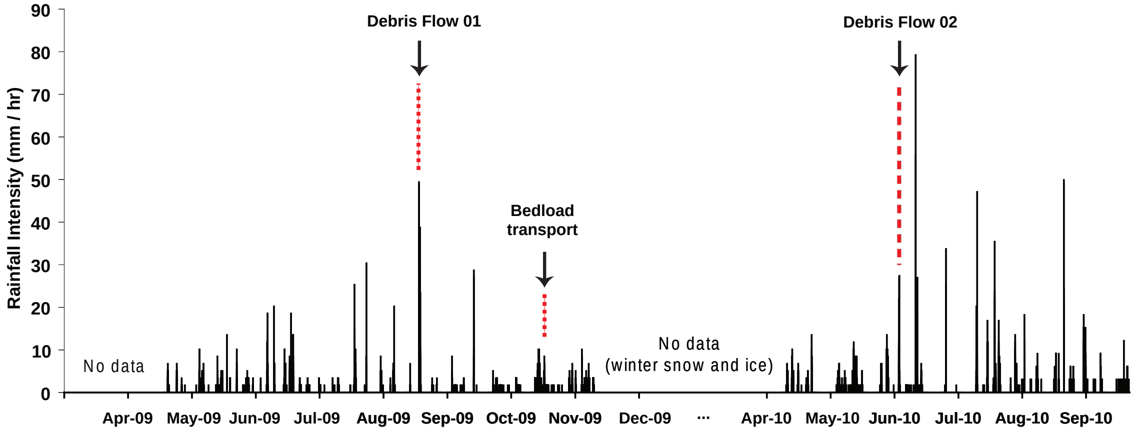

Figure 2.20: *Maximum rainfall intensity over the monitoring period measured by a rain gauge located at the top of the torrent (calculated for a 5 minutes time interval) (modified from Theule et al., 2012).*

2.6.5 The role of sediment source stability

The sediment delivery from the hillside was very low in summer, but increased significantly during autumn, meaning that debris storage was not depleted. This behaviour is somehow equivocal considering the fact that the transport capacity of ephemeral stream runoff and sheetwash related to high intensity rainstorms are larger than the one generated by low intensity – long duration rainfall, above all when gully material can be characterized as coarse and poorly sorted rockfall debris, like this is the case at Manival. The role of long lasting rainfall in sediment transfer can be related to the stability of the coarse surface layer armouring the gullies and scree slopes. Excess pore-fluid pressure in debris deposits can persist for days to weeks after sediment emplacement time (Major and Iverson, 1999; Major, 2000). One possible explanation is that the 25th August rainstorm dramatically altered the debris sources in a way that the autumn rainfalls, although of lower intensity but longer flood time, were able to transfer sediment downslope, for instance by saturating the debris deposits on the long term. This suggests though that periods of successive wetter meteorological conditions can enhance sediment transfer due to more unstable sediment sources.

The spatial pattern of geomorphic work recorded during the study showed that hillslope process activity was observed principally in gullies and scree slopes situated directly below active rock walls. Fresh rock deposits are as expected more easily destabilized than old compacted colluvium. This is supported by the rapid sediment exhaustion observed in rock couloirs of the Genièvre subcatchment for instance. The recurrent supply of fresh sediment seems especially prone to be transported downstream. Lenzi et al. (2003) for instance interpreted the annual fluctuation in sediment yield as the effect of sediment source destabilization or reactivation following a high magnitude flow event, which facilitates material entrainment by subsequent runoff. Johnson and Warburton (2006) refer to the influence of sediment source characteristics in the control of hillslope sediment discharge. These observations yield the impression that sediment source stability mentioned above affects the amount of debris supply from the hillside, despite flow capacity and sediment availability, and that fresh debris deposits are usually less stable geotechnically.

2.7 Conclusions

This investigaton of a yearly cycle of sediment dynamic evolving into a debris flow by evaluating sediment sources and transfer processes could underline that both debris flows displayed an identical behaviour in pre-event debris supply: phases of recharge preceded in time their occurrence, which could be of several months. The rate of sediment delivery recharging both hillside and low-order channels directly was essentially caused by high magnitude slope failures of low to moderate frequency and occurring mostly during winter time in particular areas of very limited extend. Consequently, material re-entrainment concentrates locally in specific scree-filled tributary gullies. As potential instabilities are widespread in the head walls (see Chapter 3), a substantial recharge is likely each winter. But the location and magnitude of sediment supply would be probably much different in a different year. During this study period, the seasonal cycle of sediment discharge from the headwater supplying the torrent with debris consisted of two phases of recharge:

1. in early spring, linked to runoff conditions and probably wet snow avalanches.
2. in autumn during long period of rainfall and wet meteorological conditions.

In the Manival, the response in terms of debris supply following the recharge period occurring in winter essentially seems therefore to be directly subordinated to the onset of a period of runoff derived from rainfall or snowmelt; debris availability is usually not a limiting factor. Conversely, the effect of intense summer rainstorms is limited by the fact that headwater subsystems follow a sediment supply-exhaustion-supply cycle as a corollary to the supply-limited model of debris flow initiation (Jakob et al., 2005; Glade, 2005). In the case of sediment depletion, as low-order channels are supply-limited, even a very competent rainstorm-derived runoff will not deliver sediment to the torrent. The time rate of exhaustion seems to be highly local, depending not only on debris availability but probably on geomorphological aspect (Mao et al., 2009). The sediment volume temporary accumulated in local topographic hollows depends on the degree of convergence and the slope gradient for instance (Reneau et al., 1990; Stock and Dietrich, 2006). And the state conditions of sediment sources stability in gullies and scree hollows in particular can influence sediment retention in the headwater. The destabilizing effect can be related to hydrometeorological conditions since the last rainstorm, rather than to the flow capacity directly. Globally, the torrent effectiveness seems to be controlled early in the season by sediment production and later in the season by the ability of the hydro-meteorological effects to weaken the remnant debris source. Low-order reaches contribute significantly to the sediment delivery mechanism of the catchment headwater by controlling the storage and routing of debris in the drainage system. Hence, the recharge threshold required for a new debris flow to occur depends primarily on the short-term debris supply, partly derived from the rate of sediment production through rockfall directly and partly derived from the availability of mobilizable debris on the hillside. The rate of sediment recharge in torrent is however greatly inconstant since production and entrainment are both highly stochastic processes. This regime of headwater sediment delivery may have been identified in other close mountainous environments, but little literature exists (Alvarez and Garcia-Ruiz, 2000; Veyrat-Charvillon and Memier, 2006; Berger et al., 2011, among others) that have explored in sufficient detail the time scale of sediment discharge on a seasonal basis.

Debris flow magnitudes have been mostly determined so far based on volume estimates derived from past events, reducing the susceptibility analysis to the known history. A monitoring of the in-storage changes in torrent linked to the debris supply can readily improve knowledge on recharge threshold leading to debris flow activity, and therefore their prediction. 10’000 m^3/yr of debris supplying the headwater channels can be expected at Manival over a century, according to the rock slope production observed in this study. Although the multiplicity of sediment sources and mode of transfer operating at different spatial and temporal scales, the pattern of processes governing the sediment dynamic can be considered precisely on a seasonal basis using TLS techniques. The maximum discharge that can initiate an extreme event that would mobilize the entire torrent storage could be specified. Without direct measurements of the rate of sediment flux and observations of the coupling between hillslope and channel processes, this cannot be rigorously determined. The timing of monitoring sediment budget in channels is however a crucial aspect for their interpretations.

Table 2.11: *Sediment budgets for all catchment subsystems revealed by comparing the successive TLS surveys operated over 16 months of monitoring. Each survey period is expressed separately in volumetric unit [m^3] with uncertainty.*

1^{st} monitoring period.

1^{st} MP	Col du Baure			Roche Ravine				Manival		Grosse Pierre		Genièvre[1]
	Gulliy Series		Baure Ravine	lower		upper						
	Hillside	Channel	Hillside	Hillside	Channel	Hillside	Channel	Hillside	Channel	Hillside	Channel	Hillside
Rockfall	1.9 ±0.1		25.5 ± 2.2	3.4 ±0.5		37.4 ±0.6		24.9 ±1.5		2.5 ± 0.5		3.8 ±0.5
Deposition	0.0 ±0.0	79.7 ±3.7	72.2 ± 2.4	10.0 ±1.2	69.4 ±7.2	0.0 ±0.0	0.0 ± 0.0	11.1 ±1.1	0.0 ± 0.0	309.2 ±30.1	0.0 ±0.0	5.8 ±0.7
Erosion	19.2 ±0.7	60.2 ±2.0	159.5 ±12.4	14.2 ±1.0	102.9 ±6.8	14.5 ±1.1	107.1 ±11.7	22.3 ±1.6	366.2 ±22.8	302.3 ±31.5	0.0 ±0.0	15.1 ±1.3
Subtotal	-2.1 ±0.7	-10.0 ±4.2	-103.4 ±12.8	-7.7 ±1.6	-51.0 ±9.9	-51.9 ±1.3	-107.1 ±11.7	-36.1 ±2.5	-366.2 ±22.8	-13.1 ±43.6	0.0 ±0.0	-13.1 ±1.5

2^{nd} monitoring period.

2^{nd} MP	Col du Baure			Roche Ravine				Manival		Grosse Pierre		Genièvre[1]
	Gulliy Series		Baure Ravine	lower		upper						
	Hillside	Channel	Hillside	Hillside	Channel	Hillside	Channel	Hillside	Channel	Hillside	Channel	Hillside
Rockfall	1.2 ±0.1		5.2 ±0.9	1.4 ±0.2		18.0 ±0.7		23.5 ± 0.9		0.0 ±0.0		1.2 ±0.2
Deposition	42.3 ±1.5	15.1 ±0.9	50.6 ±3.1	4.1 ±1.1	1.1 ±0.4	0.2 ±0.1	11.0 ±0.5	5.2 ± 0.6	100.0 ± 6.4	79.4 ±5.8	0.0 ±0.0	0.0 ±0.0
Erosion	76.9 ±2.7	39.4 ±1.0	112.5 ±6.8	95.0 ±4.7	0.6 ±0.3	9.0 ±0.5	39.6 ±2.2	270.0 ± 7.4	442.9 ±15.8	76.1 ±5.0	0.0 ±0.0	0.3 ±0.1
Subtotal	-44.8 ±3.1	-15.6 ±1.4	-60.9 ±7.5	-92.23 ±4.9	0.4 ±0.5	-26.8 ±0.8	-28.6 ±2.3	-278.3 ±61.1	-322.8 ±17.1	3.4 ±2.1	0.0 ±0.0	-1.5 ±0.2

3^{rd} monitoring period.

3^{rd} MP	Col du Baure			Roche Ravine				Manival		Grosse Pierre		Genièvre[1]
	Gulliy Series		Baure Ravine	lower		upper						
	Hillside	Channel	Hillside	Hillside	Channel	Hillside	Channel	Hillside	Channel	Hillside	Channel	Hillside
Rockfall	17.7 ±0.3		825.5 ±25.1	8.6 ± 1.2		256.6 ±17.2		2034.8 ±39.7		145.3 ± 2.5		116.3 ± 3.0
Deposition	148.6 ±1.5	3.2 ±0.3	1671.1 ±71.6	212.0 ±30.0	0.0 ±0.0	67.6 ± 4.8	147.9 ±18.2	515.9 ± 9.4	948.1 ±17.4	343.8 ±16.9	6.2 ±0.5	204.5 ±13.6
Erosion	58.5 ±2.3	97.1 ±3.5	453.3 ±33.2	274.8 ± 5.8	21.6 ±1.7	379.6 ±16.3	44.0 ± 3.4	196.1 ± 4.8	486.5 ±19.8	129.2 ± 4.7	1.7 ±0.2	450.1 ±13.7
Subtotal	72.4 ±2.8	-93.8 ±3.5	392.3 ±79.3	-91.5 ±30.6	-21.6 ±1.7	-558.7 ± 9.6	104.0 ±18.5	-1715.0 ±11.9	461.6 ±26.4	69.3 ±11.0	4.5 ±0.5	-361.8 ±19.6

[1] *The downstream reaches of the Genièvre first-order channel was not monitored, as they displayed barely any in-channel debris storage.*

Part II

Morphological implications and structural control of geomorphic process activity

Chapter 3

Morphological and structural analyses of a torrent catchment: implications for debris supply at channel heads

Abstract Debris supply and channel recharge rates inducing debris flows are implicitly linked to slope instabilities. Hence, the incorporation of terrain morphology and rock structures may be relevant to better understand sediment dynamics of debris flow prone catchments. In this chapter, rock and hill slope sediment processes of the Manival upper catchment are evaluated using DEM and field surveys by: a) a topographic classification in major morphological units and a morphological analysis per lithology, both based on the slope angle frequency distribution; b) a morphostructural analysis of topography performed at different spatial scales to extract the dominant joint sets; c) an identification of potential unstable slopes and their failure modes using kinematics and a susceptibility assessment of rock slope production considering the number of potential failures per unit area and weighted with simple geotechnics. The combination of morphological units and topographic observation extracted from shaded relief maps enable to characterize modes of geomorphic process activity such as debris production by rockfall or material reworking on hillslope. Results of the morphological and structural analysis were compared with sediment budgets collected over 16 months, especially with the rockfall inventory, to study their implications in geomorphic activity. Rockfall source areas, detected with either slope angle statistics or kinematics according to dominant structures, comprise more than 97% of recorded rockfall. Conversely, the density of potential plane failure was not able to deduce classes of susceptibility, neither from rockfall frequency nor size. The inventory is probably too short to represent a whole range of events encountered in the long term. However, the assumption that rock slope production may depend on the density of potential failure is supported by a clear correlation with the net balances of sediment budgets performed in headwater gullies. This global approach provides parameters that can be used as proxies for evaluating geomorphic process activity from DEM-based morphological elements and most influent rock mass structures. They enable to quantify degrees of susceptibility to rock mass wasting and contribute therefore to characterize rockfall activity and sediment flux dynamics of torrent systems at gully scale.

3.1 Introduction

Debris flows can transport large amounts of debris over geological time-scale (Benda and Dunne, 1987). The size of debris fans accumulated at the outlet of valley margins attests of the intensity of geomorphic process activity. Several investigation could demonstrate that bedrock landslides and progressive rock slope failures (rockfall) are a first-order control of hillslope erosion rate (Densmore et al., 1997; Shroder and Bishop, 1998; Hovius and Stark, 2006). From cursory field observations, mass-wasting processes leading to recharge debris-flow channels with debris (directly or indirectly) seem to be implicitly linked to the morphological and geological conditions prevailing at the source areas. Sediment production depends on one side from the lowering rate of local base levels (Davis, 1899; Hack, 1960): the valley slopes steepen, become progressively unstable and collapse, involving not only overlying sediment deposits but also the bedrock (Burbank et al., 1996). On the other side, debris production is controlled by lithologic and structural characteristics and their influence upon the local state of stress of topography (Sauchyn et al., 1998; Erismann and Abele, 2001; Cruden, 2003). Especially, the properties of joint sets and their geometry according to topography influence more the rock slope stability than the intrasic properties of the intact rock mass (Norrish and Wyllie, 1996; Rouiller et al., 1997). As well, tectonic deformation such as fold positions must be taken into account when considering rock slope stability (Coe and Harp, 2007). In the Swiss Alps, historical investigation have shown that periods of high debris flow frequency and magnitude result from intense rockslide events or rock avalanches of Mm^3 (Eisbacher and Clague, 1984; Bardou et al., 2003), highlighting the existence of two types of processes describing the forming of debris flows (Haeberli et al., 1991; Bardou and Jaboyedoff, 2008):

- *Continuous*, such that debris supply is linked to hillslope process activity in steady-state (or constant); mass-wasting behaves gradually and is related to weathering and rainfall intensity (climate-erosion relationship).
- *By pulse*, through the occurrence of high magnitude events of debris supply (e.g. bedrock landslides), which deviate from steady-state (extraordinary) sediment dynamics. This implies additional geological and structural predispositions.

In many catchments, both behaviours coexist. A threshold volume distinguishing one process to the other was assessed ranging around 5 x 10^4 m^3 to 7 x 10^4 m^3 for the western Swiss Alps (Bardou and Jaboyedoff, 2008).

Studies focusing on morphometric and topoclimate factors to enhance the understanding of processes governing mass-wasting and sediment flux are often limited by the small scale of investigation: topography, tectonic setting and climate are rather similar locally, whereas rates and mechanisms of sediment production can be very heterogeneous throughout adjacent subcatchments. According to the fact that rock slope instabilities strongly influence debris supply in both frequency and magnitude, incorporation of bedrock structures and terrain morphology may be relevant to study sediment budgets and debris flow hazard assessment at basin-scale. The interaction between surface processes and topographic landforms has been highlighted by decades of investigation on process geomorphology (e.g. Gilbert 1877; Carson and Kirkby, 1972; Roering et al., 2007). However, only little rigorous attention has been devoted so far to the geological and morphostructural aspect of a catchment to characterize geomorphic activity.

The present study attempts to document about debris production in the Manival catchment, a very active debris flow catchment of the Chartreuse Massif (northern French Alps). The approach bases on morphological and structural elements that can be extracted from digital elevation models (DEM) and improved with geological maps. Rates and mechanisms of debris production are characterized in terms of process-related landforms and susceptibility to slope failure according to the structural setting. They are used as proxies for evaluating terrain implications in the process of debris supply or for preliminary assessing potential zones of production.

3.2 Study site

Regional setting

The Chartreuse mountain range (Isère – France) belongs to the northern subalpine domain (helvetic) and corresponds to the Mesozoic cover of the external alpine crystalline belt (Fig. 3.1). This massif has formed in an alternation of marl and limestone ranging from upper Jurassic to early Cretaceous and embedded in layers of centimetric to decimetric thickness. It displays a structure of inclined folds from Miocene age containing important and continuous overthrust faults (thin-skin fold-and-thrust belt) in response to the northwestern – southeastern crustal shortening of the Alpine orogeny (Gidon, 1991). In the eastern part, the Chartreuse folding displays a relative great homogeneity. The fold geometry exhibits a succession of 5 major folds of equal amplitude, well-constrained around straight axes striking toward nord – south and plunging gently into the north (Fig. 3.2). A slightly discrepancy in axis orientations arises from very persistent thrust faults crossing the massif in a continuous way. Erosion has then deeply entrenched the folds, like in the Manival catchment, leaving a dissected relief with high rock walls.

Local setting

The Manival is a tributary catchment of the Grésivaudan valley located about 20 km northeast from Grenoble on the eastern border of the Chartreuse Massif (Fig. 3.1). The catchment covers an area of 3.7 km^2 from the top (1738 m a.s.l.) to the apex of the alluvial fan (500 m a.s.l.). The morphology displays a dissected topography made of series of rock walls and steep slopes mantled with scree deposits (Fig. 3.3). Towards the ridge, the slopes are made of massif (Tithonic) to stratified limestone (Kimmeridgien superior) interbedded by layers of marl (Kimmeridgien) in the lower parts (Fig. 3.4). Depending on the marl thickness, they form well-defined escarpments (Charollais et al., 1986). Below, the bedrock is composed of marly limestone from Sequanien age (Argovien-Kimmerigdien

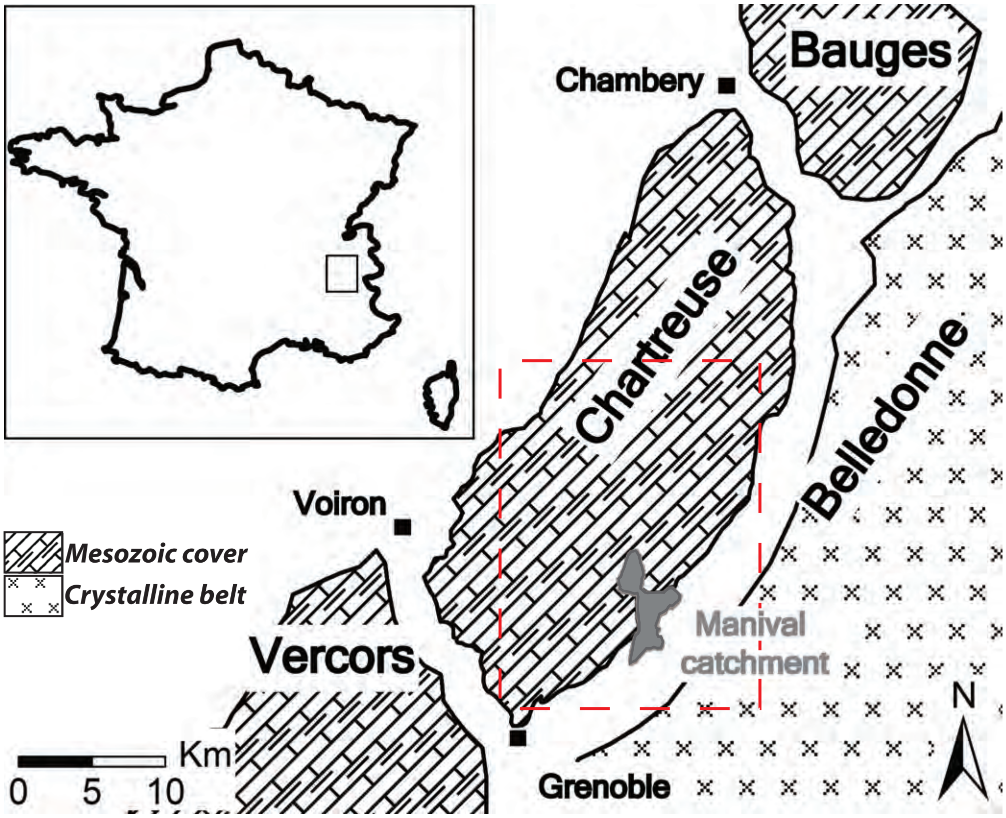

Figure 3.1: *Location of the Chartreuse Massif in the northern subalpine domain of the French Alps. The Manival catchment is displayed in light gray. The red dash line corresponds to the extent of the figure 3.2.*

stage limit). This lithology forms most of the steep rock slopes of the headwater and series of rock walls down the valley. The low-elevation hillslope and the valley-bottom exhibits calcareous marl of decimetric beds, alternating with marl from upper Argovien age. These lithologies are mostly covered by debris deposits, but form steep rock slopes in the upper catchment.

The valley has developped in an anticline where the hinge zone is cut by a system of two major thrusts that cut sidelong the axis of the valley (Fig. 3.3 and 3.4). It results a higher elevation of the western limb and the eastern limb is reversed, leading to an inclined fold. The fold axis is estimated to strikes N010-S190 and plunges 20° towards north based on the orientations of the bedding planes and using the Pi diagram method (Ramsay and Huber, 1987). Other minor faults exist, especially an inverse compressive fault in the top of the catchment (Fig. 3.4), probably ante- or syn-folding (Gidon, 1998). Those tectonic features and different lithologic properties have probably played a major role in the impressive headward entrenchment depth of the catchment.

The Manival torrent has built one of the largest alluvial fan surfaces from the french Alps made of torrential debris (Bénévent, 1915). The slope angle of the fan varies between 8% to 12%. Today, the erosion is still very active, but concentrated es-

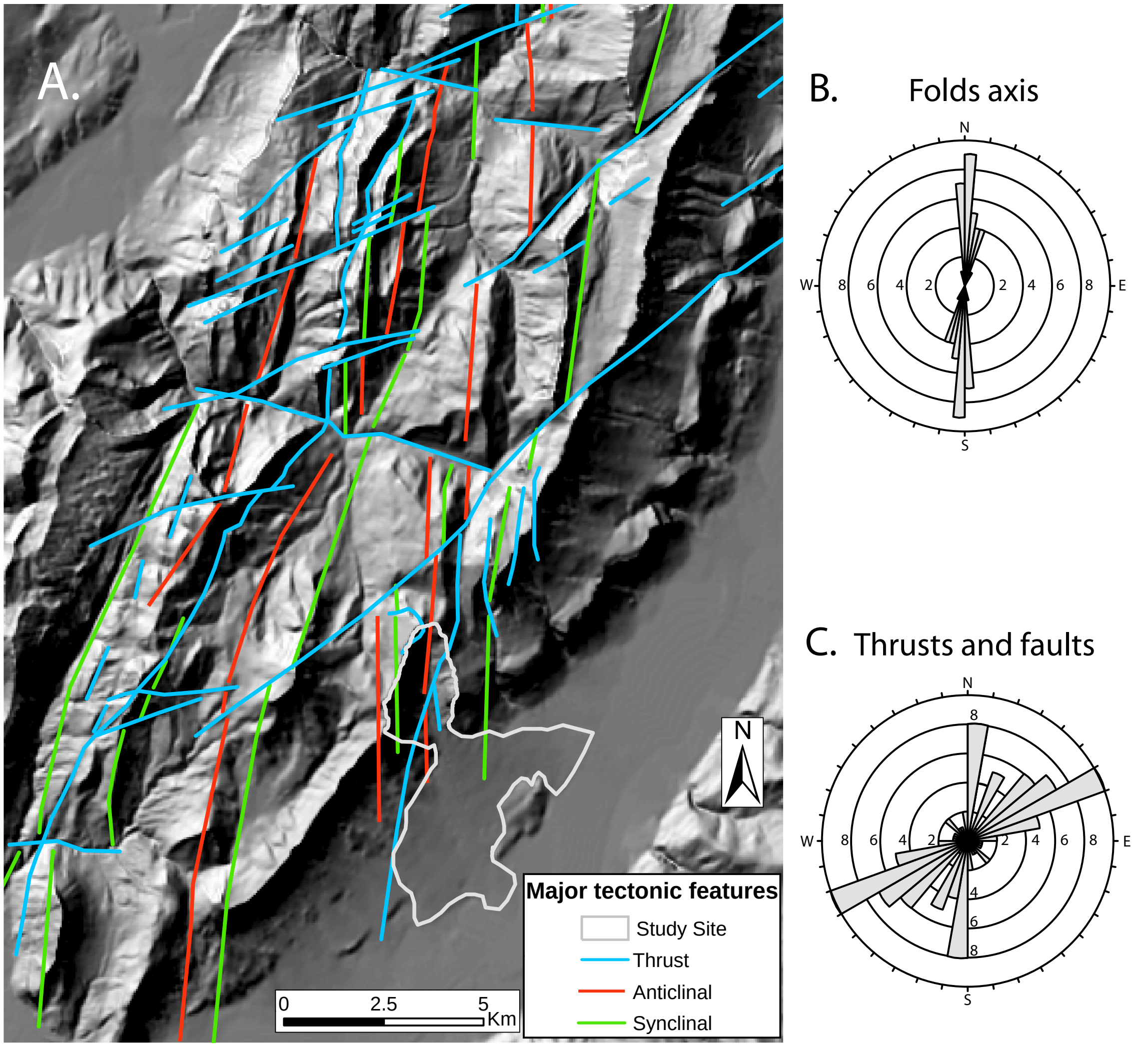

Figure 3.2: *(A) Major tectonic features of the eastern Chartreuse Massif displaying the geometry of the folds, faults and thrusts determined from shaded relief DEM analysis, geological maps and information from (Gidon, 1991). (B) Rosette projection of the axis geometry of the major folds and (C) apparent strikes of the major faults and thrusts showing the trend of deformation (mainly post-folding tectonic). The study area is regularly well-folded and tectonic deformations are relatively moderate.*

sentially in the upper catchment. Steep slope gradient coupled with low vegetation cover and permeability induce an important runoff as a response to heavy rainstorms that occur regularly due to enhanced convective cells. These are also responsible for interfluve sediment transport in the hillslope, for the erosion of screes covered slopes and ravines, for an important bedload transport along channels and for the initiation of debris flow in the torrent. The middle and down parts of the catchment, although quite steep as well, are well-vegetalized between rock walls. Hillslope process activity seems less intense and the contribution in terms of debris supply is reduced. Most of hillside gullies and debris slope deposits are not connected to the torrent at the moment.

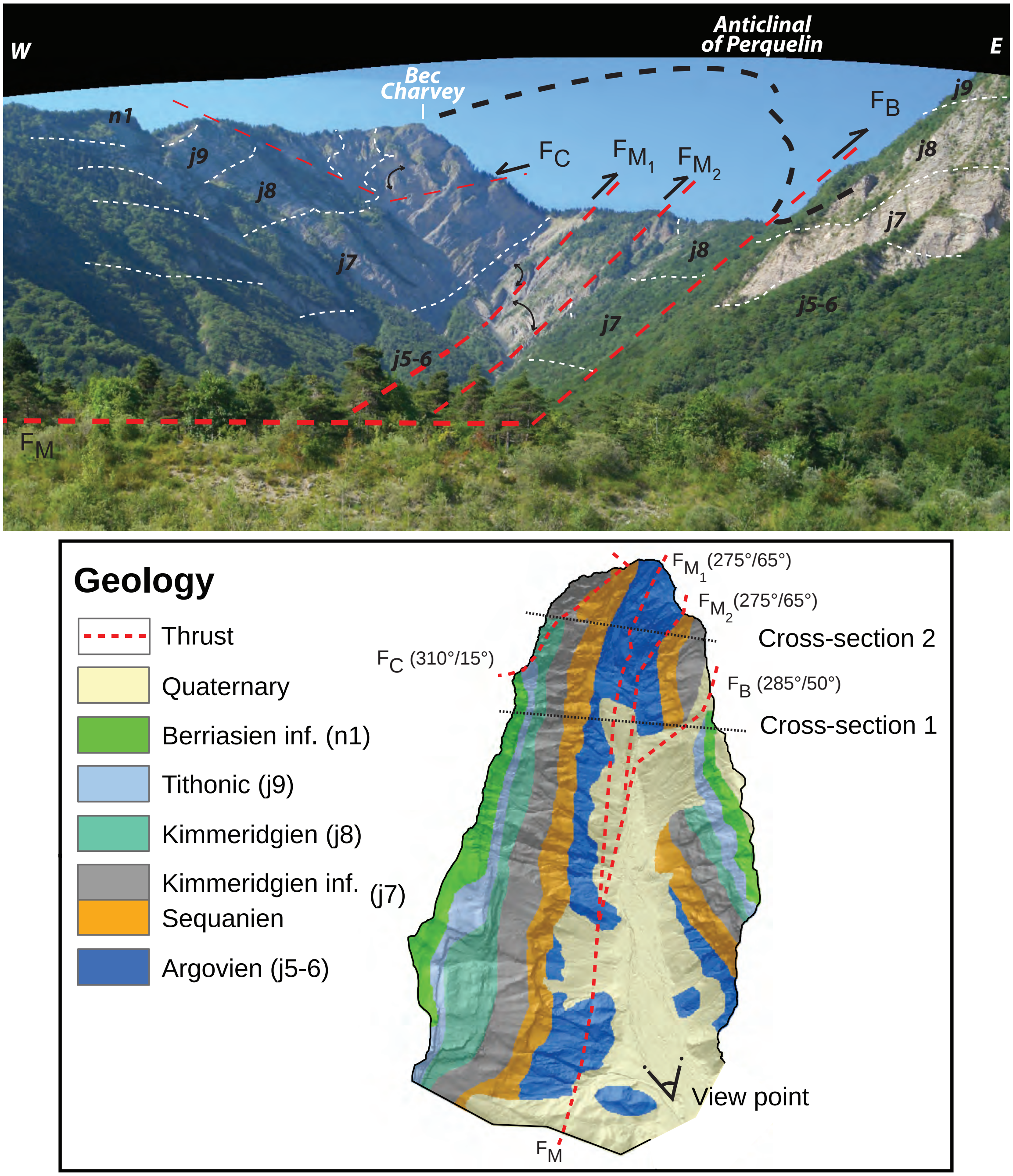

Figure 3.3: *(Above) Photograph of the study area taken from the view point showing lithology and faults; (Below) geological map of the Manival catchment (adapted from Charollais et al., 1986). The Manival thrust seems to split at least in two major fault planes (F_{M_1} and F_{M_2}) that may only be satellites of the Baure thrust (F_B). Note the impressive entrenchment of the headwater below the top peak representing a relief of 900 m. (Legend of the photograph modified after Gidon, 1998).*

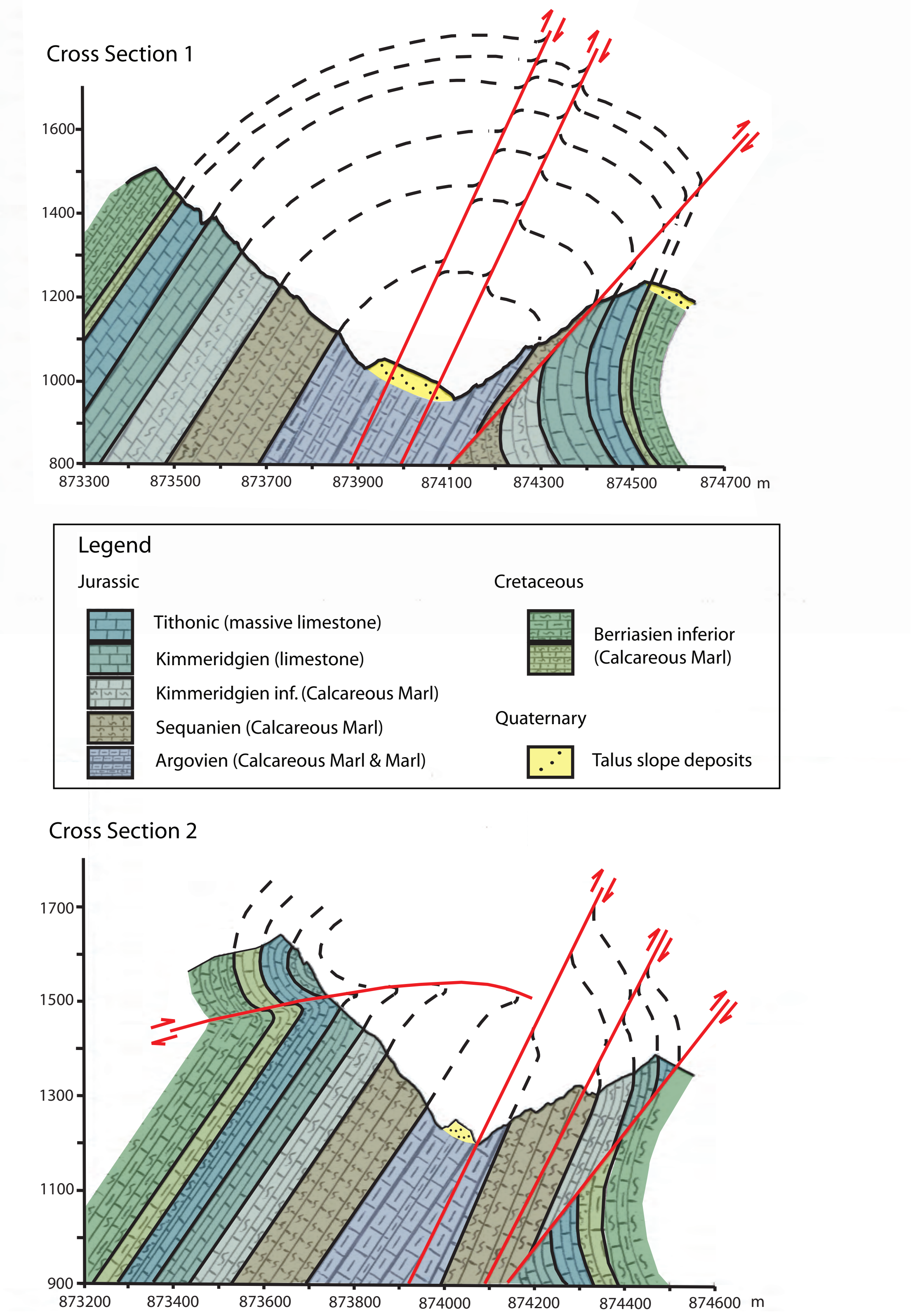

Figure 3.4: *Geological cross-sections drawn E-W through the catchment headwater (Fig. 3.3). Note in cross-section 2 the inverse compressive fault at the top west. This low angle fracture has the upper part reversely folded towards west. This thrust is as least as old as the folding (Gidon, 1998).*

3.3 Methods

3.3.1 General approach

The morphology of mountain topography reflects the compounded influence of geometrical and mechanical properties of the rock type (e.g. rock mass strength, cohesion), the stratigraphic (bedding) and tectonic aspect of the rock mass (folds, faults, joint sets) as well as the slope behaviour against mass wasting processes (Locat et al., 2000). Hence, a fine-scale representation of topography that enables the identification of dominant geological and morphological features can provide information on the nature and mode of geomorphic process activity. The characterization can be achieved using DEM within a GIS environment, for instance with a 3-D shaded relief map. The approach presented here consists of series of terrain-derived morphological and structural analyses based on observational investigation that incorporate at map scale information available in standard, high resolution DEM and high density point clouds performed with terrestrial laser scanner (TLS) surveys. This morphological information enable to interpret the role of major features of topography, such as the main structural sets shaping the slopes and the hillslope process characteristic shapes (e.g. Jaboyedoff et al., 2004; Jaboyedoff et al., 2006). This consists of:

1. a morphological investigation, through:
    - the creation of a classified map of slope steepness.
    - a slope angle frequency distribution analysis per lithology.
2. a structural analysis, through:
    - the detection and characterization of the most influencing joint sets in terms of rock mass conditions of stability.
3. a susceptibility assessment to rock slope failures:
    - based on the number of potential failures per unit area using kinematics and simple geotechnical parameters.

These parameters are then combined with other sources of information:

- with geological and structural data contained in geological map and field survey.
- with the geomorphic activity using aerial photo interpretation or field investigation.

in order to characterize debris production and the general modes of sediment dynamics.

3.3.2 Morphological study

Slope angle frequency distribution analysis

The slope angle is the most fundamental component of shear stress intensity upon mass (Selby, 1993). Hence, the topographic steepness is directly involved in rock slope stability and soil mass movement, such that surface processes are reflected in the slope angle derived from the morphology of geomorphic features. According to the Strahler's law of constancy of slopes (1950): "*the slope morphology of a local topography has the tendency to group closely around a mean slope angle value, implying that maximum slope angles (of a major topographic form) tend to be normally distributed with low dispersion around a local mean value determined by the combined factors of drainage density, relief and slope profile curvature*" (Fig. 3.5). Consequently, the predominant types of geomorphic features, such as torrential plain, debris fans, scree-slope deposits and rock walls in a mountain catchment, induce a range of distinctive slope angle values. Therefore, the analysis of the slope angle frequency distribution (SAFD) of a catchment enables to give prominence to several major morphological units characteristic of the topography. This classified map of slope steepness can be related to terrain morphology and enables a spatial analysis of dominant hillslope processes, such as area of debris production by rockfall and deposition in the form of debris fans, levees, terraces, etc. .

On the hillslope, soil creeping processes tend to dominate low slope angles, whereas landslides and other rock slope instabilities concentrate on higher slope angles (Densmore et al., 1997; Wolinsky and Pratson, 2005). These two dominant hillslope processes are separated in such way that only one set of slope angles declines once at a time. For instance, when sheet runoff operates, only creep and other fine material removal occur, contributing to decrease the set of low slope angles. The SAFD can therefore reflect the balance between weathering in weak rock or soil mass and mass wasting processes, such as rockfalls and rockslides. Several authors mention the SAFD of topography as the expression of a stage of erosional development (Carson and Kirkby, 1972; Montgomery, 2001; Korup et al., 2005). As a corollary, the SAFD of each lithology was analysed in this sense, according to the proportion of area lying above and below a certain slope angle.

3.3.3 Structural study

Detection of major discontinuity sets

The significance of geological structures on the stability of bedrock slopes has been demonstrated in the discipline of rock mechanics (Terzaghi, 1962; Hoek and Bray, 1981; Selby, 1982, among others). Studies that have focused on the structural control of erosion could show the link between structural geomorphic aspect and mass wasting (Rapp, 1960; Gerber and Scheidegger, 1973; Sauchyn and Gardner, 1983; Griffiths and Webb, 2004, among others). In order to evaluate the contribution of structures to rock slope instabilities responsible for debris and scree production across the catchment, the major discontinuity sets are identified based on the analysis of discontinuity surfaces contained

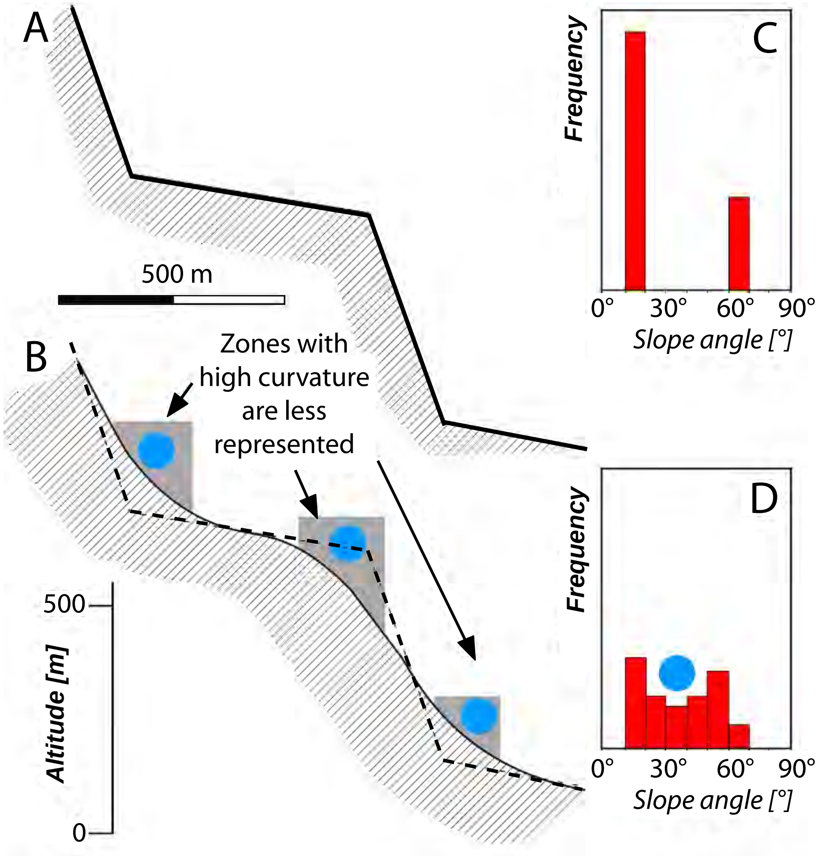

Figure 3.5: *Illustration of the Strahler's law of constancy of slope: (A) Ideal and (B) realistic sketch profile of an Alpine hillside valley representing two rock walls and two breaks of slope; (C/D) their respective slope angle distribution (modified from Rouiller et al., 1998). These two morphological features vary around a local maximum slope angle (20° for the breaks of slopes and 60° for the rock walls), leading to a bimodal distribution of the slope angles. More details can be found in Appendix D: Loye et al., 2009a.*

in the topography. Considering that topography of a bedrock dominated terrain is the expression of the structural setting, the sets of discontinuities (at least the most persistent ones) are reflected in the morphology of the landscape (Fig. 3.6). The structural characteristics can be therefore extracted from surface models (DEM, TLS point clouds) using GIS techniques. Depending on the degree of details, such approach of structural analysis provides a rather regional (using ALS-) or more local (using TLS-derived DEM) rock mass characterization (Fig. 3.6), and therefore defines the scale and the scope of the morphostructure interpretation (Jaboyedoff et al., 2009a).

Identification and susceptibility assessment of potential rockfall areas

Considering the spatial arrangement of joints in rock slopes, the confrontation between the structural sets and the topography according to kinematics represents a simple approach to localize potential instable slopes given a mode of failure (Fig. 3.7) (Wagner et al., 1998;

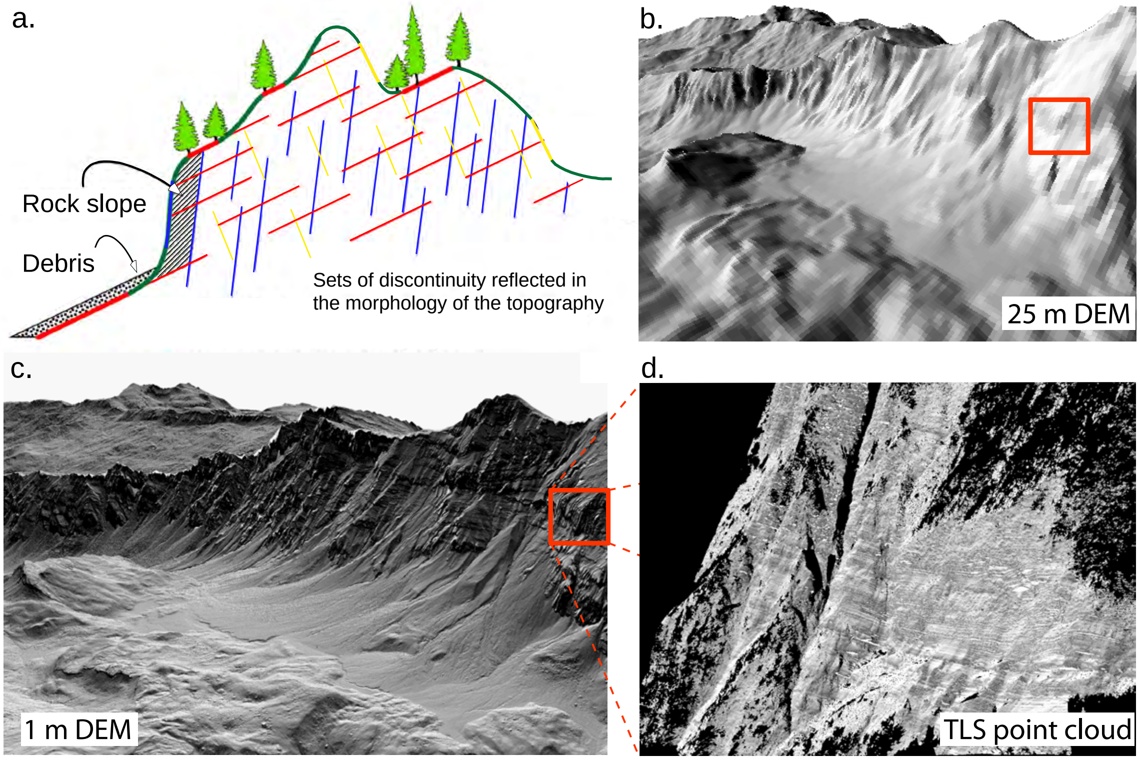

Figure 3.6: *(a) Illustration of sets of discontinuity reflected in the landscape morphology (modified from Baillifard, 2004) that can be extracted from an analysis of the topography using shaded-relief maps derived from standard DEM (b), airborne LiDAR DEM (c) or TLS point clouds (d).*

Gokceoglu et al., 2000; Günther et al., 2004). Hence, degrees of susceptibility to slope failure can be quantified by the number of potential failure mechanisms identified per surface area (InterregII, 2001). The susceptibility of each potential failure area can be also weighted by parameters derived from local slope conditions and lithology. For instances:

- the mechanical characteristics of joints
  (condition, roughness, filling, water saping)
- the properties of the rock mass
  (rock quality, rock strength, stress reduction factor)
- the outcropping location
  (proximity to a fault, seismic disturbance, permafrost)

Several rock mass classification systems exist, e.g. RQD (Deere and Miller, 1996); GSI (Hoek and Brown, 1997); RMR (Bienawski, 1973, 1989); SMR (Romana, 1985, 1993); RES (Mazzocola and Hudson, 1996); Matterocking (Rouiller et al., 1997), but require rock mass and slope property information that can hardly be obtained without accurate site investigation. As a willing to achieve the investigation on rock surface characteristics that can be deduced (more or less accurately) from DEM or TLS data, the density of potential failure mechanisms is combined with an assessment of the factor of safety (FS) using the conventional limit equilibrium analysis along distinct discontinuities, considering that the strength of potential sliding planes is determined by the Mohr-Coulomb failure criterion under dry conditions (Eberhardt, 2003). Another parameter used for the investigation is the number of joints encountered in the direction of topography (Jaboyedoff et al., 1996, see Chapter 4: Fig. 4.5), assuming that rock slopes prone to instability should be influenced by the orientation of the highest density of joints. The deduced susceptibility was compared to field observation to discuss whether the joint system extracted from morphostructural analyses can contribute to inform about rock slope production, and thus debris supply in the torrent system.

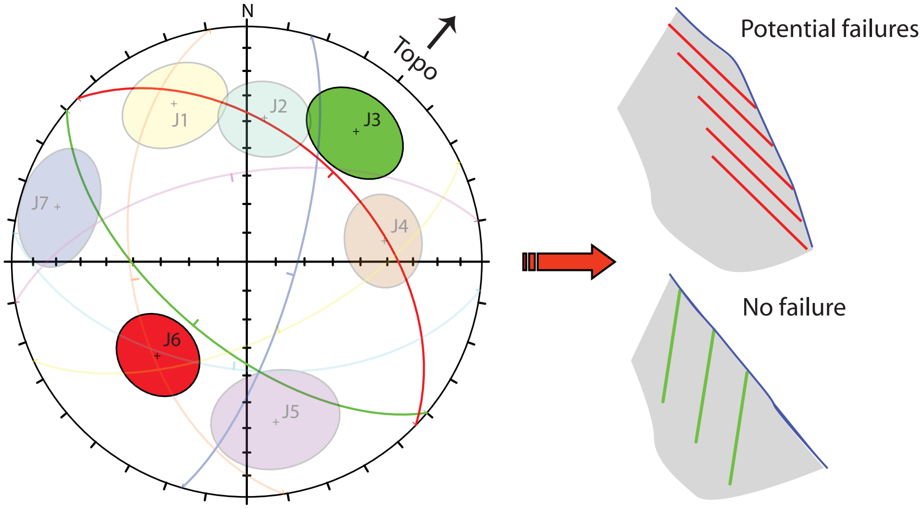

Figure 3.7: *Slope stability assessment for planar sliding using kinematics based on the confrontation of joint sets and topography derived from DEM. Planar sliding, wedge failure and toppling were considered in this study.*

3.4 Data processing

3.4.1 Classified map of slope steepness

The map of slope steepness was conducted on a LiDAR DEM of 1 m cell size derived from airborne survey of the entire catchment operated on the 1^{st} of June 2009. The slope angles are computed using a matrix of 3 x 3 DEM cells (Horn, 1981) and classified in 1° of angle. The class frequency is normalized considering their effective area of occurrence (see Appendix D: Loye et al., 2009a). The SAFD of the entire catchment is decomposed in several normal distributions using the freeware Histofit (2009), an Excel©-based application that computes in an iterative way the most likely series of Gaussian curves until their sum fits at best a target function represented here by the SAFD. The fitting process is done by minimizing the standard error using an optimisation procedure of the Excel© solver. The initial values are defined according to the shape of the SAFD, where local extrema can be identified visually. The morphological units are then delimited where a Gaussian curve representing a set of slope angles becomes dominant over the others. The SAFD of individual features was computed in the same way. The spatial distribution of scree-mantled slopes was extracted from the geomorphic process map (see Chapter 2: Fig. 2.3). The extents of the lithologies came from a modified geological map derived from the 1/50'000th map (Charollais et al., 1986) and adapted to the scale of the catchment with field observations.

3.4.2 Morphostructural analysis

The major discontinuity sets of the study area are identified using the software Coltop 3D (Jaboyedoff et al., 2007). Coltop 3D enables a detailed analysis of the discontinuities shaping the topography by representing the dip and dip direction of the slopes of a DEM with a unique colour code, the Hue saturation intensity system (HSI). The topography is displayed as a 3-D shaded relief map and the colour code is ranged in values of a Schmidt Lambert projection that enable stereographic interpretation (Fig. 3.8). The structural analysis was performed on point clouds derived from TLS (see Chapter 2), providing a 3-D representation of topography at a resolution ranging between 150 – 600 pts/m^2. Given this high resolution data, this approach enables to visualize the topography in a way closely similar to field survey. The orientation of the discontinuity planes are directly measured on the 3-D shaded relief map. A total of 14 structural stations homogeneously distributed in the upper catchment was carried out and their morphostructures were plotted in a stereonet. The morphostructural analysis was also performed over the entire catchment using the 1 m cell size DEM. When such analysis is based on airborne-based DEM acquisition, slopes with overhanging structures cannot be detected. They can be identified, however, in other parts of the slopes where they outcrop. The analysis was extended to the surrounding eastern Chartreuse Massif using a DEM of 50 m grid cell size (BD ALTI®–IGN). Despite the rough DEM resolution, this could inform about the regional structural geometry and document on the major discontinuity sets involved regionally in the shaping of the massif.

3.4.3 Areas of potential rock slope failure (using kinematic tests)

The identification of potential unstable slopes according to the geometrical characteristics of joint sets and the topography is performed with the software Materrocking (Jaboyedoff et al., 2004). This GIS tool enables to assess potential plane and wedge failure areas on DEM following conventional kinematic tests (Markland, 1972) (Fig. 3.9). Toppling is not implemented in Matterocking. This mode of failure is computed using a common GIS environment following the geometric criterion described in the Slope Mass Rating System (Romana, 1993). For each discontinuity j and a facet of topography f_j:

$$(Azimut_j + 180°) + 20° > Azimut_{f_j} > (Azimut_j + 180°) - 20° \tag{3.1}$$

$$Slope\,angle_{f_j} + Slope\,angle_j \geq 120° \tag{3.2}$$

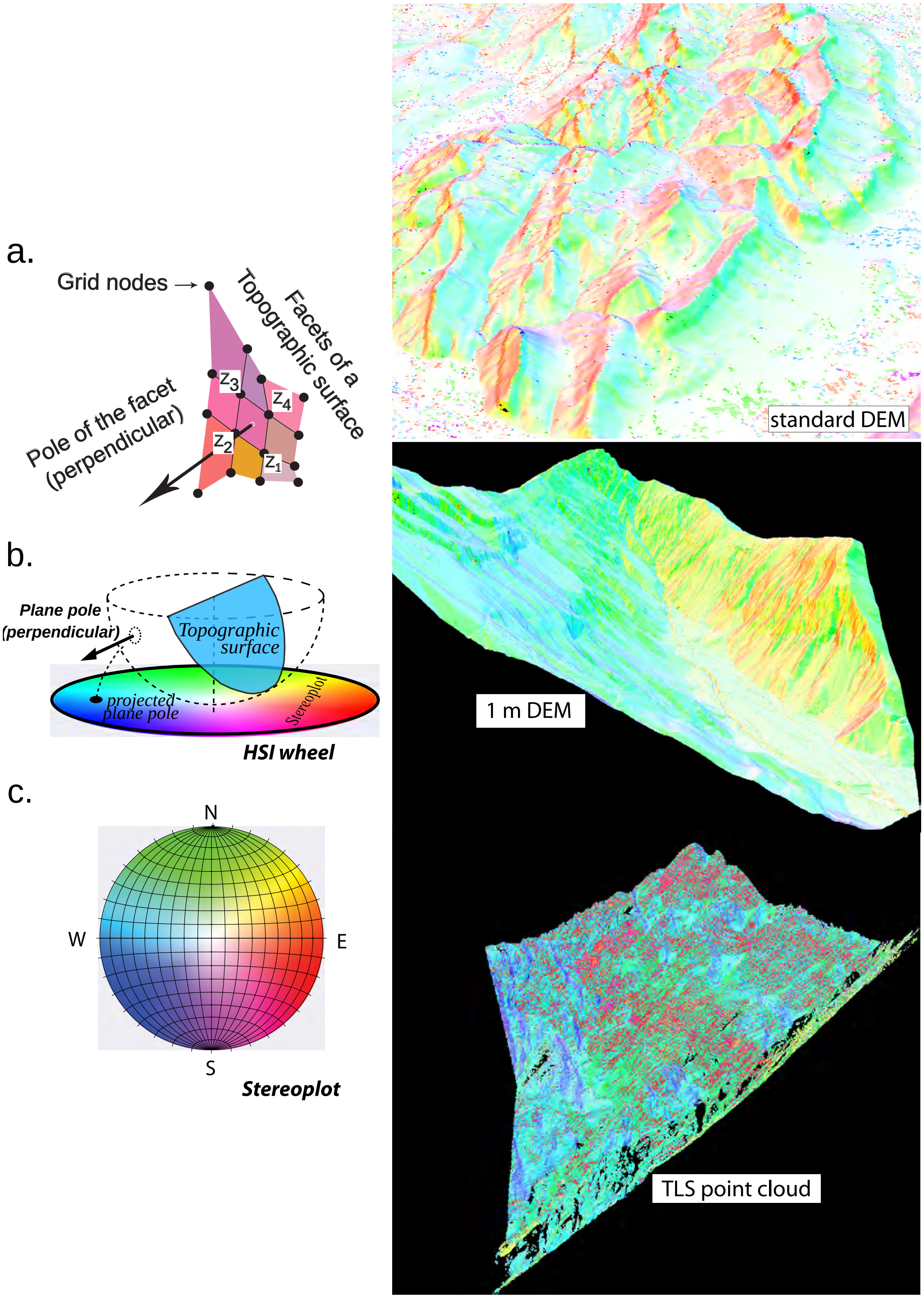

Figure 3.8: *(Left) The COLTOP 3D concept: computation of the orientation (slope angle and aspect) of a facet of DEM/TLS point cloud (a) and relation between the HSI wheel color code (b) and the Schmidt-Lambert projection for stereographic interpretation of the discontinuity surfaces (c). (Right) Representation of a standard DEM, airborne LiDAR DEM of 1 m cell size and point cloud-derived TLS with the COLTOP 3D software.*

All discontinuities were processed according to their mean dip and dip direction and the LiDAR DEM of 1 m cell size was used to represent the topography. After analysis, wedges with plunge axes lower than 15° were considered as marginally potential and were not further taken into account.

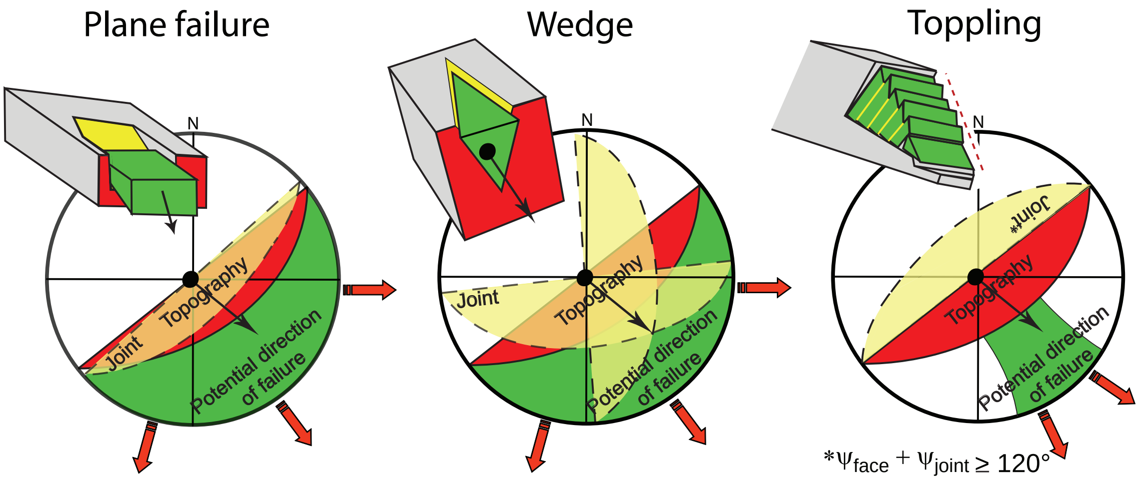

Figure 3.9: *Kinematic rules applied in the software Matterocking: the requirement for potential plane and wedge failure is that the dip angle of the joint, respectively the intersection line of joints (wedge axis) has to be lower than the one of the topography (in the direction where sliding is possible). Toppling is not handled in Matterocking, although this is possible through plane failure module, and was performed as illustrated here with other GIS tools (see details in text). (Drawings modified from Jaboyedoff et al., 2004).*

3.4.4 Susceptibility assessment to rock slope failure

Matterrocking also provides the average number of potential failure mechanisms per unit surface according to a given spacing and joint persistence. For each facet of topography of area A_i, each discontinuity featuring a potential failure plane represents an area A (in section view) defined by the trace length T (persistence) and the distance L with the next discontinuity (spacing), such that (Fig. 3.10):

$$A = L \times T \tag{3.3}$$

The projection of this section on a facet of topography gives an apparent section of area A':

$$A' = \frac{A}{\sin(\alpha)} \tag{3.4}$$

where α is the angle between the discontinuity and the facet. Hence, the number of potential plane failures n_p contained in the facet can be calculated as:

$$n_p = \frac{A_i}{\frac{A}{\sin(\alpha)}} \tag{3.5}$$

The number of potential topplings n_t per facet of topography is calculated in a similar way. As wedges are defined by two discontinuity sets, the number of wedges n_w in a facet perpendicular to the line of intersection of the wedge would be (assuming $T = \infty$):

$$n_w = \frac{A_i}{\frac{L_1 \times L_2}{sin(\gamma)}} \tag{3.6}$$

where L_1 and L_2 are the respective spacing of the discontinuities and γ the angle of wedge. When the facet is not perpendicular, the wedge area is only apparent and must be corrected, such that:

$$n_w = \frac{A_i \times cos(\beta)}{\frac{L_1 \times L_2}{sin(\gamma)}} \tag{3.7}$$

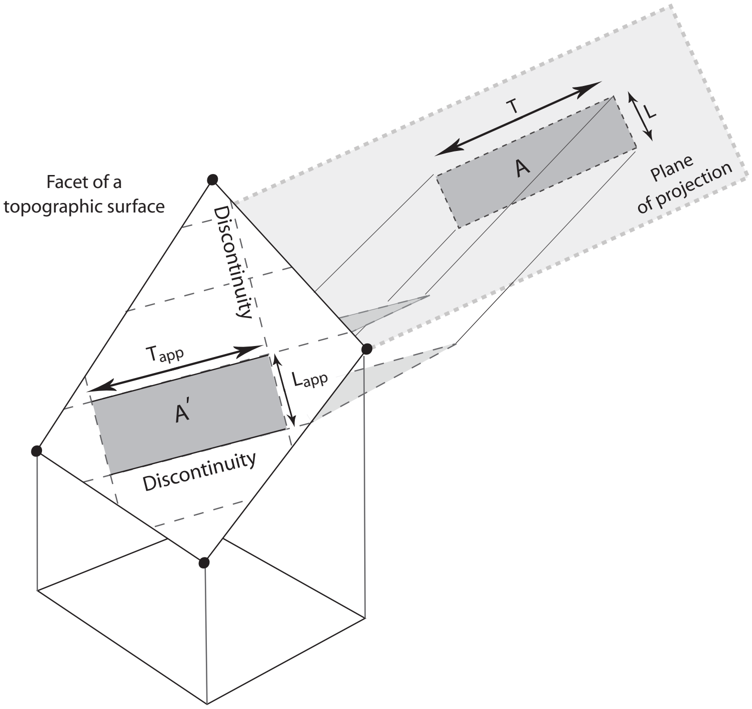

Figure 3.10: *Definition of the number of discontinuity crossing a topographic facet: A = area made by two discontinuities of spacing L and persistence T. A' = apparent A. The plane of projection is defined as perpendicular to the discontinuity greatest slope. See text for details on the different failure modes (modified from Jaboyedoff et al., 2004).*

where β is the angle between the intersection line of the wedge and the pole of the facet. The analysis of susceptibility to rock slope failures was performed in three different ways:

1. The number of potential failures n is determined for all joints j_i assuming an arbitrary spacing of 1 m (corresponding to the DEM resolution). The total density of failure N_U is obtained by summing up all joints and failure modes on a cell-by-cell basis:

$$N_U = \sum_{j_{i=1}}^{k} (n_{p_{j_i}} + n_{w_{j_i}} + n_{t_{j_i}}), \quad \text{with } j_i \text{ of uniform spacing} \tag{3.8}$$

2. The joint spacings are set proportional to each other (Tab. 3.1) based on measurements collected from scan lines in the field (Wyllie and Mah, 2004) and on an estimation defined with the sampling window approach (see Chapter 4: Fig. 4.5). There results to a density of failure N_S with relative true spacings in rock mass:

$$N_S = \sum_{j_i=1}^{k} (n_{p_{j_i}} + n_{w_{j_i}} + n_{t_{j_i}}), \quad \text{with } j_i \text{ of relative spacing} \tag{3.9}$$

Table 3.1: *Factors of proportionality between all joint spacings deduced from mean joint spacings estimated from the sampling window approach on TSL data and from scan lines performed on the field. Bedding plane S0 was set to minimum as suggested by field data, although the mean spacing defined with the sampling window suggests to be more spaced out in comparison to the other joints. Depending on TLS data and slope orientations, tight spacings are hardly detectable with precision.*

Joint set	Mean spacing [m]		Factor of
	Sampling window	Field data[1]	Proportionality
J1	6.1	0.23	1.5
J2	5.4	0.3	1.5
J3	3.7		1
S0	8.7	0.18	1
J5	7.6		2
J6	15.1	0.45	4
J7	4.1	0.15	1

[1] blank = nodata

3. The number of potential failures per unit cell is weighted by two geotechnical parameters:

    (a) The factor of safety (FS) that emphasizes slopes potentially unstable against the ones potentially stable (Tab. 3.2). For plane and wedge failure, this is determined after the Mohr-Coulomb failure criterion, assuming a null cohesive strength of the failure surface (Norrish and Wyllie, 1996). A FS for toppling can be computed for an arbitrary block b/h of base b and height h assuming that direct toppling occurs when the center of gravity of the discrete block lies outside the outline of the base of the block (Wyllie and Mah, 2004). However, both toppling and/or sliding must be considered on an inclined plane (Hoek and Bray, 1981), which make the computation more complex on DEM. The number of potential toppling presented in this chapter was therefore not weighted with a FS.

    (b) The maximum number of joints m encountered in the direction of the facet as an index of structural weakness of the rock mass (see Chapter 4).

Table 3.2: *Factor of safety computation using limit equilibrium analysis under dry conditions (Norrish and Wyllie, 1996) (See text for toppling).*

Type of failure	FS	Parameters
Plane	$\frac{\tan(\phi)}{\tan(\beta)}$	$\phi = 30°$; $\beta =$ dip of the failure plane
Wedge	$\kappa \cdot \frac{\tan(\phi)}{\tan(\beta_w)}$	$\phi = 30°$; $\kappa =$ wedge factor; $\beta_w =$ plunge of the wedge axis
Toppling	$\frac{b}{h} \cdot \frac{1}{\tan(\psi_b - 10°)}$	h = $\sqrt{3}$; b = 1m (Δx); $\psi_b =$ dip of the basal plane (= $90 - \psi_t$)

The weighted density of failure N_{WS} comprising all joints j_i of relative spacing is therefore expressed for each cell of DEM as:

$$N_{WS} = \left[\frac{\sum_{j_i=1}^{k} n_{p_{j_i}}}{FS_{plane}} + \frac{\sum_{j_i=1}^{k} n_{w_{j_i}}}{FS_{wegde}} + \frac{\sum_{j_i=1}^{k} n_{t_{j_i}}}{FS_{toppling}} \right] \times m \tag{3.10}$$

Finally, the degree of susceptibility of a given area is defined by summing up the susceptibility attributed for each DEM cell comprised in this area. The sets of joints extracted from the Coltop 3D analysis using TLS point clouds were used for the susceptibility assessment.

3.5 Results

3.5.1 Identification of the morphological units

The decomposition of the SAFD with the tool Histofit was achieved using 5 normal distributions (Fig. 3.11). Several initial values were tested, which yield to similar normal curve patterns for most of the cases. The sum of the normal curves reproduces the SAFD of the Manival topography with a coefficient of determination close to 1, meaning that the morphology is clearly constrained. Threshold slope angles delimiting the sets of slope steepness are summarized in Table 3.3. Overlying this classified map of slope steepness on the shaded relief map (Fig. 3.12) enables to identify 4 morphological units:

1. The lowest set corresponds to the *torrential flood plain*. This range of slope angles delineates the valley-bottom full of sediment deposited by torrential floods.
2. The 2^{nd} set of slope steepness displays *hillside debris fans* deposited at the outlet of tributary gullies and *bottom-slope deposits* located at the margin of the torrential flood plain.

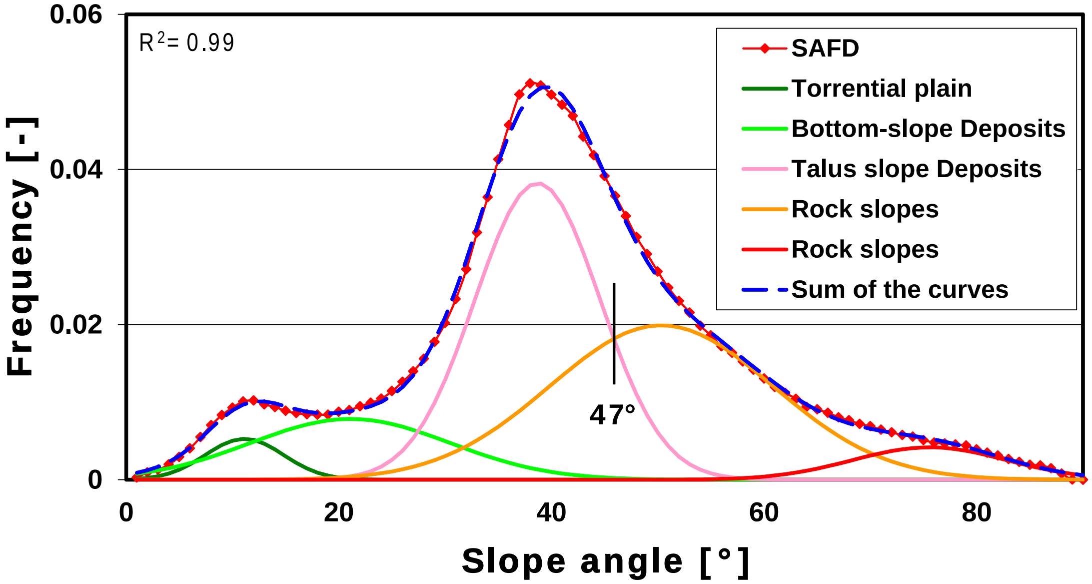

Figure 3.11: *Slope angle frequency distribution (SAFD) of the Manival catchment and decomposition in major morphological units (Tab. 3.3) using Gaussian curves. 47° is the threshold slope angle above which the topography is considered as outcropping bedrock and rock slopes prone to rockfall.*

3. The 3^{rd} range of slope angles encompasses *talus slope deposits* lightly covered with vegetation and *scree-mantled slopes*. They are located both down- and up-slope from rock walls.

4. The steepest sets delineate *rock walls, escarpments and steep outcropping bedrock slopes*. Two sets of Gaussian curves were input for a better fitting of the SAFD.

The SAFD of scree-mantled slopes derived from field mapping and the SAFDs of each lithology are given in Figure 3.13. The curve of the scree slopes approaches standard normal distribution with a mode of 35°, but deviates over a slope angle below 20°. About the lithologies, except of the Tithonic formation, all distributions are rather positively skewed. They can be characterized by a very steep increase of the limb to the highest frequency values and exhibit a large proportion of slope above their peak slope angle value.

3.5.2 Structural analysis performed in the field

Field survey could identify the presence of 5 discontinuity sets (Fig. 3.14). In the west side to the top of the catchment, the outcropping rock slopes display thick and low-weathered anaclinal beds with well-defined joints and planar structures. The structural pattern can be clearly measured. In the opposite side of the valley, the rock mass is highly weathered creating closely-spaced discontinuities that increase rock mass fragmentation. Consequently,

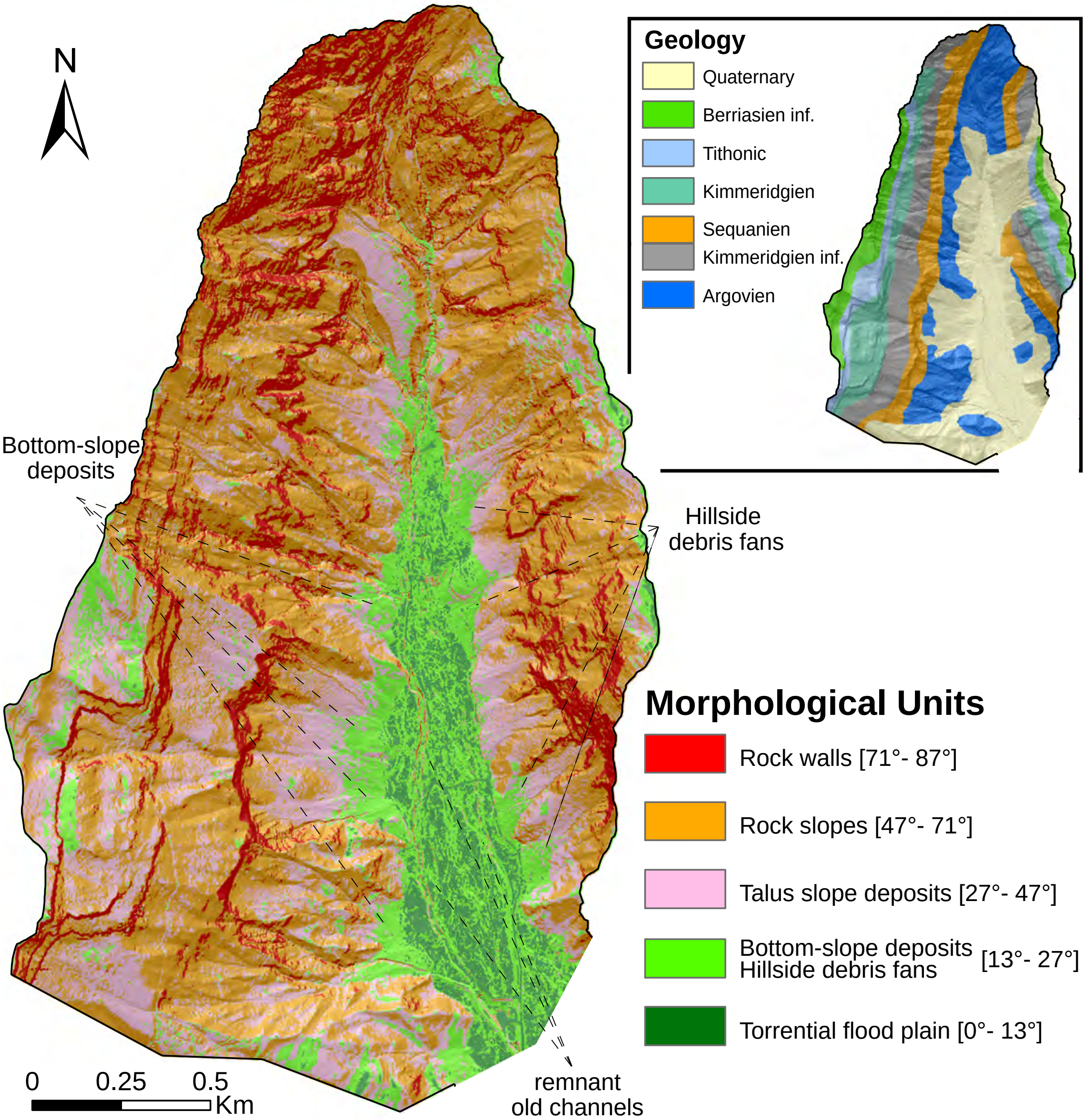

Figure 3.12: *Classified map of slope steepness highlighting the major morphological units. Note the rugged torrential plain and the remnant old channels, the hillside debris fan on the east side and the bottom-slope deposits and the west side of the valley.*

the typical bed-shape of marl and limestone alternation is identified with more difficulties since the structures are easily dislocated at the surface and mostly recovered with debris. Moreover, relevant outcrops are very difficult to access. Nevertheless, discontinuity sets J1, J2 and J6 were observed in all locations where structural field measurements were performed. Their orientations are similar, except for J1 that displays a large dispersion. The bedding plane shows constant dip direction, but the dip angle varies from 20° to 50° between stations. Discontinuity J7 was only detected in the structural field stations located on the rising limb of the fold (location 1 and 2). Globally, joints contained within limestone propagated between beds such that they show to be at least of low (1 – 3 m)

Table 3.3: *Threshold slope angles deduced from the SAFD analysis that define the morphological units.*

Threshold slope angle		Morphological units
Range	Mode	
0° – 13°	11°	Torrential plain
13° – 27°	21°	Hillside debris fans / Bottom-slope deposits
27° – 47°	37°	Talus slope deposits
47° – 87°	72°	Outcropping bedrock / Rock faces

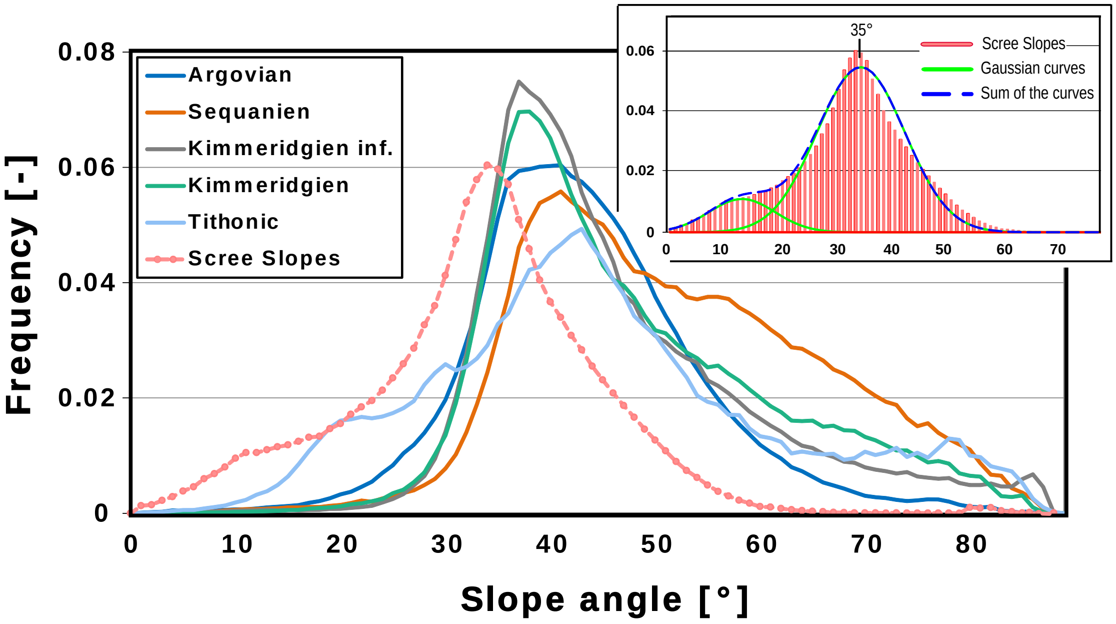

Figure 3.13: *Individual SAFDs of the morphological feature Scree-mantled slopes derived from field mapping (see Chapter 2: Fig. 2.3) and of each lithology. Note that the curve of the scree slopes approaches standard normal distribution with a mode = 35° and deviates over a slope angle below 20°.*

to medium (3 – 10 m persistence (ISMR, 1978)). In lithology dominated by marl, joint propagation between bed contact exists as well, but is more difficult to follow over a certain distance. Within a location of structural field measurement, the pattern of joints does not differ much from one bed to the next.

3.5.3 Structural analyses using COLTOP 3D:

Applied to TLS data

The structural analysis of the upper Manival catchment performed at the scale of the outcrop with COLTOP 3D on TLS point clouds could identify 8 major topographic planes

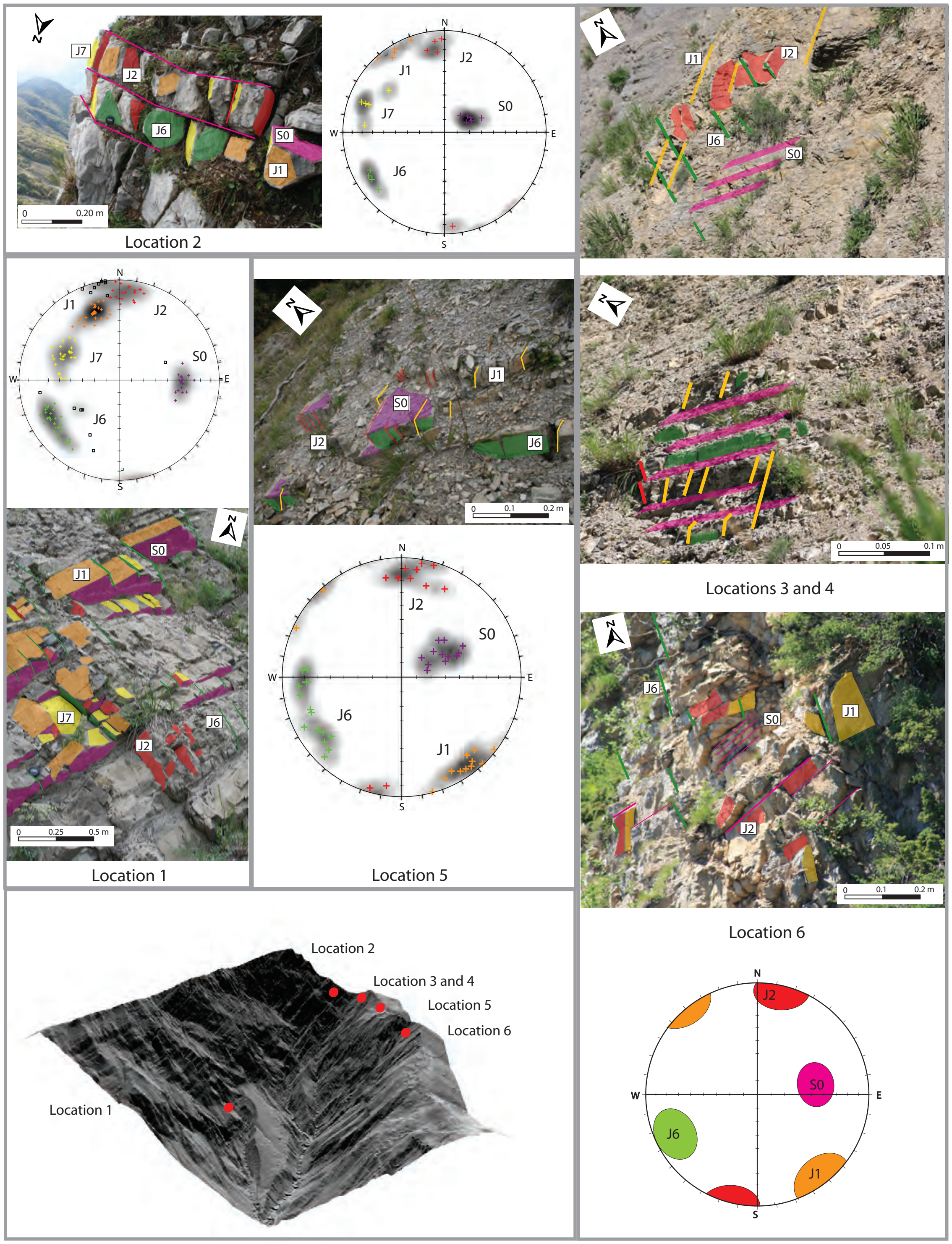

Figure 3.14: *Field illustration and stereoplot projections of structural data measured in the field. Outcrops with well-defined structures are difficult of access in the upper Manival catchment, reason why the locations of structural field measurements are mostly located on the ridge.*

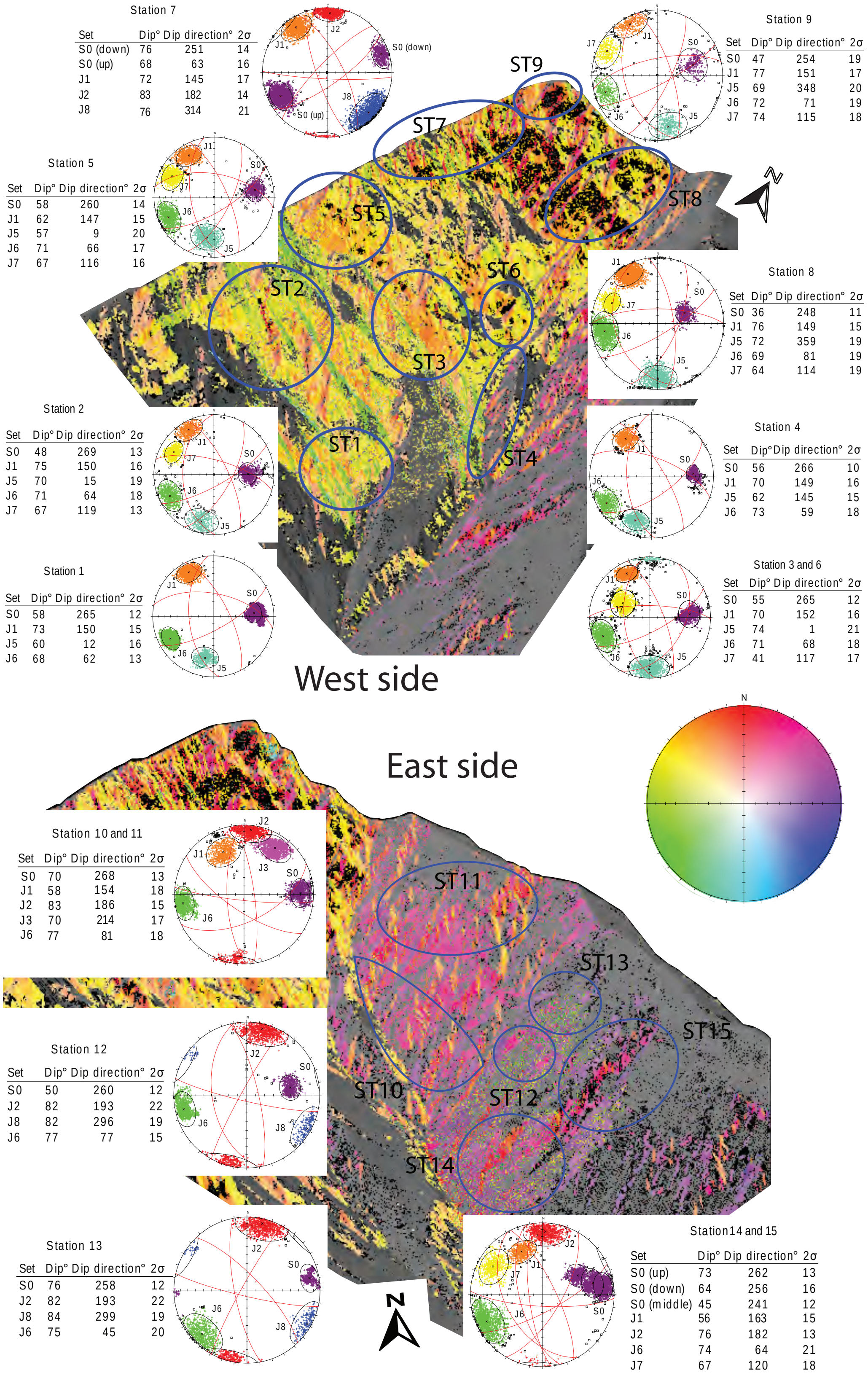

Station 7

Set	Dip°	Dip direction°	2σ
S0 (down)	76	251	14
S0 (up)	68	63	16
J1	72	145	17
J2	83	182	14
J8	76	314	21

Station 9

Set	Dip°	Dip direction°	2σ
S0	47	254	19
J1	77	151	17
J5	69	348	20
J6	72	71	19
J7	74	115	18

Station 5

Set	Dip°	Dip direction°	2σ
S0	58	260	14
J1	62	147	15
J5	57	9	20
J6	71	66	17
J7	67	116	16

Station 8

Set	Dip°	Dip direction°	2σ
S0	36	248	11
J1	76	149	15
J5	72	359	19
J6	69	81	19
J7	64	114	19

Station 2

Set	Dip°	Dip direction°	2σ
S0	48	269	13
J1	75	150	16
J5	70	15	19
J6	71	64	18
J7	67	119	13

Station 4

Set	Dip°	Dip direction°	2σ
S0	56	266	10
J1	70	149	16
J5	62	145	15
J6	73	59	18

Station 1

Set	Dip°	Dip direction°	2σ
S0	58	265	12
J1	73	150	15
J5	60	12	16
J6	68	62	13

Station 3 and 6

Set	Dip°	Dip direction°	2σ
S0	55	265	12
J1	70	152	16
J5	74	1	21
J6	71	68	18
J7	41	117	17

Station 10 and 11

Set	Dip°	Dip direction°	2σ
S0	70	268	13
J1	58	154	18
J2	83	186	15
J3	70	214	17
J6	77	81	18

Station 12

Set	Dip°	Dip direction°	2σ
S0	50	260	12
J2	82	193	22
J8	82	296	19
J6	77	77	15

Station 13

Set	Dip°	Dip direction°	2σ
S0	76	258	12
J2	82	193	22
J8	84	299	19
J6	75	45	20

Station14 and 15

Set	Dip°	Dip direction°	2σ
S0 (up)	73	262	13
S0 (down)	64	256	16
S0 (middle)	45	241	12
J1	56	163	15
J2	76	182	13
J6	74	64	21
J7	67	120	18

Figure 3.15: *Stereoplot projections of the discontinuity sets extracted from TLS data using COLTOP 3D in the sampling stations (ST) of the west and east side of the upper Manival catchment. The black circles represent a variability of orientation of 2σ and the values are given in the side tables. The blue circles delineate the extent of the sampling stations.*

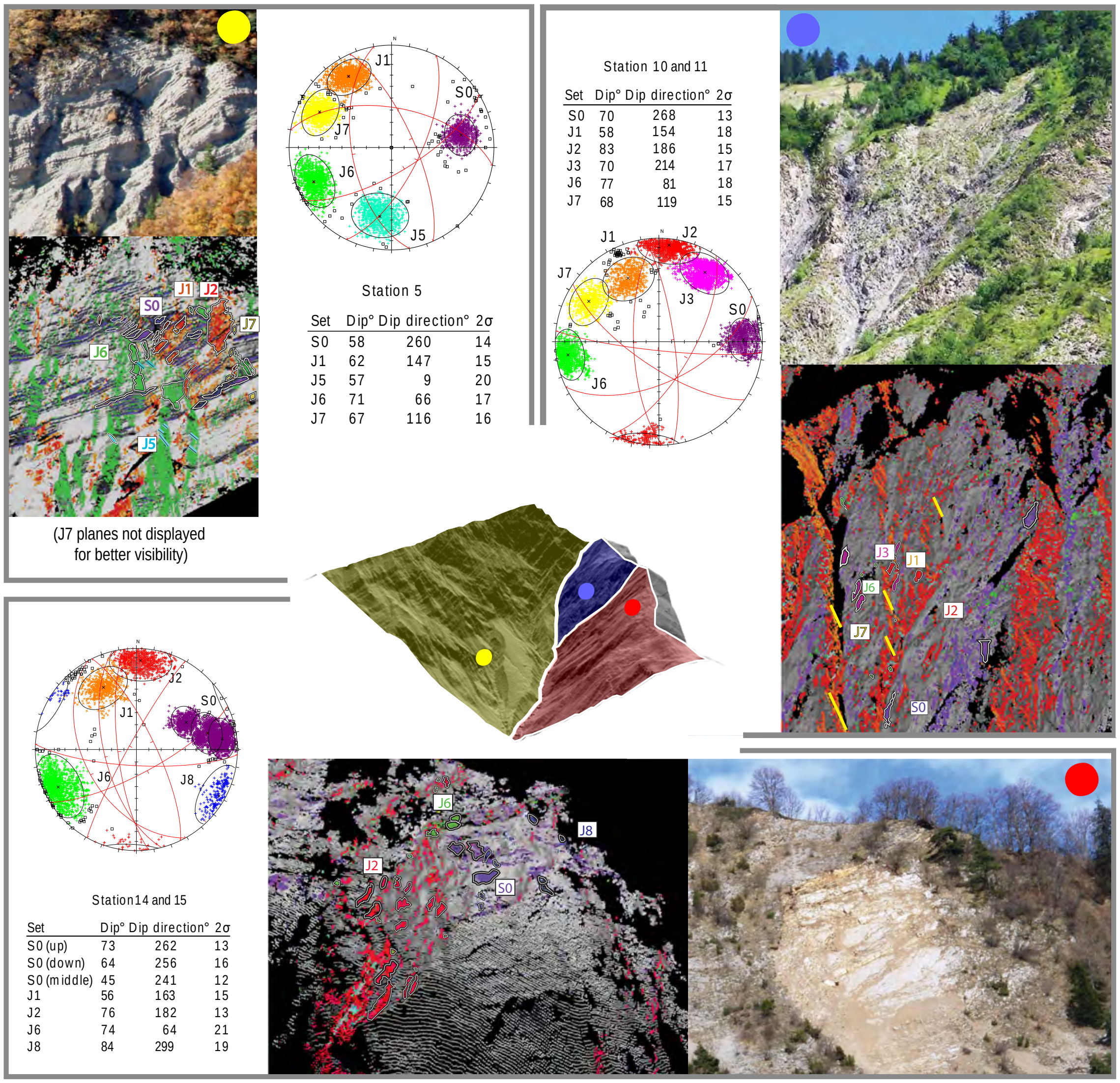

Station 5

Set	Dip°	Dip direction°	2σ
S0	58	260	14
J1	62	147	15
J5	57	9	20
J6	71	66	17
J7	67	116	16

Station 10 and 11

Set	Dip°	Dip direction°	2σ
S0	70	268	13
J1	58	154	18
J2	83	186	15
J3	70	214	17
J6	77	81	18
J7	68	119	15

Station14 and 15

Set	Dip°	Dip direction°	2σ
S0 (up)	73	262	13
S0 (down)	64	256	16
S0 (middle)	45	241	12
J1	56	163	15
J2	76	182	13
J6	74	64	21
J8	84	299	19

Figure 3.16: *Illustration of the major structural sets extracted from TLS data using COLTOP 3D in different parts of the catchment and their stereoplot projections featuring three distinctive structural agencements (colored map in center) depending on the sets of discontinuity detected in the sampling stations (Fig. 3.15). They correspond to the sets of joints used for the susceptibility assessment to rock slope failure.*

(Fig. 3.15). Four discontinuity sets (S0, J1, J6 and J7) define clear bedrock structures that affect the overall catchment morphology. On the east side, J1, J6 and J7 can be identified in the entrenchment of deep gullies and on rockslide scars. On the west side, J7 shapes the general planes of topography facing the valley-bottom, while J1 and J6 cut laterally the beds of marl and limestone with persistence. The orientation of the bedding plane (S0) displays a great consistency in geometry in sampling stations of the west side. In the ones located side east, the mean dip decreases gently toward the ridge but the dip direction remains rather constant. J5 develops clear geomorphic discontinuities only in sampling stations (ST) side west of the valley. However, the slope surface belonging closely to these orientations is very small. Discontinuity J2 was detected in all measurements performed on the east side of the valley, whereas these orientations appear only clearly in the west side in the station 7 where they shape the rock walls facing perpendicular to the valley axis. J3 is a well-defined discontinuity surface that affects the morphology developed in the vicinity of Station 10 and 11. A clear occurrence of orientations J3 in other parts of the catchment could not be observed. On the east side, J2, J3 and S0 represent large portions of topography. In the sampling stations south-east (ST 12 to ST 14) and station 7 west side, a very steep set of discontinuity J8 of more dispersed orientations is developed. These are clear geomorphic planes involved in the local entrenchment of hillside gullies and rock couloirs. Discontinuity J2, J6 and J8 are there clearly involved in the morphology of an active rockslide scar, whose mode of failure is controlled by the bedding plane S0. The mean orientation of the different discontinuity sets derived from the compilation of all structural stations are illustrated in Figure 3.16.

Applied to airborne LiDAR DEM

The major morphostructures extracted from the airborne LiDAR DEM show 7 discontinuity sets in the entire Manival catchment (Fig. 3.17). Four of them (J1, J5, J6 and J7) are essentially involved in the morphology of the west side of the valley. Discontinuity J1 and J6 are well-defined geomorphic features and represent there the dominant sets of topography. J1 defines in association with topographic planes J6 and accessory J5 the shape of deeply entrenched rock couloirs. Side west, J7 affects the hillside morphology by shaping the successive rock walls. J1 and J7 are also observable in the east side of the valley, but their occurrence as discontinuity surfaces concentrated in the gully morphology. J5 and J6 are quasi not encountered at the surface of the valley side east. There, the morphology is largely expressed by discontinuities J2, J3 and bedding planes S0, which developed discontinuity surfaces up to the top of the catchment. J2 is clearly involved in the development of gullies and can be clearly identified in the morphology of rock couloirs in the west side as well. J3 and S0 affect predominantly the shape of the hillside, whereas J3 is particularly well-developed near the thrusts. Discontinuity J2, J3 and S0 are however not developed at the surface west side. The morphostructures identified in the LiDAR DEM analysis are illustrated by photographs of the upper catchment (Fig. 3.18). More about the morphostructures of the Manival catchment can be found in Chapter 4.

Applied to standard DEM

The morphostructural analysis performed on surrounding areas of the Manival catchment using standard DEM of 50 m cell size resolution identified 5 major topographic orientations spatially well-distributed and continuously occurring in the eastern Chartreuse Massif (Fig. 3.19). The cut-through morphology of folds induced by the major Chartreuse faults reveals two dominant orientations J1 and J2, which are also encountered away from the fault zones. J3 and J5 appear to express the average morphology of fold limbs. J4 defines however a geomorphic orientation well-developed in slopes characterized by large surfaces of escarpment and geomorphic process activity. Only 4 of these dominant surface geometries are reflected in the coarse DEM morphology of the Manival. Orientation

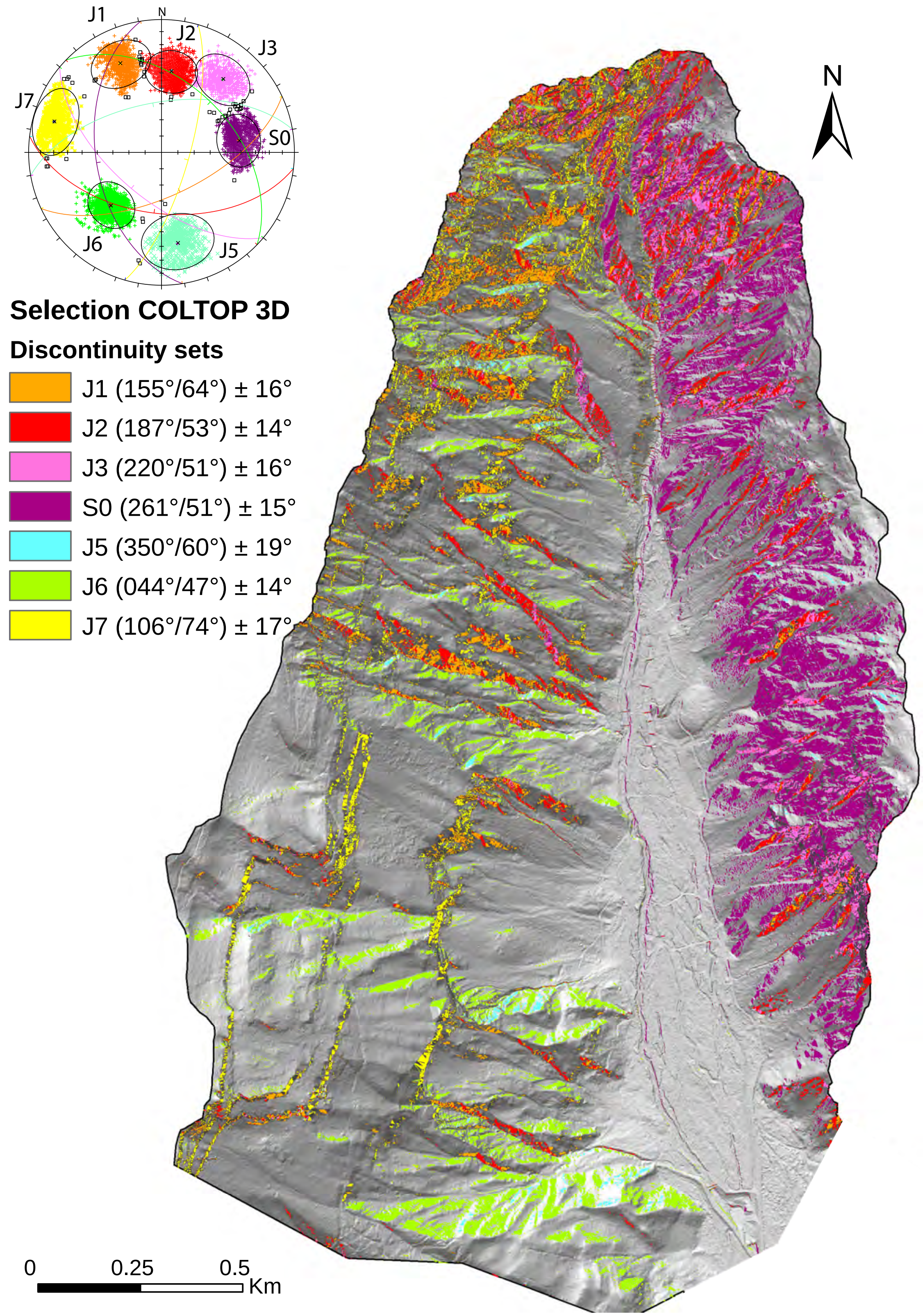

Figure 3.17: *Morphostructures identified at the surface of the catchment using COLTOP 3D on LiDAR DEM. The geometry of each discontinuity set is given with 2σ of variability.*

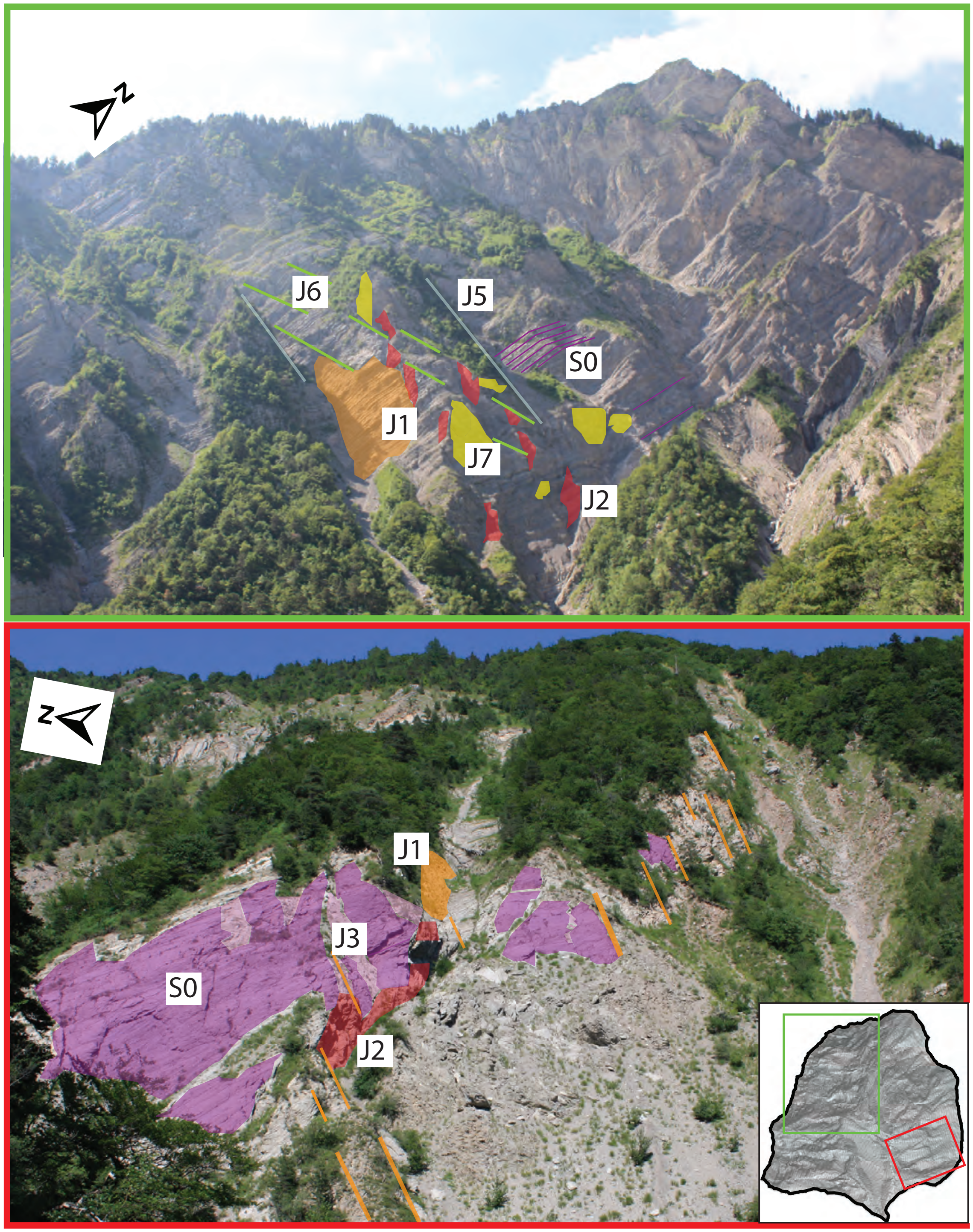

Figure 3.18: *Field illustration of the morphostructures extracted from LiDAR DEM using COLTOP 3D. Not every discontinuity could be clearly identified from the position where the photographs were taken. (Inset) Position of the photograph.*

J2 comprises large planes of the east side topography, whereas the relief of the west side is largely expressed by orientation J5. J1 and J4 complete highlighting the major geomorphic features side west.

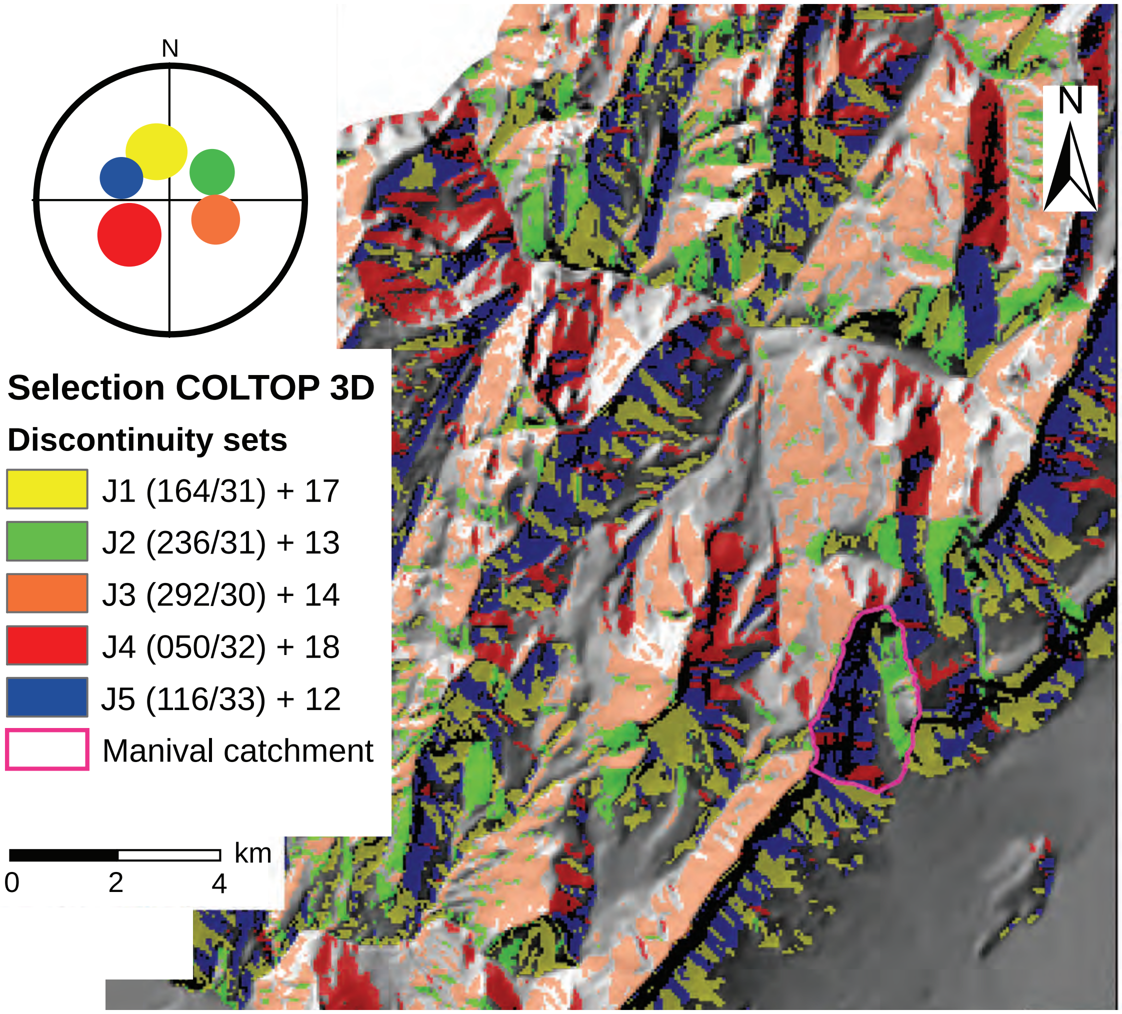

Figure 3.19: *Shaded relief map of the eastern Chartreuse Massif and related morphostructures extracted from the standard DEM using COLTOP 3D. The geometry of each set is given in the legend with a variability of 2σ.*

3.5.4 Zones of susceptibility to rock instability

The map of potential number of failures derived from the airborne LiDAR DEM using a uniform spacing between joints (Fig. 3.20) is very similar to the one using relative true spacings (Fig. 3.21). Large parts of the high-relief topography facing south-east are highly concerned with slope failures. On the west side of the valley, rock walls surrounding rock couloirs show also a very high potential number of failures. Rock walls of orientation dipping to the valley-bottom display in general a lesser proportion to failure. On the east side, gully entrenchments show large zones of potential instability, but the number is very low in average. The most exposed slopes concern the ones facing south-west towards the valley-bottom. Globally, geomorphic features highlighting rock slope process activity, such as rock walls, gullies and rock couloirs are very differently exposed to the potential number of failures. The introduction of the FS and maximum joint frequency orientations (Fig. 3.22) emphasized the zone of relative high number of failures over the ones with less failures, but the proportionality revealed previously is respected. The results are exposed here below for each failure mechanism.

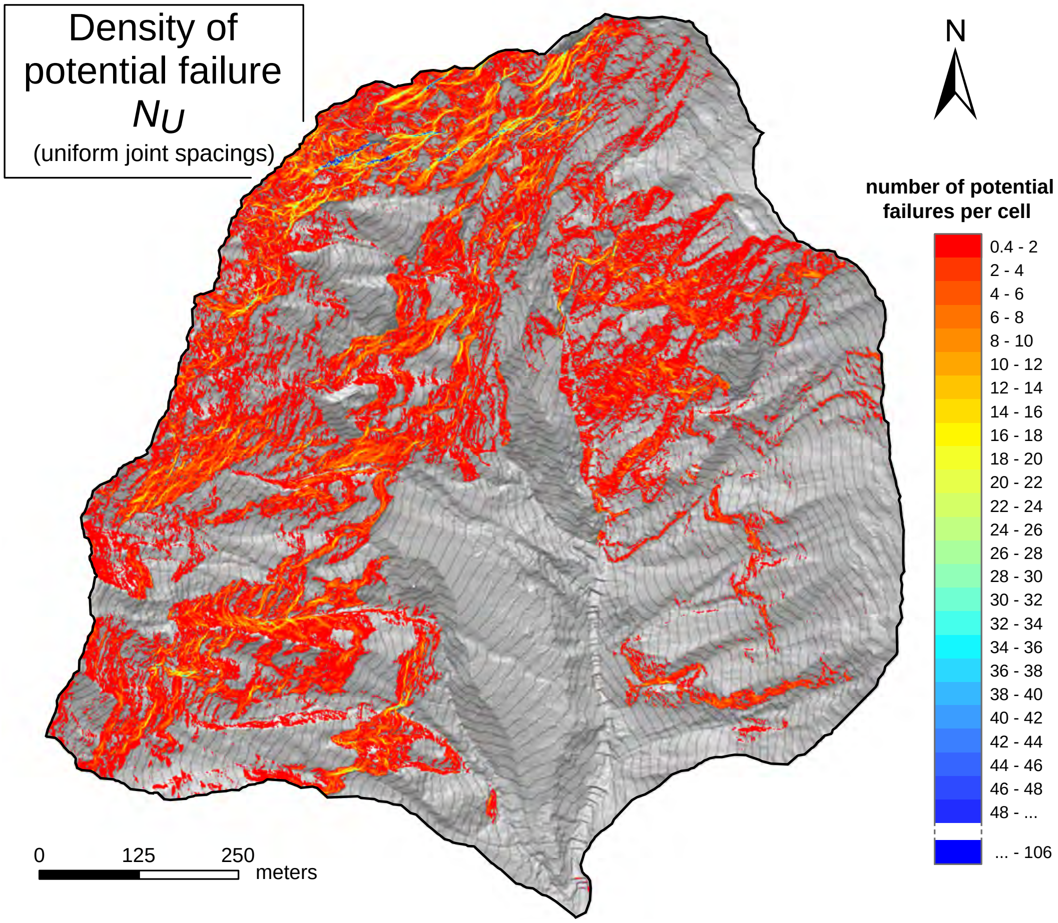

Figure 3.20: *Map of density of potential failure per DEM cell derived from summing up all structures that fulfills kinematic conditions of planar, wedge and toppling with a uniform joint spacing. The study area is particularly well-exposed to rock instabilities, but the number of potential failures per cell is very differently distributed throughout the rock slopes.*

Susceptibility to plane failure

Potential plane failures are disseminated all over the upper catchment (Fig. 3.23). High number of failures (4 to 10 per cell) is found essentially in steep slopes facing south-east, which are controlled by joint sets J1 and J2 and in lesser extent by J7. This concerns the slopes forming rock couloirs and gullies of both sides of the catchment and high-relief rock walls towards the top. J6 and in lesser extent J5 expose steep slopes facing

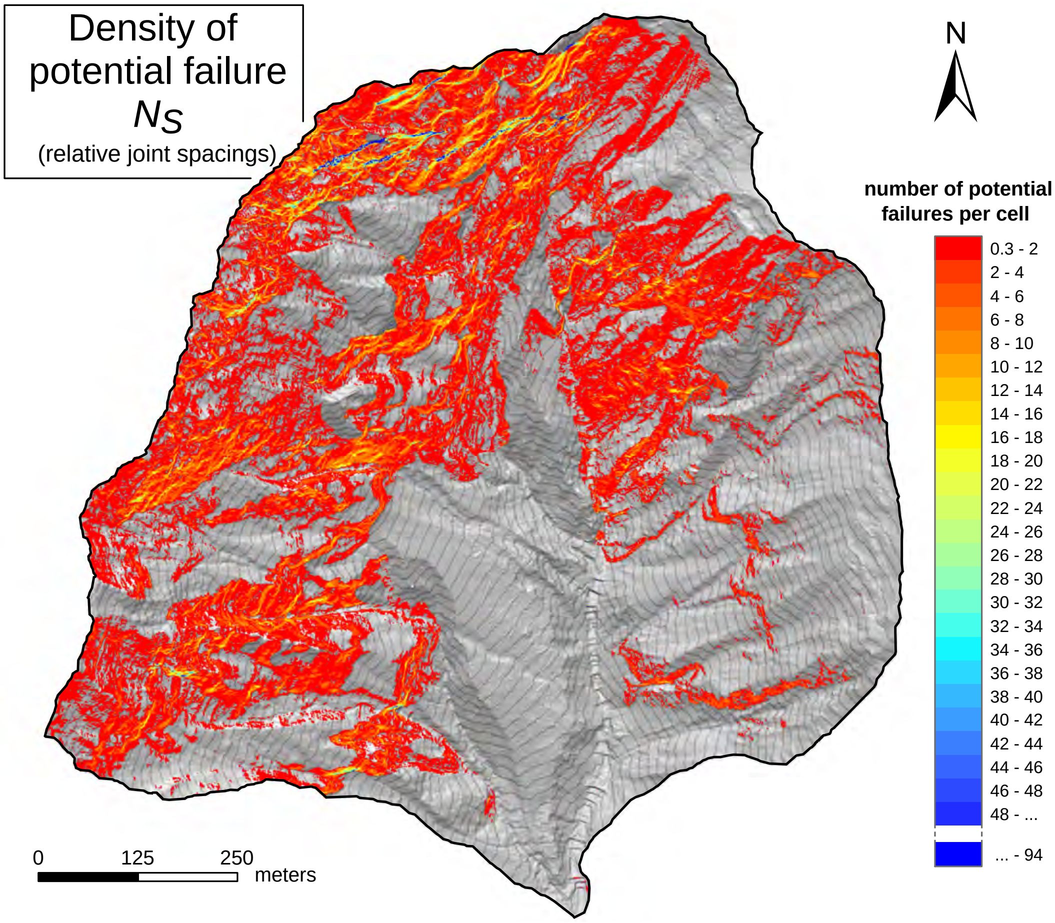

Figure 3.21: *Map of density of potential failure per DEM cell computed with a relative spacing between joints (Tab. 3.1) corresponding to the joint spacing proportionality encountered in the rock mass.*

east-northeast to plane failures. They are encountered almost exclusively in lateral entrenchments of the valley side west and the density is much lower in great majority (0.5 to 3.5 per cell). On the east side, potential plane failures are also well-dispersed over the rock slopes, particularly in the ones facing down to the valley-bottom. They develop essentially through bedding plane S0. In the zones between the thrusts, they are also developed through J3. In both areas, the number of failure remain however significantly lower than what is encountered in the west slopes (0.1 to 3 per cell unit).

Adding the relative true spacing of joints does not modify significantly the distribution of density of plane failures per cell. The susceptibility pattern remains proportionally similar to the one revealed with uniform joint spacings. A slightly increase of number of failures derived from the more tight spacing of the bedding plane SO can be however noticed in the slopes facing from east to north-east. The weighting parameters FS and maximum joint frequency orientations underline areas of high number more clearly, but do not rise or reduce the proportionality between zones. Orientations of maximum joint frequency seem less influent than the slope angle in this case, as this parameter only poorly affects the relative number of plane failures.

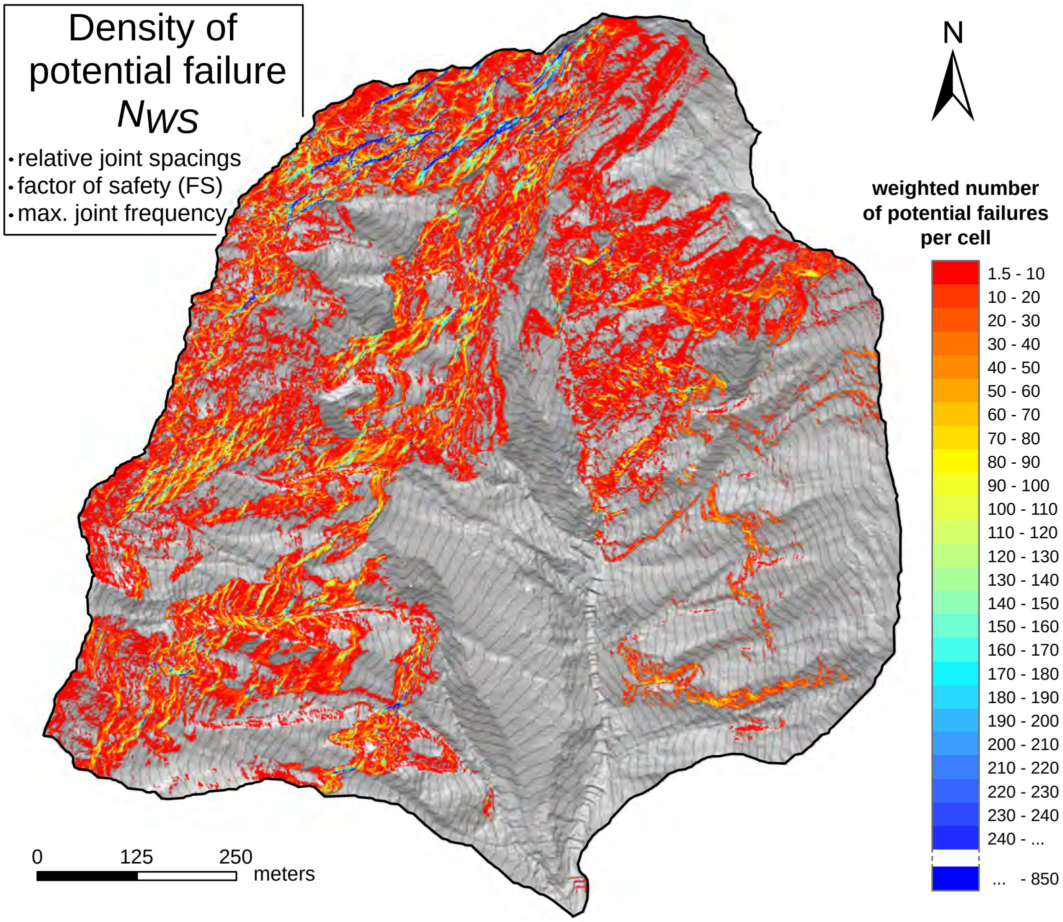

Figure 3.22: *Map of the weighted number of potential failures per DEM cell according to the relative true spacings of the joint sets, their FS and the maximum joint frequency. The zones with high number of failure determined in the previous maps are emphasized over the ones with low density of failure. Exceptions are rare.*

Susceptibility to wedges

Potential wedges are widespread in all parts of the catchment (Fig. 3.24), but the number of failures is very low (< 0.5 wedge per cell) for more than half of detected locations. Zones with high number of wedges are found primarily in steep slopes facing from east to south. They can reach from 10 up to 65 wedges per cell in the very steep areas of the top. They are controlled by joint configuration combining J1, J2, J6 and J7, which all involve a wedge axis plunge over 30°. (Stereonet of the joint system and the list of potential wedges prevailing in the upper Manival catchment can be found in Fig. 4.17 and Tab. 4.2 of the chapter 4). The steep slopes facing north-east display also a fairly high number of potential wedges per cell. They are exposed to steeply-dipping wedges J5^J6, J5^J7 and J6^J7. This concentration of wedge orientations develops essentially on slopes surrounding the deep entrenchments of topography, such as rock couloirs and gullies as well as in rock faces side west dipping perpendicular to the valley axis. In the east slopes of the valley, potential wedge failures are not only located in gullies, but over

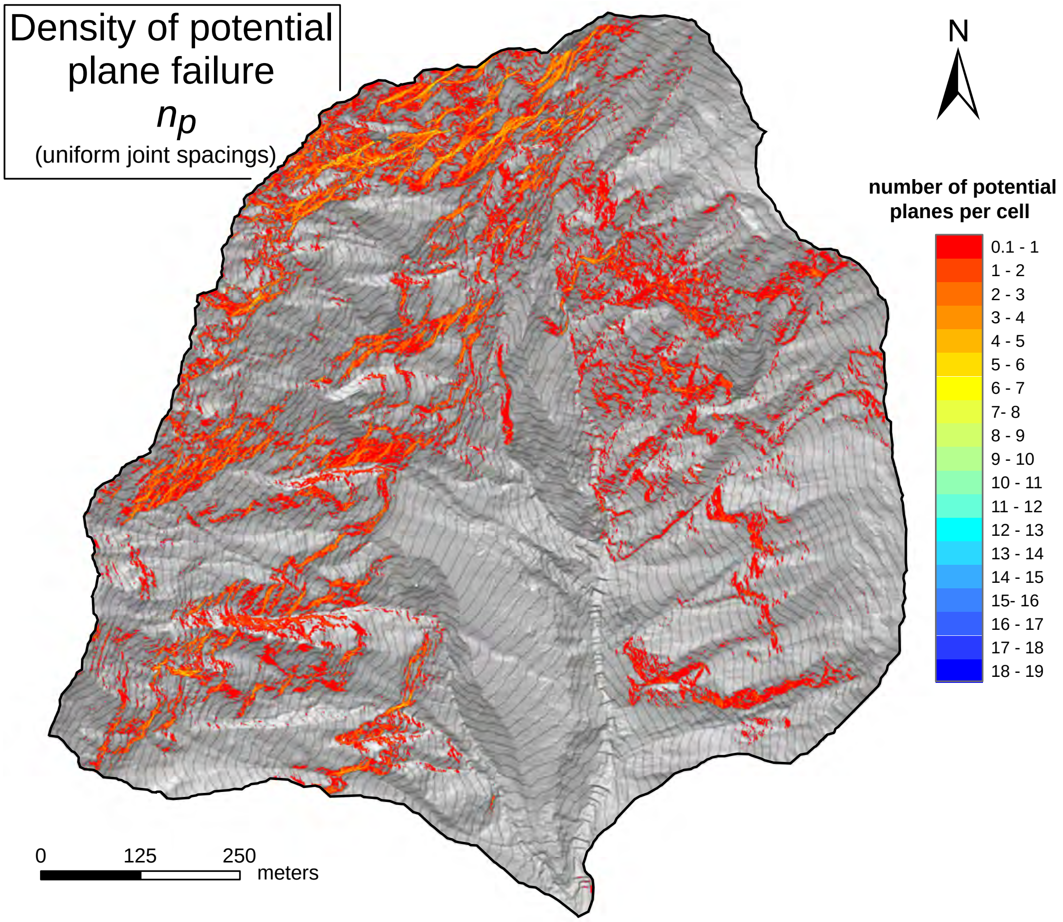

Figure 3.23: *Map of density of potential plane failures per DEM cell given a uniform spacing of 1 m between the joint sets determined after the morphostructural analysis. High numbers of failures are found essentially in steep slopes side west facing from north-east to south-east and involve joints J1, J2 and J6 particularly. The bedding plane S0 controls plane failures in the east side of the valley. The density distribution computed with relative true joint spacings and weighted with geotechnical parameters displays a trend pattern closely similar.*

the entire hillside facing from west to south-west. The density is however very low (< 0.2) for most of the hillslope, but can reach up to 5 wedges per cell in steep rock slopes. This concerns joint configuration involving the bedding plane S0. Configuration S0^J6 and S0^J7 have their wedge axis plunging around 20°, but the ones involving J1 and J2 plunge much steeper (45°). The zone between the thrusts is particularly well-exposed to wedge failures controlled by joint set J3. The number range between 0.02 to 4.3 and a large part comes from joint configuration J3^J6 having a wedge axis plunge of 15° only. The slopes facing north-west show potential wedge failures through joint configuration involving J6 and the bedding plane S0, leading to a low-dipping wedge axis around 20° and a density reaching 2.5 wedges. In the west side, their occurrence is limited to the deep entrenchment of rock couloirs.

The map of potential wedges computed with relative true joint spacings indicates that the zone between the thrusts increase their potential number, while the slopes facing north-east decrease their number of wedges proportionally. This results mainly from the large spacing of J6 in proportion to other joint spacings. The change in failure density is only of a few wedges per cell however. Adding the weighting parameters increases the number of failures of slopes facing from south-east to south-west significantly in regards to the other areas. These orientations correspond not only to steeply-dipping wedge axes (e.g. J1^J7 = 64°; J1^J3 = 59°) but also to a relatively high joint frequency, which combination contribute to emphasize the relative number of failures per cell. The slopes facing north-east display also an important increase, which is essentially due to steeply-dipping wedges.

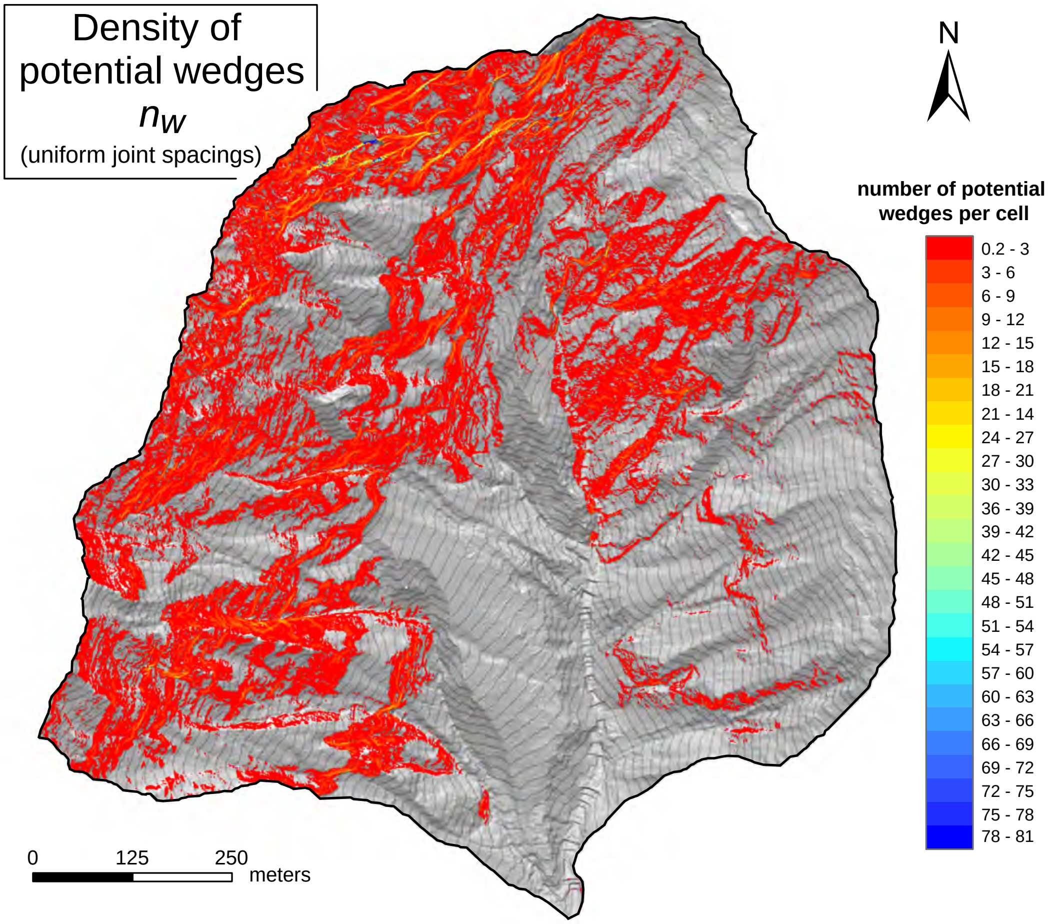

Figure 3.24: *Map of density of potential wedges per DEM cell given a uniform spacing between the joint sets. Wedge J1^J5 was removed as the axis plunges less than 15°. Wedges oriented from east to south show a high number of failure controlled by joint configurations J1, J2, J6 and J7. In the eastern part of the valley, they concern the very steep slopes facing from west to south-west, involving J3. The distribution of number of failure computed with relative true joint spacings and weighted with geotechnical parameters displays a similar pattern.*

Susceptibility to toppling

The occurrence of potential toppling is much more limited in the upper catchment (Fig. 3.25). In the west side, toppling can develop on the very steep slopes facing south south-east through joint set J5 and the bedding plane S0. The density can reach up to 17 failures per cell in the top part. On the east side, but particularly in the thrust zone, potential toppling locations are sparse. They concentrate in the very steep slopes facing south-west with a density not exceeding 5 potential failures per cell. They are controlled by joint J1 and J6 and in rare cases by J7. Potential toppling detected with the other joints are marginal. Considering the true spacing of joints, the number of failures increases significantly for the slopes controlled by J1. On the east side, the number of failures is quasi constant and even slightly decreases in the side walls of the gullies facing south-west. Combining the number of failures with the parameter maximum joint frequency orientations emphasizes significantly the slopes facing east in the west side and the ones facing south-west in the east side of the valley; there, the influence is more widespread. The overall differences remain minor compared with the rest of potential failure locations.

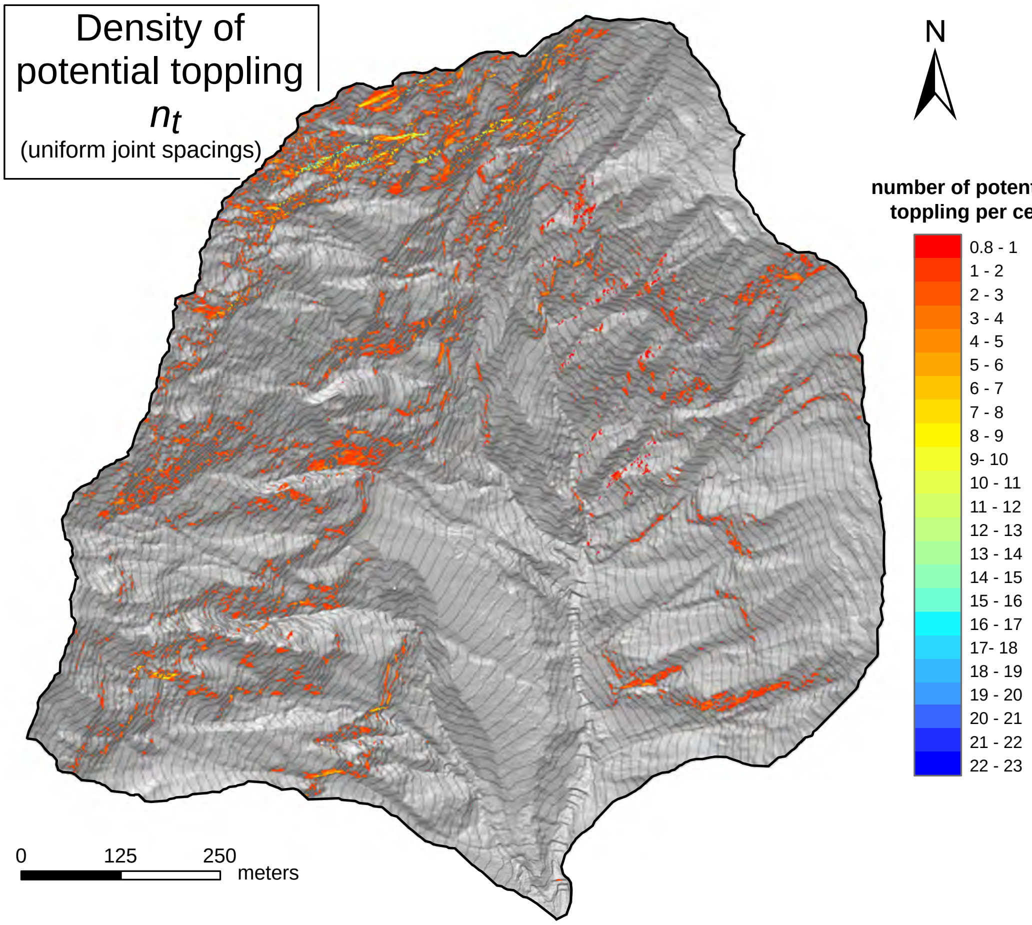

Figure 3.25: *Map of density of potential toppling per DEM cell according to a uniform spacing between joints. Potential toppling is located almost exclusively in very steep slopes and involves joint J1, S0, J5 and J6.*

3.6 Analysis and discussion

3.6.1 Hillslope process activity derived from morphological units

Combining the classified map of slope steepness (Fig. 3.12) with observation that can be drawn from a shaded-relief map and field surveys can document about the mode of geomorphic process activity:

- The torrential flood plain exhibits a very rugged surface inherited from several remnant old channels. Their high amount attests of high magnitude debris flow events that could change the course of the main torrent. The mode of slope gradient is 11° (20%). This corresponds to the mean angle of repose of granular-type debris flow (Rickenmann, 1995), referring to a frictional-collisional rheological regime with a prevalent non-cohesive coarse fraction and poor clay content (Ancey, 1999).

- The second morphological unit of slope steepness characterizes two type of process according to their shape and break of the slope angle at the interface with the torrential flood plain:

    1. Fan-shaped deposits at the outlet of hillside gullies entrenched by ephemeral channels. They are mostly encountered on the east side of the valley. The relative steep slope angles of deposition suggest a colluvial-dominant type of deposit, such as debris slide/flow, dry ravelling and snowflow derived from highly immature coarse sediment. More cohesive debris flows and water-dominated fans are usually less steep, because they are composed of finer and more mature material (Blikra and Nemec, 1998).
    2. Hillside bottom-slope deposits: They are gently-flatten slopes made of clastic waste and finer-grained soil material covered with mature vegetation undergoing progressive creep and slopewash processes. These geomorphic features are mostly found on the west side. They are also expressed on the rising limb of the SAFD of the mapped layer scree-mantled slopes between 10°-19°. The deviation from the trend of the slope angle distribution (Fig. 3.13) suggests that parts of the scree slopes were remobilised and deposited further down by sheet wash and creep processes.

- Comparison of the morphological unit talus-slope deposits with the corresponding scree-mantled slopes derived from field mapping shows a close agreement in both amplitude and variance. This reveals that major morphological units of mountain topography can be extracted through SAFD analysis with accuracy. The SAFD of the effective scree-mantled slopes exhibits a close-shaped normal distribution around a mean value of 35°. This mode corresponds to what can be expected from undisturbed deposition of clastic fragments inherited from rock slope failure, as a corollary to the angle of repose of a sand pile (see Appendix D: Loye et al., 2009a). A mode around 35° is also noticed in the morphological unit Talus slopes deposits. In both SAFD, the standard deviation is small, implying that this unit is rather straight morphologically. This is often the case for intermediate scree slope deposits underneath rock walls (Loye et al., 2009a).

- The threshold slope angle above which the topography is considered as rock slopes and outcropping bedrock is 47°. This is comparable to what is obtained in the similar Helvetic Swiss Alps (Loye et al., 2009a). In the lower part of the catchment, the Argovien lithology is mostly covered by talus slope deposits, but contains many rock walls in the upper part. The Sequanien formation exhibits a very high proportion of steep bedrock slopes and rock walls. But rock walls (defined by the highest Gaussian curve) can be encountered in all lithologies. Steep bedrock slopes and cliffs are not concentrated in any lithology in particular. This unit is dominated by rock slope failures, such as rockfall and rockslides. Comparison with the rockfall inventory reveals that only 21 (1%) of the 1866 events detected between April 2009 and July 2010 (see Chapter 2) were not located in the *Rock slope* morphological unit, also happened on lower slope gradient. Rockfall locations on DEM were considered with an uncertainty of 1 m. The slope angle is therefore a reliable parameter for the delineation of debris derived from rock slope production.

In the upper catchment, debris detached from rock walls reach debris flow channels directly or accumulate on the side where they progressively migrate downslope. However, any significant hillside fan or similar geomorphic shapes are displayed, suggesting an absence of long-term mass wasting deposits coming from tributary gullies and thus a high connectivity of the entire upper catchment to transport debris away. Debris flow frequency seems therefore to be supply-limited according to Bovis and Jakob (1999).

3.6.2 Stage of erosion development in lithologies

The Tithonic formation outcrops near the ridge of the catchment only, a portion of topography were the slopes become convex, which can explain the high frequency of low slope angles. The shape of the SAFD of other lithologies is typical of a mechanical desagreggation dynamic related to slope failures (Strahler, 1954). The upper lithologies (Kimmeridgien inf. and Kimmeridgien) display a similar curve characterized by a small standard deviation, implying a constant morphology of their slopes. The Sequanien formation underneath shows in the opposite a very high proportion of high steepness slopes in comparison to the other lithologies, that may suggest a competency of the rock slopes much higher. This significant positive skewness in the SAFD can also come from the enhanced lowering of the channel floor, inducing the rock slopes to oversteepen their natural apparent angle of stability. This is suggested by the fact that the lithologies exhibiting the highest proportion of very steep slopes are located at the heart of the catchment, where the erosion (entrenchment) is the most active. The highest frequency of rockfall recorded in the 2009 – 2010 inventory was located in the Sequanien formation followed by the Argovien one (Fig. 3.26). These lithologies seem to be the most instable ones in the stage of erosion development.

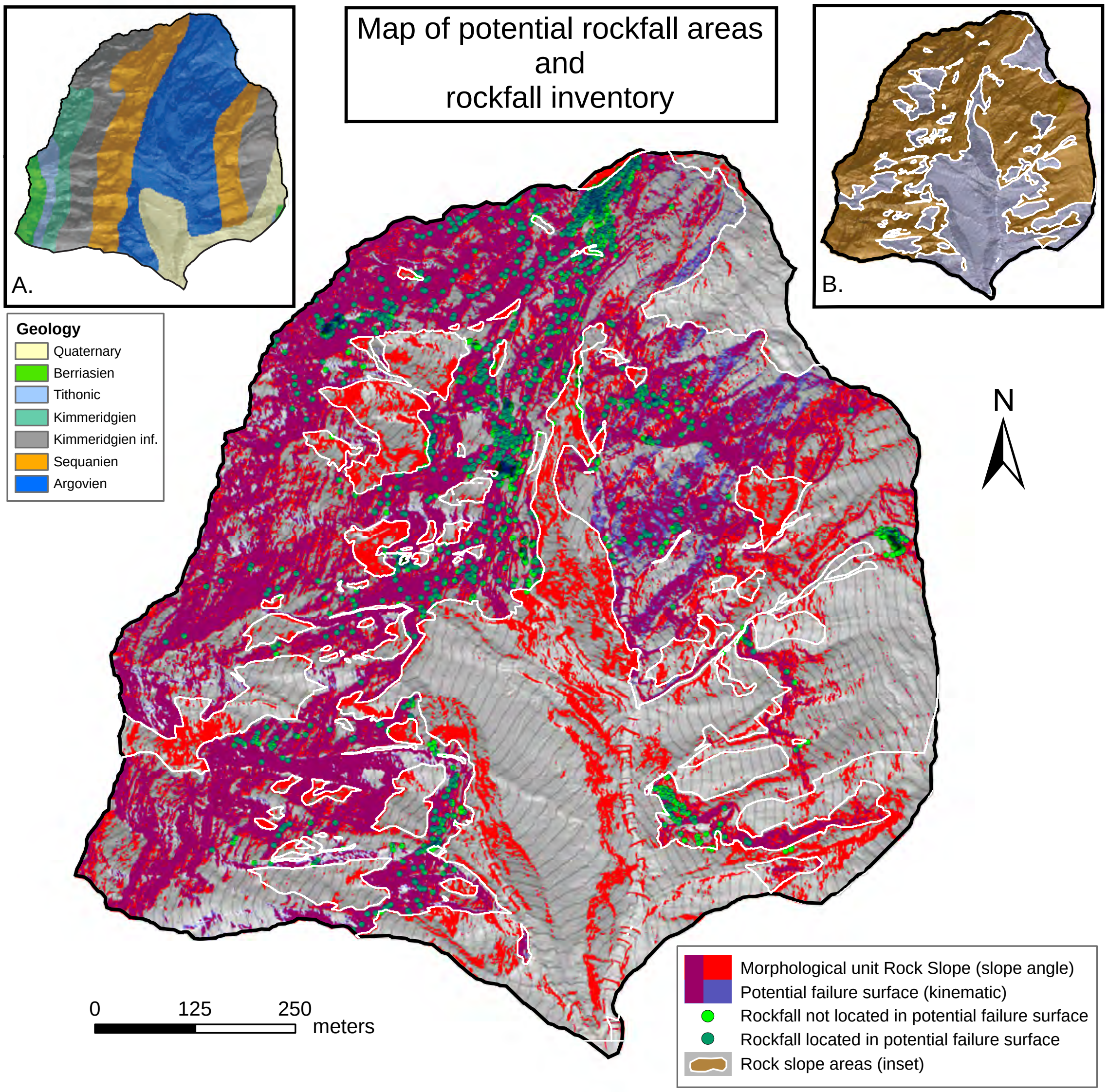

Figure 3.26: *Locations of rockfall events from the 2009 – 2010 inventory compared to the extent of potential rockfall areas delineated by the morphological and structural approaches. The white lines display the extent of the rock slopes. A 1 m uncertainty in rockfall locations was admitted for the statitics. (Inset A) Geological map. (Inset B) Areas of the outcropping bedrock.*

3.6.3 Structural investigation based on DEM of different resolution

The morphostructures identified with airborne LiDAR DEM without any information from field surveys show that all sets can be related to discontinuity orientations identified using TLS data, which measurements approaches more field data acquisitions. The difference in geometry comes essentially from a better precision of topographic resolution. The morphology displayed in HR-DEM is smoothed in comparison to the more angular discontinuity surfaces derived from high density point clouds (Loye et al., 2009a) and consequently tends to lower the dip angle particularly. The greatest difference of measurement between HR-DEM and TLS data comes in fact from the selected geomorphic features. They are mainly surfaces affected by erosion that exhibit therefore averaged topographic structures, as opposed to very local observations that can be made on point clouds, where only steep planar surfaces are more likely to be measured. For instance, discontinuity surfaces J2 and J6 highlighting morphostructures of rock couloirs and gullies have much lower dip angles in the DEM analysis. In the contrary, discontinuity J7 highlighting high relief rock walls dips in a similar way in both analyses considering the mesh size of the data.

The structural analysis using TLS point clouds, and therefore using HR-DEM, is in good agreement with field data, particularly for measurements performed in the west side up to the top of the catchment. J5 was not detected in field data, which does not mean that this discontinuity cannot be found elsewhere. J2 was not identified in all stations of the valley side west, but field data show clearly that it represents a true discontinuity. The non-detection can be related to the small size of structural planes J2 perpendicular to the bedding as well as the close orientation to discontinuity J1, which shapes the slopes with greater surface. In the other side of the valley, the trend pattern of three discontinuities (J1, J2 and J6) and bedding plane S0 is similar to DEM analysis, but with greater dispersion for field data. The steeply-dipping discontinuity J8 detected in TLS data only is also visible in field data. The structural sets observed in the field may not be completely representative of the discontinuity sets due to the important grade of weathering affecting the rock mass (mostly freeze and thaw cycles, maybe exfoliation), particularly in the marl-rich Sequanien and Kimmeridgien lithology. One can assume however that gravitational fractures, for instance the ones observed on the catchment ridge side east (Fig. 3.14 – Location 6), follow the predominant joint sets. Discontinuity J3 and J7 were not observed in any field outcrops sampled in this study, but structural stations of the east side were performed along the ridge only. As shown on DEM data, these two sets are mostly encountered on the hillside between both Manival thrusts and seem to be much less present outside this zone.

The Coltop 3D analysis performed on the standard DEM does not provide enough topographic resolution to provide distinct planes of morphostructures. The morphology is greatly influenced by the coarse DEM resolution, particularly the slope angle. The dip directions show however a concordance with the morphostructural investigation using higher resolution DEM. Topographic orientations J1, J4 and J5 derived from the standard DEM can be clearly associated respectively to discontinuity sets J1, J6 and J7. Topographic orientation J2 represents an intermediate direction between discontinuity set J3 and the bedding plane orientation. This may come from the fact that the topography represents only the mean orientation of both discontinuity surfaces. All these topographic orientations respect the tectonic lines identified previously. This pattern of morphostructures strongly suggests that those discontinuities represent predominant joint sets at the scale of the catchment and more regionally in the whole massif. Those joints can be considered as the most persistent ones.

3.6.4 Interpretation of the discontinuity sets

The structural analysis performed from the outcrop to a more regional scale of investigation allows proposing following observation. In the field, any discontinuity sets were reported to be folded and must be therefore related to late- to post-folding tectonic. In the Manival catchment, the discontinuities associated to the regional structural trend (J1, J6 and J7) control the shapes of deeply-entrenched rock couloirs, hillside gullies developed in bedrock and scars of rock instabilities. They define wedges with a direction of intersection of about 105°/67° (± 030°/20°). Discontinuity J1 is oriented perpendicular and J6 parallel to the fold axis and both are perpendicular to the bedding plane. They can be interpreted as extensional fractures generated during folding (Price and Cosgrove, 1990). The great consistency detected on HR-DEM and the planarity of these structures support the assumption that they are caused by regional faults. They are all oriented nearly longitudinal to the major faults that cut through the Chartreuse folding. No displacement could be observed however.

Discontinuity J2 and J5 are more difficult to interpret. They are also involved in the geomorphic control of gullies and rockslide scars. According to DEM analysis, J2 can be interpreted as conjugated joints with J1, while J5 is mixed with break of slopes associated with J6 exclusively. At the scale of the outcrop, they define lateral discontinuities with low persistence. In the east side of the catchment, J2 forms in association with the bedding plane a succession of small gullies and v-shape geomorphic features. J5 could not be observed in the field and the orientation is not only poorly constrained around a mean value (sigma = 20°), but also differs toward east between TLS and DEM analysis. These observations suggest that discontinuity J2 and J5 may correspond to rock structures derived from geomorphic activity rather than fold-induced predominant joints. By the way, J2 is similar than the maximum joint frequency orientations , suggesting that J2 is the product of a composite surface (Jaboyedoff et al., 1996, see Chapter 4). In the west side of the catchment, the bedding plane displays great consistency in orientation. Near the top of the catchment, the geometry is more variable, induced by local deformation (secondary folding) related to the inverse compressive fault (Gidon, 1998).

The topography side east is primary influenced by discontinuity J2, J3 and S0. The rock slope morphology is either in dip slopes or overdip slopes (cataclinal), so that the topography (erosion, channel incision) is strongly controlled by the varying bedding plane orientation. The discontinuity J3, which is only visible on DEM analysis in the local thrust zone, corresponds to the maximum joint frequency orientations. J3 represents an intermediate orientation between J2 and S0. Slope failure combining S0 and J2 may generate a preferential surface orientation in a wedge-style configuration. J3 can also be a variation of bedding geometry induced by local slope deformation related to the thrusts (post-folding). The existence of J3 as associated conjugated faults to the Baure and Manival Thrusts, which strike N070 like most of the thrusts in Chartreuse cannot be excluded though. A simple characterization of morphostructure J3 is complex according to low rock mass quality and strong erosion processes affecting the true discontinuity geometry of the slopes. The steeply-dipping discontinuity J8 detected on DEM seems to belong to discontinuity J1 measured in the field. The variable orientations are either induced by local deformations or gravitational movements.

These seven morphostructures are expressed in the morphology of the catchment for about 32% of the topographic surface, respectively 43% considering only the upper catchment (headwater), and suggests that these discontinuity sets strongly influence the morphological development of the catchment.

3.6.5 Areas potentially exposed to rock slope instability

The map of potential rock slope failures, which combines all areas respecting kinematic conditions of plane failure, wedge and toppling, indicates that the upper Manival catchment is well-exposed to rock instabilities. Potential failure surfaces correspond to about 50% of the contributing area of the Manival torrent (i.e. the headwater extent, see chapter 1). And about 60% of the rock slopes outcropping in the headwater can develop failures with the major sets of joints derived from morphostructural analyses. Areas potentially exposed to wedges represent the greatest contribution (71%). This is actually well-reflected in the morphology of the east and top parts of the catchment, through wedge-like configuration of geomorphic features (see chapter 4). Plane failures influence also greatly slope stability (46%), while toppling is much more local in the upper Manival catchment. This represents only 15%. A large portion area exhibits both plane and wedge failures.

Comparison with the rockfall inventory (Fig. 3.26) reveals that only 43 events (2.3%) occurred outside zones delimited as potential failures, considering a buffer of 1 m uncertainty for rockfall locations. Volumes of undetected rockfalls range between 0.03 m^3 to 1 m^3. The DEM resolution could be the reason, as the great majority of those rockfalls were situated on gentle slope angles (<30°). Specific rock mass conditions implying local joint sets or particular triggering factors may be another reason, like e.g. sliding on dip slope. Indeed, this very high correspondence shows that the kinematic approach based on major joint sets can be used to identify areas prone to rockfall with a very high level of confidence. This suggests also a pronounced influence of the major joint sets prevailing at Manival.

These potential zones of instabilities are comprised at 98% in the rock slopes morphological unit delineated from the SAFD analysis. The discrepancy arises almost exclusively in the thrust zone and results from potential wedges with low plunge axes. In the opposite, 70% of the surface delineated as rock slopes with the morphological approach develops potential failure mechanisms. This correspondence is interesting since the morphological unit can incorporate slopes with no bedrock or bedrock slopes covered with vegetation, which were not considered in the structural method using kinematics.

3.6.6 Susceptibility assessment

Geomorphic elements featuring erosion process activity, such as rock walls, gullies and rock couloirs, reveal very different density of potential failure. Considering that this reflects degrees of susceptibility to rock slope instabilities, one could therefore expect that the greater the number of potential failures of a given area, the larger the rockfall production would be in this area. Comparison with the rockfall inventory reveals that any positive correlation exists between volumes of events and the number of potential failures at the place where they detached, even by considering an uncertainty of 1 m in rockfall locations, and so for the three ways of defining susceptibility (Fig. 3.27 left). In the contrary, large size events such as rockslides of several hundred of m^3 are found exclusively in areas showing numbers ranging from 0,65 to 15 failures per cell (considering uniform joint spacings), and hence, having relatively low density (incl. maximum values). Only few rockfall of volumes above 1 m^3 occur in areas reaching 30 failures per cell unit. All events located above 1/3 of the maximum number of failures have their volume smaller than 1 m^3. Areas with high density values correspond to events of very small sizes and are rare.

This absence of direct relationship is also well-expressed in rockfall frequency (Fig. 3.27 right). The higher concentration of events corresponds clearly to the lower density of failures and the distribution decreases homogeneously as this latter increases. Local extrema (clusters) are hardly distinguishable and cannot provide information on rockfall distribution in relation with specific thresholds of failures. The introduction of relative true joint spacings does not modify significantly the spatial distribution of number of failures and therefore does not improve the correlations. Both volume and frequency distribution remain pretty close to what was obtained with a homogeneous spacing between joints. The attempt to weight the number of failures provided by each joint set with simple geotechnical parameters (FS and orientations of the maximum joint frequency) has only minor influences. Both volume and frequency distributions are more spread over a failure scale that is bigger, but the trend pattern is similar. Rockfall inventory remains negatively well-correlated against the weighted number of failures. The frequency distribution suggests two threshold density values surrounding local maxima, between [25;75] and [75;200]. However, their interpretation in terms of susceptibility to failures is difficult.

In both cases, these inverse relationships may be explained by analyzing the susceptibility distribution to failures at rockfall locations. This can be characterized by a Poisson law (Fig. 3.28). Even the distribution of the weighted number of failures approaches a Poisson law. Consequently, rockfall locations suggest being randomly distributed over the potential number of failures developed in the headwater. They suggest also being mutually independent, and that the probability to find any number of failures in regards to the rockfall inventory is constant. The investigation period seems therefore to be too short to represent the whole range of volumes, especially the occurrence of large rock slope instabilities characterized by very low frequency. This may explain the absence of data in areas with high theoretical susceptibility. Rockfall is a complex process where small rockfall events are very often preceding in time the occurrence of larger collapses (Rosser et al., 2007; Abellán et al., 2009b, 2012). Hence, small volumes are very likely to be encountered in area mapped with high susceptibility, like here. A longer period of record with larger contributions would probably help defining degrees of susceptibility to rock slope failure at the scale of rockfall events.

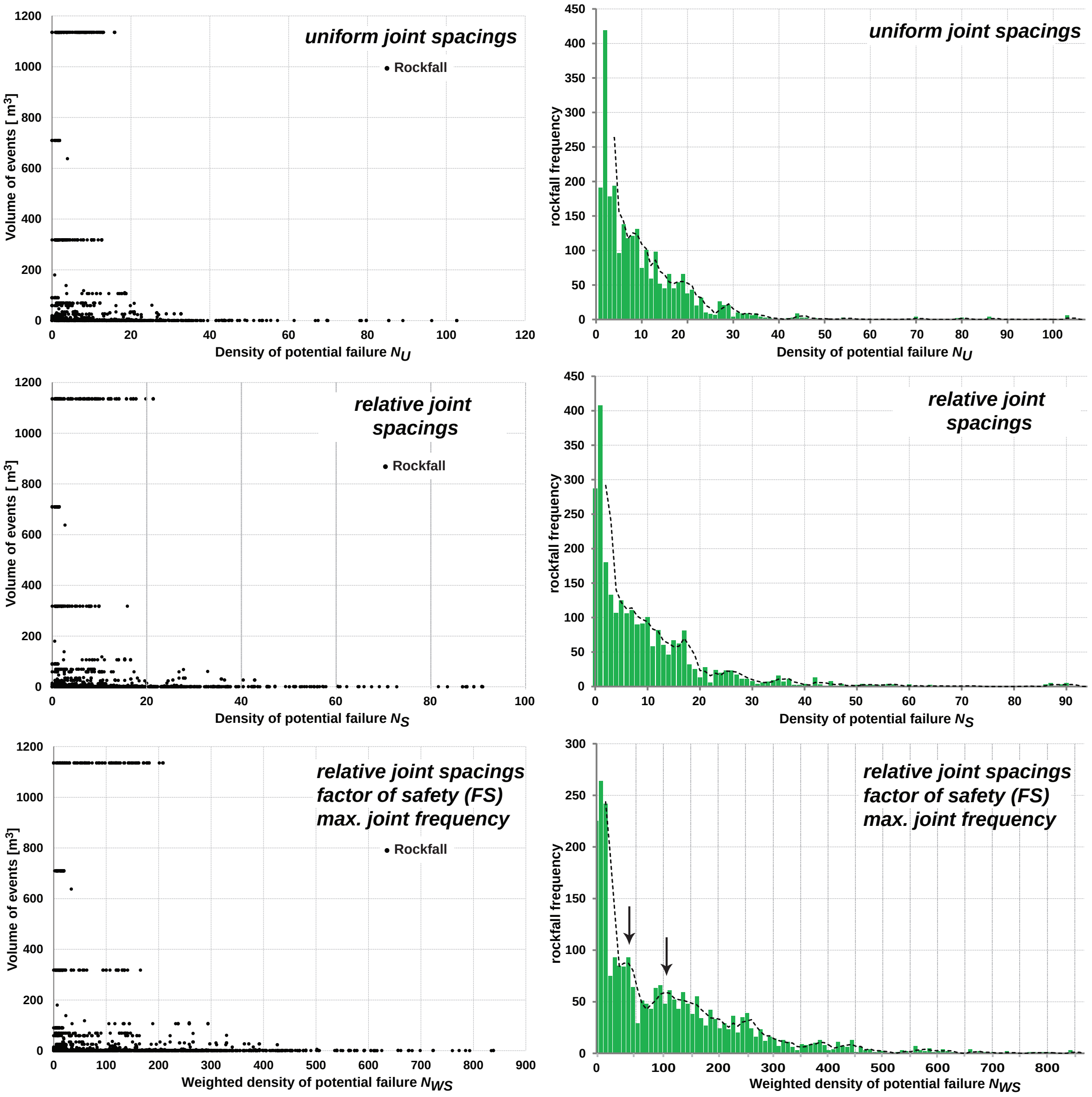

Figure 3.27: *(Left) Rockfall volume inventory expressed as function of the density of potential failure for the three ways of defining susceptibility to rock slope failures. The plots show rather an inverse correlation where large rockfall events are related to small numbers of failures. (Right) Rockfall frequency per number of potential failures. Note the homogeneous decrease of events when the number of failure increases. The frequency distribution including geotechnical weighting parameters (F) suggests however local extrema at 40 and 100 failures per cell that could provide information upon susceptibility thesholds to rock slope failures.*

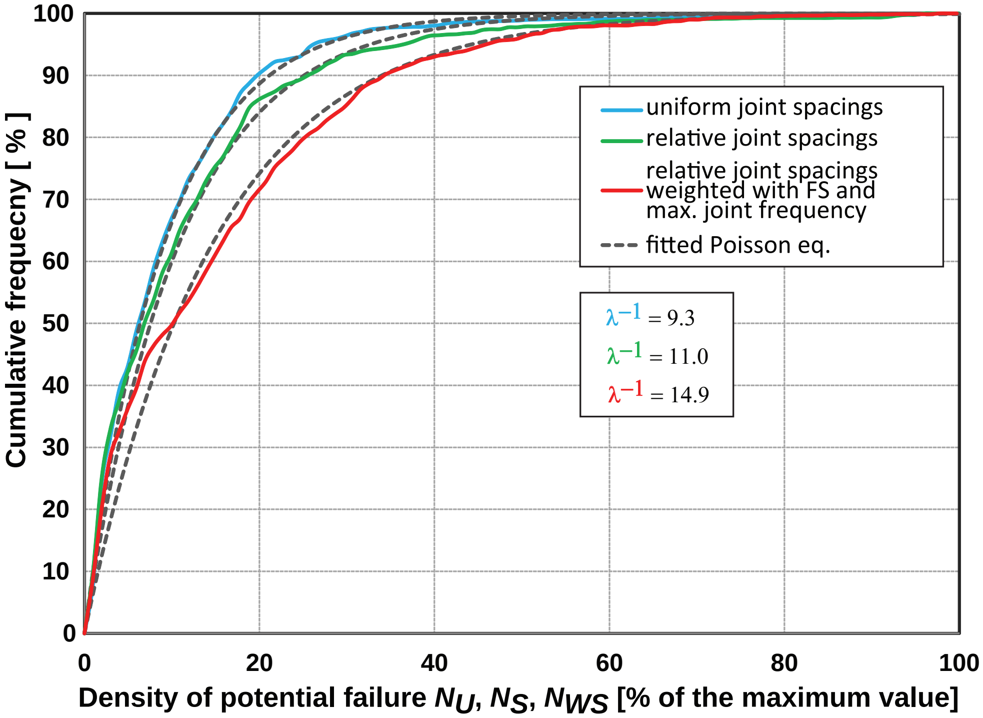

Figure 3.28: *Normalized cumulative frequency distribution of the density of potential failure at rockfall locations observed in the inventory. In the three cases, the frequency distributions approach a Poisson law.* λ^{-1} *is the mean number of failure computed by the fitted Poisson equation.*

3.6.7 Implication for debris supply

Nevertheless, although degrees of susceptibility to rock slope failure could not be set from the number of failures at the scale of rockfall events, the susceptibility to rock slope production was analyzed at the scale of the hillslope. The total number of potential failures integrated over each tributary subsystem of the headwater was compared to their rock slope production measured during the 16 months of investigation (Fig. 3.29). The correlation are scattered and characterized by a wide range of total failure densities producing volumes of similar order of magnitude. In several subcatchments, like the Baure Ravine, the susceptibility distribution barely reaches a few tens of failures per cell unit, although they produced a relatively large rockfall volume. Others exhibit a range of failure density of one order of magnitude more for a very low debris production. Only the Manival subcatchment shows an interesting correspondence with a large rockfall volume for a high total density of failures.

Considering a scale dependency upon surfaces, both total density of failures and volumes were averaged over the extent of their rock slopes respectively (Fig. 3.30). The correlation remains poor, but suggests however a trend in the characterization of volumes as function of the total density of potential failure. This tendency must be interpreted with caution, since neither budgets of rock slope production nor the total density of failures may depend on rock slope areas (Fig. 3.30). As well, the total density of failures is also poorly dependent on the slope angle either. Despite of a lack of consistency in data, those results are

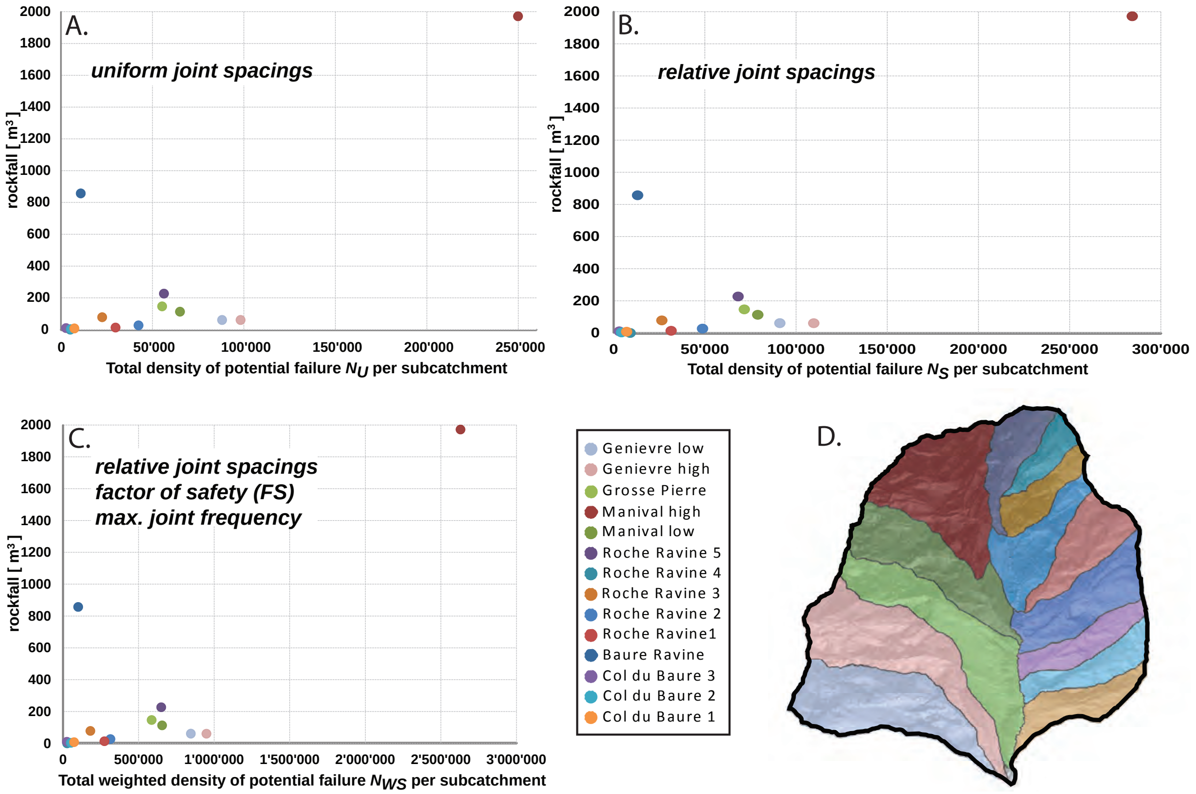

Figure 3.29: *Rockfall volumes expressed as function of the total density of potential failure with (A) a uniform joint spacings, (B) relative true joint spacings and (C) weighted with geotechnical parameters for each tributary subsystem (subcatchment) of the upper Manival (D). All plots are closely similar and display rather scattered correlations where rock slope production of similar order of magnitude has a total density of potential failure ranging over several orders of magnitude. The Baure Ravine subcatchment for instance deviated substantially from what can be expected, while the Manival high subsystem shows a clear positive correspondence.*

promising in regards to observation performed at the scale of rockfall events previously. The relationships are strongly affected by the short period of investigation as well.

A mean of considering rock slope production over a longer time period is to incorporate the entire geomorphic activity (erosion and deposition) recorded during the investigation period. At Manival, rock slope production is implicitly reflected in sediment process activity, since past rockfall activity governs the supply of debris and the rate of recharge in gullies (Chapter 2). Net sediment balances recorded in different subsystems of the headwater (see Chapter 2: Fig. 2.4) are clearly associated to the total density of failures (Fig. 3.31) and indicate that the observed geomorphic activity can be expressed as function of susceptibility to rock slope failure. This suggests that over a long period of record, the assumption that rock slope production may be dependent on the potential number of rock slope failures is valid and can be used to define a susceptibility index of debris production or to quantify degrees of susceptibility to mass wasting and geomorphic process activity, and so by using a uniform spacing between joints already.

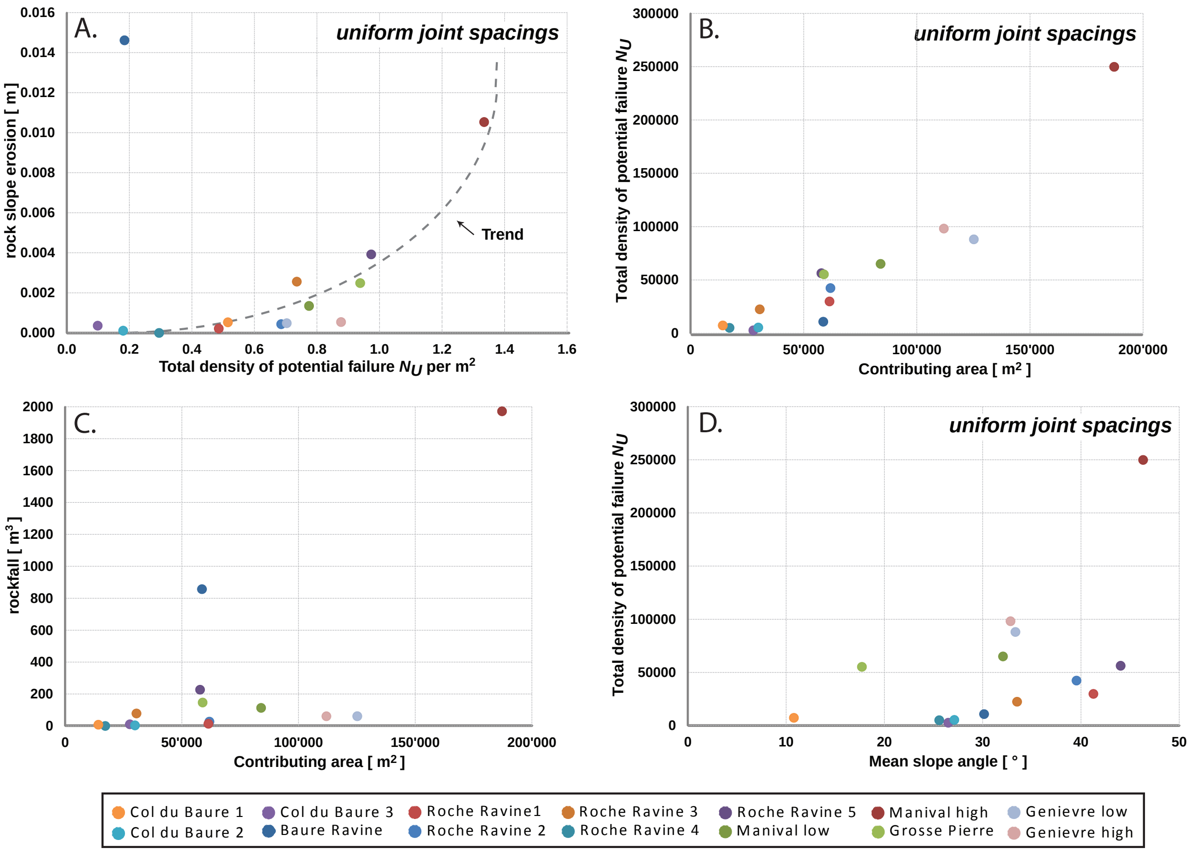

Figure 3.30: *(A) Rock slope erosion rate expressed as function of the total density of potential failure considering a uniform joint spacing for each subcatchment of the upper Manival. The plot suggests a trend in correlation that must be interpreted with caution since both input data may not depend on the rock slope extent (B and C). The Baure Ravine subcatchment (dark blue point) seems definitively to be an outliner. (D) Total potential failure density as function of the average slope angle of each subcatchment. The plots that consider relative true joint spacings and geotechnical parameters display similar results.*

3.7 Conclusions

This attempt to characterize debris supply related to rockfall activity based on morphological and structural investigation demonstrates evidence between hillslope process activity and morphostructural aspects of the Manival catchment. DEM-based parameters developed in this case study do not only assess degrees of susceptibility to rock mass wasting qualitatively, but quantitatively, contributing therefore to characterize rock slope failures and sediment dynamics of torrent systems at gully scale.

The topographic classification in major morphological units provides a systematic and homogeneous way to identify areas dominated by rock slope instabilities. The kinematic approach considers the spatial arrangement of joints with topography and therefore introduces more local geometrical and geomechanical elements for slope stability analysis. Comparison with the rockfall inventory shows that both methods can be used to map potential areas prone to rockfall and rockslides with a high level of confidence. Areas de-

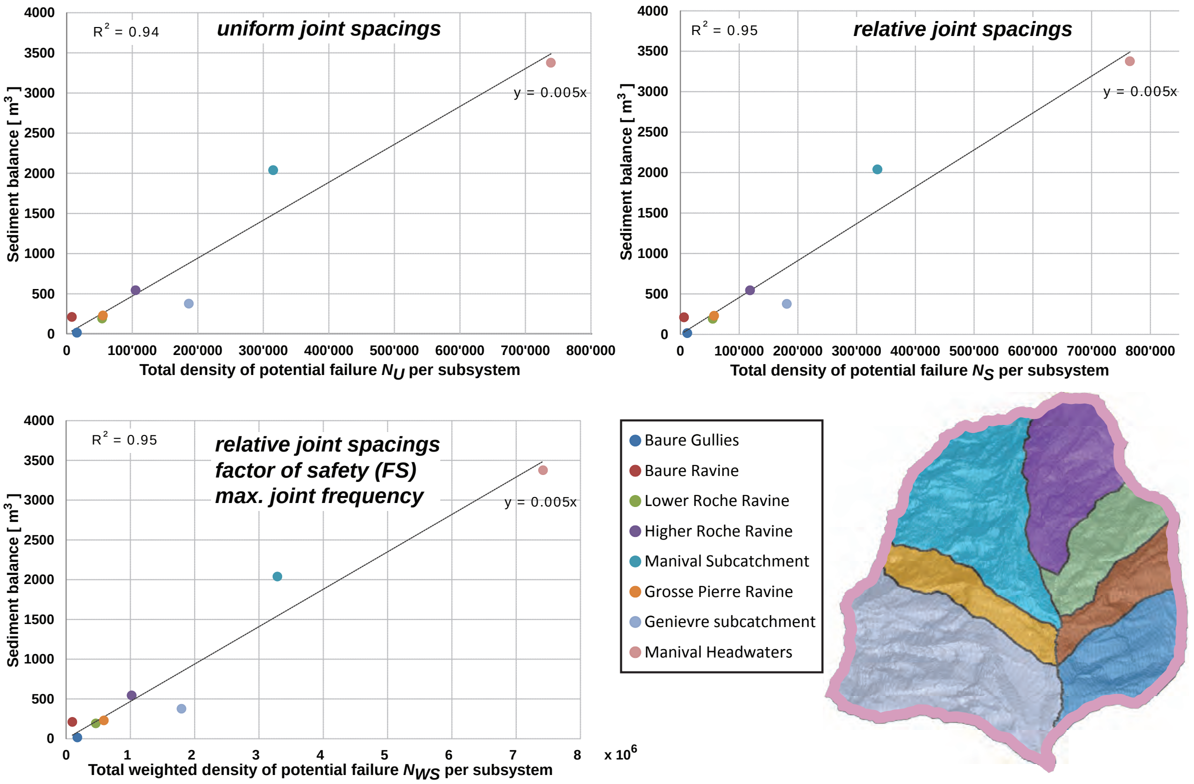

Figure 3.31: *Net sediment balances observed in the Manival headwaters displaying a strong positive correlation with the total density of potential failure. This supports the assumption that rock slope production (rockfall) is associated with the density of potential failure encountered at the scale of a gully over few years. In this case study, the introduction of relative true joint spacings and geotechnical parameters do not improve the relationship between data.*

lineated by the morphology only are large, but in regards that they may in great majority develop several mechanisms of failure according to the prominent joint setting, this can be qualified as reasonable over a long period of time. Such approaches provide therefore a preliminary overview for locating sources of debris supply and rockfall hazard assessment.

The structural analysis performed with the morphostructural method enables the extraction of the major discontinuity sets prevailing in rock mass in regards to the scale of investigation. The analysis performed with TLS data provides certainly the most precise geometry of local structural sets, while HR-DEM displays some averaged discontinuities that must be considered as geomorphic features highlighting rock slope process activity. However, both topographic data reflect the general pattern of structures with significative resolution to be used in slope stability assessment using kinematics for instance. The morphostructural analysis using standard DEM provide only an assessment of the most dominant structures at regional scale. As this latter is very often correlated to major tectonic features such as faults and other large-scale surficial lineaments, this can inform about the geostructural conditions inducing a (morpho-) structural control of the terrain for evaluating implications in process-related debris production from rock slopes.

A quantitative characterization of rock slope production from the number of potential failures suffers from the short rockfall inventory of this study case. The inconvenience of short-term records of events to set degrees of susceptibility was less the occurrence of small volumes in areas with high potential of failure than the observation of larger volumes detached at locations with low theoretical susceptibility. According to the prediction of occurrence of much larger rockslides (see Chapter 2), one can argue that the inventory largest events cannot be considered as large volume contributions and that most of them did not fail during the inventory. A longer period of record would probably help defining degrees of susceptibility to rock slope failures at the scale of rockfall events. This is also supported by the clear relationship with the overall sediment balances encountered in headwater subsystems. Geomorphically active zones may be quantitatively evaluated for long-term assessment. For short term prediction of sediment production, process related to rock slope instability seems to be more site-specific and require local field investigation.

Chapter 4

Influence of bedrock structures on the spatial pattern of erosional landforms in small alpine catchments

Abstract Structural settings and lithological characteristics are traditionally assumed to influence the development of erosional landforms, such as gully networks and rock couloirs, in steep mountain rock basins. The structural control of erosion of two small alpine catchments of distinctive rock types is evaluated by comparing the correspondences between the orientations of their gullies and rock couloirs with (1) the sliding orientations of potential slope failures mechanisms, and (2) the orientation of the maximum joints frequency, this latter being considered as the direction exploited primarily by erosion and mass wasting processes. These characteristic orientations can be interpreted as structural weaknesses contributing to the initiation and propagation of erosion. The morphostructural analysis was performed using digital elevation models and field observations. The catchment comprised of magmatic intrusive rocks shows a clear structural control, mostly expressed through potential wedges failure. Such joint configurations have a particular geometry that encourages the development of gullies in hard rock, e.g. through enhanced gravitational and hydrological erosional processes. In the catchment underlain by sedimentary rocks, penetrative joints that act as structural weaknesses seem to be exploited by gullies and rock couloirs. However, the lithological setting and bedding configuration prominently control the development of erosional landforms, and influence not only the local pattern of geomorphic features, but the general morphology of the catchment. The orientations of the maximum joints frequency are clearly associated with the gully network, suggesting that its development is governed by anisotropy in rock strength. These two catchments are typical of bedrock-dominated basins prone to intense processes of debris supply. This study suggests a quantitative approach for describing the relationship between bedrock jointing and geomorphic features geometry. Incorporation of bedrock structures can be relevant when studying processes governing the transfer of clastic material, for the assessment of sediment yields and in landforms evolution models.

4.1 Introduction

In steep mountain environments, contemporary landscape morphology may be explained from geodynamics, folding and faulting, long-term conditions of rock uplift, climate and surface processes (Hack, 1960; Ahnert, 1970; Barsch and Caine, 1984; Burbank et al., 1996; Willet, 2004). This multiple process origin remains complex (Desloges and Gardner, 1984; Roering et al., 2007). Indeed, whilst morphotectonic conditions and topoclimatic factors are relatively homogeneous throughout adjacent subcatchments, erosional landforms and hillslope processes are much less regular in their spatial pattern (Evans, 1997; Cruden, 2003). There is a great variability in the spatial distribution of landslides and rockfall activity, reflecting the local conditions that contribute to slope instability (Erismann and Abele, 2001). There is also considerable contrast in the spatial variability of erosional processes, suggesting that geomorphic features like gullies, debris flows channels, chutes and rock couloirs, may be strongly influenced by the underlying geology. In particular, their development may result from long-term factors that condition slope failure, such as bedrock structural features (i.e. bedding, folds, foliation, faults, and local joints) and lithological characteristics. The major role played by these geological features in landscape morphology is recognized in rock mechanics and rock slope stability analysis (Terzaghi, 1962; Hoek and Bray, 1981; Selby, 1982). The structural setting and the spatial distribution of joint sets within the bedrock slope inherently control the fragmentation and the modes of failure, which predetermine their geomorphic expression through erosion and mass wasting processes leading to the morphological development of the catchment (Selby, 1993; Sauchyn et al., 1998). Concerning the spatial distribution of geomorphic features, the influence of geological structures and lithological variations have also been mentioned in several studies related to steep mountain slopes (Davis, 1962; Luckmann, 1977; Craig, 1989; Weissel and Seidl, 1987). However, their implications are very often assumed or only explained implicitly, despite of their significance for debris flux and mass wasting processes. Less attention in the literature so far has been given to analysing quantitatively whether the geological structures controls significantly the spatial initiation and subsequent development of erosional landforms in steep mountain rock basins. Among several contributions, the spatial association between rock couloirs and their drainage basin with the geological lineaments such as faults is explicitly established: for example by Scheidegger (1980) in the Canadian Rockies and by Marchi et al. (2008) in the Italian Dolomites. The role of the major joint sets in predetermining gully location and bedrock channels is clearly recognized in Bulter and Walsh (1990), Eyles and Scheidegger (1995) and Sas and Eaton (2008). Less directly, Gardner (1986) notes that ephemeral channels coincide with steeply-dipping bedding planes. The relationship between the degree of fracturing of bedrock jointing and the location of erosion paths (debris flow, snow avalanches) is illustrated by Markgren (1964) in Fennoscandia and by Pippan (1981) in high calcareous Alps. The fractures density is mentioned in the works of Olyphant (1981; 1983) as being a key factor imposing a dominant local influence on the erodibility of rock slopes, demonstrating that zones of densely fractured rocks develop the largest talus accumulation. Other studies (Bloom, 1978; Sturzenegger et al., 2007a, among others) note that the direction that encounters the greatest number of fractures (highest joint density) should be more favourably exploited by erosion and mechanical weathering.

The present study documents the structural implications on the landforms derived from erosional processes of two small alpine catchments chosen for their intense geomorphic activity and their characteristic lithologies: (1) The Saxé and Métin catchment, a small basin of the Swiss Alps shaped in magmatic intrusive rocks; and (2) the Manival catchment, a small tributary valley of the French Alps located in Mesozoic sedimentary rocks. The spatial distribution of their gully network and rock couloirs is first characterized in terms of structural setting. The correspondences with the sliding orientations of potential slope failure are further studied. This analysis is then extended to the regional morphostructural context of the catchment, i.e. according to the main confluent valley and the geological lineaments such as thrust zones and local faults. Finally, the influence of the spatial distribution of the joints is investigated based on the orientations of the highest joint frequency, which are assumed to represent a structural weakness. The implications of structurally controlled erosional processes on the spatial distribution of hard rock gullies are discussed. Topographic and structural elements were extracted from High Resolution Digital Elevation Models (HRDEM) using GIS methods and coupled to structural information derived from geological maps, aerial photographs interpretation and field observations. The overall conditions associated with slope failure are presented in order to analyse whether the local joint systems, through influences on the most likely sliding orientations, contribute to the formation and propagation of gullies and rock couloirs across the catchment.

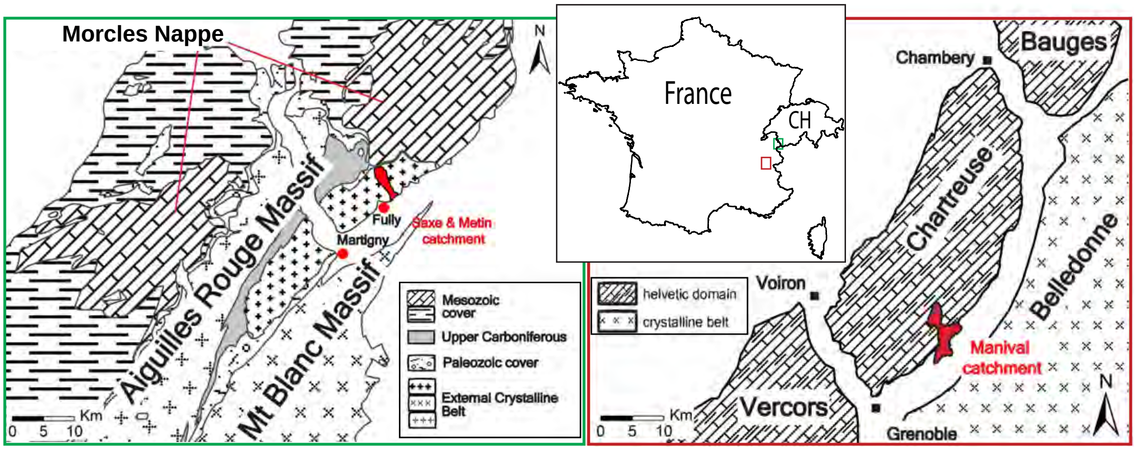

Figure 4.1: *Simplified tectonic maps showing the location, size and geological context of the two study areas. For the Manival catchment (right), note the very large debris fan recovering the confluent valley.*

4.2 Study sites

4.2.1 The Saxé and Métin catchment

The Saxé and Métin torrents (Fig. 4.1 left) form a common catchment located in the northern end of the Aiguilles-Rouges Massif, about 10 km northeast from the town of Martigny

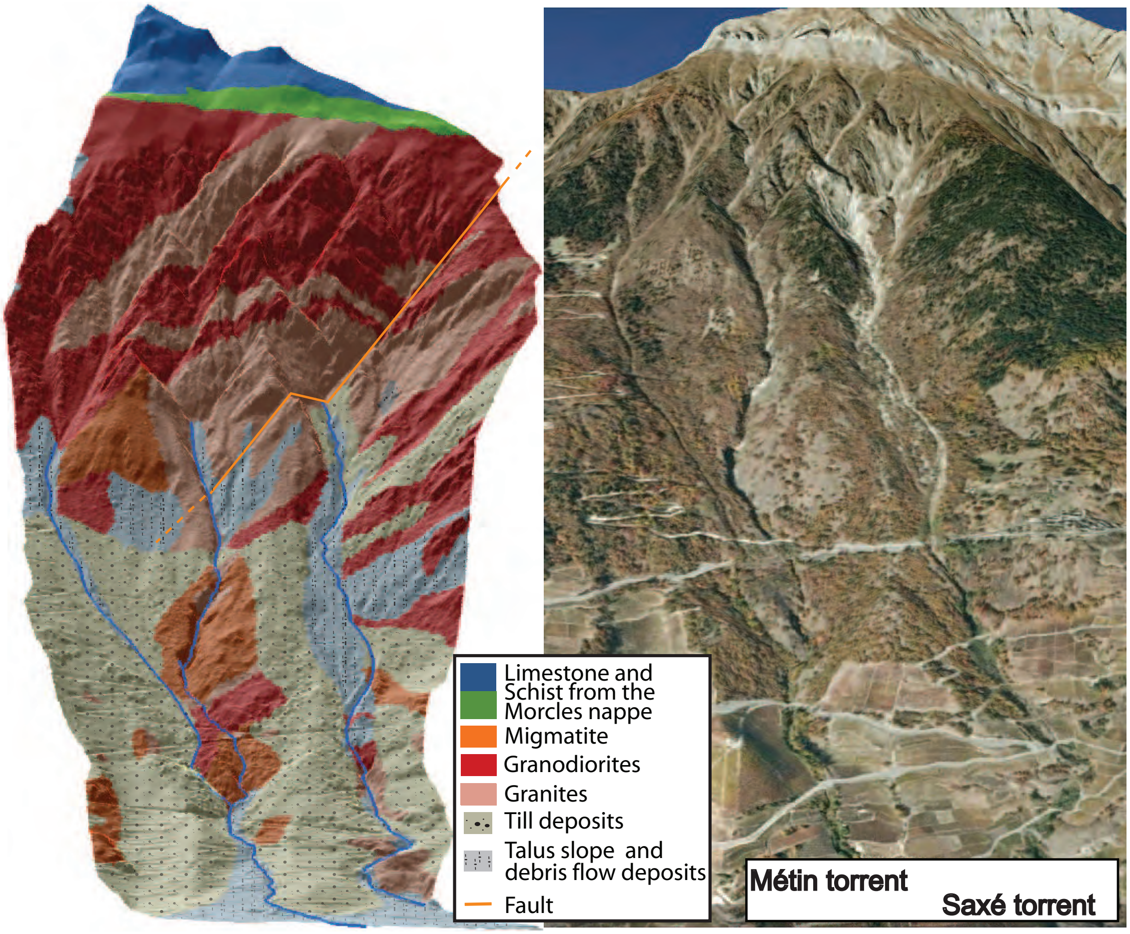

Figure 4.2: *Saxé and Métin catchment: (Left) projection of the geological map onto a 3-D shaded DEM displaying the dominant rock types of topography. (Right) View of the field area showing the gully network, which is particularly well-defined in the upper part of the catchment, where the bedrock dominates.*

(Valais). This mountain range is part of the external crystalline belt of the western Swiss Alps, which corresponds to the pre-Mesozoic basement. The lithologies have experienced several orogenic episodes, leading to a high variability of metamorphic grade and local anatexis (Krummenacher, 1959). The catchment has been developed in magmatic intrusive rocks (Fig. 4.2 left), mainly coarse-grained granodiorite and granite (Bussy et al., 2000). As the study site is located in the external part of the belt, the tertiary alpine orogeny had relatively little effect and pre-Alpine structures have been well-preserved (vonRaumer, 1974). Due to the low grade Alpine metamorphism, the rock types show therefore no systematic internal structures (e.g. foliation) and a modest brittle deformation only. Field reconnaissance suggests that the lithologies are very resistant to erosional processes, forming finely cut escarpments and steep rock cliffs. Large-scale tectonic features, beside a probably ante-alpine fault (vonRaumer et al., 2009) of orientation N45 crossing the Saxé torrent, were not detected. The top is covered with Mesozoic sediments of the Morcles Nappes. The contrast between both domains is very clear; the well-cut wedge shape bedrock gullies of the lower part disappear when they reach the tertiary lithologies,

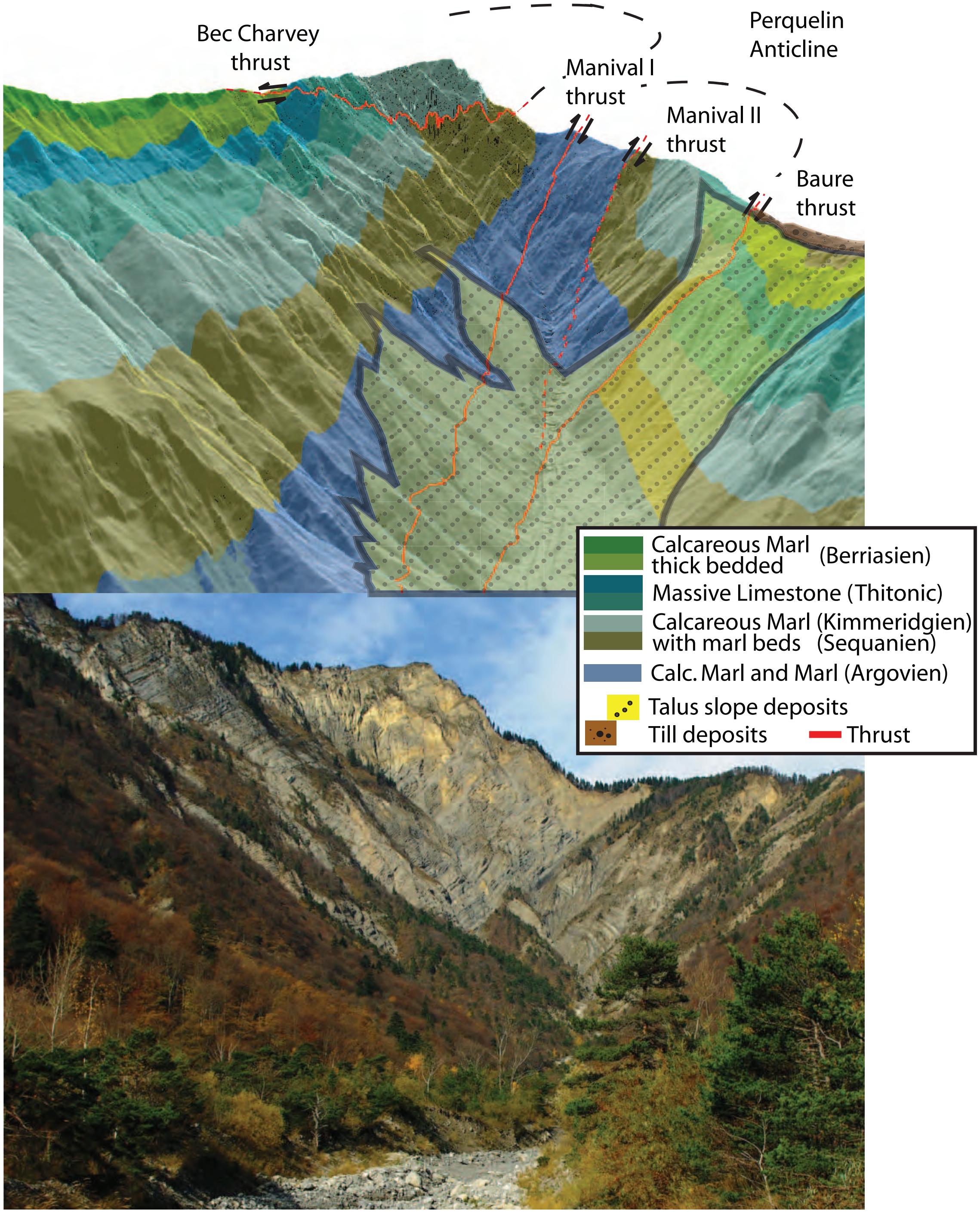

Figure 4.3: *The Manival catchment: (above) projection of the geological map and major tectonic features of the fold onto a 3-D shaded DEM. (below) View of the field area displaying the bedrock cirque below the summit and the rock couloirs and gullies of the upper valley.*

replaced by steep bedrock talus slopes and cliff ridges developed in the Malm massif limestone. The catchment covers a surface of 2 km^2 with a local relief varying from 500 m a.s.l. to 2000 m a.s.l. and an average slope angle exceeding easily 45° (Fig. 4.2 right). The erosional landforms are expressed through a network of channels incised in the bedrock. The erosional activity seems to be supply-limited, as debris availability is low. Recent debris flow events carried along a few 100 m^3 of sediment (Bardou and Jaboyedoff, 2008). However, in the middle part of the Saxé torrent, an important accumulation of loose sediment has been deposited. In 1939, a large volume of this deposit was mobilized in a debris flow estimated at 120'000 m^3 with dramatic consequences for the village beneath (Montandon, 1940). This catchment seems to proceed in the long term with rare, but high volume catastrophic events.

4.2.2 The Manival catchment

The Manival is a small basin, tributary to the Isère River in the Grésivaudan Valley, situated 20 km northeast of the town of Grenoble (France). This catchment covers an area of 3.7 km^2 from the top (1738 m a.s.l.) to a sediment trap built on the top of the alluvial fan (565 m a.s.l.) and belongs to the northern subalpine domain of the Chartreuse Massif, which corresponds to the Mesozoic cover of the external alpine crystalline belt. The lithologies consist of an alternation of limestone and marl ranging from the upper Jurassic to early Cretaceous (Fig. 4.3 above) and embedded in layers of decimetric to metric thickness (Charollais et al., 1986). The upper catchment has developed in an anticline, where the two valley sides correspond to the fold limbs. It displays a structure of inclined folds from Miocene age containing important and continuous overthrust faults (Gidon, 1991). The hinge zone is cut by a system of inverse faults that crosses sidelong the axis of the valley, leading to a higher elevation of the western limb and the east side is reversed (Gidon, 1991). Erosion has then deeply entrenched the fold, leaving a dissected relief with steep cliff faces, and built one of the largest alluvial fan of the western Alps made of torrential debris (Besson, 1996). These tectonic features, like the lithologies, have probably played a major role in the impressive headward entrenchment depth of the catchment. Today, the erosion is still very active, but hillslope process activity is concentrated essentially in the upper catchment (Fig. 4.3 below), where the bedrock basin displays steep cliff walls. The torrent channels experience significant bedload transport and debris flows of thousands of m^3 almost every year, where their initiation is linked to a certain level of the headwater sediment production. The largest volume of debris measured during the 20^{th} century deposited about 60'000 m^3 (Péteuil et al., 2008).

4.3 Data sources, methods and statistical analysis

4.3.1 Morphostructural analysis using DEM

The major joints sets were identified based on a morphostructural analysis of the topography displayed by DEM. When bedrock dominates, the morphological expression of

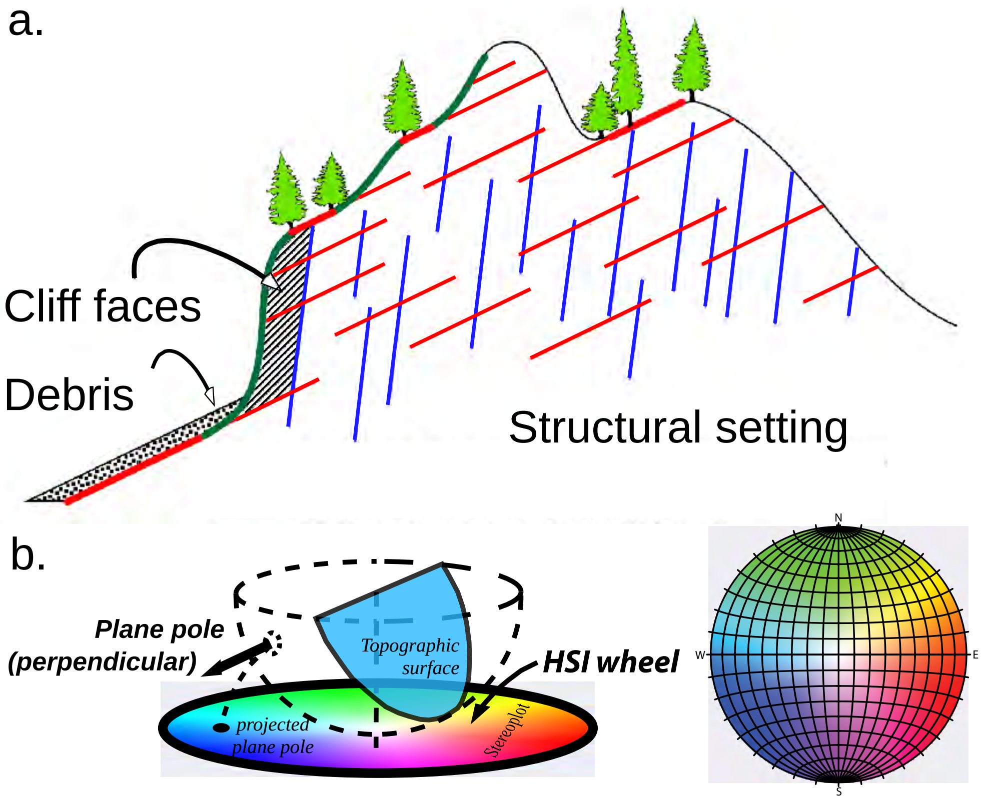

Figure 4.4: *(a) Illustration of the fact that in bedrock-dominated terrains, the joint sets are expressed in the morphology of the topography and can be therefore extracted from a 3-D morphostructural analysis of the topography (modified after Baillifard, 2004). (b) Relationship between the Schmidt-Lambert projection and the HSI wheel colour code used in Coltop 3D to display the spatial orientations of the terrain in a stereographic projection mode.*

the topography reflects the overall structural pattern shaping the terrain (Terzaghi, 1962; Selby, 1982; Jaboyedoff et al., 2004). Geostructural lineaments, such as faults, joints and bedding surfaces are therefore represented in the discontinuities of the topography (Fig. 4.4a). Hence, a 3-D morphostructural analysis using HRDEM provides a uniform and full overview (at the catchment scale) of the major morphostructures and tectonic features with high degree of detail. Such data are not always identifiable from field reconnaissance (Jaboyedoff et al., 2009a; Sturzenegger and Stead, 2009; Pedrazzini et al., 2011). The identification of the discontinuity sets was performed with the software Coltop 3D (Jaboyedoff et al., 2007), which represents the azimuth and slope gradient of the DEM cells with a unique colour code, the HUE saturation intensity system (HSI). The colour code ranges between values of a Schmidt Lambert projection. The terrain orientations are therefore expressed in terms of dip angle and dip direction (Fig. 4.4b). The topography is displayed as a 3-D shaded relief model that enables to analyse visually the major tectonic lineaments and the characteristic shapes linked to particular hillslope processes. Uncertainties remain when a structural assessment is carried out on joint observation made from limited outcrops, due to the fact that their orientation can vary considerably over a relatively small area. The advantage of performing a morphostructural analysis within HRDEM is not only an alternative to very local structural studies performed on accessible outcrops, when conditions for measuring become too hazardous, but is complementary to a structural field study.

4.3.2 Relevance of the discontinuity pattern for the catchment morphology

According to Priest and Hudson (1976), sets of non-random individual discontinuities create a random occurrence of discontinuity sets when put together after a series of geological events. Considering that all orientations of discontinuity planes can be found in a terrain morphology undergoing surface processes, the spatial occurrence of each discontinuity that shapes the catchment topography can be compared with a uniform spatial distribution of the discontinuity orientations. By doing so, the non-random spatial occurrence of the identified sets of discontinuity is established and their weight in the expression of the catchment morphology can be discussed. The relevance of each discontinuity set for the catchment morphology was therefore explored on the basis of their statistical occurrence as topographic planes at the surface of the catchment. The topographic surfaces corresponding to the joint sets orientation were estimated by computing the topographic area, given the mean orientation of each joint set, plus an increasing variability corresponding up to 2σ. Their surface was then normalized over the entire study area. Each surface ratio was then compared with their corresponding surface ratio A_{stereo} as follows:

$$A_{stereo} = 1 - cos(\alpha) \tag{4.1}$$

α being the variability, that is displayed in the stereoplot as a unitary surface ratio.

4.3.3 Correspondence between gully network and potential slope failure geometry

In order to study their correspondences, the sliding orientations of potential slope failure mechanism (planar – wedge – toppling) were compared with the orientations of the geomorphic features at the scale of the gully reaches. This was performed following the kinematic criteria commonly established in the literature (Markland, 1972; Hoek and Bray, 1981) and the topographic orientations. In particular, the variability of the wedge axis direction was set following the variability of the joints according to the discontinuity sets selected with Coltop 3D. However, the large variability of certain joints results in a very large range of possible orientations in the wedge axis direction. Although this is not incorrect following the variability of the structural sets, this large distribution of potential failure directions increases considerably the correlation with the orientation of geomorphic features. Therefore, to refine the correspondences between both geometries, the analysis was carried out by using the wedge axis direction computed following the mean orientation of the joints with a variability that was progressively added. Their geometric correspondence was then quantitatively evaluated as a percentage of segments influenced by the considered mode of failure.

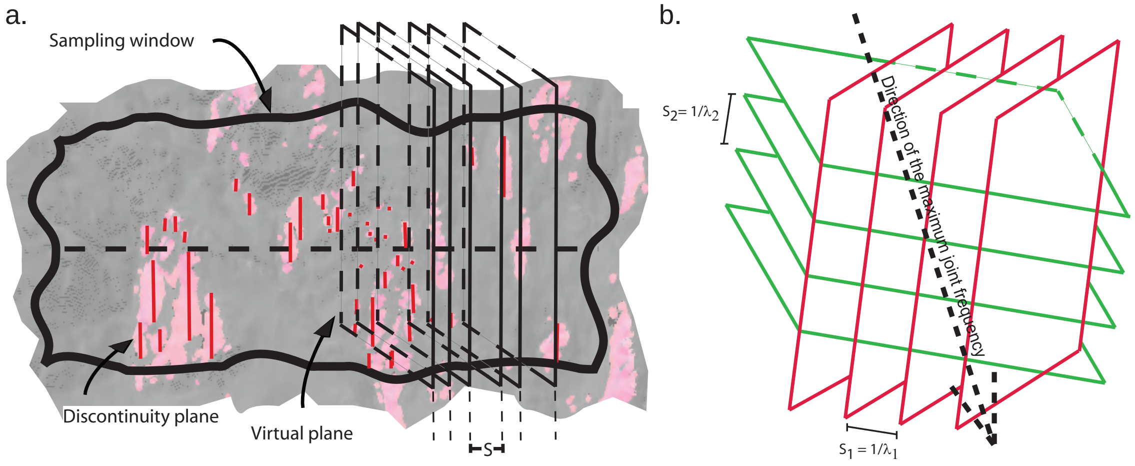

Figure 4.5: *(a) Sketch of the sampling window approach that enables an estimation of the mean spacing of a discontinuity set. The distance S between two consecutive virtual planes can be measured for each trace of sets of discontinuities extracted within Coltop 3D at the surface of DEM. (b) Sketch illustrating the joints frequency in space, which is more prominent along a certain direction.* λ *= linear frequency of the spacing of the joint (modified from Sturzenegger et al., 2007).*

4.3.4 Orientation of the maximum joints frequency

As local patterns of joints include sets that have typically preferred orientations, the number of joints is not equal in all directions across a fracture network. The joint density encountered along certain directions is significantly bigger, such as erosional processes can be assumed to be located or at least facilitated in the direction where the encountered number of joints is the most important. The influence of the spatial distribution of joints was therefore studied based on the computation of the joint frequency in all directions of space (Fig. 4.5b). This was performed by using the equation proposed by Hudson and Priest (1983) and implemented for stereographic visualization in Jaboyedoff et al. (1996). Information about the mean joint spacings (ISMR, 1978) is required, at least a corresponding ratio of spacing between the joint sets. This was estimated using the spatial distribution of the traces, as they appear with Coltop 3D on the DEM and following the sampling window approach (Rohrbaugh et al., 2002). A sampling window is drawn over the most relevant and representative part of the catchment (Fig. 4.5a) and the orientation is chosen to avoid subparallel discontinuity traces (Sturzenegger and Stead, 2009). A plane with the mean orientation of the considered joint is set to each trace. The distance between two consecutive planes is then measured considering that the traces represent joints that are persistent over the whole sampling window (a succession of infinite plane). This method was chosen rather than the traditional scanline approach due to the fact that impersistence is difficult to account for in DEM data, and already implicitly incorporated in the measure when sampling at such a large scale (Sturzenegger et al., 2011). As the spacing extracted from a DEM can range from a few tens of centimetres to hundreds of meters, a scale effect is expected when sampling at such large scales, creating a cut-off at a certain level due to the fact that the large spacing distribution is probably underestimated considering the size of the sampling window. Therefore, as suggested in Jaboyedoff et al.

(1996) and Hudson and Priest (1983), all joints are assumed to have a random occurrence that enables comparison of the distribution of their spacing to a 1-D Poisson process. The spacing distribution was thus assessed using a negative exponential distribution, where the number of fractures per unit length λ is assumed to be:

$$\lambda = 1/\frac{\sum S}{n} \tag{4.2}$$

where λ is the linear frequency, *S* the spacing between two consecutive joints and *n* the amount of joints considered. The random distribution following a Poisson law is expressed as a cumulative distribution function as follows:

$$F(x \leq s) = 1 - e^{\lambda x} \tag{4.3}$$

where *F* corresponds to the amount of discontinuities where their spacing x between two consecutive planes is smaller than a given spacing s. For each cumulative frequency of each joint spacing, the function *F* was adjusted using the least square fitting method in order to minimize the error between both distributions and to define an optimal mean spacing value λ^{-1}.

4.3.5 Data processing

All data were processed in a similar way for both catchments. The topographic data were extracted from airborne LIDAR-derived HRDEM of grid resolution 2 m cell size for the Saxé and Métin catchment, respectively 1 m for the Manival. The discontinuity sets were extracted with Coltop 3D by analysing the occurrence of the significant topographic planes shaping the DEM bedrock topography. Their orientations were selected on the shaded relief model and displayed in a stereoplot. The geometry of each joint set was then given with its mean orientation and a variability of 2σ, assuming a Fisher distribution (Wyllie and Mah, 2004). When such analysis is based on airborne DEM acquisition, structures subparallel to the topography or overhanging planes cannot be detected. However, they very often outcrop in some other parts of the topography where they can be identified and their orientations measured.

The gully network and rock couloir geometries were defined with a combined analysis of DEM and aerial photographs mapping using GIS techniques. They were delineated initially using the river extraction D8 algorithm (O'Callaghan and Mark, 1984) in the HRDEM and considering a minimum contributing area of 500 m^2. These virtual flow paths were completed manually for gullies that have a too small contributing area to be automatically extracted. Erroneous flow paths were manually removed. Geomorphic features lying in the lower part of the catchment, where the Quaternary deposits are dominant, were not considered in this study as they are not structurally controlled (by definition). Each erosion path was cut in segments corresponding to the DEM resolution. Each segment was characterized in terms of both direction (azimuth) and slope gradient. Using the trend and plunge notation allows the frequencies of gully geometries to be shown on a stereoplot, which can be directly linked to joint settings. The correspondences were inspected by overlying the joint sets stereoplot.

In the Manival, the mean spacing value of the bedding plane does not correspond to the true mean spacing, as some lithologies (e.g. calcareous marl) have a more tight spacing that is not detectable with the HRDEM, but is likely to correspond to the mean spacing of the more competent calcareous layers. This could give at least an overall estimation of the influence of this joint plane as expressed in the topography.

4.3.6 Structural data validation

Validation and interpretation of the structural setting were performed using field observation and information taken from geological maps and previous published literature, concerning e.g. faults and foliation influences. The structural sets extracted with Coltop 3D for the Saxé and Métin catchment were compared with field measurements performed on some outcrops at the lower part of the catchment. At Manival, a few field measurements were taken, but the cliffs are rather hazardous for field work. For this reason, HRDEM were acquired with terrestrial laser scanner (TLS) on both sides of the valley. The high density of point cloud datasets (150 – 600 pts/m^2) allows an accurate reconstruction of the rock surface in the form of a 3-D interpolated surface. An identification of the major discontinuity sets that shape the bedrock topography was carried out for the detailed TLS point cloud with Coltop 3D. These local structural measurements were then compared with the overall morphostructural data.

4.4 Results

4.4.1 Morphostructural analysis of the Saxé and Métin catchment

Six major discontinuity sets were identified in the crystalline complex (Fig. 4.6), for which a mean spacing was estimated (Fig. 4.7). All joints are spatially well-distributed across the catchment, such as different structural domains are therefore unlikely. J1 (226°/44°) and J4 (063°/55°) form large topographic planes shaping the slopes regularly. J1 covers a relatively large proportion of the surface with a low dispersion orientation that can be therefore linked to a well-defined joint set with a great persistency (Fig. 4.8). J2 (284°/59°) and J3 (021°/51°) are encountered at the surface in the inner gullies slopes exclusively. These two joints are mostly anaclinal and consequently cover a smaller surface area, although they have a more dispersed orientation. However, they define clear bedrock structural sets rather than geomorphic features as they are encountered clearly in the neighbouring catchments as well. J5 (148°/70°) and J6 (182°/71°) are two sets of planes facing down towards the major Rhône Valley and forming the steep cliffs. They cover a large portion of the topography with low dispersion. J5 seems to be particularly persistent.

Comparison of the joint patterns detected with Coltop 3D with field measurements for the lower part of the catchment shows some similar trends for joints J1 to J4 (Fig. 4.6b). J5 has a lower dip angle in the field data, which can be explained by local orientation changes. The discrepancy of steepness between the discontinuities J6 can result from the

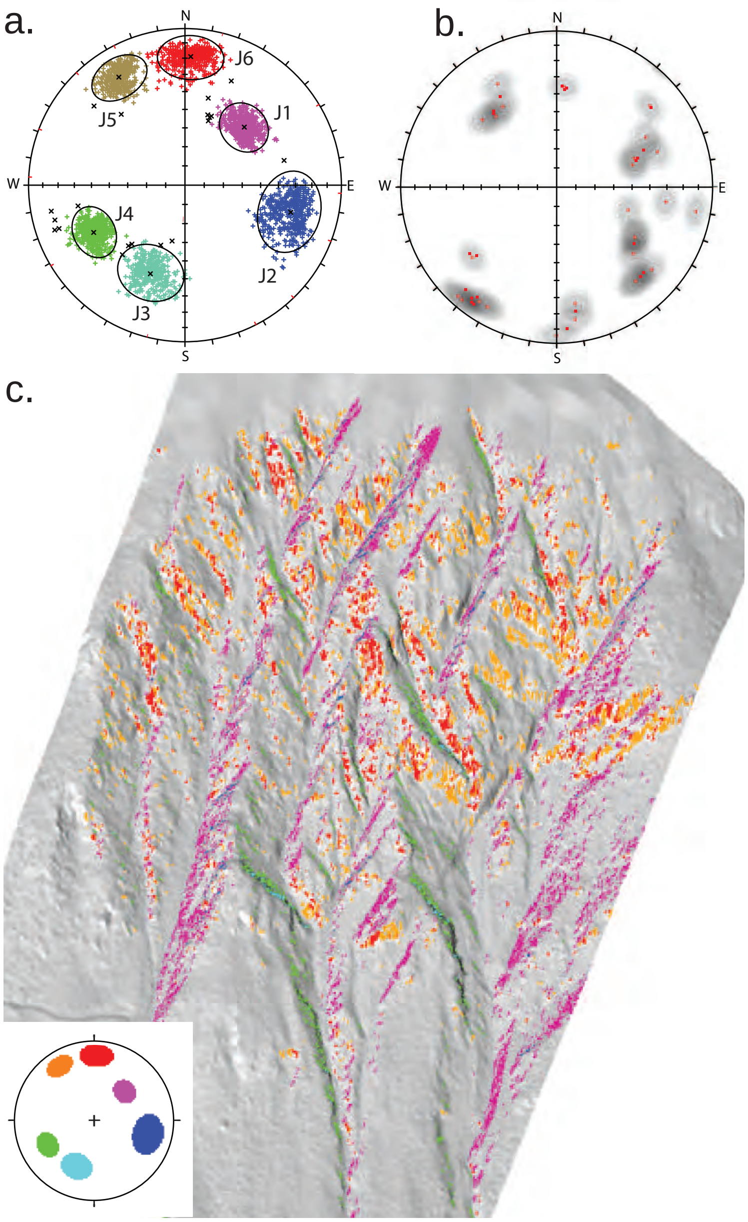

Major discontinuity sets detected in
the Saxé and Métin using Coltop 3D

Discontinuity set	Coltop 3D data			
	Dip Direction	Dip	Variability (2σ)	Mean spacing
J1	226°	44°	12°	9.6 m
J2	284°	59°	18°	26.0 m
J3	21°	51°	15°	19.8 m
J4	63°	55°	12°	35.1 m
J5	148°	70°	12°	5.4 m
J6	182°	71°	14°	18.8 m

Figure 4.6: *Saxé and Métin catchment: (a) Discontinuity sets extracted from the morphostructural analysis of the DEM using Coltop 3D and displayed on a 3-D shaded relief map (c). The black circles represent the variability (2σ); the values are given in the table below. (b) Field measurements carried out in several outcrops of the lower part of the catchment.*

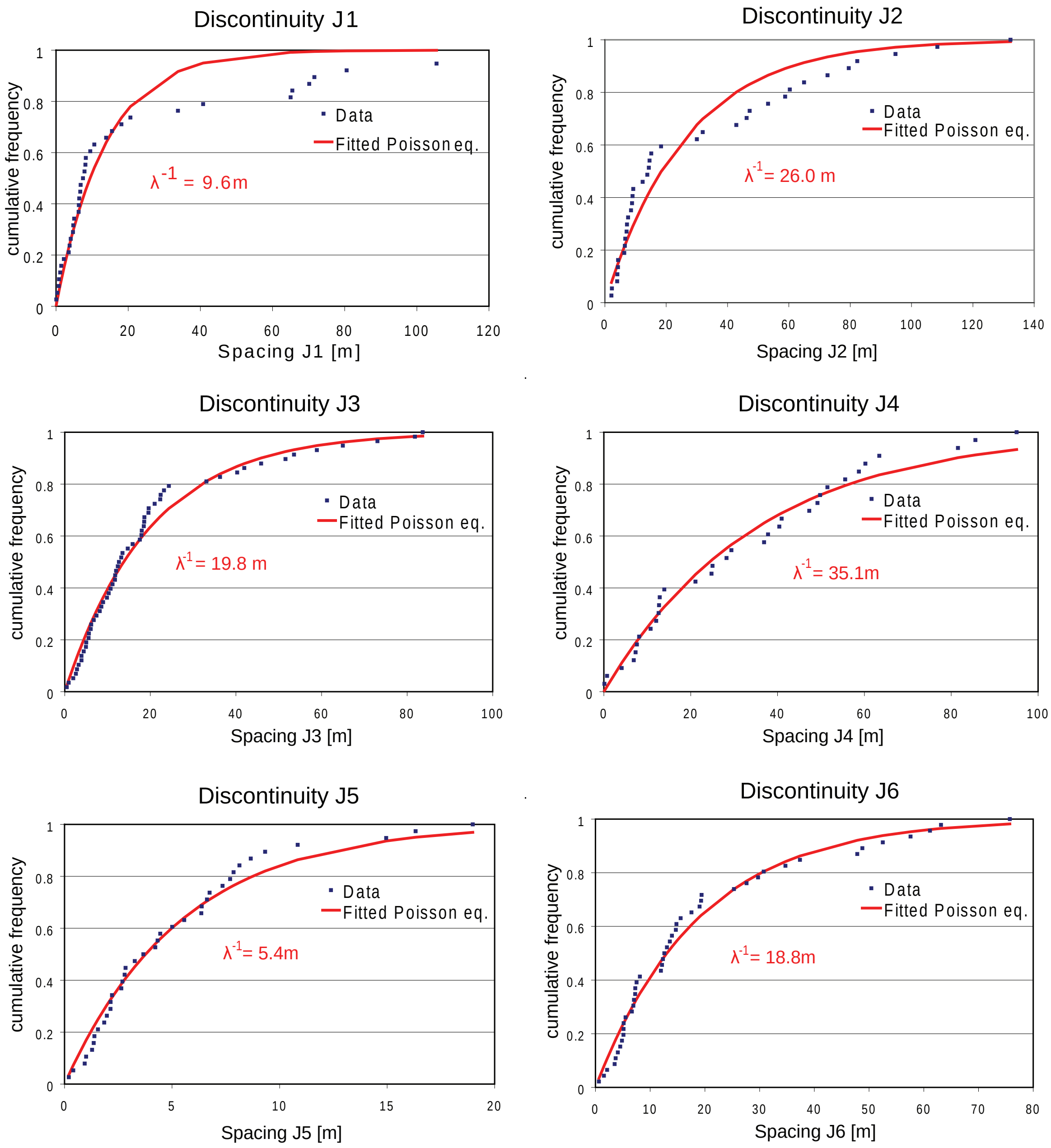

Figure 4.7: *Joint spacing distribution of the discontinuity sets determined after the sampling window approach in the Saxé and Métin catchment.* λ^{-1} *is the mean spacing deduced by the Poisson equation.*

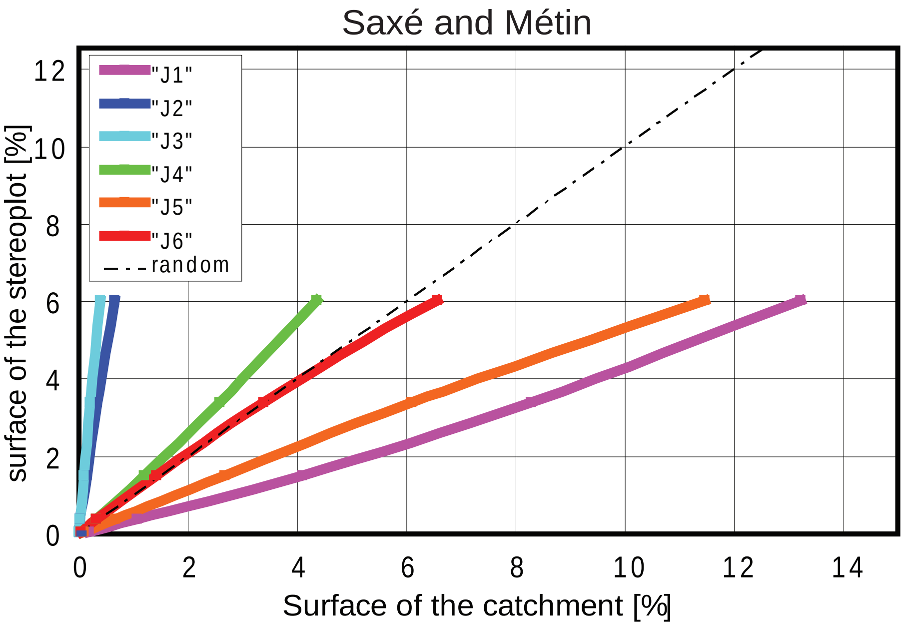

Figure 4.8: *Influence of joint orientations on the morphology of the topography in the Saxé and Métin catchment. The surface of the catchment (x-axis) corresponds to the topographic area (in %) covered by each discontinuity set given a certain variability of their orientation ranging from 1° to 20°; such orientations with their increasing variability are expressed as an ordered pair with the corresponding unitary surface ratio of the considered orientation (surface of the stereoplot in %). The random line indicates that the topography expressed by a given discontinuity equals the unitary surface ratio* A_{stereo}*. Discontinuity J1 shows e.g. a surface ratio of about 2.5 x* A_{stereo} *for a variability of orientation of* 2σ*, whereas surface ratio J3 only 0.05 x* A_{stereo}*.*

local outcrops downslope, but also from the fact that the DEM cannot display overhanging joint sets. Based on these field data, the morphostructural analysis carried out with Coltop 3D can be assumed to display the general patterns of the major joint sets occurring in this catchment.

The orientation of the maximum joint frequency is shown in Figure 4.9 (right). The distribution ranges towards 185°/70° with a variability of 25°. The maximum density is directed basically towards north south, steeply-dipping, and decreases progressively towards west and east. Assuming an identical mean spacing for all joints yields to a similar trend, but more constrained in the north east direction. This is due to the influence of J5, which has a very tight mean spacing in comparison with the other joints. A comparison with the orientations of the catchment topography highlights the cliffs and steep slopes facing south towards the main Rhône Valley (Fig. 4.10).

4.4.2 Morphostructural analysis of the upper Manival catchment

Seven major discontinuity sets were identified at the surface of the upper Manival catchment (Fig. 4.11). Their mean spacing is given in Figure 4.12. All discontinuities are encountered on both sides of the valley, except J3 (220°/62° ± 16°) that outcrops only dis-

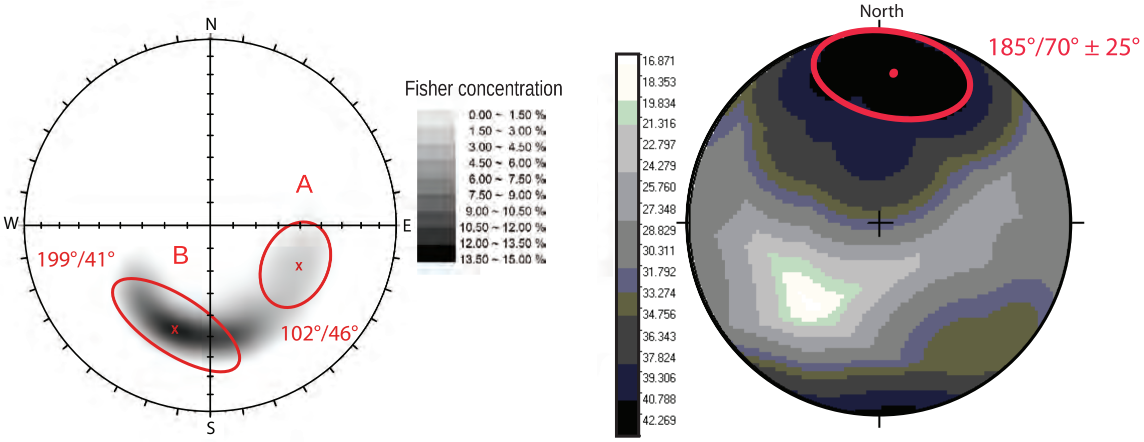

Figure 4.9: *(Left) Stereoplot of the frequencies of orientations of the geomorphic features highlighting two populations of gullies in the Saxé and Métin catchment. The concentration corresponds to the number of gully and rock couloir segments for a given orientation expressed in percent of the whole geomorphic features. (Right) Stereoplot of the orientation of the joint frequency according to the mean joint spacing deduced from the sampling window approach. The geometry of the maximum frequency considering all the joints is in the circle in red and represents a variability of 25° around the maximum orientation 185°/70°.*

tinctly in the eastern side and J5 (350°/60° ± 19°) in the western side (Fig. 4.11c). They all show a good similarity to the structural pattern revealed by the Coltop 3D analysis performed on detailed TLS data. Variations should come mostly from the more accurate resolution of the topography. Joint set J2 (187°/53° ± 14°) and J3 occur only in the region situated between the Baure and Manival I thrusts (Fig. 4.3), whereas J5 is absent. J7 (106°/74° ± 17°) defines only a few discontinuities and was not detected on the outcrops sampled with TLS data in the thrusts region. The thrusts zone can be therefore considered as a structural domain separately. J1 (155°/64° ± 16°) is well-distributed on both valley sides but seems particularly persistent in the western limb as it defines large topographic planes. J2 and J3 are similar to J1, whereas they cover a smaller surface as they occur only in the structural domain of the thrusts zone. These three discontinuity sets shape most of the cliffs facing in the direction of the valley axis. The topographic orientation described by S0 (261°/50°) covers the greatest surface, although having a variability of 15° (Fig. 4.13). It shapes the eastern topography of the valley with large planes. Field observations show that these orientations correspond to the bedding planes. On the western limb, the bedding is anaclinal and its occurrence at the surface of the DEM is rare. J5 was not detected in the structural domain of the thrusts zone. This discontinuity is encountered mostly in the deep entrenchments of the western side, mostly associated with J6. It covers a very low portion of the topography, although a larger variability. J6 is particularly well-defined in the western valley side, where it shows distinct and persistent topographic planes that appear regularly from the top to the bottom of the valley. The topographic area described by discontinuity J7 follows a trend as its influence on the morphology would be random (Fig. 4.13). However, field observations confirmed that J7 defines a clear bedrock structure that can be found in both structural domains. Its orientation corresponds to large and steep cliffs oriented parallel to the Manival torrent.

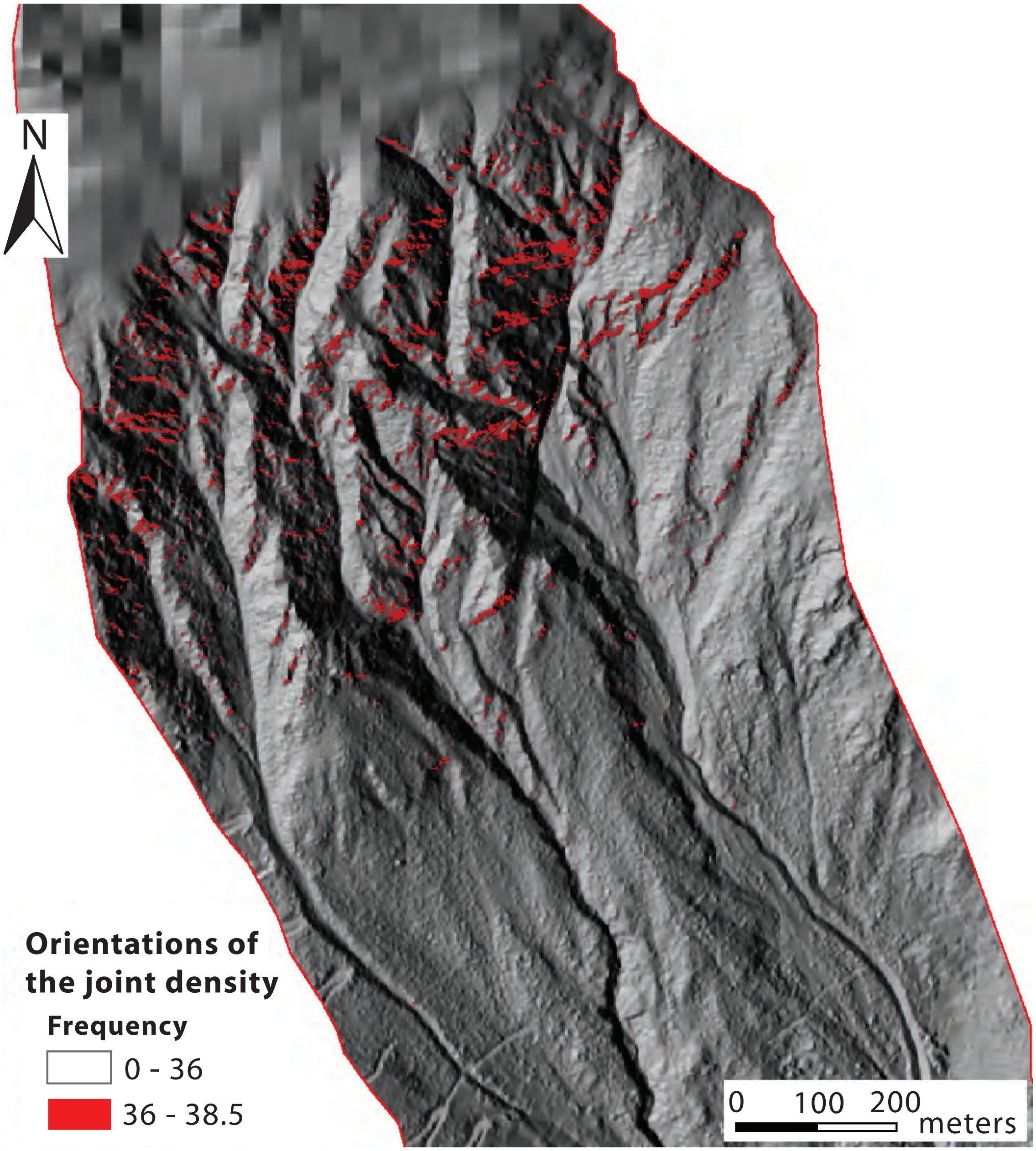

Figure 4.10: *Shaded relief map of the Saxé and Métin catchment showing the topography oriented in the direction of the maximum joint frequency. There are the cliffs and steep slopes facing south towards the main confluent valley.*

The joint frequency on the stereoplot shows a maximum orientation towards 175°/60° ± 20° (peak A) and 225°/75° ± 10° (peak B) (Fig. 4.14 right). Assuming a uniform mean spacing of the joints shows that the maximum direction is oriented more towards south east, and is steeper dipping. J6 particularly has a mean spacing much larger than the others (Fig. 4.12), minimizing its influence on the maximum orientation. The bedding planes influence greatly the joint density distribution by highlighting the orientations surrounding the peak B as a maximum frequency orientation. This shows a trend in the orientations delineating the steep cliffs facing south-southwest (Fig. 4.15).

4.4.3 Geomorphic feature orientation analysis of the Saxé and Métin catchment

The orientations of more than 80% of the gullies have azimuths between [150°–230°] for an inclination ranging within [27°–55°] (Fig. 4.9 left). The frequency distribution appears to be normally distributed around a mode defined at 199°/41° ($2\sigma = 24°$). A second population of gullies with orientations [90°–135°] and dip angles [35°–60°] and a mode at 102°/46° ($2\sigma = 22°$) exists as well, but represents less than 20% of all geomorphic segments. The orientations located on both sides of the distribution show a clear agreement with the mean direction of several potential slope failures (Fig. 4.16). Two groups of wedges create potential sliding directions corresponding to the peak frequency orientation of the geomorphic feature segments. Notably, the failure directions of the wedges W2 (111°/44°) and W5 (086°/53°) correlate with about 15% (18%) of all geomorphic features segments using a variability of maximum 15° (20°) of their wedge axis. They concern precisely the gullies directed towards the most eastern direction. Considering the aforementioned variability of their axis orientation, the bulk failure direction of the group of wedges W6 (222°/38°), W7 (218°/44°), W8 (230°/44°) and W10 (245°/52°) coincide with about 25% (31%) of all geomorphic segments, comprising a very large majority of gullies located west from the peak frequency B. More detailed values on these correspondences are given in Table 4.1.

Concerning potential planar sliding, J1 can be closely related to the peak frequency B, especially the western end-members of the distribution. Although the mean dip direction of J1 somehow offsets the higher frequency orientations of these geomorphic features, there is a very consistent alignment of the dip angle of the geomorphic segments with the dip of the plane J1.

The remnant possible joints acting as potential sliding planes or wedge structures defining potential failure orientations are either too flat or dip into the slope. They are therefore difficult to be considered as having a direct structural control on the orientations of the geomorphic features. Conversely, the geomorphic segments that have not been considered so far by potential failure modes linked to the structure are the ones roughly parallel to the orientation approaching the maximum slope of the catchment. This general orientation is however oriented between the dip direction of joints J5 and J6, and concordant with their common wedge structure W4 (160°/70°). But also, wedge-toppling formed by J2^J3

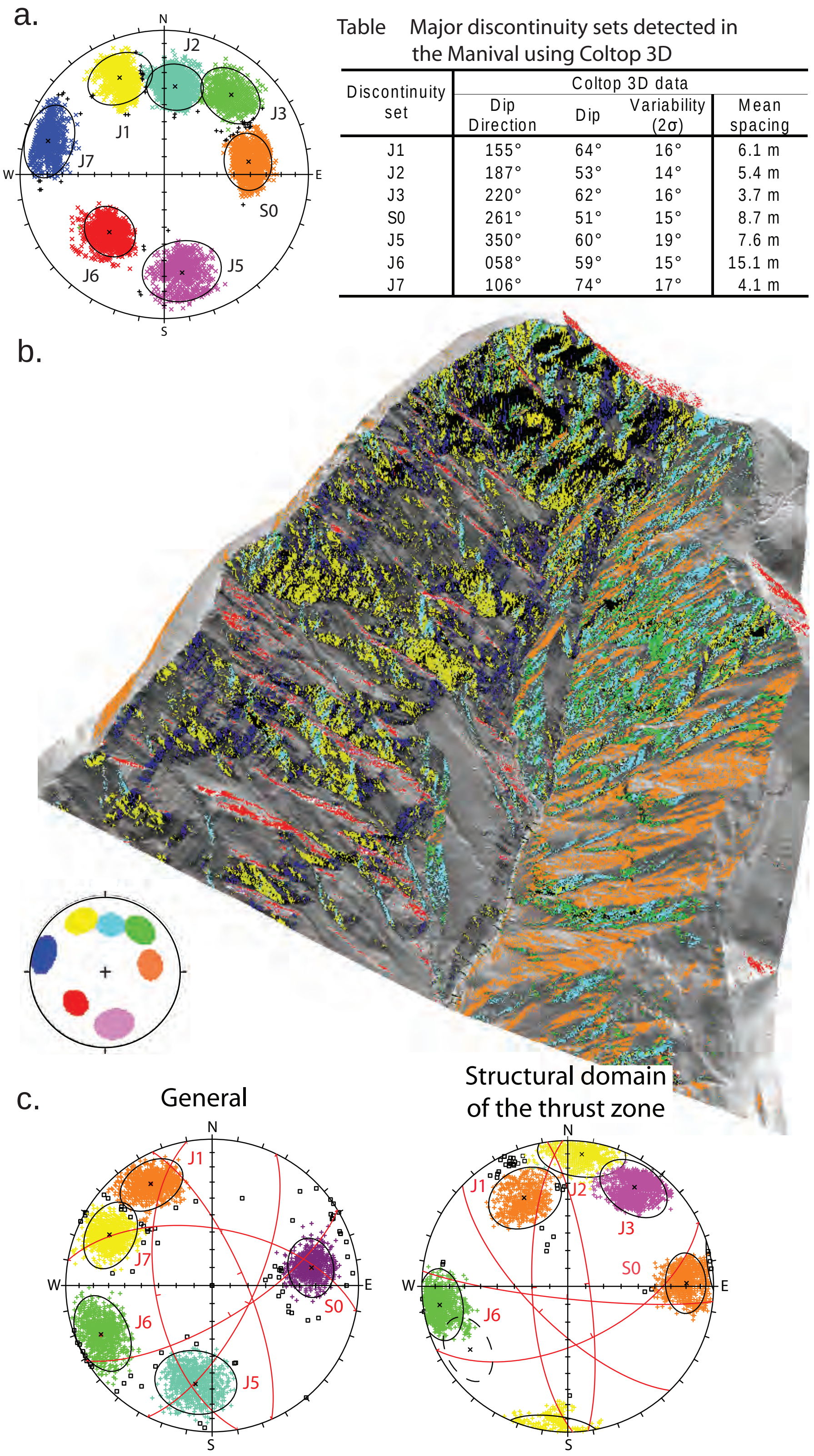

Table Major discontinuity sets detected in the Manival using Coltop 3D

Discontinuity set	Coltop 3D data			
	Dip Direction	Dip	Variability (2σ)	Mean spacing
J1	155°	64°	16°	6.1 m
J2	187°	53°	14°	5.4 m
J3	220°	62°	16°	3.7 m
S0	261°	51°	15°	8.7 m
J5	350°	60°	19°	7.6 m
J6	058°	59°	15°	15.1 m
J7	106°	74°	17°	4.1 m

Figure 4.11: *Manival catchment: (a) Discontinuity sets extracted from the morphostructural analysis of the DEM using Coltop 3D and displayed on a 3-D shaded relief map (b); The black circles represent the variability (2σ); the values are given in the table hereby. (c) Results of the Coltop 3D analysis performed with TLS data for several locations within the field area.*

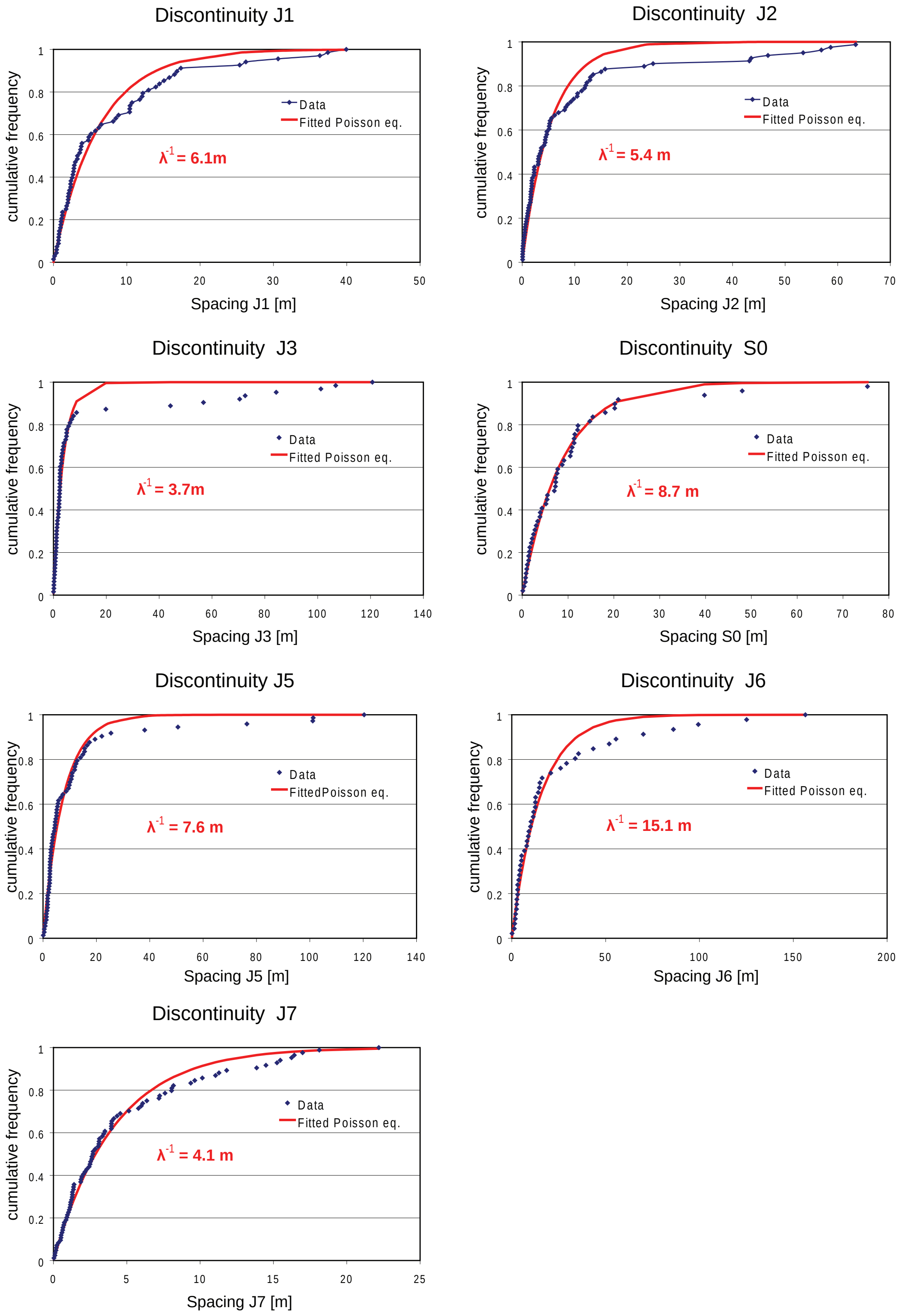

Figure 4.12: *Joint spacing distributions of the discontinuity sets considered in the Manival. Each spacing was determined after the sampling window approach.* λ^{-1} *is the mean spacing computed by the Poisson equation.*

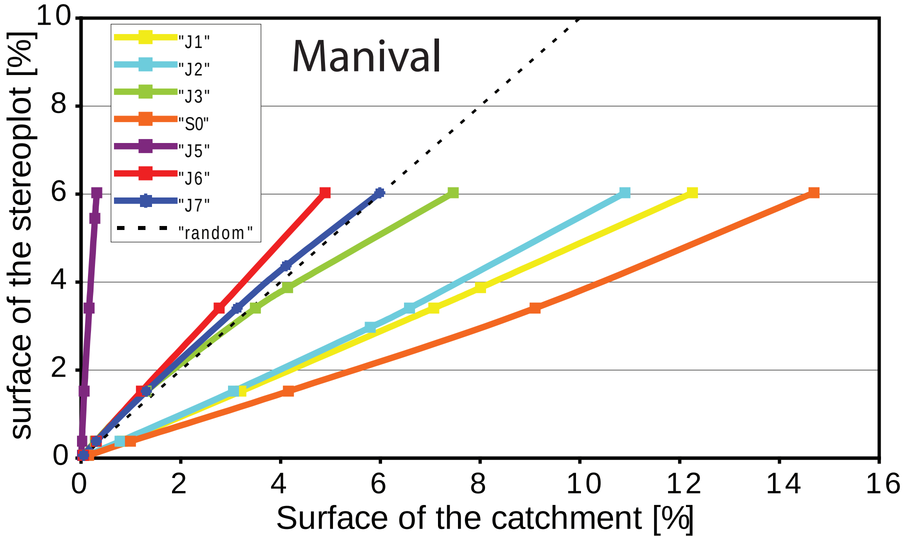

Figure 4.13: *Influence of joint orientations on the morphology of the topography in the Manival catchment (same as Fig. 4.8). The surface ratio of discontinuity S0 is about 2.8 x A_{stereo} for instance, whereas surface ratio J3 is about 1.2 x A_{stereo}.*

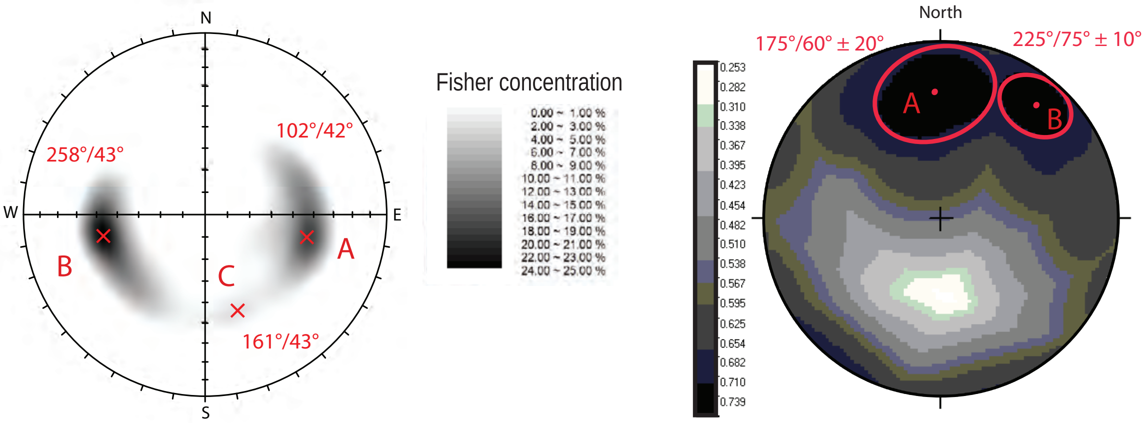

Figure 4.14: *(Left) Frequencies of orientations of the geomorphic features in the Manival catchment, highlighting three distinctive populations of gullies and rock couloirs direction. (Right) Orientations of the maximum joints frequency A and B according to the mean joint spacing deduced from the sampling window approach.*

and J5 and J6 at the base is kinematically possible, or even toppling purely due to the steeply-dipping failure plane. Nevertheless, discontinuities J5 and J6 can be assimilated to steeply-dipping fractures as they are involved at the surface of numerous escarpments and rock slopes instabilities detected in the catchment. Field data showed that J6 can form overhanging planes directed towards south, implying potential toppling.

The orientation of the maximum joint frequency, given the joint variability, corresponds closely to the highest frequency orientation of the gully network (199°/39°). Conversely, the dip is significantly steeper.

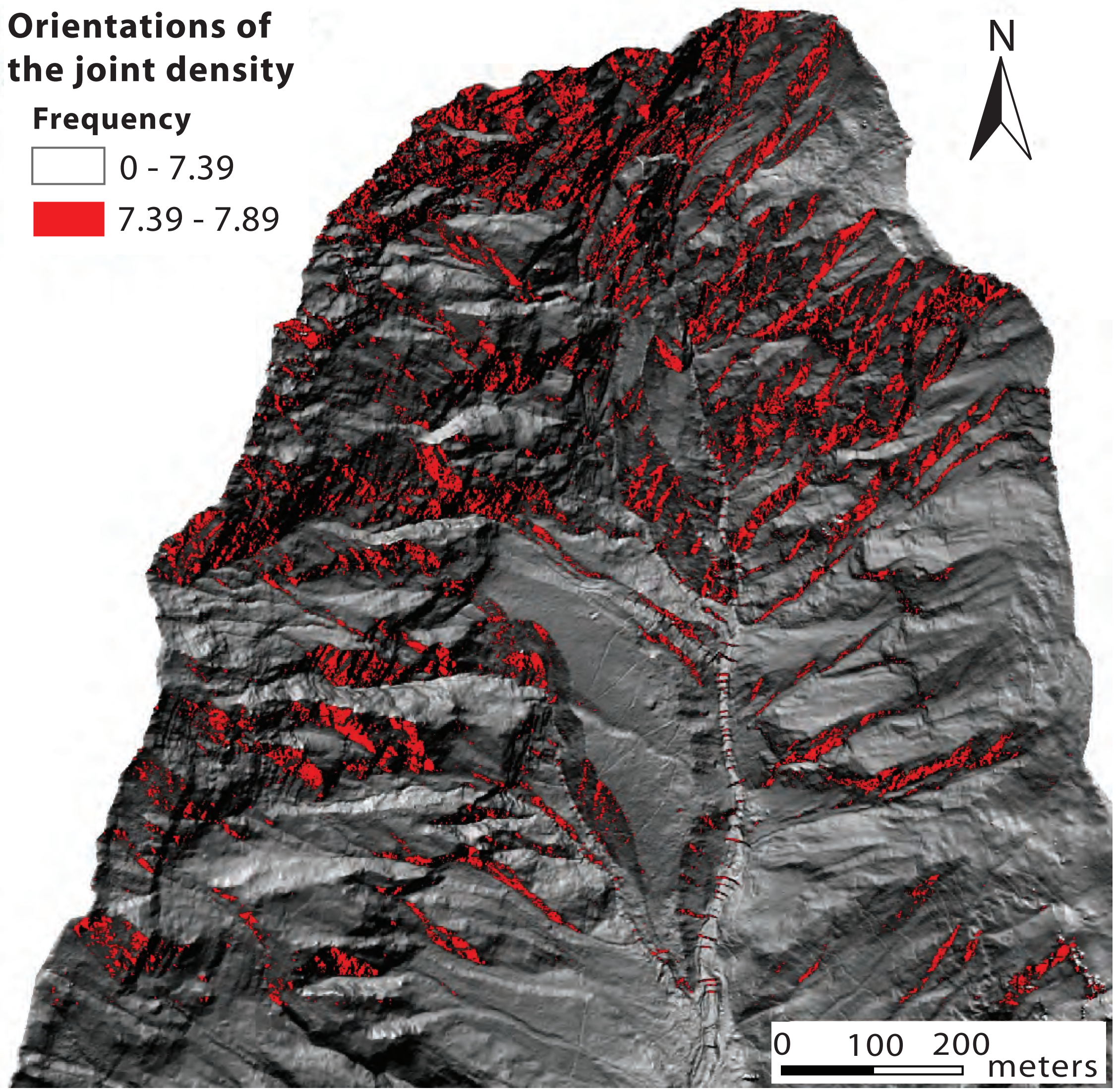

Figure 4.15: *Shaded relief map of the upper Manival catchment showing the topography oriented in the direction of the maximum joint frequency. These orientations are clearly associated with the pattern of gullies and the rock couloirs.*

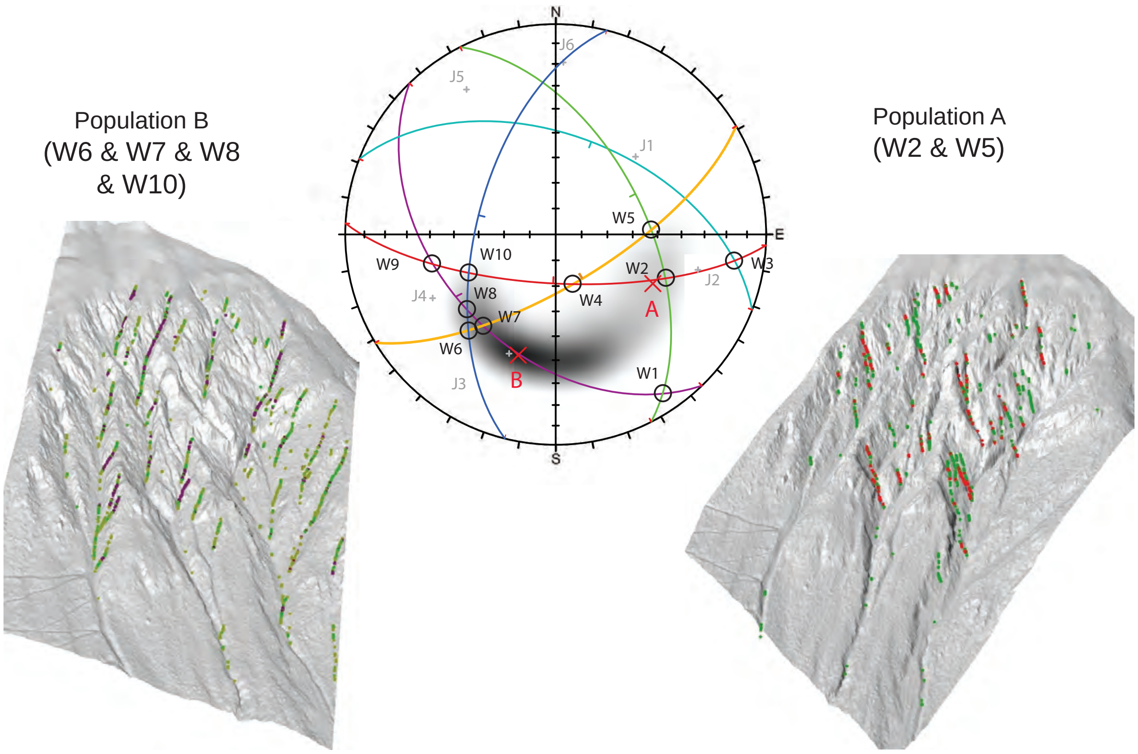

Figure 4.16: *Populations of geomorphic features and groups of potential wedges according to the joint systems prevailing in the Saxé and Métin catchment and using a 15° variability of the wedge axis orientations. Each point represents a segment of the gully network (see text for details). The associations are quantitatively expressed in Tab. 4.1*

4.4.4 Geomorphic feature orientation analysis of the upper Manival catchment

The frequency orientations of the gullies and rock couloirs in the upper catchment display two major populations (Fig. 4.14 left). Population A has a peak value of 102°/42° and corresponds to the mean direction of the features located in the west side: their azimuth ranges between [50°–130°] and their dip angle between [35°–70°]. Population B with a peak value of 258°/43° is linked to the geomorphic segments of the east side, including the structural domain of the thrusts zone. The variability is more constrained around the mean value, but of similar range ([200°–280°]). A third population C with a very low frequency and a mean orientation 161°/43° (±15°) is associated with gullies and rock couloirs situated below the top of the catchment.

Several potential planar or wedge failure orientations coincide with both end-members of the geomorphic features distributions (Fig. 4.17), similar to the Saxé and Métin catchment. Conversely, the two major peak frequencies A and B also correspond closely to the orientations of potential failure modes. On the east part, joint plane S0 and potential wedge W16 (271°/50°) show a correspondence of about 15% of all geomorphic segments using a variability of 15° of the wedge axis (Tab. 4.2). In addition, potential wedge structures can be treated in two groups defining very close axis orientations that correspond

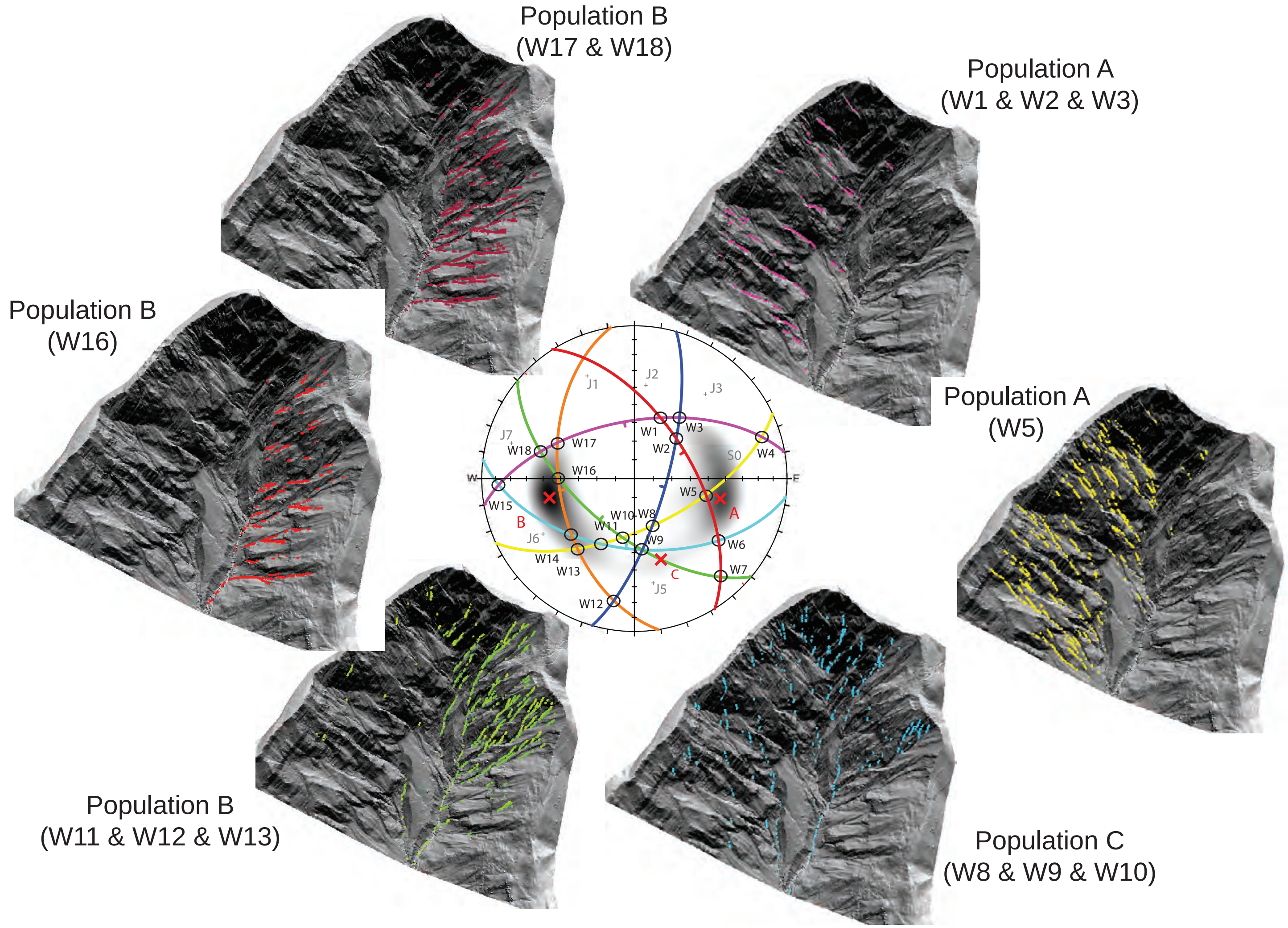

Figure 4.17: *Populations of geomorphic features and groups of potential wedges according to the joint system prevailing in the Manival catchment and using a 15° variability of the wedge axis orientations. Each point represents a segment of gullies or rock couloirs (see text for details). The associations are quantitatively expressed in Tab. 4.2.*

Table 4.1: *Potential wedges prevailing in the Saxé and Métin catchment according to the joint system. The variability of the wedge axes used to compute the geomorphic correspondences cannot exceed the variability defined by their joint orientations. Group of wedges W6, W7 and W8 correspond to 9%, 16%, 23% and 29% of the total segments of geomorphic features (population B, Fig. 4.16) given the variability of their axis; with W10, they reach together 10%, 20%, 25% and 31%. The group of wedges W2 and W5 contribute for 2%, 7%, 15%, and 18% (population A).*

Potential wedges		Wedge axis		Variability		Geomorphic correspondences according to a variability of the wedge axis of			
No	Joints	Trend	Plunge	Trend	Plunge	5°	10°	15°$^{(*)}$	20°$^{(*)}$
1	J1^J4	146°	10°	12°	12°	0%	0%	0%	1%
2	J4^J6	111°	44°	18°	18°	2%	5%	10%	14%
3	J3^J6	98°	16°	14°	19°	0%	0%	0%	1%
4	J5^J6	160°	70°	69°	24°	0%	1%	2%	5%
5	J4^J5	86°	53°	30°	13°	0%	2%	5%	7%
6	J2^J5	222°	38°	16°	25°	2%	9%	16%	23%
7	J1^J5	218°	44°	28°	12°	4%	12%	20%	27%
8	J1^J2	230°	44°	50°	14°	3%	8%	13%	18%
9	J1^J6	255°	40°	48°	17°	0%	0%	2%	4%
10	J2^J6	245°	52°	33°	22°	1%	3%	6%	9%

*or the maximum variability defined by the variability orientation of the joints

to both end-members of the distribution of orientations group B. On one side, there are wedge W17 (295°/45°) and W18 (286°/37°); on the other side, there are W11 (208°/51°), W13 (219°/42°) and W14 (228°/45°). All together, they coincide with about 27% (34%) given a variability of 15° (20°) of their axis orientation. These statistics were derived by separate consideration of the structural domain of the thrusts zone. Note that several of these wedges involve the bedding plane S0 and that J2 was only clearly detected in the thrusts zone, acting therefore as a potential sliding plane only in this structural domain. Joints J6 and J7 are potential failure planes that could kinematically trigger (wedge)-toppling on the east side, but they are more likely to develop as steep planar sliding along sliding plane J3.

Concerning the geomorphic features linked to the west side of the valley, the peak frequency of population A shows a very close statistical agreement to potential wedge W5 (101°/50°). A group of wedges W2 (043°/58°), W3 (036°/50°) and accessory W1 (026°/55°) may be structurally attributed to the extreme end-members of the distribution. W6 (126°/32°) seems to influence the gullies oriented towards south east, although the line of intersection is somehow less steep than the majority of these geomorphic segments. Together, they virtually agree for about 26% (35%) of all geomorphic features orientations given a maximum variability of 15° (20°) of their axis orientation. A wedge-toppling formed by S0^J5 and sliding along J7 at the base is kinematically possible and shows a chute azimuth closely related to the mean frequency orientation of the geomorphic segments.

Table 4.2: *Potential wedges prevailing in the Manival catchment according to the joint system. Here, the correspondences with the geomorphic feature populations (Fig. 4.17) are already given by group of wedges.*

Potential wedges		Wedge axis		Variability		Geomorphic correspondences according to a variability of the wedge axis of			
No	Joints	Trend	Plunge	Trend	Plunge	5°	10°	$15^{\circ(*)}$	$20^{\circ(*)}$
1	J5^J6	26°	55°	43°	19°	1.9%	3.6%	5.5%	7.1%
2	J6^J7	43°	58°	80°	22°				
3	J5^J7	36°	50°	30°	26°				
4	J1^J5	72°	14°	17°	25°	0%	0%	0%	<1%
5	J1^J6	101°	50°	30°	20°				
6	J2^J6	126°	32°	15°	18°				
7	J3^J6	139°	15°	16°	20°	0%	0%	>0%	1.4%
8	J1^J7	160°	64°	81°	24°				
9	J2^J3^J7	174°	52°	83°	39°	2.3%	5.3%	9.5%	13.6%
10	J1^J3	191°	59°	48°	18°				
12	S0^J7	190°	21°	17°	28°	0%	>0%	1.9%	3.9%
11	J1^J2	208°	51°	88°	44°				
13	J1^S0	219°	42°	28°	23°	7.3%	11.9%	16.3%	20.5%
14	J2^S0	228°	45°	39°	18°				
15	J2^J5	267°	12°	17°	20°	0%	0%	0%	0%
16	J3^S0	271°	50°	80°	31°	1.4%	6.7%	14.4%	19.4%
17	S0^J5	295°	45°	38°	22°	2.7%	5.4%	8.9%	9.9%
18	J3^J5	286°	37°	18°	27°				

[*] or the maximum variability defined by the variability orientation of the joints

To complete, sliding plane J2 and the group of wedges W8 (160°/64°) to W10 (191°/59°) display a failure direction that associates population C. This wedges concentration corresponds to about 10%, given a variability of 15° in the wedge axes.

Consideration of the geometry of the maximum joints frequency with the entire topography defines particularly well the slopes alongside the gullies in the east part of the catchment. In the west part, these orientations are associated with the inner steep walls of the rock couloirs. In the north part, they display a large portion of the terrain as the cliffs are very steep and facing mostly southwest. However, this cannot be directly related to a particular population of geomorphic segments.

4.5 Discussion

In both catchments, the orientations of a large number of gully segments are concordant with potential slope failure directions derived from kinematic analysis. The results suggest a strong relationship between geomorphic patterns and local joint systems.

4.5.1 Saxé and Métin catchment

In the Saxé and Métin catchment, this strong correlation is concerned with the geomorphic features whose orientation is located in both tails of the frequency distribution. The bulk failure direction of several potential groups of wedges coincides considerably with a large majority of geomorphic features. Considering joint spacing, these local wedge failures promote the detachment of rock slope units in a preferential direction, contributing to guide the spatial development of erosion and slope instabilities. These failure directions can be interpreted as structural weaknesses where geomorphic processes in gullies and rock couloirs are not only preferentially initiated, but propagated, for instance by allowing rock mobilization through gravitational and hydrological erosion processes directly (Whipple et al., 2000; Whipple, 2004). The close correlation between joint set J1 and the western portion of the population B suggests a dominant influence of J1, which display as well the largest morphostructure of the catchment (surface ratio = 2.5 x A_{stereo}). Planes J1 define large and persistent topographic discontinuities, mostly related to the inner slopes of the gullies and rock couloirs. This topography suggests that J1 has a control effect on the lateral erosion of these geomorphic features, by acting as a failure plane. Small bedrock landslides and debris collapses can occur preferentially on this sliding plane, which can be cut laterally by some other joints (especially J2 and J5). And the gully incision over time maintains the lateral slope adjustment through failure plane J1 in a structural configuration of dip slope. The asymmetry of the landforms topography delineated by the discontinuity J1 shows that the geomorphic features directed towards southwest (population B) appear to have developed preferentially normal to the strike of failure plane J1, which strikes similarly to the fault crossing the catchment.

From these observations, this is clear that the more the orientations of geomorphic segments offset the direction of maximum slope of the catchment, the more likely this discrepancy can be attributed to structural control and expressed as potential slope failure linked to wedge configuration and subsequently planar sliding. The spatial orientation of the remnant geomorphic features is thus directed in the azimuth of the maximum slope of the catchment, towards the major confluent Rhône Valley. However, this direction is also in agreement with the chute azimuth of several potential failure modes (plane failures J5 and J6; wedge structure W4; wedge-toppling J2^J3). Those joint configurations can be considered to structurally influence the geometric development of geomorphic features by facilitating bedrock destabilisation and gullies or rock couloir incision.

The two peak frequencies of the gully network orientations in the Saxé and Métin catchment differ from the mean slope orientation of the catchment, which faces towards the Rhône Valley (∼150°/38°). At the same time, the close statistical agreement between both azimuths of the overall peak frequency orientations of the gully segments and the one of the maximum joint frequency suggests that the joint density according to the slope face influences the landforms at the scale of the catchment, as this latter becomes significantly less important when directed progressively towards the east and towards the west. These orientations correspond de facto to the geomorphic features that have been clearly recognized as being potentially structurally controlled, reinforcing the observation that both end-members of the geomorphic distribution are clearly related to potential wedges and failure planes. The orientation of the maximum joints frequency is therefore less related to the geometry of geomorphic features, but more linked to bedrock scars and slope escarpments. The structural dependence seems to influence the general landforms of the catchment, which are controlled by rockfall and bedrock landslides.

4.5.2 Manival catchment

In the Manival catchment, there is primarily a close statistical agreement between the peak frequency orientations of the geomorphic features and the joint systems leading to potential slope failures. There is also a clear correspondence of the side-members of the distribution of orientations of geomorphic features. On the east side, potential wedge failures imply a structural control of a large number of geomorphic segments. They involve the discontinuities defining the most imposing morphostructures in the catchment (surface ratio = 1.2 to 2.8 x A_{stereo}). Several of these failure mechanisms involve the bedding plane S0, acting as a sliding plane. In the upper part of the catchment, the eastern fold limb is reverse in an overfolded configuration (Gidon, 1991), such that the bedding plane is in a dip slope configuration. Aerial photographs comparison coupled with field observations allow identification of active scarps in the eastern slopes, where rock fragments have become detached along failure plane S0.

Apart from the kinematic analysis, control of the gully geometries by the bedding planes can be explained by the higher rock mass strength of the bed faces compared to the ones in the direction of the inter-bedded layers. The development of the geomorphic features is influenced by anisotropic substrate resistance, such as the face of the bedding planes have a larger erosional resistance due to very low infiltration capacities and decreased pore pressures, and follows therefore the orientations of S0. An analysis of the distribution of the orientations of the eastern geomorphic features according to the different lithologies shows no particular variation in geometry. The lithological influence, for instance between thin-bedded calcareous marl and massif limestone, seems not to be clearly expressed in the geometry of geomorphic features. The structural control can therefore be assumed to be related principally to the bedding plane orientation, and only locally influenced by the rock type and their bed thicknesses. The geometry of the bedding plane defines an extremely dominant morphostructure in the eastern side, in such a way that the actual overall morphology, and thus the trend in the azimuth of the maximum slope in this part of the catchment, then follows the bedding plane direction. This suggests a strong structural control influencing dominantly the general shape of the eastern fold limb and into the scale of the rock slope where the geomorphic features propagate.

On the western side of the valley, the correlations suggests a relative predominance of the joint systems on the orientations of geomorphic segments, the statistical agreement of the groups of potential wedges being however considerably lower than what is observed on the east side. The mean frequency orientation of the geomorphic segments is concordant with the maximum slope orientation directed towards the main valley. DEM observations of the discontinuities corresponding to the joints prevailing in this part of the catchment reveal that some of them (J5, J6 and J7) are not significantly expressed in the morphostructures (Fig. 4.7b). J7 in particular seems randomly distributed and could correspond only to a bedrock structure derived from geomorphic activity rather than a penetrative discontinuity. Conversely, J1 is a penetrative structure in the carbonate rocks that clearly shapes the topography.

In the north part of the catchment, some geomorphic segments define a morphology oriented towards the axis of the valley. Considering that they can be structurally controlled, it is interesting to note that the group of wedges W8 to W10 displays a failure direction towards the main axis valley, which also corresponds to the direction of the fold axis. Their joints seem to influence the slope stability of the upper cirque basin, which may influence the development of the geomorphic features.

The geomorphic features in the western limb of the Manival are mostly anaclinal rock couloirs, deeply entrenched through inner walls that are apparently controlled by joints J5 and J6 on one side and J1 on the other side. A very steep slope gradient coupled with this lithological configuration may be a reason why the rock couloir geometries follow the maximum slope gradient instead of one preferential structural configuration. The rock slope detachment is governed by the formation of overhanging walls along the bedding plane due to the degradation of the downward talus slopes. The progressive overhang collapses then occur in the azimuth of the maximum slope gradient. The joint systems prevailing along the rock couloirs can be interpreted as structural weaknesses that influence the location of these geomorphic features by promoting rock detachment and lateral erosion propagation.

In the Manival catchment, the orientation of the maximum joint frequency coincides with the steep slopes that define the sides of the gullies and rock couloirs. However, the topographic elements delineated by these orientations are not homogeneous within the study area. A large proportion of slopes describing the orientations of the maximum joint frequency is found in the structural domain between both thrusts and in the upper part. The trend in the azimuth of the maximum joint frequency is also in agreement with the fold axis direction, which corresponds to the axis of the valley. Similar to the Saxé and Métin catchment, the orientations with a very high joint density corresponds to sets of cliff faces. However, they concern only the steep slopes located alongside the gullies and inner walls of the rock couloirs, not the ones facing towards the contributory valley that can be taken as the bulk chute azimuth. Since rockfall activity and debris slides preferentially occur where the topographic orientation corresponds to a high density of joints, the geomorphic feature orientations appear to be clearly influenced by zones of preferential slope instabilities and erosion processes. The structural implications of the joint systems controlling the geomorphic features can be interpreted first as a dominant factor of initiation, where the structural weaknesses are preliminary exploited by erosional activity and mass wasting processes. But, the structural implications continue to contribute to the development of these gullies and rock couloirs by controlling their lateral adjustment. The bedrock jointing, and the bedding in particular, play a predominant role in the slope stability of the inner walls and alongside slopes, which is certainly determined by the hillslope evolution, particularly entrenchment following erosional activity.

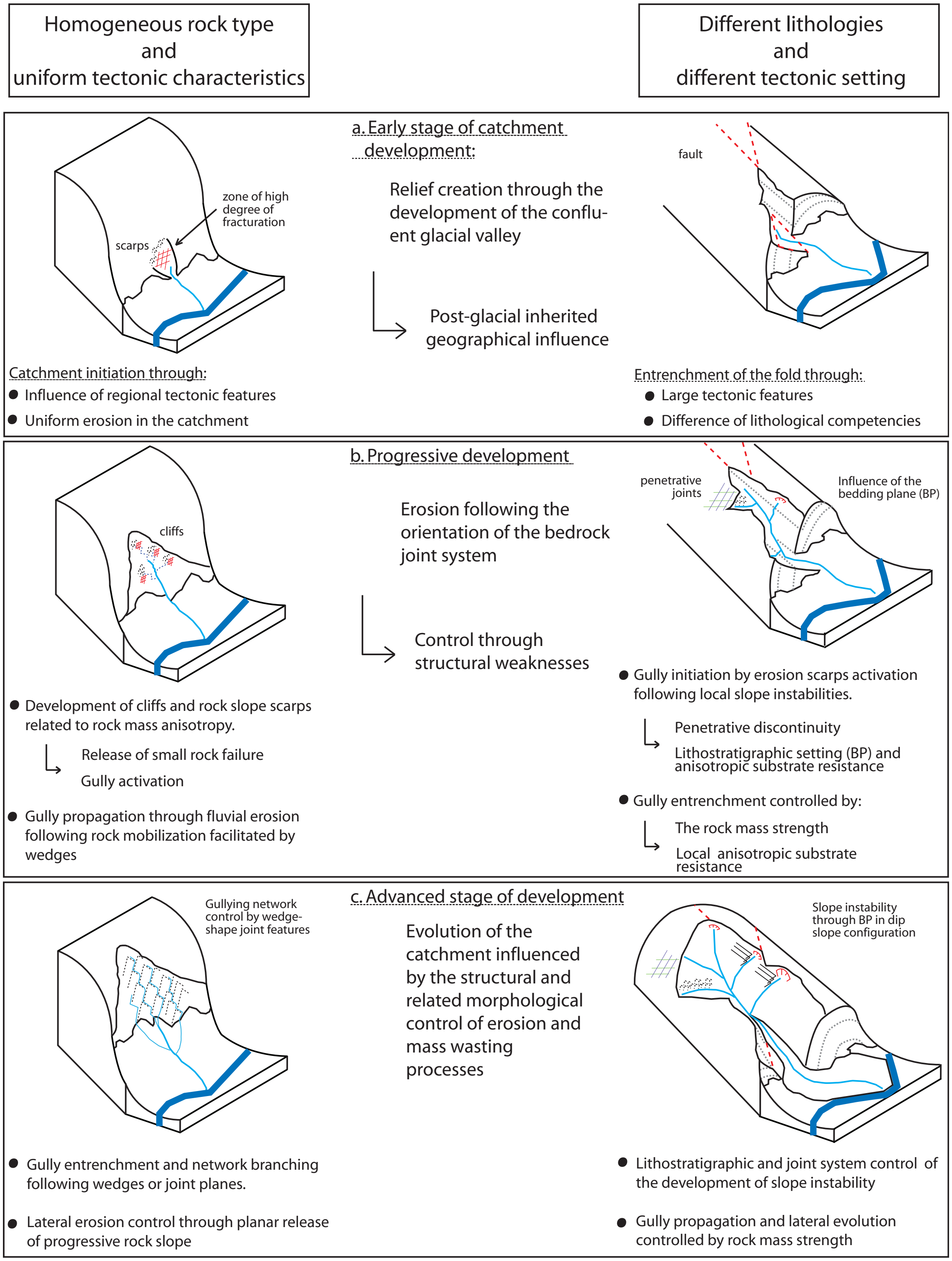

Homogeneous rock type
and
uniform tectonic characteristics

Different lithologies
and
different tectonic setting

a. Early stage of catchment development:

Relief creation through the development of the confluent glacial valley

Post-glacial inherited geographical influence

Catchment initiation through:

- Influence of regional tectonic features
- Uniform erosion in the catchment

Entrenchment of the fold through:

- Large tectonic features
- Difference of lithological competencies

b. Progressive development

Erosion following the orientation of the bedrock joint system

Control through structural weaknesses

- Development of cliffs and rock slope scarps related to rock mass anisotropy.
  - Release of small rock failure
  - Gully activation
- Gully propagation through fluvial erosion following rock mobilization facilitated by wedges

- Gully initiation by erosion scarps activation following local slope instabilities.
  - Penetrative discontinuity
  - Lithostratigraphic setting (BP) and anisotropic substrate resistance
- Gully entrenchment controlled by:
  - The rock mass strength
  - Local anisotropic substrate resistance

c. Advanced stage of development

Evolution of the catchment influenced by the structural and related morphological control of erosion and mass wasting processes

- Gully entrenchment and network branching following wedges or joint planes.
- Lateral erosion control through planar release of progressive rock slope

- Lithostratigraphic and joint system control of the development of slope instability
- Gully propagation and lateral evolution controlled by rock mass strength

Figure 4.18: Conceptual model describing the development of the geomorphic features involving a structural control of erosion in a small alpine catchment. The left column illustrates the Saxé and Métin catchment, whereas the right one corresponds to the Manival catchment.

4.6 Structural control of erosion

The observations for both catchments are in agreement with the idea that rock mass strength, in terms of rock mass anisotropy, promotes the development of rock faces, and the structural setting, in terms of discontinuity sets, is related to the orientation, type and frequency – magnitude of planes of weakness that may be subsequently exploited by mass wasting processes (Selby, 1987; Abrahams and Flint, 1983; Beavis, 1999). Such a concept describing the structural control of erosion is illustrated in Figure 4.18. Among potential structural joint configurations, wedges seem in particular to have a geometry that encourages the development of geomorphic processes, for instance, through enhanced channelized runoff caused by intense rainstorms. Similar morphostructural settings involving failure planes with a steep dip angle and a wedge-like geometry have been observed in other debris flow prone catchments and active debris slide areas (Lee, 1989; Volk, 2000). Wedge geometry enables a deep entrenchment and persistent failure planes contribute to the slope destabilization that borders the geomorphic features. Debris is then transported further by surface runoff and debris flows. The same characteristics were recognized in rock couloirs of the Dolomites (Marchi et al., 2008). Toppling is a failure mechanism that requires a steep dipping plane and a favourable topography to occur. Hence, toppling influences predominantly the stability of the cliffs and steep bedrock slopes, but cannot significantly control the spatial geometry of gullies and rock couloirs on its own. This may do in combination with other modes of failure and surface erosional processes.

4.7 Conclusions

An assessment of the sliding orientations of potential failure mechanisms linked to joint systems shows the importance of structural controls of the geomorphic features for small bedrock-dominated catchments. The strong correspondences between a large majority of geomorphic segments and the sliding directions of potential wedges failure in the Saxé and Métin catchment, and in the case of the Manival between the lithological setting and the bedding plane, suggest that the underlain geology plays a strong influence in determining gully network and rock couloirs characteristics, in terms of both initiation and subsequent development.

In magmatic intrusive rock, as in the Saxé and Métin catchment, the structural pattern is usually well-defined through sets of joints, which seem to control the initiation and subsequent geomorphic development. In catchments with carbonate rock (as per the Manival catchment), former tectonic structures can disappear through recrystallization. Predisposing factors are linked to the regional setting, so that at the scale of the catchment, the geomorphic features are influenced on the one hand by the surface geometry of the terrain. On the other hand, they are controlled by the actual rock mass strength, as influenced by lithological factors and fracture density, in both processes of initiation and propagation. This work describes a quantitative approach to document the landscape morphology involving bedrock-related structures governing erosional processes. The two catchments are representative of small alpine basins dominated by steep rock slopes and prone to large debris flow events, in both sedimentary and magmatic lithologies. In such hillslope context, the spatial heterogeneity of mass wasting processes on cliffs and rock slopes, which contribute to produce debris and sliding masses, influences erosional landforms initiation and geomorphic feature development at the scale of individual catchments. Investigating the role played by bedrock structures may be used to inform about the sources of debris supply in order to characterize channel recharge rate, a factor essential in debris flow hazard assessment (Bovis and Jakob, 1999). The structural setting and lithological characteristics appear to be a significant aspect for the assessment of sediment yield and denudation rate. A better understanding of the geological control of geomorphic features may provide some insight for improving geomorphic-transport laws (e.g. Stock and Dietrich, 2006) and landscape evolution models (e.g. Hovius, 2000).

Part III

Modeling sediment budgets of torrent systems

Chapter 5

Alpine catchment sediment budget modeling through a quantitative sediment cascade procedure

Abstract Solid waste management in mountain environment requires the prediction of reliable sediment yield estimates. Within the MATEROSION project, a dynamic semi-distributed sediment cascade algorithm was developed to assess sediment budgets in torrent systems. This takes into account the probable variation of sediment production and conveyance in relation to climate changes and the possible occurrence of big landslides. Potential sediment delivery is simulated following a spatially-structured conceptual model reflecting hillslope and torrent sediment dynamics. This sediment cascade is implemented in a sediment flux routine based on mass balance conservation, where channel recharge rates and bedload transfer are governed by stochastic processes simulating the trend pattern of runoff conditions. Material supply derived from landslides and debris flows events of empirically-defined intensity are generated randomly following their return period. Model parameters are calibrated with field observation and results are averaged over a great number of randomly-generated time series, providing the most probable sediment yield to the torrent system. Here is given only a brief overview (in English) as the detailed description (in French) of the algorithm, model application and results are found in Appendix A.

5.1 Introduction

Debris flows and other channelized processes involving landslides derived sediment flux dominate the sediment budgets of mountain catchments (Dietrich and Dunne, 2007). Material deposited in higher-order channels and valley bottoms over the time requires the development of proper strategies of hazard mitigation and solid waste management (e.g. sustainable dredging of sediment trap). Sediment budgets of mountain catchments have been previously defined by summing up the volumes or masses of geomorphic features prevailing in and near the drainage system (e.g. Rapp, 1960; Jäckli, 1957). Since them, a panel of more evolved approaches ranging from empirically-based dynamic models to numerical sediment flow routing based on deterministic physical principles of simulating sediment activity has been introduced in distributed model structures (see Chapter 1, section 1.1: 3^{rd} §). This last chapter presents a very brief summary (in English) of the sediment budget method and sediment discharge modeling developed in the framework of the MATEROSION project. The part of the project involved with consists of addressing the issue of predicting the amount of material that would accumulate to small alpine basin outlets prone to debris flows at short, middle and long term, considering probable climate changes. An extensive description of the quantitative approaches for defining sediment budget estimates and simulating sediment yield with the sediment flux routine MatErosion 1.0 is found in Appendix A (in French).

5.2 Study site

The sediment budget predictions are illustrated by two small but active Alpine catchments (Lirec and Perrec torrents) situated up the Anniviers Valley (southern Walliser Alps, Switzerland) (Fig. 5.1). Their catchment area is about 2 km^2, 1800 m relief watershed and composed of gneiss and michaschist of the penninic zone (Marthaler and Sartori, 2005). Their common outlet forms a fan of 5 ha attesting of the past activity. Today, small debris flow events of several hundreds of m^3 occur at a frequency estimated to 0.2/yr, but may reach up to 10'000 m^3 once every 30 years (Idealp Sàrl, 2009). Mass wasting deposited in the sediment trap downstream recorded about 4000 m^3 between 1990 - 2003 (Ayer, 2003). Bedload contribution is estimated to 300 m^3/yr. The magnitude and frequency of debris flows, as well as a massive debris supply induced by landslides, remain uncertain due to the fact that any remarkable event was noticed during the last decades. And so the management of their sediment yields.

5.3 The quantitative and dynamic sediment cascade

5.3.1 The sediment budget approach

The evaluation of sediment budgets in mountain catchments comprises all kinds of geomorphic processes that are likely to supply the channel network with material and then,

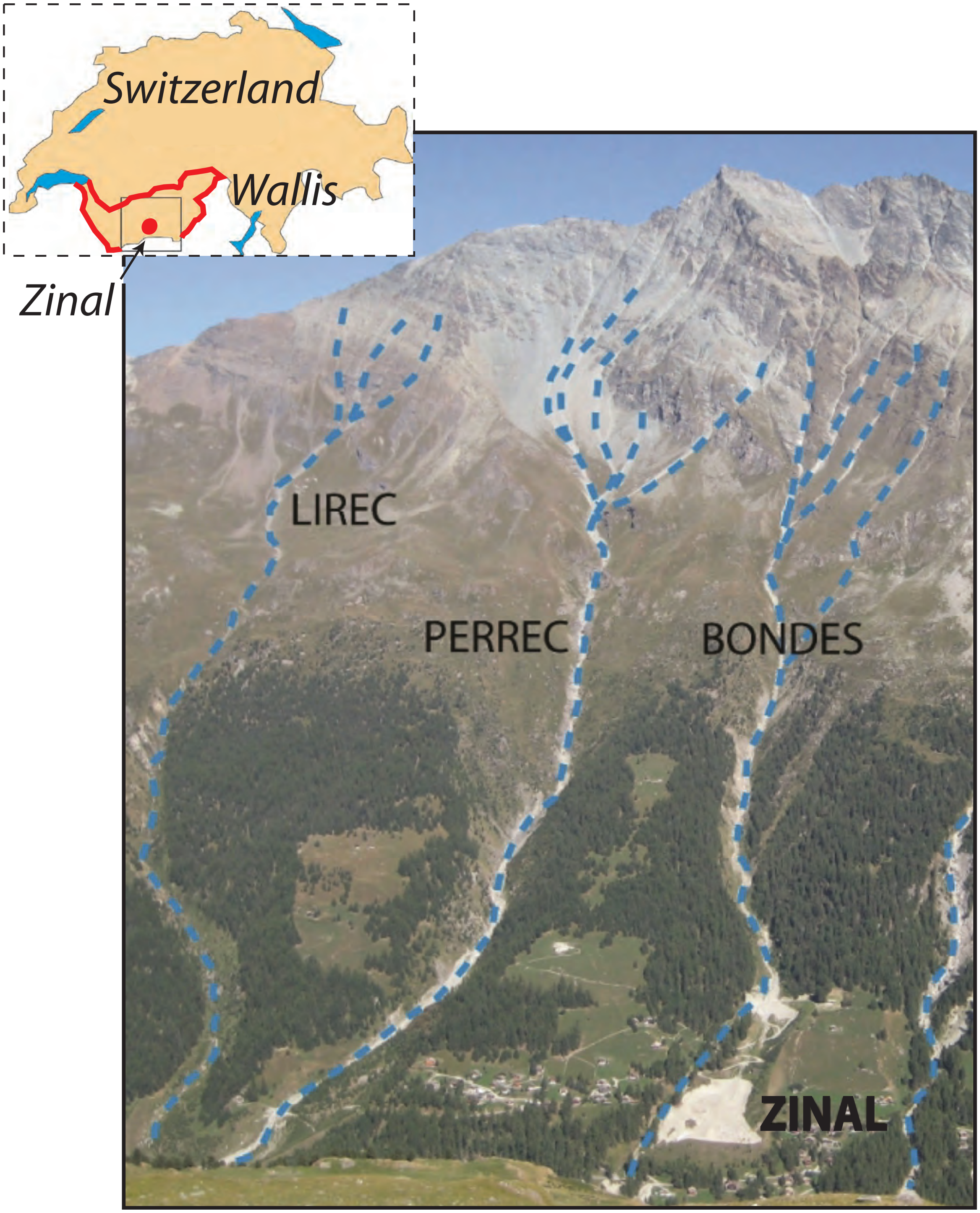

Figure 5.1: *Study site location (inset) and photograph of the Lirec and Perrec torrents above the village of Zinal. Note the impressive sediment trap of Bondes torrent. There is a similar one at the common outlet of the Lirec and Perrec torrent. They serve to protect the village against snow avalanches as well.*

that are conveyed downstream by runoff. This depends on:

- The availability of sediment stocks (mobilization of material)
- The transport capacity of the drainage system (entrainment of material)

In torrent catchments, potential mobilization of material entrained downstream from the drainage system to form sediment flows (mostly bedload and debris flows) comes from (Fig. 5.2):

1. outside the channel network, involving any kinds of fast or slow gravitational processes, snow avalanches and slope wash that accumulate material in channel heads, gullies or all along the torrent.
2. the in-torrent erosion itself, directly (re-)mobilized from the flow bed or detached from the banks.

Therefore, generating a sediment budget for torrent systems consists of both identify and quantify the pre-existing and potential sedimentary stocks, even involved only episodically during torrent floods. Available sediment stocks were therefore classified in direct (in-torrent stocks) and indirect (hillslope stocks) sources of sediment in regards to the drainage system.

5.3.2 The torrent system dynamics

In a catchment, the sediment flow dynamics induced by the interactions of these sediment stocks against hydrometerological conditions can be integrated in a sediment cascade (Chorley and Kennedy, 1971; Schrott et al., 2003; Fryirs et al., 2006), where the hillslope and channel sediment flux processes is reflected schematically in individual reservoirs interconnected to each others (Fig. 5.3). The channel network is therefore subdivided into reaches implying homogenous geomorphic processes deduced from geomorphodynamical parameters. Each channel segment is connected to its contributing area and forms a subsystem corresponding to a link of the sediment cascade. Each subsystem is composed of several reservoirs supplying the cascade links with material according to corresponding hillslope process activity.

The flux of sediment passing through the sediment cascade is driven by:

1. their mode of detachment (mobilization sensitivity), of conveyance (volume, effectiveness) and of deposition (routes and distance).
2. the speed of mobilization (erosion / production rates) and transfer (transport capacity).
3. the evolution of the sediment stocks (volume aggradation / depletion) and transfer rules with time.

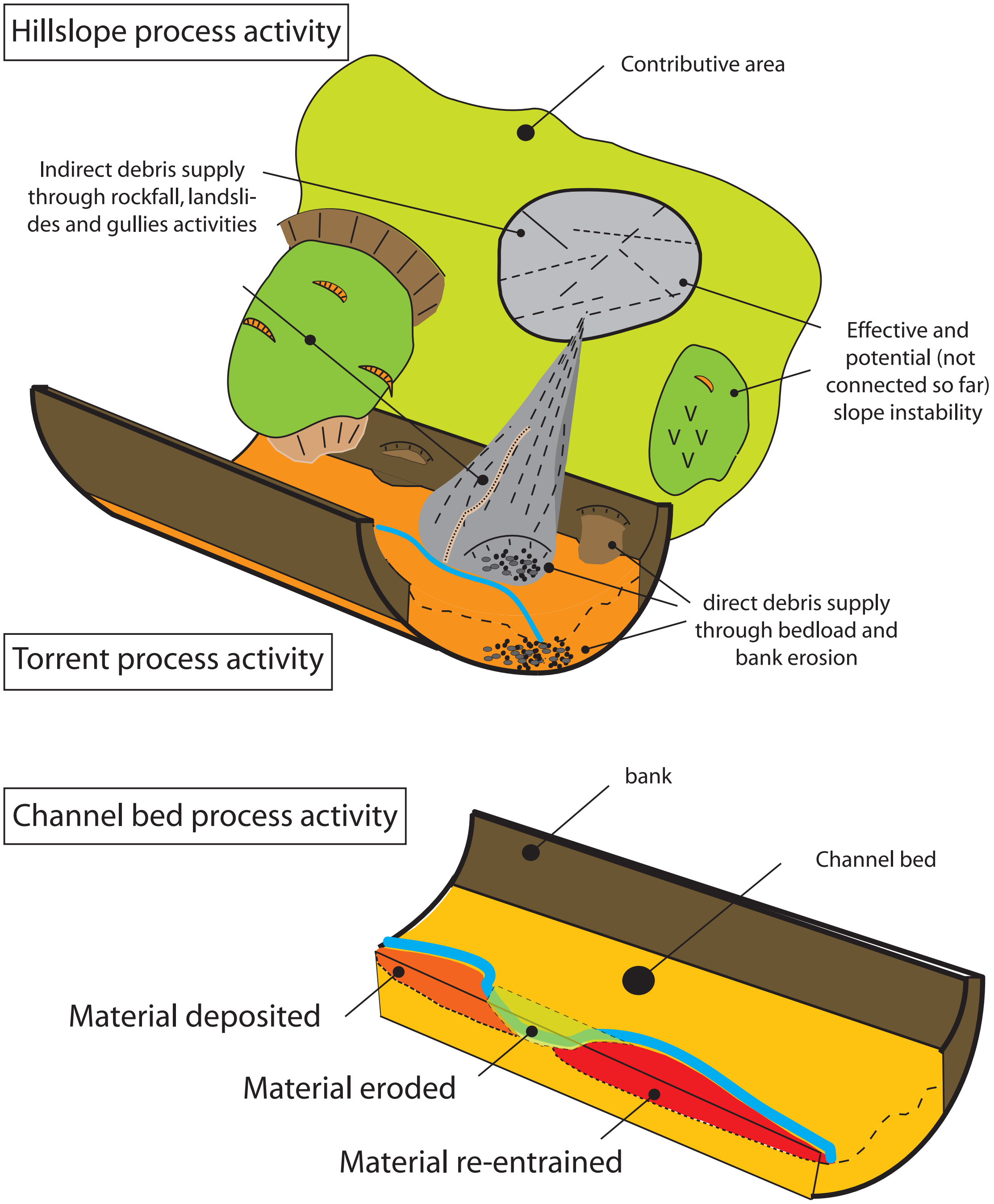

Figure 5.2: *Illustration of the sediment budget approach that consists of investigating potential and effective sediment stocks by identifying and estimating volumes of the hillslope and channel geomorphic processes contributing to supply material into the torrent system.*

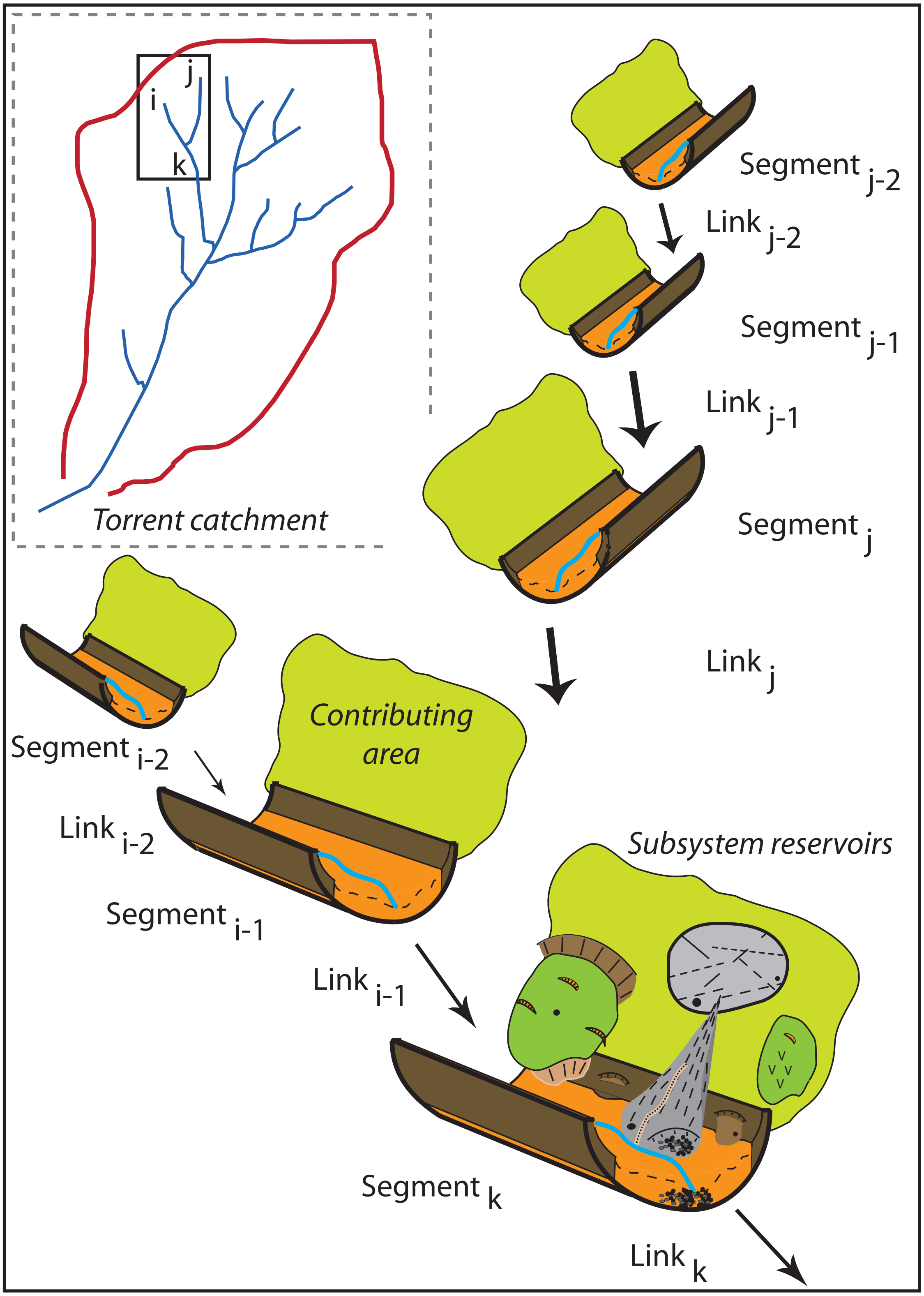

Figure 5.3: *Illustration of the sediment cascade in torrent systems. The channel network is subdivided in several individual subsystems representing a schematic structure of the catchment sediment dynamics.*

Hence, the exchange of sediment flux is governed by the mode of sediment transfer between each link of the sediment cascade following parameters controlling material initiation, entrainment rates and runout distance, e.g. sediment delivery ratio SDR, (Roehl, 1962). Although these factors of sediment dynamics may vary significantly in space for torrent catchments, the MATEROSION approach attempts to characterize in a simple way these different factors driving the erosion and sedimentation processes at a scale corresponding to the sediment cascade links (subsytems). In such a manner, the effect of major hydrosedimentological phenomena may be properly accounted for in sediment budget investigation.

5.3.3 The sediment flow routine

Whether the supply of material is a necessary condition, the in-channel sediment flux dynamics is inherently driven by stochastic processes of various intensity and duration, which are discrete in space and time (Benda and Dunne, 1997). In torrent systems, this concerns almost exclusively rainstorms and snowmelt. Therefore, the sediment yield reaching the torrent outlet depends on:

- the frequency of occurrence of events inducing runoff.
- the capacity of this latter to transport this load of material.

The conceptual sediment cascade was therefore implemented into a sediment flow routine where the computational steps follow time series of rainfalls, debris flows and other landslides occurrence, and simulate their effects upon the sediment cascade links (Fig. 5.4). At each simulation time step, each subsystem of the cascade performs an internal sediment balance (mass conservation) before being propagated into the cascade next links and sediment stocks are updated after each exchange of sediment flux. Above all, a flow routine enables to simulate a great number of time series. Therefore, a dynamic sediment cascade routine considers a great number of interactions between the hillslope and channel system and within the torrent itself, improving the result estimates.

5.4 Model application and data processing

5.4.1 Field data

This input data of this semi-distributed sediment cascade modeling was generated using only high resolution digital elevation model (DEM) of 2 m cell size, landuse and geological maps. Orthorectified aerial photographs and shaded relief maps provided the basis for geomorphological mapping and landuse characterization. Hydrometeorological data were obtained from a 1973 – 2007 records of daily precipitations. The station is located about 1 km away and 100 m of elevation below the torrent outlet. The sediment budget

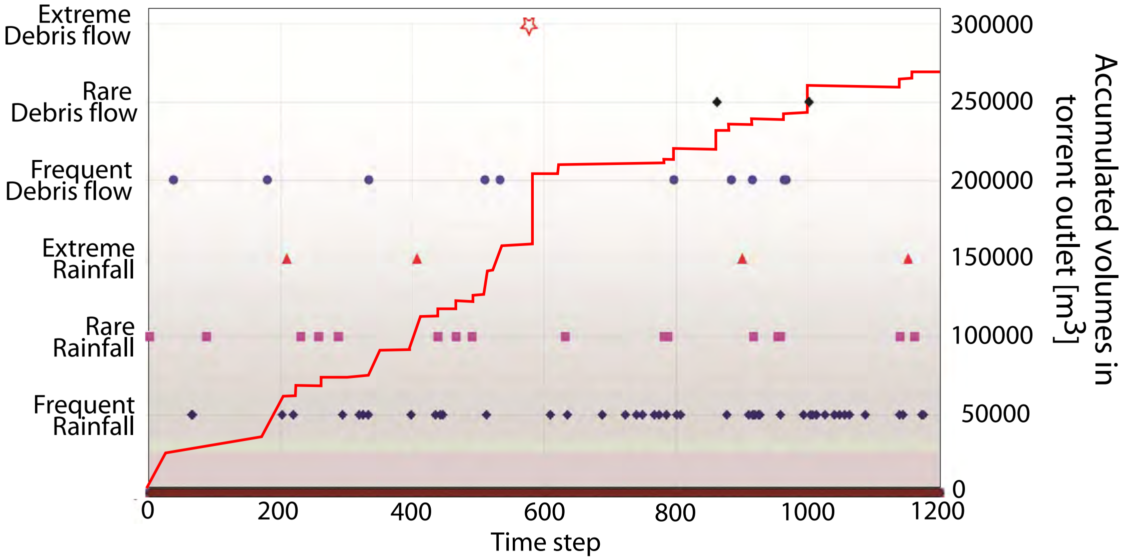

Figure 5.4: *Illustration of a time series of events simulating the stochastic perturbations encountered in the torrent system and its effects in the sediment cascade (red line).*

inventory used for calibration is derived from coarse observation performed by the people in charge of the sediment trap. Field surveys focused on the mapping of hillslope process initiation sites, run-out distance of geomorphic process activity and thickness of material deposits. In and near the torrent, they concentrate on the changes of sediment dynamics (reach dominated by erosion / deposition) and notice special features of the channel bed and banks. Field data were also used for validating the entire development of the model. The canonical structure of the sediment cascade and the integrated sediment flow routine is illustrated in the flow chart in Figure 5.5.

5.4.2 In-channel storage (direct debris sources)

The sedimentary stocks available in the torrent channels, i.e. the pre-existing and potential material that can be entrained from the bed and the banks, is estimated for each reach using the Slope local base level (SLBL) method (Jaboyedoff and Derron, 2005) and high resolution DEM. This enables to model the maximum volumes to be likely affected by cutting from torrent floods, assuming a close U-shape of the reach of limited curvature (Fig. 5.6). The maximum erosion depth H_{max} was defined with the Kronfelner-Kraus (1984) formula:

$$H_{max} = 1.5 + 12.5 \cdot J \qquad \text{where } J = \text{the slope gradient} \tag{5.1}$$

5.4.3 Recharge from hillslope (indirect debris sources)

Hillslope sediment stocks contributing to recharge the torrent channels were delineated from the analyses of shade relief DEM and geological data, aerial photograph interpreta-

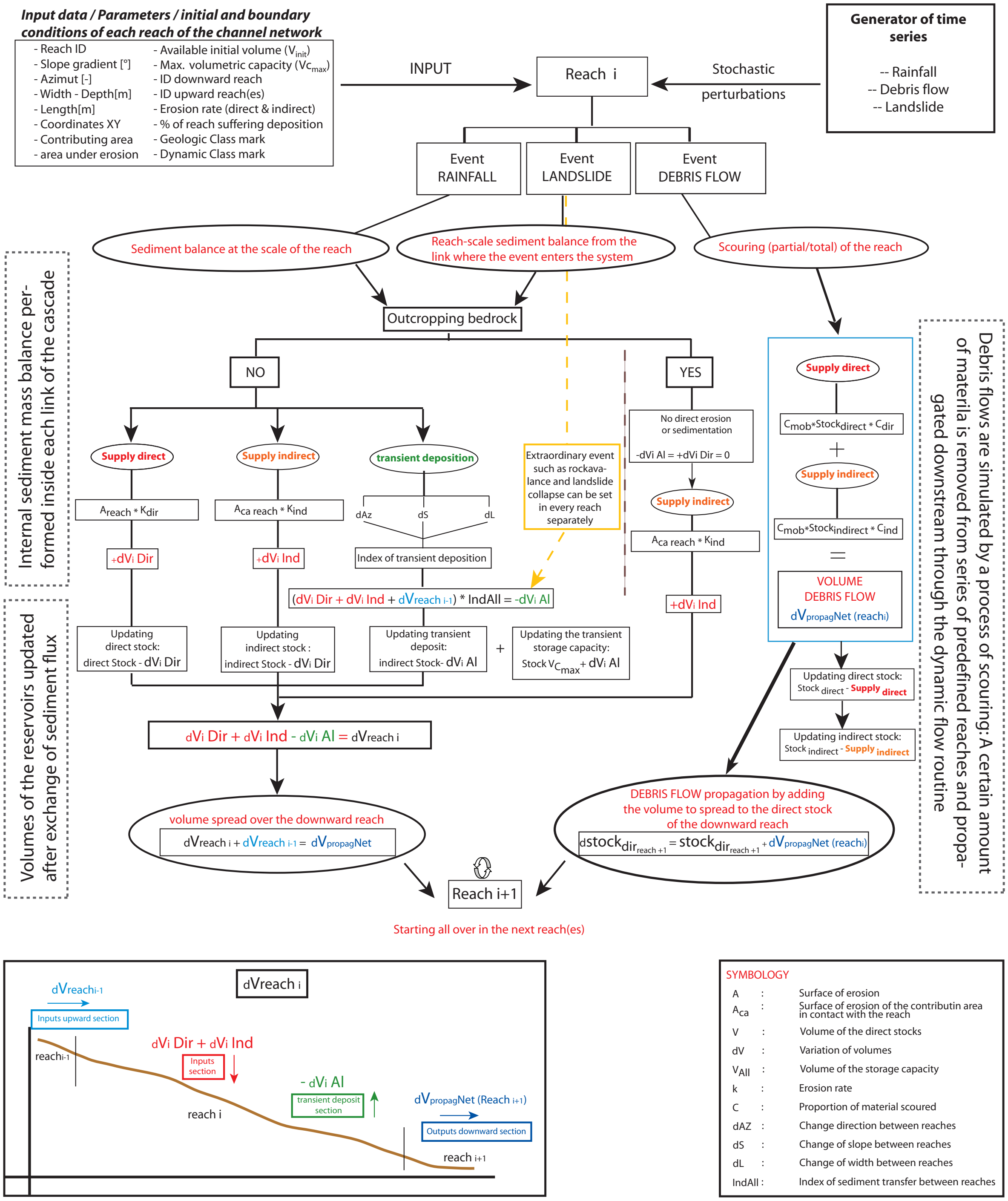

Figure 5.5: *Sediment cascade flow chart illustrating the semi-distributed sediment flow routine model with input data and time series generator.*

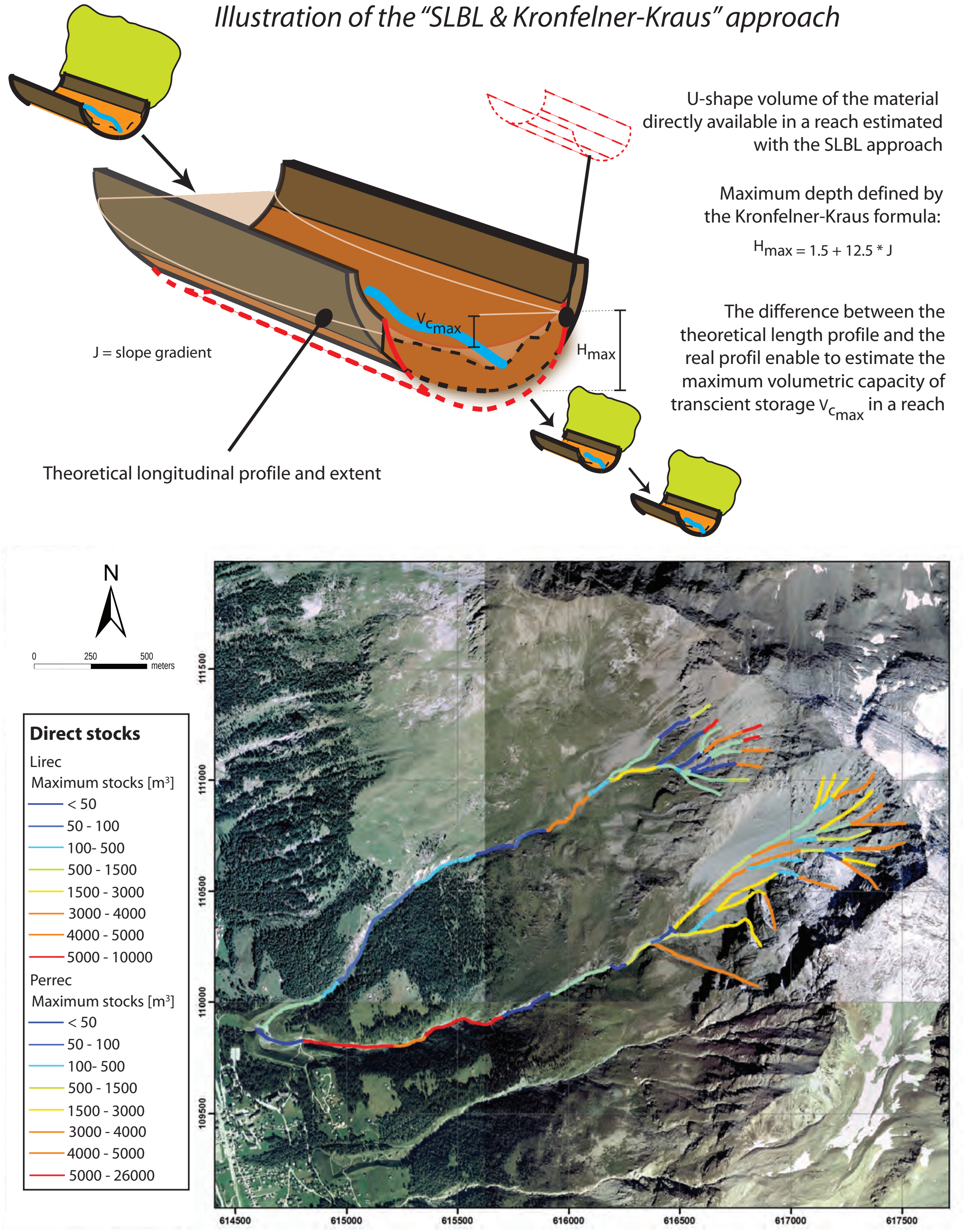

Figure 5.6: *Estimation of the maximum sediment supply in a reach using the SLBL method and the Kronfelner-Kraus formula. The analysis of the theoretical length profile informs about sediment flow dynamics (entrainment / deposition zones) and the volumetric capacity of the torrent to store material temporary.*

tion and field investigation (Fig. 5.7). The surface extent of pre-existing compacted and recently generated loose material potentially in contact with the drainage network was mapped according to their shape (morphology) and geomorphic aspect (surface cover). The thickness of the deposits such as landslides, sacking and scree deposits can be estimated with plausible geometric shapes. This represents however a major uncertainties when adressing sediment stocks estimates that must be considered over the long term, and when omitting the occurrence of extraordinary supply of material through rockslides and undetected landslides.

5.4.4 Sediment cascade structure and in-torrent sediment flow dynamics

The torrent channels were subdivided in homogenous reaches considering slope gradient and other morphological parameters and linked to their corresponding contributing area (Fig. 5.8). The characterization of the transfer of sediment flux between subsequent channel reaches was defined according to an analysis of the length profile of the torrent and its tributary gullies. Assuming that the drainage network attempts to reach its length profile in equilibrium, the propension of each reach to entrain or depose material can be defined (Fig. 5.9). The height difference between theoretical and effective topographic length profiles provides also quantitative information about the volumetric capacity $V_{C_{max}}$ of the reach to temporary store material.

Besides, channel segments are discriminated in bedrock or debris-covered reaches and classified with the Strahler's stream order (1952). All this factors were considered for generating the schematic structure of sediment cascade.

5.4.5 Volume flux and rates of sediment transfer

The discharge of material between the successive reaches, e.g. the transfer rate of flux, is governed by an index (I_{alluv}) representing a percentage of material that are potentially deposited in each reach, considering that they have limited transient storage capacity (Fig. 5.10). This proportion of sediment transfer was determined according to the change of slope gradient (S), of width (L) and of direction (A_z) between the successive reaches. As the change of direction between the reaches does not necessary induce an increase or decrease of material potentially passing through them, I_{alluv} is first defined from (ΔS) and (ΔL). Then, a certain weighting is added depending on ΔA_z. An example is illustrated in Figure 5.10 (Table down). The distance of propagation is therefore established with the volumetric balance, which determines the variation in volume ΔV_i for each link of the cascade:

$$\Delta V_i = V_i^{dir} + V_i^{ind} - V_i^{dep} + \Delta V_{i-1} \tag{5.2}$$

with ΔV_{i-1} the volume entering from the preceding reach , V_i^{dir} the in-channel storage available, V_i^{ind} the material supply from the contributing area and V_i^{dep} the volume of material deposited in the link. This index of sediment transfer is somehow similar to the

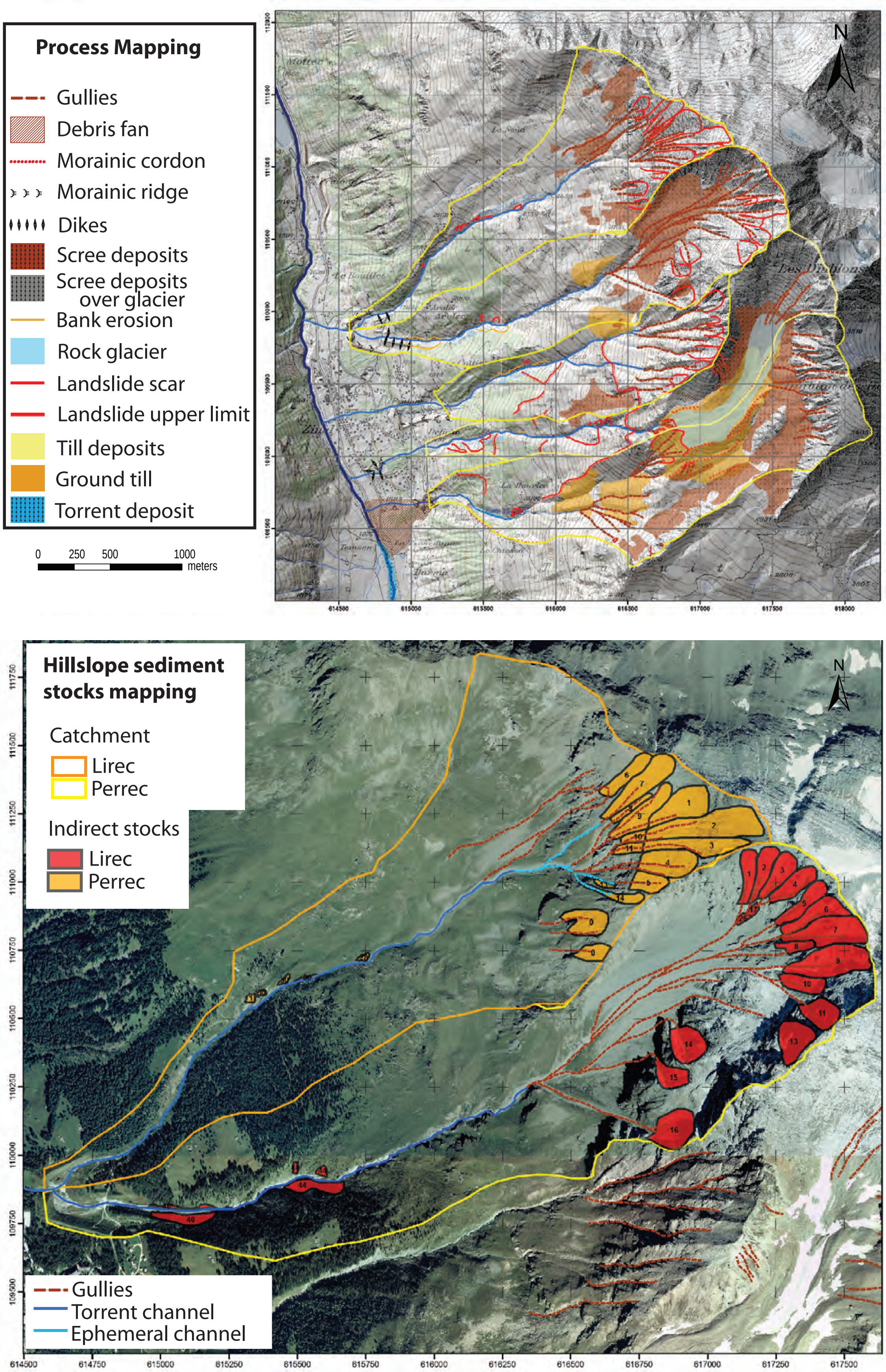

Figure 5.7: *Geomorphic process map (left) and hillslope sediment stocks (right) for the Lirec and Perrec catchment in contact with the drainage system performed with GIS data and field surveys (from Mazotti et al., 2010).*

Criteria	Classes	Implication upon channel dynamic
Mean slope gradient over 25 m	< 2° 2°-15° 15°- 40° > 40°	- Bedload - Debris flows and bedload runout - Triggering of debris flows - Rock walls
Mean mapped channel width	< 1.5 m - Bins of 2 m width until 10 m - Bins of 5 m width until 25 m < 25 m	Change of channel width between two reaches influences the runoff speed in the channel and therefore its transport capacity
Change of direction over 25 m	< 20° 20° - 60° > 60°	Change of direction between two reaches influences the transport capacity
Bedrock	- outcropping - covered with debris	Inform on sediment flux dynamic in reaches (propension to deposition / entrainment)
Strahler order	Contributive area under / over 10'000 m^2	A reach has to belong to the same Strahler's order hierarchy of the channel network

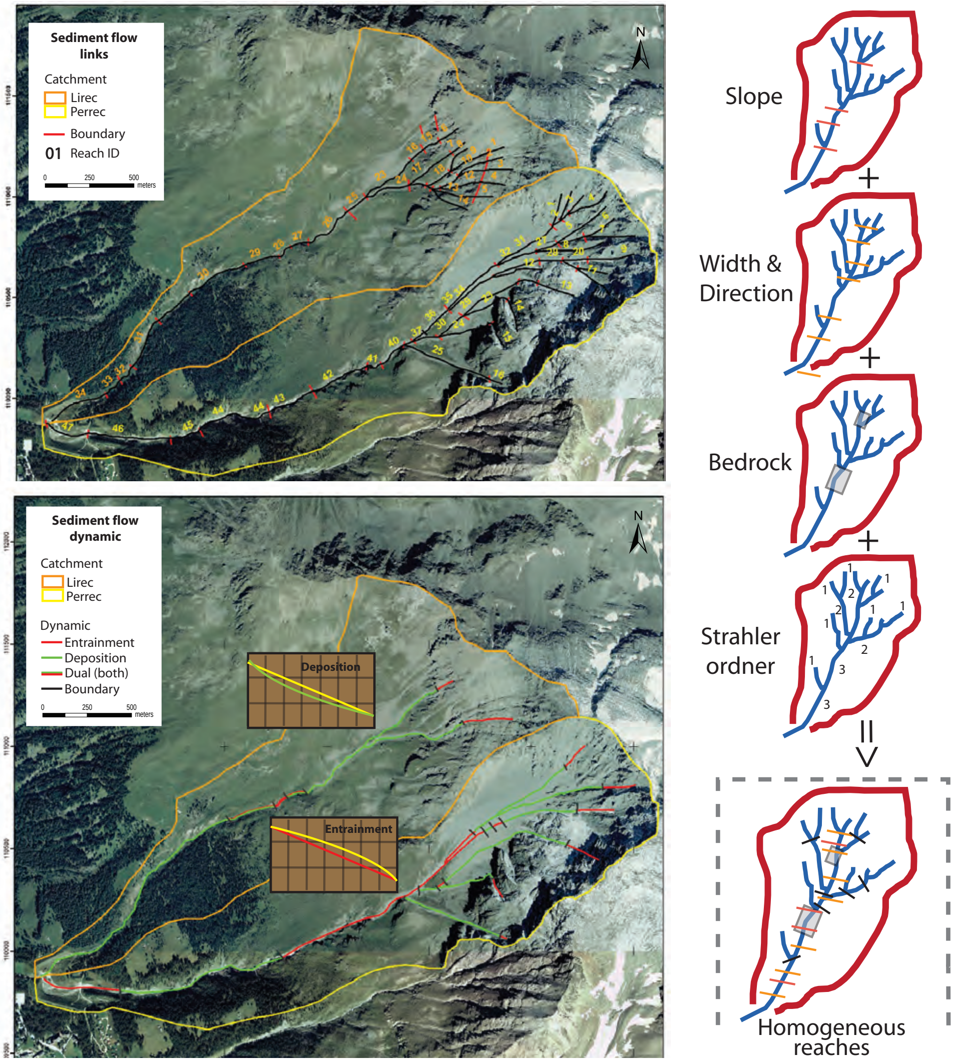

Figure 5.8: *Determination of the sediment cascade links through morphological principles (Table above) in regards to the torrent flow dynamics and division of the torrent system considering the analysis of the length profile in addition (Fig. 5.9).*

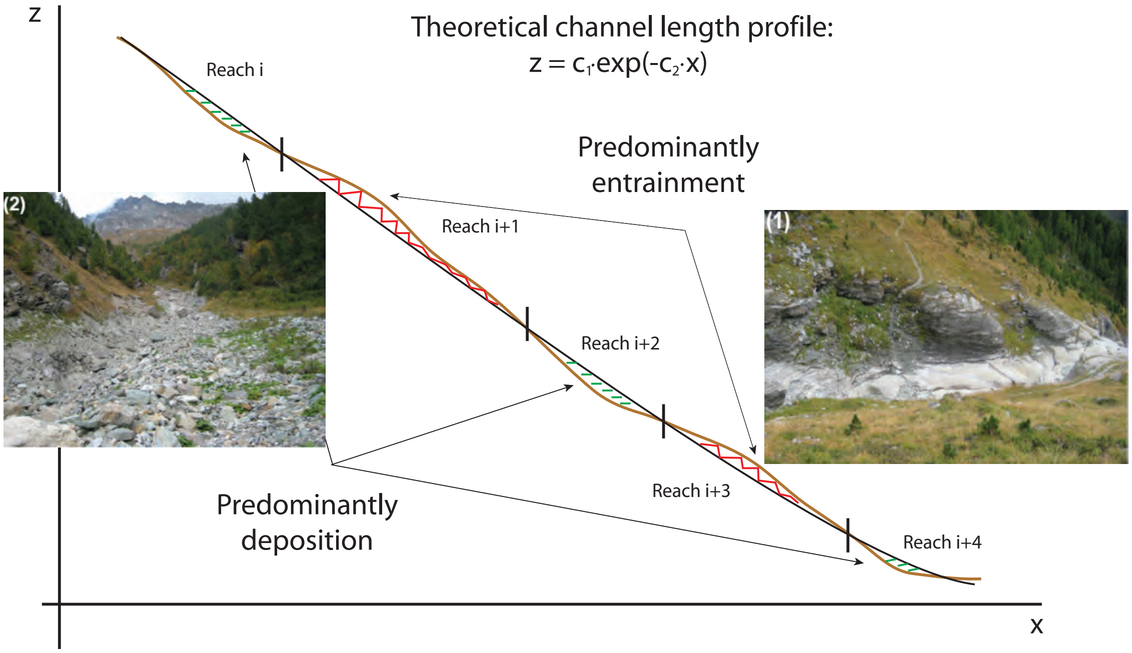

Figure 5.9: *Length profile analysis of the torrent topography providing information about the transient storage of sediment routing downstream the torrent channels. The mathematical function of the theoretical length profile was validated with field comparison. Entrainment zones (1) show mostly oucropping bedrock while deposition zones (2) are mostly loaded with debris transported from bedload and debris flow events.*

volume-based approach of Fanin and Wise (2000) in which the changes of subsequent reach morphology determine the flow behavior (entrainment / deposition) and magnitude along the downslope path. The volume of material deposited in a reach cannot however exceed the maximum capacity of storage $V_{C_{max}}$ (Fig. 5.6). Once this volumetric capacity is reached, the flux of sediment is just conveyed to the next reach without deposing any material. The possibility that material overflows a reach and leaves the torrent bed was not considered so far.

The mobilization (direct / indirect debris sources) of sediment varies all along the sediment cascade. These were defined by a parameter k proportional to the intensity of rainfall events. The volumes of sediment flux recharging each reach of the torrent are given by:

$$V^p_{i_{ind}} = A_i^{ind} \cdot k_{ind}, \qquad \mathrm{A_i^{ind}} = \mathrm{erodible\,area\,in\,contact\,with\,the\,reach} \tag{5.3}$$

The k – parameter represents a mean erosion rate in the torrent contributive area. The volumes of in-channel debris mobilized in reaches themselves are given by:

$$V^p_{i_{dir}} = A_i^{dir} \cdot k_{dir}, \qquad \mathrm{A_i^{dir}} = \mathrm{erodible\,area\,of\,the\,reach} \tag{5.4}$$

A_i^{dir} can be different from the surface of the reach depending on whether the bedrock outcrop or not. Here, the k – parameter represents a mean height of erosion of the sediment stock available in each reach.

Debris flows were simulated by considering them as an evacuation (emptying) of the sediment stocks contained in the sediment cascade links transported downstream to the

Proportion of transient deposition estimated in a reach according to

the change of slope gradient *S* and width *L* with the upward reach(es)		the change of direction A_Z with the upward reach(es)	
$\left(\frac{S_{reach}}{S_{reach\,(es)_{up}}} + \frac{L_{reach\,(es)_{up}}}{L_{reach}}\right) / 2$	Index of transient deposition I_{alluv}	ΔA_Z	Index of transient deposition I_{alluv}
0 – 0.3	80 %		
0.3 – 0.5	60 %	0° < ΔA_z	+0 %
0.5 – 0.8	40 %	20° < ΔA_z < 60°	+10 %
0.8 - 1	20 %	60° < ΔA_z < 90°	+20 %
≥ 1	0 %		

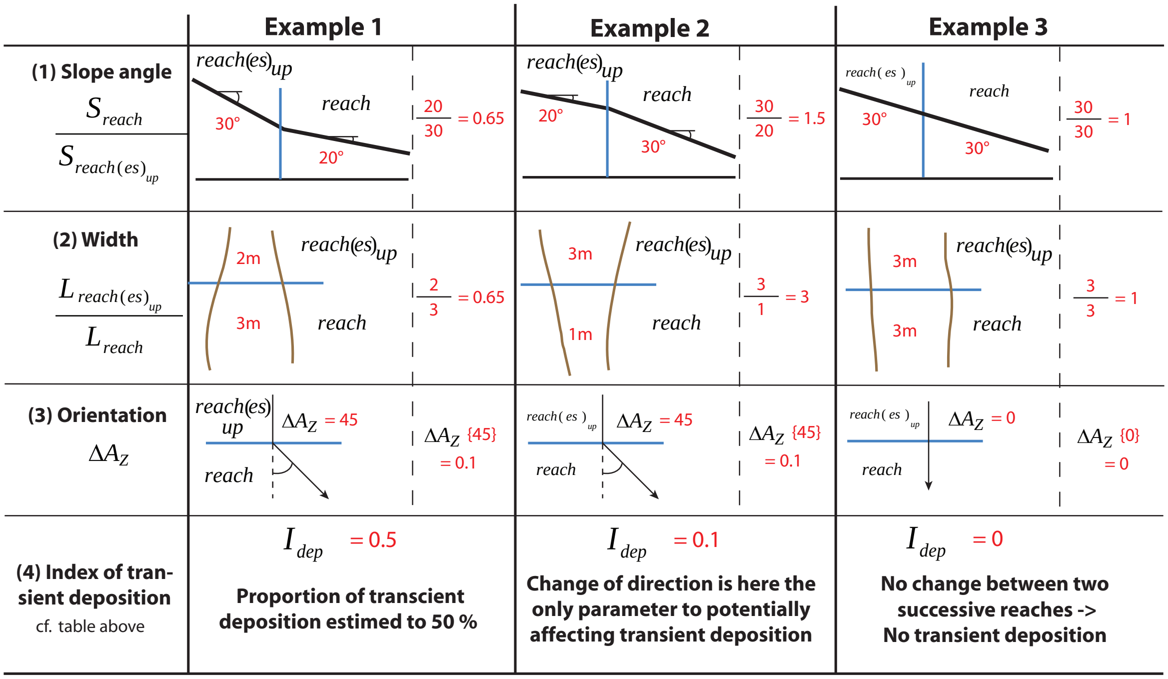

Figure 5.10: *Determination of the index of sediment transfer rates I_{alluv} illustrated by examples (Table down). Depending on the scale of the sediment cascade links, more than two reaches may be assigned to define the propension of sedimentation.*

torrent outlet. A volume of material (V^{DF}), proportional to the direct and indirect stocks available, is transfered out of each reach and propagated into the sediment cascade next reaches. This is given by:

$$V_i^{DF} = c_{mob} \cdot (Stock_i^{dir} \cdot c_{dir} + Stock_i^{ind} \cdot c_{ind}) \tag{5.5}$$

where c_{mob}, c_{dir} and c_{ind} represent factors of proportionality between the different stocks. They govern the magnitude of debris flow events. The volume of sediment for each reach are limited to the direct stocks available, whereas the indirect stocks can be considered or not to be unlimited.

All these parameters require in-situ calibration for validation. Different orders of erosion rates and conveyances within the hillslope and torrent sediment stocks (recharge) can be set proportional to the intensity of these stochastic perturbations.

5.4.6 Frequency and magnitude of stochastic events

The sediment influx of the torrent system is governed by daily rainfall of various intensity and debris flows of different magnitude:

- The precipitations of low intensity (*frequent*) determine the basic flux of sediment of the cascade. There are events that recharge the torrent reaches with material. The sediment flux consists exclusively of bedload of low intensity.
- The precipitations of high intensity (*rare*) induce a bedload of higher intensity. The sediment supply recharging the channel reaches are also more important.
- The precipitations of type *extreme* enable to define a threshold where also extraordinary events may occur, e.g. a landslide of large magnitude. This volume of material is added to the sediment cascade at a location that is determined from field data. The parameters of erosion and sediment transfer rates are also amplified in comparison to events of high runout.
- Debris flow event intensity induce a transfer of a certain volume of material in the outlet downstream taken from the sediment stocks. They follow a similar approach than precipitations.

Material production, debris supply and sediment routing were driven by randomly-generated time series of simulating the occurrence of a list of events defined according to their return period (Fig. 5.11). The occurrence of rainfall and debris flow was however limited from April to November as runoff during winter is almost stopped by large snowfall. When neither runoff induced rainfall or snowmelt nor debris flow happen, the sediment activity is considered to be dormant, so that any flux operates in the sediment cascade. So far, continuous erosion processes such as soil creeping through gelifluction for instance, as well as ground snow avalanches, are not taken into account.

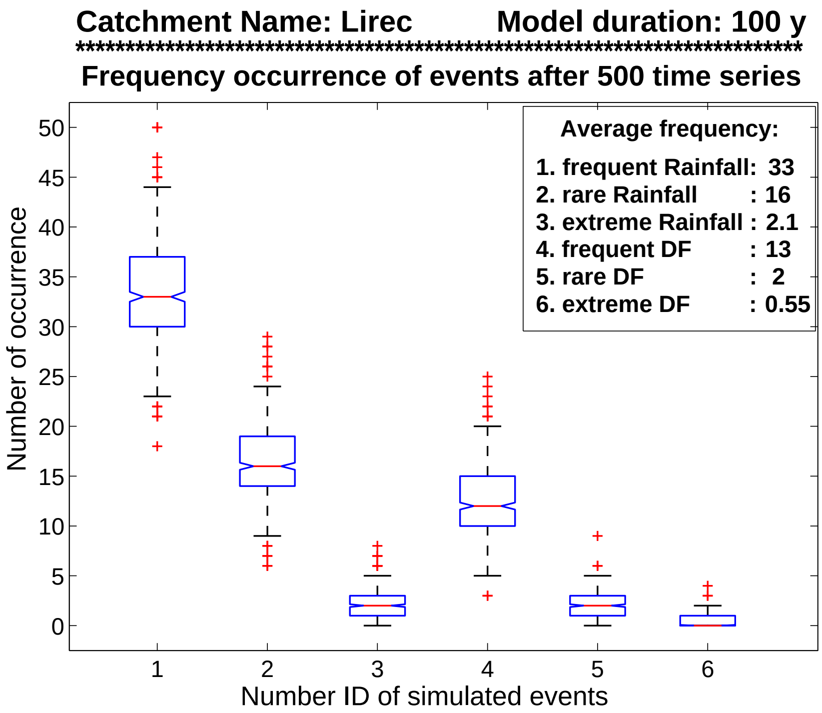

Figure 5.11: *Boxplot statistics showing the number of occurrence of the stochastic events simulated in the sediment cascade over the time: median (red line); 25th and 75th quantile (blue box); extremums (red crosses). The number of events varies greatly from one time serie simulation to another, and so the need to model a great number of time series to get significant averages.*

5.4.7 MATEROSION model application

Several scenari were simulated considering different process interactions between the hillslope and channel subsystems (limited / unlimited supply of channel recharge) or within the torrent channel themselves (rates of sedimentation and transportation). The situation with a potential occurrence of major landslides or rockslides were also considered. In the lack of evidence, extraordinary debris supply was set to 1% (25'000 m^3) of the entire sediment stocks contained in the torrent system. The sediment stocks detected in torrent catchments are given in Tab. 5.1. For want of anything better, the frequency – magnitude of modeled debris flow events were calibrated in a statistic way based on debris supply inventories of neighboring catchments. Globally, quaternary soils in the periglacial environment of the Lirec and Perrec torrents are quasi inexistent in the upper part and range in the middle and down parts between 1 m to 2 m. Their significance of material availability is rather limited. Hillslope debris supply recharging these torrent channels can be considered to be 5 times less active than the Péterey torrent. Debris flows can be recognized to be proportionally more spread out in time (Tab. 5.2). Return periods and magnitudes estimated for this study case were set in rather conservative manner, ensuring cautious sediment budget projections.

The erosion rates of indirect sediment stocks defining the volumetric conveyance from the hillslope to the torrent channels (recharge) were defined according to mean values

Table 5.1: *Total stocks of material in the torrent and the hillslope defining the amount of sediment to get potentially mobilized and the potential of recharge. The theoretical capacity corresponds to the total volume that can be temporary stored in the torrent channels.*

Catchment	Debris stocks [m^3] Direct	Indirect	Total [m^3]	Theoretical storage capacity [m^3]
Perrec	61'000	79'500	**140'500**	346'400
Lirec	9'300	48'000	**57'300**	105'200

Table 5.2: *Return period estimation of debris flows of different magnitudes in the torrent of Lirec and Perrec based on the debris supply inventory of the neighboring Péterey torrent.*

Catchment	Intensity classes	Frequent	Rare	Extreme
Perrec	Return period [y]	5	30	100
	Averaged magnitude [m^3]	750	10'000	25'000
Lirec	Return period [y]	8	50	170
	Averaged magnitude [m^3]	500	7'500	17'000

deduced from long-term observation obtained from watershed sediment budgets based on hydropower reservoir sedimentation located near the study area (see Appendix B). The three classes of rainfall intensity were appointed to these plausible erosion rates.

Sediment transfer functions controlling the flow dynamics within successive sediment cascade links (recharge, bedload and debris flow propagation) were calibrated in order that conveyed amounts of material to the torrent outlet represents certain volumes in accordance with field observation and inventory estimations. To reduce uncertainties, a number of 500 randomly generated time series was modeled over a period of 100 years at a time step of a month to provide averaged sediment budgets. A series of simulation with exaggerated parameters were also performed to consider possible modifications in the stochastic driven processes caused by climate changes. This involved a progressive increase of 25% of daily rainfall per year and debris flow frequency were doubled. Erosion and sediment transfer rates remained unchanged.

5.5 Sediment budget projections

The application of the MATEROSION model in the Lirec and Perrec torrent reveals an averaged cumulative sediment yield at their catchment outlet of 160'000 m^3 to 210'000 m^3 for the next 100 year period. In the perspective of changing climate, where the rainfall of high intensity principally would increase, the sediment budget could rise up to 450'000 m^3 for the next century. The global sediment yield would thus double in comparison to projections based on the actual hydrometeorological conditions. By limiting the hillslope supply of material to the torrent to their contemporary volumes (finite sediment stocks), the cumulative sediment yield may reduce of 50% after about 100 years. The results are summarized in Figures 5.12 and Fig. 5.13. Comparison of the projected sediment yield in terms of erosion rates of the sediment cascade modeling with other approaches based on the quantification of sediment deposits at long-term (Hinderer, 2001; Loye et al., 2009b, see Appendix B) are of similar order of magnitude.

Notice that the occurrence of catastrophic landslides events loading the torrent with several 100’000 of m^3 and comparable to the ones observed in the St-Barthélémy torrent in the 1920s (Montandon, 1940) or in the Hillgraben catchment during the 1960s (Eisbacher and Clague, 1984) was not considered so far. This might be the case in the upper periglacial part of the catchment (e.g. Bonnard rock glacier). Such situations can be added to the global sediment budget projections.

5.6 Conclusive comments

This semi-distributed sediment budget modeling method developed in the framework of the MATEROSION project attempts to discretize the torrent system in channel unit and individual process-response systems. This also looks after to include in simple manner the geological, morphological and sediment flux information that can be deduced from GIS data in each element of the sediment cascade. The preliminary results obtained in this case study are promising and show potential applications. Particularly, the sediment flow routine based on projected time series allow the generation of a great number of simulations of different scenari, providing the most probable sediment yield estimates to the torrent system. This provides therefore a mean of reducing the common sediment budget uncertainties inherent to torrent system sediment yield projections. The scale of the hillslope and channel processes in space and time can be adapted individually and their implications along the sediment cascade links can be individually analysed. The function of sediment transfer both in and near the torrent channel can be easily improved, and they must be improved to reliable sediment budget estimations. So far, this might not always be correct. In this perspective of development, this sediment cascade routine could provide to stakeholders a decision base and the means to forcast for better managing torrent solid wastes and ensuring the full capability of mitigation works.

Volumes accumulated at the outlet of the torrent of Perrec

Hypothese	**Scenario**	Average after 10 years	Variability	Average after 30 years	Variability	Average after 100 years	Standard	DR *$mm\ y^{-1}$*
constant climatic conditions	**finite stocks**	9’400	5'000 (50%)	57'200	21'000 (35%)	111’000	50'000 (45%)	0.41
	infinite stocks	14’200	8'000 (55%)	46’400	21'300 (45%)	130’000	56'000 (45%)	0.48
changing climatic conditions	**finite stocks**	26’900	8'000 (30%)	72’600	24'700 (35%)	162’500	55'000 (35%)	0.6
	infinite stocks	27’800	9'500 (35%)	92’400	28'600 (40%)	280’000	85’000 (35%)	1

**DR: Erosion rates [mm/yr] considering an averaged cumulative of 100 years over the total topographic catchment area and a bulk density of the deposits of 1800 kg/m^3*

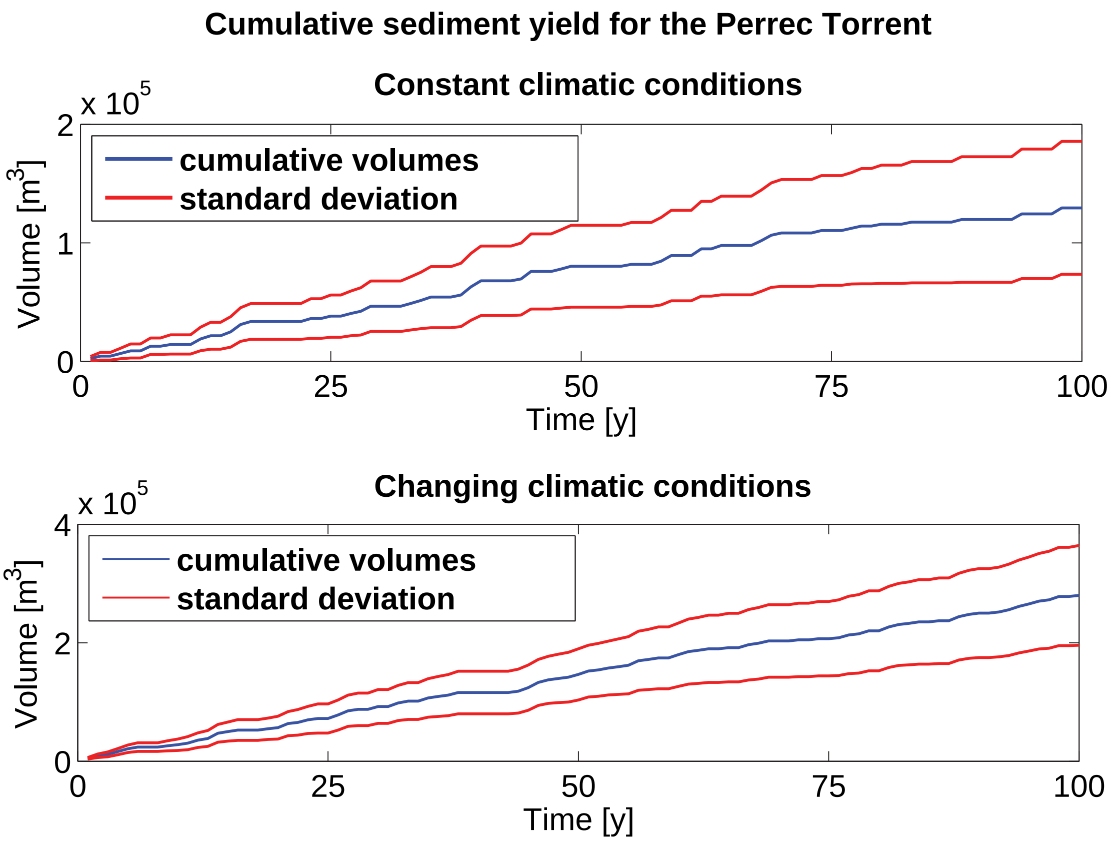

Figure 5.12: *(Table) Sediment budget projection for the Perrec torrent. (Plot) Averaged cumulative sediment yield simulated at the outlet of the Perrec torrent for a scenario with infinite sediment stocks under the contemporary and changing climate conditions.*

Volumes accumulated at the outlet of the torrent of Lirec

Hypothese	Scenario	Average after 10 years	Variability	Average after 30 years	Variability	Average after 100 years	Standard	DR $mm\ y^{-1}$
constant climatic conditions	**finite stocks**	7’200	3'500 (50%)	24'900	11'400 (35%)	57’500	30'000 (45%)	0.24
	infinite stocks	8’900	4'000 (45%)	26’700	12'200 (45%)	76’700	40'000 (50%)	0.32
changing climatic conditions	**finite stocks**	16’100	5'800 (35%)	40’000	13'500 (35%)	84’700	32'500 (40%)	0.35
	infinite stocks	16’500	5'300 (30%)	47’100	17'500 (35%)	162’500	56’000 (35%)	0.68

**DR: Erosion rates [mm/yr] considering an averaged cumulative of 100 years over the total topographic catchment area and a bulk density of the deposits of 1800 kg/m^3*

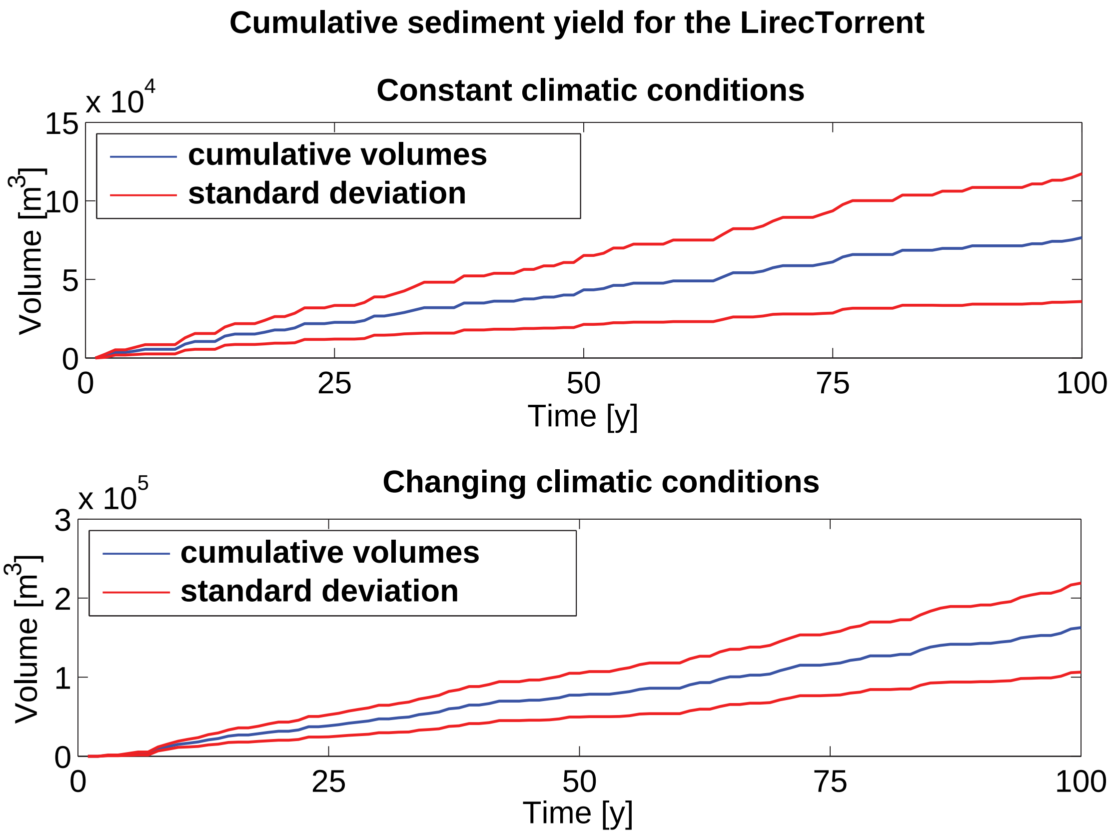

Figure 5.13: *(Table) Sediment budget projection for the Lirec torrent. (Plot) Averaged cumulative sediment yield simulated at the outlet of the Perrec torrent for a scenario with infinite sediment stocks under the contemporary and changing climate conditions.*

Conclusion

Addressing the issue of debris supply and sediment transfer in torrent channels, as well as modeling sediment delivery in catchments prone to debris flow, are a formidable task because torrent systems may be one of the most characteristic outcomes of the relation between orogeny (endogenic processes) and associated mass wasting (exogenic processes) in its entirety. All along the course of torrent systems, from headmost gullies recruiting debris-derived rock collapse to hillslope mass movement transferring sediment to be evacuated in debris flow channels, the instability principle of geomorphic equilibrium formulated by Scheidegger (1983) can be found. Erosion in torrent systems represents therefore an ultimate illustration of the geological impermanence of the Earth surface.

Debris flow channels are recharged with material by mass wasting processes and sediment entrainment occurs in the form of bedload and debris flows within the torrent system. Frequently however, debris storage fails delivering significant slugs of sediment downstream, despite of hydrological solicitations. The particular link between channel recharge rate and sediment transfer is far of being completely understood (Fig. 5.14), such that prediction of sediment yield and debris flow frequency and magnitude remains difficult yet, whether not impossible. Even though this aspect was in the center stage of this PhD thesis, this was never the point actually. The different projects developed in the frame of this PhD contribute however in many aspects to a better understanding of some of the processes related to debris flow dynamics.

One of these aspects is the response of debris flow channels to sediment recharge (Chapter 2). For that, the investigation of sediment dynamics in its whole was extensive, involving the monitoring of debris production and hillslope sediment transfer and the event-based surveys of material entrainment in the main torrent. All these measurements yield information about the volumes of material supplied and the conditions of in-channel debris storage prevailing in the torrent system. They are however only indirect observation of the processes of sediment activity occurring in response to particular events, and need to be interpreted. Still, the analysis of these "topographic snapshots" pictured one of the most detailed evolutions of sediment dynamics over a year in a debris flow catchment. Their interpretation emphasized that erosion, from both rock walls and hillslope, is highly variable in time and space and reacts differently to hydrometeorological conditions. Debris production in both frequency and magnitude is limited, occurring in great majority during the cold season, and hangs on the type of lithology. Long-lasting low intensity rainfalls foster the (re-)mobilization of debris deposits, e.g. through excess pore pressure, and therefore affect sediment transfer downstream. Not only the availability, but also the stability of debris deposits, govern sediment entrainment, and therefore influence material retention

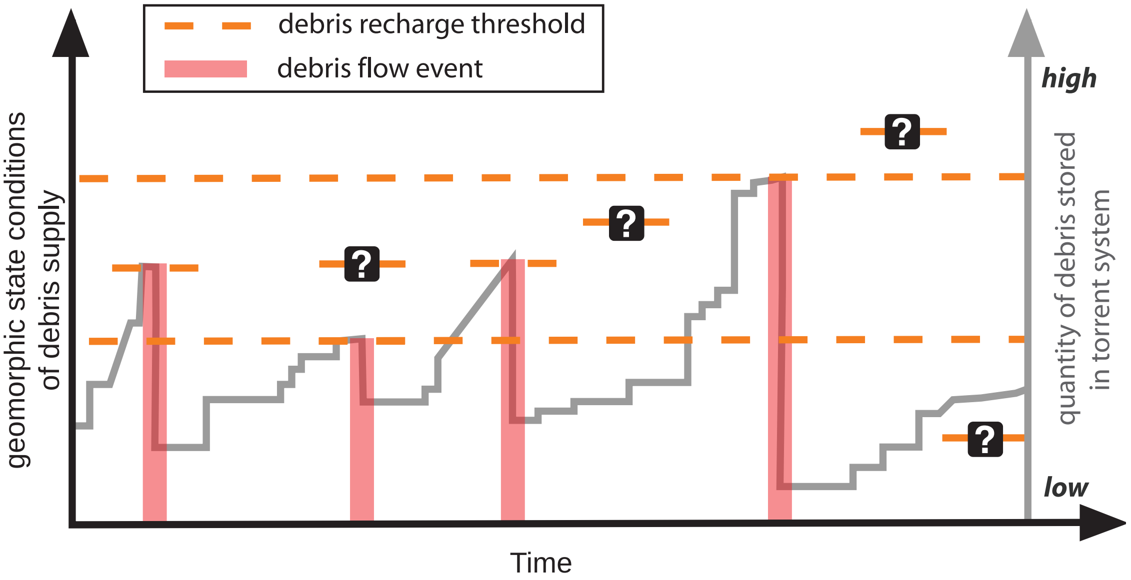

Figure 5.14: *Schematic relationship between geomorphic process activity, inducing debris supply and channel recharge/sediment load, and debris flow dynamics. Above a certain treshold, that varies constantly through time, a debris flow initiates. Assessing this geomorphic threshold is much challenging yet.*

of the catchment headwaters. Fresh debris deposits especially seem to be more easily destabilized by subsequent periods of rainfall. Our good fortune allowed to observe two major debris flows, from which we could analyze the pre-conditions of sediment recharge. Although a seasonally-based monitoring showed only the coarse phenomenology, these observations readily improved our knowledge about discontinuous occurrence of bedload transport and debris flow activity at Manival.

Another aspect concerns the debris production in catchment headwaters (Chapter 3). The generated rockfall inventory emphasized that rock slope collapse follows a power law distribution. This enables to estimate an average magnitude of debris supply that can be expected over a certain period of time. A different mode of failure for small volumes characterized by the power law roll-over could not be assessed from the observed data. But rockfall detection performed with the automated identification procedure revealed that events of very small size were probably omitted by the visual identification procedure. The existence of different physical processes of rock collapse including distinct episodic large rockfall event and more continuous erosion of rock walls remain still open.

The attempt to characterize sediment supply in terms of susceptibility according to the structural aspect of the rock mass and their geotechnical condition highlighted a clear correspondence between rockfall contribution and sediment delivery measured in catchment headwaters, considering the three main types of failure kinematics in hard rock: plane failure, wedges and toppling (Chapter 3). This relation is ultimately evident, since rock slope stability is known from many studies in mining engineering and tunneling to be essentially controlled by fractures and rock joints, which decrease the rock mass strength, and that their orientation and density play an important role on rockfall activity (e.g. Hoek and Bray, 1981). What less evident was the degree of susceptibility to rock slope production, which was not reflected in the density of potential failure at the scale of the outcrop. In the contrary, areas with high structure density corresponded to events of very small size and were rare. If any affirmation may be drawn from such a short-time rockfall inventory, particularly about the frequency of occurrence, this reveals however that rock mass cut by a high density of joint tend to generate blocks of small size, and therefore induce small size rockfall events, but of higher frequency than the one affected by only few discontinuities delimitating primarily blocks of size that induce more episodic larger rock collapse.

Bedrock structures and lithologic characteristics may not only influence rock slope stability. They may also modulate the overall morphological development and landscape evolution of a catchment (Chapter 4). The clear association between the geometry of erosional landforms and the preferential orientation of potential rock slope failure emphasized a structural control of the erosional mechanisms prevailing in bedrock-dominated catchments, and so for both crystalline and carbonate rock types. The rock mass strength, in terms of anisotropy of the structures, predisposes the initiation and propagation of erosion by facilitating the collapse of rock wall by rockfall and the incision of rock couloirs and gullies along zones of weakness. At the scale of the channel reach, particular joint configuration, like wedges or bedding planes tends to promote the detachment of rock slope units in a preferential direction through gravitational and hydrological erosion processes, contributing to guide their spatial development. The geological setting prevailing in a torrent system appear to be a first-order control in the evolution of landforms induced by erosion and mass wasting processes, and so for both initiation and subsequent development of the geomorphic processes.

The implementation of a sediment flux algorithm in a semi-distributed sediment cascade conceptual model at the scale of channel reaches revealed to be innovative (Chapter 5). Although this software remained at an early stage of development, it provides already a way to refine sediment budget estimates with numerical simulations and can therefore help managing solid mass wasting induced by torrent systems. This routine is a first step toward a more fully distributed sediment dynamic model, e.g. at the scale of a HRDEM cell. Due to the social and economic need to quantify risks associated with torrential hazard and solid waste management, the MATEROSION project could have been the research topic of a doctoral thesis on its own.

These projects included many different types of investigations that aimed to gather as many information as possible. Most of these results about processes of sediment dynamics and transfer rate need to be studied in more depth. Several of the issues could be addressed with field and laboratory experiments and by the advances in 3-D geological modeling. The following elements require to be improved:

1. The full range of sediment process was not captured as they were masked by successive sediment transfer. Higher frequency surveys could sensibly improve the interpretation of sediment process activity in response to particular event. Such investigations would require considerable effort in terms of time and resources. The

identification and extraction procedure developed in this work is an example of time and cost-effective tools for analyzing TLS data. Advances in TLS techniques for both acquiring and processing are booming by the end of this thesis. This TLS turmoil was just at its beginning when the project at Manival started.

2. 2.5-D digital elevation model are limited in modeling very steep terrain. Performing kinematic tests on real 3-D datasets, that include with high degree of details the vertically-oriented and overhanging topography could sensibly improve the slope stability analysis and hence, the susceptibility assessment to rock slope production. A Matterocking software using TLS point cloud is being developed at present.

3. Several factors contributing to weaken the rock mass in particular, such as the rock type and the local structural domain, the degree of alteration of joints, the effect of thermal stress and freeze/thaw cycles, the occurrence of water seepage and the effects of precipitation, should be considered with more attention to refine the susceptibility to rock slope production. This could be done by more intensive field work or characterize from TLS datasets. Advance in measurement techniques should make possible to adequately assess or determine those geological information in any accessible areas at the scale of the outcrop.

4. An in-situ observation of the geometric development of erosional landforms could highlight the small-scale mechanisms of erosion and processes of mass-wasting that induce a structural control of the erosion in bedrock-dominated catchment.

5. Parts of the torrent systems are not governed by hydrometeorological solicitations. They are supply-limited and depend rather on the rate of recharge of debris channels. The in-channel flow dynamic of the sediment cascade modeling should therefore be able to deliver mass flux between reaches based exclusively on recharge thresholds, using e.g. dampers or resistors. The sediment transfer functions can be improved by considering not only one reach from another, but a segment or even the entire upstream portion of the channel, so that the topographic setting of the torrent could be integrated in each reach. As well, the contributing area of each reach can be treated individually, processes of sediment recharge can be differentiated and the geological and morphological aspects can be included more specifically. All these elements would require not only a more complex model, but also more field work and in-situ calibration.

This thesis focused essentially in the headwaters of the torrent system, which made the originality of this work. Headwaters are commonly described as the “critical source area” (Hooke, 2003) as they can deliver a disproportionately large amount of material in a relative short-time. They showed to play an essential role in the occurrence of the two debris flows observed in the Manival torrent by recharging this latter with material. These phases of recharge can precede debris flow events with very long period of time. The torrent can remain inactive for several months before a debris flow occurs. For each rainstorm or period of runoff, the torrent system produces different responses that alter debris supply, complicating the assessment of failure frequency and magnitude. How complicated are sediment production and transfer within the torrent system are not necessary reflected in the sediment yield of the catchment outlet. Throughout this thesis, it becomes clear that the localization of debris supply and the study of the non-equilibrium behavior of the catchment headwaters according to large scale (e.g. landslides, earthquakes) and small scale (e.g. rockfall, frost action) disturbances is a crucial task that needs to be addressed for reliable quantitative risk management.

But the torrent itself is not the “jerky conveyor belt” (in reference to Ferguson, 1981) of the wasted material induced by on-going mountain landscape evolution. The high relief of most catchment headwaters provide enough gravitational energy gradient to potentially generate very large sediment flux compared to many earth surface processes. The torrent is therefore the noble carrier of this tremendous amount of energy accumulated through the geological time, especially when this concerns historically glaciated landscapes. And this work represents my mark of gratitude. With this in mind, the only viable solution to prevent torrential hazards, without considering mitigation structures, is to either give him enough places to live its moody temperament, or to monitor its evolving conditions of debris supply, storage and the coupling with its catchment headwaters, which should give some warning time to anticipate its insolence.

Lausanne, a Thursday of October 2012

Bibliography

Abellán, A., Calvet, J., Vilaplana, J., and Blanchard, J. (2009a). Detection and spatial prediction of rockfalls by means of terrestrial laser scanner monitoring. *Geomorphology*, 119:162–171.

Abellán, A., Carrea, D., Loye, A., Tonini, M., Jaboyedoff, M., Royan, M., and Pedrazzini, A. (2012). Understanding precursory rockfalls along cracks. In *Geophysical Research Abstracts*, Vol. 14, EGU2012-6037-1. EGU General Assembly.

Abellán, A., Jaboyedoff, M., Oppikofer, T., and Vilaplana, J. (2009b). Detection of millimetric deformation using a terrestrial laser scanner: experience and application to a rockfall event. *Natural Hazards and Earth System Sciences*, 9:365–372.

Abrahams, A. and Flint, J. (1983). Geological controls on the topological properties of some trellis channel networks. *Geological Society of America Bulletin*, 94:80–91.

Agliardi, F., Crosta, G., Zanchi, A., and Ravazzi, C. (2009). Onset and timing of deep-seated gravitational slope deformations in the eastern Alps, Italy. *Geomorphology*, 103:113–129. doi:10.1016/j.geomorph.2007.09.015.

Ahnert, F. (1970). Functional relationship between denudation, relief and uplift in large mid-latitude drainage basins. *American Journal of Science*, 268:243–263.

Aki, K. (1965). Maximum likelihood estimate of b in the formula logN=a-bM and its confidence limits. *Bull. Earthquake Res. Institute*, 43:237–239.

Alvarez, B. and Garcia-Ruiz, J. (2000). Variability of sediment yield from a high mountain catchment, central Spanish Pyrenees. 32(4):478–484.

Ancey, C. (1999). Rhéologie des laves torrentielles. Rapport scientifique final PNRN 1998–99, CEMAGREF – Grenoble, France.

Anderson, E., Thompson, J., and Austin, R. (2005). LiDAR density and linear interpolator effects on elevation estimates. *International Journal of Remote Sensing*, 26(18):3889–3900.

Arenson, L. (2002). *Unstable Alpine Permafrost: a potentially important natural hazard – Variations of geotechnical behaviour with time and temperature*. PhD thesis, No. 14801, Institute for Geotechnical Engineering, Swiss Federal Institute of Technology: Zurich.

Ashmore, P. and Church, M. (1998). Sediment transport and river morphology: A paradigm for study. In *P.C. Klingeman and R.L. Beschta and P.D. Komar and J.D. Bradley (eds), Gravel-Bed Rivers in the Environment*, pages 115–148, Water Resources Publications, LLC, Highlands Ranch, Colorado.

Ayer (2003). Rapport technique sur la mise en décharge des matériaux inertes. Document inédit, Commune d'Ayer.

Baillifard, F. (2004). *Détection par SIG des zones rocheuses à fortes susceptibilités d'éboulement.* PhD thesis, No. 194, University of Lausanne.

Bardou, E., Fournier, F., and Sartori, M. (2003). Paleofloods reconstruction on Illgraben torrent (Switzerland): a need for today frequency estimation. In *V.R. Thorndycraft and G. Benito and M. Barriendos and C. Llasat (eds), International Workshop on Paleofloods, Historical Data and Climate Variability: Application in Flood Risk Assessment*, pages 53–59, Proceedings of the PHEFRA International Workshop, Barcelona, 16–19 October 2002.

Bardou, E. and Jaboyedoff, M. (2008). Debris flows as a factor of hillslope evolution controlled by a continuous or a pulse process ? In *K. Gallagher and S.J. Jones and J. Wainwright (eds), Landscape Evolution: Denudation, Climate and Tectonic Over Different Time and Space Scales*, pages 63–78, Geological Society, London, Special Publication 296.

Barsch, D. and Caine, N. (1984). The nature of mountain geomorphology. *Mountain Research and Development*, 4(4):287–298.

Barthurst, J., Burton, A., and Ward, T. (1997). Debris flow run-out and landslide sediment delivery model tests. *Journal of Hydraulic Engineering*, 123(5):410–419.

Beavis, S. (1999). Structural controls on the orientation of erosion gullies in mid-western New South Wales, Australia. *Geomorphology*, 33:59–72.

Benda, L. and Dunne, T. (1987). Sediment routing by debris flows. In *R.L. Beschta and T. Blinn and G.E. Grant and G.G. Ice and F.J. Swanson (eds), Erosion and Sedimentation in the Pacific Rim*, pages 213–223, IAHS Publication 296.

Benda, L. and Dunne, T. (1997). Stochastic forcing of sediment supply to channel networks from landsliding and debris flow. *Water Resources Research*, 12(33):2849–2863.

Benporad, G., Alterach, J., Amighetti, F., Peviani, M., and Saccardo, I. (1997). A distributed approach for sediment yield evaluation in alpine regions. *Journal of Hydrology*, 197:370–392.

Berger, C., McArdell, B., and Schlunegger, F. (2011). Sediment transfer patterns at the Illgraben catchment, Switzerland: Implication for the time scales of debris flow activities. *Geomorphology*, 125:421–432.

Berti, M., Genevois, R., LaHusen, R., Simoni, A., and Tecca, P. (2000). Debris flow monitoring in the Acquabona watershed on the Dolomites (Italian Alps). In *Original Research Article Physics and Chemistry of the Earth, Part B: Hydrology, Oceans and Atmosphere*, pages 707–715, Volume 25, Issue 9.

Besl, P. and McKay, N. (1992). A method for registration of 3-D shapes. *IEEE Transactions on Pattern Analysis and Machine Intelligence*, 14(2):239–256.

Besson, L. (1996). *Les risques naturels en Montagne*. Editions Artès–Publialp, Grenoble. 438 p.

Bienawski, Z. (1973). Engineering classification of jointed rock masses. *Trans S. Afr. Inst. Civ. Engrs*, 15:335–344.

Bienawski, Z. (1989). Rock mass classification in rock engineering. In *Z.T.Bienawski (eds), Exploration for rock engineering, proc. of the symp.*, pages 97–106, Cape Town.

Bitelli, G., Dubbini, M., and Zanutta, A. (2004). Terrestrial laser scanning and digital photogrammetry techniques to monitor landslide bodies. In *Proceedings of the* XX^{th} *ISPRS Congress Geo–Imagery Bridging Continents, XXXV, part B5, Istanbul, Turkey, 12–23 July 2004*, pages 246–251, ISPRS.

Blikra, L. and Nemec, W. (1998). Postglacial colluvium in western Norway: depositional processes, facies and paleoclimatic record. *Sedimentology*, 45:909–959.

Bloom, A. (1978). *Geomorphology. A systematic analysis of late Cenozoic land forms*. Englewood Cliffs, New Jersey: Prentice–Hall. 510 p.

Bénévent, E. (1915). Le Manival – Etude de cône de déjection. *Recueil des travaux de l'institut de géographie alpine*, 1(3):69–100.

Bovis, J. and Jakob, M. (1999). The role of debris supply conditions in predicting debris flow activity. *Earth Surface Processes and Landforms*, 24:1039–1054.

Bozzano, F., Mazzanti, P., Prestininzi, A., and Mugnozza, G. (2010). Nine years of spatial and temporal evolution of the La Valette landslide observed by SAR interferometry. *Engineering Geology*, 7(3):381–385.

Brayshaw, D. and Hassan, M. (2009). Debris flow initiation and sediment recharge in gullies. *Geomorphology*, 109:122–131.

Bremer, M. and Sass, O. (2011). Combining airborne and terrestrial laser scanning for quantifying erosion and deposition by a debris flow event. *Geomorphology*, 138:49–60.

Brochot, S., Coeur, D., Lang, M., and Naulet, R. (2000). Historique – Isère et torrents affluents. Utilisation de l'information historique pour une meilleur définition du risque d'inondation. Rapport technique, Cemagref / Achtys, Lyon – Grenoble. 248 p.

Brochot, S., Koulinski, V., and Rovera, G. (1998). Approches globales pour l'estimation de l'érosion torrentielle (apports des versants et production de sédiments). *Ingénieries-EAT*, 15:61–78.

Brochot, S., Marchi, L., and Lang, M. (2002). Debris flow volume assessment: available methods and application to the Poucet torrent (Savoy, France). *Bulletin of Engineering Geology and the Environment*, 61(4):389–402.

Brodu, N. and Lague, D. (2012). 3D terrestrial lidar data classification of complex natural scenes using a multi-scale dimensionality criterion: Applications in geomorphology. *ISPRS Journal of Photogrammetry and Remote Sensing*, 68:121–134.

Buckley, S., Howell, J., Enge, H., and Kurz, T. (2008). Terrestrial laser scanning in geology: data acquisition processing and accuracy considerations. *Journal of the Geological Society*, 165:625–638.

Burbank, D., Leland, J., Fielding, E., Anderson, R., Brozovic, N., Reid, M., and Duncan, C. (1996). Bedrock incision, rock uplift and threshold hillslopes in the northwestern Himalayas. *Nature*, 379:505–510.

Burrough, P. and McDonnel, R. (1998). *Principals of Geographic Information Systems*. Oxford University Press. 333 p.

Bussy, F., VonRaumer, J., and Capuzzo, N. (2000). Mont Blanc–Aiguilles Rouges Massifs – External Massifs, an example of polyorogenic evolution. *University of Lausanne*, unpublished.

Butler, D. and Walsh, S. (1990). Lithologic, Structural and Topographic Influences on Snow-Avalanches Path Location, Eastern Glacier National Park, Montana. *Annals of the Association of American Geographers*, 80(3):362–378.

Byers, S. and Raftery, E. (1998). Nearest-Neighbor Clutter Removal for Estimating Features in Spatial Point Processes. *Journal of the American Statistic Association*, 93(442):577–584.

Caine, N. (1974). The geomorphic processes of the alpine environment. In *J.D. Ives and R.G. Barry (eds), Artic and Alpine Environment Chapter 12B*, pages 721–748, London.

Cannon, S., Gartner, J., Parret, C., and Parise, M. (2003). Wildfire-related debris flow generation through episodic progressive sediment-bulking process, western USA. In *D. Rickenmann and C.L. Chen (eds), Debris-flow hazard mitigation: mechanics, prediction and assessment*, Millpress, Rotterdam.

Carson, M. and Kirkby, M. (1972). *Hillslope form and process*. Cambridge University Press, Cambridge. 475 p.

Chandler, J. and Brunsden, D. (1995). Steady state behaviour of the Black Ven mudslide: the application of archival analytical photogrammetry to studies of landform change. *Earth Surface Processes and Landforms*, 20:255–275.

Charollais, J., Dondey, D., Ginet, C., Lombard, A., Muller, J., Rosset, J., and Ruchat, C. (1986). Carte géol. France (1 / 50.000^{ème}. Feuille Domène 33–34, Orléans, B.R.G.M.

Chorley, R. and Kennedy, B. (1971). *Physical Geography, A System Approach*. Prentice–Hall International, London.

Coe, J., Glancy, P., and Whitney, J. (1997). Volumetric analysis and hydrologic characterization of a modern debris flow near Yucca Mountain, Nevada. *Geomorphology*, 20:11–28.

Coe, J. and Harp, E. (2007). Influence of tectonic folding on rockfall susceptibility, American Fork Canyon, Utah, USA. *Natural Hazards and Earth System Sciences*, 7:1–14.

Coe, J., Kinner, D., and Godt, J. (2008). Initiation conditions for debris flows generated by runoff at Chalk Cliffs, central Colorado. *Geomorphology*, 96(3-4):270–297.

Craig, R. (1989). Computing Appalachian geomorphology. *Geomorphology*, 2:197–207.

Cruden, D. (2003). The shapes of cold, high mountains in sedimentary rocks. *Geomorphology*, 55:249–261.

D'Agostino, V. (1996). Analisi quantitativa e qualitativa del transporto solida torrentizio nei bacini montani del trentino orientale, i problemi dei grandi comprensori irrigui. Technical report, Associazone Italiana di Ingegneria Agraria, Novara. pages 111–123.

DallaFontana, G. and Marchi, L. (2003). GIS indicators for sediment sources study in Alpine basins. In *Hydrology, Water Resources and Ecology in Headwaters*, IAHS Publ. no. 248. Proceedings of the HeadWater 98 Conference, Merano, Italy.

Davies, M., Hamza, O., and Harris, C. (2001). The effect of rise in mean annual temperature on the stability of rock slope containing ice-filled discontinuities. *Permafrost and Periglacial Processes*, 12(1):137–144.

Davis, G. (1962). Erosional features of snow avalanches, Middle Fork Kings River, California. Professional Paper Vol. 450–D, U.S. Geological Survey. Washington: Government Printing Office.

Davis, W. (1899). The geographical cycle. *Geography Journal*, 14:481–504.

Decaulne, A. and Saemundsson, P. (2007). Spatial and temporal diversity for debris-flow meterorological control in subarctic oceanic periglacial environments in Iceland. *Earth Surface Processes and Landforms*, 32:1971–1983.

Deere, D. and Miller, R. (1996). Engineering Classification and Index Properties of Intact Rock. Technical Report AFL–TR–65–116, pages 509–513, Air Force Weapon Laboratory, Kirkland Air Force Base, New Mexico.

Dempster, A., Laird, N., and Rubin, D. (1977). Maximum Likelihood from Incomplete Data via the EM Algorithm. *Journal of the Royal Statistical Society*, 39(1):1–38.

Densmore, A., Anderson, R., McArdell, B., and Ellis, M. (1997). Hillslope evolution by bedrock landslides. *Science*, 275:369–372.

Derron, M., Jaboyedoff, M., and Blikra, L. (2004). Preliminary assessment of rockslide and rockfall hazards using a DEM (Oppstadhornet, Norway). *Natural Hazards and Earth System Sciences*, 5:285–292.

Desloges, J. and Gardner, J. (1984). Process and discharge estimation in ephemeral channels, Canadian Rocky Mountains. *Canadian Journal of Earth Sciences*, 21:1050–1060.

Desplanches, J.-L. (1999). Evolution temporelle de la production de matériaux dans les bassins-versants torrentiels: l'exemple de trois torrents des Alpes du Nord. Mémoire DEA, Université de Savoie, Chambéry. 55 p.

Dewez, T. and Rohmer, J. (2011). Probabilistic rockfall hazard: empirical computation based on ground-based lidar observations in Mesnil-Val, Normandy. In *Journée Aléa Gravitaire, 7–8 Septembre 2011, Strasbourg (France)*.

Dietrich, W. and Dunne, T. (2007). Sediment budget for a small catchment in mountainous terrain. *Zeitschrift für Geomorphologie Suppl. Bd.*, 32:1971–1983.

Downs, P. and Priestnall, G. (2003). Modelling catchment processes. In *G.M. Kondolf and H. Piégay (eds), Tools in Fluvial Geomorphology*, pages 205–230, John Wiley & Sons, Chichester.

Dunning, S., Massey, C., and Rosser, N. (2009). Structural and geomorphological features of landslides in the Bhutan Himalaya derived from terrestrial laser scanning. *Geomorphology*, 103:17–29.

Dussauge, C., Helmstetter, A., Grasso, J.-R., Hantz, D., Jeannin, M., and Giraud, A. (2002). Probabilistic approach to rock fall hazard assessment: potential of historical data analysis. *Natural Hazards and Earth System Sciences*, 2:15–26.

Eaton, S., Morgan, B., Kochel, R., and Howard, A. (2003). Role of debris flows in long-eterm landscape denudation in the central Appalachians of Virginia. *Geology*, 31:339–342.

Eberhardt, E. (2003). Rock Slope Stability Analysis – Utilization of Advanced Numerical Techniques. Course material, University of Brithish Columbia: Earth and Ocean Sciences, Vancouver, Canada. 41 p.

Eisbacher, G. and Clague, J. (1984). Destructive mass movement in high mountains: hazard and management. *Geol. Survey of Canada*, 84(16):230 p.

El-Sheimy, N., Valeo, C., and Habib, A. (2005). *Digital terrain modeling: acquisition, manipulation, and applications*. Artech House, Boston, MA. 257 p.

Erismann, T. and Abele, G. (2001). *Dynamics of rockslides and rockfalls*. Springer Verlag, Berlin. 316 p.

Evans, M. (1997). Temporal and spatial representativeness of Alpine sediment yields: Cascade Mountains, British Columbia. *Earth Surface Processes and Landforms*, 22:287–295.

Eyles, N. and Scheidegger, A. (1995). Environmental significance of bedrock jointing in Southern Ontario, Canada. *Environmental Geology*, 26:269–277.

Fanin, R. and Wise, M. (2000). An empirical – statistical model for debris flow travel distance. *Canadian Geotechnical Journal*, 38:982–994.

Ferguson, R. (1981). Channel forms and channel changes. In *Lewin, J. (eds) British Rivers*, pages 90–125. Allen and Unwin, London.

Frayssines, M. and Hantz, D. (2006). Failure mechanisms and triggering factors in calcareous cliffs of the Subalpine Ranges (French Alps). *Engineering Geology*, 86:256–270.

Fryirs, K., Brierley, G., Preston, N., and Kasai, M. (2006). Buffers, barriers and blankets: The (dis)connectivity of catchment-scale sediment cascades. *Catena*, 70:49–67.

Fuller, I. and Marden, M. (2009). Rapid channel response to variability in sediment supply: Cutting and Filling of the Tarndale Fan, Waipaoa Catchment, New Zealand. *Marine Geology*, 270:45–54.

Gabbet, E. and Mudd, S. (2006). The mobilization of debris from shallow landslides. *Geomorphology*, 74:207–218.

Gardner, J. (1970). Rockfall: a geomorphic process in high mountain terrain. *The Albertan Geographer*, 6:15–20.

Gardner, J. (1986). Sediment movement in ephemeral streams on mountain slopes, Canadian Rocky Mountains. In *A.D. Abrahams (eds), Hillslope Processes*, pages 97–113, Wincherster, MA, Allen and Unwin Inc.

Gerber, E. and Scheidegger, A. (1973). Erosion and stress – induced features of steep slopes. *Zeitschrift für Geomorphologie, N.F.*, (Suppl. Band 18):38–49.

Gertsch, E. and Kienholz, A. (2008). Geschiebelieferung alpiner Wildbachsysteme bei Grossereignissen. In *Interpraevent 2008 – Conf. Proceed. Vol. 1*, Klagenfurt, Austria.

Gidon, M. (1991). Géologie de la Chartreuse – Sentiers de la Chartreuse : Circuit de la Dent de Crolles. www.Geol–alp.com publ. 1d, 1° éd., Association "A la découverte du Patrimoine de Chartreuse". 20 p., 9 fig.

Gidon, M. (1998). *Le Bec Charvet et la gorge du Manival – Le rebord subalpin entre Saint-Ismier et Bernin.* Extrait de GEOL-ALP – Un atlas géologique des Alpes françaises, http://www.geol-alp.com.

Gilbert, G. (1877). Report on the Geology of the Henry Mountains (Utah). Technical report, U.S. Geol. Surv., Washington, D.C.

Glade, T. (2005). Linking debris-flow hazard assessments with geomorphology. *Geomorphology*, 66:189–21.

Günther, A. (2003). SLOPEMAP: programs for automated mapping of geometrical and kinematical properties of hard rock hill slopes. *Computer Geosciences.*, 29(7):865–875.

Gokceoglu, C., Sonmez, H., and Ercanoglu, M. (2000). Discontinuity controlled probabilistic slope failure risk maps of the Altindag (settlement) region in Turkey. *Engineering Geology*, 4(55):277–296.

Griffiths, J. and Stokes, M. (2008). Engineering geomorphological input to ground models: an approach based on earth systems. *Quarterly Journal of Engineering Geology and Hydrogeology*, 41(1):73–91.

Griffiths, P. and Webb, R. (2004). Frequency and initiation of debris flows in Grand Canyon, Arizona. *Journal of Geophysical Research*, 109. F04002.

Gruffaz, F. (1997). Torrent du Manival – Isère, Etude de bassin et de la plage de dépôts torrentiels. Rapport technique, RTM/ONF, Grenoble. 66 p.

Günther, A., Carstensen, A., and Pohl, W. (2004). Automated sliding susceptibility mapping of rock slopes. *Natural Hazards and Earth System Sciences*, 4:95–102.

Guzzetti, F., Peruccacci, S., Rossi, M., and Stark, C. (2008). The rainfall intensity – duration control of shallow landslides and debris flows: an update. *Landslides*, 5:3–17.

Hack, J. (1960). Interpretation of erosional topography in humid temperate regions. *American Journal of Science*, 258–A:80–97.

Haeberli, W., Rickenmann, D., and Roessli, U. (1991). Murgänge, Ursacheanalyse der Hochwasser 1987. Ergebnisse der Untersuchung. Mitteilung No. 14, Landeshydrologie und -geologie, Bern.

Haeberli, W., Wegmann, M., and VonderMühll, D. (1997). Slope stability problems related to glacier shrinkage and permafrost degradation in the Alps. *Eclogae Geologicae Helvetiae*, 90:407–414.

Hampel, R. (1980). Geschieberechnung für Gefahrenzonenpläne in Wildbachgebieten. In *International Symposium Interpraevent*, pages 83–91, Bad Ischl, Austria.

Hantz, D. (2011). Quantitative assessment of diffuse rock fall hazard along a cliff foot. *Natural Hazards and Earth System Sciences*, 11:1303–1309.

Hantz, D., Dussauge, C., Jeannin, M., and Vengeon, J.-M. (2002). Rock fall hazard: from expert opinion to quantitative evaluation. In *Symposium Geomorphology: from expert opinion to modeling (2002), Strasbourg (France).*

Hantz, D., Vengeon, J.-M., and Dussauge, C. (2003). An historical, geomechanical and probabilistic approach to rockfall hazard assessment. *Natural Hazards and Earth System Sciences*, 3:693–701.

Harris, C. (2005). Climate Change, Mountain Permafrost Degradation and Geotechnical Hazard. In *Global Change and Mountain Regions. Advance in Global Change Research. U.M. Huber, H.K.M. Bugmann and M.A. Reasoner (eds)*, pages 215–224. Springer Netherlands.

Hinderer, M. (2001). Late quaternary denudation of the Alps, valley and lake fillings and modern river loads. *Geodinamica Acta*, 14:231–263.

Histofit (2009). Histofit 1.0 – slope angle frequency analysis for mapping rockfall hazard. Technical report, Institute of Geomatics and Risk Analysis, Uuniversity of Lausanne. http://www.unil.ch/igar/page88464_fr.html.

Hoek, E. and Bray, J. (1981). *Rock Slope Engineering*. Spon Press, London. 525 p.

Hoek, E. and Brown, E. (1997). Practical estimates of rock mass strength. *International Journal of Rock Mechanics and Mining Sciences*, 34:1165–1186.

Hooke, J. (2003). Coarse sediment connectivity in river channel systems: a conceptual framework and methodology. *Geomorphology*, 56:79–94.

Horn, B. (1981). Hill Shading and the reflectance map. *Proceedings of the IEEE*, 1(69):14–47.

Hovius, N. (2000). Macro scale process systems of mountain belt erosion. In *M. Summerfield (eds), Geomorphology and Global Tectonics*, pages 77–105, New York. John Wiley and Sons.

Hovius, N. and Stark, C. (2006). Landslide-driven erosion and topographic evolution of active mountain belts. In *S.G. Evans et al. (eds) – Landslides from massive rock slope failure*, pages 573–590. Springer Verlag.

Hudson, J. and Priest, S. (1983). *Discontinuity frequency in rock masses*, volume 20. Int. J. Rock Mech. Min. Sci. Geomech. Abstr. p. 73–89.

Hungr, O. (2011). Characterizing debris flows for design of hazard mitigation. In *R. Genevois and D.L. Hamilton and A. Prestininzi (eds), Proceedings of the 5th International Conference on Debris Flow Hazards Mitigation/Mechanics, Prediction, and Assessment, Padova, Italy*. Italian Journal of Engineering Geology and Environment. Book of abstracts – Keynote lecture p. 5.

Hungr, O., Evans, S., Bovis, M., and Hutchinson, J. (2001). A Review of the Classification of Landslides of the Flow Type. *Environmental and Engineering Geoscience*, VII(3):221–238.

Hungr, O., Evans, S., and Hazzard, J. (1999). Magnitude and frequency of rockfalls along the main transportation corridors of southwestern British Columbia. *Canadian Geotechnical Journal*, 36:224–238.

Hungr, O., McDougall, S., and Bovis, M. (2005). *Entrainment of material by debris flows. Chapter 7.* Debris Flow Hazards and Related Phenomena, M. Jakob and O. Hungr (eds), Springer Verlag, Heidelberg, Germany. IJn association with Praxis Publishing Ltd.

Hungr, O., Morgan, G., and Kellerhals, R. (1984). Quantitative analysis of debris torrent hazards for design of remedial measure. *Canadian Geotechnical Journal*, 21:663–677.

Idealp Sàrl (2009). Conceptes de protection et cartes des dangers dus aux crues pour le Val d'Anniviers. Rapport technique, IDEALP Sàrl and BISA SA and BINA SA. 3 Carnets.

InnovMetric Software Inc. (2009). *PolyWorks – 3D scanner and 3D digitizer software*. InnovMetric Inc., 2014 Rue Cyrille – Duquet, Quebec City, QC G1N 4N6, Canada.

InterregII (2001). Falaises: Prévention des mouvements de versants et des instabilités de falaises – confrontation des méthodes d'étude des éboulements rocheux dans l'arc alpin. Programme INTERREG II C, Presso la Tipografia Valdostana – Aosta.

ISMR (1978). *International society for rock mechanics commission on standardization of laboratory and field test*, volume 15. Pergamon Press Ltd, Int. J. Rock Mech. Min. Sci. Geomech. Abstr. p. 319–168.

Iverson, R. (1997). The Pysics of Debris Flows. *Reviews of Geophysics*, 35(3):245–296.

Jaboyedoff, M. (2002). Matterocking 2.0: A program for detecting rockslide instabilities. User Guide, CREALP – Centre de recherche sur l'environnement alpin, Valais, Switzerland. www.crealp.ch.

Jaboyedoff, M., Baillifard, F., Couture, R., Locat, J., and Locat, P. (2004). New insight of geomorphology and landslide prone area detection using DEM. In *W.A. Lacerda and M. Ehrlich and A.B. Fontoura and A. Sayao (eds), Landslides Evaluation and Stabilization*, pages 199–205, Rotterdam. Balkema.

Jaboyedoff, M., Couture, R., and Locat, P. (2009a). Structural analysis of Turtle Mountain (Alberta) using digital elevation model: Toward a progressive failure. *Geomorphology*, 103:5–16. doi: 10.106/j.geomorph.2008.14.012.

Jaboyedoff, M. and Derron, M.-H. (2005). A new method to estimate the infilling of alluvial sediment of glacial valleys using a sloping local base level. *Geog. Fis. Dinam. Quat.*, 28:37–46.

Jaboyedoff, M., Giorgis, D., and Riedo, M. (2006). Apports des modèles numériques d'altitude pour la géologie et l'étude des mouvements de versant. *Bull. Soc. vaud. Sc. nat.*, 90(1):1–21.

Jaboyedoff, M., Metzger, R., Oppikofer, T., Baillifard, F., Couture, R., Locat, J., Derron, M., and Turmel, D. (27–31 May 2007). New insight techniques to analyze rock-slope relief using DEM and 3D-imaging cloud points: COLTOP–3D software. In *E. Eberhardt and D. Stead and T. Morrison (eds), Rock Mechanics: Meeting Society's Challenges and Demands: Proceedings of the 1st Canada–U.S. Rock Mechanics Symposium, Vancouver, Canada*, pages 61–68. Taylor and Francis, London. Vol. 1.

Jaboyedoff, M., Oppikofer, T., Abellán, A., Derron, M., Loye, A., Metzger, R., and Pedrazzini, A. (2012). Use of LiDAR in landslide investigations: a review. *Natural Hazards*, 61(5):5–28.

Jaboyedoff, M., Oppikofer, T., Locat, A., Turmel, J., Robitaille, D., Demers, D., and Locat, P. (2009b). Use of ground-based LIDAR for the analysis of retrogressive landslides in sensitive clay and of rotational landslides in river banks. *Canadian Geotechnical Journal*, 46:1379–1390. doi: 10.1139/T09-073.

Jaboyedoff, M., Philippossian, F., Mamin, M., Marro, C., and Rouiller, J. (1996). Distribution spatiale des discontinuités dans une falaise: approche statistique et probabilistique. Rapp. Trav. PNR 31, Hochschulverlag AG an der ETH Zürich, Switzerland.

Jakob, M., Bovis, M., and Oden, M. (2005). The significance of channel recharge rates for estimating debris-flow magnitude and frequency. *Earth Surface Processes and Landforms*, 30:755–766.

Jäckli, H. (1957). *Gegenwartsgeologie des bündnerischen Rheingebietes. Ein Beitrag zur exogenen Dynamik alpiner Gebirgslandschaften (Exogene dynamics of an Alpine landscape).* Beiträge zur Geologie der Schweiz, Geotechnische Serie 36. 136 p. and 5 maps.

Johnson, A. M. and Rodine, J. R. (1984). Debris flow. In *Slope Instability, D. Brundsden and D. B. Prior (eds)*, page 257–361. John Wiley & Sons, Chichester.

Johnson, P., McCuen, R., and Hromadka, T. (1990). Magnitude and frequency of debris flows. *Journal of Hydrology*, 123:69–82.

Johnson, R. and Warburton, J. (2006). Variability in sediment supply, transfer and deposition in an upland torrent system: Iron Crag, northern England. *Earth Surface Processes and Landforms*, 31:844–861.

Johnson, R., Warburton, J., Mills, A., and Winter, C. (2010). Evaluating the significance of event and post–event sediment dynamics in a first order tributary using multiple sediment budgets. *Geogr. Ann.*, 92 A(2):189–209.

Kemeny, J. and Turner, K. (2008). Ground-based LIDAR. Rock slope Mapping and Assessment. Technical report of the Central Federal Lands Highway Division US Department of Transportation FHWA-CFL/TD-08-006. www.ieag.info.

Konz, M., Chiari, M., Rimkus, S., Turowski, J., Molnar, P., Rickenmann, D., and Burlando, P. (2011). Quantitative analysis of debris torrent hazards for design of remedial measure. *Hydrology and Earth System Sciences*, 21:663–677.

Korup, O., Schmidt, J., and McSaveney, M. (2005). Regional relief characteristics and denudation pattern of the western southern alps, new zealand. *Geomorphology*, 71:402–423.

Kronfellner-Kraus, G. (1984). Extreme Feststofffrachten und Grabenbildungen vonWildbächer. In *International Symposium Interpraevent*, pages 109–118, VHB, Villach, Austria.

Krummenacher, D. (1959). Le cristallin de la région de Fully (Valais). *Schweizerische Mineralogische und Petrographische Mitteilungen*, 39:51–266.

Lane, S., James, T., and Crowell, M. (2000). Application of digital photogrammetry to complex topography for geomorphological research. *Photogrammetric Record*, 95(16):793–821.

Lane, S., Westaway, R., Murray, M., and Hicks, D. (2003). Estimation of erosion and deposition volumes in a large, gravel-bed, braided river using synoptic remote sensing. *Earth Surface Processes and Landforms*, 28:249–271.

Lato, M., Diederichs, M., Hutchinson, D., and Harrap, R. (2008). Optimization of LiDAR scanning and processing for automated structural evaluation of discontinuities in rock masses. *Int. J. Rock Mech. Min. Sci.*, 46:194–199. doi: 10.1016/j.jrmms.2008.04.007.

Lee, F. (1989). Slope movements in the Cheshire Quartzite, south western Vermont. In *A.P. Schultz and R.W. Jibson (eds), landslide processes of the Eastern United States and Puerto Rico*, pages 89–102. Special Paper – Geological Society of America.

Lehmann, C. (1993). Zur Abschätzung der Feststofffracht in Wildbächen. *Geographica Bernensia, Bern.*

Lenzi, M., Mao, L., and Comiti, F. (2003). Interannual variation of suspended sediment load and sediment yield in an alpine catchment. *Hydrological Sciences – Journal des sciences hydrologiques*, 48(6).

Lin, C., Shieh, C., Yuan, B., Shieh, Y., Liu, S., and Lee, S. (2003). Impact of Chi-Chi earthquake on the occurrence of landslides and debris flows: example from the Chenyulan river watershed, nantou, taiwan. *Engineering Geology*, 71:49–61. doi:10.1016/S0013-7952(03)00125-X.

Locat, J., Leroueil, S., and Picarelli, L. (2000). Some considerations on the role of geological history on slope stability and estimation of minimum apparent cohesion of rock mass. In *E. Bromhead and N. Dixon and M.L. Ibsen (eds) – Landslides in research, theory and practice*, pages 935–942. 8th International Symposium on Landslides in Cardiff in 2000.

Loye, A. (2006). Gornergletscher – Evolution of the drainage system during a jökulhlaup as revealed by dye tracer experiments. Diploma Thesis, unpublished, Versuchsanstalt für Wasserbau, Hydrologie und Glaziologie der ETH Zürich. ETH – Zurich.

Loye, A., Jaboyedoff, M., and Pedrazzini, A. (2009a). Identification of potential rockfall source areas at a regional scale using a DEM-based geomorphometric analysis. *Natural Hazards and Earth System Sciences*, 9:1643–1653.

Loye, A., Jaboyedoff, M., Pedrazzini, A., Theule, J., Liébault, F., and Metzger, R. (2011). Morphostructural analysis of an alpine debris flow catchment: implication for debris supply. In *R. Genevois and D.L. Hamilton and A. Prestininzi (eds), Proceedings of the 5th International Conference on Debris Flow Hazards Mitigation/Mechanics, Prediction, and Assessment, Padova, Italy*, pages 115–126. Italian Journal of Engineering Geology and Environment. doi:10.4408/IJEGE.2011-03.B-014.

Loye, A., Minoia, R., and Jaboyedoff, M. (2009b). Estimation des quantités de matériaux érodés dans le bassin versant de Zinal, basés sur l'étude de l'alluvionnement des ouvrages hydroélectriques valaisans. Rapport technique, Institut de Géomatique et Analyse du risque, Université de Lausanne. Document inédit.

Loye, A., Pedrazzini, A., Theule, J., Jaboyedoff, M., Liébault, F., and Metzger, R. (2012). Influence of bedrock structures on the spatial pattern of erosional landforms in small alpine catchments. *Earth Surface Processes and Landforms*, 37(13):1407–1423.

Loye, A., Theule, J., Jaboyedoff, M., and Liébault, F. (submitted). Debris supply and torrent response inducing debris flows: the case of the manival catchment. *Journal of Geophysical Research.*

Luckmann, B. (1977). The geomorphic activity of snow avalanches. *Geografiska Annaler*, 59(A):31–48.

Major, J. (2000). Gravity-driven consolidation of granular slurries – implications for debris-flow deposition and deposit characteristics. *Journal of Sedimentary Research*, 70(1):64–83. doi:1073-130X/00/070-64/$03.00.

Major, J. and Iverson, R. (1999). Debris-flow deposition – effects of pore-fluid pressure and friction concentrated at flow margins. *Geological Society of American Bulletin*, 111:1424–1434.

Mao, L., Cavalli, M., Comiti, F., Marchi, L., Lenzi, M., and Aratto, M. (2009). Sediment transfer processes in two Alpine catchments of contrasting morphological settings. *Journal of Hydrology*, 364:88–98.

Marchi, L., DallaFontana, G., Cavalli, M., and Tagliavini, F. (2008). Rocky Headwater in the Dolomites, Italy: Field Observations and Topographic Analysis. *Arctic and Alpine Research*, 40(4):685–694.

Markgren, M. (1964). Geomorphological studies in Fennoscandia, Chute slopes in northern Fennoscandia, B, Systematic studies. *Lund Studies In Geography, Series A, Physical Geography 28*, 2:51 p.

Markland, J. (1972). A useful technique for estimating the stability of rock slope when the rigid wedge sliding type of failure is expected. Rock Mech. Res. Rep. 19, Imp. Coll., London.

Marthaler, M. and Sartori, M. (2005). Carte géologique feuille 1307 – Vissoie. Atlas de la Suisse, Service hydrologique et géologique national, Berne.

Mathys, N., Brochot, S., Meunier, M., and Richard, D. (2003). Erosion quantification in the small marly experimental catchment of draix (Alpes de Haute Provence, France): Calibration of the ETC rainfall-runoff-erosion model. *Catena*, 50:527–554.

Matsuoka, N. and Sakai, H. (1999). Rockfall activity from an alpine cliff during thawing period. *Geomorphology*, 28:309–328.

May, C. and Gresswell, R. (2003). Processes and rates of sediment and wood accumulation in headwater streams of the Oregon Coast Range, U.S.A. *Earth Surface Processes and Landforms*, 28(4):409–424.

May, C. and Gresswell, R. (2004). Spatial and temporal patterns of debris flow deposition in the Oregon Coast Range, U.S.A. *Geomorphology*, 57:135–149.

Mazotti, B., Loye, A., and Jaboyedoff, M. (2010). Création d'un modèle d'estimation du bilan sédimentaire de torrents en milieu alpin. Carnet méthodologique, IGAR – Université de Lausanne. (inédit).

Mazzocola, D. and Hudson, J. (1996). A comprehensive method of rock mass characterization for indicating natural slope instability. *Q. J. Eng Geol. Hydroge.*, 1(29):37–56.

Melton, M. (1965). Magnitude and frequency of debris flows. *Journal of Geology*, 73:1–38.

Merritt, W., Letcher, R., and Jakeman, A. (2003). A review of erosion and sediment transport models. *Environmental modeling and Software*, 18:761–799.

Montandon, F. (1940). La coulée d'éboulis de Saxé. *Globe*, 79.

Montgomery, D. (2001). Slope distributions, threshold hillslopes, and steady state topography. *American Journal of Science*, 301:432–454.

Norrish, N. and Wyllie, D. (1996). Rock slope stability analysis. Transportation Research Board. Special Report, Serial 247, Published in Washington D.C. 509–513.

O'Callaghan, J. and Mark, D. (1984). The Extraction of Drainage Networks From Digital Elevation Data, Computer Vision. *Graphics and Image Processing*, 28:328–344.

Olyphant, G. (1981). Interaction among controls of cirque development: Sangre de Cristo Mountains, Colorado, USA. *Journal of Glaciology*, 27:449–58.

Olyphant, G. (1983). Analysis of the factors controlling cliff burial by talus within Blanca Massif, Southern Colorado, USA. *Arctic and Alpine Research*, 15(1):65–75.

Oppikofer, T. (2009). *Detection, analysis and monitoring of slope movements by high-resolution digital elevetion models*. PhD thesis, University of Lausanne.

Oppikofer, T., Jaboyedoff, M., and Keuzen, H. (2008). Collapse of the eastern Eiger flank in the Swiss Alps. *Nature Geoscience*, 1:531–535. doi: 10.1038/ngeo258.

Optech, I. (2008). *ILRIS 3D, Intelligent Laser Ranging and Imaging System*. Advanced Visual Systems Inc., 300 Interchange Way, Vaughan, ON L4K 5Z8, Canada, summary specification sheet – ILRIS enhanced range mode edition.

Pedrazzini, A., Froese, C., Jaboyedoff, M., Hungr, O., and Humair, F. (2011). Combining digital elevation model analysis and run-out modelling to characterize hazard posed by a potentially unstable rock slope at Turtle Mountain, Alberta, Canada. *Engineering Geology*, 128:76–94. doi: 10.1016/16j.enggeo.2011.03.015.

Peiry, J. (1990). Les torrents de l'Arve: dynamique des sédiments et impact de l'aménagement des bassins versants sur l'activité torrentielle. *Rev. Géog. Alpine*, 78:25–58.

Pelfini, M. and Santilli, M. (2008). Frequency of debris flows and their relation with precipitation: A case study in the Central Alps, Italy. *Geomorphology*, 101:721–730. doi:10.1016/j.geomorph.2008.04.002.

Perroy, R., Bookhagen, B., Asner, G., and Chadwick, O. (2010). Comparison of gully erosion estimates using airborne and ground-based LliDAR on Santa Cruz Island, California. *Geomorphology*, 118:288–300.

Pippan, T. (1981). Studies on present-day geomorphological processes of high morphogenetic intensity in the High Calcareous Alps of Salzburg. *Zeitschrift für Geomorphologie Suppl. Bd.*, 37:73–90.

Price, N. and Cosgrove, M. (1990). *Analysis of Geological Structures*. Cambridge Press, UK. 516 p.

Priest, S. and Hudson, J. (1976). Discontinuity spacing in rock. *J. Rock. Mech. Min. Sci. Geomech.*, Abstracts 13:135–148.

Prokop, A. and Panholzer, H. (2009). Assessing the capability of terrestrial laser scanning for monitoring slow moving landslides. *Natural Hazards and Earth System Sciences*, 9:1921–1928.

Péteuil, C., Maraval, C., Bertrand, C., and Monier, G. (2008). Torrent du Manival: Schéma d'aménagement et de gestion du basin versant contre les crues. Rapport technique, 107 p., Office National des Forêts, Service de Restauration des terrains en Montagnes de l'Isère, Grenoble, France.

Ramsay, J. and Huber, M. (1987). *Techniques of Modern Structural Geology*, volume 2, Folds and Fractures. Academic Press, London, UK. 700 p.

Rapp, A. (1960). Talus slopes and Mountain Walls at Tempelfjorden, Spitzbergen. Special Report, Serial. 119, Nor. Polarins. Skr. 96 p.

Reneau, S., Dietrich, W., Donohue, D., Jull, A., and Rubin, M. (1990). Late quaternary history of colluvial deposition and erosion in hollows, central California Coast Ranges. *Geological Society of America Bulletin*, 102:969–982.

Rickenmann, D. (1990). Bedload transport capacity of slurry flows at steep slope. Mitteilung 169, Versuchsanstalt für Wasserbau, Hydrologie und Glaziologie der ETH Zürich. 249 p.

Rickenmann, D. (1995). Beurteilung von Murgängen. *Schweizer Ingenieur und Architekt*, 48:1004–1008.

Rickenmann, D. (1999). Empirical relationship for Debris Flows. *Natural Hazards*, 19:47–77.

Rickenmann, D. (2005). Runout prediction models. In *Jakob M. and Hungr O. (eds), Debris flow hazard and related phenomena*, pages 305–324. Praxis, Springer, Berlin.

RisquesTV (2012). Manival, le mauvais torrent – Episode I. Movie, Institut des Risques Majeurs (IRMa), Grenoble, France. www.risques.tv/video.php?id_DTvideo=225.

Roehl, J. (1962). Sediment source area, delivery ratios and influencing morphological factors. In *Symposium of Bari (Commission of Land Erosion), 1–8 October, 1962*, pages 202–213, Wallingford, UK. IAHS Publ. 59, IAHS Press.

Roering, J., Stimely, L., Mackey, G., and Schmidt, D. (2009). Using DInSAR, airborne LIDAR and archival air photos to quantify landsliding and sediment transport. *Geophysical Research Letters*, 36:L19402, 5 p., doi: 10.1029/2009GL040374.

Roering, J., TaylorPerron, J., and Kirchner, J. (2007). Functional relationships between denudation and hillslope form and relief. *Earth and Planetary Science Letters*, 264:245–258.

Rohrbaugh, M., Dunne, W., and Mauldon, M. (2002). Estimating fracture trace intensity, density, and mean length using circular scan lines and windows. *American Association of Petroleum Geologists Bulletin*, 86(12):2089–2104.

Romana, M. (1985). New adjustement ratings for application of Bienawski classification to slopes. In *Int. Symp. on the role or rock mechanics ISRM*, pages 49–53, Zacatecas.

Romana, M. (1993). *A Geomechanical Classification for Slopes: Slope Mass Rating*, volume 3. J.A. Hudson (eds), Imperial College of Science, Technology and Medecin, London, UK. Pergamon Press Ltd, 45 p.

Rosser, N., Lim, N., Petley, D., Dunning, S., and Allison, R. (2007). Patterns of precursory rockfall prior to slope failure. *Journal of Geophysical Research*, F04014(112).

Rouiller, J.-D., Jaboyedoff, M., Marro, C., and Philippossian, F. (1997). Matterock : méthodologie d'étude d'instabilités de falaise et d'appréciation du danger. Publications de la Soc. Suisse de Méc. Sols et Roches No. 135. 13–16.

Rouiller, J.-D., Jaboyedoff, M., Marro, C., Philippossian, F., and Mamin, F. (1998). Pentes instables dans le Pennique valaisan. matterock: une méthode d'auscultation des falaises et détection des éboulements majeurs potentiels. Rapport final du PNR31, VDF Hochschulverlag AG, ETH Zürich, Switzerland.

RTM (2010). Le torrent du Manival – 150 ans de lutte contre les risques naturels. Notification RTM 38, Office National des Forêts, RTM 38 Grenoble–Isère–France.

Sas, R. and Eaton, S. (2008). Quartzite terrains, geologic controls and basin denudation by debris flows: their role in long-term landscape evolution in the central Appalachians. *Landslides*, 5:97–106.

Sauchyn, D., Cruden, D., and Hu, X. (1998). Structural control of the morphometry of open rock basins, Kananaski region, Canadian Rocky Mountains. *Geomorphology*, 22:313–324.

Sauchyn, D. and Gardner, J. (1983). Morphometry of open rock basins, Kananaskis area, Canadian Rocky Mountians. *Canadian Journal of Earth Sciences*, 20:409–419.

Scheidegger, E. (1980). Alpine joints and valleys in the Neotectonic stress-field. *Rock Mech. Suppl.*, 9:109–124.

Scheidegger, E. (1983). Instability principle in geomorphic equilibrium. *Zeitschrift für Geomorphologie, N.F.*, 27:1–19.

Scheidl, C., Rickenmann, D., and Chiari, M. (2008). The use of airborne lidar data for the analysis of debris flow events in Switzerland. *Natural Hazards and Earth System Sciences*, 8:1113–1127.

Schlunegger, F., Badoux, A., McArdell, B., Gwerder, C., Schnydrig, D., Rieke-Zapp, D., and Molnar, P. (2009). Limits of sediment transfer in an alpine debris-flow catchment, Illgraben, Switzerland. *Quaternary Science reviews*, 28:1097–1105.

Schrott, L., Hufschmidt, G., Hankammer, G., Hoffmann, T., and Dikau, R. (2003). Spatial distibution of sediment storage types and quantification of valley fill deposits in an alpine basin, Reintal, Bavarian Alps, Germany. *Geomorphology*, 55:45–63.

Selby, M. (1982). Controls on the stability and inclinations of hillslopes formed on hard rock. *Earth Surface Processes and Landforms*, 7(5):449–467.

Selby, M. (1987). *Rock slopes*. M.G. Anderson and K.S. Richards (eds) Slope stability: geotechnical engineering and geomorphology, Chichester: Wiley. 475–504.

Selby, M. (1993). *Hillslope Material and Processes*. Oxford University Press, Oxford. 451 p.

Shaw, P. (2003). *Multivariate statistics for the Environmental Sciences, Hodder-Arnold*. ISBN 0-3408-0763-6.

Shroder, J. and Bishop, M. (1998). Mass movement in the Himalaya: new insights and research directions. *Geomorphology*, 26:13–35.

Smith, L., Alsdorf, D., Magilligan, F., Gomez, B., Mertes, L., Smith, N., and Garvin, J. (2000). Estimation of erosion, deposition and net volumetric change caused by the 1996 Skeidararsandur Jökulhlaup, Iceland, from SAR interferometry. *Water Resources Research*, 36(6):1583–94.

Squarzoni, C., Delacourt, C., and Allemand, P. (2003). Nine years of spatial and temporal evolution of the La Valette landslide observed by SAR interferometry. *Engineering Geology*, 68:53–66.

Stark, C. and Hovius, N. (2001). The characterisation of landslides size distributions. *Geophysical Research Letters*, 6(26):1091–1994.

Stock, J. and Dietrich, W. (2006). Erosion of steepland valleys by debris flows. *Geological Society of America Bulletin*, 118(9-10):1125–1148.

Strahler, A. (1950). Equilibrium theory of erosional slopes approached by frequency distribution analysis. *American Journal of Science*, 248:673–696 and 800–814.

Strahler, A. (1952). Dynamic basis of geomorphology. *Geological Society of America Bulletin*, 63:923–938.

Strahler, A. (1954). Statistical analysis in geomorphic research. *Journal of Geology*, 62:1–25.

Sturzenegger, M., Sartori, M., Jaboyedoff, M., and Stead, D. (2007a). Regional deterministic characterization of fracture networks and its application to GIS-based rock fall risk assessment. *Engineering Geology*, 94:201–214.

Sturzenegger, M. and Stead, D. (2009). Quantifying discontinuity orientation and persistence on high mountain rock slopes and large landslides using terrestrial remote sensing techniques. *Natural Hazards and Earth System Sciences*, 9:267–287. doi: 10.5194/nhess–9–267–2009.

Sturzenegger, M., Stead, D., and Elmo, D. (2011). Terrestrial remote sensing-based estimation of mean trace length, trace intensity and block size/shape. *Engineering Geology*, 119(3–4):96–111.

Sturzenegger, M., Yan, M., Stead, D., and Elmo, D. (2007b). Application and limitation of ground-based laser scanning in rock slope characterization. In *E. Eberhardt and D. Stead and T. Morrison (eds) Rock Mechanics: Meeting Society's Challenges and Demands: Proceedings of the 1st Canada–U.S. Rock Mechanics Symposium, Vancouver, Canada*, pages 29–36, London. Taylor and Francis.

Takahashi, T. (1991). Estimation of potential debris flows and their hazardous zones: soft countermeasures for a disaster. *Journal of Natural Disaster Science*, 3:57–89.

Taylor, J. (1997). *An Introduction to Error Analysis*. University Science Books, Sausalito, California. 327 p., 2^{nd} Ed.

Terzaghi, K. (1962). Stability of slopes on hard unweathered rock. *Geotechnique*, 12:251–263.

Theule, J. (2012). Geomorphic study of sediment dynamics in active debris-flow catchments (French Alps). PhD Thesis, IRSTEA – Grenoble (France).

Theule, J., Liébault, F., Loye, A., Laigle, D., and Jaboyedoff, M. (2012). Sediment budgets of the Manival debris-flow torrent. *Natural Hazards and Earth System Sciences*, 12:731–749.

Trauth, M. (2007). *Matlab© Recipes for Earth Sciences*. Springer – Verlag, Berlin Heidelberg. 2^{nd} Ed.

Trevisani, T., Cavalli, M., and Marchi, L. (2012). Surface texture analysis of high-resolution DTM: Interpreting an alpine basin. *Geomorphology*, 161–162:26–39.

VanDine, D. (1985). Debris flow and debris torrents in the Southern Canadian Cordillera. *Canadian Geotechnical Journal*, 22:44–68.

VanRompaey, A., Verstraeten, G., VanOost, C., Govers, G., and Poesen, J. (2001). Modelling mean annual sediment yield using a distributed approach. *Earth Surface Processes and Landforms*, 26:1221–1236.

VanSteijn, H. (1996). Debris flow magnitude – frequency relationships for mountainous regions of Central and Northwest Europe. *Geomorphology*, 15:259–273.

Varnes, D. (1978). Slope movement and types of processes. In *Landslides, Analysis and Control, R.J. Schuster and R.J. Krized (eds)*, pages 176: 11–33. (Special Report 176: 11- 33), Washington, Transportation Research Board, National Academy of Sciences.

Veyrat-Charvillon, S. (2005). *Elaboration d'une méthode de prédiction du volume maximal d'une lave torrentielle (PREVENT)*. PhD thesis, Université Blaise Pascal Clermont–Ferrant 2. 354 p.

Veyrat-Charvillon, S. and Memier, M. (2006). Stereophotogrammetry of archive data and topographic approaches to debris-flow torrent measurements: Calculation of channel-sediment states and a partial sediment budget for Manival torrent (Isère, France). *Earth Surface Processes and Landforms*, 31(2):201–219.

Veyrat-Charvillon, S. and Mémier, M. (2006). The use of archive data by stereophotogrammetry with a topographic methodology of debris-flow torrent measurements: calculation of channel sediment states and partial sediment budget on manival torrent (isère, france. *Earth Surface Processes and Landforms*, 31(2):201–219.

Volk, H. (2000). The tatopani Landslide in the Kali Gandaki Valley of western Nepal: cause and relation to mass rock creep. *J. Nepal Geol. Soc.*, 22:405–412.

vonRaumer, J. (1974). Zur Metamorphose amphibolitischer Gesteine im Altkristallin des Mont Blanc und Aiguilles-Rouges Massives. *Schweiz. Mineral. Petrogr. Mitt.*, 54:471–488.

vonRaumer, J., Bussy, F., and Stämpfli, G. (2009). The Variscan evolution in the External Massifs of the Alps and place in their Variscan framework. Comptes Rendus Geosciences 341(2-3): 239-252.

Wagner, A., Olivier, R., and Leite, E. (1998). Rock and debris slide risk maps applied to low-volume road in Nepal. TRB, National Research Council, Washington, DC 255-267, Transportation Research Record 1106.

Weissel, J. and Seidl, M. (1987). Inland propagation of erosional escarpments and river profile evolution across the southeast Australian passive continental margin. In *K.J. Tinkler and E.E. Wohl (eds), Rivers over rock: fluvial processes in bedrock channels*, pages 189–206. Am. Geophys. Union Monogr. 107.

Whipple, K. (2004). Bedrock rivers and the geomorphology of active orogens. *Annual Review of Earth and Planetary Sciences*, 32:151–85.

Whipple, K., Hancock, G., and Anderson, R. (2000). River incision into bedrock: Mechanics and relative efficacy of plucking, abrasion and cavitation. *Geological Society of America Bulletin*, 112:490–503.

Wichmann, V. and Becht, M. (2005). Modelling of geomorphic processes in an alpine catchment. In *P.M Atkinson and G. M. Foody and S. E. Darby and F. Wu (eds), GeoDynamics*, pages 151–167, CRC Press, Boca Raton.

Wicks, J. and Bathurst, J. (1996). Shesed: a physically-based, distributed erosion and sediment yield component for the SHE hydrological modeling system. *Journal of Hydrology*, 123(1-4):213–238.

Willet, S. (2004). Orogeny and orography: The effects of erosion on the structure of mountain belts. *Journal of Geophysical Research*, 104(B12):28’957–28’981.

Wolinsky, M. and Pratson, L. (2005). Constraints on landscape evolution from slope histograms. *Geology*, 33:477–480.

Wolman, M. and Gerson, R. (1978). Relative scales of time and effectiveness of climate in watershed geomorphology. *Earth Surface Processes*, 3:189–208.

Wu, Y. and Cheng, H. (2005). Monitoring of gully erosion on the Loess Plateau of China using a global positioning system. *Catena*, 63:154–166.

Wyllie, D. and Mah, C. (2004). *Rock Slope Engineering: Civil and Mining*. Spon Press, London. 4^{th} Ed.

Zimmermann, M., Mani, P., Gamma, P., Gsteiger, P., Heiniger, O., and Hunziker, G. (1997a). Murganggefahr und Klimaänderung – ein GIS-basierter Ansatz. Schlussbericht NFP Vol. 31.

Zimmermann, M., Mani, P., and Romang, H. (1997b). Magnitude – frequency aspects of alpine debris flows. *Eclogae Geologicae Helvetiae*, 90:415–420.

Acknowledgments

I would like to thank my "boss", Prof. Michel Jaboyedoff, for giving me the opportunity to make a PhD in his Institute of Geomatics and Risk Analysis (IGAR), for providing input to my work, for supporting the field work I performed, for sending me to summer schools, to numerous conferences, to the UN project in Pakistan and for the working skills collected through the various expertises and assignments that he gave me to do. This has been a rich experience that will accompagny me on my next occupations.

I wish to thank also the people at IGAR and CEMAGREF of Grenoble that have contributed directly or indirectly to the successful completion of these works. My gratitute goes particularly to Josh for his help during field work, for his compagny during the never-ending TLS surveys, for all the fun we had in the field and downtown Grenoble and for providing me his cosy accomodation. It has been a great pleasure to get to know him better all along the Manival project. I am also grateful to Marc-Henri Derron for the interesting conversations we had, for reading through my papers and this manuscript, for being on my PhD committee and for having me working over at the Geological Survey of Norway (NGU) for couple of months. I discovered Norway and experienced what does it mean to live far north at the edge of the continent during Spring and in Summer. A special gratitude goes to my good mates at the office, Andrea, Pascal, Thierry, Richard, Julien, Romain, Lorenzo, Ivan, Lucien, Benoît M. and Benoît F. , Battista, Florian and Marie. Working with them was not only a lot of fun, but also stimulating, productive, conforting and hanging out with them was distracting, relaxing, screaming. Lots of unforgettable memories come to my mind. Andrea in particular has been of great scientific influence on me: his geological knowledge was a invaluable help and the numerous interesting discussions we had contributed greatly to improve my PhD thesis. Our good collaboration was inspiring; without that all the things we did for our PhD and for the institute would have never gone as easily as they did. I thank all my workmates of the Risk Team for the good atmosphere and assistance they provided at work, at coffee breaks and during the outstanding aperitifs. I thank also the fellows of the Geomatic Team; their advises on statistics and computer programming were appreciated.

Several people that I got to know along this PhD have had a strong influence on me. A special thought to Luuk, Olga, Benni, Emma, Oliver, Christophe. Coming across them was of great fortune that provided the other good feeling about these years of hard labor.

A heartfelt thanks to Stéphanie for all the love she gives me on everyday life, for her understanding and patience she had, for staying close during all this life experience and for making my mornings so bright.

A special gratitude to my brother and sister, to make family life such great time, to grandma who still wunders what do I do so far from home and to grandpa that passed away on the fourth year of my stay at the University of Lausanne. I would have wished to share with him the joy and resulting satisfaction of completing this step of life.

And to my parent, whose encouraged me to continue my studies in geology, for their resolute support during the rough time, for their affection and their love.

Appendix A

The MatErosion project

Technical report – *Sediment budgets estimation and sediment flux modeling at short, middle and long time scale in torrent systems.*

The case of the Lirec and Perrec catchment (Zinal, Valais, Switzerland)

UNIL | Université de Lausanne
Faculté de Geosciences et Environnement
Institut de Géomatique et Analyse de Risque
Amphipôle
CH-1015 Lausanne

Projet MatErosion

Méthodologie d'estimation de bilans sédimentaires prévisionnels en milieu alpin.

Synthèse du Projet

Faculté de Géosciences et Environnement
Institut de Géomatique et Analyse du Risque
Alexande Loye, Dipl. EPFZ en Sciences de la Terre
Mazotti Benoît, MSc en Géosciences et Environnement
Dr. Michel Jaboyedoff, Professeur

Rapport: IGAR - AL – R004

Faculté des géosciences et de l'environnement
Institut de géomatique et d'analyse du risque

Tél.+41 21 692 35 47 | Fax.+41 21 692 35 35 |Alexandre.loye@unil.ch

TABLE DES MATIERES

1 PRÉAMBULE 5

2 TRAVAUX ET OUVRAGES DE RÉFÉRENCES 7

3 LE SYSTÈME ÉROSIF « LAVES TORRENTIELLES » 8

3.1 INTRODUCTION.. 8
3.2 FONCTIONNEMENT DU SYSTEME EROSIF TORRENTIEL.................... 9

4 MÉTHODE (SYNTHÈSE DE MAZOTTI ET AL., 2010).....10

4.1 ANALYSE GENERALE ET CARTOGRAPHIE DE LA DISPONIBILITE DES MATERIAUX D'EROSION 10
4.2 CARACTÉRISATION DE LA DYNAMIQUE GÉNÉRALE DU TORRENT.................... 10
4.3 ESTIMATION DES STOCKS SÉDIMENTAIRES ET APPORTS DE MATÉRIAUX POTENTIELS DANS LE SYSTÈME TORRENTIEL.................... 12
4.4 FLUX ET VITESSE DE TRANSFERT DES STOCKS SEDIMENTAIRES 13
4.5 FREQUENCE D'OCCURRENCE DES EVENEMENTS ET INTENSITES 16
4.6 PRINCIPE DE PROPAGATION DES FLUX DE MATERIAUX ET EVOLUTION DES STOCKS SEDIMENTAIRES 18
4.6.1 La cascade sédimentaire....................18
4.7 LE PROGRAMME MATEROSION 21

5 APPLICATION AUX BASSINS VERSANTS PILOTES.....26

5.1 LES TORRENTS DE PERREC ET LIREC.................... 26
5.2 CARTOGRAPHIE DES PHÉNOMÈNES 28
5.3 DIVISION DES TORRENTS EN BIEFS HOMOGÈNES......................... 39**ERREUR ! SIGNET NON DEFINI.**
5.4 ESTIMATION DE LA DYNAMIQUE GÉNÉRALE DES BIEFS PAR L'ANALYSE DES PROFILS EN LONG 39**ERREUR ! SIGNET NON DEFINI.**
5.5 ESTIMATION DES STOCKS DE MATÉRIAUX DIRECTS ET INDIRECTS 30
5.6 ESTIMATION DES TEMPS DE RETOUR DES EVENEMENTS 34
5.6.1 Temps de retour des précipitations 34
5.6.2 Temps de retour des laves torrentielles.................... 37
5.7 PARAMÈTRES DE SIMULATION DE LA CASCADE SÉDIMENTAIRE 38

6 BUDGET SÉDIMENTAIRE GLOBAL.............................41

7 RÉSULTATS DES BILANS SÉDIMENTAIRES SIMULÉS .46

7.1 OCCURRENCE DES EVENEMENTS DANS UNE SERIE TEMPORELLE 46
7.2 SIMULATION AVEC STOCKS FINIS 47
7.3 SIMULATION AVEC STOCKS INFINIS 51
7.4 SYNTHESE: PERREC.................... 55
7.5 SYNTHESE : LIREC.................... 56

8 RÉSULTATS LIÉS À UN CHANGEMENT CLIMATIQUE...57

8.1 OCCURRENCE DES EVENEMENTS ... 58
8.2 RESULTATS DES SIMULATIONS AVEC STOCKS FINIS ... 59
8.3 RESULTATS DES SIMULATIONS AVEC STOCKS INFINIS ... 61
8.4 SYNTHÈSE PERREC ... 63
8.5 SYNTHÈSE LIREC ... 64

9 SENSIBILITÉ DE LA CASCADE SÉDIMENTAIRE ... 65

9.1 VARIATION DES BILANS SÉDIMENTAIRES PAR RAPPORT AUX NOMBRES DE SIMULATIONS ... 65
9.2 SENSIBILITÉ PAR RAPPORT À L'INDICE D'ALLUVIONNEMENT ... 65
9.3 INCERTITUDES SUR LES STOCKS SÉDIMENTAIRES ET VITESSE D'ÉROSION ... 66

10 SYNTHÈSE ... 67

10.1 RESULTATS TORRENT DU PERREC ... 67
10.2 RESULTATS TORRENT DU LIREC ... 69
10.3 RESULTATS GLOBAUX ... 72

11 CONCLUSION ET SUGGESTIONS ... 73

12 BIBLIOGRAPHIE ... 75

Annexe I : Données topographiques et de volumes pour le torrent de Lirec ... 77

Annexe I : Données topographiques et de volumes pour le torrent de Perrec ... 78

Annexe II : Résumé du travail de terrain effectué ... 79

A. Identification et quantification de l'apport de matériaux solides dans le torrent ... 79

B. Estimation du volume de matériel déposé et déposable dans le torrent ... 81

C. Identification des stocks sédimentaires ... 82

D. Localisation de particularités des torrents ... 83

E. Localisation des ouvrages de protection ... 84

1 Préambule

Dans le cadre d'un projet de gestion des matériaux inertes transportés dans les torrents alpins valaisan à court, moyen et long terme, l'institut de Géomatique et Analyse du Risque (IGAR) de l'Université de Lausanne a été mandaté par M. le Géologue cantonal Jean-Daniel Rouiller afin de développer une approche quantitative d'estimation et de prédiction de bilans sédimentaires à l'échelle du bassin versant torrentiel. La méthode a pour but d'estimer les volumes d'apports sédimentaires attendus à l'exutoire de ces torrents ces prochaines décennies compte tenu de possibles variations de la dynamique sédimentaire liées aux éventuels changements climatiques et autres évènements exceptionnels (glissements de terrain, éboulements).

Une première étude (Loye et al. 2009) opérée en 2008, basée sur des mesures de l'alluvionnement observé dans 12 des plus grands aménagements hydroélectriques valaisans, avait permis d'estimer des ordres de grandeurs de transport de sédiments dans quelques bassins versants valaisans de haute altitude depuis la seconde moitié du XX$^{\text{ème}}$ siècle. Par la suite, l'étude s'est orientée vers le développement d'une méthodologie prévisionnelle d'estimation quantitative de bilans sédimentaires dans les torrents alpins. Cette approche est applicable de façon non-spécifique à un torrent particulier (Mazotti et al. 2010). Sur la base de cette méthodologie, une routine informatique de simulation de la dynamique sédimentaire (érosion, transport, dépôt) d'un système torrentiel a été développée selon le concept de la cascade sédimentaire. Dans sa phase de développement, cette modélisation de l'apport sédimentaire dans le dépotoir d'un torrent alpin a été testée sur deux torrents pilotes (le Lirec et le Perrec) situés en amont du village de Zinal dans le haut Val d'Anniviers (fig. 1.1). Le projet final, dénommé MatErosion, consistera à l'estimation sur le moyen et long terme du bilan sédimentaire de tous les torrents situés en rive droite de la haute vallée d'Anniviers.

Ce rapport présente les résultats finaux des bilans sédimentaires prévisionnels obtenus dans les deux torrents tests de Perrec et Lirec lors de la phase de développement du projet MatErosion. La première partie de ce document rappelle de façon synthétique les bases méthodologiques développées dans Mazotti et al. (2010), lequel rapport interne comporte une explication plus détaillée de l'estimation des stocks sédimentaires. Il peut être consulté sur demande à l'IGAR. La seconde partie illustre l'application de la cascade sédimentaire aux deux systèmes torrentiels pilotes. S'en suive les résultats préliminaires de l'estimation des bilans sédimentaire ainsi qu'une analyse détaillée des volumes simulés.

En outre, ce document comprend une estimation globale des taux d'érosion observés sur le long terme (chapitre 6), illustrant des ordres de grandeur du remplissage sédimentaire dans le haut Val d'Anniviers. Ces taux d'érosion sur le long terme peuvent être mis en perspective avec les volumes à moyen terme simulés obtenus à l'exutoire des torrents.

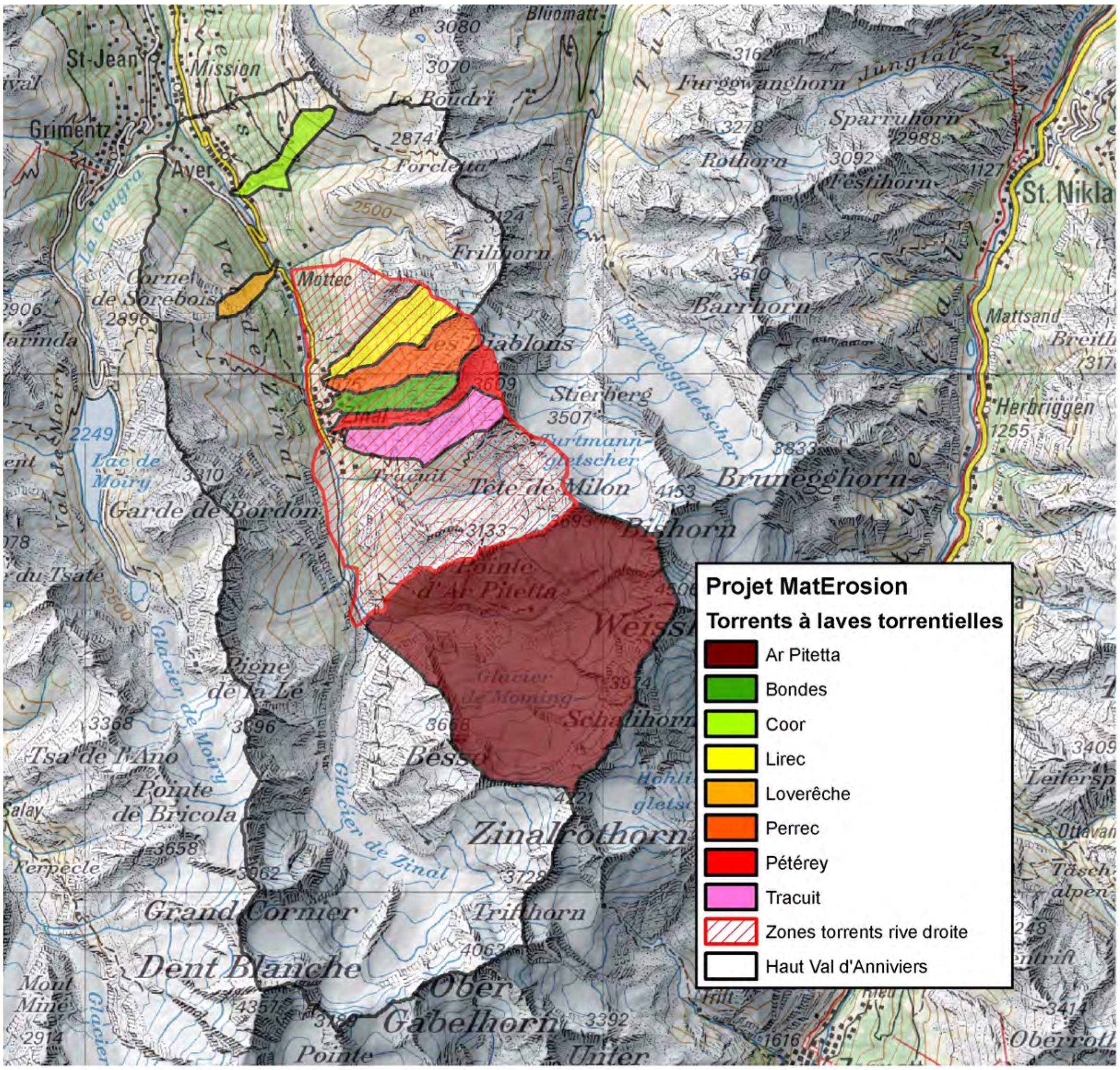

***Figure 1.1** : Localisation des torrents cibles avec leur bassin versant étudiés dans le projet MatErosion. La phase de développement s'est concentrée sur les torrents de Lirec et Perrec. La phase finale concerne tous les torrents à laves torrentielles de la région de Zinal, principalement ceux situés en rive droite, ainsi que le val d'Ar Pitteta.*

2 Travaux et ouvrages de références

Le tableau ci-dessous présente les principaux travaux (liste non exhaustive) permettant un aperçu de l'activité sédimentaire dans le haut Val d'Anniviers. Ils viennent s'ajouter aux ouvrages déjà mentionnés dans la bibliographie de Loye et al. 2009.

***Tableau 2.1** : récapitulatif des ouvrages existant sur la thématique concernant la région de Zinal.*

Rapports d'étude concernant les torrents de la région de Zinal

Nom du document	Description
Heim, G., 2005, Schüsselstellenanalysen im Gerinne, Untersuchung im Hinblick auf den Feststoffverlagerungsprozess in Wildbächen bei Murgangereignissen, Diplomarbeit, Universität Bern.	Analyse détaillée de l'activité torrentielle dans le torrent du Pétérey.
Ayer, 2002, Modification partielle du plan d'aménagement des zones pour l'ouverture de décharges de matériaux inertes, Service pour la protection de l'environnement, Etat du Valais.	Rapport technique sur l'entretien des dépotoirs et la gestion des matériaux inertes de la commune d'Ayer. Il contient une analyse précise de chaque torrent de la commune ainsi qu'un historique des événements.
Nivalp SA, 2009, Zone de dépôt de matériaux au Plat de la Lé, document inédit.	Projet visant l'implantation d'un dépôt de matériel inerte dans la région du Plat de la Lé.
CREALP, Torrent du Pétérey, analyse précise du torrent, document inédit non daté. **CREALP**, Evénement historiques du torrent du Pétérey, document inédit non daté.	Rapports d'étude du torrent du Pétérey comportant tout particulièrement une analyse des périodes de retour des laves torrentielles.
Favre-Bulle, G., Sartory, M. et Métraux, V., 2009, Glacier Bonnard, cartographie, interprétation et calcul des volumes, CREALP, document inédit.	Rapport d'étude sur le glacier (volumes, événements, localisation de la glace, mouvements, etc.).
IDEALP et UNI-Fribourg , 2007, Glacier rocheux Bonnard, mesures de déplacement en 2006 et 2007, document inédit.	Mesure des mouvements du glacier couvert Bonnard.
Service des forêts et du paysage, Commune d'Ayer, IDEALP, GEOSAT SA, UNI-Fribourg, Torrent du Pétérey et Tracuit, rapport technique.	Mesures des mouvements dans la zone du glacier couvert Bonnard, sources de laves torrentielles.
Stoffel, M. and Bollschweiler, M., 2009, Tree-ring reconstruction of past debris flows based on a small number of samples - possibilities and limitations, Landslides, 6: 225-230.	Analyse des événements passés du torrent du Pétérey à partir d'analyses dendrochronologiques sur le cône de déjection (dépotoir actuel)
IDEALP Sàrl, BISA SA, BINA SA, 2009, Concept de protection et cartes des dangers dus aux crues pour le Val d'Anniviers (Rapport général, rapport par torrents, annexes).	Rapports présentant les résultats de l'analyse du danger lié aux crues pour les torrents du Val d'Anniviers comportant des informations intéressantes sur les temps de retour et les volumes mobilisables.
Huss, M., Farinotti D., Bauder, A. and Funk, M. (2008). Modelling runoff from highly glacierized alpine drainage basins in a changing climate. Hydrological Processes, 22(19), 3888-3902.	Article qui s'intéresse au retrait glaciaire futur en fonction du changement climatique et traite des glaciers du fond du Val d'Anniviers.
Gertsch, E. 2009, Geschiebelieferung alpiner Wildbachsysteme bei Grossereignissen - Ereignisanalysen eines Abschätzverfahrens, Doctorthesis, Universität Bern.	Travail de fond très important sur un grand nombre de torrents en Suisse (y.c. torrent de Pétérey) et création d'un outil d'estimation des volumes charriés par les laves torrentielles.

3 Le système érosif « laves torrentielles »

3.1 Introduction

Le système sédimentaire des torrents alpins se compose de tous les processus érosifs susceptibles dans une échelle de temps propre de venir s'accumuler progressivement dans le chenal torrentiel et ensuite d'y être transportés en aval par l'activité du torrent. Sa dynamique sédimentaire est gouvernée par l'interaction entre :

- la disponibilité de sédiments (matériaux mobilisables).
- la capacité de transport par le torrent (entrainement).

L'apport de matériaux potentiellement mobilisables dans le système torrentiel se caractérise par un double apport de sédiments :

1. de l'extérieur du torrent, transporté par les processus érosifs du bassin versant dans la zone de départ ou tout au long du torrent. Ceci inclut l'érosion du sol, le démantèlement des affleurements rocheux par chutes de blocs, la dégradation des versants par glissements de terrain et coulées boueuses ainsi que les avalanches de fond.
2. de l'intérieur du torrent, érodé ou remobilisé directement depuis les berges et dans le lit.

Dès lors, la création de bilans sédimentaires des systèmes torrentiels érosifs implique une identification et quantification des apports de matériaux (stocks) qui affectent les zones susceptibles d'atteindre le lit du torrent, même seulement épisodiquement lors de crues par exemple. A cela s'ajoute une estimation de leur mode d'acheminement pouvant entrer en contact avec le torrent (vitesse de mobilisation) ainsi qu'une estimation de l'évolution dans le temps de ces stocks.

Si l'apport de matériaux en contact avec le torrent est une condition nécessaire, le régime torrentiel sous forme de précipitations ou d'apports d'eau de fonte est réellement le moteur du transport sédimentaire (flux de sédiments).

Ainsi, la quantité de matériaux atteignant l'exutoire du système torrentiel est définie par la fréquence des évènements ainsi que l'intensité du transport torrentiel. Selon la dynamique du bassin versant et du torrent le long de son cours, ces transferts de matériaux à l'extérieur comme dans le torrent lui-même ne sont pas continus, mais alternent entre les zones de dépôts et des zones de charriage. Le matériel mobilisé peut nécessiter plusieurs événements torrentiels avant d'atteindre l'exutoire. Il s'agit donc de connaître les vitesses auxquelles les volumes des différents processus sont transportés dans le système torrentiel.

Enfin, ces apports sédimentaires évoluent avec le temps et le climat. Il est donc nécessaire d'établir plusieurs scénarios qui prévoient les modifications du système sédimentaire dans le temps, tant au niveau des apports que du transfert de flux.

3.2 Fonctionnement du système érosif torrentiel

Un système érosif torrentiel peut être vu comme une cascade sédimentaire ou les éléments du système sont des réservoirs et les liens entre ces réservoirs sont les volumes de transferts de sédiments des différents processus érosifs à travers le bassin versant (fig. 3.1). Le torrent est divisé en une suite de bacs pouvant contenir un volume sédimentaire qui se remplissent et se vident successivement les uns dans les autres. Les éléments d'une cascade sédimentaire peuvent être regroupés sous trois catégories :

1. les stocks sédimentaires préexistants (actifs et dormants).
2. les apports potentiels de nouvelles masses sédimentaires.
3. la capacité du bassin versant (y.c. le torrent lui-même) à charger le torrent en matériel et la capacité du torrent à transporter ce matériel à l'exutoire du système (flux sédimentaire).

Les réservoirs regroupent des processus dynamiques qui évoluent dans le temps. Un stock peut rester invariant jusqu'à l'érosion de sa base (processus rapide), lequel peut provoquer un glissement (processus plus lent) pouvant s'ajouter au bilan. Une instabilité de versant a tendance à se dé/stabiliser, influençant la vitesse et les flux de sédiments. Dès lors, la vitesse de transfert est contrôlée par le phénomène le plus lent. Le flux de matériaux vidant ou remplissant simultanément un réservoir est établi en fonction des processus observés dans l'évolution du versant et de son système torrentiel (régime hydrographique). Le déclenchement des laves torrentielles ou d'événements de charriage majeurs est simulé sur la base d'une analyse des prédispositions impliquant les évènements récents. Dans la perspective de changements climatiques, un modèle de cascade sédimentaire permet une analyse du démantèlement d'un bassin versant par système torrentiel sur la base des processus observés (et non des dommages) en les faisant évoluer dans le temps (déclenchement lié aux changements des conditions climatiques). Le profil ainsi que la dynamique du cours d'eau est cependant en perpétuel changement, influençant son érodabilité (potentiel érodable) propre.

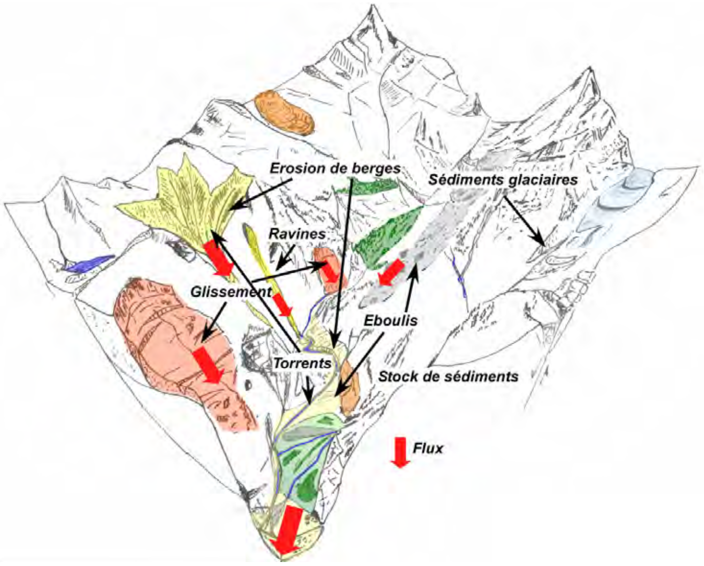

Figure 3.1 *: Illustration des phénomènes participant à la production et au transport de sédiments vers l'exutoire du bassin. Ces processus sont identifiés, caractérisés et cartographiés sur la base de visites de terrain et par l'analyse de photos aériennes dans un environnement SIG.*

4 Méthode (synthèse de Mazotti et al., 2010)

4.1 Analyse générale et cartographie de la disponibilité des matériaux d'érosion

Une cartographie des phénomènes a permis d'identifier l'ensemble des apports en matériaux potentiellement mobilisables dans le système torrentiel. Les apports peuvent provenir à la fois de stocks de sédiments meubles préexistants et de sédiments nouvellement formés. Les sédiments préexistant sont anciens, mais générés par des processus encore en cours actuellement. Tout particulièrement, Il s'agit de cartographier les processus directement mobilisables au contact du torrent :

- érosion de berges
- apports latéraux dus aux phénomènes torrentiels
- apports latéraux dus aux mouvements de versants (chutes de blocs, glissements, avalanches de neige)

Il s'agit aussi d'effectuer un relevé des éléments indirectement mobilisables :

- dépôts glaciaires
- glissements de terrain stabilisés, dormants ou actifs
- éboulis fossiles ou actifs et colluvions de toute sorte (ex. avalanches de neige)
- dépôts lacustres et éoliens (Loess)

Pour chacun de ses processus illustrés dans la figure 3.1, le volume, l'apport annuel et la vitesse de mobilisation ont été évalués dans la mesure du possible. La « *philosophie du terrain* » est illustrée en Annexe II.

4.2 Caractérisation de la dynamique générale du torrent

Une caractérisation de la dynamique sédimentaire du torrent a été effectuée à partir du profil en long des chenaux principaux et de ses affluents. Le torrent est divisé en biefs homogènes en fonction de 5 critères découpés en classes (fig. 4.1):

1. Les critères morphologiques de pente, largeur et direction de segment du torrent permettent de discrétiser le chenal en unité (bief) où la dynamique du transport sédimentaire (ex. variation de la capacité d'entrainement/déposition) le long du chenal est semblable (tab. 4.1). Cette tendance des segments du torrent à entrainer/déposer du matériel le long de son cour est ensuite défini par un indice d'alluvionnement (cf. chap. 4.4).
2. De plus, les biefs sont différentiés entre le cas où le lit du torrent est recouvert de sédiments et le cas où le bedrock affleure.

3. Enfin, pour qu'un bief soit considéré comme homogène, il doit faire partie de la même hiérarchisation des branches du réseau torrentiel (classification de Strahler, 1952).

***Tableau 4.1** : Critères morphologiques liés à la dynamique du torrent pour la division du torrent en biefs homogènes (d'après Mazotti et al., 2010)*

Critères	Classes	Implication sur la dynamique du torrent
Pente moyenne sur 25 m	< 2° :	- Charriage
	2°-15° :	- propagation laves torrentielles et charriage
	15°- 40° :	- déclenchement de laves torrentielles
	> 40° :	- falaises
Largeur moyenne cartographiée	< 1.5 m	La variation de largeur entre deux biefs influence la vitesse d'écoulement et ainsi sa capacité de transport. Exemple : Lorsque le flux devient plus confiné, la capacité d'entrainement augmente.
	1.5 - 2 m	
	2 - 5 m	
	5 - 7 m	
	7 – 10 m	
	10 - 15 m	
	15 - 20 m	
	> 25 m	
Changement de la direction moyenne sur 25 m	< 20°	Le changement de direction le long du chenal influence la capacité de transport.
	20° - 60°	
	> 60°	

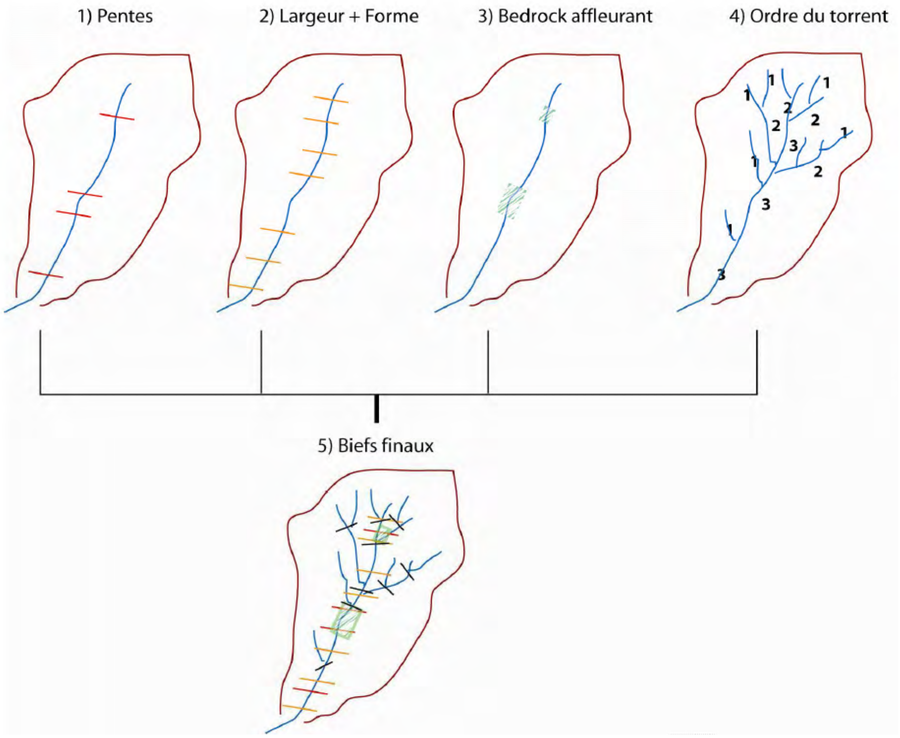

***Figure 4.1** : Illustration des 5 critères utilisés pour la subdivision du torrent en biefs homogènes. Le découpage est effectué dans l'ordre indiqué dans le schéma en appliquant les classes décrites dans le tab 3.1.*

Partant de l'hypothèse qu'un torrent tend à se rapprocher de son profil théorique, il est possible de différencier la dynamique (déposition/entrainement) du flux sédimentaire dans chaque bief (fig. 4.2). L'écart entre le profil réel et celui théorique indique les secteurs du torrent ou la tendance du flux sédimentaire est au dépôt ou à l'inverse des zones où l'entrainement (érosion) de sédiments dans le bief semble prépondérant. Le profil théorique peut être défini en ajustant une fonction mathématique simple de type exponentielle sur le profil topographique réel, depuis l'apex du cône jusqu'au pied des falaises où les affluents des torrents prennent leur source.

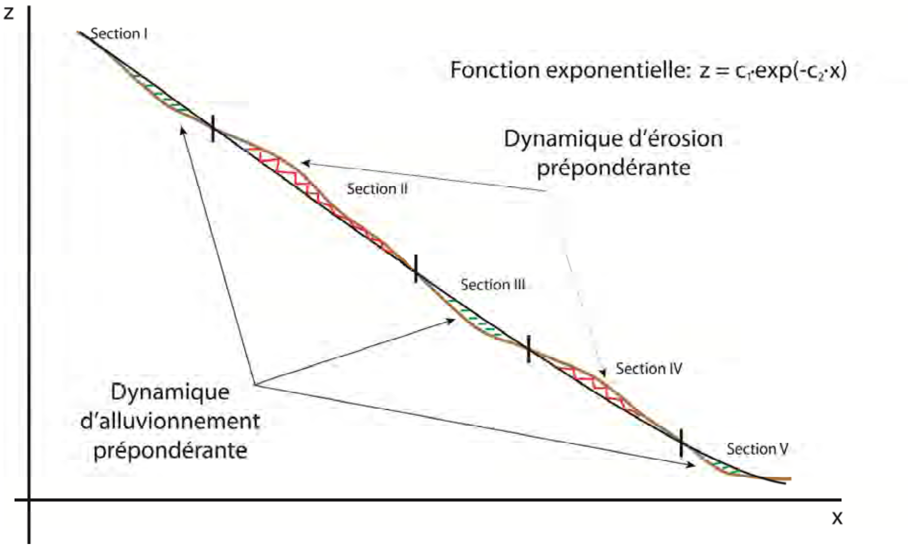

***Figure 4.2** : Illustration de l'analyse du profil en long du torrent permettant de délimiter les zones de dépôt et d'érosion dans les biefs (en brun, le profil réel ; en noir, le profil théorique défini par une courbe exponentielle).*

4.3 Estimation des stocks sédimentaires et apports de matériaux potentiels dans le système torrentiel

Le flux sédimentaire à l'exutoire du torrent dépend des stocks de sédiments mobilisables présents et pouvant entrer dans le système (Lehmann et al. 1999). Il s'agit d'une part des volumes de matériaux actuellement stockés (stock direct) dans ou à proximité du torrent. D'autre part, il s'agit de volumes ne provenant pas de l'activité du torrent, mais produit par l'érosion générale du versant (par ex. suite à des précipitations) ou par des mouvements de versant (phénomène ponctuel). Cet apport externe de sédiments (stock indirect) est présent tout au long du torrent:

1. Les apports de matériaux provenant directement du lit et des berges du torrent ($Stock_{direct}$) ont été estimés pour chaque bief à l'aide de la méthode du **S**lope **L**ocal **B**ase **L**evel (SLBL) (Jaboyedoff et Derron, 2005). Cette approche permet une estimation du volume maximum de matériel potentiellement mobilisable (érosion maximale du lit et des berges du torrent) lors d'événements extrêmes. La méthode du SLBL creuse le MNT selon une surface du 2ème degré ($z \sim ax^2$) suivant deux

conditions initiales de courbure et profondeur afin de représenter la forme en U du bief après une telle érosion (fig. 4.3). La profondeur maximale (H_{max}) de l'érosion est définie à partir de la formule de Kronfelner-Kraus (1984) :

$$H_{max} = 1.5 + 12.5 * J \qquad J = \text{la pente en } [m/m]$$

et permet ainsi de limiter le creusement du bief avec la méthode du SLBL à une profondeur maximum :

$$Stock_{direct} = \{Volume_{SLBL} \mid H_{SLBL} \leq H_{max}\}$$

où la différence entre la topographie réelle et celle creusée par le SLBL forme le volume de sédiments dans le bief directement mobilisable.

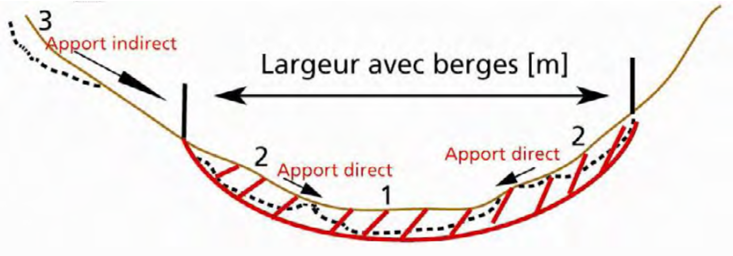

***Figure 4.3** : Profil en large d'un bief illustrant la méthode du SLBL pour l'estimation du volume directement mobilisable dans chaque bief. Seule la masse se trouvant entre les berges est creusée. La profondeur limite maximale a été déterminée par l'équation de Kronfelner-Kraus.*

2. Les stocks indirects de matériaux mobilisables ($Stock_{indirect}$) sont obtenus en multipliant la surface ($A_{Erosion}$) de ces zones d'érosion (obtenue par la cartographie de terrain), par une hauteur ($H_{Erosion}$) estimée à partir des observations sur le terrain ou à partir d'informations provenant de la littérature :

$$Stock_{indirect} = A_{Erosion} * H_{Erosion}$$

4.4 Flux et vitesse de transfert des stocks sédimentaires

La quantification des apports de matériaux dans un système torrentiel nécessite non seulement les volumes mobilisables mais leur vitesse de mobilisation.

La quantité de l'alluvionnement dans les biefs, c.-à-d. la proportion du torrent à déposer du matériel d'un bief à l'autre, a été définie à partir du changement de pente (S), de largeur (L) ainsi que de direction entre biefs (ΔA_Z) (Lehmann et al. 1999 ; Bardou 2002 ; Lan & al. 2008 ; Gertsch 2009). Un indice d'alluvionnement (I_{alluv}) est défini pour chaque bief selon que la pente diminue, la largeur augmente et le torrent change de direction entre le bief considéré par rapport à son bief amont (tab. 4.2). Cette démarche s'approche tout particulièrement des travaux de Fanin & Wise (2000), dans lesquels est établie de façon empirique une relation linéaire entre les facteurs (gradient de pente et morphologie du chenal) influençant la propagation/déposition et le volume de matériel entrainé de biefs en biefs. L'indice d'alluvionnement représente un pourcentage de matériel potentiellement déposable dans chaque bief. Comme un changement de direction à lui tout seul entre bief n'implique pas forcément une augmentation du potentiel à déposer du matériel, I_{alluv} obtenu en fonction du score de S et L est augmenté d'un certain pourcentage en fonction de ΔA_Z. Un exemple de calcul de I_{alluv} est présenté dans le tableau 4.3.

***Tableau 4.2 et 4.3**: (En haut) Exemples du calcul de l'indice d'alluvionnement. Le pourcentage de matériel potentiellement déposable dans chaque bief est estimé à partir de la variation de pente (S), largeur (L) et direction (A_Z) entre le bief considéré et son bief amont, selon le calcul présenté dans le tableau du bas.*

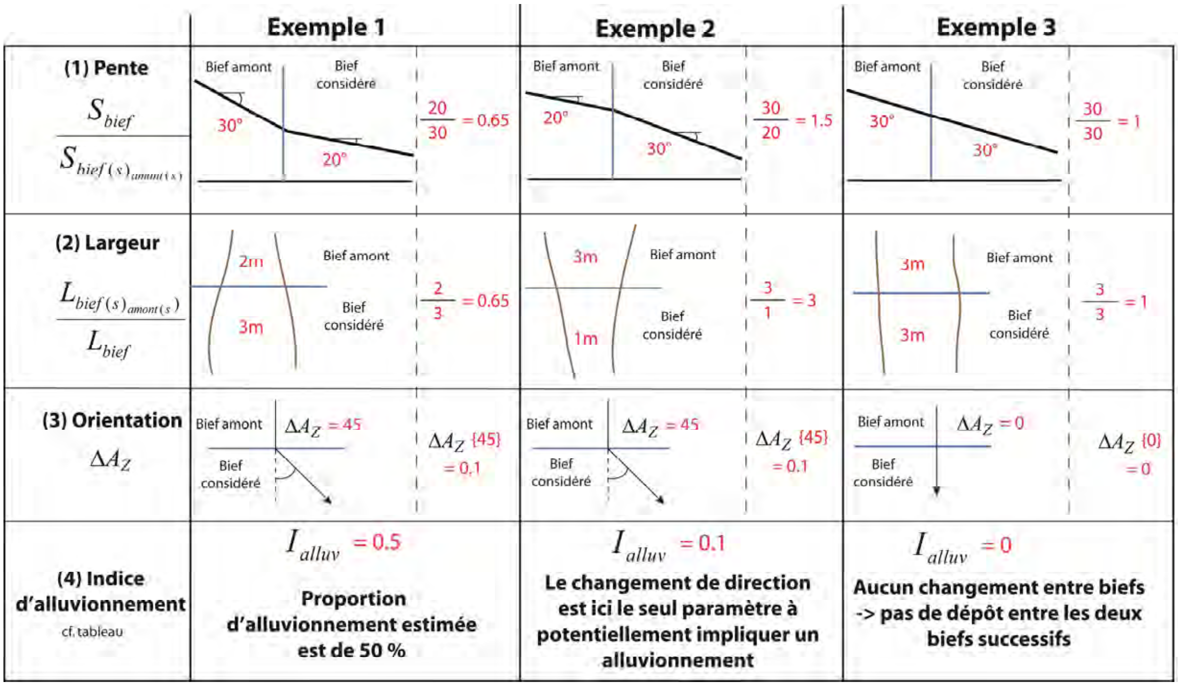

	Exemple 1	Exemple 2	Exemple 3
(1) Pente $\frac{S_{bief}}{S_{bief(s)_{amont(s)}}}$	$\frac{20}{30} = 0.65$	$\frac{30}{20} = 1.5$	$\frac{30}{30} = 1$
(2) Largeur $\frac{L_{bief(s)_{amont(s)}}}{L_{bief}}$	$\frac{2}{3} = 0.65$	$\frac{3}{1} = 3$	$\frac{3}{3} = 1$
(3) Orientation ΔA_Z	$\Delta A_Z \{45\} = 0.1$	$\Delta A_Z \{45\} = 0.1$	$\Delta A_Z \{0\} = 0$
(4) Indice d'alluvionnement cf. tableau	$I_{alluv} = 0.5$ **Proportion d'alluvionnement estimée est de 50 %**	$I_{alluv} = 0.1$ **Le changement de direction est ici le seul paramètre à potentiellement impliquer un alluvionnement**	$I_{alluv} = 0$ **Aucun changement entre biefs -> pas de dépôt entre les deux biefs successifs**

Proportion de matériel déposé dans le bief considéré selon la variation de pente et largeur entre ce bief et son bief amont :		**Proportion de matériel déposé dans le bief selon le changement de direction avec son bief amont:**	
$\left(\frac{S_{bief}}{S_{bief(s)_{amont(s)}}} + \frac{L_{bief(s)_{amont(s)}}}{L_{bief}} \right) / \ 2$	I_{alluv}	ΔA_Z	I_{alluv}
0 – 0.3	80 %		
0.3 – 0.5	60 %	0° < ΔA_z < 20°	+0 %
0.5 – 0.8	40 %	20° < ΔA_z < 60°	+10 %
0.8 - 1	20 %	60° < ΔA_z < 90°	+20 %
≥ 1	0 %		

Le volume de matériel déposé dans un bief ne peut cependant pas excéder sa capacité maximale de remplissage ($\text{Stock}_{\text{max}}$) du bief défini par le profil théorique du torrent (fig. 4.4). Ce volume de déposition maximum dans un bief est estimé par la différence d'altitude entre le profil réel et le profil théorique (ΔH_{profil}) multiplié par la surface du bief (A_{bief}) :

$$\text{Stock}_{\text{max}} = A_{\text{bief}} * \Delta H_{\text{profil}}$$

Un fois cette capacité atteinte, le flux sédimentaire ne peut plus être déposé dans le bief et est propagé au bief suivant. La possibilité que du matériel déborde d'un bief et quitte le torrent n'est pas pris en compte dans cette approche, bien qu'elle soit tout à fait envisageable. Les biefs situés au-dessus de leur profil théorique n'ont pas de capacité de stocker du matériel, le matériel charrié ne fait que transiter dans le bief.

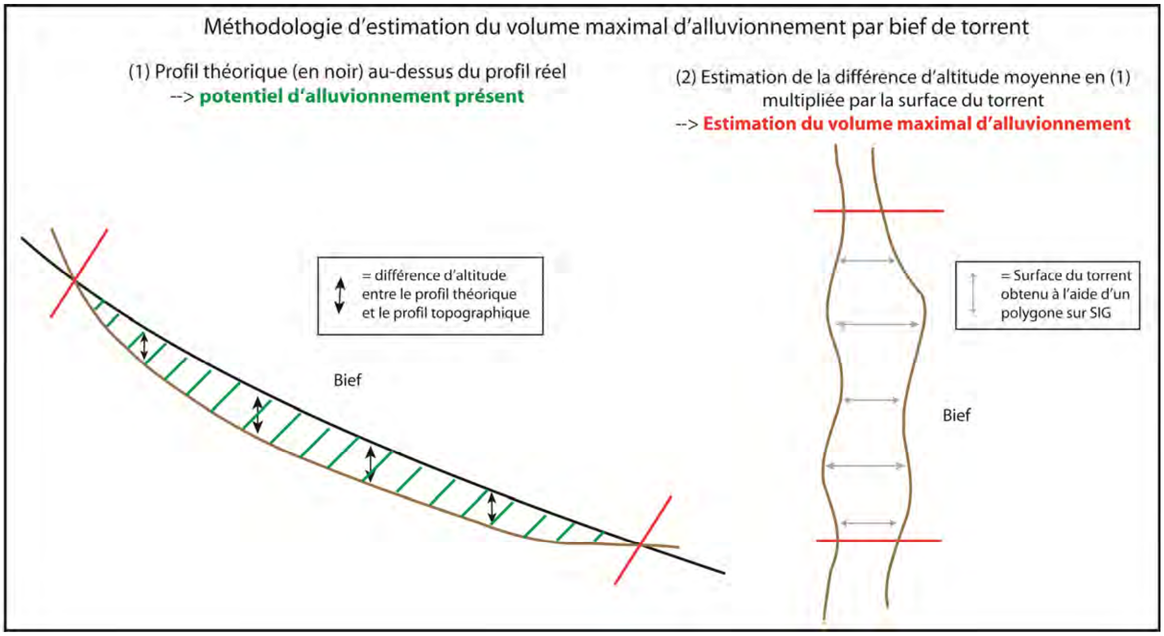

***Figure 4.4** : Illustration du calcul de la capacité volumique maximal d'un bief suivant la différence d'altitude entre le profil réel et théorique.*

Les apports directs et indirects tout au long de la cascade sédimentaire sont définis par les vitesses de transfert de sédiments propres aux différents phénomènes en jeu que sont les précipitations et laves torrentielles. Le flux sédimentaire se décompose de façon simple en deux étapes, lesquelles possèdent chacun leur vitesse propre et un flux variable :

1. Lorsqu'il s'agit du flux sédimentaire provoqué par *les précipitations*, les volumes d'apport indirect de sédiments (V^{P}_{ind}) par type de précipitations peuvent être définis sur la base de taux moyen de l'érosion (k_{ind}) dans le bassin versant et défini dans un temps donné:

$$V^{P}_{\text{ind}} = A_{\text{bv bief}} * k_{\text{ind}} \, ; \qquad A_{\text{bv bief}} = \text{surface érodable en contact avec le bief.}$$

L’apport direct de sédiment, c.-à-d. le volume mobilisés (V^{P}_{dir}) dans chaque bief du torrent par type de précipitations, est défini en fonction de la surface (totale ou partielle selon que le bedrock affleure) du bief (A_{bief}), multipliée par une valeur d’érosion moyenne k_{dir} , k_{dir} représentant une hauteur du stock direct contenu dans chaque bief :

$$V^{P}{}_{\_dir} = A_{bief} * k_{dir}$$

2. Lorsqu’il s’agit d’évènements *laves torrentielles*, le flux sédimentaire s’apparente à une vidange des matériaux mobilisables contenus dans le torrent plus ou moins importante selon le type de laves torrentielles. Un certain volume de sédiments (V^{LT}), calculé à partir d’un pourcentage du volume direct et indirect de sédiments mobilisables par bief, est purgé dans chaque bief, tel que :

$$V^{LT} = c_{mob} * (Stock_{direct} * c_{dir} + Stock_{indirect} * c_{ind})$$

c_{mob} représente le pourcentage de matériel mobilisable dans chaque bief, c_{dir} représente la proportion de matériel purgé dans le stock direct de chaque bief et c_{ind} la proportion du stock indirect.

Lorsque les stocks directs ($Stock_{direct}$) et indirects ($Stock_{indirect}$) deviennent insuffisants, les apports mobilisables sont limités aux flux disponibles. Cependant, les stocks indirects peuvent être considérés comme infinis selon le scénario choisi.

4.5 Fréquence d’occurrence des évènements et intensités

La mise en mouvement des matériaux n’est pas régulière et linéaire mais ponctuée de pics plus ou moins important du flux de matériaux. La dynamique sédimentaire est principalement causée par des précipitations de fortes intensités. Au cours d'un seul événement extrême, d’énormes quantités de matériaux peuvent être mobilisés. Les flux sédimentaire dans la cascade sont déterminés à partir de la connaissance des temps de retour des précipitations ainsi que des laves torrentielles en fonction de leur intensité :

- les précipitations avec une intensité de type fréquente déterminent le flux sédimentaire de base. Il s’agit d’événements qui rechargent le torrent en matériel ; le flux sédimentaire dans le torrent est composé d’un léger charriage exclusivement.
- les précipitations avec une intensité de type rare provoquent un charriage important dans le torrent. Et l’apport sédimentaire depuis les stocks indirects y est aussi plus important.
- le temps de retour de précipitations de type extrême permet de définir un seuil d’occurrence d’événements exceptionnels, ex. un glissement de terrain ou éboulement de volume important entrant dans le système torrentiel. Il s’agit d’un volume extraordinaire introduit dans la cascade sédimentaire à un lieu déterminé par les

données de terrain. Ce volume s'ajoute au fonctionnement de la cascade sédimentaire, laquelle est déterminé par des paramètres d'érosion extrêmes par rapport à la normal. Le transfert sédimentaire se fait aussi de façon très soutenu.

- les temps de retour des laves torrentielles en fonction de leur intensité déterminent le flux de matériaux transporté par de tels évènements dans le dépotoir. Une certaine quantité de sédiments (en % du volume direct et indirect de sédiments mobilisables par bief) est purgée du potentiel total du torrent. Leurs intensités (volumes) liés aux temps de retour des laves torrentielles sont définies sur la base des observations recensées dans le dépotoir. L'approche est semblable aux données de précipitations. Cependant, les données sont souvent manquantes et il faut composer avec les observations de terrain (traces de laves torrentielles anciennes et récente, volume des dépôts et levées, observation de la couverture végétale du torrent, etc…) et les comparer sur la base de la carte des évènements (potentiel de matériel mobilisable, zones de production de matériel, etc…). Le phénomène laves torrentielles a été classifié selon 3 degrés d'intensité : les laves torrentielles fréquentes, rares et exceptionnelles.

Lorsqu'il n'y a pas de précipitations ou laves torrentielles, l'activité sédimentaire est considérée comme dormante. Aucun flux sédimentaire dans les stocks ou dans le torrent n'a lieu. Il faut en outre relever que certaines roches tendres peuvent produire en continu des matériaux dans le lit des torrents. Ceci n'est cependant pas considéré dans ce modèle.

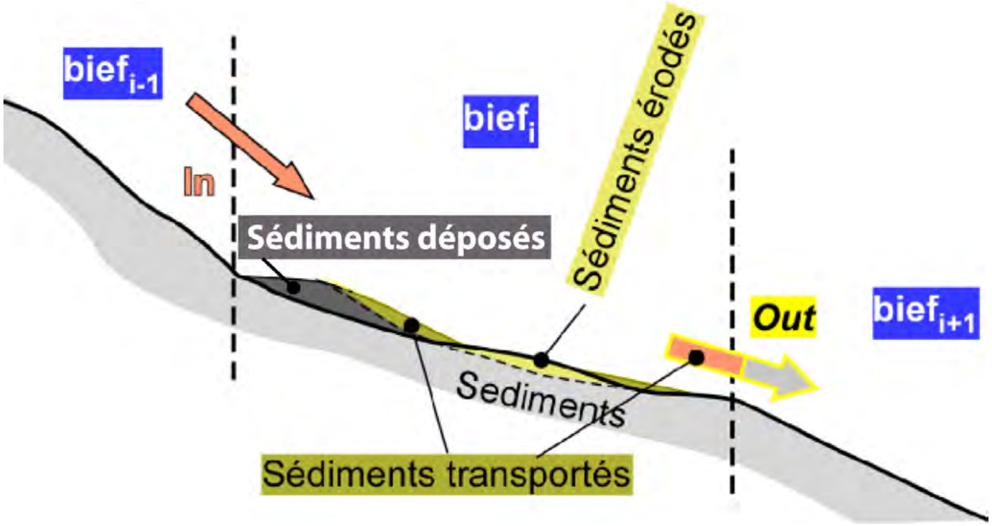

Figure 4.5 : *Illustration du principe de la cascade sédimentaire.*

4.6 Principe de propagation des flux de matériaux et évolution des stocks sédimentaires

4.6.1 La cascade sédimentaire

Le concept de cascades pour simuler la dynamique sédimentaire d'un torrent alpin développé dans ce projet s'inspire de plusieurs travaux antérieurs : Chorley and Kennedy, 1971 ; Lehmann et al. 1999 ; Schrott et al. 2003 ; Fryirs et al. 2006 ; Gertsch, 2009 ; Wichmann et al. 2009. Le principe consiste à définir un bilan sédimentaire à l'échelle du bief (fig. 4.5) et de faire propager ce bilan de bief en bief à partir des vitesses de flux discutés précédemment:

$$\Delta \mathrm{vol}_{\mathrm{bief\ i}} = \Delta \mathrm{vol}_{\mathrm{bief\ i\text{-}1}} + \mathrm{vol\ direct}_{\mathrm{bief\ i}} + \mathrm{vol\ indirect}_{\mathrm{bief\ i}} - \mathrm{vol\ déposé}_{\mathrm{bief\ i}}$$

La variation du volume dans le bief i ($\Delta \mathrm{vol}_{\mathrm{bief\ i}}$) est définie par l'addition du volume propagé depuis le(s) bief(s) précédent(s) ($\Delta \mathrm{vol}_{\mathrm{bief\ i\text{-}1}}$) avec le volume direct ($\mathrm{vol\ direct}_{\mathrm{bief\ i}}$) et indirect ($\mathrm{vol\ indirect}_{\mathrm{bief\ i}}$) mobilisables dans le bief auxquels est retenue une certaine quantité de matériaux déposée dans le bief ($\mathrm{vol\ déposé}_{\mathrm{bief\ i}}$) en fonction des conditions morphologiques du bief et de sa capacité de stockage. Chaque bief possède un stock direct et indirect de matériel mobilisable prédéterminé (fig. 4.6), lesquels sont actualisés après chaque bilan intrabief. Ils font office de conditions limites à la quantité de sédiments entrainés dans la cascade sédimentaire. L'exécution de la cascade sédimentaire correspond à un pas de temps. A chaque pas de temps, le flux sédimentaire dans la cascade sédimentaire est déterminé par la probabilité d'occurrence qu'une précipitation ou lave torrentielle d'une intensité définie ait

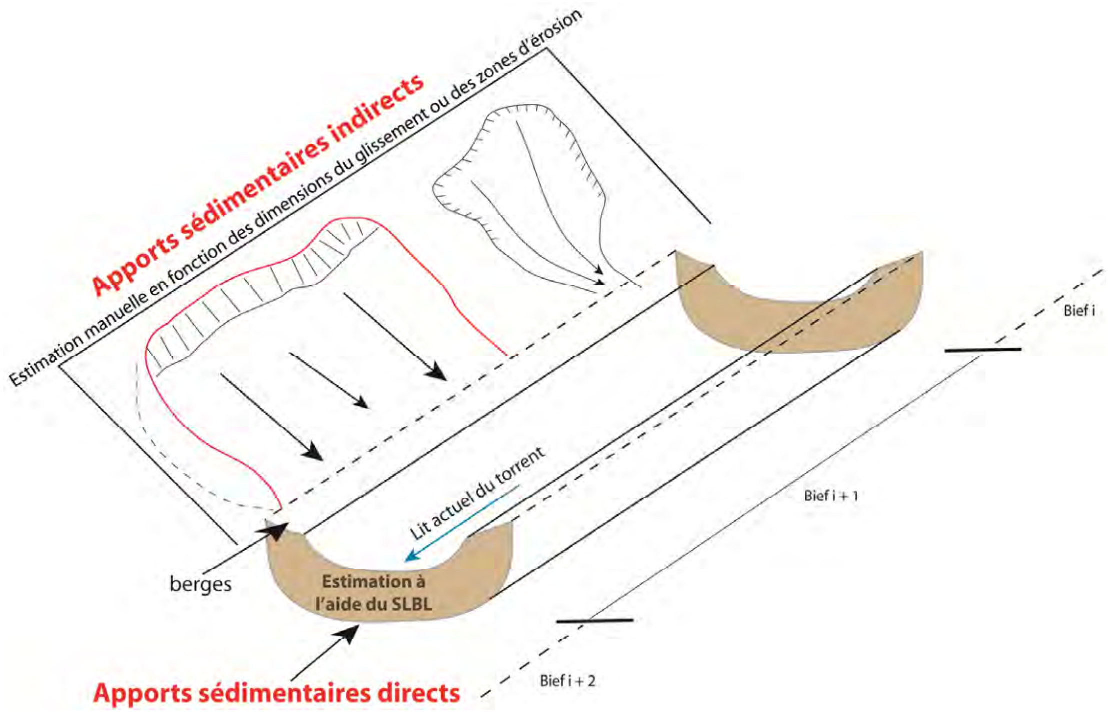

Figure 4.6 *: Illustration des stocks sédimentaires directs et indirects pris en compte dans chaque bief du torrent.*

lieu selon un tirage aléatoire (loi normale) déterminé par leur temps de retour ainsi qu’un cheminement prédéfini, et ceci pour chaque phénomène considéré dans le model (fig. 4.7). Ainsi, il est possible que pour un même pas de temps, plusieurs phénomènes (ex. une précipitation et une lave torrentielle) soient simulés. Dans cette phase du projet, les types d’évènements retenus sont (chap. 4.5) :

1. les précipitations fréquentes
2. les précipitations rares
3. les précipitations extrêmes
4. les laves torrentielles fréquentes
5. les laves torrentielles rares
6. les laves torrentielles extrêmes

Les transferts de sédiments selon les stocks présents dans les réservoirs de la cascade sédimentaire sont contrôlés par le flux sédimentaire. Il s’agit d’une représentation simplifiée de la dynamique des phénomènes en jeu :

- Un processus lent (érosion du pied d’un glissement) est modélisé lors de l’occurrence de précipitations fréquentes.
- Un processus rapide (débâcle due à l’effondrement de ce même glissement) peut être modélisé lorsqu’une précipitation extraordinaire survient.
- Les laves torrentielles peuvent être modélisées par des coulées de débris purgeant une quantité de sédiments de biefs en biefs jusqu’au dépotoir.

Selon l’évolution climatique après une certaine période de simulation, les paramètres de fréquences d’événements et de vitesses de flux peuvent être modifiés selon plusieurs scénarii sur la base des critères actuels, permettant ainsi une analyse de sensibilité de l’évolution de la dynamique sédimentaire du torrent.

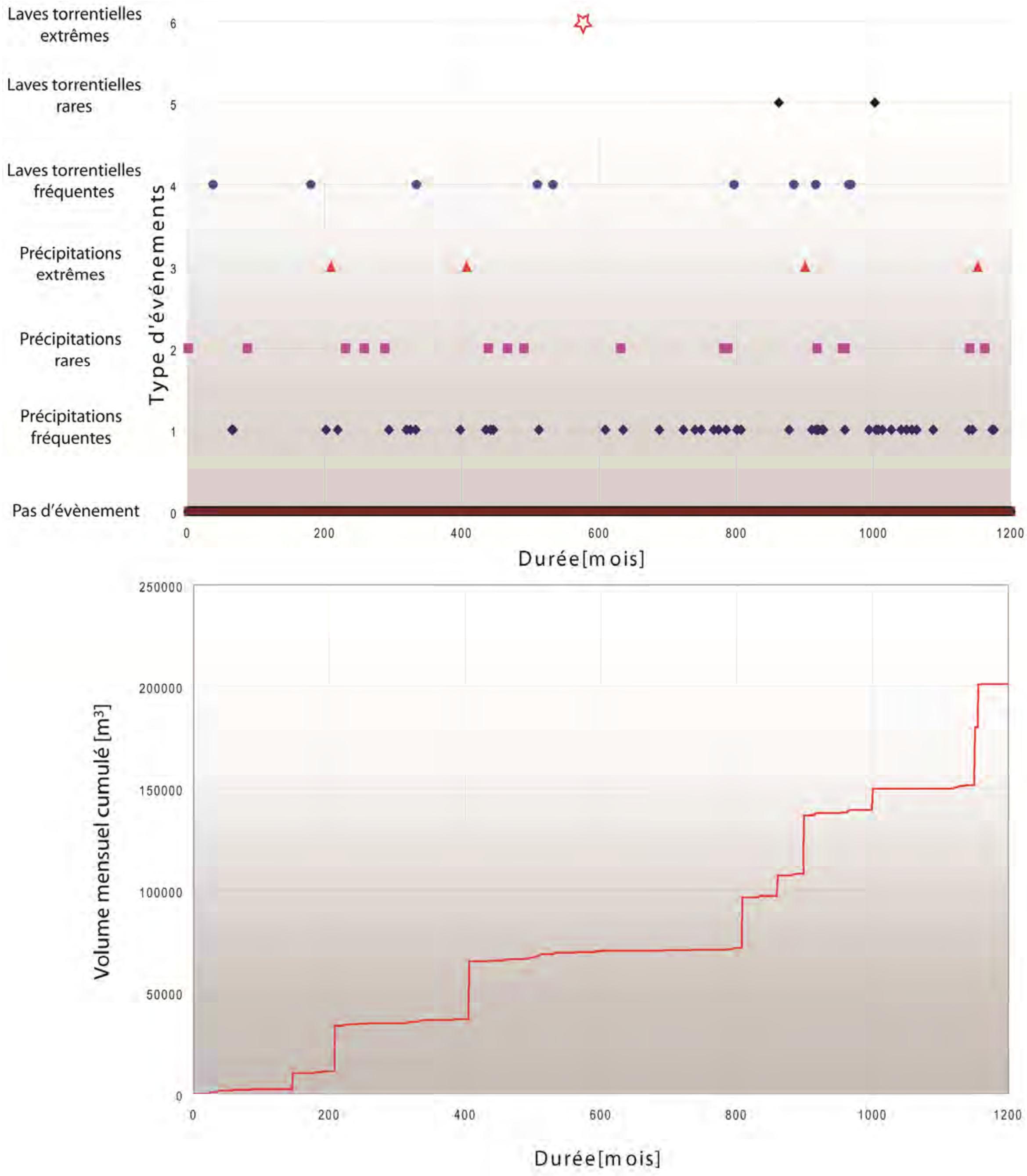

***Figure 4.7** : (Haut) Séquence aléatoire déterminant l'occurrence des phénomènes dans la série temporelle. (Bas) Implication sur les flux sédimentaires et volumes accumulés dans un bief.*

4.7 Le programme MatErosion

Cette cascade sédimentaire a été implantée dans une routine informatique programmée dans l'environnement Matlab©. Le flux sédimentaire du torrent tel qu'il est simulé de bief en bief dans la cascade sédimentaire de MatErosion est détaillé dans la figure 4.13. La routine informatique peut être pilotée à partir d'une interface graphique (fig. 4.8). Une simulation nécessite environ 1 à 2 secondes de temps de calcul.

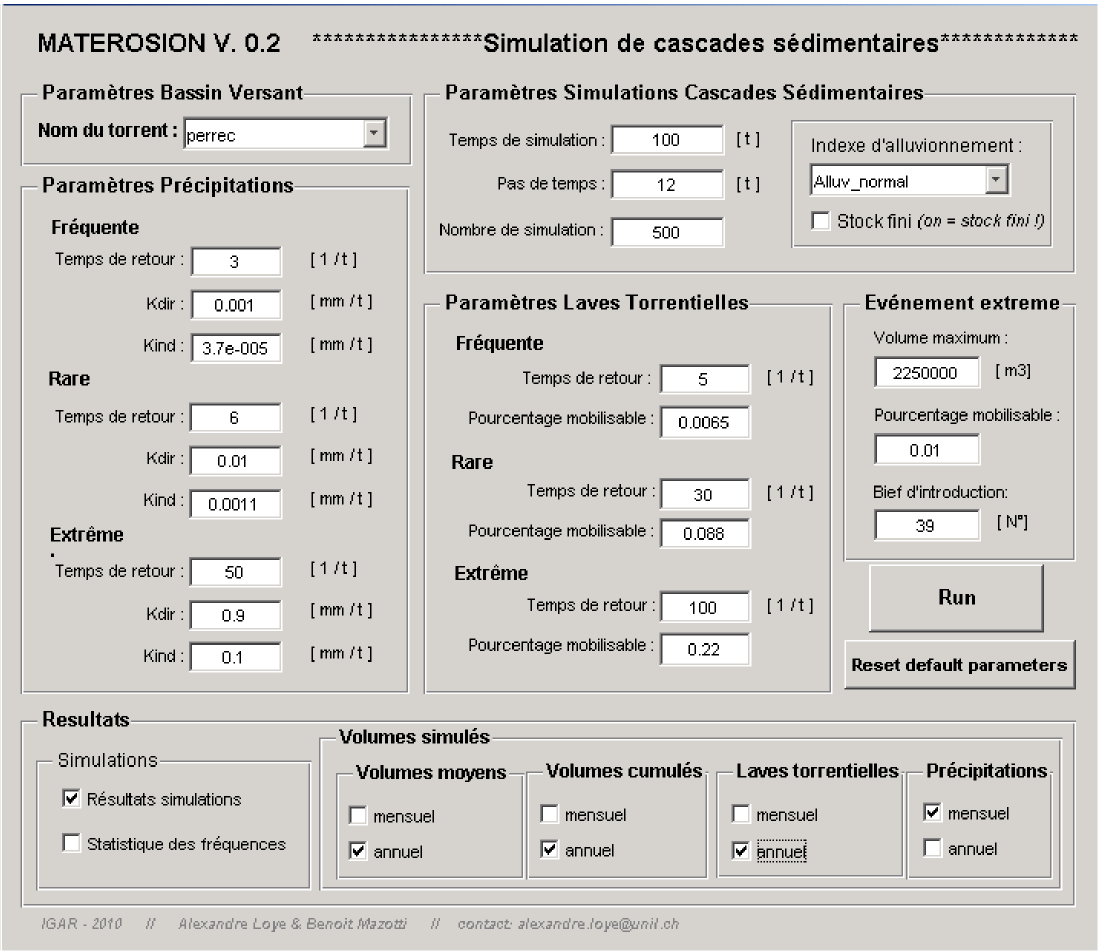

MATEROSION V. 0.2 ****************Simulation de cascades sédimentaires*************

Paramètres Bassin Versant

Nom du torrent : perrec

Paramètres Précipitations

Fréquente

Temps de retour : 3 [1 / t]

Kdir : 0.001 [mm / t]

Kind : 3.7e-005 [mm / t]

Rare

Temps de retour : 6 [1 / t]

Kdir : 0.01 [mm / t]

Kind : 0.0011 [mm / t]

Extrême

Temps de retour : 50 [1 / t]

Kdir : 0.9 [mm / t]

Kind : 0.1 [mm / t]

Paramètres Simulations Cascades Sédimentaires

Temps de simulation : 100 [t]

Pas de temps : 12 [t]

Nombre de simulation : 500

Indexe d'alluvionnement : Alluv_normal

☐ Stock fini *(on = stock fini !)*

Paramètres Laves Torrentielles

Fréquente

Temps de retour : 5 [1 / t]

Pourcentage mobilisable : 0.0065

Rare

Temps de retour : 30 [1 / t]

Pourcentage mobilisable : 0.088

Extrême

Temps de retour : 100 [1 / t]

Pourcentage mobilisable : 0.22

Evénement extreme

Volume maximum : 2250000 [m3]

Pourcentage mobilisable : 0.01

Bief d'introduction: 39 [N°]

Resultats

Simulations

☑ Résultats simulations

☐ Statistique des fréquences

Volumes simulés

Volumes moyens: ☐ mensuel ☑ annuel

Volumes cumulés: ☐ mensuel ☑ annuel

Laves torrentielles: ☐ mensuel ☑ annuel

Précipitations: ☑ mensuel ☐ annuel

***Figure 4.8** : Interface du programme MatErosion développée dans l'environnement Matlab©, mais pouvant aussi fonctionner sous la forme d'un exécutable indépendant de l'environnement Matlab©.*

Le bilan intrabief s'effectue à partir de plusieurs modules :

1. Le calcul de l'apport direct de sédiments dans le bief est détaillé dans la figure 4.9. Lors de chaque « boucle » (pas de temps), le stock de base d'apport direct (cf. chap. 4.3) est mis à jour. Si lors de la boucle suivante le stock est insuffisant, seul le flux restant sera utilisé dans le bilan sédimentaire du bief.

Le calcul de l’apport indirect de sédiment est semblable à celui de l’apport direct (fig. 4.10). Par contre, il est possible de ne pas mettre à jour le stock indirect lors de chaque pas de temps du modèle. Le stock indirect de matériel mobilisable reste ainsi à sa valeur initiale.

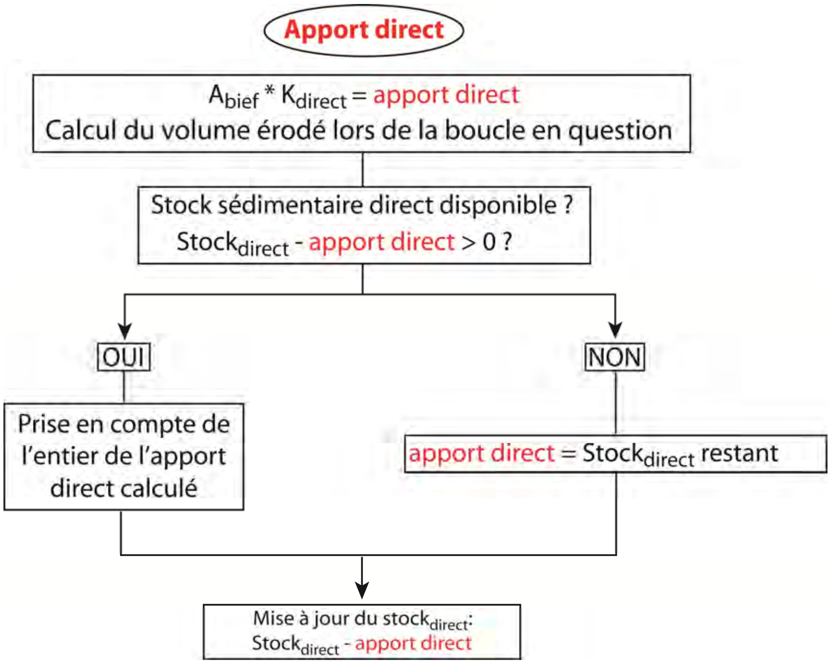

***Figure 4.9** : Détails des étapes de calcul de l’apport direct dans la routine MatErosion.*

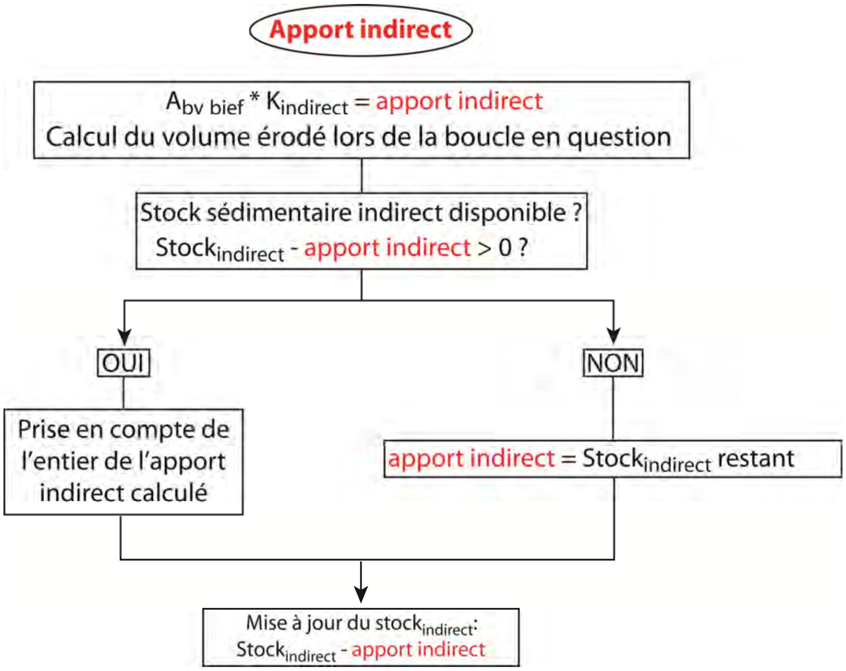

***Figure 4.10** : Détails des étapes de calcul de l’apport indirect dans la routine MatErosion.*

Le volume alluvionné à l'intérieur du bief est calculé à partir du volume entrant du/des biefs amont(s), des apports directs et indirects et de l'indice d'alluvionnement (cf. chap. 4.4). Le stock direct est mise à jour à chaque pas de temps, de même que sa valeur limite d'alluvionnement (fig. 4.11). En effet, la quantité de matériel qui n'est pas propagée dans le bief suivant reste dans le bief sélectionné et doit donc être ajoutée au stock direct du bief. La capacité maximale de remplissage ($\text{Stock}_{\text{max}}$) du bief en est aussi diminuée. Le schéma pour la propagation des volumes apportés par les laves torrentielles est décrit dans la figure 4.12.

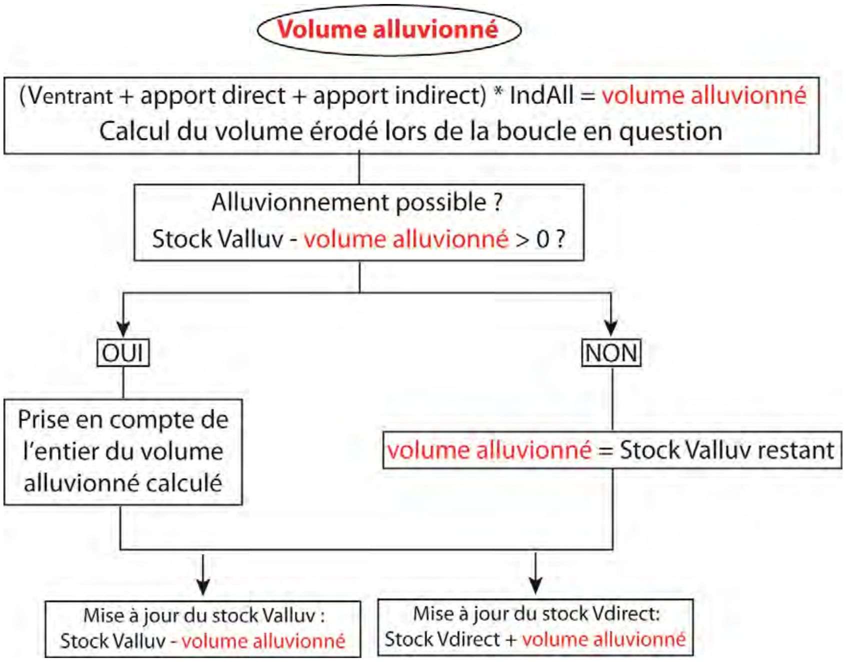

Figure 4.11 *: Représentation schématique des étapes de calcul de l'alluvionnement dans le modèle.*

Figure 4.12 *: Représentation schématique des étapes de calcul du volume propagé lors de la simulation de laves torrentielles.*

Le flux sédimentaire dans la cascade n'est gouverné que par la fréquence des évènements précipitations et laves torrentielles ainsi que de leur intensité. Ceci se traduit dans MatErosion par la création d'une séquence temporelle au pas de temps déterminé où viennent se greffer les phénomènes et leur intensité (ex. fig. 4.7). Selon la durée de simulation choisie, chaque phénomène se retrouvera un certain nombre de fois dans une simulation, ce nombre de fois étant produit par un tirage aléatoire de fréquence moyenne égale à l'inverse de leur temps de retour. Le pas de temps de la cascade sédimentaire est déterminé par le pas de temps des séries d'évènements précipitations et laves torrentielles. La simulation d'un grand nombre de séquences temporelles permet ainsi de simuler un grand nombre de scénarios de séquences de précipitations et laves torrentielles. Les données d'entrée nécessaires à l'exécution du bilan sédimentaire à l'échelle du bief sont résumées dans le tableau 4.4.

***Tableau 4.4** : Paramètres, variables et conditions initiales de chaque bief dans la cascade sédimentaire*

Données topographiques	**Information sur la dynamique**	**Stocks sédimentaires initiaux**	**Potentiel d'alluvionnement**
Identifiant du bief Pente (°) Longueur (m) Largeur (m) Orientation (Azimut, direction)	Surface érodable (apport direct) (m^2) Surface érodable (apport indirect) (m^2) Dynamique (érosion, dépôt, mixte) Bedrock affleurant ou non Identifiant du bief aval	Volume initial direct (m^3) Volume initial indirect (m^3) Volume maximum érodable (m^3)	Hauteur potentielle de dépôt (m) Potentiel maximum d'alluvionnement (m^3)

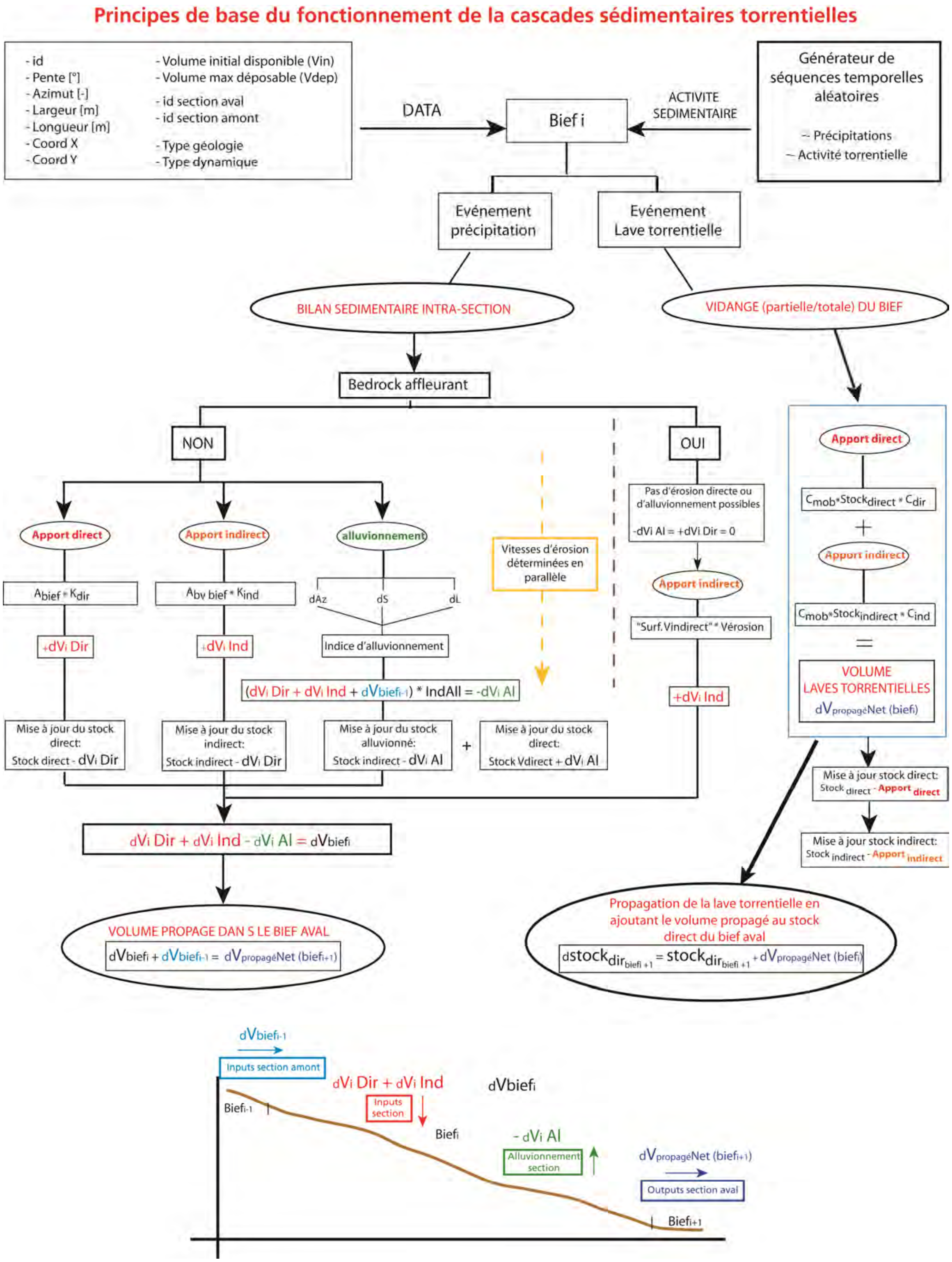

***Figure 4.13** : Concept final de simulation des flux sédimentaires dans un torrent en milieu alpin sous la forme d'une cascade sédimentaire.*

5 Application aux bassins versants pilotes

5.1 Les torrents de Perrec et Lirec

Cette démarche de simulation de la dynamique sédimentaire des torrents alpins a été appliquée sur deux torrents tests, le Perrec et le Lirec, situés au-dessus de Zinal en rive droite de la haute vallée d'Anniviers (fig. 5.1 et 5.2). Leur bassin versant couvre une surface respectivement de 1.8 km^2 et 1.6 km^2. En aval, les torrents s'écoulent dans les gneiss et micaschistes de la zone de Siviez-Michabel. En amont, ils atteignent les schistes lustrés de la Nappe du Tsaté. Dans leur partie sommitale, un lambeau de roches ophiolitiques les sépare des gneiss de la nappe de la Dent Blanche (Marthaler & Sartori, 2005). Les deux torrents se rejoignent au sommet du village pour former un cône de déjection de 5 ha environ. Sa pente moyenne est de 25%. A la confluence des deux torrents, une partie du cône a été réaménagée en ouvrage de protection contre les avalanches. Il fait office de dépotoir d'une capacité théorique de 200'000 m^3 pour stocker les matériaux provenant des avalanches, du charriage ainsi que des laves torrentielles (Ayer, 2003). Les sédiments transportés par le torrent proviennent principalement de la zone périglaciaire située au pied des Diablons, où le permafrost y est très probablement généralisé (OFEV, 2006). Le long de leur cours, plusieurs zones de glissements actifs et d'érosion le long des berges contribuent à recharger les torrents en matériaux.

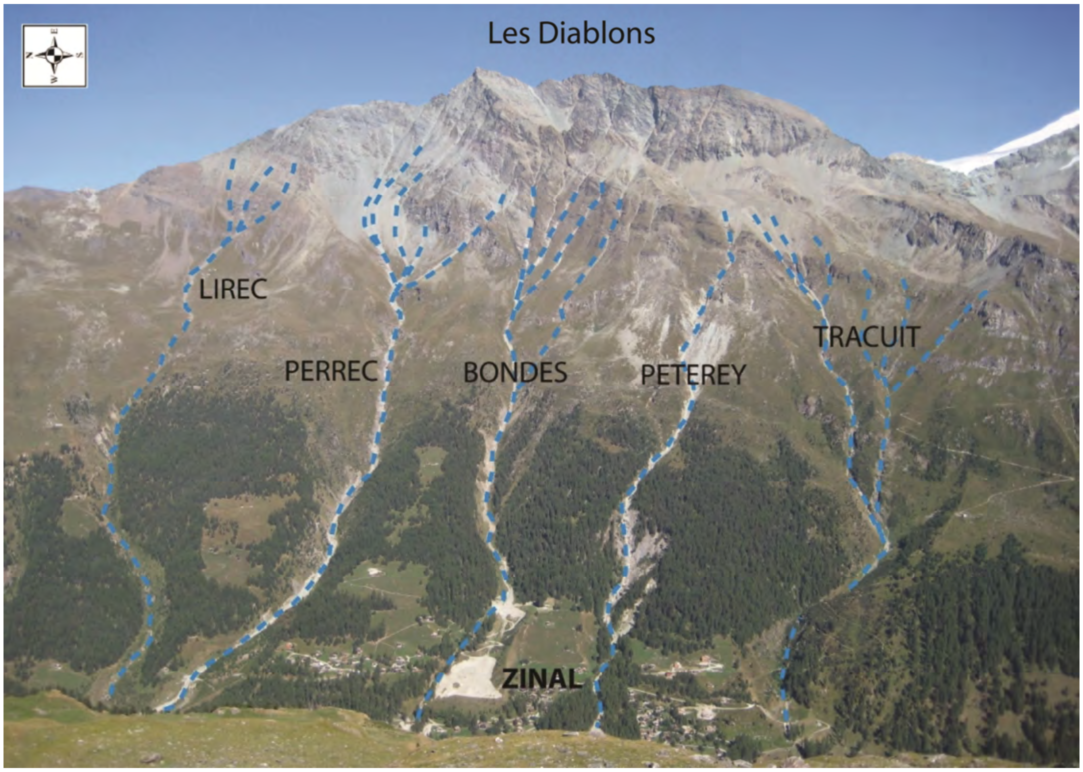

***Figure 5.1** : Torrents situés en amont du village de Zinal mentionnés dans cette étude.*

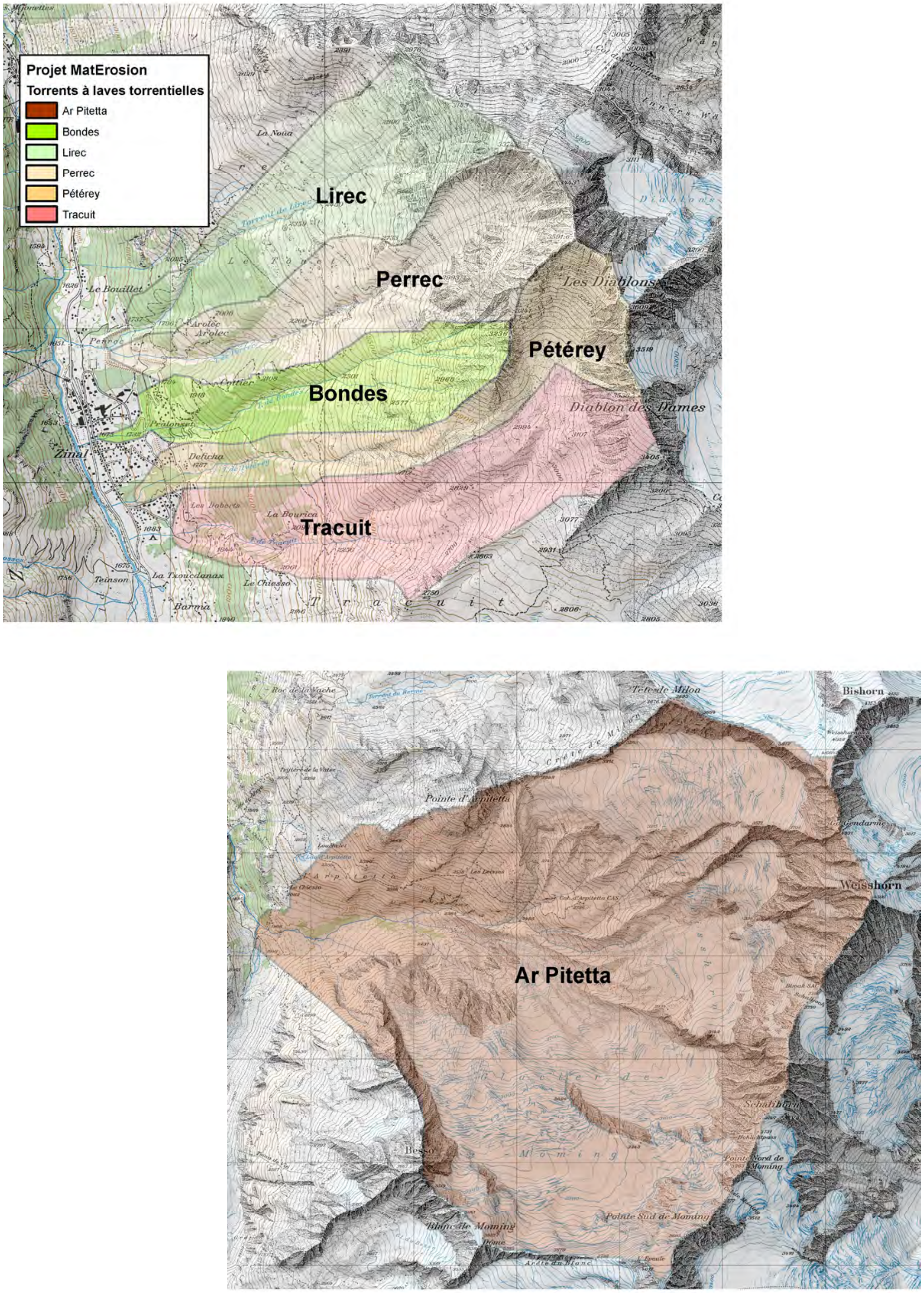

Figure 5.2 *: Localisation sur la carte topographique au 25'000ème des torrents à laves torrentielles et leur bassin versant situés en amont du village de Zinal ainsi que le Val D'Ar Pitetta (swisstopo).*

5.2 Cartographie des phénomènes

Plusieurs visites de terrain ont permis de récolter les informations spécifiques à l’estimation des stocks et des flux sédimentaires liés à la dynamique de transport dans le torrent et dans le bassin versant. Ces informations ont été complétées par une analyse des documents SIG (MNT et photos aériennes). Plus particulièrement (cf. annexe II et Mazotti et al. 2010,) :

1. un relevé des changements de dynamique du torrent a permis de diviser le torrent en :
    - zones de dépôts (Dep)
    - zones d’entrainement de matériaux (Er)
    - zones présentant des caractéristiques dynamiques mixtes (Bim)
    - zones où le bedrock affleure (Géologie = 1)
2. les dépôts quaternaires (surfaces, hauteurs moyennes supposées), spécialement les zones de matériaux meubles facilement entrainables ont été cartographiés (ex. formes périglaciaires, éboulis, etc.).
3. les instabilités de versants (glissements, niche d’arrachements, zones de chutes de blocs) potentielles et effectives pouvant d’une manière ou d’une autre accéder au torrent ont été relevées. Même si un glissement de terrain éloigné du chenal ne constitue pas une source immédiate de matériaux, il rapproche progressivement des matériaux de la zone de transport.
4. les particularités du torrent et les ouvrages d’aménagement et de protection.

Toutes ces informations sont résumées dans une carte des phénomènes sédimentaires (fig. 5.3) représentant les zones et phénomènes effectifs et potentiels d’apports de sédiments dans le système torrentiel. Un aperçu du travail de cartographie effectué dans les torrents de Zinal est illustré en annexe II.

5.3 Division des torrents en biefs homogènes

La division des torrents en biefs homogènes (fig. 5.4) à l’aide des critères de pentes, largeur et forme ainsi que de leur ordre dans le torrent (cf. tab. 4.1) a été effectuée sur la base du modèle numérique de terrain de 25 m de résolution (CREALP) dans un environnement SIG. Le paramètre *bedrock affleurant* est déduit des observations de terrain.

5.4 Estimation de la dynamique générale des biefs par l’analyse des profils en long

Le profil en long des torrents permettant d’estimer la dynamique générale sédimentaire a été extrait à partir du MNT 25 m sur la base de la couche rivière contenu dans le vecteur25 (CREALP). Le profil théorique ainsi que le volume de dépôt maximum pour chaque bief ($Stock_{max}$) a été calculé selon l’approche décrite aux chapitres 4.2 et 4.4. Les zones de dépôt et les zones d’érosion où le stockage temporaire de matériel dans les biefs est impossible sont présenté dans la figure 5.5 et le Stock$_{max}$ dans la figure 5.7. Le détail des valeurs pour chaque bief est donnée en annexe I.

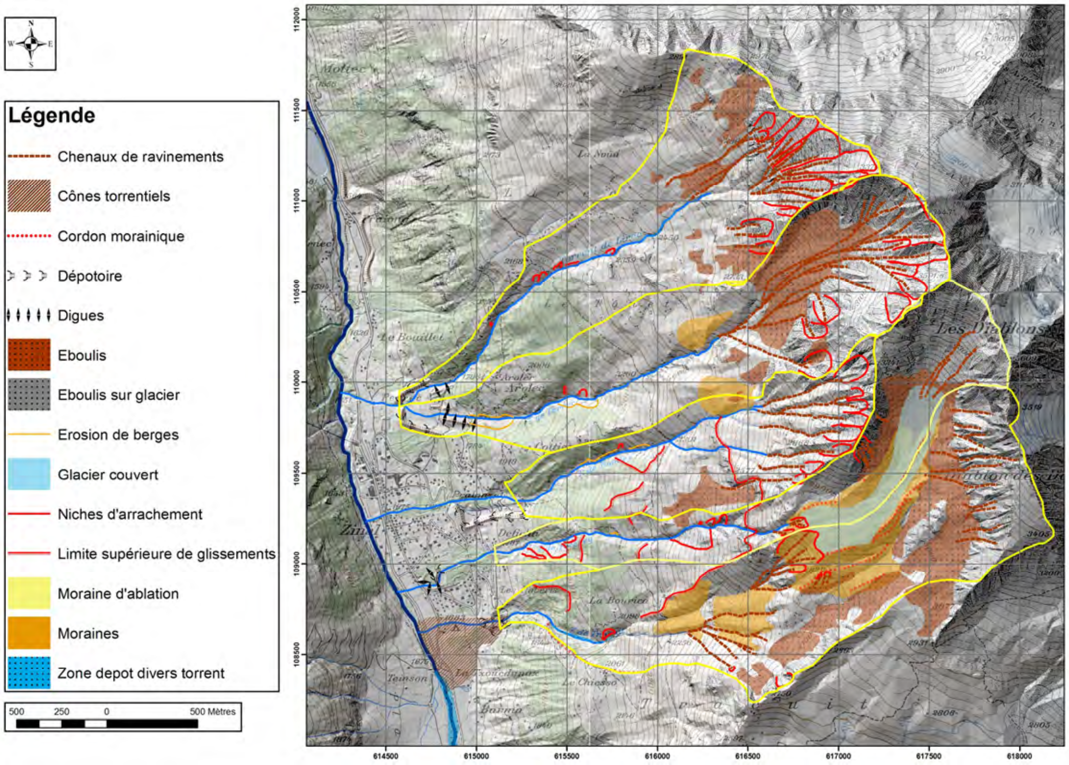

Figure 5.3 : Carte des phénomènes obtenue à partir des relevés de terrain et les données SIG.

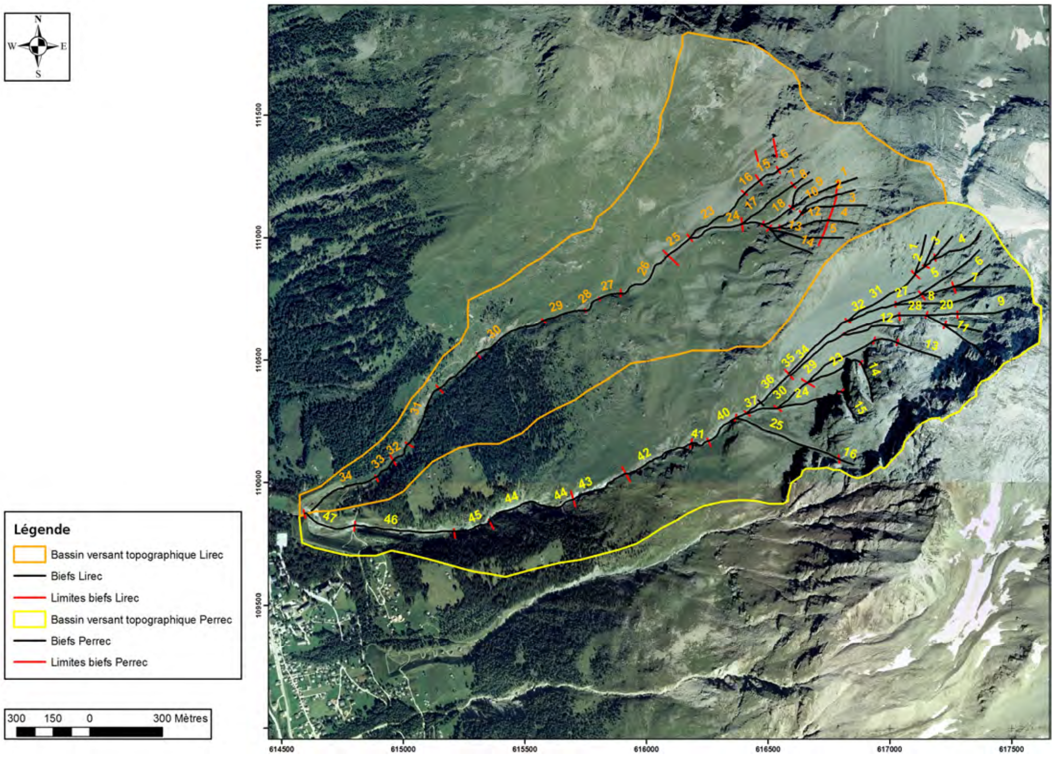

***Figure 5.4** : Divisions des torrents de Lirec et Perrec en biefs homogènes.*

L’analyse du profil en long avec les données de terrain montre une corrélation significative entre le régime dynamique des biefs identifiés à partir du profil en long et leur capacité à stocker du flux de matériaux (fig. 5.5, fig. 5.6 et fig. 5.8).

5.5 Estimation des stocks de matériaux directs et indirects

L’estimation des stocks de sédiments mobilisables directs ($Stock_{direct}$) pour chaque bief du torrent a été effectuée selon la méthode du SLBL décrite au point 1 (chap. 4.3). Le paramètre de courbure a été fixé à -0.1 m et la profondeur maximum définie par la formule de Kronfelner-Kraus. Les limites du torrent ont été délimitées dans un SIG sur la base des observations de terrain et des photos aériennes (fig. 5.9 et 5.10).

Les stocks indirects de matériaux mobilisables ont été définis à partir de la carte des événements sédimentaires selon l’approche décrite au point 2 (chap. 4.3), puis associés aux biefs correspondant (fig. 5.11).

L’estimation des stocks de sédiment mobilisables directs et indirects pour chaque bief des torrents de Lirec et Perrec est présentée en annexe I. Ils représentent les volumes de matériaux imputables à chaque bief. Les volumes totaux que cela représentent sont présentés plus en détails dans Mazotti et al. (2010). Ils sont résumés dans le tableau 5.1.

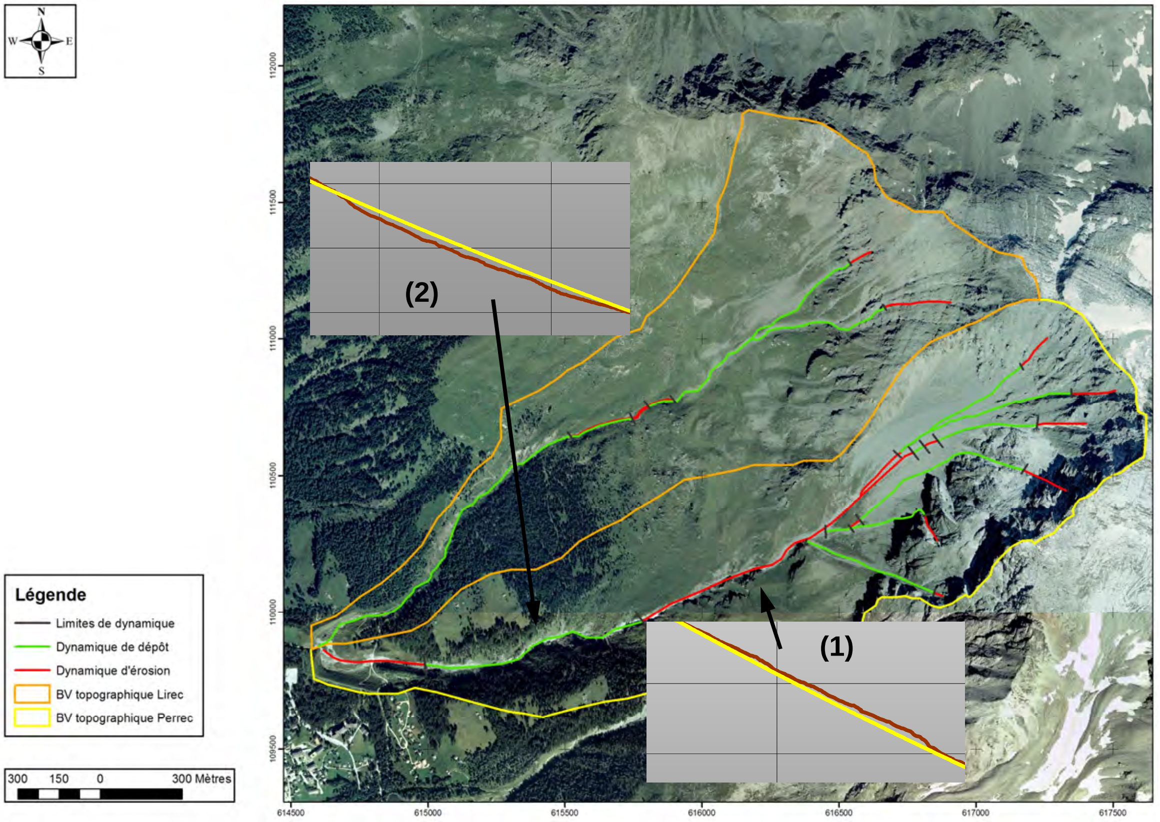

***Figure 5.5** : Résultat de l’estimation de la dynamique sédimentaire des torrents de Lirec et Perrec. Les zones d’érosion (exemple 1) sont représentées en rouge et les zones de dépôt en vert (exemple 2).*

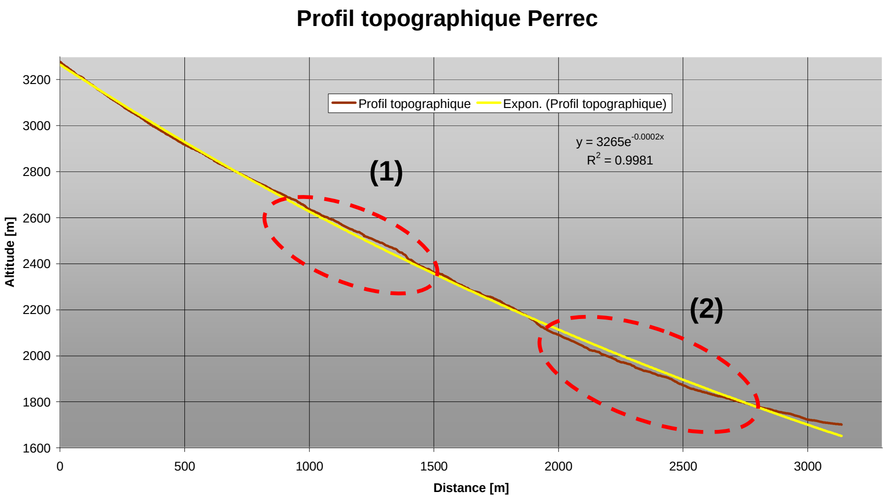

***Figure 5.6** : Profil topographique en long du torrent de Perrec en brun et le profil théorique obtenu avec une courbe exponentielle extrapolée sur le profil topographique en jaune. (1) Zones d'érosion, (2) zones de déposition.*

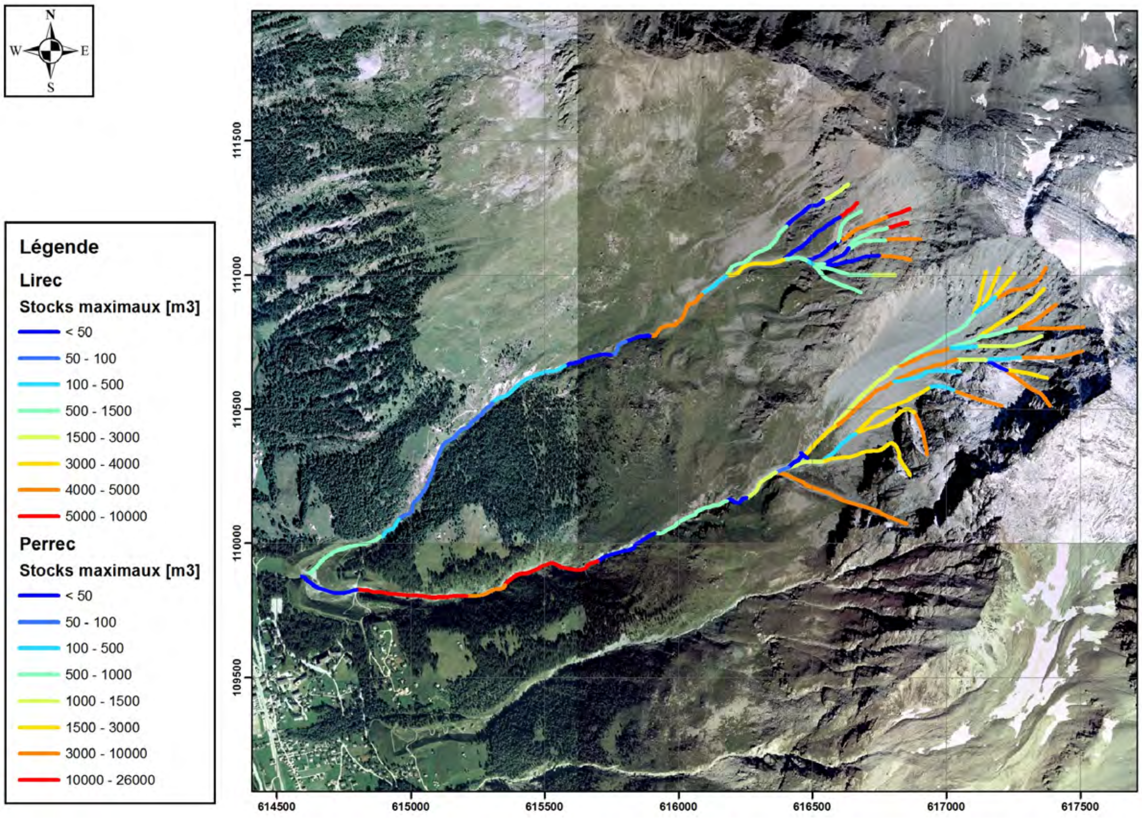

***Figure 5.7** : Volume de dépôt maximum pour chaque bief (Stock$_{max}$) calculé à partir de la différence d'altitude moyenne entre le profil théorique et réel et la largeur moyenne de chaque bief. La partie inférieure du Perrec montre des valeurs particulièrement importantes.*

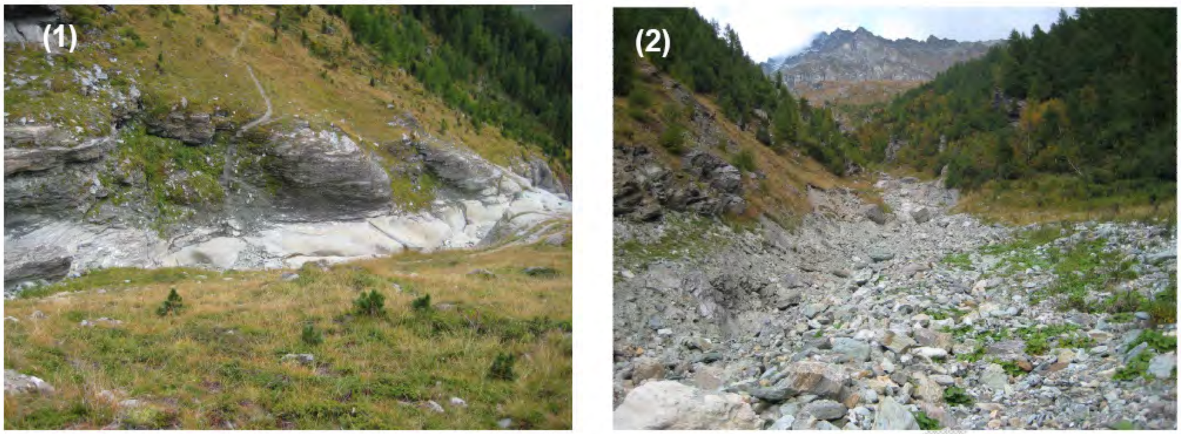

***Figure 5.8** : Vérification in-situ des zones d’érosion et dépôt déterminées à partir du profil en long dans le torrent du Perrec. (1) Zone d’érosion : profil topographique supérieur au profil d’équilibre ; le bedrock y est souvent affleurant (matériel mobilisable faible) et les dépôts sont sporadiques. (2) Zone de déposition : profil topographique inférieur au profil d’équilibre : présence de matériel remobilisé (charriages et dépôt de laves torrentielles).*

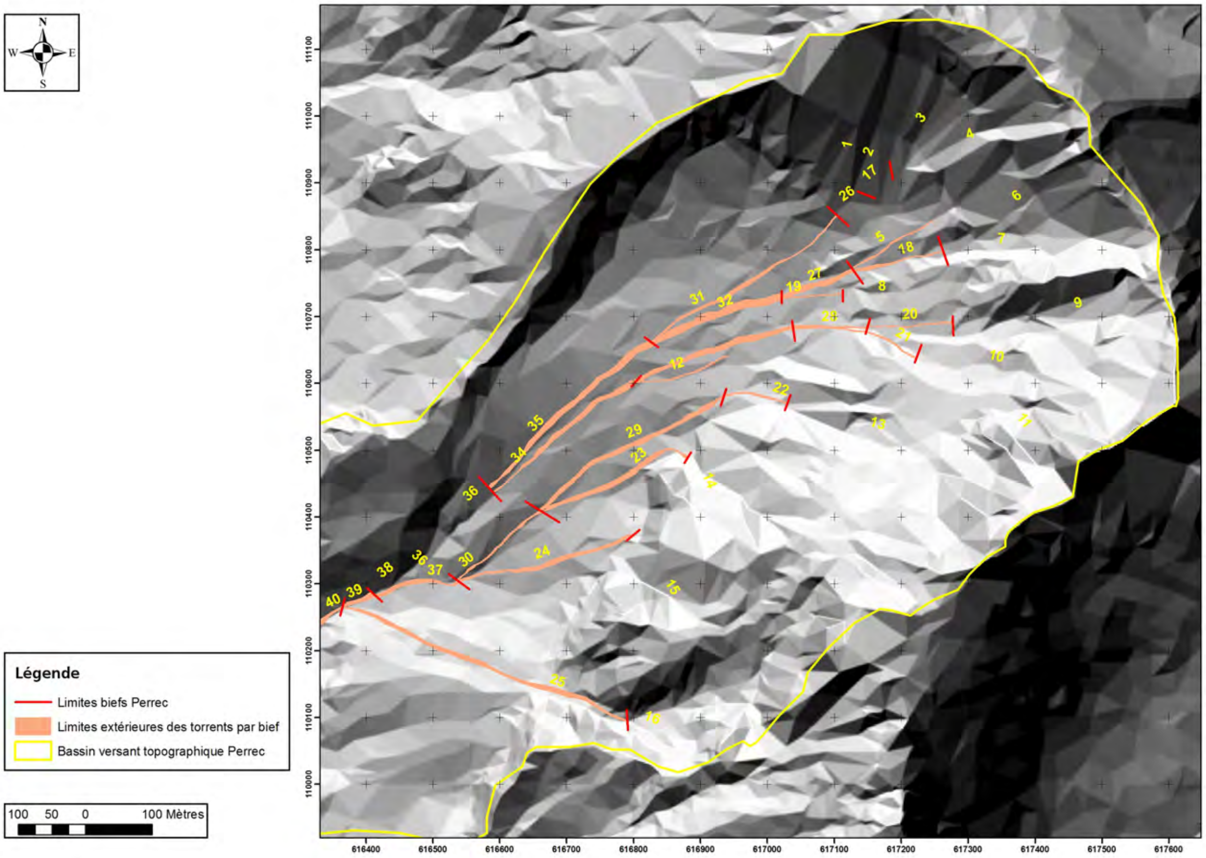

***Figure 5.9** : Partie sommitale du bassin versant de Perrec avant le « creusement » des torrents à l’aide de la méthode SLBL. Les polygones en rose illustrent la largeur maximale cartographiée des différents chenaux.*

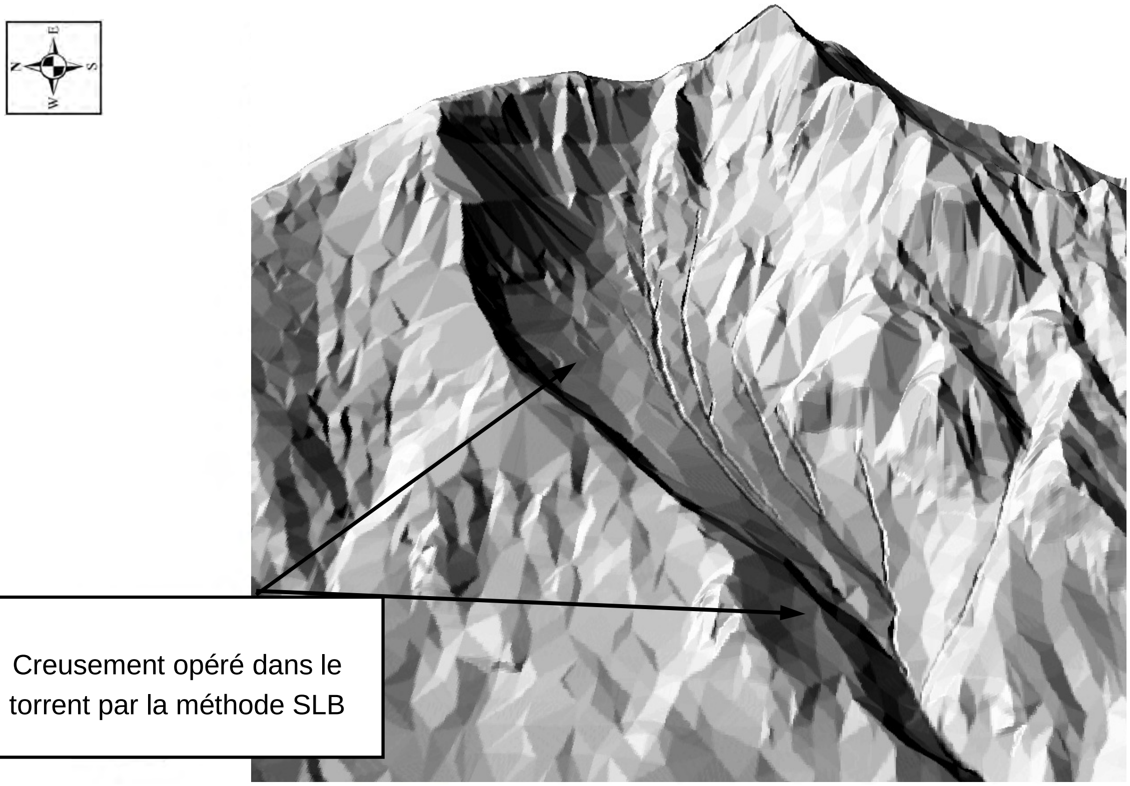

Creusement opéré dans le torrent par la méthode SLB

***Figure 5.10** : Relief ombragé du mnt après creusement opéré dans le torrent par la méthode SLBL permettant une estimation du stock maximum de sédiments mobilisable dans et à proximité du torrent (Stock$_{direct}$).*

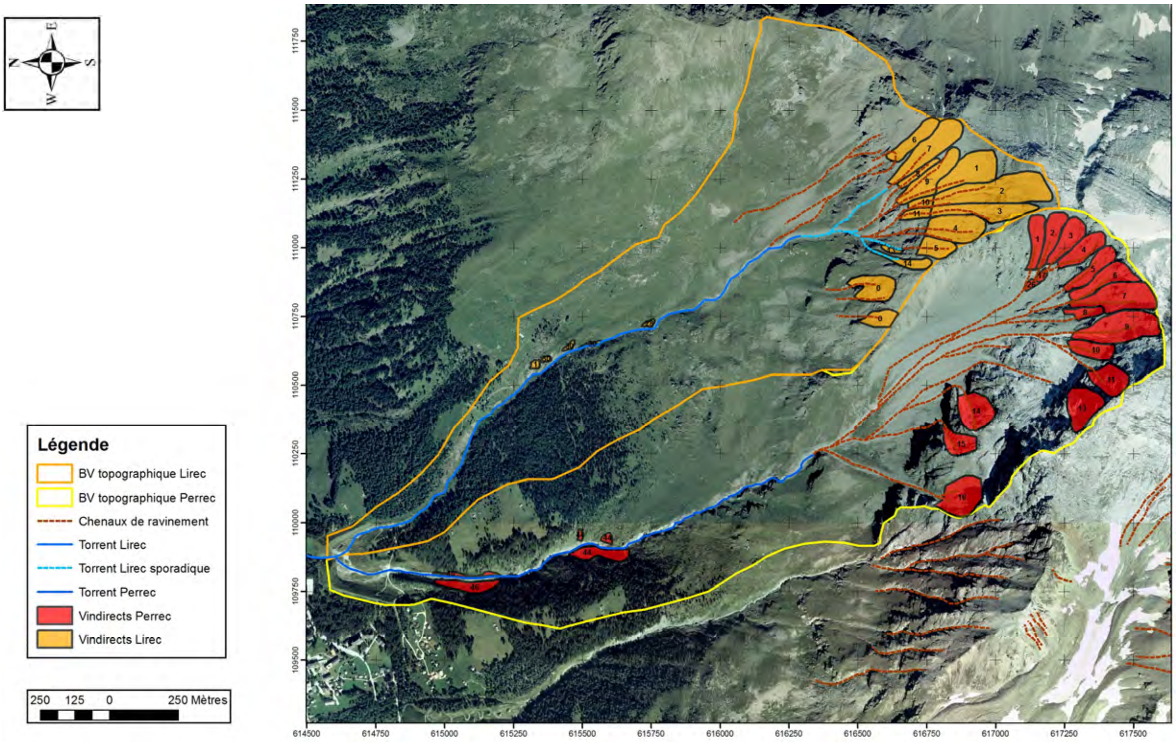

***Figure 5.11**: Localisation des zones d'érosion indirecte dans les bassins versants de Lirec et Perrec. Chaque numéro est associé à un polygone qui représente cette surface d'érosion.*

***Tableau 5.1**: stocks sédimentaires pouvant être mobilisés par les torrents pilotes sur le long terme.*

	Lirec (1.64 km^2)	**Perrec (1.84 km^2)**
Stock direct [m^3]	10’000	61’000
Stock indirect [m^3]	48’000	80’000
Total [m^3]	58’000	140’000

5.6 Estimation des temps de retour des événements

Les temps de retour des différentes intensités de précipitations et de laves torrentielles ont été déterminés à partir des archives d’événements (Evénements historiques du torrent du Pétérey, CREALP), du rapport sur les cartes de dangers du Val d’Anniviers (IDEALP, 2009), des données de précipitations de la station de Mottec (MétéoSuisse) et de l’ATLAS Hydrologique Suisse (2006).

5.6.1 Temps de retour des précipitations

A partir des précipitations mesurées à la station météorologique de Mottec de 1973 à 2007 (614025/111240, 1560 m, mesures journalières), il a été possible de calculer des intensités de pluie en fonction de temps de retour définis à 2, 5, 10, 20 et 50 ans (Hingray et al., 2009, cf. tableau 5.2).

***Tableau 5.2** : Intensités de pluie attendues pour des temps de retour de 2 à 50 ans.*

Temps de retour [an]	**Normal**	**2**	**5**	**10**	**20**	**50**
Intensité pluie à 24h [mm]	< 40.3	40.3 – 51.9	51.9 – 59.6	59.6 – 67.0	67.0 – 76.6	> 76.6

La figure 5.12 illustre les pluies maximales par année entre 1973 et 2007 à la station de Mottec avec les limites d’intensité de pluie en couleurs. Ces résultats sont visibles dans le tableau 5.4 et interprétés dans le tableau 5.3.

A partir du tableau 5.4, il a été possible d’estimer leur temps de retour respectif et ainsi de définir une fréquence d’occurrence pour chaque type d’évènement précipitations fréquentes, rares et extrêmes. Ainsi les temps de retour pour les précipitations fréquentes ont été fixés à 3 ans, pour les précipitations de type rares à 6 ans et les précipitations extrêmes à une tous les 100 ans (tab. 5.5).

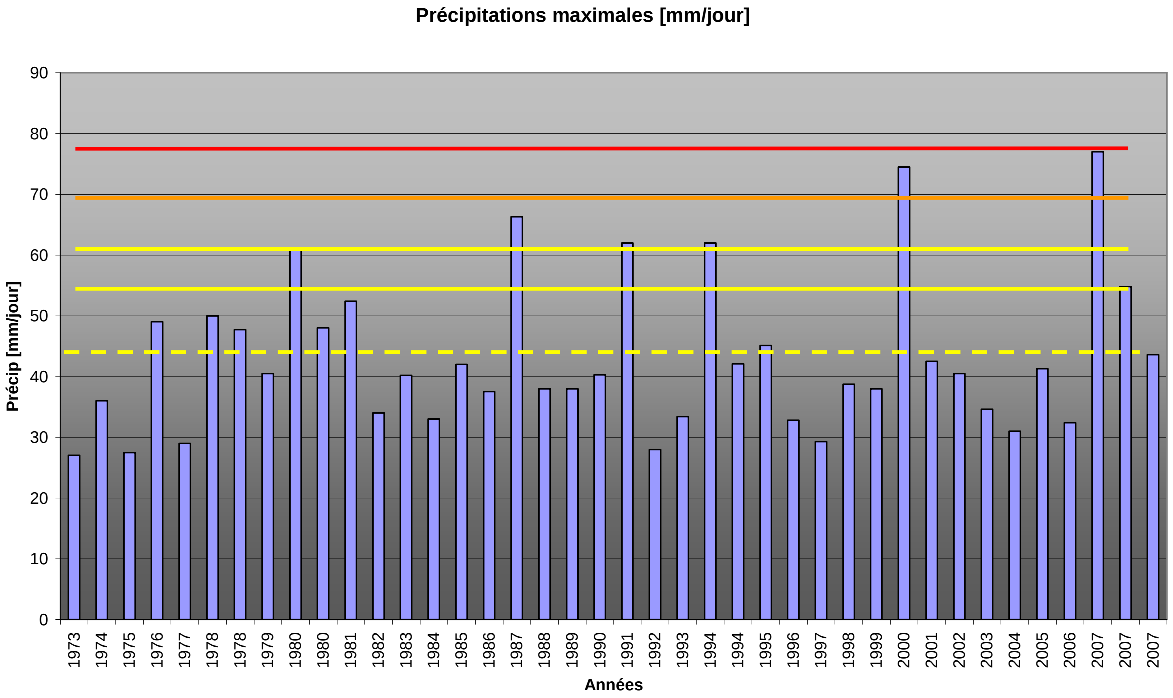

***Figure 5.12** : Illustration graphique des intensités de pluies maximales mesurées sur une année [$^{mm}/_{jour}$]. Lorsque plusieurs précipitations supérieures à la moyenne surviennent dans une même année, elles sont toutes indiquées sur le graphique. C'est le cas des années 1978, 1980, 1994 et 2007. Les différentes lignes représentent les seuils limites pour chacun des temps de retour (traits-tirés jaune = 2 ans trait rouge = >50).*

***Tableau 5.3**: Estimation et interprétation de la fréquence d'occurrence des différentes intensités de pluie.*

Intensité pluie à 24h [mm]	**Fréquence d'occurrence** $\frac{nombre\ d'\ occurrence}{nombre\ total\ d'\ année}$	**Interprétation**
40.3 – 51.9	11/34 = 0.35	Ce type d'année avec une intensité de pluie fréquente survient environ tous les 3 ans au minimum.
51.9 – 59.6	2/34 = 0.05	Ce cas de figure est spécial puisqu'une précipitation avec un temps de retour à priori plus petit a une *fréquence* d'occurrence plus faible que celle avec une plus forte intensité. Il en a été déduit que cette intensité limite n'avait pas de sens dans le cas de la région de Mottec. Il a donc été décidé de relier les intensités entre 51.9 et 67.0 pour obtenir une *fréquence* annuelle d'occurrence de 0.17, soit une pluie de cette intensité environ tous les 6 ans.
59.6 – 67.0	4/34 = 0.11	
67.0 – 76.6	1/34 = 0.02	Dans ces deux cas, il est difficile d'établir une réelle statistique pour des temps de retour élevé en fonction de la série temporelle de 37 années disponible. Toutefois, ce type de précipitation rare à extrême semble survenir environ tous les 50 ans.
> 76.6	1/34 = 0.02	

***Tableau 5.4** : Analyse du temps de retour des différentes intensités de précipitation. Les précipitations maximales sont prises en compte pour chaque année et comparées aux intensités de pluies du tableau 2-1. Il est ainsi possible d'en déduire une première approximation des temps de retour des événements normaux, fréquents, rares et extrêmes.*

Années	Mois	Jours	Précipitations maximales annuelles [mm/jour]	Types d'années
1973	Maximum annuel		27	normal
1974	Maximum annuel		36	normal
1975	Maximum annuel		27.5	normal
1976	4	23	49	2
1977	Maximum annuel		29	normal
1978	3	20	50	2
1978	8	7	47.7	2
1979	12	11	40.5	2
1980	2	4	60.8	10
1980	10	17	48	2
1981	3	31	52.4	5
1982	Maximum annuel		34	normal
1983	11	26	40.2	normal
1984	Maximum annuel		33	normal
1985	5	8	42	2
1986	Maximum annuel		37.5	normal
1987	10	11	66.3	10
1988	Maximum annuel		38	normal
1989	Maximum annuel		38	normal
1990	2	14	40.3	normal
1991	12	21	62	10
1992	Maximum annuel		28	normal
1993	Maximum annuel		33.4	normal
1994	5	18	62	10
1994	11	5	42.1	2
1995	5	30	45.1	2
1996	Maximum annuel		32.8	normal
1997	Maximum annuel		29.3	normal
1998	Maximum annuel		38.7	normal
1999	Maximum annuel		38	normal
2000	10	14	74.5	20
2001	2	3	42.5	2
2002	11	16	40.5	2
2003	Maximum annuel		34.6	normal
2004	Maximum annuel		31	normal
2005	8	2	41.3	2
2006	Maximum annuel		32.4	normal
2007	5	27	77	> 50
2007	8	8	54.8	5
2007	8	29	43.6	2

Tableau 5.5 *: Temps de retour des types de précipitations prédéfinis par rapport aux intensités de pluie.*

Classe d'Intensité	**Fréquent**	**Rare**	**Extrême**
Temps de retour [an]	**3**	**6 – 10**	**> 50**
Intensité de pluie à 24h [mm]	< 40.3	40.3 – 67.0	> 67.0

5.6.2 Temps de retour des laves torrentielles

Le cadastre des événements de la commune d'Ayer (Ayer, 2003) indique un volume de matériaux déposé dans le dépotoir commun des torrents de Lirec et Perrec de 4000 m^3 entre 1990 et 2003 (300 m^3/an). Cependant, il ne comporte pas de détail sur la fréquence et l'intensité de ces événements (une partie peut être attribuée aux avalanches ?). Ce manque d'information signifie sans doute qu'aucun événement important ne s'est produit durant cette période. A partir des connaissances actuelles, la moyenne annuelle semblerait se situer plutôt autour de 800 -1000 m^3/an (comm. pers. E. Bardou, CREALP). D'après les observations de terrain (stocks sédimentaires disponibles, état du torrent, traces d'évènements), le torrent de Perrec semble être au moins la source de 60 % à 80 % du matériel transporté jusqu'au dépotoir. Devant ce peu d'informations, les fréquences d'événements laves torrentielles ont été déterminés sur la base des données statistiques des apports de laves torrentielles dans le torrent voisin du Pétérey (Ayer, 2003). Des événements sont observés quasiment chaque année dans ce torrent avec un volume moyen transporté dans le dépotoir de 4000 m^3/an (tout processus confondus) pour les 30 dernières années. Les évènements rares surviennent chaque 20 ans en moyenne avec des apports annuels maximum observés de 13'000 m^3. Les apports annuels des torrents de Perrec et Lirec sont 5 fois moins importants. En admettant l'hypothèse que leur mise en charge est plus longue, le temps de retour des laves torrentielles au Lirec et Perrec est proportionnellement plus espacé.

Tableau 5.6 *: Temps de retour supposés des intensités de laves torrentielles dans les torrents de Lirec et Perrec basés sur les données statistiques du torrent voisin du Pétérey.*

Classe d'Intensité	**Fréquent**	**Rare**	**Extrême**
Temps de retour [an] Perrec	**5**	**30**	**100**
Intensité moyenne [m^3]	**750**	**10000**	**25000**
Temps de retour [an] Lirec	**8**	**50**	**170**
Intensité moyenne [m^3]	**500**	**7500**	**17000**

Ainsi, les temps de retour du torrent du Perrec sont supposés de 5 ans pour une lave torrentielle de type fréquent, de 30 ans pour une de type rare et 100 ans pour une lave torrentielle d'intensité extrême. Le torrent du Lirec ne représentant en moyenne que 30 % des apports dans le dépotoir, ses temps de retour sont aussi ajustés (tab. 5.6). Les intensités moyennes de laves torrentielles pour le torrent de Perrec ont été estimées afin que la somme des volumes représente 70'000 m^3 sur une période de 100 ans, c.-à-d. 700 m^3 an^{-1} (tab. 5.7). Pour le torrent du Lirec, le volume est de 31'000 m^3 en 100 ans (tab. 5.8).

***Tableau 5.7** : Exemple d'estimation des volumes moyens par type de laves torrentielles pour le torrent de Perrec pour 100 ans.*

Type de Laves torrentielles	Nombre Moyen d'événements	volume	total
fréquente	20	750	15000
rare	3	10000	30000
extrême	1	25000	25000
			70'000

***Tableau 5.8** : Exemple d'estimation des volumes moyens par type de laves torrentielles pour le torrent de Lirec sur 100 ans.*

Type de Laves torrentielles	Nombre Moyen d'événements	volume	total
fréquente	12	500	6000
rare	2	7500	15000
extrême	0.59	17000	10000
			31'000

5.7 Paramètres de simulation de la cascade sédimentaire

Les données d'entrée nécessaires à l'exécution du bilan sédimentaire à l'échelle du bief sont présentées dans le tableau en annexe, laquelle comporte les valeurs et volumes spécifiques utilisées dans le cadre de cette étude.

Les paramètres de flux sédimentaire des stocks indirects (**k_{ind}**) représentent la hauteur d'érosion moyenne de ce stock. Ils ont été repris des taux d'érosion estimés dans le bassin versant de Zinal dans le rapport de Loye et al. (2009) (cf. p. 24-25 et tableau 16, p. 31). Ils sont résumés dans le tableau 5.9.

Tableau 5.9 : taux d'érosion estimés dans le bassin versant de Zinal dans le rapport de Loye et al. 2009 (cf. p. 24-25 et tableau 16, p. 31) et utilisés comme paramètres k_{indt} du flux sédimentaire des stocks indirects.

Evénements Précipitation	k_{ind}
fréquente	**0.024 mm/an**
rare	**0.7 mm/an**
extrême	**3 mm/an**

Le flux de sédiment transporté d'un bief à l'autre est contrôlé d'une part par l'indice d'alluvionnement (tab. 5.11) et de l'autre part par la vitesse d'érosion du stock contenu dans le bief (**k_{dir}**). Ils ont été définis compte tenu des observations de terrain et du taux de remplissage / vidange des biefs (tab. 5.10).

Tableau 5.10 : Paramètre k_{dir} défini à partir d'observations de terrain et calibré pour les torrents.

Evénements Précipitations	k_{dir}	Remarques
fréquente	**0.001 m/ évènement**	La hauteur d'eau dans le torrent ne permet pas un charriage significatif
rare	**0.1 m/ évènement**	La hauteur d'eau dans le torrent permet un charriage important
extrême	**0.9 m/ évènement**	La hauteur d'eau dans le torrent permet une vidange importante des biefs

Tableau 5.11 : Indice d'alluvionnement appliqué aux torrents du Perrec et de Lirec

I_{alluv}	**0 – 0.3**	**0.3 – 0.5**	**0.5 – 0.8**	**0.8 – 1**	**> 1**
Proportion de matériel déposé selon la variation de pente et largeur	55%	35%	15%	5%	0
I_{alluv}	**$0° < \Delta A_z < 20°$**		**$20° < \Delta A_z < 60°$**		**$\Delta A_z > 60°$**
Proportion de matériel déposé selon le changement de direction	+ 0%		+ 5%		+15%

Les paramètres déterminant le flux de matériaux transporté par des laves torrentielles dans le dépotoir ont été calibrés de façon à obtenir les intensités décrites dans les tableaux 5.7 et 5.8. Ces volumes représentent la somme des quantités (en % du volume direct et indirect de sédiments mobilisables par bief) prélevés dans chaque bief et propagés intégralement jusqu'à l'exutoire (cf. Mazotti et al. 2010). Lors de laves torrentielles, l'apport indirect est semblable à l'apport par les précipitations. Et la proportion de matériel directement purgé dans chaque bief est proportionnelle au remplissage de chaque bief (mais ne peut pas dépasser 100%).

Pour le Perrec :

Evénements Laves Torrentielles	c_{mob}	c_{dir}	c_{ind}
fréquente	0.65% par évènement	$\min\left[\frac{Stock_{direct}}{Stock_{max}},1\right]$	$c_{ind} = k_{ind}$
rares	8.8% par évènement		
extrêmes	22% par évènement		

Pour le Lirec :

Evénements Laves Torrentielles	c_{mob}	c_{dir}	c_{ind}
fréquente	0.93 % par évènement	$\min\left[\frac{Stock_{direct}}{Stock_{max}},1\right]$	$c_{ind} = k_{ind}$
rares	13.75% par évènement		
extrêmes	31% par évènement		

Le pas de temps (Δt) de la cascade sédimentaire a été fixé au mois. Chaque mois, la cascade sédimentaire est exécutée suivant un scénario d'événements défini aléatoirement selon la fréquence d'occurrence des événements précipitations et laves torrentielles. A chaque pas de temps, les simulations ont été effectuées 500 fois sur une période de 100 ans. Ce grand nombre de simulation permet ainsi de s'approcher des valeurs moyennes de matériaux attendu dans le dépotoir (cf. chap. 9.1).

Le volume simulant l'occurrence d'un événement exceptionnel a été fixé à 1% du stock sédimentaire global de chaque bassin versant. Ce volume extraordinaire a été introduit dans la cascade sédimentaire à la confluence des petits torrents amont de chaque torrent (tab. 5.12).

***Tableau 5.12** : Simulation d'un évènement exceptionnel à partir d'un volume supplémentaire introduit à la confluence du torrent et défini par le temps de retour des précipitations extrêmes.*

Torrent	Volume extraordinaire (1% du stock global)	introduit dans bief n°
Perrec	0.01 * 2'250'000 = 22'500 m^3	39
Lirec	0.01 * 1'850'000 = 18'500 m^3	23

6 Budget sédimentaire global

Une quantification des volumes de sédiments accumulés durant l'Holocène dans les bassins versants de la région de Zinal permet une estimation (ordre de grandeur) à long terme des taux d'érosion rencontrés dans la vallée. Cette approche globale d'estimation des stocks sédimentaires consiste à évaluer la quantité de sédiments accumulés dans le fond de vallée depuis le retrait glaciaire. Pour obtenir ce résultat, nous partons du principe que la section moyenne de la vallée est parabolique. L'origine de la parabole est au point bas (fig. 6.1). Si A est la surface sous la parabole, alors la section moyenne de la vallée est donnée par :

$$S = 2\left(\frac{w}{2}z_0 - A\right) \qquad (5.1)$$

Sachant que w est la largeur moyenne de la vallée, z_0 la profondeur moyenne. En intégrant la parabole on obtient :

$$S = \frac{2}{3}wz_0 \qquad (5.2)$$

Le volume est obtenu en multipliant la longueur du tronçon (L) par la section moyenne (S) :

$$V = L\frac{2}{3}wz_0 = L \times S \qquad (5.3)$$

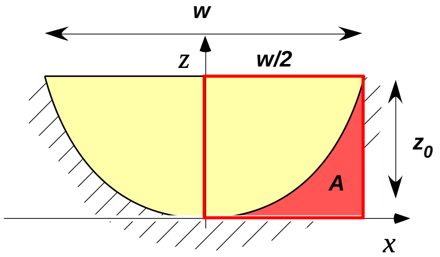

Figure 6.1 : La demi-section de la vallée vaut la surface du carré rouge moins la zone rouge.

La largeur moyenne w est obtenue sur SIG et la profondeur déduite des données de forage. (CREALP) Cette dernière a été estimée entre 80 et 100 mètres. Cependant, les forages effectués dans la plaine de Zinal n'ont pas atteint le fond à 80 mètres de profondeur. La longueur est prise en compte depuis le fond du Val d'Ar Pitetta jusqu'à la sortie de Zinal, ce qui représente environ 6 km, divisés en 7 sections de largeur plus ou moins homogène (fig. 6.3). La période d'accumulation s'étend depuis la fin du Dryas récent (~9400 BP) (fig. 6.2). Le remplissage de la vallée a été estimé entre 85'000'000 m^3 et 107'000'000 m^3 (tab. 6.1). En fonction d'une période de 9'500 ans d'accumulation, le volume annuel est compris entre 9'000 et 11'500 m^3an^{-1}. Rapporté à la surface contributive totale (~83 km^2), l'érosion annuelle moyenne est de 0.07 – 0.09 mm par an[1]. En ne considérant seulement le volume accumulé par les torrents de Lirec, Perrec, Bondes, Pétérey et Tracuit (7.38 km^2) dans la section 1, l'érosion annuelle moyenne est de 0.25 – 0.3 mm par an.

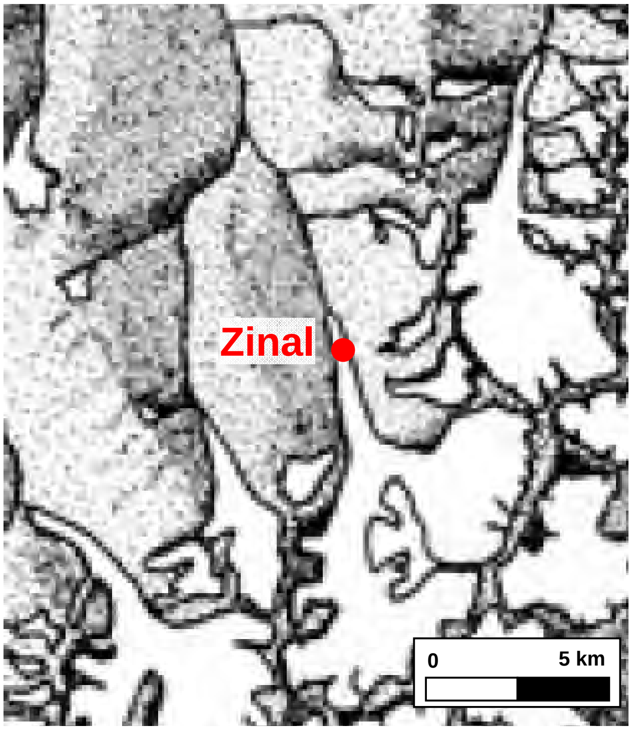

***Figure 6.2** : Extension du glacier de Zinal durant le Dryas récent. La couverture glaciaire recouvre encore tout le plat de la Lé jusqu'en aval du village (d'après Burri 1990, tiré de:Schweizerische Gesellschaft für Ur- und Frühgeschichte 1993.*

Tableau 6.1 : volumes accumulés dans le plateau de Zinal sur une période moyenne de 10'000 ans.

No section	Largeur moyenne [m]	Longueur [m]	Volume accumulé à 80 m de profondeur [m^3]	Volume accumulé à 100 m de profondeur [m^3]
1	330	1'500	26'400'000	33'000'000
2	437	1'100	25'637'340	32'046'670
3	350	380	7'093'340	8'866'670
4	240	650	8'320'000	10'400'000
5	130	560	3'882'670	4'853'340
6	60	540	1'728'000	2'160'000
7	150	1'600	12'800'000	16'000'000
Total			**85'860'000**	**107'325'000**

---

[1] En admettant une densité sèche de 1800 kg m^{-3} (cf. Loye et al. 2009).

Les stocks sédimentaires globaux contenus dans chaque bassin versant en rive droite de la vallée sont estimés à partir d'une couverture quaternaire uniforme. L'épaisseur moyenne du « sol quaternaire » a été fixée à 1 m, car selon les observations de terrain, il est quasiment inexistant au-dessus de 2'000 mètres, et en-dessous, son épaisseur[2] varie entre 1 et 2 m. Les surfaces se basent sur la carte des phénomènes (fig. 5.3). Ces volumes sont résumés dans le tableau 6.2. Les volumes très importants estimés pour le Val d'Ar Pitetta sont dus aux imposantes moraines et éboulis sur glaciers présents dans ce secteur. Les formes périglaciaires, glaciaires et éboulis ont été comptabilisés dans les « stocks sédimentaires ».

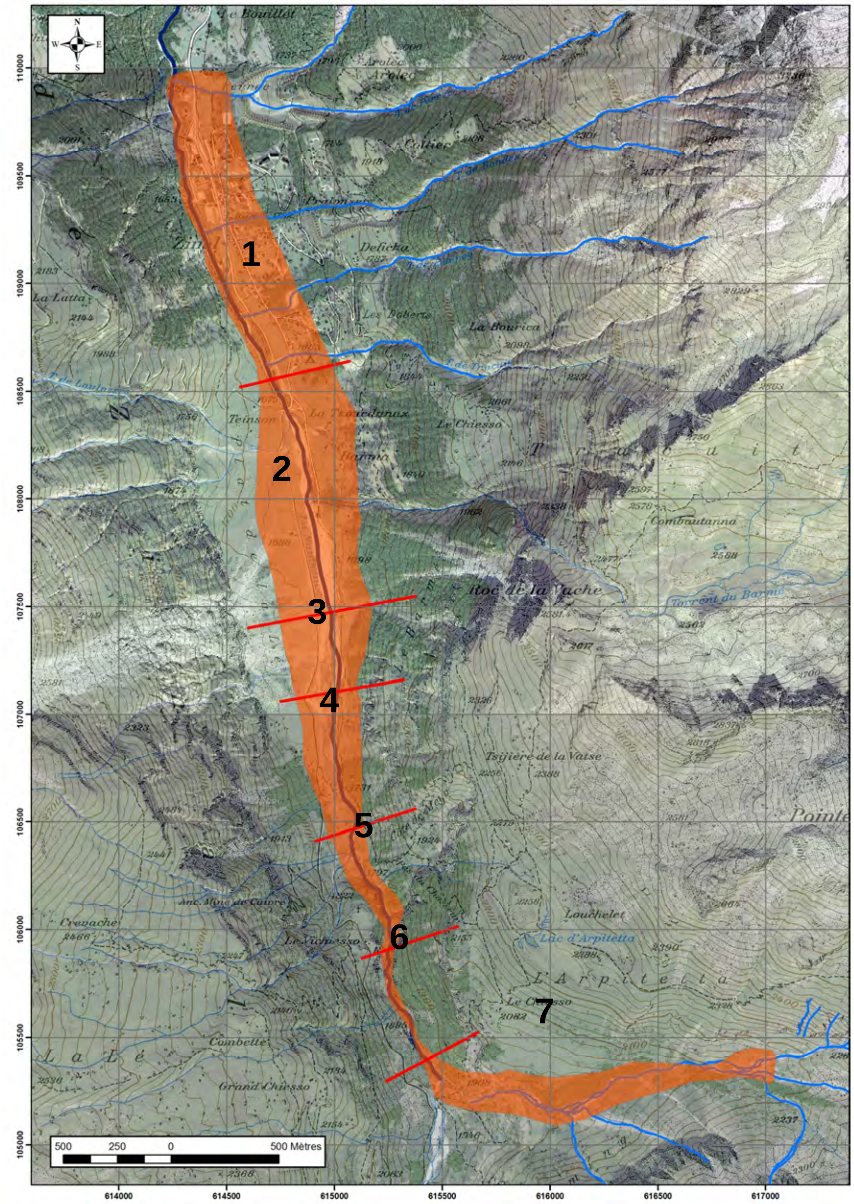

Figure 6.3 : *Sections de la vallée définies dans le tableau 5-1.*

---

[2] Cette estimation ne prend pas en compte l'accumulation quaternaire dans la plaine de Zinal qui a été estimée auparavant dans ce chapitre.

***Tableau 6.2** : Stocks sédimentaires globaux des différents bassins versant en rive droite de la vallée de Zinal. L’érosion moyenne est obtenue pour une période prospective de 1'000 ans. (Les taux d’érosion moyen sont obtenus sur la base d’une densité sèche de 1800 kg* m^{-3}*.)*

Bassin versant	**Volumes stocks sédimentaires [m^3]**	**Volumes sol quaternaire (~1m) [m^3]**	**Total [m^3]**	**m^3/an**	**Surface (km^2)**	**mm/an**
LIREC	220’000	1'600’000	**1'820’000**	1’820	1.64	**0.72**
PERREC	450’000	1’800’000	**2'250’000**	2’250	1.84	**0.79**
BONDES	100’000	500’000	**600’000**	600	1.17	**0.33**
PETEREY	840’000[3]	1'000’000	**1'840’000**	1’840	1.3	**0.92**
TRACUIT	1’500’000	1'900’000	**3'400’000**	3’400	2.01	**1.1**
AR PITETTA	36'000’000	6'500’000	**42'500’000**	42’500	19.85	**1.4**
Totaux	39’610’000	13’300’000	**52’410’000**	52’410	27.81	**1.23**

Loye et al. (2009) indiquent des taux d’érosion moyen sur quelques autres bassins de l’ordre de 0.70 mm an^{-1}. Les valeurs obtenues pour chaque bassin versant à partir des stocks sédimentaires globaux sont dans cet ordre de grandeur. En conséquence, cela correspondrait à une purge totale des bassins versants sur une période de 1’000 ans.

En considérant une période de 100 ans, les taux d’érosion sont dans l’ordre de grandeur du cm an^{-1}. A l’exception d’Ar Pitetta, si les bassins versants déversaient 1% de leur stock chaque année (et ainsi se vidaient complètement de leur stock en un siècle), cela représenterait un volume de 100'000 m^3 an^{-1} au total. Une telle intensité est cependant très improbable. Le volume total de matériaux charrié par les torrents en rive droite récence dans Loye et al. (2009) se situent entre 8’350 m^3 an^{-1} et 36’700 m^3 an^{-1}. Les auteurs de ce rapport supposent qu’au maximum 10’000 – 30’000 m^3 par an peuvent être produits en moyenne dans les torrents de Zinal sur une période de 100 ans.

Les ordres de grandeur par bassin versant des volumes maximaux mobilisables lors d’événements extrêmes obtenus à l’aide des formules empiriques de Kronfelner-Kraus (1984) et de Rickenmann (1995) sont présentés dans le tableau 6.5. Les études des torrents de Lirec et Perrec menées lors de ce projet montre une surestimation des volumes par ces formules. En conséquence, Rickenmann 95 et Kraus 84 n’ont pas été retenus pour le modèle.

---

[3] Volumes du glacier couvert Bonnard obtenus à partir du rapport Favre-Bulle et al., 2009 (CREALP).

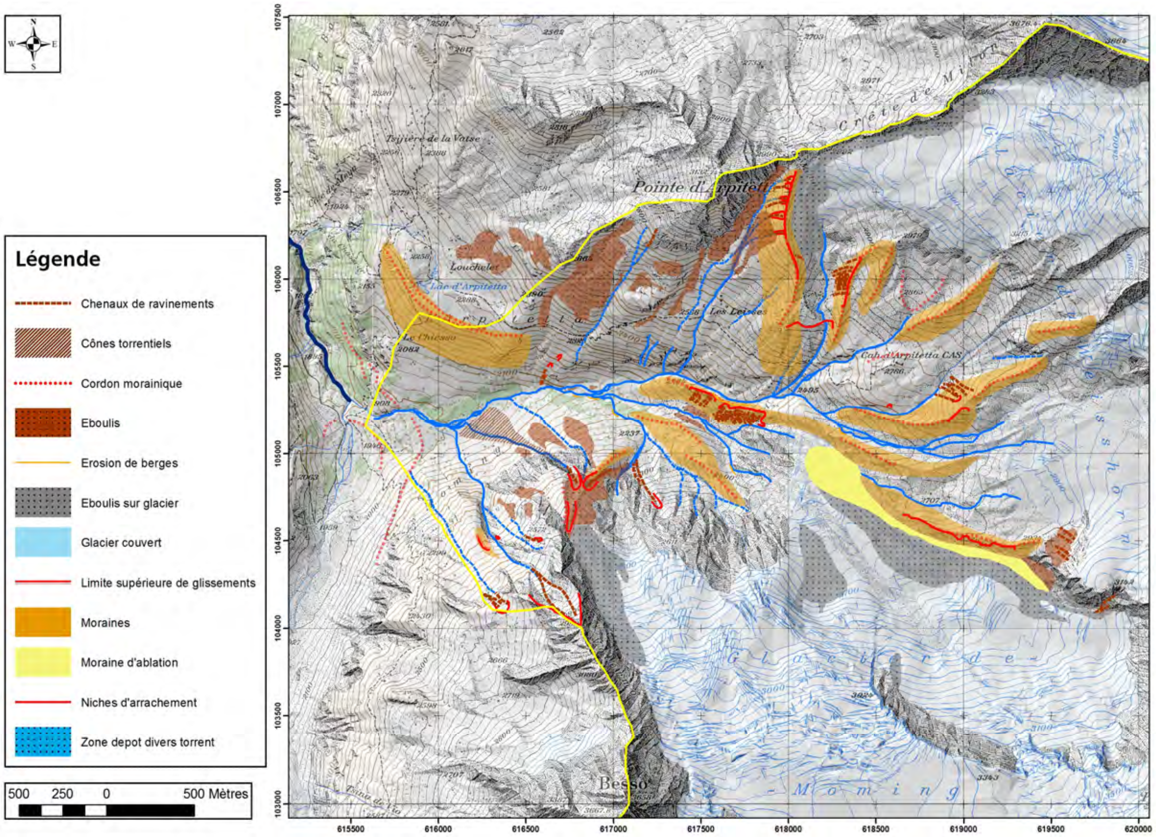

Figure 6.4 : Carte des phénomènes obtenue à partir des relevés de terrain et les données SIG dans le Val D'Ar Pitetta. La carte des phénomènes concernant les autres bassins versants est présentée à la figure 5.3.

***Tableau 6.5** : Stocks sédimentaires globaux définis par les formules de Kronfelner-Kraus et Rickenmann. Les différences correspondent au pourcentage de volumes estimés dans cette étude, lesquelles différences sont probablement dues à l'effet de la dynamique locale. L'estimation des stocks sédimentaires globaux proviennent de Mazotti et al. (2010) et correspondent aux tableaux de données en annexe.*

Bassins versant	**V_{max} événementiel Kronfelner-Kraus 84 [m^3]**	**V_{max} événementiel Rickenmann 95 [m^3]**	**Estimations des stocks sédimentaires globaux (Mazotti et al. 2010) [m^3]**
Lirec	148'200 (+150%)	140'000 (+144%)	57'300
Perrec	182'200 (+30%)	155'000 (+10%)	140'500
Bondes	58'500	135'000	
Pétérey	67'600	132'000	
Tracuit	104'900	156'000	
Total	**413'200**	**718'000**	

7 Bilans sédimentaires obtenus par simulations

7.1 Occurrence des évènements dans une série temporelle

La variation du nombre d'événements générés aléatoirement à partir de leur temps de retour entre les 500 simulations des séries temporelles est illustrée de façon statistique dans les boxplots de la figure 7.1. L'indice correspond aux évènements simulés (chap. 4.5) : précipitations fréquentes (1), rare (2) et extrêmes (3), laves torrentielles fréquentes (4), rares (5) et extrêmes (6). D'une simulation à l'autre, le nombre de mois rencontrant des précipitations et laves torrentielles, même sur un échantillon de 1'200 mois (100 ans), peut varier énormément, impliquant un apport sédimentaire très différent dans le dépotoir.

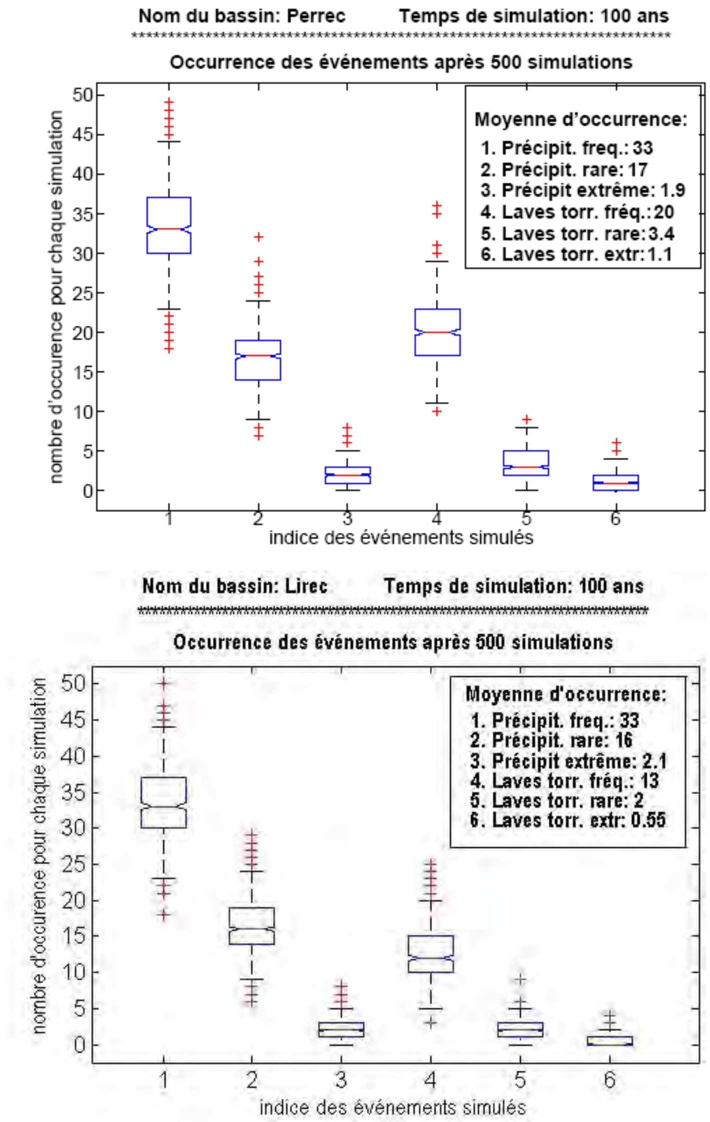

Figure 7.1 : *Boxplot illustrant de façon statistique le nombre de précipitations et laves torrentielles présentes lors des simulations (Trait rouge = médiane, box bleu = 25ème et 75ème percentile, croix rouge (extrémum) = 1.5 fois la valeur des quartiles). Le nombre d'évènements sur 100 ans peut varier grandement d'une simulation à l'autre.*

7.2 Simulation avec stocks finis

Les volumes accumulés dans le dépotoir après chaque simulation (une série temporelle de 100 ans), en supposant que l'apport sédimentaire indirect n'est pas réalimenté et diminue avec le temps, sont illustrés dans la figure 7.2. Pour chaque mois, un bilan statistique de toutes les simulations est effectué. Le volume moyen de toutes les simulations avec écart-type (1) accumulé après chaque mois dans le dépotoir est illustré dans la figure 7.3. Il est extrait des événements d'une série temporelle prise au hasard. D'un mois à l'autre, selon les occurrences d'évènements de la série temporelle générée, de grand écart de volumes sont simulés dans le dépotoir, respectant la dynamique irrégulière et ponctuée de pics important de flux de matériaux.

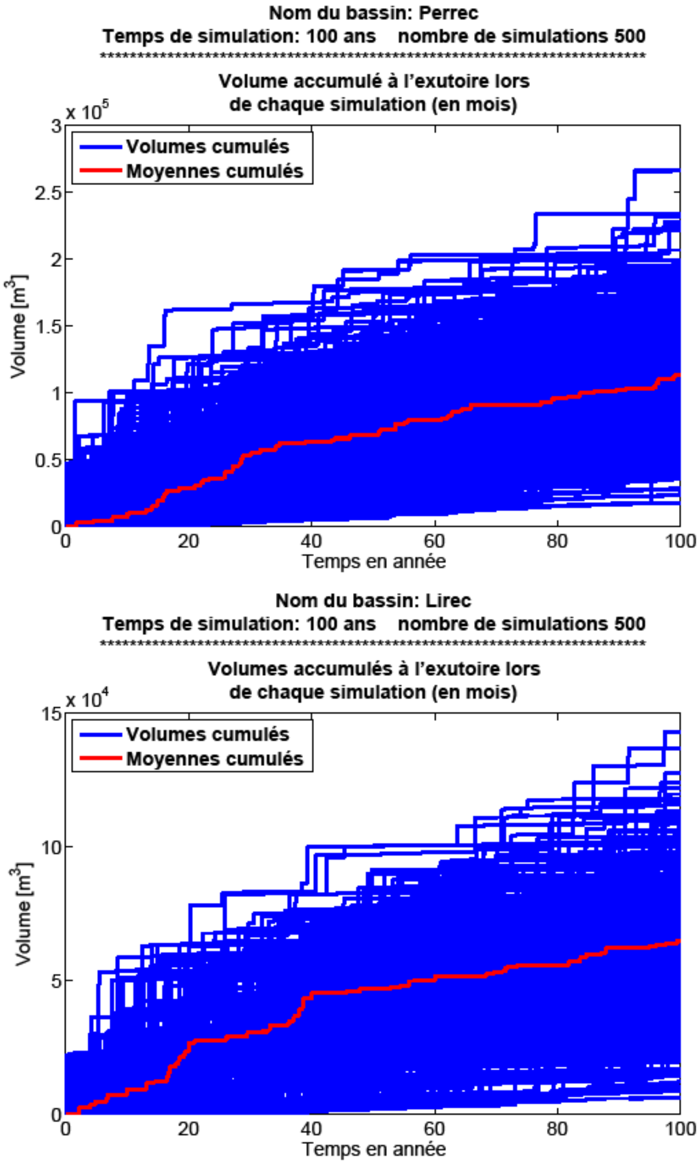

Figure 7.2 : *Résultats des 500 simulations de l'apport de matériaux cumulé à l'exutoire selon une série d'évènements définie sur 100 ans. Torrent du Perrec (haut): volume minimum = 17'600 m^3; moyenne = 113'000 m^3 ; maximum = 266'000 m^3. Torrent de Lirec (bas): volume minimum = 6'100 m^3; moyen = 65'000 m^3 ; maximum = 143'000 m^3.*

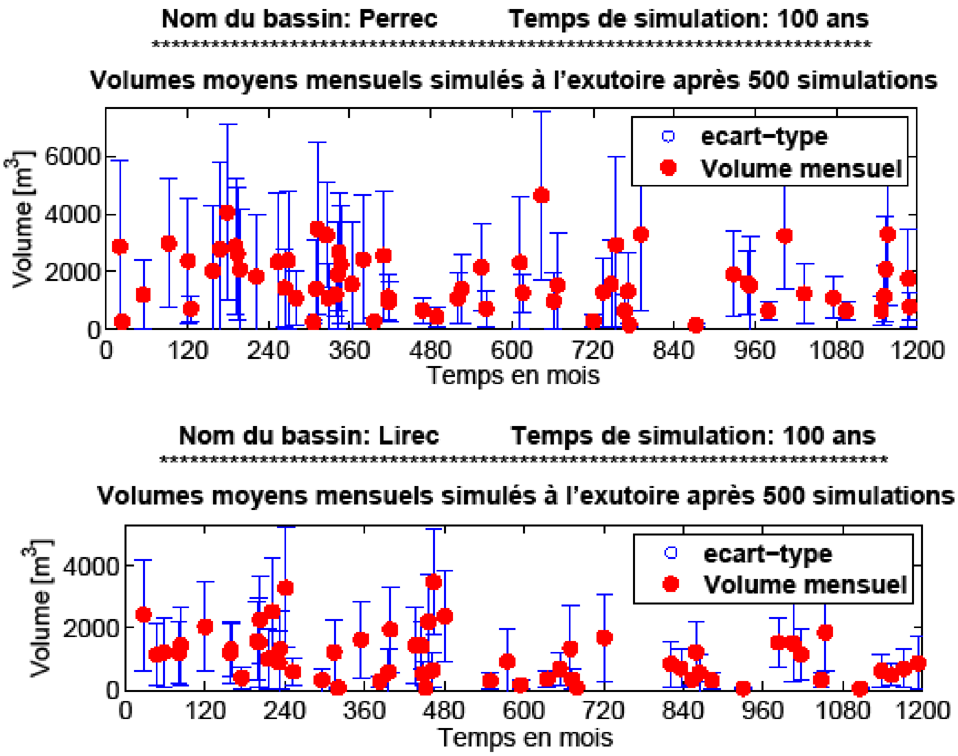

***Figure 7.3** : Volumes accumulés à l'exutoire pour le torrent de Perrec (haut) et Lirec (bas), extrait d'une simulation (une série temporelle). Les volumes correspondent à la quantité moyenne (donnés avec leur écart-type) de 500 simulations. Ils diminuent avec le temps, du fait que les stocks diminuent.*

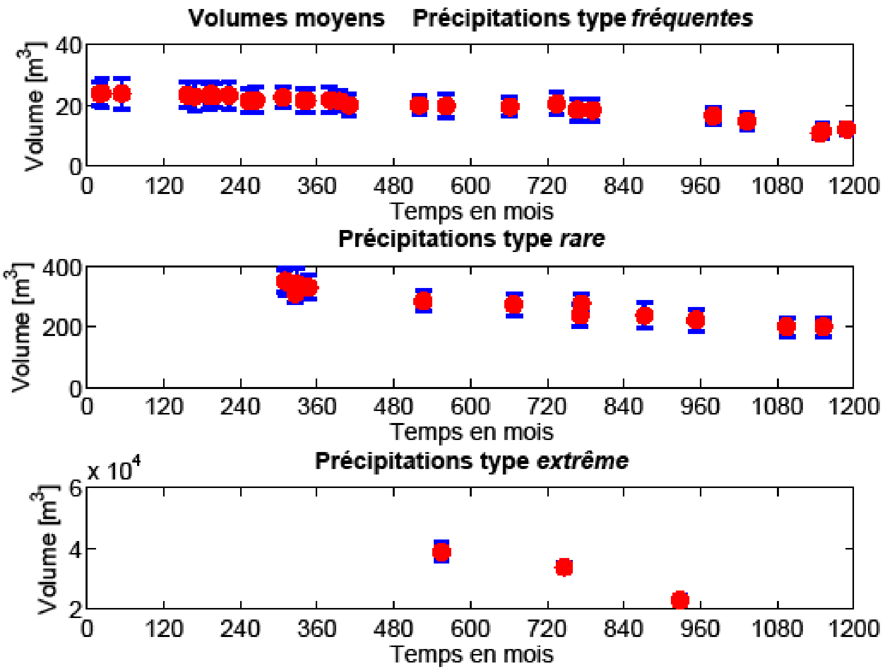

***Figure 7.4** : Exemple d'une simulation montrant les volumes (avec écart-type calculé sur la moyenne de 500 simulations) de matériaux apportés à l'exutoire par les précipitations pour le torrent de Perrec. Une pluie fréquente apporte en moyenne 25 m^3 ; une pluie rare représente un charriage de 375 m^3, un événement extrême 47'500 m^3 dans le dépotoir (y.c. les 25'000 m^3 des événements extraordinaires). Ils diminuent avec le temps, du fait que les stocks diminuent. Le volume pour les précipitations extrêmes est de l'ordre 10^4.*

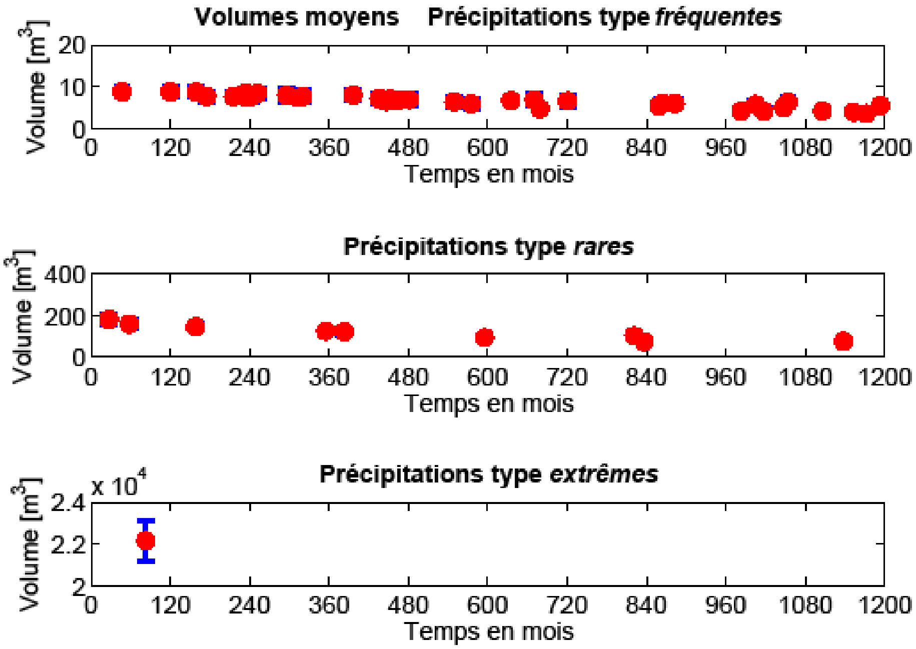

***Figure 7.5** : Extrait d'une série temporelle illustrant les volumes (avec écart-type calculé sur la moyenne de 500 simulations) de matériaux apportés à l'exutoire par les précipitations pour le torrent de Lirec. Une pluie fréquente apporte en moyenne 9 m^3 ; une pluie rare représente un charriage de 150 m^3, un événement extrême 25'000 m^3 dans le dépotoir (y.c les 18'300 m^3 de l'événement extraordinaire). Ils diminuent avec le temps, du fait que les stocks diminuent. Le volume pour les précipitations extrêmes est de l'ordre 10^4.*

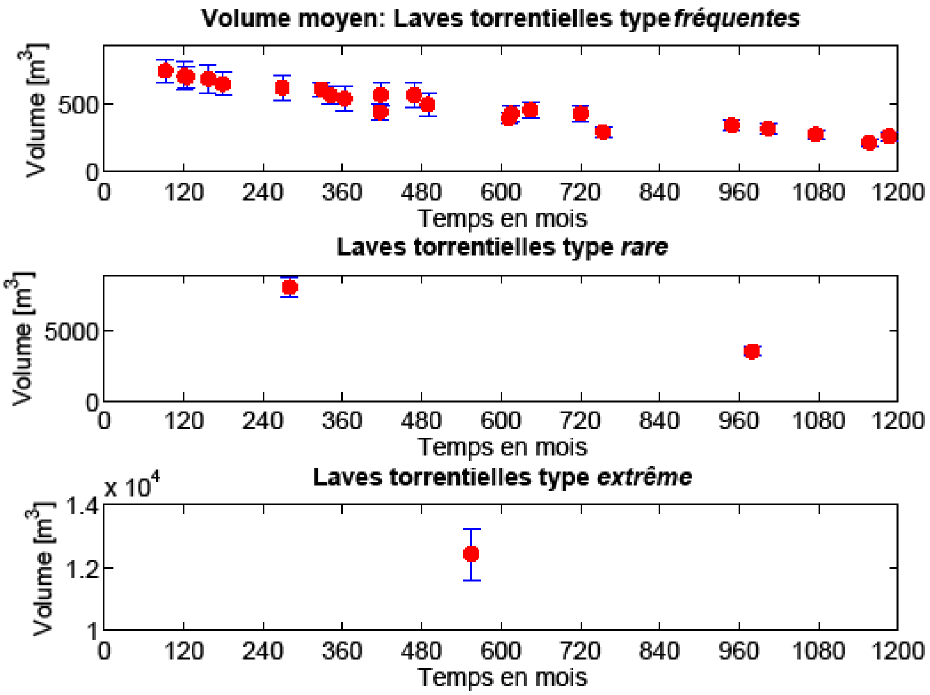

***Figure 7.6** : Extrait d'une simulation montrant les volumes (avec écart-type calculé sur la moyenne de 500 simulations) de matériaux apportés à l'exutoire par les laves torrentielles dans le torrent du Perrec. Dans les premières années de simulation, ils correspondent aux volumes définits dans les tableaux chapitre 5, puis diminuent à cause que les stocks indirects diminuent aussi. Le volume des laves torrentielles extrêmes est de l'ordre 10^4.*

Les volumes moyens accumulés dans le dépotoir lors de précipitations sont illustrés dans les figures 7.4 et 7.5. Ils ont été définis à partir des taux d'érosion moyen observés dans les bassins versants de Zinal et calibrés à l'aide des paramètres contrôlant le flux de sédiments dans la cascade (ex. indice d'alluvionnement). Ils diminuent avec le temps, du fait que le stock indirect est remis à jour après chaque simulation. L'apport de matériel mobilisable est ainsi limité.

Les volumes moyens accumulés dans le dépotoir par les laves torrentielles sont illustrés dans les figures 7.6 et 7.7. Leurs volumes ont été définis en partie sur la base des données statistiques des apports de laves torrentielles dans le torrent voisin du Pétérey (cf. chap. 5). La diminution de l'intensité des laves torrentielles dans le temps provient de la diminution du matériel mobilisable des biefs en raison de la diminution des stocks indirects rechargeant les biefs.

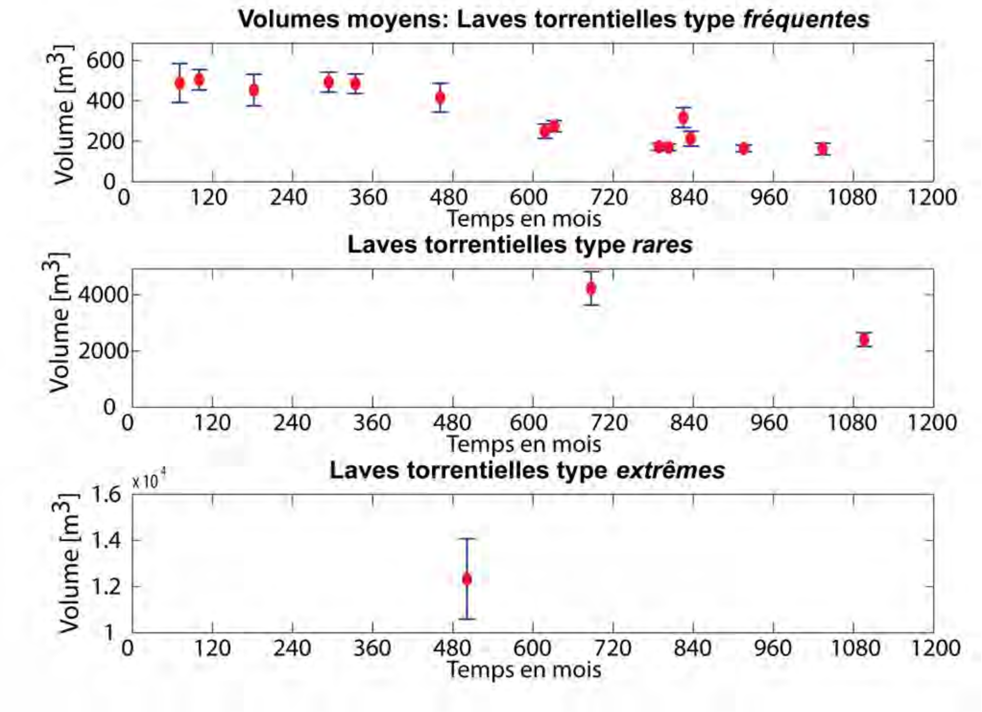

Figure 7.7 : Exemple d'une simulation montrant les volumes (avec écart-type calculé sur la moyenne de 500 simulations) de matériaux apportés à l'exutoire par les laves torrentielles dans le torrent de Lirec. Dans les premières années de simulation, ils correspondent aux volumes définis dans les tableaux, chapitre 5, puis diminuent à cause que les stocks indirects diminuent. Le volume des laves torrentielles extrêmes est de l'ordre 10^4.

7.3 Simulation avec stocks infinis

En admettant que la dynamique du massif alpin est une source continue de sédiments d'érosion qui alimente le système torrentiel, les stocks indirects ne sont pas mis à jour dans la cascade sédimentaire après chaque pas de temps. Les volumes mobilisables provenant de l'extérieur sont supposés infinis. Les figures suivantes (fig. 7.8 – 7.13) présentent les résultats.

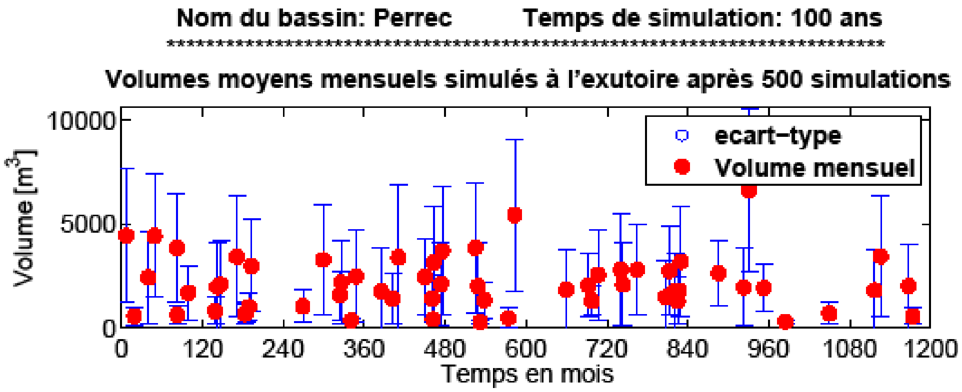

Figure 7.8 : *Volumes accumulés à l'exutoire du torrent de Perrec (idem fig. 7.1) .En maintenant le stock indirect à son volume initial, les volumes accumulés à l'exutoire ne diminuent pas dans le temps.*

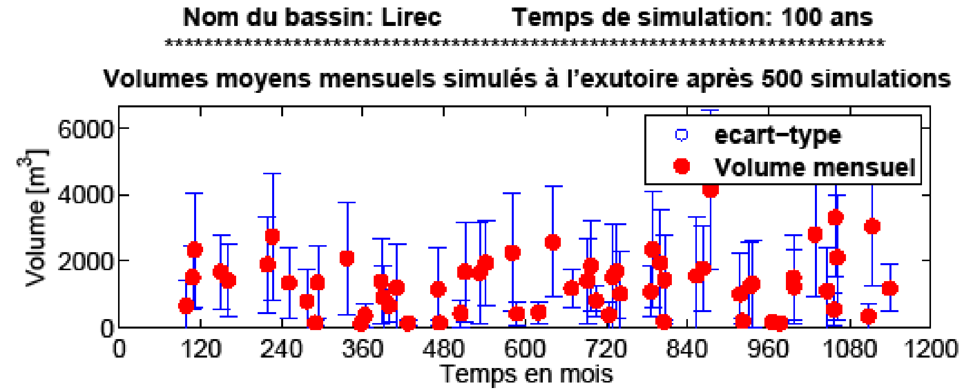

Figure 7.9 : *Volumes accumulés à l'exutoire du torrent de Lirec (idem fig. 7.2). En maintenant le stock indirect à son volume initial, les volumes accumulés à l'exutoire ne diminuent pas dans le temps.*

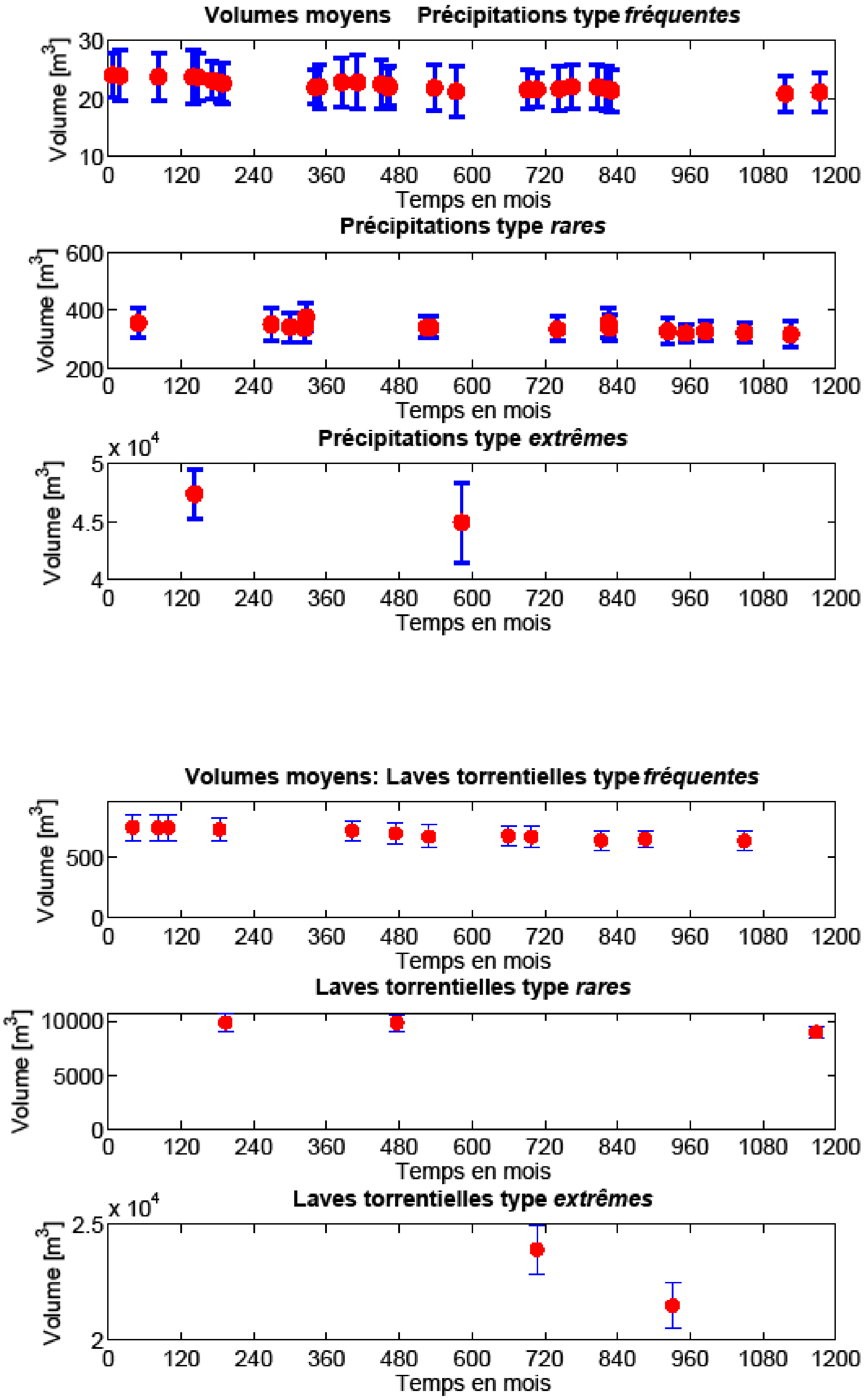
Volumes moyens Précipitations type *fréquentes*

Précipitations type *rares*

Précipitations type *extrêmes*

Volumes moyens: Laves torrentielles type *fréquentes*

Laves torrentielles type *rares*

Laves torrentielles type *extrêmes*

***Figure 7.10** : Volumes apportés à l'exutoire du torrent du Perrec par les précipitations (haut) et laves torrentielles (bas), extraits d'une série temporelle (idem fig. 7.4 et fig. 7.6). En maintenant les stocks indirects, les entrées de matériaux dans le système torrentiel ne diminuent pas dans le temps. Les volumes accumulés dans le dépotoir par les précipitations et laves torrentielles ne dépendent que de la dynamique sédimentaire dans la cascade (volume stock direct et stockage temporaire dans les biefs de matériel).*

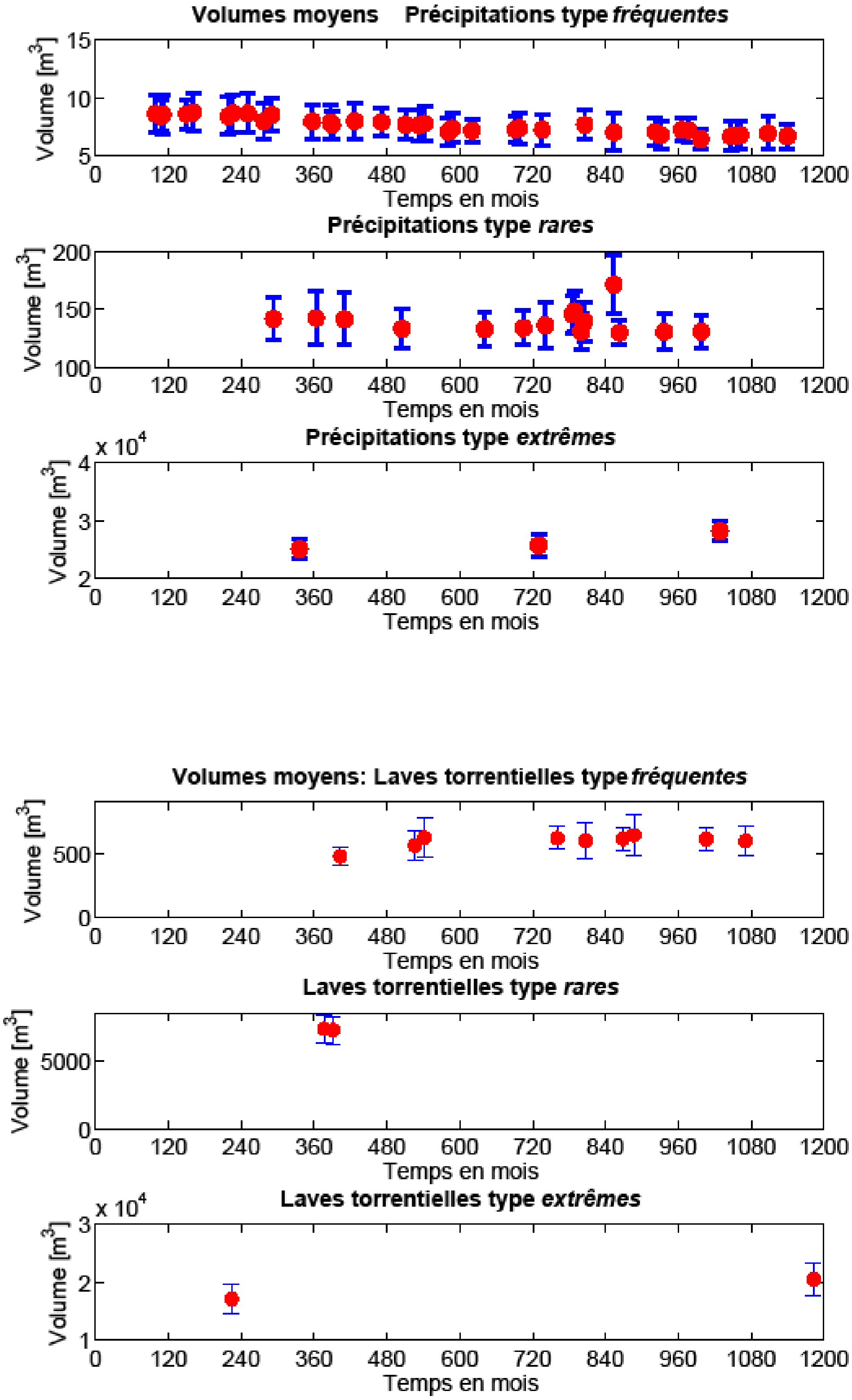

***Figure 7.11** : Volumes moyens (avec écart-type) apportés à l'exutoire du torrent du Lirec par les précipitations (en haut) et laves torrentielles (en-bas), extraits d'une série temporelle (idem fig. 7.5 et fig. 7.7). En maintenant les stocks indirects à leur valeur initiale, l'apport sédimentaire externe ne diminue pas dans le temps. Les variations dans le temps de l'apport sédimentaire sont provoqués par le stockage temporaire de matériel dans les biefs.*

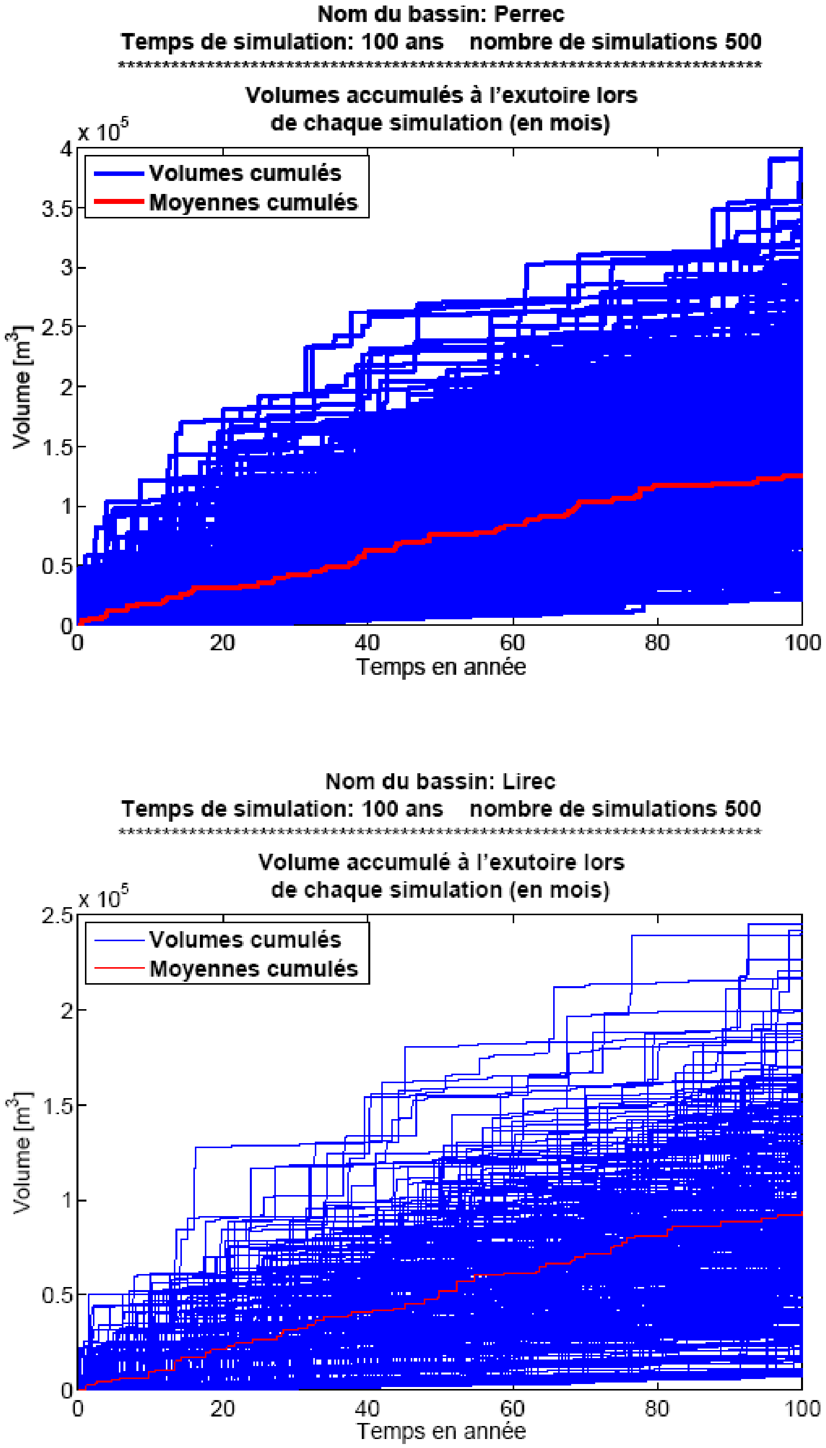

***Figure 7.12** : Volumes accumulés à l'exutoire pour le torrent du Perrec (haut) et Lirec (bas) engendré par chaque simulation avec des apports de matériaux mobilisable infinis (les volumes sont notés 10^5). Selon les occurrences d'évènements de la série temporelle générée pour le torrent du Perrec, le volume cumulé s'étend de 22'000 m^3 à 397'000 m^3, avec un volume moyen cumulé de 126'000 m^3 en 100 ans. Pour celle du torrent du Lirec, le volume cumulé s'étend de 10'000 m^3 à 245'000 m^3, avec un volume moyen cumulé de 92'000 m^3 en 100 ans.*

7.4 Synthèse: Perrec

Les volumes accumulés à l'exutoire du torrent de Perrec pour les scénarios *stock fini* et *stock infini* sont présentés dans le tableau 7.1 et illustrés dans la figure 7.14. Le volume mensuel cumulé représente la somme du volume moyen de toutes les simulations accumulés mois après mois dans le dépotoir. Son écart-type devient très large car il reflète le très large écart de volumes cumulés possibles après 100 ans. Les valeurs *Minimum* et *Maximum* représente la simulation la plus pauvre, respectivement la plus riche en apport de matériaux (fig. 7.2 et fig. 7.12).

Tableau 7.1 *: Volumes cumulés dans le dépotoir du Perrec après 100 ans et 500 simulations*

Volumes simulés à l'exutoire du torrent de Perrec après 100 ans (en m^3)

Scenario	Moyenne	Ecart-type	Minimum	Maximum
Stock fini	113'000	95'000	18'000	266'000
Stock infini	126'000	100'000	25'000	219'000

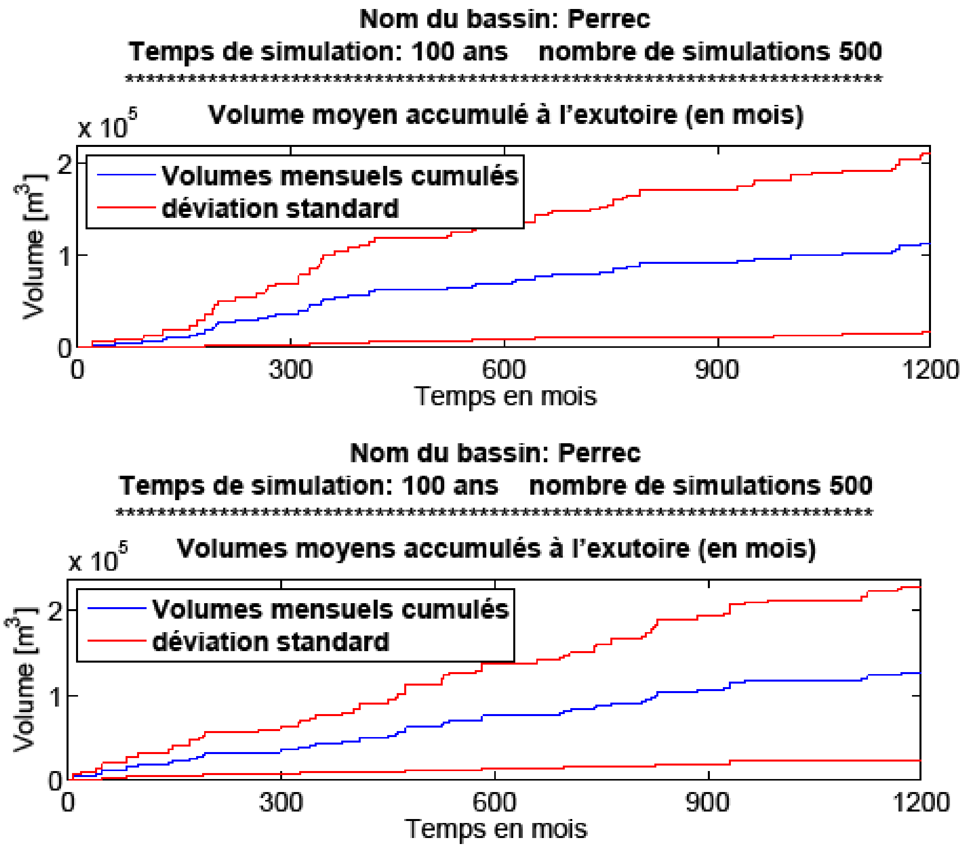

Figure 7.14 *: Volumes accumulés mois après mois à l'exutoire du torrent du Perrec pour un stock indirect fini (haut) et infini (bas). Les volumes de chaque mois sont une moyenne de toutes les simulations. Ils sont décrits dans le tableau 7.1. Le large écart-type (déviation standard) provient du très large écart de volume cumulé possible ([min ; max] d'une série temporelle à l'autre. De plus, l'évolution de cet écart-type est due au nombre limité de 500 simulations, lequel n'englobe pas tous les scénarios possibles (voir chap. 9.1).*

7.5 Synthèse : Lirec

Les volumes accumulés à l'exutoire du torrent de Lirec pour les scénarios *stock fini* et *stock infini* sont présentés dans le tableau 7.2 et illustré dans la figure 7.15.

Tableau 7.2 : Volumes cumulés dans le dépotoir du Lirec après 100 ans et 500 simulations

Volumes simulés à l'exutoire du torrent de Lirec après 100 ans (en m3)

Scenario	Moyenne	Ecart-type	Minimum	Maximum
Stock fini	65'000	45'000	6'000	143'000
Stock infini	92'500	65'000	10'000	245'000

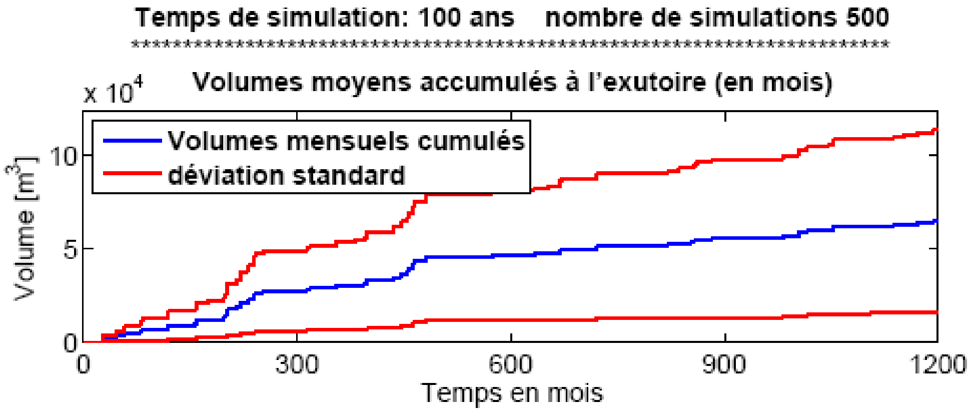

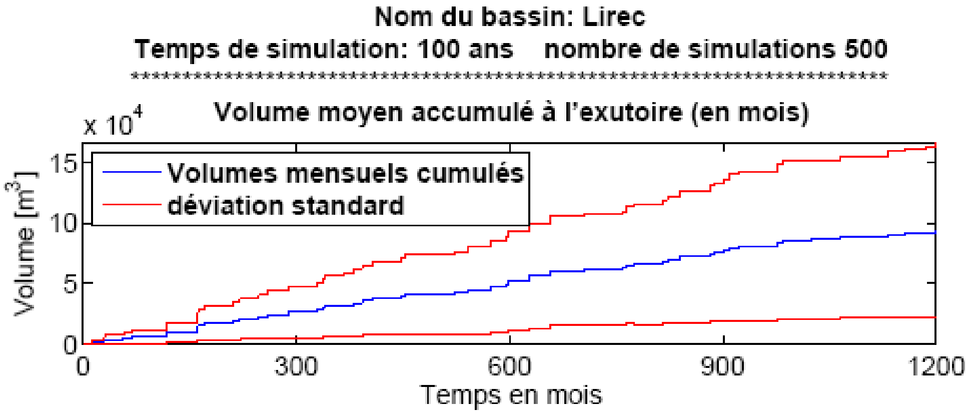

***Figure 7.15** : Volumes accumulés mois après mois à l'exutoire du torrent du Lirec pour un stock indirect fini (haut) et infini (bas). Les volumes de chaque mois sont une moyenne de toutes les simulations. Ils sont décrits dans le tableau 7.2. Le large écart-type (déviation standard) provient du très large écart de volume cumulé possible ([min ; max] selon une série temporelle à l'autre. De plus, son évolution est due au nombre limité de 500 simulations, lequel n'englobe pas tous les scénarios possibles (voir chap. 9.1).*

8 Résultats liés à un changement climatique

Les paramètres de simulations ont été modifiés afin de fournir quelques bilans sédimentaires prévisionnels incorporant l'incidence de changements climatiques. De récentes études ont montrées que les températures moyennes lors du siècle dernier (1900 – 2006) ont augmenté de 1.47°en Suisse (moyenne hémisphère nord = +0.87°) (OFEV, 2007). L'augmentation de la température a donc été beaucoup plus marquée en Suisse, et dans les Alpes particulièrement. L'augmentation moyenne de température en Suisse est d'autant plus importante si l'on ne considère que les mesures postérieures à 1961 (+0.4° par décennie en moyenne). Cette tendance au réchauffement se confirme avec une multiplication des années chaudes durant les dernières décennies. De telles températures devraient provoquer des modifications sur le régime des précipitations et du régime hydrologique des bassins versants qui pourraient être localement importantes. Les observations montrent que les précipitations ont surtout augmentées en hiver (+20 - +30%) au cours du dernier siècle, particulièrement dans le centre et le sud des Alpes (OFEV, 2007). Dans notre cas, l'altitude des bassins versants font que l'activité sédimentaire hivernale devrait rester nulle malgré cette augmentation, car les précipitations continueront de tomber principalement sous forme de neige malgré le réchauffement. Cependant, le régime hydrographique lors des périodes de fonte devrait être plus intense. Concernant les événements extrêmes relatifs aux précipitations, la rareté de ces événements ainsi que l'incertitude statistique qui s'y rapporte font que l'analyse des tendances ne peut être définie que de façon très floue à l'échelle locale (OcCC, 2003). Pendant la même période d'observation, la fréquence des précipitations journalières intenses a augmentée entre 15% et 70% dans la plupart des stations de mesures du nord des Alpes en hiver et en automne (OFEV, 2007). Au printemps et en été, les précipitations journalières intenses ne montrent aucun changement systématique. En l'état actuelle des connaissances, il est toutefois possible d'envisager que les précipitations devraient d'avantage varier d'une année à l'autre et les épisodes intenses devenir plus nombreux, principalement en automne et en hiver.

Ainsi, le scénario suivant a été retenu, tiré du GIEC (Cubasch et al, 2001) :

- augmentation maximum annuel de précipitation journalière de 10 - 25%.
- accroissement d'un facteur deux et plus de la fréquence des précipitations intenses.

La fréquence des précipitations est ainsi augmentée de 25% et l'occurrence moyenne des laves torrentielles est doublée (fig. 8.1). Les vitesses de flux sédimentaire ainsi que les taux d'érosion annuelle restent inchangés.

***Tableau 8.1** : Fréquences modifiés des évènements incorporant l'hypothèse d'un changement climatique.*

Classes d'intensités			Fréquent	Rare	Extrême
Perrec	Temps de retour [an]	Précipitations	2.25	4.5	35
		Laves torrentielles	3	15	50
Lirec	Temps de retour [an]	Précipitations	2.25	4.5	35
		Laves torrentielles	4	25	85

8.1 Occurrence des évènements

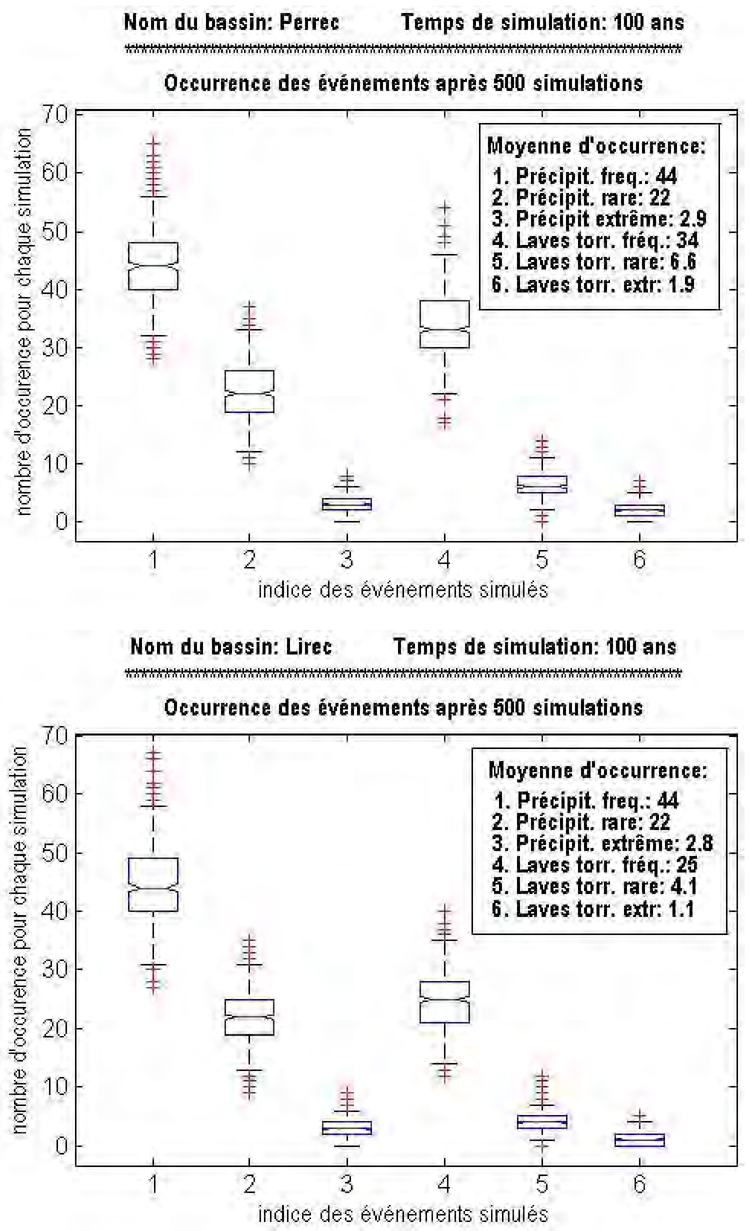

***Figure 8.1** : Panel d'occurrence des événements précipitations et laves torrentielles simulées pour le torrent du Perrec et Lirec compte tenu d'un changement climatique. La fréquence des précipitations est augmentée de 25% et l'occurrence moyenne des laves torrentielles est doublée.*

8.2 Résultats des simulations avec stocks finis

L’augmentation de la fréquence des précipitations et laves torrentielles sur un lot de simulations avec stocks finis a pour effet d’augmenter de 50% dans les deux torrents la charge sédimentaire accumulée dans le dépotoir par rapport au scénario actuel (fig. 8.2). Et ceci, malgré que la diminution des volumes apportés par les différents événements simulés (fig. 8.3) soit accélérée. L’augmentation du volume provient du plus grand nombre d’événements simulés, en particulier ceux qui apportent un volume conséquent de matériel dans le dépotoir.

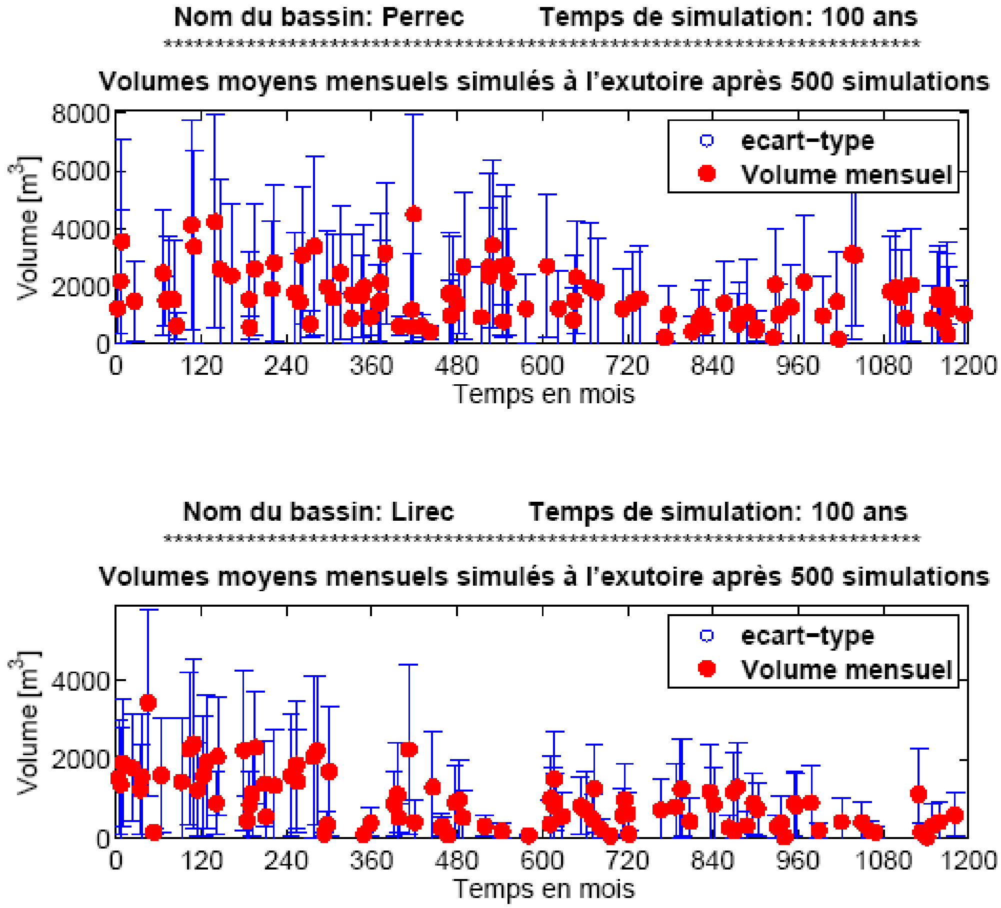

***Figure 8.2**: Volumes accumulés à l’exutoire pour le torrent de Perrec et Lirec compte tenu d’un changement climatique et d’un stock indirect fini. Malgré que les apports diminuent plus rapidement, le nombre plus important d’évènements contribue à augmenter le volume moyen cumulé sur 100 ans de 50 %.*

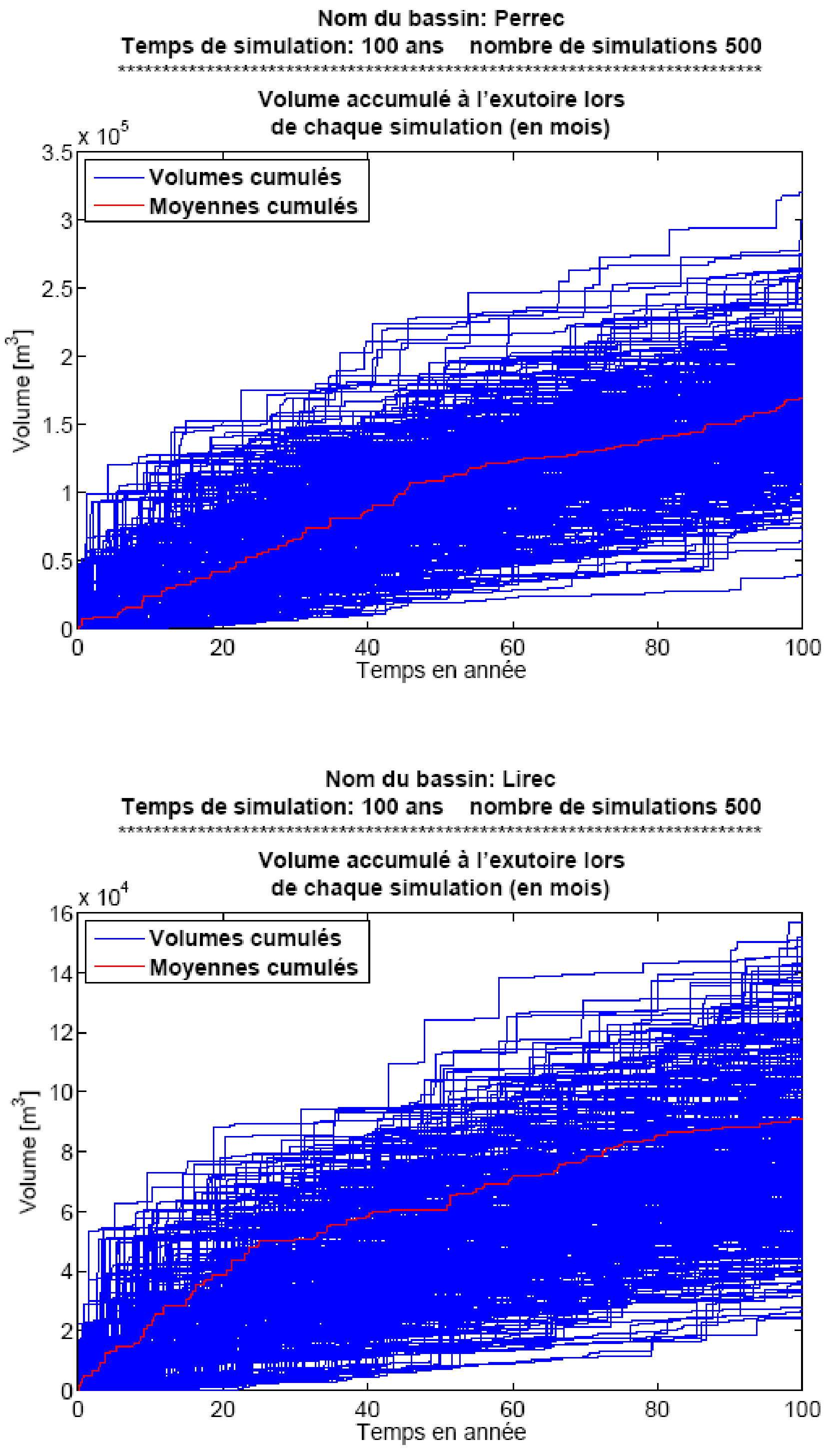

Figure 8.3 : Résultats des 500 simulations simulant l'apport de matériaux à l'exutoire selon une série d'évènements définie sur 100 ans selon l'hypothèse d'un stock fini et tenant compte d'un changement climatique. Torrent du Perrec (haut): volume minimum = 38'800 m^3; moyenne = 169'000 m^3 ; maximum = 320'800 m^3. Torrent de Lirec (bas): volume minimum = 24'000 m^3; moyen = 90'700 m^3 ; maximum = 157'100 m^3.

8.3 Résultats des simulations avec stocks infinis

En maintenant les apports indirects (stock infini) à leur valeur initiale (fig. 8.4), l'augmentation du volume moyen accumulé sur 100 ans est de 130 %, et ceci pour les deux torrents (fig. 8.5).

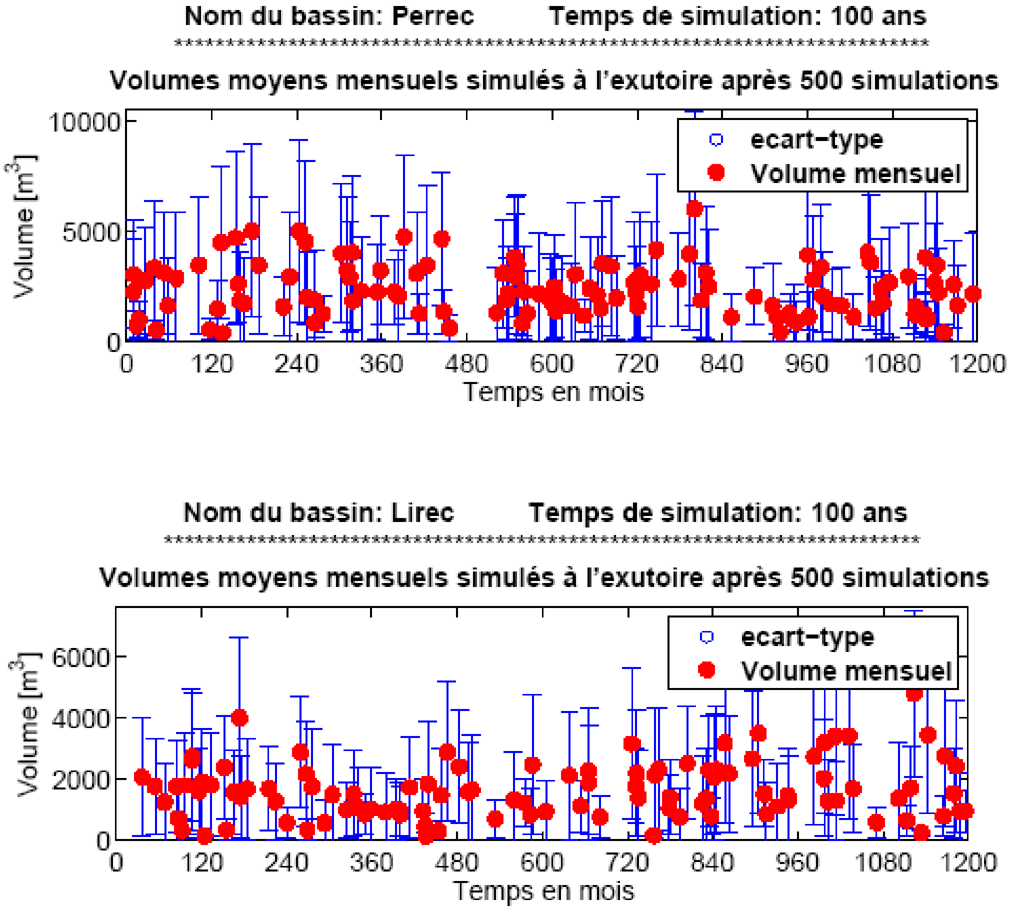

***Figure 8.4**: Exemples de série temporelle montrant les volumes accumulés à l'exutoire pour le torrent de Perrec et Lirec compte tenu d'un changement climatique et des stocks infinis.*

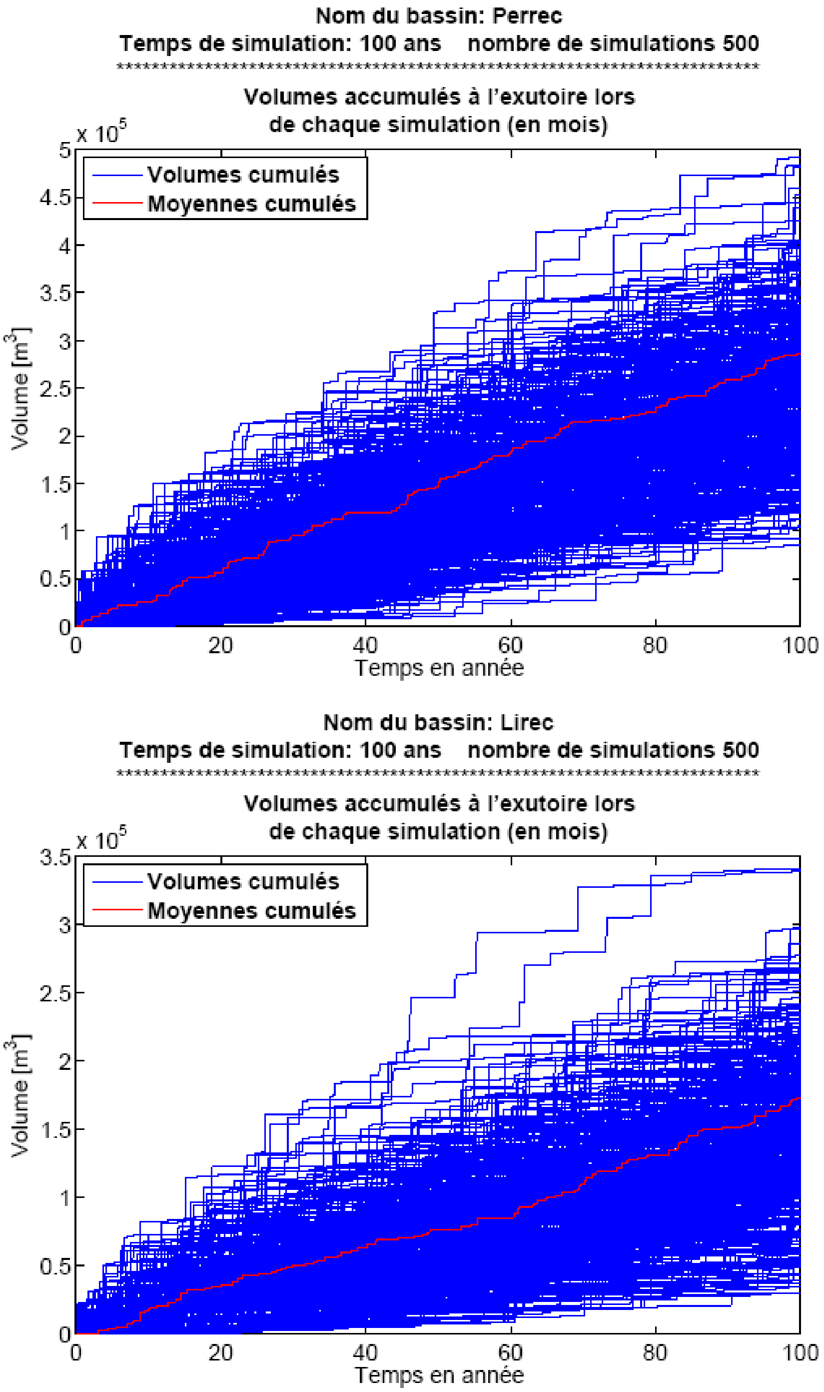

Figure 8.5 : Résultats des 500 simulations simulant l'apport de matériaux à l'exutoire selon une série d'évènements définie sur 100 ans selon l'hypothèse d'un stock infini et tenant compte d'un changement climatique. Torrent du Perrec (haut): volume minimum = 92'000 m^3; moyenne = 287'000 m^3 ; maximum = 491'500 m^3. Torrent de Lirec (bas): volume minimum = 29'500 m^3; moyen = 173'000 m^3 ; maximum = 339'000 m^3.

8.4 Synthèse Perrec

Les volumes accumulés à l'exutoire du torrent de Perrec basés sur un lot de 500 simulations incorporant les effets d'un changement climatique majeur sont présentés ci-dessous. Les valeurs correspondant aux figures ci-dessous sont données dans le tableau 8.3.

***Tableau 8.3** : Volumes cumulé dans le dépotoir du Perrec après 100 ans (en m^3). (Légende cf. tab. 7.1)*

Volumes simulés à l'exutoire du torrent de Perrec après 100 ans (en m^3)

Scenario	Moyenne	Ecart-type	Minimum	Maximum
Stock fini	169'000	170'000	39'000	321'000
Stock infini	287'000	260'000	92'000	492'000

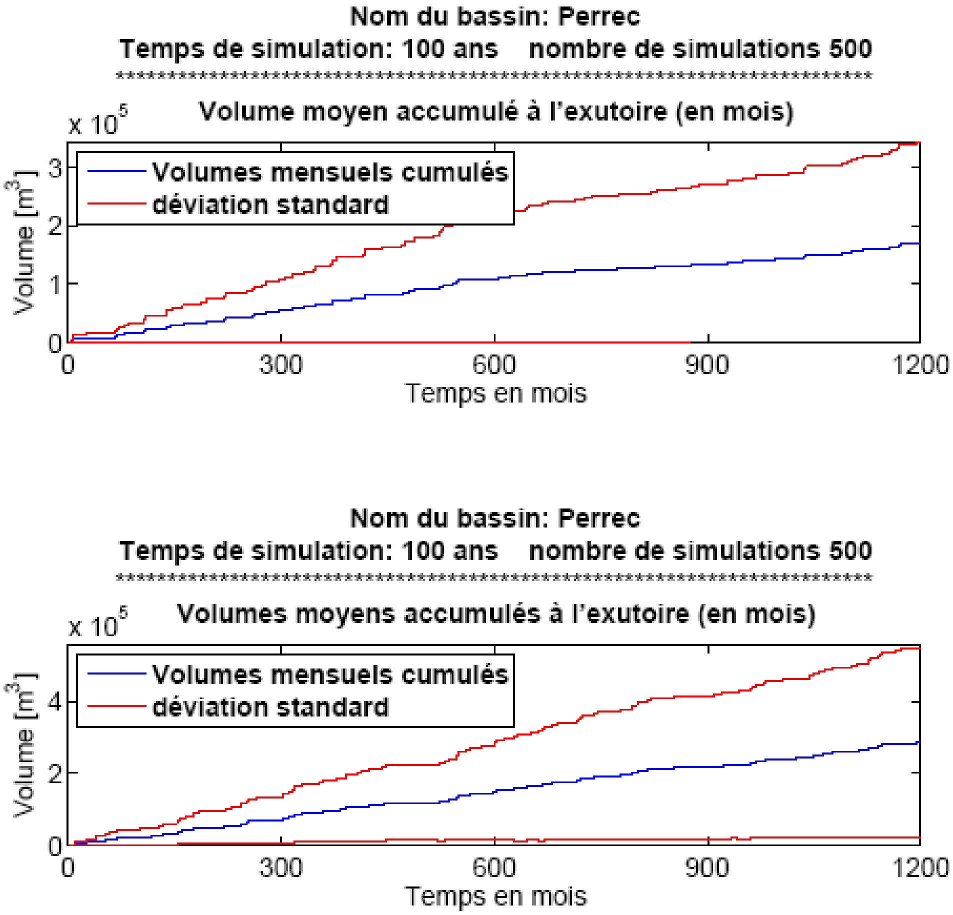

***Figure 8.6** : Volumes accumulés mois après mois à l'exutoire du torrent du Perrec pour un stock indirect fini (haut) et infini (bas) incorporant un changement climatique majeur (idem fig.7.14).*

8.5 Synthèse Lirec

Les résultats des volumes cumulés à l’exutoire du torrent de Lirec sont présentés ci-dessous. Les valeurs correspondant aux figures ci-dessous sont données dans le tableau 8.4.

***Tableau 8.4** : Volumes cumulé dans le dépotoir du Perrec après 100 ans (en m^3).*

Volumes simulés à l’exutoire du torrent de Lirec après 100 ans (en m^3)

Scenario	Moyenne	Ecart-type	Minimum	Maximum
Stock fini	91’000	85’000	24’000	157’000
Stock infini	173’000	150’000	29’500	339’000

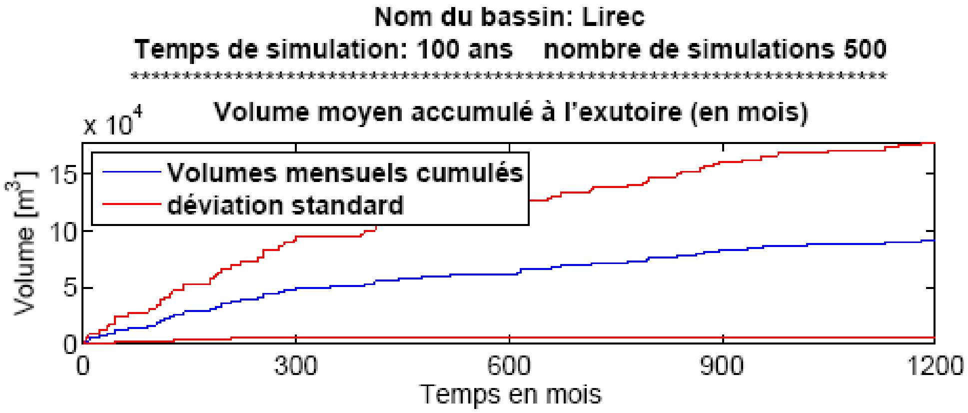

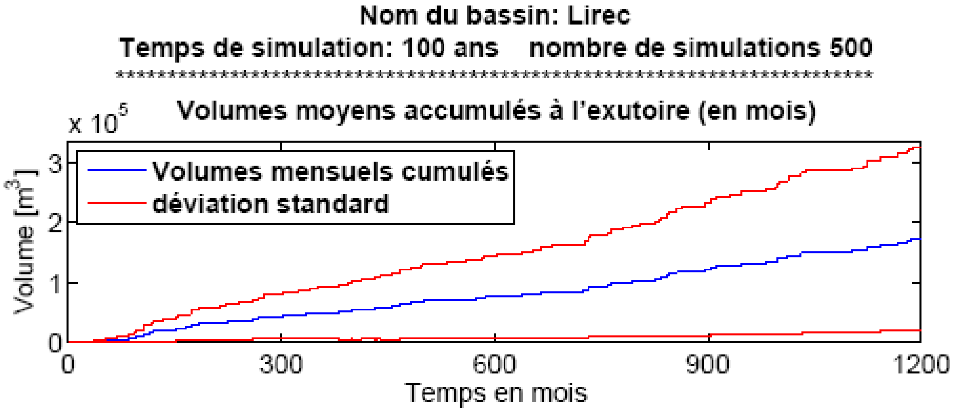

***Figure 8.7**: Volumes accumulés mois après mois à l’exutoire du torrent du Lirec pour un stock indirect fini (haut) et infini (bas) incorporant un changement climatique majeur (idem fig.7.14).*

9 Sensibilité de la cascade sédimentaire

9.1 Variation des bilans sédimentaires par rapport aux nombres de simulations

500 séries temporelles ne couvrent pas toutes les possibilités d'occurrence d'événements. Pour chaque mois, il y a 47 scénarios d'évènements possibles. Multiplié par le nombre de mois de simulations, cela fait 56'400 possibilités et cela sans tenir compte de l'ordre auxquelles elles apparaissent dans la série temporelle. Des lots de simulations plus longs (2000 simulations) ont été testés afin de quantifier la dépendance des bilans par rapport au nombre de simulations. Ils fournissent un volume moyen dans une fourchette de ±10%. Cependant, l'écart-type dépend des processus simulés. Ainsi le relatif petit lot de scénarios simulés par rapport à toutes les possibilités d'événements fait varier l'écart-type dans le temps, ce qui ne devrait pas être le cas lors des simulations avec un stock infini (mais peut être le cas lors de simulation avec stock fini). Sans effectuer un nombre de simulation s'approchant du total des possibilités, l'écart-type à court et moyen terme est quelque peu biaisé. Pour cette raison, il est plus juste de parler d'une variabilité indicative pour les résultats de bilans sédimentaires obtenus sur une moyenne de 10 ans et 30 ans. Par contre, sur le long terme (100 ans), l'écart-type (exprimé en %) est une estimation plus précise.

9.2 Sensibilité par rapport à l'indice d'alluvionnement

Plusieurs indices d'alluvionnement ont été testés afin de quantifier la différence de volumes par rapport à une augmentation/diminution de cet indice. Bien qu'il ne soit pas évident de quantifier ce paramètre, les différents tests nous montrent qu'une augmentation de 5% de l'indice d'alluvionnement dans les biefs fait diminuer le bilan sédimentaire dans la majorité des simulations de 3 à 12%. A contrario, une diminution de l'indice d'alluvionnement de 5% implique une augmentation de la charge sédimentaire dans le dépotoir de 5 à 15%. L'incertitude concernant l'indice d'alluvionnement peut être estimée de façon prudente à 20% dans le bilan sédimentaire intrabief. Relié aux résultats des volumes moyens accumulés à la fin de la cascade sédimentaire, c.-à-d. dans le dépotoir des torrents, compte tenu que l'apport sédimentaire des événements laves torrentielles ne dépend pas de ce paramètre, une incertitude de 10% sur l'indice d'alluvionnement fait varier le volume moyen cumulé de 10 à 15% au maximum. Cette incertitude est donc comprise dans l'écart-type des résultats moyens produits à partir d'un grand nombre de simulations. L'incertitude sur la dynamique sédimentaire ne dépend pas seulement de cet indice, mais aussi de la capacité maximum de remplissage du bief et de la découpe du torrent en biefs homogènes.

9.3 Incertitudes sur les stocks sédimentaires et vitesse d’érosion

Les stocks sédimentaires directement mobilisables sont certainement quelque peu surestimés par la méthode du SLBL à cours et moyen terme, mais raisonnable sur une période de 100 ans. Elle prend en compte les possibles changements du cours du torrent. Les stocks indirects de chaque bief doivent être considérés comme des approximations. La variabilité des données de stocks ne peut pas être quantifiée précisément. L’imprécision devrait être cependant balancée entre les différents apports indirects des biefs.

Les vitesses d’érosion liées aux précipitations et laves torrentielles sont définies à partir de moyennes observées sur une période. Les taux d’érosion employés dans cette étude sont dans les ordres de grandeurs standards pour ce type de bassin versant, lesquels ont été déduits à partir de plusieurs approches (en plus des nôtres). Par contre, les intensités et fréquences de calibrage des laves torrentielles dans les bassins de Lirec et Perrec pourraient être sous-évaluées. La période d’observation est relativement courte et aucun gros évènement n’a été recensé durant cette période ou émane de la mémoire collective des habitants de Zinal. Une analyse plus détaillée des temps de retour des précipitations et laves torrentielles sera menée dans la prochaine étape du projet MatErosion.

Les volumes d’entrées de la cascade sédimentaire ainsi que les vitesses d’érosion doivent être appréhendées avec une imprécision inhérente à toute étude de bilan sédimentaire. Cependant, le mode de simulation pseudo stochastique de la cascade sédimentaire permet de prendre en compte cette incertitude en produisant un grand nombre de scénarios possibles. Une étude plus détaillée des stocks sédimentaires indirects potentiels, tels que la possibilité d’un écroulement rocheux de grand volume ainsi que la présence de matériaux meubles potentiellement instables (exemple : moraines fossiles, glacier couvert Bonnard au dessus du torrent de Tracuit) sera entreprise dans la suite du projet.

10 Synthèse

Les résultats du bilan sédimentaire relatif à chaque scénario sont présentés sur la base d'un bilan statistique annuel de toutes les simulations effectuées pour un pas de temps de un mois. Un bilan des simulations sur l'année (moyenne sur 12 mois) permet de réduire le très large écart de volumes possibles cumulés dans le dépotoir provoqué par la grande variabilité d'occurrence des évènements dans les séries temporelles, et ainsi de réduire la variabilité indicative (écart-type) des bilans. Les volumes moyens cumulés calculés par mois ou par année restent quasiment les mêmes. Ils sont dans la fourchette des variations de résultats observés entre plusieurs lots de simulations. Les résultats à court et moyen terme des simulations avec stock fini et stock infini sont donnés avec l'écart-type obtenu sur le long terme (100 ans).

10.1 Résultats torrent du Perrec

A partir des observations actuelles de volumes sédimentaires et de la dynamique torrentielle, la modélisation effectuée sur le torrent du Perrec révèle (tab. 10.1) un volume moyen cumulé de 9'400 (±45%) m^3 après 10 ans, 57'280 (±45%) m^3 après 30 ans et 111'000 (±45%) pour les 100 prochaines années, considérant un apport de matériel limité aux observations actuelles. Ceci représente une moyenne oscillant entre 950 an^{-1} et 1'400 (±45%) m^3 an^{-1} (fig. 10.1).

***Tableau 10.1** : Résultats du bilan sédimentaire simulé dans le torrent de Perrec.*

Volumes simulés à l'exutoire du torrent de Perrec après 100 ans (en m^3)

Hypothèse	**Scénario**	Moyenne après 10 ans	Variabilité	Moyenne après 30 ans	Variabilité	Moyenne après 100 ans	Ecart-type	DR *mm an^{-1}*
constante	**Stock fini**	9'400	5'000 (50%)	57'200	21'000 (35%)	111'000	50'000 (45%)	0.41
	Stock infini	14'200	8'000 (55%)	46'400	21'300 (45%)	130'000	56'000 (45%)	0.48
Changement climatique	**Stock fini**	26'900	8'000 (30%)	72'600	24'700 (35%)	162'500	55'000 (35%)	0.6
	Stock infini	27'800	9'500 (35%)	92'400	28'600 (40%)	280'000	85'000 (35%)	1

DR : taux d'érosion [mm an^{-1}] par rapport au volume moyen cumulé sur 100 ans ramené à la surface total du bassin versant et une densité moyenne des dépôts de 1800 kg m^{-3}.

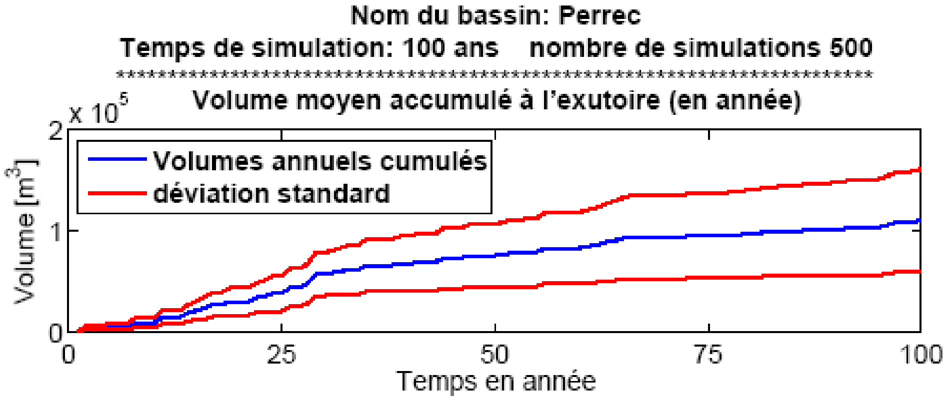

Figure 10.1 : Volumes moyen annuel accumulés à l'exutoire du torrent du Perrec pour un stock indirect fini selon l'hypothèse constante.

En supposant que l'apport sédimentaire indirect ne diminue pas avec le temps dans le torrent du Perrec, le volume moyen cumulé après 10 ans est de 14'200 m^3 (±45%), 46'400 m^3 (±45%) après 30 ans et 130'000 m^3 (±45%) après 100 ans (fig. 10.2).

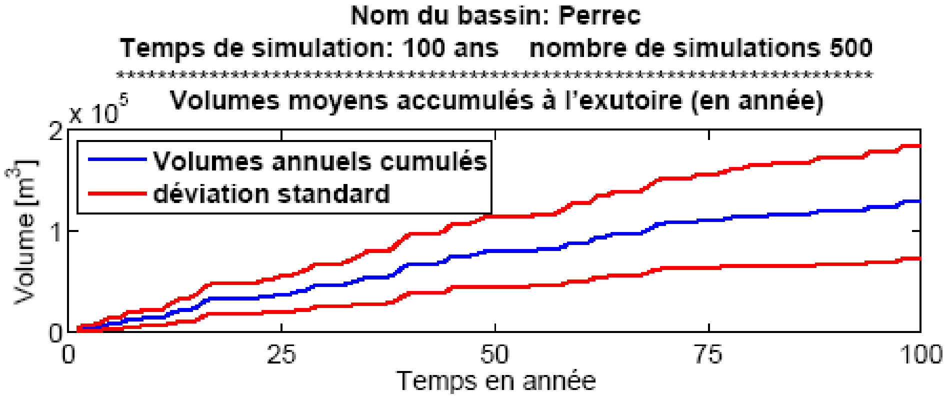

Figure 10.2 : Volumes moyen annuel accumulés à l'exutoire du torrent du Perrec pour un stock indirect infini selon l'hypothèse constante.

Le scénario incorporant les effets d'un changement climatique fait augmenter de façon significative les volumes moyens accumulé dans le dépotoir. Pour une configuration de stocks indirects finis, il représente un volume moyen de 26'900 (±35%) m^3 après 10 ans, 72'600 (±35%) m^3, après 30 ans et 162'500 (±35%) m^3 après 100 ans (fig. 10.3). En maintenant les stocks à leur valeur actuel, le volume moyen de 27'800 (±35%) m^3 après 10 ans, 92'400 (±35%) m^3 et 280'000 (±35%) m^3 après 100 ans (fig. 10.4). En comparant les résultats entre l'hypothèse *constant* et *changement climatique*, il en ressort qu'une augmentation de la fréquence et intensité des précipitations contribue à grossir le volume moyen cumulé dans le dépotoir du torrent du Perrec en 100 ans de 46% en admettant que les stocks soient limités, et de 115% avec des apports sédimentaires illimités.

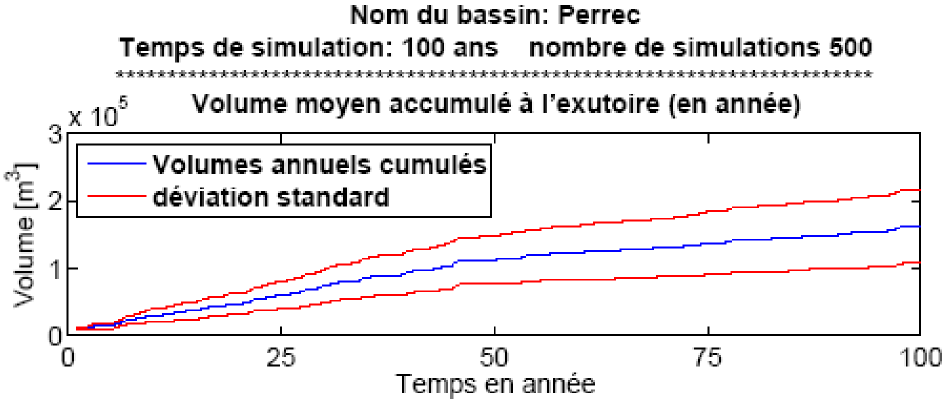

Figure 10.3 *: Volumes moyen annuel accumulés à l'exutoire du torrent du Perrec pour un stock indirect fini incorporant un changement climatique majeur.*

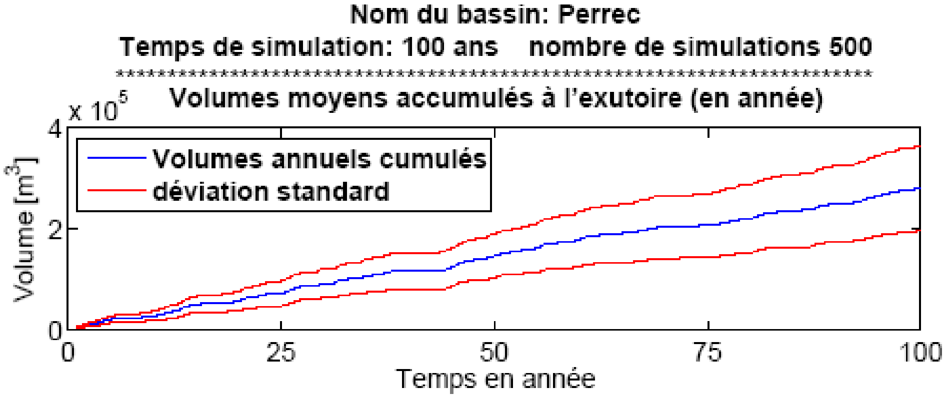

Figure 10.4 *: Volumes moyen annuel accumulés à l'exutoire du torrent du Perrec pour un stock indirect infini incorporant un changement climatique majeur.*

10.2 Résultats torrent du Lirec

Selon les volumes sédimentaires actuels et de la dynamiques torrentielles du torrent de Lirec, le bilan sédimentaire modélisé révèle un volume moyen cumulé de 7'200 (±45%) m^3 après 10 ans, 24'900 (±45%) m^3 après 30 ans et 57'500 (±45%) pour les 100 prochaines années, considérant un apport de matériel limité aux observations actuelles (fig. 10.5). En supposant que l'apport sédimentaire indirect ne diminue pas avec le temps dans le torrent de Lirec, les volumes moyens accumulés s'élèvent après 10 ans à 8'900 (±50%) m^3, 26'700 (±50%) m^3 après 30 ans et 76'700 (±50%) m^3 après 100 ans (fig. 9.6).

Tableau 10.2 *: Résultats du bilan sédimentaire simulé dans le torrent de Lirec.*

Volumes simulés à l'exutoire du torrent de Lirec après 100 ans (en m^{3})

Hypothèse	Scénario	Moyenne après 10 ans	Variabilité	Moyenne après 30 ans	Variabilité	Moyenne après 100 ans	Ecart-type	DR* *mm an*$^{-}$
constante	**Stock fini**	7'200	3'500 (50%)	24'900	11'400 (35%)	57'500	30'000 (45%)	0.24
	Stock infini	8'900	4'000 (45%)	26'700	12'200 (45%)	76'700	40'000 (50%)	0.32
changement climatique	**Stock fini**	16'100	5'800 (35%)	40'000	13'500 (35%)	84'700	32'500 (40%)	0.35
	Stock infini	16'500	5'300 (30%)	47'100	17'500 (35%)	162'500	56'000 (35%)	0.68

*DR : taux d'érosion [mm an^{-1}] par rapport au volume moyen cumulé sur 100 ans ramené à la surface total du bassin versant et une densité moyenne des dépôts de 1800 kg m^{-3}.

Dans l'hypothèse d'un changement climatique, pour un stock supposé limité, le bilan s'élève après 10 ans à 16'100 (±40%) m^{3}, 40'000 (±40%) m^{3} après 30 ans et 84'700 (±40%) m^{3} après 100 ans (fig. 10.7). Pour un apport sédimentaire illimité, le bilan s'élève après 10 ans à 16'500 (±35%) m^{3}, 47'100 (±35%) m^{3} après 30 ans et 162'500 (±35%) m^{3} après 100 ans (fig. 10.8). L'augmentation des volumes moyens cumulés dans l'hypothèse d'un changement climatique par rapport au scénario actuel est de 47% en limitant les stocks indirects et de 112% en maintenant les apports sédimentaires illimités.

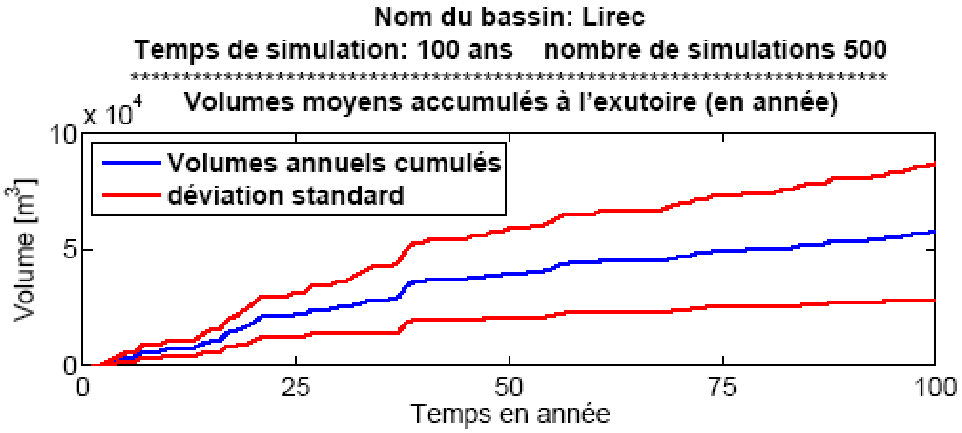

***Figure 10.5** : Volumes moyen annuel accumulés à l'exutoire du torrent du Lirec pour un stock indirect fini selon l'hypothèse constante.*

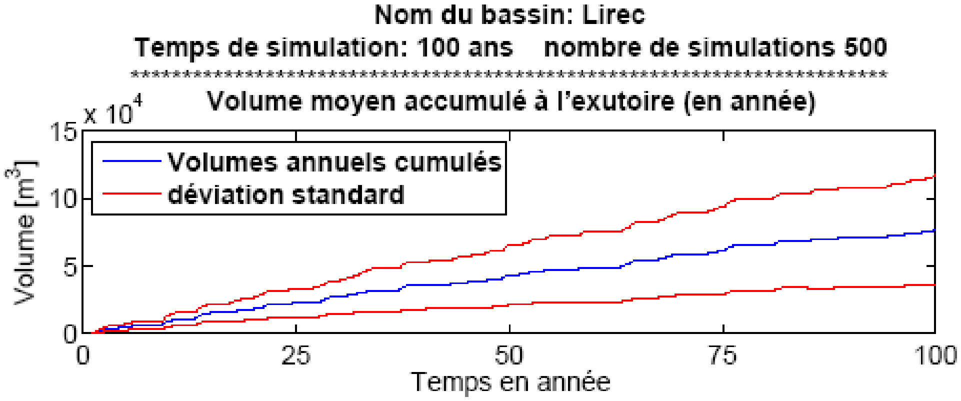

Figure 10.6 : Volumes moyen annuel accumulés à l'exutoire du torrent du Lirec pour un stock indirect infini selon l'hypothèse constante.

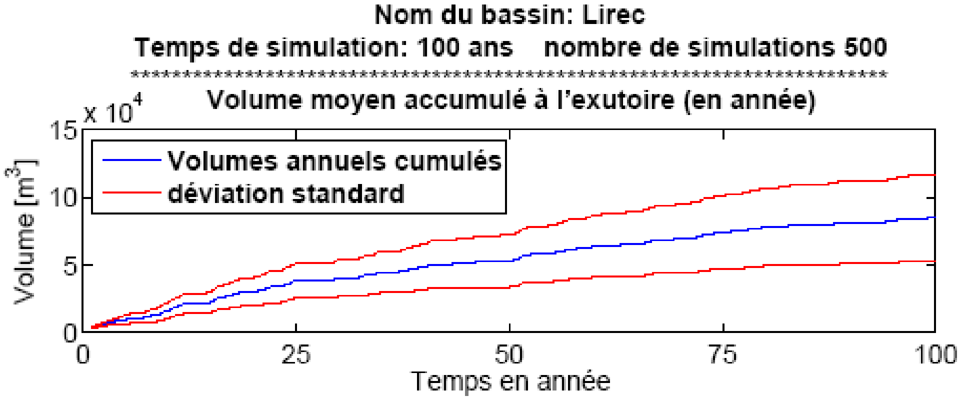

Figure 10.7 : Volumes moyen annuel accumulés à l'exutoire du torrent du Lirec pour un stock indirect fini incorporant un changement climatique majeur.

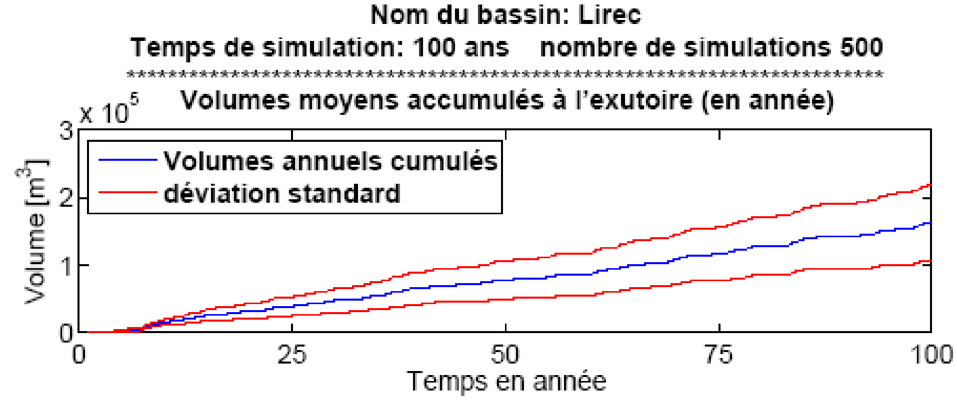

Figure 10.8 : Volumes moyen annuel accumulés à l'exutoire du torrent du Perrec pour un stock indirect infini incorporant un changement climatique majeur..

10.3 Résultats globaux

La présente étude indique qu'un volume moyen de 1'100 m^3 par an (±45%) (stock fini : 110'000 sur 100 ans) à 1'300 m^3 par an (±45%) (stock infini : 130'000 sur 100 ans) devrait se déposer dans le dépotoir du torrent du Perrec au cours des 100 prochaines années, avec des fluctuations sur des périodes plus courtes se situant entre 900 m^3 (±45%) (9'400 sur 10 ans) et 1'900 m^3 (±45%) (57'200 sur 30 ans) en moyenne annuelle. Dans le cadre d'un changement de l'activité climatique vers des scénarios comme annoncé par le GIEC (groupe d'experts intergouvernemental sur l'évolution du climat), un volume moyen de 1'625 m^3 par an (±35%) (stock fini : 162'500 sur 100 ans) à 2'800 m^3 par an (stock infini : 280'000 sur 100 ans) (±35%) pourrait s'accumuler dans le dépotoir sur le long terme, avec des fluctuations à moyen terme situées entre 2'400 m^3 (72'600 sur 30 ans) et 3'000 m^3 (92'400 sur 30 ans) en moyenne annuelle.

Les résultats pour le torrent de Lirec indiquent que 500 m^3 par an (±45%) (stock fini : 57'500 sur 100 ans) à 800 m^3 par an (±50%) (stock infini : 76'700 sur 100 ans) par an devrait se déposer à son exutoire sur une période de 100 ans, avec des variations à moyen terme pouvant atteindre 900 m^3 (±50%) (26'700 sur 30 ans) en moyenne annuelle. Dans le cadre d'une évolution climatique défavorable, des volumes moyens situés entre 850 m^3 (±40%) (stock fini : 84'700 sur 100 ans) et 1'650 m^3 (±35%) (stock infini : 162'500 sur 100 ans) pourrait être déposés dans le dépotoir sur une période de 100 ans avec des moyennes annuelles sur le moyen terme plutôt de l'ordre de 1'300 m^3 (±40%) (40'000 sur 30 ans) à 1'600 m^3 (±35%) (47'100 sur 30 ans).

Il s'agit de résultats qui peuvent encore être améliorés en affinant les données des stocks sédimentaires et la connaissance de la dynamique torrentielles. Cependant, ces résultats obtenus lors de cette phase de développement du projet MatErosion fournissent des bilans sédimentaires très cohérents par rapport aux connaissances actuelles. Les taux d'érosion découlant de ces bilans sédimentaires peuvent permettre de réduire l'écart d'incertitude des mêmes taux d'érosion précédemment estimés dans le rapport de Loye et al. (2009).

.

11 Conclusion et perspectives

Cette méthode développée dans cette première partie du projet « MatErosion » permet d'estimer dans le temps l'apport sédimentaire dans le torrent ainsi que le bilan de la charge sédimentaire accumulée tout au long ou à l'exutoire du torrent. Elle se base sur trois types de données qui peuvent être acquis par des observations et mesures de terrain ainsi que par les données topographiques sur SIG:

1. les stocks sédimentaires et la dynamique générale du torrent ;
2. les vitesses d'érosion dans le bassin et le transfert des flux sédimentaires dans le torrent
3. la fréquence d'événements de type précipitations et laves torrentielles.

La dynamique sédimentaire du bassin et de son torrent est modélisée sur la base d'une cascade sédimentaire, où les événements gouvernent les apports et transferts de matériaux dans le torrent. Son application n'est pas spécifique à un type de systèmes torrentiels.

L'application de cet outil sur les torrents de Perrec et Lirec ont permis d'estimer un apport sédimentaire moyen probable de 160'000 à 210'000 m^3 accumulé dans leur dépotoir commun sur une période de 100 ans. Ces volumes ont été estimés sur la base des observations des stocks sédimentaires essentiellement meubles et potentiellement mobilisables actuellement, ainsi que des taux d'érosion moyen mesurés dans la région. Dans l'hypothèse d'un changement climatique où les précipitations de fortes intensités doubleraient de fréquence, le bilan sédimentaire pourrait augmenter à 450'000 m^3 sur 100 ans. Il serait ainsi doublé par rapport aux projections basées sur des scénarios climatiques actuels. En limitant les apports sédimentaires à leur volume actuel, l'apport sédimentaire estimé dans le dépotoir pourrait diminuer après 100 ans de 50% environ. Cependant, l'occurrence d'un événement de plusieurs millions de m^3 venant alimenté le torrent, comparable à ceux qui a pu être observé dans le bassin versant de l'Illgraben dans les années 1960, ou dans le St-Barthélémy fin des années 1920, n'a pas été considéré dans cette phase actuelle du projet, bien que le modèle le permet. De même, la présence de glaciers couverts, comme celui de Bonnard au sommet du torrent de Tracuit, n'a pas encore été introduit dans les simulations. De telles hypothèses peuvent être ajoutées aux bilans globaux.

La comparaison des volumes moyens (sous forme de taux d'érosion annuels) calculés par la cascade sédimentaire avec d'autres approches basées sur la quantification des dépôts à long terme (cf. chap. 6; Loye et al. 2009 ; Hinderer 2001) sont dans un ordre de grandeur semblable. En outre, les présentes estimations permettent de réduire les écarts d'incertitude présentées dans ces approches quand il s'agit de les appliquer à des systèmes torrentiels. Cet outil développé dans le projet MatErosion permet ainsi de fournir aux services concernés une base de décision et des moyens d'anticipation pour une meilleure gestion économique et environnementale de ce type de matériaux à long terme. Une gestion intégrée des matériaux inertes déposés dans les ouvrages de protections contre les dangers naturels permet d'assurer leur fonction de protection ou d'écoulement.

Si la cascade sédimentaire permet de simuler un événement exceptionnel (ex. glissements, éboulements, etc) en l'introduisant dans un bief déterminé par la carte des événements, la possibilité que du matériel quitte le torrent avant l'exutoire (débordements) est à envisager. Le moteur de la cascade sédimentaire sont les fréquences des événements précipitations et laves torrentielles, lesquelles dans la configuration actuelle permettent de simuler la dynamique irrégulière et ponctuée de pics importants (pulses) de flux sédimentaires (Bardou & Jaboyedoff, 2008). Ceci est régit par des fréquences mensuelles d'évènements qui peuvent être encore affinées. D'ailleurs, une étude sur le choix du pas de temps le plus adapté devra être opérée dans l'étape prochaine. De plus, la dynamique sédimentaire de certains bassins (ou parties de bassins) n'est pas régie par les précipitations (transport-limited), mais plutôt par le temps de recharge de ses biefs (supply-limited). Il s'agit dès lors d'introduire des déclenchements de flux sédimentaire par seuils, lesquelles peuvent être simulés dans la cascade sédimentaire par des « fusibles » dans le transfert sédimentaire opéré de biefs en biefs. L'indice d'alluvionnement peut être amélioré en prenant en compte une série de biefs (amont et aval) afin d'intégrer le contexte topographique du bief dans son ensemble. De même, les apports indirects pourraient dans un future développement se baser sur des vitesses de transport propre à chaque bief (incluant la géologie par exemple), et non pas seulement sur un taux d'érosion local. Pour tout cela, il faudrait instrumenter le torrent pour un certain temps au moins.

Lausanne, le 20 novembre 2010

12 Bibliographie

Ayer, 2003, rapport technique sur la mise en décharge des matériaux inertes, document inédit, commune d'Ayer.

Bardou, E., 2002, Méthodologie de diagnostic des laves torrentielles sur un basin versant alpin, Ph.D. thesis, Section Génie-Civil, EPFL.

Bardou, E. & Jaboyedoff, M., 2008, Debris flows as a factor of hillslope evolution controlled by a continuous or a pulse process, Geol.Society of London, Special Publication, v. 296, 63-78.

Chorley, R.J. & Kennedy, B.A., 1971. Physical Geography, A Systems Approach. Prentice-Hall International, London.

Cubasch, U., Mehl, G. A. et al., 2001, Projections of future climate change. Chapter 9 in: Climate Change 2001: Basis. 3th Assessment Report of the Intergovernmental Panel on Climate Change (IPCC), Cambridge Press, Camebridge, U.K. 525–582, 2001.

Fanin, R. J. & Wise, M. P., 2000, An empirical-statistical model for debris flow travel distance. Can. Geotech. J. 38 : 982-994.

Favre-Bulle, G., Sartory, M. et Métraux, V., 2009, Rapport CREALP Glacier Bonnard, Cartographie, interprétation et calcul des volumes, rapport technique.

Fryirs, K. A., Brierley G. J., Preston N. J. et Kasai M., 2006, Buffers, barriers and blankets: The (dis)connectivity of catchment-scale sediment cascades, Catena 70, 49-67, 10.1016/j.catena.2006.07.007.

Gertsch, E., 2009, Geschiebelieferung alpiner Wildbachsysteme bei Grossereignissen - Ereignisanalysen eines Abschätzverfahrens Institut de Géographie, Université de Berne.

Hinderer, M., 2001, Late quaternary denudation of the Alps, valley and lake fillings and modern river loads, Geodinamica Acta 14, 231-263.

Hingray B., Picouet C. et Musy, A., 2009, Hydrologie 2, Une science pour l'ingénieur, Presse Polytechniques et universitaires romandes.

Jaboyedoff, M. & Derron, M.-H., 2005, A new method to estimate the infilling of alluvial sediment of glacial valleys using a sloping local base level, Geogr. Fis. Dinam. Quat, 28,37-46.

Kronfellner-Kraus, G.,1984, Extreme Festofffrachten und Grabenbildungen von Wildbächen. INTERPRAEVENT. VHB, Villach, 109–118.

Lan, H., Martin, D. and Zhou, C. H., 2008, Estimating the size and travel distance of Klapperhorn Mountain debris flows for risk analysis along railway, Canada, International Journal of sediment Research, Vol. 23, No.3, pp. 275-282.

Loye, A. & Jaboyedoff M., 2009, Estimation des quantités de matériaux érodés dans le bassin versant de Zinal, basée sur l'étude de l'alluvionnement des ouvrages hydroélectriques valaisans, IGAR, FGSE, Université de Lausanne, rapport technique.

Marthaler, M. & Sartori, M., 2005, Feuille 1307 Vissoie avec notice explicative, Altas de la Suisse, Service hydrologique et géologique national, Berne.

Mazotti B., Loye A. et Jaboyedoff, M., 2010, Création d'un modèle d'estimation du bilan sédimentaire de torrents en milieu alpin, carnet méthodologique, IGAR - Université de Lausanne, rapport technique inédit.

OcCC, 2003, Evènement extrêmes et changements climatiques. Organe consultatif sur les changements climatique (OcCC), Berne

Rickenmann, D., 1995. Sediment transport in Swiss torrents. Earth Surface Processes and Landforms, 22, 937–951.

Schrott L., Hufschmidt, G., Hankammer, G., Hoffmann, T. and Dikau, R., 2003, Spatial distibution of sediment storage types and quantification of valley fill deposits in an alpine basin, Reintal, Bavarian Alps, Germany, ***Department of Geography, University of Bonn***, Geromorphology 55, 45-63.

Strahler, A. N. 1952, Dynamic basis of geomorphology. Geological Society of America Bulletin, 63, 923 – 938.

Lehmann, C., Spreafico, M., and Naef, O., 1999, Recommandations concernant l'estimation de la charge sédimentaire dans les torrents, Manuel, Phase I, bases techniques et exemples pratique, Phase II, Bundesamt für Umwelt, BAFU (GHO).

Wichmann, V., Heckmann, T., Haas, F. and Becht, M., 2009, A new modelling approach to delineate the spatial extent of alpine sediment cascades, Geomophology 111, 70-78, 10.1016/j.geomorph.2008.04.028.

OFEV, 2006, Carte indicative du permafrost en Suisse, Office fédéral de l'environnement (OFEV).

OFEV, 2007, Changement climatique en Suisse : indicateurs des causes, des effets et des mesures. Office fédéral de l'environnement (OFEV).

Annexe I : Données topographiques et de volumes pour le torrent de Lirec

	Caractéristiques topographiques des bief										Caractéristiques dynamiques des biefs				Volumes de base des biefs					
No Bief	Coord X	Coord Y	altitude [m]	Pente (°)	Longueur (m)	Longueur réelle (m)	Largeur (m)	Orientation (Az)	Surfaces érodables du bief	Surfaces érodables Vind	Dynamique	Type Section	Géologie	ID Bief aval	Vinitial direct [m3]	Vinitial indirect [m3]	Vmax limite [m3]	Profondeur moyenne dépôt	% bief concerné par du dépôt	Vmax dépôt
1	616820.4	111230.6	3040	38	89.80	113.96	2	245	0	26140	Er	gen_er	0	9	0	5300	5300	0	0	0
2	616817.4	111185.9	3027	37	78.83	98.71	2	240	0	47010	Er	gen_er	0	10	0	9500	9500	0	0	0
3	616837.9	111133.1	3038	38	132.51	168.16	2	268	0	23880	Er	gen_er	0	11	0	4800	4800	0	0	0
4	616808.2	111066.6	3011	39.2	119.44	154.13	2	277	0	24370	Er	gen_er	0	12	0	4900	4900	0	0	0
5	616764.2	110999.5	2982	37	90.69	113.55	2	270	0	10780	Er	gen_er	0	13	0	2200	2200	0	0	0
6	616589.9	111305.2	2910	40.4	111.46	146.36	2	254	0	13440	Er	gen_er	0	15	0	2700	2700	0	0	0
7	616636.8	111240.6	2930	36	84.49	104.43	2	223	0	27680	Er	gen_er	0	17	0	5600	5600	0	0	0
8	616619.5	111196.4	2896	39	150.60	193.78	2	225	0	5750	Er	gen_er	0	18	0	1200	1200	0	0	0
9	616685.6	111178.7	2925	39.8	196.11	255.25	2	241	0	21560	Er	cf	0	18	0	4400	4400	0	0	0
10	616700.5	111149.8	2931	42	167.07	224.82	2	249	0	4540	Er	cf	0	19	0	1000	1000	0	0	0
11	616700.8	111126.4	2928	42	142.65	191.96	2	271	0	4970	Er	cf	0	19	0	1000	1000	0	0	0
12	616647.5	111052.2	2865	42	210.93	283.84	2	261	0	0	Bim	cf	1	20	0	0	0	30	0.1	900
13	616610.0	111009.2	2840	40	216.26	282.31	2	294	340	1740	Bim	cf	0	21	250	400	650	30	0.2	1700
14	616585.1	110972.6	2834	37	206.15	258.13	2	296	0	7020	Bim	cf	0	21	0	1500	1500	30	0.3	2400
15	616501.1	111258.7	2820	46.3	94.02	136.08	4	262	0	0	Bim	tf	1	16	0	0	0	25	1	3500
16	616433.0	111208.3	2749	34.6	78.11	94.90	7	221	280	0	Dep	tf	0	23	50	0	50	25	1	2400
17	616494.9	111140.1	2790	39	262.37	337.61	5	225	0	0	Dep	tf	1	24	0	0	0	25	0.1	900
18	616544.2	111085.0	2791	36.2	143.78	178.17	5	237	0	0	Bim	tf	1	22	0	0	0	30	0.5	2700
19	616596.0	111065.6	2822	38	108.28	137.41	5	251	0	0	Dep	tf	1	20	0	0	0	30	0.2	900
20	616524.4	111039.4	2770	32	39.98	47.14	10	263	360	0	Dep	tf	0	21	570	0	570	30	1	1500
21	616490.0	111047.4	2747	32	28.16	33.21	10	273	300	0	Dep	tf	0	22	120	0	120	30	1	1000
22	616435.9	111063.0	2711	37	86.27	108.02	10	244	580	0	Dep	tf	0	23	1130	0	1130	30	1	3300
23	616296.1	111084.3	2644	28	299.79	339.53	7	222	1700	0	Dep	tf	0	25	700	0	700	30	1	10200
24	616280.3	111042.4	2621	32	228.52	269.46	10	220	2640	0	Dep	tf	0	25	3410	0	3410	30	1	8100
25	616134.1	110961.4	2539	28	112.45	127.36	10	200	920	0	Bim	tf	0	26	430	0	430	30	1	3900
26	616006.4	110828.7	2463	25	267.16	294.78	7	210	1840	0	Dep	tf	0	27	1280	3500	4780	30	1	8900
27	615848.1	110768.2	2393	28	91.15	103.23	5	224	350	0	Bim	tf	0	28	30	0	30	30	0.5	1600
28	615773.5	110729.6	2357	30	81.36	93.95	5	201	250	0	Er	tf	0	29	65	0	65	0	0	0
29	615661.2	110690.4	2290	29	178.21	203.76	5	236	300	900	Bim	tf	0	30	50	0	50	33	0.5	3400
30	615431.6	110611.4	2173	30	313.40	361.88	5	219	690	3410	Dep	tf	0	31	200	0	200	33	1	12000
31	615124.8	110370.8	1986	26	479.30	533.27	5	207	1080	0	Dep	tf	0	32	100	0	100	33	1	17600
32	615000.2	110114.1	1856	28	97.81	110.78	5	207	240	0	Dep	tf	0	33	100	0	100	33	1	3700
33	614926.4	110052.7	1812	26	100.75	112.10	5	190	330	0	Dep	tf	0	34	120	0	120	33	1	3700
34	614741.9	109977.6	1742	20	307.56	327.30	7	223	310	0	Dep	tf	0	35	700	0	700	33	1	10900
														Totaux	**9305**	**48000**	**57305.00**			**105200.00**

Annexe I : Données topographiques et de volumes pour le torrent de Perrec

	Caractéristiques topographiques des biefs										Caractéristiques dynamiques des biefs				Volumes de base des biefs					
No Bief	Coord X	Coord Y	altitude [m]	Pente (°)	Longueur (m)	Longueur réelle (m)	Largeur (m)	Orientation (Az)	Surfaces érodables du bief	Surfaces érodables Vind	Dynamique	Type Section	Géologie	ID Bief aval	Vinitial direct [m3]	Vinitial indirect [m3]	Vmax limite [m3]	Profondeur moyenne dépôt	% bief concerné par du dépôt	Vmax dépôt
1	617128.0	110927.8	3140.0	37	169.52	212.26	2	194	0	11560	Er	gen_er	0	31	0	2320	2320	0	0	0.00
2	617171.1	110955.3	3173.0	41	150.99	200.07	2	202	0	13120	Er	gen_er	0	26	0	2630	2630	0	0	0.00
3	617219.0	110961.6	3206.0	37	113.60	142.24	2	223	0	13720	Er	gen_er	0	17	0	2750	2750	0	0	0.00
4	617288.3	110950.6	3248.0	43	238.94	326.71	2	238	0	15070	Er	gen_er	0	17	0	3020	3020	0	0	0.00
5	617252.1	110852.6	3175.0	40	301.21	393.20	2	233	400	14260	Er	cf	0	27	123	2860	2983	0	0	0.00
6	617340.0	110836.1	3235.0	40	175.45	229.03	2	248	0	17750	Er	gen_er	0	18	0	3550	3550	0	0	0.00
7	617383.9	110800.5	3258.0	43	255.99	350.02	2	286	0	32290	Er	gen_er	0	18	0	6460	6460	0	0	0.00
8	617238.1	110733.6	3142.0	38	250.36	317.71	2	270	0	6050	Dep	gen_er	0	19	0	1210	1210	5	1	3200.00
9	617393.9	110691.9	3257.0	40	231.51	302.22	2	265	0	34910	Er	gen_er	0	20	0	6990	6990	0	0	0.00
10	617302.7	110634.0	3191.0	40	152.26	198.76	2	289	0	11950	Er	gen_er	0	21	0	2390	2390	0	0	0.00
11	617311.0	110581.1	3217.0	42	212.59	286.07	2	303	0	15700	Er	gen_er	0	21	0	3140	3140	0	0	0.00
12	616924.6	110639.0	2929.0	31	254.23	296.60	2	257	350	0	Dep	cf	0	34	256	0	256	5	1	3000.00
13	617117.7	110537.3	3063.0	39	185.93	239.24	2	270	0	18950	Er	gen_er	0	22	0	3790	3790	0	0	0.00
14	616914.3	110410.4	2940.0	43	161.99	221.50	2	308	0	19390	Er	gen_er	0	23	0	3880	3880	0	0	0.00
15	616829.6	110309.1	2868.0	42	131.01	176.29	2	213	0	11990	Er	gen_er	0	24	0	2400	2400	0	0	0.00
16	616822.0	110083.6	2855.0	37	64.77	81.10	2	280	0	21570	Er	gen_er	0	25	0	4320	4320	0	0	0.00
17	617164.7	110901.0	3142.0	37	49.48	61.96	3	223	0	1610	Bim	tf	0	26	0	400	400	10	0.6	1200.00
18	617194.9	110781.8	3110.0	37	138.93	173.96	3	263	500	0	Dep	cf	0	27	625	0	625	13	1	6800.00
19	617065.0	110730.3	3016.0	32	95.16	112.22	5	256	200	0	Dep	cf	0	32	300	0	300	13	1	7300.00
20	617213.4	110685.6	3115.0	38	127.69	162.03	5	250	300	0	Bim	cf	0	28	238	0	238	5	0.8	3300.00
21	617186.6	110663.0	3028.0	38	87.24	110.71	5	287	300	0	Dep	cf	0	28	40	0	40	5	1	2800.00
22	616982.5	110584.9	2954.0	37	98.19	122.95	5	255	400	0	Dep	tf	0	29	230	0	230	14	1	8700.00
23	616775.6	110451.8	2793.0	34	247.20	298.18	7	233	1700	0	Dep	tf	0	30	1900	0	1900	12	1	25100.00
24	616677.0	110334.5	2720.0	34	285.87	344.82	7	252	1500	0	Dep	tf	0	37	2100	0	2100	12	1	29000.00
25	616579.1	110177.9	2576.0	36	454.48	561.77	7	280	2800	0	Dep	tf	0	40	3600	0	3600	7	1	27600.00
26	617127.2	110870.9	3100.0	36	43.65	53.96	5	223	0	1610	Dep	tf	0	31	0	400	400	10	1	2700.00
27	617075.3	110747.3	3029.0	39	113.24	145.71	5	285	900	0	Dep	tf	0	32	750	0	750	13	1	9500.00
28	617092.9	110683.7	3029.0	41	110.64	146.60	7	307	600	0	Dep	tf	0	33	1040	0	1040	5	1	5200.00
29	616790.0	110505.9	2817.0	33	322.99	385.13	7	231	2200	0	Dep	tf	0	30	2100	0	2100	14	1	37800.00
30	616599.0	110358.0	2677.0	31	161.04	187.88	7	206	600	0	Bim	tf	0	37	121	0	121	12	0.8	12700.00
31	616970.0	110752.1	2969.0	32	340.16	401.11	7	243	1400	0	Dep	tf	0	35	852	0	852	13	1	36600.00
32	616919.6	110699.7	2932.0	40	202.12	263.84	10	295	2300	0	Dep	tf	0	35	5800	0	5800	13	1	34300.00
33	616924.4	110650.9	2840.0	38	240.00	304.56	10	290	2000	0	Bim	tf	0	34	3300	0	3300	5	0.8	12200.00
34	616794.0	110596.5	2700.0	37	270.00	338.08	10	270	1700	0	Bim	tf	0	36	1300	0	1300	5	0.2	3400.00
35	616698.8	110561.5	2785.0	35	324.75	396.45	10	243	2600	0	Bim	tf	0	36	2600	0	2600	13	0.4	20700.00
36	616525.5	110383.9	2780.0	34	191.83	231.39	10	206	0	0	Er	cf	1	38	0	0	0	0	0	0.00
37	616474.3	110302.6	2596.0	34	125.21	151.03	10	246	800	0	Bim	tf	0	39	1200	0	1200	5	0.7	5300.00
38	616439.9	110305.9	2589.0	28	70.99	80.40	10	207	0	0	Er	tf	1	39	0	0	0	0	0	0.00
39	616388.5	110274.1	2556.0	27	48.49	54.42	10	252	400	0	Er	tf	0	40	70	0	70	0	0	0.00
40	616303.2	110221.1	2502.0	29	149.18	170.57	15	198	1400	0	Er	tf	0	41	1300	0	1300	0	0	0.00
41	616220.0	110150.5	2490.0	31	81.90	95.55	15	210	0	0	Er	cf	1	42	0	0	0	0	0	0.00
42	616046.3	110101.4	2326.0	33	301.47	359.46	15	215	2000	0	Bim	tf	0	43	757	0	757	0	0	0.00
43	615812.4	109974.0	2000.0	33	240.71	287.01	10	220	0	0	Bim	cf	1	44	0	0	0	0	0	0.00
44	615644.7	109904.1	1985.0	32	380.77	448.99	10	260	500	11420	Dep	tf	0	45	9200	17000	26200	5	1	22500.00
45	615285.3	109814.2	1904.0	25	154.39	170.35	10	258	200	0	Dep	tf	0	46	5979	0	5979	5	1	8600.00
46	615004.2	109804.2	1804.0	24	410.24	449.06	15	234	500	10430	Bim	tf	0	47	15235	10000	25235	5	0.5	16900.00
47	614689.8	109822.0	1800.0	20	224.97	239.41	15	270	0	0	Er	tf	0	48	0	0	0	0	0	0.00
														Totaux	**61016**	**79510**	**140526**			**346400.00**

ANNEXE II : Résumé du travail de terrain effectué

Les travaux de terrain ont permis d'obtenir les données qualitatives et quantitatives nécessaires au fonctionnement du modèle MatErosion. Cette approche ne nécessite pas de cartographie géomorphologique de précision (GPS, Lidar) du torrent et de son bassin versant. Il s'agissait avant tout de :

- *relever les changements de la dynamique du torrent (érosion, dépôt, les deux, etc.) le long de son chenal ;*
- *relever les épaisseurs moyennes de la couche quaternaire ;*
- *relever les épaisseurs moyennes des différents glissements, des niches d'arrachement, des formes périglaciaires et glacières, des éboulis et des autres stocks sédimentaires ;*
- *noter d'éventuelles particularités du torrent.*

Avant de se rendre sur le terrain, une première analyse sur SIG a été au préalable effectuée en parcourant les photos aériennes et les cartes topographiques et géologiques. Cela a permis de planifier le parcours en notifiant les secteurs qui devaient à priori être visités. Cette première analyse a été suivie d'une identification à distance (cf. fig. 5.1) permettant ainsi de se faire une idée de la forme du torrent, des zones (visibles) d'apports de sédiments ainsi que le relevé d'éventuelles particularités qui n'avaient pas été identifiées dans la première étape. Il a ainsi été possible de mettre en relation les données SIG préalablement analysées avec la réalité du terrain et de déceler d'éventuelles incohérences ou modifications, lesquelles ont été vérifiées de plus près par la suite.

Toutes les informations quantitatives de terrain sur les volumes « potentiels » et « dormants » du torrent ont été enfin complétées par une nouvelle analyse SIG, afin d'obtenir une carte des phénomènes la plus complète possible. Les points suivant illustrent la démarche par quelques observations effectuées sur le terrain.

A. Identification et quantification de l'apport de matériaux solides dans le torrent

Il s'agit de cartographier les zones d'érosion connectées au torrent (fig. II.1 et II.4). Une délimitation spatiale a été réalisée en prenant en compte le potentiel d'extension de la dite zone. L'estimation du volume d'apport potentiel de ces zones d'érosion s'effectue en estimant la profondeur potentielle de l'érosion maximale (fig. II.2). La surface est calculée par la suite sur SIG (une estimation grossière peut toutefois être effectuée).

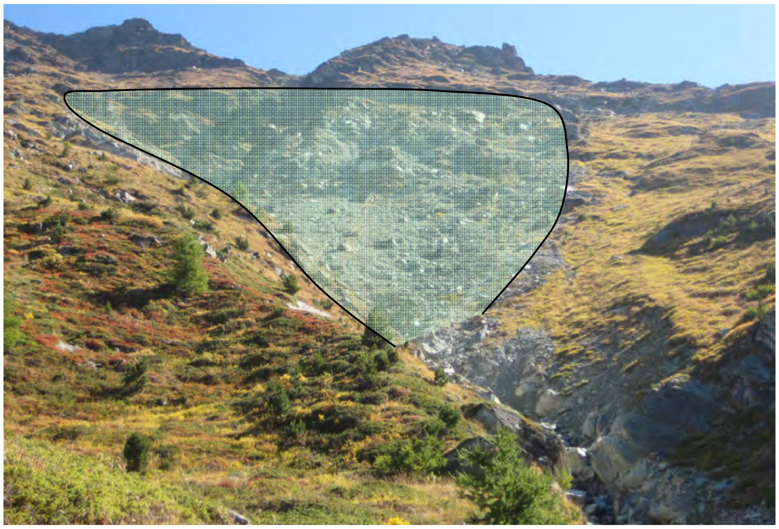

Figure II. 1 *: Illustration d'une zone le long du torrent de Pétérey cartographiée comme zone d'érosion.*

Figure II. 2 *: Quantification de la profondeur de l'érosion potentielle maximale pour cette zone d'érosion (Dynamique = Dep) dans le torrent de Lirec.*

Figure II. 3 *: Illustration d'un secteur de torrent (torrent de Perrec) où le bedrock affleure et classifié selon une dynamique d'érosion uniquement (Dynamique = ER). En conséquence, le modèle ne calculera pas d'érosion directe de matériel meuble dans celui-ci.*

Figure II. 4 *: Zone de démantèlement rocheux (Garde de Bordon) au-dessus du plat de la Lé.*

B. Estimation du volume de matériel déposé et déposable dans le torrent

En parallèle à l'estimation du potentiel d'érosion, il faut relever le potentiel de dépôt dans certaines parties du torrent en estimant le volume de matériel déposé (ou potentiellement déposable) (fig. II.3 et II.5). Il peut être aussi convenu d'effectuer des mesures plus précise du potentiel d'érosion (ou de dépôts suivant les cas choisis) en faisant recours à des outils tels que le GPS ou le LIDAR par exemple (fig. II.6).

Figure II.5 *: Estimation du volume de matériel déposé dans ce secteur du torrent de Lirec.*

***Figure II.6** : Mesures LIDAR d'une moraine en aval du glacier de Zinal effectués en septembre 2009.*

C. Identification des stocks sédimentaires

Il s'agit de cartographier les volumes stockés et potentiellement mobilisables par le torrent dans le futur. Cela passe par la localisation ainsi qu'une estimation de l'épaisseur de ce type de forme géomorphologique que sont les éboulis, les moraines, les éboulis sur glacier, les glaciers rocheux, les glaciers couverts, etc. (exemples fig. II.7 et II.8). Leur surface ainsi que leur épaisseur peuvent être estimées plus précisément sur SIG par la suite.

***Figure II.7** : Localisation d'imposantes moraines dans le val d'Ar-Pitteta (Le cercle rouge indique où a été prise la photo de la figure II.10)*

Figure II.8 *: Moraine imposante du glacier du Weisshorn. Son épaisseur (~30 m) peut facilement être déterminée sur SIG.*

D. Localisation de particularités des torrents

Le relevé de particularités dans et autour du torrent, qui pourrait modifier certains paramètres à court, moyen ou long terme, n’est pas nécessaire au modèle directement. Il est toutefois indispensable à l’élaboration de scénarios concernant l’évolution de la dynamique sédimentaires des bassins versants étudiés. Il s’agit par exemple d’un changement brusque de direction du torrent dans une zone de colluvion, d’un torrent captif, d’un risque d’embâcle-débâcle ou d’un événement extrême de type écroulement rocheux ou glissements de terrain qui viendraient modifier le bilan sédimentaire et la dynamique de transport de sédiments du torrent. Ce type de scénarios doit être pris en compte afin d’obtenir des estimations englobant l’activité torrentielle potentielle future.

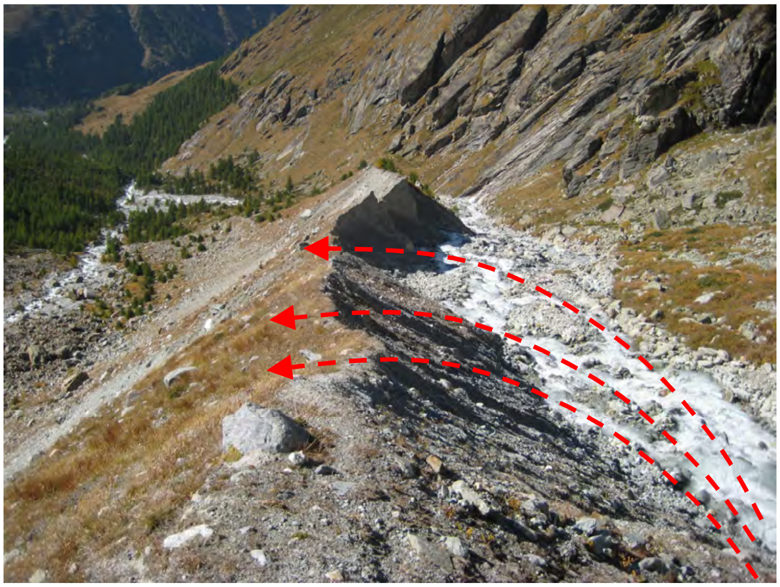

Figure II.9 : *Illustration d’un secteur où il est fort probable que ce torrent érode suffisamment le sommet de la moraine et déborde sur la gauche de l’image emportant par la même occasion une quantité importante de matériel solide et asséchant une partie du torrent auparavant active.*

E. Localisation des ouvrages de protection :

Ce type d'ouvrage peut avoir une influence sur la dynamique sédimentaire d'un torrent et doit être relevé sur la carte des phénomènes (fig. II.10). Une estimation (au moins qualitative) de son impact sur la dynamique sédimentaire doit être effectuée.

***Figure II. 10** : Dépotoir du torrent du Pétérey contenant des aménagements et ouvrages pouvant influencer la dynamique sédimentaire.*

Appendix B

Watershed sediment balance and local denudation rate based on hydropower reservoir sedimentation data

Abstract Hydropower reservoirs built in the lateral valleys of Valais (Switzerland) trap the sediment flux, so that their catchment areas become a sedimentary almost closed system, depending on hydrological regime and storage capacity. The rate of sediment infilling supplies data of sediment balance on the watershed. In this study, data of sediment volumes accumulated behind 11 hydropower dams and 3 settling basins were collected through bathymetrical surveys and camera or visual observations. Data analysis allows quantifying the sediment flux deposited since the time of dam construction and a local mean denudation rate can be assessed from a geographic information system. Estimated volumes are corrected according to the sediment trap efficiency of the reservoirs. The conversion of sediment volume into denudation rate is obtained according to the ratio of dry bulk density of the deposited material to solid bedrock density. Hence, density of loose sediment stored in the reservoir is estimated through grain-size distribution and degree of compaction. In some reservoirs, this evaluation was strongly restricted due to fragmentary information in space and time, so that the interpretation was limited to a general overview. In three watersheds, however, more data is available. A short-term trend of the sediment supply magnitude in the lake could be reconstructed. Local mean denudation rates range between 0.39 mm/yr to 0.62 mm/yr for 7 of 12 of the investigated watersheds. 2 highly-glaciated watersheds show a mean denudation rate of about 1.5 mm/yr and 2 other have a rate below 0.15 mm/yr. The overall mean denudation rate of the considered catchment areas is about 0.7 mm/y, which corresponds of an eroded mass of about 2'000 t/km^2 per year. Results are compared to characteristic surface processes and discussed according to the geomorphology, the recent glacial retreat and the fluvial network connectivity.

Quantitative data analysis of hydropower reservoir sedimentation is a complementary approach to existing methods, such as measurement of river sediment load and debris trap structures. The watershed sediment balance is fundamental information for the classification and understanding of slope erosion processes, as well as the inception condition of debris flows, which are key parameters in hazard assessment and reservoir management.

UNIL | Université de Lausanne
Faculté de Geosciences et Environnement
Institut de Géomatique et Analyse de Risque
Amphipôle
CH-1015 Lausanne

Estimation des quantités de matériaux érodés dans le bassin versant de Zinal

basée sur l'étude de l'alluvionnement des ouvrages hydroélectriques valaisans

Rapport final

Faculté de Géosciences et Environnement
Institut de Géomatique et Analyse du Risque
Loye Alexandre, Assistant PhD
Jaboyedoff Michel, Professeur

Avec la collaboration de
Minoia Romain, Assistant

Rapport: IGAR - AL - R001

Table des Matières

1 Préambule 5
2 Introduction 6
3 Présentation de la méthode 7
4 Estimation de l'alluvionnement 8
4.1 Capacité de rétention de la retenue 8
4.2 Conversion de l'alluvionnement en taux d'érosion 10
4.2.1 Densité des sédiments 11
4.2.2 Formulation de Miller incluant la compaction 11
5 Estimation de l'erreur des données 15
6 Données d'alluvionnement et taux d'érosion 16
6.1 Emosson 16
6.2 Les Toules 16
6.3 La Fouly 16
6.4 Grande Dixence 17
6.5 Zmutt et Cleuson 17
6.6 Mattmark 17
6.7 Mattsand 17
6.8 Gebidem 18
6.9 Ferden 18
6.10 Mauvoisin 19
6.11 Moiry 20
6.12 Turtmann 21
6.13 Sénin 22
6.14 Gries 22
7 Analyse des résultats 24
8 Estimation des volumes érodés dans le bassin versant de Zinal 29
9 Conclusion 33
10 Bibliographie 34
11 Annexe I 36
12 Annexe II 37

1 Préambule

Dans le cadre d'une réflexion liée à la gestion à long terme des matériaux inertes dans le canton du Valais, l'Institut de Géomatique et d'Analyse du Risque (IGAR) de l'Université de Lausanne a été mandaté par M. le Géologue cantonal Jean-Daniel Rouiller afin de quantifier, par une approche empirique, l'érosion annuelle dans le bassin versant de Zinal (Val d'Anniviers). Le mandat consiste à appréhender les bilans sédimentaires par la mise en relation de l'érosion des bassins versants avec l'alluvionnement des ouvrages hydroélectriques des vallées environnantes. Une étude des volumes de sédiments accumulés depuis leur mise en service dans 12 des plus grands aménagements hydroélectriques valaisans a permis d'estimer le taux d'érosion moyen de leur bassin versant respectif. Sur la base des quantités observées dans les systèmes sédimentaires valaisans, des ordres de grandeur des volumes de sédiments érodés chaque année dans la région de Zinal et plus particulièrement sur les zones des torrents ont pu être estimés.

Cette étude prospective sectorielle tente de tirer profit des données d'alluvionnement des ouvrages hydroélectriques. Elle présente ainsi une méthode d'analyse quantitative complémentaire aux démarches existantes, telles que les mesures de charriages sur la base de relevés dans les dépotoirs (GHO, 2004) ou les transports de charges sédimentaires en suspension dans les rivières (Grasso, 2003). En outre, ces valeurs empiriques sont des informations primordiales dans la classification (par ex. Gertsch, 2004) et la modélisation de ces systèmes érosifs, lesquelles conduisent à une mitigation des risques encourus.

Ce travail est une approche supplémentaire dans la connaissance des volumes sédimentaires sujets aux processus d'érosion. En lien avec les autres démarches, il contribue à présenter une image quantitative des bilans sédimentaires estimés annuellement dans les bassins versants valaisans de hautes altitudes et documente sur la quantité de matériaux qui devront être entreposés dans le future.

2 Introduction

Les retenues hydroélectriques, à partir d'une certaine taille, forment en théorie une zone d'accumulation sédimentaire close. Les volumes de sédiments accumulés dans ces retenues correspondent:

- à la déposition de la charge solide de tous les affluents contributifs (érosion par ruissellement d'eau).
    - Les matériaux grossiers se déposent en cônes de déjection aux embouchures des affluents.
    - Les particules plus fines sont transportés plus loin avant de se sédimenter.
    - Les matières dissoutes ne se décantent généralement pas dans la retenue et sont turbinées plus loin (USBR, 2006).
- à tous les processus de surface surplombant la retenue, tels qu'avalanches, glissements de terrain, coulées de boues ou torrentielle et chute de blocs.

Leur remplissage successif est fonction des processus de l'activité érosive dans le bassin versant contributif. L'historique stratigraphique des dépôts constitue une clé pour quantifier ces processus. La part d'alluvions autochtones (zooplanctons et algues) dans les lacs de montagnes est quasi inexistante et peut être écartée dans les bilans de masse. Ainsi, la documentation des volumes sédimentaires accumulés dans ces retenues permettent d'établir le taux d'érosion mécanique de leur bassin versant (Hinderer, 2000).

Cette approche se limite cependant à des mesures reflétant les volumes déposés à un endroit précis (c.-à-d. la retenue) durant une période de temps donnée. Selon les phénomènes, la charge sédimentaire érodée n'est pas transporté à la même cadence dans la zone d'accumulation qui sert de point de mesure. De plus, la topographie du bassin versant ainsi que son régime fluvial détermine le régime de transport des sédiments vers le point de mesure en contrebas. Les dépôts qui se forment ne sont pas pris en compte dans cette approche.

3 Présentation de la méthode

Une recherche de données précises sur le volume et la granulométrie des sédiments accumulés dans les dessableurs, captages et bassins d'accumulation a été entreprise auprès des exploitants des aménagements hydroélectriques ainsi que du service cantonal de l'énergie et force hydraulique. Les informations obtenues en retour ont été de fortune très diverses :

- Mauvoisin, Turtmann et Gebidem sont bien documentés dû aux problèmes d'exploitation liés à un fort alluvionnement.
- Moiry, Ferden, Sénin et Grande Dixence ont fait l'objet d'une ou deux bathymétries sur toute la surface du plan d'eau.
- D'autres installations (Emosson et Mattmark) ne possèdent que des mesures effectuées à des endroits précis, telles les prises d'eau et vannes de fonds. Elles sont difficilement extrapolables à l'étendue du réservoir, principalement à cause des courants de turbidité qui entrainent les sédiments contre le barrage ou à l'existence à l'amont d'une ancienne retenue aujourd'hui immergée.
- Mattsand, La Fouly et Zmutt se basent sur les mesures de purges ou vidanges lors des contrôles quinquennaux.
- Cleuson, Gries et Zeuzier : aucune donnée pertinente n'existe.

Ces volumes de sédiments déposés dans les retenues, lesquels sont sensés représenter l'apport en sédiments solides de leur bassin versant respectif, ont tous été quantifiés en suivant la même approche :

- Les données de volumes ont été reconsidérées en comparant différentes sources d'information (quand cela était possible), afin de ne garder que les estimations de volume les plus vraisemblables. Cependant, suivant la disparité et la qualité des données brutes disponibles, l'incertitude liée à ces valeurs est très variable d'un bassin versant à l'autre.
- Les retenues bien documentées ont fait l'objet d'une reconstitution de leur alluvionnement, permettant ainsi d'analyser son évolution dans le temps. Cela a permis en outre de détecter d'éventuelles périodes ou les estimations de volumes étaient peu vraisemblables, même erronées.
- Les volumes moyens de sédiments alluvionnés ont été corrigés selon la capacité de rétention de la retenue et convertis en taux d'érosion à partir d'une estimation de la densité moyenne du matériel déposé.
- Les taux d'érosion ainsi obtenu ont été ensuite normalisés (mm an^{-1}) pour permettre une comparaison entre les différents bassins versants investigués ainsi qu'avec les résultats d'autres études de bilans d'érosion.
- Enfin, les volumes de sédiments érodés annuellement dans la région de Zinal ont été estimés en tenant compte des taux d'érosion de l'ensemble des bassins versants étudiés dans cette étude et comparés avec les bilans des dépotoirs de la commune.

4 Estimation de l'alluvionnement

Le chapitre suivant présente les étapes successives à la conversion en taux d'érosion moyen des volumes de sédiments accumulés dans les retenues provenant de leur bassin versant contributif. A la fin de chaque partie, les variables utilisées et résultats obtenus concernant chaque étape du calcul de l'alluvionnement sont résumés dans un tableau. Une table récapitulative comportant toutes les données avec sources concernant le calcul de l'alluvionnement est ajoutée en Annexe I.

4.1 Capacité de rétention de la retenue

Selon la taille du plan d'eau, les sédiments solides apportés ne se dépose pas complètement dans la retenue, mais les particules les plus fines traversent le réservoir et sont turbinées vers l'aval (Snyder et al., 2004). Le volume d'alluvion déposé est ainsi corrigé suivant l'équation suivante :

$$V_s = 100 \times \frac{V_{ps}}{R} \qquad [1]$$

V_s : apport total de sédiments [m^3]

V_{ps} : volume de sédiments déposé dans la retenue [m^3]

R : capacité de rétention de la retenue [%]

La capacité de rétention des retenues n'est pas statique mais varie selon la quantité de sédiments déjà déposés, de la gestion de la hauteur d'eau (remobilisation) ainsi que des conditions hydrologiques (USBR, 2006). Sur la base des informations disponibles sur chaque retenue, une valeur peut être estimée à l'aide de la formule empirique d'Avendaño Salas et al. (1995 ; citée dans Beyer Portner, 1998) :

$$R = 100 \times \left[1 - \frac{1}{1 + \frac{ITE \cdot V_e}{S}} \right] \qquad [2]$$

ITE : indice du type d'exploitation de la retenue [-]

V_e : volume en eau de la retenue [10^3 m^3]

S : surface du bassin versant contributif [km^2]

Pour les retenues de productions hydroélectriques, la valeur ITE préconisée est de 1.43, car elles ne rencontrent que des variations modérées du plan d'eau. Pour les retenues hebdomadaires[1] de Ferden et Gebidem, lesquelles subissent des variations plus importantes du volume d'eau accumulé, une valeur ITE de 0.76 a été choisie. Quant aux dessableurs de Moiry et Turtmann, leur remplissage n'étant pas influencé, l'indice ITE est de 2.1. Les surfaces des bassins versants contributifs ont été calculées dans un environnement SIG sur la base du MNT 25m (CREALP) et comparées avec les données fournies par les exploitants.

Seules les petites retenues ont fait l'objet d'une correction. Quant aux grands barrages, leur capacité de retenue approchant les 100% [comm. Person. N. Bretz], le volume déposé n'a donc pas été corrigé.

Les retenues hydroélectriques ne collectent pas seulement les eaux de leur bassin versant naturel, mais sont reliées à de très nombreux captages récoltant l'eau des bassins avoisinants. Ces apports d'eau latéraux contribuent au transport de matériaux solides dans le lac, malgré qu'ils soient tous dotés d'un dessableur. Devant l'absence de données concernant ces contributions externes, seul le bassin versant naturel a été pris en compte dans cette étude.

Retenue	**Apport sédimentaire total V_s [m^3 an^{-1}]**	**Volume déposé V_{ps} [m^3 an^{-1}]**	**capacité de rétention R [%]**	**indice type d'exploitation ITE**	**volume V_e [mio m^3]***	**surface bassin versant naturel S [km^2]**
Les Toules	1750	1750	100	1.43	20.15	39
La Fouly	37037	20000	54	1.43	0.02	48.8
Grande Dixence	50000	50000	100	1.43	401	44.6
Mattmark	26700	26700	100	1.43	101	38
Mattsand	445044	200270	45	1.43	0.21	324
Gebidem	463918	450000	97	0.76	9.2	197.6
Ferden	21978	20000	91	0.76	1.89	132.6
Mauvoisin	348000	348000	100	1.43	211.5	114.6
Moiry	35102	35102	100	1.43	77	29.4
Moiry dessableur	9765	9082	93	2.1	env. 0.46	14
Turtmann	12680	12300	97	1.43	0.78	28.1
Turtmann dessableur	5893	4950	84	2.1	env. 0.15	21.93
Emosson	22414	22414	100	1.43	227	25.52
Sénin	3385	3385	100	1.43	2.8	11.35

*Aménagement le plus récent

Tableau 1: Données concernant le calcul de la capacité de rétention des retenues (les calculs des volumes sont référencés à la section 6).

---

[1] Caractéristique de la retenue, laquelle peut être statistiquement remplie de façon hebdomadaire.

4.2 Conversion de l'alluvionnement en taux d'érosion

À partir du volume total de sédiments accumulés dans la retenue, correspondant à l'érosion de surface du bassin versant contributif, le taux d'érosion est calculé à l'aide de l'équation suivante (Hinderer, 2000):

$$DR = \frac{V_S}{S \cdot T} \cdot \frac{\rho_S}{\rho_b}$$

DR : taux d'érosion dans le bassin versant naturel [$m^3\ km^{-2}\ an^{-1}$]

S : surface du bassin versant contributif [km^2]

T : période d'alluvionnement considérée par le volume déposé [an]

ρ_s : densité sèche des sédiments (dry bulk density) [$kg\ m^{-3}$]

ρ_b : densité solide du sol et bedrock érodé [$kg\ m^{-3}$]

Le taux d'érosion est exprimé dans ce rapport en $mm\ an^{-1}$, ce qui correspond à 1 km par million d'années :

ER : taux d'érosion dans le bassin versant naturel, exprimé en [$mm\ an^{-1}$]

Retenue	ρ_s [$kg\ m^{-3}$]	ρ_b [$kg\ m^{-3}$]	année de mise en service	DR [$m^3\ km^{-2}\ an^{-1}$]	ER [$mm\ an^{-1}$]
Les Toules	1450	2700	1963	24	0.024
La Fouly	1750	2700	1972	422	0.422
Grande Dixence	1500	2700	1937	623	0.623
Mattmark	1500	2700	1967	390	0.39
Mattsand	1280	2700	1962	610	0.61
Gebidem	1625	2700	1967	1261	1.26
Ferden	1500	2700	1975	92	0.092
Mauvoisin	1500	2700	1956	1687	1.69
Moiry	1400	2700	1958	619	0.62
Moiry dessableur	1615	2700	1972	417	0.42
Turtmann	1330	2700	1960	228	0.23
Turtmann dessableur	1800	2700	1972	179	0.18
Emosson	1330	2700	1975*	433	0.43
Sénin	1350	2700	1965	149	0.15

*Aménagement le plus récent

Tableau 2 : Données concernant le calcul du taux d'érosion de chaque bassin versant

4.2.1 Densité des sédiments

Le volume des sédiments V_s déposé dans la retenue est lié au volume de matériel érodé par le ratio de la densité sèche sur la densité solide ρ_s / ρ_b.

La densité solide du matériel érodable ρ_b dépend du type de lithologie ainsi que de sa couverture sédimentaire (Robitaille & Tremblay, 1997) . Il varie entre *2’500* et *2’800 kg m*$^{-3}$ pour des terrains de sources mixtes (calcaire, granite). Pour les bassins versants composés de roche en place plus basiques et ultrabasiques, leur densité est plus élevée. Par contre, la densité moyenne des dépôts morainiques varie entre *1’750 – 2’000 kg m*$^{-3}$ (Schlüchter, 1989). Dès lors, une densité solide du matériel en place (mean bedrock density) de *2’700 kg m*$^{-3}$ fut appliquée comme valeur moyenne de ρ_b.

Concernant les dépôts sédimentaires non consolidés des retenues, nous n’avons pas bénéficié de mesures in situ. A partir des données granulométriques des différents lacs étudiés, la densité sèche moyenne ρ_s des alluvions a donc été estimée sur la base d’une équation empirique fondée sur des mesures in situ établies dans plus de 500 lacs de retenues à travers le monde. Cependant, toutes ces démarches empiriques, bien que largement utilisées, assument un taux de sédimentation constant dans le temps ainsi qu’une distribution constante de la composition des grains alluvionnés. Ces conditions sont rarement rencontrées dans les barrages valaisans et l’application de ces formules sur des mesures in situ ont révélé de sérieux décalages (> 50%) dans les valeurs comparées (Verstraeten & Poesen, 2000). Les erreurs associées avec l’estimation de la densité sèche moyenne ayant un impact significatif sur le calcul du taux d’érosion, les valeurs obtenues furent comparées avec d’autres campagnes de mesures faites sur d’autres retenues ainsi que les données classiques de littérature à ce sujet.

Ainsi, devant une telle incertitude pour déterminer la densité totale moyenne des volumes de sédiments déposés dans les retenues, le ratio ρ_s / ρ_b choisi doit être considéré comme une valeur probable. Elle correspond à un ordre de grandeur indicatif mais en aucun cas comme une prédiction certaine.

4.2.2 Formulation de Miller incluant la compaction

La densité totale sèche dépend essentiellement de la distribution granulaire des sédiments. Elle dépend aussi de la profondeur de l’eau, de l’épaisseur de la couche de sédiments et du degré de compactage (Morris & Fan, 1998). Les sédiments tendent à se compacter à la longue, sous l’effet des pressions de surcharge, mais aussi de l’alternance de mise à sec et d’immersion lors de variations du niveau de la retenue. De plus, la densité humide globale varie selon la grandeur des grains et peut varier de 20% selon le type de dépôts (Hinderer, 2002). Enfin, des études basées sur des carottages montrent que la densité n’augmente pas nécessairement avec la profondeur, car les couches inférieures comportent dans certains cas un pourcentage de sédiments fins plus élevés (Snyder & al., 2004).

A partir de l’hypothèse que le dépôt s’effectue de façon continue, une relation a été établie entre la densité sèche, la granulométrie et le temps écoulé T [an] :

$$\rho_s = \rho_{s_0} + 0.4343 \cdot K \cdot \left\{ \frac{T}{T-1} \cdot \ln(T) - 1 \right\}$$

(Koelzer & Lara, 1958)

Dans notre cas *T* correspond à la durée d’exploitation de la retenue. ρ_{so} [kg m^{-3}] correspond à la densité sèche initiale des sédiments juste après déposition. Il se calcule sur la base des classes granulométriques comme suit :

$$\rho_{s_0} = \frac{\rho_{(argile)_0} \cdot \%Argile + \rho_{(limon)_0} \cdot \%Limon + \rho_{(sable)_0} \cdot \%Sable + \rho_{(gravier)_0} \cdot \%Gravier}{100}$$

Le coefficient *K* est un facteur déterminant la vitesse de compactage des sédiments dans la retenue. Sa valeur est calculée selon :

$$K = \frac{K_{(argile)} \cdot \%Argile + K_{(limon)} \cdot \%Limon + K_{(sable)} \cdot \%Sable + K_{(gravier)} \cdot \%Gravier}{100}$$ (cf. Tableau 3)

Type de réservoir	***gravier (>1000μm)***		***sable (50-1000μm)***		***limon (5-50μm)***		***argile (<5μm)***	
	$\rho_{So\ i(gravier)}$	$K_{gravier}$	$\rho_{So\ i(sable)}$	K_{sable}	$\rho_{So\ i(limon)}$	K_{limon}	$\rho_{So\ i(argile)}$	K_{argile}
Retenue toujours (ou presque) pleine$^{(1)}$	*1600*	*0*	*1490*	*0*	*1041*	*91*	*481*	*256*
Retenue à variation modérée du plan d'eau $^{(2)}$	*1600*	*0*	*1490*	*0*	*1185*	*43*	*737*	*171*
Retenue à variation intensive du plan d'eau$^{(3)}$	*1600*	*0*	*1490*	*0*	*1266*	*16*	*961*	*96*
Retenue normalement vide	*1600*	*0*	*1490*	*0*	*1314*	*0*	*1245*	*0*

(1) Retenue type dessableur, (2) Retenue type accumulation, (3) Retenue type hebdomadaire comme Ferden et Gebidem.

Tableau 3 : Valeur ρ_{So} [kg m^{-3}] et K pour l’équation 2 et 3 d’après Lane and Koelzer (1943 ; tirées de Verstraeten & Poesen, 2000).

Les valeurs de densité sèche initiale après *T* années d’exploitation de dépôt sont résumées dans le Tableau 4.

Une autre formule empirique basée sur des mesures de plus de 600 réservoirs de part le monde s’exprime par l’équation :

$$\rho_{s_0} = 817 \cdot (p+2)^{0.13}$$ (Lane & Koelzer, 1943 ; citée dans Verstraeten & Poesen, 2000)

Ou *p* représente le pourcentage de sédiments grossiers > 0.05 mm. Les valeurs obtenues sont résumées dans le Tableau 4.

Des mesures in situ ont été effectuées par « multisensor-core-logger » dans une retenue hydroélectrique d'Englebright (Californie du nord) par Snyder et al. (2004). Ce lac artificiel est de taille moyenne (86 mio m^3) et possède un alluvionnement mixte composé de charriage et de fines (hauteur des dépôts maximaux: ~35m). La distribution de la taille des grains ainsi que sa teneur en matière organique sont comparables à celles observées dans les grands barrages valaisans. Ainsi, il comporte de nombreuses similitudes avec le type de dépôts observé dans les Alpes. Les résultats de leurs investigations sont résumés dans le Tableau 5.

Retenue	**Coefficient K**	**% gravier**	**% sable**	**% limon**	**% argile**	**Densité sèche initiale (équation de Miller)**	**densité sèche après T = 30 ans**	**Densité sèche initiale (équation de Lane & Koelzer)**
La Fouly	216	56.7	36.2	7.2	<1	1532	1769	1477
Mattsand	78	0	26	58	16	1193	1276	1260
Gebidem	166		85	15	>1	1444	1626	1460
Mauvoisin	136	20	33	47	-	1369	1518	1376
Turtmann	77		20	80	-	1246	1331	1221
Moiry	98	10	20	70	-	1287	1395	1282
Moiry dessableur	203	60	25	5	-	1392	1614	1460
Turtmann dessableur	228	-	60	40	-	1556	1806	1397
Sénin	90	-	30	55	15	1225	1350	1282
Toules	116	-	47	53	-	1327	1453	1355

Tableau 4 : Analyse granulométrique disponible de différents barrages valaisans. Les données de densité sont exprimées en [kg m^{-3}]. (Pour les références : voir section 6).

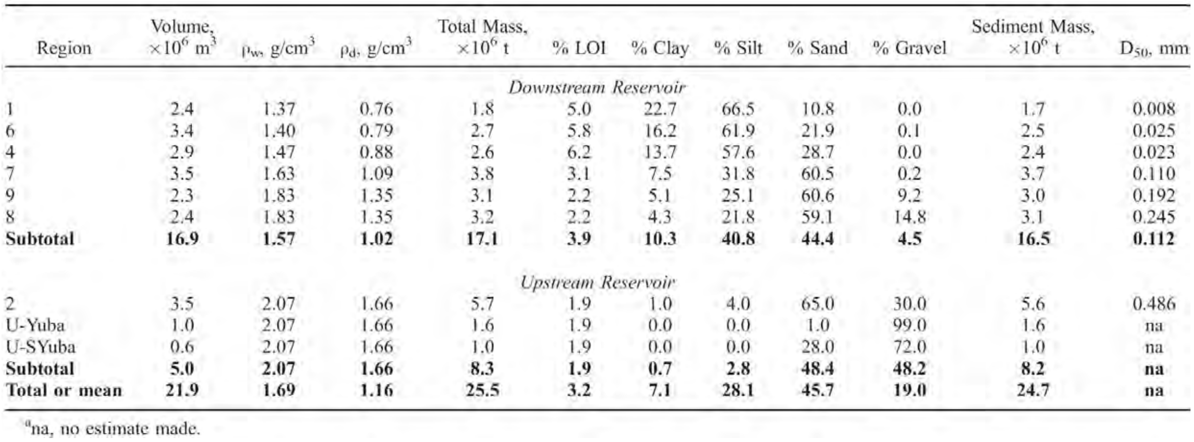

Region	Volume, $\times 10^6$ m^3	ρ_w, g/cm^3	ρ_d, g/cm^3	Total Mass, $\times 10^6$ t	% LOI	% Clay	% Silt	% Sand	% Gravel	Sediment Mass, $\times 10^6$ t	D_{50}, mm
					Downstream Reservoir						
1	2.4	1.37	0.76	1.8	5.0	22.7	66.5	10.8	0.0	1.7	0.008
6	3.4	1.40	0.79	2.7	5.8	16.2	61.9	21.9	0.1	2.5	0.025
4	2.9	1.47	0.88	2.6	6.2	13.7	57.6	28.7	0.0	2.4	0.023
7	3.5	1.63	1.09	3.8	3.1	7.5	31.8	60.5	0.2	3.7	0.110
9	2.3	1.83	1.35	3.1	2.2	5.1	25.1	60.6	9.2	3.0	0.192
8	2.4	1.83	1.35	3.2	2.2	4.3	21.8	59.1	14.8	3.1	0.245
Subtotal	**16.9**	**1.57**	**1.02**	**17.1**	**3.9**	**10.3**	**40.8**	**44.4**	**4.5**	**16.5**	**0.112**
					Upstream Reservoir						
2	3.5	2.07	1.66	5.7	1.9	1.0	4.0	65.0	30.0	5.6	0.486
U-Yuba	1.0	2.07	1.66	1.6	1.9	0.0	0.0	1.0	99.0	1.6	na
U-SYuba	0.6	2.07	1.66	1.0	1.9	0.0	0.0	28.0	72.0	1.0	na
Subtotal	**5.0**	**2.07**	**1.66**	**8.3**	**1.9**	**0.7**	**2.8**	**48.4**	**48.2**	**8.2**	**na**
Total or mean	**21.9**	**1.69**	**1.16**	**25.5**	**3.2**	**7.1**	**28.1**	**45.7**	**19.0**	**24.7**	**na**

[a] na, no estimate made.

Tableau 5 : Caractéristiques des quantités de sédiments accumulés dans le lac Englebright (Californie). Notez la densité sèche ρ_d exprimée en [g cm^{-3}] (tiré de Snyder et al., 2004).

Les valeurs contenus dans la littérature, concernant les sédiments submergés de façon permanente dans les retenues de montagnes, varies entre *700* et *2'000 kg* m^{-3}. Leur densité sèche dépend fortement des conditions de dépôts et du type et taille des grains. Le Tableau 6 présente les valeurs recensées par dominance spécifique des grains.

Taille des grains dominants	Sédiments submergés de façon permanente	
	Minimum [kg m^{-3}]	Maximum [kg m^{-3}]
Argile	641	961
Limon	881	1202
Mélange Argile - Limon	641	1041
Mélange Limon - Sable	1202	1522
Mélange Argile – Limon - sable	801	1282
Sable	1362	1602
Gravier	1362	2003
Sable et gravier pauvrement classé	1522	2083

Tableau 6 : Éventail des masses volumiques sèches pour des classes de sédiments submergées en permanence (tiré de H. P. Guy, 2001).

La comparaison des valeurs types avec les valeurs obtenues par les formules empiriques montre une bonne adéquation avec les maximums. En considérant les données granulométriques, elles tendent à corroborer les résultats obtenus par les formules empiriques, lesquelles sont relativement similaires (cf. Tableau 4). Les mesures d'Englebright par Snyder et al. (2004) sont par contre plutôt en adéquation avec les valeurs types minimums. Leurs résultats sont plausibles dans les premières dizaines de centimètre des dépôts, c-à-d la vase, ou les alluvions s'apparentent à une matrice argileuse. Ils semblent cependant bas si on considère un alluvionnement solide de plusieurs mètres. Ainsi, les densités sèches moyennes obtenues par l'équation de Miller ont servi d'estimation pour le calcul du taux d'érosion. Les densités des retenues de Mattmark, Grande Dixence et Ferden, lesquelles ne comportent pas d'informations granulométriques, ont été calquées sur la densité de Mauvoisin. Cette hypothèse semble raisonnable au vue du système fluvio-glaciaire de leur bassin versant ainsi que la grandeur des lacs. Emosson est réputé pour ses eaux claires. Selon l'exploitant, les dépôts d'alluvions sont peu importants. Ainsi une densité ρ_{so} arbitraire de $1'250\ kg\ m^{-3}$ (correspondant à une granulométrie argilo-sableux à dominance limoneuse) a été appliquée. Cette densité est semblable à ce qui est observé dans le lac de Sénin, et son bassin versant est composé des mêmes unités lithologiques (cf. Tableau 2 et Tableau 4).

5 Estimation de l'erreur des données

Les volumes des dépôts obtenus par mesures bathymétriques sont assez précis. Les sources d'imprécision proviennent essentiellement de la détection de l'interface eau-dépôts sédimentaires au fond du barrage et de la détermination des hauteurs d'eau lors des mesures. Selon un spécialiste des bathymétries (comm. Pers. Alexandre Gal), l'erreur du calcul des volumes alluvionnés est de *~5%*. Les pertes de volumes de sédiments contenus dans les retenues entre les mesures sont plus difficiles à estimer : si la perte due au turbinage dans les grands barrages est insignifiant, dans les petites retenues, selon la charge solide en suspension, les volumes mesurés peuvent être sous-estimés. La correction de la capacité de rétention des retenues tend à minimiser cette erreur. La pertinence des données de volumes obtenus par estimation ne peuvent pas être quantifiées. Il est cependant important de préciser que la motivation première des barragistes à l'étude de l'alluvionnement n'est point de connaître de façon précise les volumes et la composition des dépôts recensés, mais s'intéressent avant tout à l'ensablement de leurs installations par mesures de sécurité et d'usure des turbines. Comme mentionné déjà précédemment, la densité sèche varie grandement entre faciès des grains et profondeur des sédiments. En prenant une valeur moyenne pour toute l'étendue du dépôt, la masse des dépôts de surface est certainement surestimée et ceux déposés depuis plusieurs décennies ont une densité plus élevée à la valeur moyenne choisie. Dans la plupart des cas, l'imprécision devrait être cependant balancée. Ainsi, tous les volumes obtenus par mesures bathymétriques ou dragage des retenues peuvent être appréhendé avec une imprécision inhérente à toutes études de bilan de masses.

Les densités sèches varient dans une proportion de 20% selon les différents types de dépôts considérés.

Toutes les autres valeurs doivent donc être considérées comme des approximations.

6 Données d’alluvionnement et taux d’érosion

6.1 Emosson

Selon l’exploitant, les eaux du barrage d’Emosson sont claires et l’alluvionnement y est très restreint. Une bathymétrie fut effectuée durant l’été 2004 (Emosson, 2004) devant le couronnement et aux alentours de la prise d’eau. Le rapport fait mention de levés antérieurs (1988 et 1993) non communiqués. Un volume de sédiments d’environ 650’000 m^3 a été mesuré par comparaison avec les données précédentes pour toute la surface du barrage. Malgré ces relevés physiques, ce volume reste une estimation à cause de la présence en amont de la digue de Barberine, laquelle influence la répartition des alluvions au fond du lac. L’apport en sédiments dans les lacs d’Emosson se fait principalement par des apports en eau indirects, lesquelles proviennent des vallées glaciaires actives environnantes. Il n’est cependant pas aisé de quantifier la part d’alluvion indirect, car ces sédiments sont en partie décantés dans des dessableurs ou entrainés hors du lac par turbinage. Cependant, Emosson pratique essentiellement un turbinage d’été et les apports indirects ne restent que très peu de temps dans la retenue (comm. pers. de l’exploitant), empêchant un dépôt important des alluvions.

En partant dès lors de l’hypothèse que le volume provient essentiellement de son bassin versant naturel et en ne tenant pas compte du bassin versant du barrage du Vieux Emosson, le taux d’érosion peut être estimé à *0.43 mm an*$^{-1}$, en admettant une densité sèche de 1’330 kg m^{-3} des alluvions correspondant à un faciès 80% limon et 20% sable.

6.2 Les Toules

La retenue des Toules ne possède pas de mesures particulières de son alluvionnement, malgré qu’elle a été vidée complètement il y a quelques années. L’apport par charriage est estimé à 1’000 m^3 an^{-1} et le dépôt des sédiments fin à 750 m^3 an^{-1} (Beyer Portner, 1998).

Compte tenu d’un bassin versant naturel de 39 km^2, l’estimation du taux d’érosion dans la haute vallée du Grand St-Bernard s’élève à *0.024 mm an*$^{-1}$.

6.3 La Fouly

Cette petite retenue de 20’000 m^3 est en faite une prise d’eau pour le complexe hydroélectrique d’Emosson. Les dépôts contenus dans le dessableur et la retenue sont dragués chaque année. Les volumes estimés sont de l’ordre de 5’000 m^3 de gravats dans le dessableur et de 15’000 m^3 de matériaux plus mélangés dans le lac (comm. pers. Emosson SA).

En tenant compte de sa capacité de rétention ainsi que de la granulométrie analysée par Rosset (1990 ; cité dans N. Beyer Portner, 1998), l’érosion moyenne se monte à *0.42 mm an*$^{-1}$ pour la haute vallée de Ferret.

6.4 Grande Dixence

Dans les années 80, Bezinge (1989) avait estimé l'apport solide direct dans le barrage de la grande Dixence à 28'000 m^3 an^{-1}. Dans les années 90, Grande Dixence SA estimait l'apport solide du bassin versant naturel à 50'000 m^3 environ. En 2006, une étude bathymétrique a révélé un ensablement d'env. 9 mio m^3 depuis la mise en service en 1937. Le rapport (Bretz, 2006) sur la gestion de l'ensablement de Grande Dixence indique un apport solide total de 100'000 m^3 an^{-1}. L'apport provenant du bassin versant naturel s'élève à ~50'000 m^3 confirmant grossièrement les valeurs antérieures.

Compte tenu de la complexité du réseau hydrologique de Grande Dixence SA (cf. Zmutt et Cleuson), seul le volume concernant son apport par ruissellement direct a été retenu pour l'analyse. Le volume moyen de sédiments érodés dans le Val des Dix est estimé à *0.62 mm* an^{-1}.

6.5 Zmutt et Cleuson

Selon Grande Dixence SA, la retenue de Cleuson n'est que très peu chargée en sédiments. Son eau est claire. Il existe aucune donnée à leur connaissance.

Des purges annuelles ont lieu dans la retenue de Zmutt. L'ensablement est important, en particulier dû au retrait des glaciers qui l'alimentent. Il n'existe cependant pas de données précises sur le volume des dépôts purgés (entre 10'000 et 40'000 m^3). Des mesures sont effectuées pour s'assurer que les masses en suspension ne dépassent pas le seuil autorisé. Mais les débits des apports d'eau externes (Gorner – Findelen) servant à diluer ces particules ne sont pas mesurés. Il n'est ainsi pas possible de raccrocher de façon judicieuse ces estimations à un bassin versant précis pour évaluer un taux d'érosion.

6.6 Mattmark

Quelques levées bathymétriques ont été accomplies sur les embouchures des affluents du lac pour y étudier l'alluvionnement de ses deltas. Un taux d'érosion de 1 mm an^{-1} fut estimé par comparaison avec d'autres bassins versants (Willi, 1996 ; cité dans N. Beyer Portner, 1998). Sur la base de ces données, une extrapolation sur toute la surface du lac estime le volume de sédiment déposé entre 1967 et 1995 à 747'000 m^3.

Sur la base de cette estimation, le taux de dénudation dans le bassin naturel du lac de Mattmark est évalué à *0.39 mm* an^{-1}.

6.7 Mattsand

Une grande partie des eaux du bassin versant de la vallée de Zermatt sont détournés dans les aménagements hydroélectriques de la Grande Dixence. De ce fait, l'apport en eau chargée de masses solides est grandement influencé par tous ces ouvrage rendant difficilement estimable sa contribution brute dans la retenue de Mattsand. Dès lors, l'eau de ruissellement captée par la retenue de Zmutt n'a pas été considérée dans le calcul de surface de son bassin versant naturel. Des mesures effectuées dans la fin des années 70 lors des purges des dessableurs et du bassin de compensation lui-même estimaient un alluvionnement global d'env. 200'000 m^3 par an (Beyer Portner, 1998).

En tenant compte de sa faible capacité de rétention et qu'en outre les sédiments ne restent qu'une année dans la retenue, le taux d'érosion est d'environ *0.61 mm* an^{-1}.

6.8 Gebidem

Des mesures effectuées durant un an par EDF avant la construction du barrage avait révélé un transport solide dans la Massa de 500'000 m^3 an^{-1} environ. Durant les années 1970-90, des mesures de concentration durant les purges annuelles estimaient l'apport sédimentaire à 230'000 m^3 (Vischer 1981). A partie de 1991, des études détaillées de l'alluvionnement ont été effectuées lors de chaque vidange par EOS (Rechsteiner, 1996) durant 6 ans :

Année	Volume des sédiments déposés [m^3 an^{-1}]	Volume des sédiments turbinés et purgés [m^3 an^{-1}]	Volume total [m^3]
<1970			500000
1970-1990	160000	70000	230000
1991	240000	70000	310000
1993	400000	80000	480000
1994	320000	110000	430000
1995	350000	120000	470000
1996	325000	95000	420000
Moyenne sur 50 ans			380400
Moyenne 1993-96	348750	101250	450000
Tendance 2000			>500000

Tableau 7 : Bilan de l'alluvionnement dans la retenue de Gebidem (G. Rechsteiner, 1996)

Compte tenu des vidanges annuelles, les sédiments ne se compactent pas dans la retenue. Le taux de dénudation obtenu pour la moyenne sur 50 ans est de *1.06 mm* an^{-1} malgré un bassin versant naturel d'env. 200 km^2. Pour le volume moyen obtenu dans les années 90, l'estimation de l'érosion atteint *1.26 mm* an^{-1}. La tendance depuis l'an 2000 semble s'approcher des valeurs mesurées dans le cours d'eau avant la construction du barrage, correspondant à *1.36 mm* an^{-1} d'érosion.

6.9 Ferden

Cette retenue hebdomadaire contient des relevés bathymétriques effectués chaque deux an depuis 1982. Avant cela, l'alluvionnement annuel se basait sur des estimations. Le volume moyen accumulé durant ces 40 dernières années est estimés entre 16'000 et 20'000 m^3 par an (Comm. KW Lötschen AG).

Comparé à l'étendue de son bassin versant, le taux d'érosion se situe entre *0.074* et *0.092 mm* an^{-1}.

6.10 Mauvoisin

La vidange complète du lac effectuée en 1985 a révélé un niveau important d'alluvionnement dans la retenue de Mauvoisin. Afin de remédier à l'envasement des prises d'eau qui ne cessait d'augmenter à l'époque, un concept général a été adopté par Mauvoisin SA. Ainsi, quelques études détaillées ont été effectuées sur l'alluvionnement du barrage et le volume de sédiments déposés est bien documenté dans le temps (Schleiss, 1996 ; Electrowatt, 1997 ; Seiler & Thomann, 2002 ; Ecotec 1998) :

Année	Commentaires	Alluvionnement mesuré [m^3]	Perte en particules fines due aux purges [m^3]	alluvionnement [m^3]	Taux d'alluvionnement [m^3 an^{-1}]	Erosion spécifique de surface [mm an^{-1}]
1956-1985	Estimation par photogrammétrie lors de la vidange complète	9.5 mio (80% fines)	0.335 mio (vidange)	9835000	339138	1.64
1985-1995	1ème bathymétrie* :	2 mio (fines)	0.01 mio an-1	2600000	260000	1.26
1995-1997	2ème bathymétrie** :	31700	560	1140381	570190	2.76
1997-1998	3ème bathymétrie** :	7100	1900	128810	128810	0.63
1998-2000	4ème bathymétrie** :	19100	3200	523810	261905	1.27
2000-2004	5ème bathymétrie*** :	88254	-	2270354	567588	2.75
					Moyenne 1956 - 1985	1.64
					Moyenne 1956 - 1995	1.55
					Moyenne 1956 - 2000	1.55
					Moyenne 1956 - 2004	1.67
					Moyenne 1985 - 2004	1.7
					Moyenne 1995- 2004	2.2

Tableau 8 : Résumé de l'alluvionnement observé dans la retenue de Mauvoisin. * L'estimation fut faite par rapport à 1985 ; ** Surface de la fenêtre d'observation : 42'000 m^2 (2.02% du plan d'eau) ; * Surface de la fenêtre d'observation : 57'600 m^2 (2.77% du plan d'eau).**

Les relevés bathymétriques (Mauvoisin SA) ont été établis sur la portion avale du lac de Mauvoisin, principalement aux alentours de la prise d'eau et de la vanne de fond. Ces installations sont en outre séparées par une digue batardeau qui influença l'ensablement à l'amont du barrage jusqu'au début des années 90. La fenêtre d'observation a donc été extrapolée sur toute la surface du lac de façon non linéaire à cause des courants de turbidités qui remobilisent et concentrent les dépôts dans la partie avale du lac (De Cesare, 1998) ou s'effectuèrent les levés bathymétriques. Les observations de ces courants de densité sur d'autres ouvrages ont révélé que ces transports subaquatiques de matériaux solides viennent mourir contre le barrage et finissent leur course sur la partie aval du lac.

Ainsi, en se basant sur l'hypothèse que les courants de densité V_{cd} amènent environ 35'000 m^3 an^{-1} (Electrowatt, 1997) dans les parties proches de la retenue (10% de la surface totale A_{tot}), un volume d'alluvion V_{all} peut être estimé par le calcul suivant:

$$V_{all} = V_{cd} \cdot \frac{A_{bath}}{A_{tot}} \cdot \frac{1}{p}$$

où A_{bath} est la surface d'observation de la bathymétrie et p le facteur équivalent au pourcentage de la surface en question. Le calcul du volume total de sédiments déposés dans les fenêtres d'observation tient compte donc de quelques 7'000 m^3 d'alluvions remobilisés provenant depuis l'arrière du lac pour les bathymétries antérieures à 2004, et respectivement quelque 9'500 m^3 pour celle de 2004.

Par rapport au volume moyen des 50 dernières années, l'alluvionnement mesuré correspond à un taux d'érosion de *1.7 mm an^{-1}*. Et en ne considérant que les données bathymétriques, le résultat est semblable : la moyenne des 20 dernières années est similaire à ce qui a été observé sur plus long terme. Toutefois, les mesures semblent indiquer une augmentation importante de l'alluvionnement (~30%) depuis 1995.

6.11 Moiry

La retenue de Moiry possède deux grands dessableurs situés environ 1 km à l'amont du lac. Leur ensablement est quelque peu documenté dans un rapport des possibilités du rehaussement de leur digue (Colenco, 2001).

Année	commentaires	Perte volume utile digue inférieure [m^3]	Alluvionnement digue inférieure [m^3 an^{-1}]	Perte volume utile digue supérieure [m^3]	Alluvionnement digue supérieure [m^3 an^{-1}]	Volume total déposé dans les dessableurs [m^3 an^{-1}]	Erosion spécifique de surface DESSABLEUR [mm an^{-1}]
1958-1972		133000	3500			3760	0.16
1972 -1996	Construction digue supérieure	133000	3500	212000	8833	13248	0.57
1996-2006		100000	10000	0*	0	10742	0.46
Total		233000		212000		9765	0.42

* digue pleine

Tableau 9 : Résumé de l'alluvionnement observé dans les dessableurs de Moiry (Colenco, 2001)

Le barrage possède 2 campagnes bathymétriques. Les levées ont été opérées sur toute la surface du plan d'eau avec des profiles s'écartant de 20 m à l'avant du lac pour atteindre presque 200 m à l'arrière (Gougra SA, 2002).

Contenu de ces mesures, il en ressort un taux d'érosion de *0.62 mm an^{-1}* pour la période 1958 – 2002. Les dernières estimations font état d'une augmentation du taux d'érosion de 27% ces dernières années comparé à la moyenne. L'analyse des données des dessableurs fournissent un taux d'érosion quelques peu inférieur à celui observé dans le barrage. Mais il reste dans le même ordre de grandeur.

Année	Commentaires	Volume des sédiments déposés [m^3]	Volume des sédiments déposés [m^3 an^{-1}]	Erosion spécifique de surface Barrage [mm an^{-1}]
1958 – 1997	1ère bathymétrie	163000	41795	0.74
1997 – 2002	2ème bathymétrie	90000	18000	0.32
2002 – 2007	Estimation*	280000	56000	0.99
Total	1958 – 2002 (2007)		35102	0.62 (0.72)

*sur la base d'observations récentes (Comm. Pers. F.M. de la Gougra SA)

Tableau 10 : Résumé de l'alluvionnement dans le lac de Moiry (Gougra SA, 2002)

6.12 Turtmann

Depuis sa mise en eau en 1960, l'alluvionnement de la retenue de Turtmann n'a cessé d'augmenter. La dernière bathymétrie de 2002 fait état d'une perte de volume utile supérieure à 20% (623'000 m^3 contre 780'000 m^3 en 1960). Au vue de cette situation irréversible, les forces motrices de la Gougra SA ont étudié depuis les années 70 les diverses possibilités pour remédier à cet ensablement (Zuber, 2005). Il en ressort un registre très fourni en comparaison avec les autres aménagements de son alluvionnement, lequel est résumé dans le Tableau 11.

Année	Commentaires	Perte volume utile du barrage [m^3]	Volume des sédiments déposés [m^3 an^{-1}]	Volume extrait du barrage [m^3]	Purge [m^3 an^{-1}]	Alluvionnement dessableur [m^3 an^{-1}]
1960 - 70	1^{ère} bathymétrie et début de la purge annuelle	167860	15260			
1963 - 69				34000		
1970 - 78	construction de la digue et 2^{ème} bathymétrie	38000	4750	32100	1500	5700
1979 - 89			2280		1500	4550
1978 - 97	3^{ème} bathymétrie et surrélévation de la digue	50880	3360			
1990 - 92	Surrélévation de la digue			13900	1500	
1992 - 97					1100	4940
1997 - 02	4^{ème} bathymétrie	7500	1500		750	5000

Tableau 11 : Résumé de l'alluvionnement observé dans la retenue de Turtmann et son dessableur depuis sa mise en eau. Les données proviennent de plusieurs sources (Dufour, 2004 ; Alpreserv 2005b; De Cesare, 2006).

Devant la variabilité des sources, une tentative de reconstruction de l'alluvionnement année après année a été tentée (cf. Annexe II). Ce tableau présente le scénario le plus probable de l'alluvionnement enregistré dans la retenue et le dessableur. Ce scénario obtient une perte de volume utile dans la retenue de 18.2% (638'100 m^3) en 2002 contre 21.1% observé par la bathymétrie est peut être donc appréhendé avec confiance. On observe ainsi un taux d'érosion de *0.28 mm* an^{-1} pour la période 1960 – 2002.

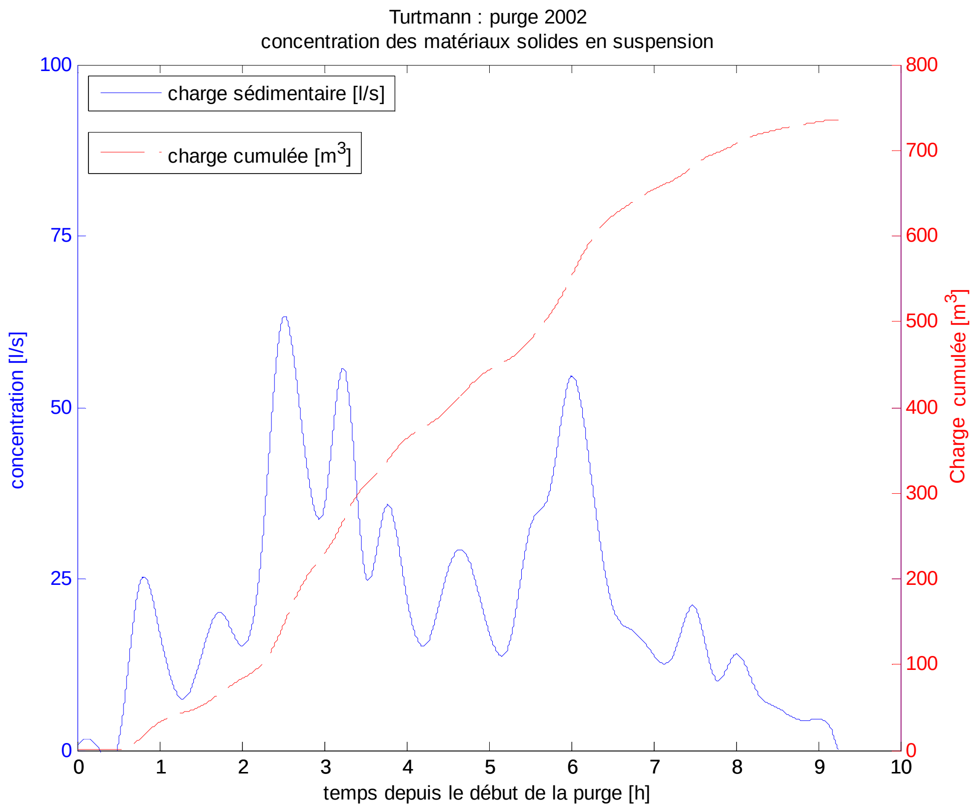

Figure 1 : Calcul du volume de sédiments évacué du barrage de Turtmann le 8 octobre 2002 lors de la purge annuelle. Les débits d'eau et les concentrations de matières solides en suspension (MES) peuvent être connus avec une certaine précision car les sédiments sont dilués dans le barrage même par de l'eau provenant de la retenue de Mottec (Val d'Anniviers) . Cette purge a évacué env. 750 m^3 d'alluvions. (Données brutes obtenues auprès de E. Zufferey, F.M. de la Gougra SA)

6.13 Sénin

Le lac du Sanetsch a fait l'objet d'une étude qualitative et quantitative de son alluvionnement en 2004 (Brethaut & Zahnd, 2006). Le relevé bathymétrique a révélé un volume de sédiments déposé dans la retenue depuis sa mise en eau en 1965 estimé à 132'000 m^3. Les prélèvements par carottages ont montré une granulométrie fine (sablo-limoneux).

Par rapport à son alluvionnement, la présente méthode estime un taux d'érosion moyen pour le bassin versant de Sénin de *0.15 mm an*$^{-1}$.

6.14 Gries

Une recherche de donnée a été intentée auprès du barrage du Gries. Son bassin versant est fortement recouvert de glace et le glacier qui l'alimente s'étendait encore jusqu'au lac dans les années 80. Des dires de l'exploitant, des observations par caméra sont effectuées depuis les années 90 pour contrôler l'ensablement des prises d'eau. Et l'alluvionnement peu important au début de son exploitation semble avoir augmenté depuis le retrait du glacier. La rivière en amont a changé de lit entre temps. Aucune donnée chiffrée n'existe à son sujet.

Retenue	Taux d'érosion [mm an^{-1}]	Références	Méthode
Les Toules	0.024	Beyer Portner, 1998	Estimation
La Fouly	0.422	Emosson SA; Beyer Portner, 1998	Dragage du dessableur et estimation
Grande Dixence	0.623	Bezinge, 1989; Bretz 2006	Estimation dans les prises d'eau et bathymétrie
Mattmark	0.39	Beyer Portner, 1998	Etude de l'alluvionnement des deltas et extrapolation
Mattsand	0.61	Beyer Portner, 1998	Estimation sur les purges
Gebidem	1.26	Vischer, 1981; Rechsteiner, 1996	Mesures de purges et études bathymétriques détaillées
Ferden	0.092	KW Lötschen AG	Estimation et bathymétrie
Mauvoisin	1.69	Schleiss, 1996; Electrowatt, 1997; Seiler & Thomann, 2002 (Mauvoisin AG)	Bathymétries extrapolée sur toute la surface et étude détaillée
Moiry	0.62	Gougra SA, 2002	Bathymétrie et estimation par observation
Moiry dessableur	0.42	Colenco, 2001	
Turtmann	0.23	Dufour, 2004; Alpreserv 2005b; Zuber, 2005; De Cesare, 2006;	Bathymétrie et mesures de purges
Turtmann dessableur	0.18		
Emosson	0.43	Emosson, 2004	Bathymétrie
Sénin	0.15	Bréthaut & Zahnd, 2006	Bathymétrie

Tableau 12 : Taux d'érosion obtenus à partir des volumes de sédiments alluvionnés dans les principales retenues hydroélectriques valaisannes depuis leur mise en eau.

7 Analyse des résultats

Le taux d'érosion des bassins versants étudiés dans ce rapport varient entre un maximum de *1.68 mm an*$^{-1}$ pour Mauvoisin et un minimum de *0.024 mm an*$^{-1}$ pour la vallée du Gd St-Bernard. 7 bassins versants sur 12 investigués indiquent un taux d'érosion compris entre *0.39 mm an*$^{-1}$ et *0.62 mm an*$^{-1}$. L'érosion moyenne par unité de surface comprenant tous les bassins versants étudiés est de *0.72 mm an*$^{-1}$ ou *714 m*^{3} *km*$^{-2}$ *an*$^{-1}$. Ce qui correspond à une masse sédimentaire érodée de *1'928 t km*$^{-2}$ *an*$^{-1}$ calculée à partir d'un volume de densité moyenne[2] de 2'700 kg m^{-3}.

Les résultats obtenus dans ce rapport diffèrent sensiblement des valeurs présentées dans d'autres études similaires (cf. Tableau 13). Les taux d'érosion présentés par Electrowatt (1997) ne sont pas accompagnés d'explications quant au mode de calcul, rendant impossible toutes comparaisons. Par rapport aux taux d'érosion résultant de la thèse de Beyer Portner (1998), de De Cesare (2006) et de Brethaut & Zahnd (2006), lesquels sont très bien documentés, les résultats de la présente analyse sont dans la plupart des cas entre 20% à 50% inférieurs. D'un bassin versant à l'autre, cependant, la proportion est assez bien gardée. Les paramètres de densité choisis quant à la corrélation des volumes observés avec le taux d'érosion peuvent expliquer cette variation. Ainsi, malgré cette apparente disparité, l'estimation des taux d'érosion de la présente étude semble être en adéquation avec les autres bilans sédimentaires.

Retenue	Présente étude	Etude de Beyer Portner, 1998		Autres études	
	ER [mm an^{-1}]	ER [mm an^{-1}]	Références	ER [mm an^{-1}]	Références
Les Toules	0.024	0.044	FM d'Orsière SA		
La Fouly	0.422	0.645	Emosson SA ; Rosset 1990		
Grande Dixence	0.623	1.137	Grande Dixence SA		
Mattmark	0.39	0.721	Willi, 1996		
Mattsand	0.61	1.78	Fux, 1981 ; Alusuisse-Lonza Energie AG		
Gebidem	1.26	2.113	Vischer, 1981; Rechsteiner, 1996	2.5	Electrowatt, 1997
Ferden	0.092	0.12	Alusuisse-Lonza Energie AG		
Mauvoisin	1.69	1.479	Bezinge, 1985; Schleiss, 1996	2.2 - 2.9	Electrowatt, 1997
Turtmann	0.23			0.32	De Cesare, 2006
Sénin	0.15			0.3	Bréthaut & Zahnd, 2006

Tableau 13 : Comparaison des taux d'érosion obtenus dans la présente étude avec ceux tirés d'autres études similaires.

---

[2] Si on considère que le matériel érodé est uniquement de la roche en place. Pour des terrains de sources mixtes (rocher, moraine, débris, sols), la densité moyenne est inférieure de 10% à 30%.

Si on compare nos résultats avec des études se basant sur une approche différente :

- le taux d'érosion actuel moyen obtenu pour la vallée du Rhône par Hinderer (2000) à partir de mesures de la charge des rivières et de l'étude du remplissage de la plaine du Rhône est de *0.22 mm an*$^{-1}$. En considérant la période depuis le dernier maximum glaciaire, ce taux et de *1.01 mm an*$^{-1}$, mais atteignait une vitesse de *2.87 mm an*$^{-1}$ durant la période post-glaciaire. En considérant toutes les Alpes, le taux moyen actuel est de *0.125 mm an*$^{-1}$, respectivement *0.62 mm an*$^{-1}$ depuis le dernier maximum glaciaire et *1.76 mm an*$^{-1}$ pour l'époque post-glaciaire.
- le taux d'érosion actuel moyen obtenu pour le Valais par Schlunegger & Hinderer (2003) à partir de mesures opérées sur la charge des particules solides transportée dans le Rhône par rapport à la taille du bassin versant est de *0.151 mm an*$^{-1}$ à la Porte du Scex et de *0.355 mm an*$^{-1}$ à Brig, mais s'élève à *0.716 mm an*$^{-1}$ pour les mesures effectuées dans la Vispa (Viège). Cette dernière valeur est comparable au résultat de *0.61 mm an*$^{-1}$ obtenu pour le bassin versant de Zermatt (Mattsand).

La comparaison avec Hinderer est intéressante comparée aux données obtenus dans ce rapport, compte tenu que les bassins versants étudiés sont dans une période post-glaciaire depuis la fin du XIX$^{\text{ème}}$ siècle.

Bien que les taux d'érosion maximum et minimum obtenus par notre étude correspondent à la plus haute et respectivement la plus basse couverture glacière, aucune corrélation claire n'apparait entre les deux variables (cf. Figure 2). Pour le bassin versant de Gebidem, l'important retrait du glacier d'Aletsch enregistré ses dernières années (1.2 km depuis la construction du barrage) est une hypothèse sérieuse pour expliquer ce taux relativement élevé en comparaison des autres bassins versants. Tourtemagne, cependant, malgré une couverture de glace importante (45%) et un retrait proportionnellement similaire, enregistre un taux d'érosion 9 fois moins important. Ceci peut être dû au fait que les sédiments érodés mécaniquement par les glaciers ne sont pas transportés à la même cadence d'un système à l'autre, à cause d'une topographie moins prononcée par exemple. Un bassin versant aura plus tendance à former des dépôts, alors que l'autre subit un régime fluvial entraînant simultanément le matériel vers le barrage en contrebas.

Dans le même ordre d'idée, la distance entre la langue glaciaire et le lac de retenue n'indique pas de liens entre les différents taux d'érosion.

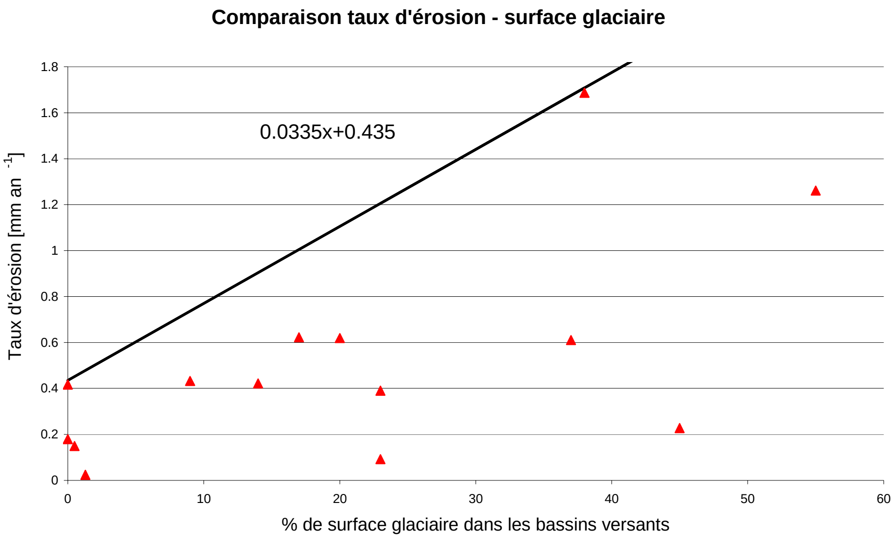

Figure 2: Comparaison des taux d'érosion avec la surface glaciaire de chaque basin versant. La droite indique le taux d'érosion maximum observé dans cette étude pour une couverture glaciaire donnée.

L'application de critères morphologiques suggérés par Hinderer (2000), tels que l'élévation maximale ou la différence entre l'élévation moyenne et minimum, ne permettent pas non plus d'extraire des corrélations positives entre les différents taux d'érosion investigués dans ce rapport (cf. Figure 3).

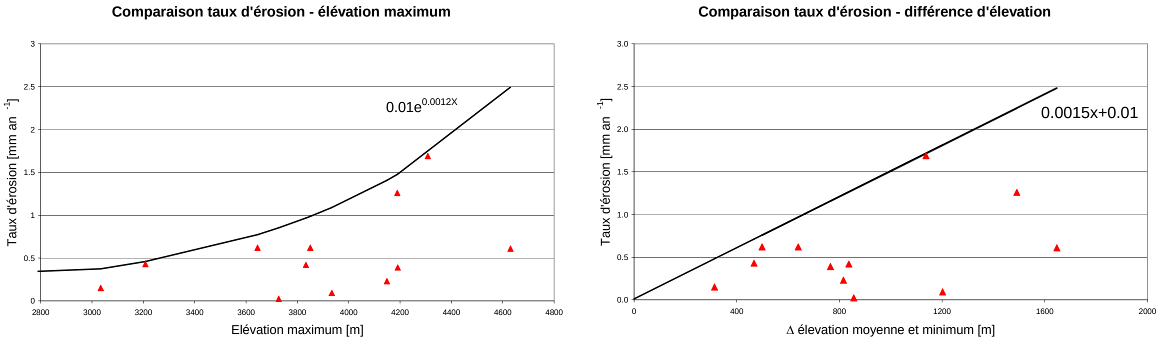

Figure 3 : Comparaison des taux d'érosion avec des critères morphologiques. La line noire indique le taux d'érosion maximum observé dans cette étude par rapport au critère morphologique respectif.

Enfin, l'étude détaillée de l'alluvionnement de quelques retenues ne révèle pas de corrélation similaire quant à l'évolution du taux d'érosion entre les bassins versant. Si la tendance depuis une dizaine d'année semble être une augmentation significative de l'alluvionnement dans les retenues, donc d'un taux d'érosion plus important, les données ne sont pas toutes univoques quant à un changement clair dans la quantité de sédiments érodés entre la période froide des années 1967 – 1990 et la période très chaude qui s'ensuit. Comme le montre l'exemple de Tourtemagne, les travaux entrepris pour limiter l'alluvionnement pourrait être une cause à l'absence d'un signal fort convergeant dans ce sens.

D’une façon générale, et comme le montre l’analyse des bathymétries dans le lac de Moiry, les volumes de sédiments apportés peuvent être fortement modifiés par des évènements isolés. Les avalanches, les grandes crues et les débâcles glaciaires peuvent constitués une grande partie de l’apport annuel moyen des alluvions dans les lacs de retenue. Même si l’érosion est avant tout causée par les rivières, ces évènements extrêmes peuvent expliquer les variations de l’apport sédimentaire moyen sur des périodes d’observation relativement courtes (< 60 ans). Les phénomènes d’érosion à l’échelle régionale forment des systèmes complexes que l’alluvionnement enregistré à l’exutoire ne reflète pas en tout temps l’érosion actuelle, mais contient un certain décalage dans le temps.

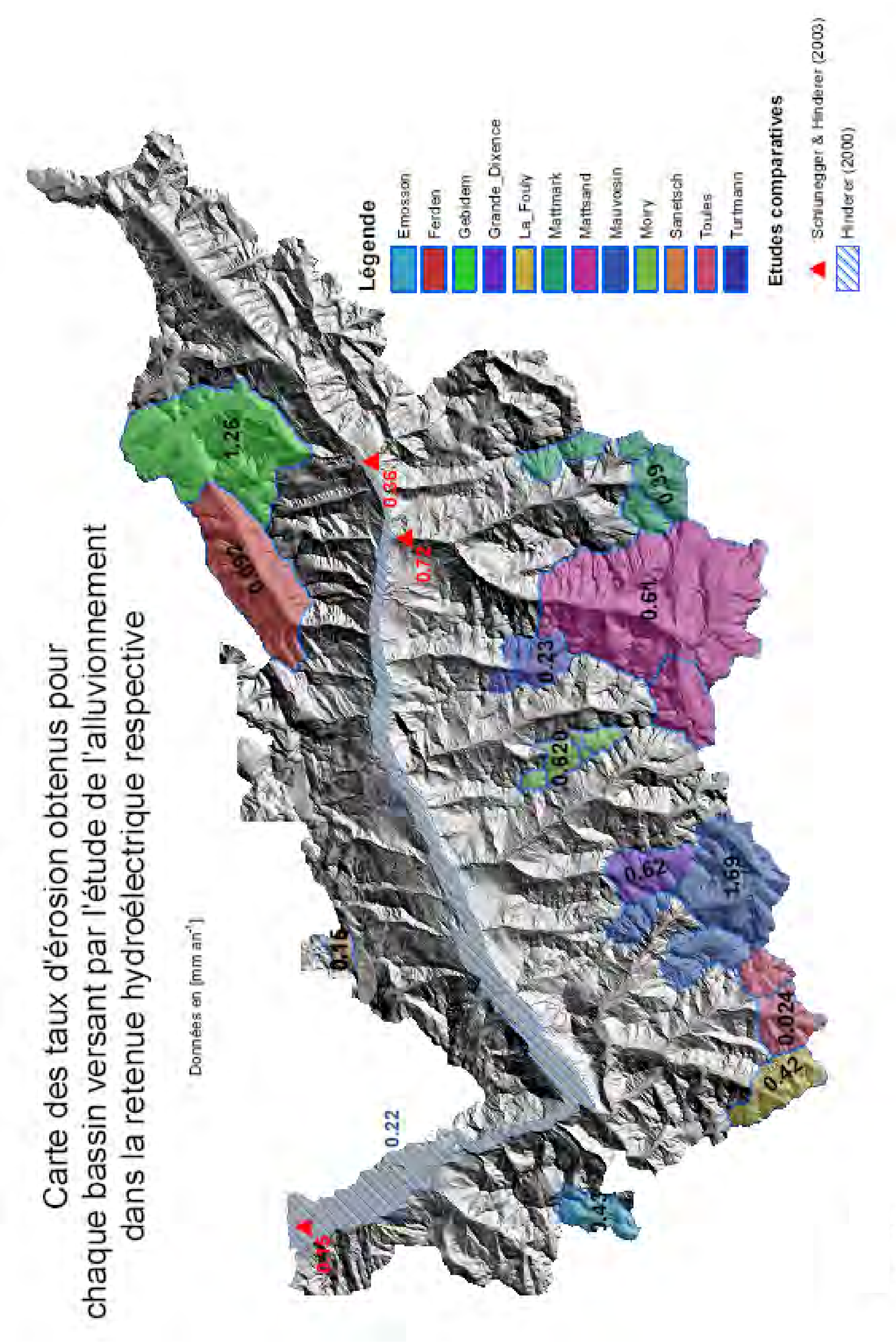

Carte des taux d'érosion obtenus pour chaque bassin versant par l'étude de l'alluvionnement dans la retenue hydroélectrique respective

Données en [mm an^{-1}]

8 Estimation des volumes érodés dans le bassin versant de Zinal

La comparaison des taux d'érosion des différents bassins versants investigués dans cette étude ne permet pas d'extraire des corrélations positives avec des paramètres morphologiques. De même, la couverture glaciaire ou la lithologie n'apparaissent pas être des facteurs contrôlant le taux d'érosion des bassins versants. Dès lors, l'attribution d'un taux d'érosion moyen pour la région de Zinal par comparaison d'un ou l'autre bassin versant environnent semble quelque peu aléatoire. L'estimation des volumes de matériaux érodés s'est donc effectuée de la manière suivante :

1. Dans une première démarche, le volume total de matériaux érodés dans le bassin versant du haut Val d'Anniviers est déterminé sur la base des taux d'érosion minimum, maximum et moyen observés sur le plan valaisan (cf. Tableau 14). Ce volume est estimé entre *2'750* m^3 an^{-1} et *193'150* m^3 an^{-1}, avec un volume moyen de *81'750* m^3 an^{-1}. Si on ne considère que la surface contributive autour du village de Zinal, le volume total de matériaux érodés varie entre *930* m^3 an^{-1} et *65'350* m^3 an^{-1} avec un volume moyen de *27'650* m^3 an^{-1}.

Sous bassin versant	Surface bassin versant [km^2]	Volume en m^3 an^{-1}		
		pour un taux d'érosion moyen de 0.71 mm an^{-1}	pour un taux d'érosion minimum de 0.024 mm an^{-1}	pour un taux d'érosion maximum de 1.69 mm an^{-1}
Haut Val d'Anniviers	114.5	81747	2748	193146
Glacier de Zinal et Moming	53.0	37808	1271	89330
Des torrents à laves torrentielles	38.5	27500	924	64976
Autour du village de Zinal	38.7	27656	930	65344

Tableau 14 : Volume de matériaux érodés dans les sous basins versants du vallon de Zinal, sur la base des taux d'érosion observés sur le plan valaisan (cf. Error! Reference source not found.**).**

La rive droite de Zinal contient plusieurs torrents produisant fréquemment des laves torrentielles. Sur la base du taux d'érosion moyen estimés ci-dessus, les volumes de matériaux charriés sont de l'ordre de *27'500* m^3 an^{-1} (cf. Tableau 14).

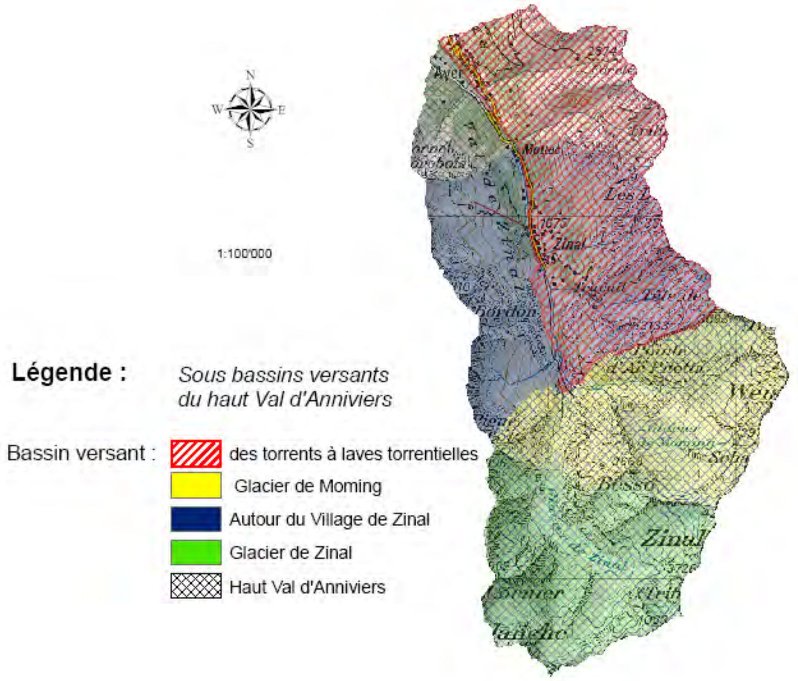

Figure 4 : Découpage du haut Val d'Anniviers en surfaces contributives pour l'estimation des volumes érodés.

Torrent	Surface bassin versant [km^2]	Volume en m^3 an^{-1}			Evènements observés [m^3 an^{-1}]	Volumes potentiellement mobilisables [m^3]
		pour un taux d'érosion minimum de 0.024 mm an^{-1}	pour un taux d'érosion moyen de 0.71 mm an^{-1}	pour un taux d'érosion maximum de 1.69 mm an^{-1}		
Perrec	1.84	44	1314	3073	300	
Lirec	1.64	39	1171	2739		
Péterey	1.30	31	928	2171	3600 - 4000	800 à 13000 par an
Tracuit	2.01	48	1435	3357	4000	
Bondes	1.17	28	835	1954	100	
Coor	0.97	23	690	1615		
Loverêche	0.46	11	329	770	60 - 80	1500 à 6000, voir 10000

Tableau 15 : Estimation de Volume érodés dans différents torrents du vallons de Zinal pour un taux d'érosion comparable à la moyenne des bassins versants valaisans, respectivement pour les valeurs minimums et maximums obtenus dans ce rapport. Les 2 dernières colonnes de droite résument les volumes répertoriés dans le cadastre des évènements de la commune d'Ayer ainsi que les volumes des zones de production potentielle (Ayer, 2003).

2. Dans une seconde étape, les taux d'érosion mesurés par la présente étude ont été appliqués aux 7 torrents provoquant les laves torrentielles aux alentours de Zinal (cf. Tableau 15). Cette démarche permet ainsi de comparer les estimations de volumes érodés par cette étude avec les évènements observés dans le passé.

Le cadastre des évènements de la commune d'Ayer (Ayer, 2003) dénombre 8 laves torrentielles entre 1990-2000 dans le torrent de la Loverêche avec des dépôts de l'ordre de 60 – 80 m[3]. Dans les années 1965 -1970, un évènement avec des volumes plus conséquent est mentionné. Le rapport technique de la commune (Ayer, 2003) estime les volumes potentiellement mobilisables entre 1500 m^3 à 6'000 m^3 pour des évènements fréquents à rares, et 10'000 m^3 dans le cas extrême.

Le volume de matériaux déposé dans le dépotoir commun du torrent du Lirec et Perrec atteind 4'000 m^3 en 13 ans.

Le dépotoir du torrent des Bondes a observé une moyenne de 100 m^3 an^{-1} durant ces 50 dernières années.

L'apport de matériaux charriés dans le dépotoir du torrent du Péterey varie de 800 m^3 an^{-1} à 13'000 m^3 an^{-1} selon les années. Le volume moyen des 25 dernières années est estimé entre 3'600 et 4'000 m^3 an^{-1}. Le torrent de Tracuit ne comporte pas de données chiffrées, mais se situe dans ce même ordre de grandeur.

Sur la base de ces données, les volumes érodés annuellement pour les torrents du Péterey et de Tracuit sont entre 15% et 40% supérieurs au taux d'érosion maximum estimé par l'analyse de l'alluvionnement. Pour les autres torrents, les volumes érodés observés lors d'évènements se situent entre le taux d'érosion minimum et moyen déterminé dans ce rapport.

Le volume total charrié par ces torrents se situent entre *8'350 m^3 an^{-1}* et *36'700 m^3 an^{-1}*. En admettant une densité sèche de 1800[3] kg m^{-3}, cela correspond à un taux d'érosion moyen de *0.66 mm an^{-1}* pour les évènements fréquent à rare, respectivement *2.91 mm an^{-1}* dans des évènements extrêmes (cf. Tableau 16). Ce taux d'érosion moyen est sensiblement proche de celui calculé pour la Vallée de Moiry (*0.62 mm an^{-1}*) dans cette présente étude ainsi que de la moyenne des bassins versants valaisans (*0.71 mm an^{-1})*. Il peut être le fruit du hasard des chiffres. Cependant, l'auteur de ce rapport est convaincu que le régime climatique semblable entre les deux bassins versants, ainsi que les nombreuses similitudes dans les caractéristiques morphodynamiques et lithologiques, tendent à justifier une comparaison entre les deux régions. Quant au taux d'érosion des évènements extrêmes, il se situe dans l'ordre de grandeur estimé par Hinderer (2000) pour la période qui suivit la dernière époque glaciaire. Cette estimation est fort probable, car ces torrents (particulièrement Tracuit et Péterey) sont alimentés en matériel de charriage par des glaciers rocheux ou des glaciers à l'agonie.

Volume totaux charriés par les torrents dans le vallon de Zinal [m^3 an^{-1}]		**Taux d'érosion [mm an^{-1}]**
Minimaux	8350	0.66
Maximaux	36700	2.91

Tableau 16 : Volumes totaux charriés par les laves torrentielles dans le bassin versant de Zinal sur la base d'observations répertoriées par la commune d'Ayer, et l'estimation du taux d'érosion respectif pour une densité sèche de 1'800 kg m^{-3}.

---

[3] La masse volumique moyenne du mélange formant une lave torrentielle est de 2300 kg m^{-3} avec une concentration solide de 78 %vol. (Bardou, 2002)

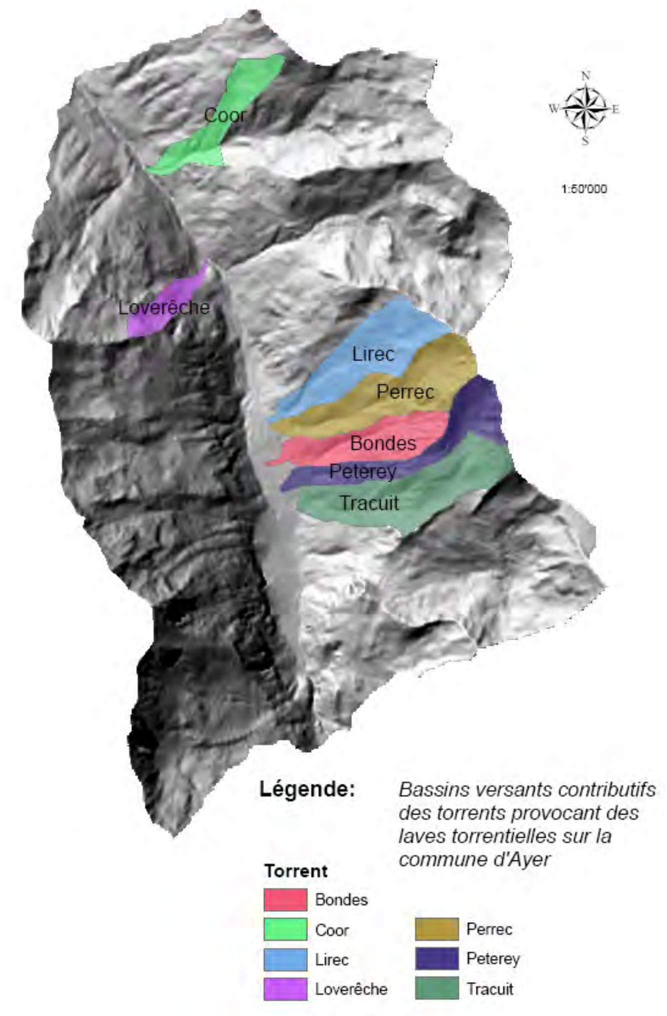

Figure 4 : Torrents ayant provoqué des laves torrentielles ces dernières années dans le vallon de Zinal (Ayer, 2003).

9 Conclusion

L’étude des volumes de sédiments déposés dans les principales retenues hydroélectriques valaisannes a révélé un taux d’érosion moyen pour les bassins versants de haute altitude sur le plan cantonal de *0.71 mm an*$^{-1}$. Plus de la moitié des bassins versants investigués indiquent un taux d’érosion compris entre *0.39 mm an*$^{-1}$ et *0.62 mm an*$^{-1}$. Les tentatives de corrélation de ces différents taux d’érosion avec des critères simples, tels que la surface glaciaire de chaque bassin versant ou les paramètres morphométriques de leur relief n’ont pas permis d’extraire des classifications distinctes. Il semblerait cependant que les taux d’érosion minimaux estimés par la présente étude dans le bassin versant du Gd St-Bernard (0.024 mm an^{-1}) et du Sanetsch (0.15 mm an^{-1}) soient liés à l’absence de surface glaciaire. Et que l’alluvionnement des retenues de Mauvoisin et Gebidem, influencés par les énormes glaciers qui les alimentent, joue un rôle prépondérant dans l’estimation des taux d’érosion de la présente étude (*1.69 mm an*$^{-1}$, resp. *1.26 mm an*$^{-1}$).

L’application des taux d’érosion minimaux, moyens et maximaux déterminé dans cette étude au bassin versant du haut Val d’Anniviers (Zinal) estime le volume de matériaux érodés entre *2’750 m*^{3} *an*$^{-1}$ et *193’000 m*^{3} *an*$^{-1}$, avec une quantité moyenne de *82’000 m*^{3} *an*$^{-1}$. Une comparaison des quantités de volumes déposées dans les dépotoirs des torrents de la région de Zinal ainsi que les volumes des zones de production potentielles indique que le taux d’érosion moyen calculé sur les autres bassins versants cantonaux correspond aux volumes annuels minimaux observés durant les 25 dernières années dans cette région. Et le taux d’érosion maximum calculé à partir de l’alluvionnement sur les autres bassins versants valaisans sous-estime de 40% les volumes potentiellement mobilisables dans les torrents de Zinal.

Sur la base de la présente étude, les volumes érodés chaque année dans toute la vallée de Zinal (haut Val d’Anniviers) peuvent être estimés entre *82’000 m*^{3} *an*$^{-1}$ et *193’000 m*^{3} *an*$^{-1}$. En ne considérant que les torrents ayant provoqué ces dernières années des laves torrentielles, le volume charrié est estimé à *10'000 m*^{3} *an*$^{-1}$ pour les années à évènements fréquents, mais peut atteindre *40'000 m*^{3} *an*$^{-1}$ pour les années à évènements extrêmes.

Si l’estimation des volumes de sédiments érodés chaque année dans le bassin versant de Zinal peut être appréhendée avec confiance, l’estimation des volumes charriés par les torrents doit être quelque peu relativisée car le processus d’érosion est issu de systèmes complexes et locaux qui ne peuvent être directement mis en relation avec les volumes de sédiments alluvionnés dans les retenues hydroélectriques environnantes. Les granulométries mesurées sont différentes. Et seule une étude prospective des zones d’érosion potentielles ainsi que l’évaluation des contributions aux processus érosifs des bassins versants de chaque torrent permettrait d’affiner l’estimation de ces bilans sédimentaires. Cependant, les taux d’érosion qui ressortent de la présente analyse sont des valeurs très vraisemblables car ce sont des ordres de grandeurs correspondant à ce qui est observé dans ce type de système érosif. Et les matériaux mesurés dans les dépotoirs, lesquels provenant essentiellement du charriage provoqué par des évènements brusques et alimenté par des instabilités de terrain (glissements, glaciers rocheux, fonte du permafrost), forment des volumes comparables quand ils sont mesurés sur des périodes de temps assez longue (Q_{30} ou Q_{100}).

RÉFERENCES

Alpreserv 2005b. Gestion globale des sédiments de la retenue de Tourtemagne - Génération et évaluation de variantes. Projet Alpreserv - INTERREG IIIB. Martinerie R., De Cesare G., Jordan F., Boillat J.-L. (2005). LCH - EPFL Lausanne. 21

Ayer, 2003. Rapport technique sur la mise en décharge des matériaux inertes. document inédit 2003, commune d'Ayer. 31

Bardou, E. 2002. Méthodologie de diagnostic des laves torrentielles sur un bassin versant alpin. Thèse de doctorat n° 2002, EPFL Lausanne. 31

Beyer Portner, N. 1998. Erosion des bassins versants alpins par ruissellement de surface. Thèse de Doctorat, Communication 6, LCH- EPFL Lausanne. 8

Bezinge A. (1989). The management of sediment transported by melt-water streams and its significance for the estimation of sediment yield. 17

Bretz, 2006. Gestion de l'ensablement dans le barrage de la grande Dixence. Grande Dixence SA, Sion. 17

Colenco 2001. Geschiebewirtschaftung Turtmanntal, Variantenstudium, 2001. Kraftwerke Gougra AG 21

De Cesare, 1998. Alluvionnement des retenues par courants de turbidité. Thèse de doctorat no 1820 (1998). LCH - EPFL Lausanne. 19

De Cesare, 2006. Turtmann Pilot project, Workpackage 8. Document inédit, LCH - EPFL Lausanne. 21

Dufour, 2004. Assainissement des ocours d'eau en Valais / Analyse de l'hydrosystème de la Tourtemagne. ESM-Ruppen Ingéenieurs SA, Monthey. 21

Ecotec 1998. Enquête préliminaire d'impact sur le réhaussement de la prise d'eau et vidange de fond. Ecotec Environnement SA. 19

Electrowatt, 1997. Rapport réhaussement de la prise d'eau et installation de la purge. Electrowatt Ingenieering, 1997. 19

Emosson, 2004. Rapport des levés bathymétriques du 25.08.2004. Electricité d'Emosson SA. 16

Rechsteiner, G. 1996. Verlandung con Stauseen und Stauhaltungen, Sedimentprobleme in Leitungen un Kanälen. VAW Mitteilung no 142, ETH Zürich. 18

Gertsch, E. 2004. Geschievelieferung alpiner Wildbachsysteme bei Grossereignissen. Thèse de doctorat. AGNAT - Uni Berne. 5

GHO, 2004. Das geschiebemessnetz - Gruppe für operationelle Hydrologie (GHO). FAN - Agenda 1/04. OFEV 5

Gougra SA, 2002. Rapport des leveés bathymétriques 2002. Forces Motrices Gougra SA, Sierre. 20

Grasso, A. 2003. Charge de sédiments en suspension - Bericht gwa 12/2003. BAFU. 5

H. P. Guy, 2001. Fluvial sediments concepts, chapter C1. U.S Geological Survey, Techniques of Water-Resources Investigations, Book 3, 2001. 14

Hinderer, M. 2000. Late Quaternary denudation of the Alps, valley and lake fillings and modern river loads. Geodinamica Acta 14 (2001) 232 - 263 6

Koelzer & Lara, 1958. Densities and compaction rates of deposited sediement. Journal of the Hydraulics Division, ASCE 84(HY2); Proceedings Paper 1603 11

Mauvoisin SA. Rapports des relevés bathymétriques. Documents inédits, Mauvoisin SA, Sion. 19

Morris and Fan, 1998. Reservoir Sedimentation Handbook; Design and Management of Dams, Reservoirs and Watersheds for Sustainable Use. McGraw-Hill: New York 11

OFEG, 2005b. Hydrologie de la Suisse. Rapports de L'OFEG, Série Eaux No.7 - Berne 2005 24

Robitaille & Tremblay, 1997. Mécanique des sols, Théorie et pratique. Modulo Éditeur, 1997. 11

Schleiss, 1996. Verlandungsprobleme im Stausee Mauvoisin. VAW Mitteilung 142, ETH Zürich. 19

Schlüchter, 1989. Eiszeitliche Lockergesteine - Geologie, Genese und Eigenschaften. Lehrbuch Quartärgeologie, ETH Zürich 11

Seiler & Thomann, 2002. Verlandungsprobleme im Stausee Mauvoisin: Ausmass, Auswirkungen und möglivhe Massnahmen. VAW Mitteilung 174, ETH Zürich 19

Snyder et al., 2004. Estimating accumulation rates and physical properties of sediment behind a dam: Englebright Lake, Yuba River, northern California. Water resources research, vol. 40, W11301, 2004. 8

USBR, 2006. Erosion and Reservoir Sedimentation. Erosion and sedimentation Manual, Chapter II. U.S. Dept. of the Interior - Sedimentation and River Hydraulics Group, Denver (Colorado). 6

Verstraeten & Poesen, 2000. Variability of dry sediment bulk density between and within retention ponds and its impact on the calculation of sediment yields. Earth surface Processes and Landforms. Landforms 26, 375 - 394 (2001). 12

Vischer D. 1981. Verlandung von Stauseen. Schweizer Ingenieur und Architekt; Heft 47/1981. Publikation VAW, ETH Zürich. 18

Zuber, 2005. Problématique du lac de Tourtemagne. INTERREG IIIB, Projet Alpreserv 2005. LCH - EPFL Lausanne. 21

10 Annexe I

Retenue	surface basin versant naturel S [km^2]	surface bassin versant total [km^2]	surface du plan d'eau [km^2]	Surface glacière [%]	année de mise en service*	volume V_e [mio m^3]*	capacité de rétention R [%]	indice type d'exploitation ITE	indice de retenue K [-]	% Gravier	% Sable	% Limon	% Argile
Les Toules	39	64	0.599	1.3	1963	20.15	100	1.43	116	-	47	53	-
La Fouly	48.8			14	1972	0.02	54	1.43	216	56.5	36	7	>1
Grande Dixence	44.6	340	4.000	17	1937	401	100	1.43					
Mattmark	38	90.8	1.741	23	1967	101	100	1.43					
Mattsand	324	380.1	0.044	37	1962	0.21	45	1.43	78	-	26	58	16
Gebidem	197.6		0.204	55	1967	9.2	97	0.76	166		85	15	
Ferden	132.6		0.106	23	1975	1.89	91	0.76					
Mauvoisin	114.6	173.1	2.250	38	1956	211.5	100	1.43	136	20	33	47	
Moiry	29.4	35.5	1.300	20	1958	77	100	1.43	98	10	20	70	
Moiry dessableur	14		0.115	0	1972	env. 0.46	93	2.1	203	60	25	5	
Turtmann	28.1	37.2	0.098	45	1960	0.78	97	1.43	77		20	80	
Turtmann dessableur	21.93		0.045	0	1972	env. 0.15	84	2.1	228		60	40	
Emosson	25.52	46.79	3.214	9	1975	227	100	1.43					
Sénin	11.35		0.284	0.5	1965	2.8	100	1.43	90		30	55	15

*Aménagement le plus récent

Retenue	V_s [m^3 an^{-1}]	V_{ps} [m^3 an^{-1}]	ρ_{s0} [kg m^{-3}]	$\rho_{s\,(T=30)}$ [kg m^{-3}]	ρ_b [kg m^{-3}]	DR [m^3 km^{-2} an^{-1}]	ER [mm an^{-1}]	Références
Les Toules	1750	1750	1350	1450	2700	24	0.024	Beyer Portner, 1998
La Fouly	37037	20000	1500	1750**	2700	422	0.422	Emosson SA; Beyer Portner, 1998
Grande Dixence	50000	50000	1375	1500	2700	623	0.623	Bezinge, 1989; Bretz 2006
Mattmark	26700	26700	1375	1500	2700	390	0.390	Beyer Portner, 1998
Mattsand	445044	200270	1200	1280**	2700	610	0.610	Beyer Portner, 1998
Gebidem	463918	450000	1450	1625**	2700	1261	1.261	Vischer, 1981; Rechsteiner, 1996
Ferden	21978	20000	1375	1500	2700	92	0.092	KW Lötschen AG
Mauvoisin	348000	348000	1375	1500	2700	1687	1.687	Schleiss, 1996; Electrowatt, 1997; Mauvoisin AG
Moiry	35102	35102	1285	1400	2700	619	0.619	Gougra SA, 2002
Moiry dessableur	9765	9082	1400	1615	2700	417	0.417	Colenco, 2001
Turtmann	12680	12300	1250	1330	2700	228	0.228	Dufour, 2004; Alpreserv 2005b
Turtmann dessableur	5893	4950	1550	1800	2700	179	0.179	Zuber, 2005 ; De Cesare, 2006;
Emosson	22414	22414	1250	1330	2700	433	0.433	Emosson, 2004
Sénin	3385	3385	1225	1350	2700	149	0.149	Bréthaut & Zahnd, 2006

** à titre indicatif

Annexe 1 : Récapitulatif des données concernant les bassins versants investigués dans cette étude

11 Annexe II

année	commentaires	alluvionnement barrage [m^3 an^{-1}]	Volume extrait du barrage [m^3]	Purge [m^3 an^{-1}]	alluvionnement dans le dessableur [m^3 an^{-1}]	Volume sédiments déposés (digue + dessableur)	Erosion spécifique de surface [m^3 km^2 an^{-1}]
1959	construction du barrage						
1960	mise en eau du barrage	15260				15260	373
1961 -1969		15260				15260	373
1970	1er Bathymétrie et debut de la purge annuelle	15260				15260	373
1971		4750		1500	5700	11950	312
1972	construction de la digue	4750	34000	1500	5700	11950	312
1973 - 1977		4750		1500	5700	11950	312
1978	surélévation de la digue et 2ème bathymétrie	4750	32100	1500	5700	11950	312
1979 - 1990		2280		1500	4550	8330	220
1991		3360		1500	4550	9410	246
1992		3360		1500	4550	9410	246
1993	surélévation de la digue	3360	13900	1100	4940	9400	248
1994		3360		1100	4940	9400	248
1995		3360		1100	4940	9400	248
1996		3360		1100	4940	9400	248
1997	3ème bathymétrie	3360		1100	4940	9400	248
1998		1500		750	5000	7250	195
1999		1500		750	5000	7250	195
2000		1500		750	5000	7250	195
2001		1500		750	5000	7250	195
2002	4ème bathymétrie	1500		750*	5000	7250	195

*Quantité de sédiments purgés en 2002 sur la base des relevés de matériel en suspension (MES) mesuré en contrebas du barrage (cf. Figure 1)

Annexe 2 : reconstruction de l'alluvionnement annuel de l'aménagement hydroélectrique de Tourtemagne.

EGU General Assembly 2009
EGU2009-12933, Session HS11.2

Watershed sediment balance and local denudation rate based on hydropower reservoir sedimentation data

A. Loye (1), R. Minoia, M. Jaboyedoff (1), J.-D. Rouillier (2), J.-L. Boillat (3); Contact: Alexandre.loye@unil.ch
(1) Institute of Geomatics and Risk Analysis, University of Lausanne, Switzerland, (2) CREALP, Research center in alpine environment, Sion, Switzerland, (3) Laboratory of Hydraulic Constructions, Ecole Polytechnique Fédérale de Lausanne, Switzerland

UNIL | Université de Lausanne
Institut de géomatique
et d'analyse du risque

Abstract

Hydropower reservoirs built in the tributary valleys of Wallis (Switzerland) trap the sediment flux, so that their catchment area have become a sedimentary close system or almost close depending on the water regime and storage capacities. Their rates of sediment infilling can supply dataset of sediment budget at the watershed scale. In this study, sediment volumes accumulated behind 11 hydropower dams and 3 desilting lakes were collected through bathymetric surveys and camera or visual observation, in order to quantify the sediment flux since their commissioning. A local mean denudation rate could then be assessed within GIS information. Results are now getting characterised according to each watershed geomorphology, lithology, recent glacial retreat and fluvial network connectivity.

Sediment infilling rate

Dataset about sediment quantities and their physical properties (e.g. grain size distribution) not only in the lake, but in their sediment traps, were supplied directly by dams operators and the state authorities for hydropower. The collected datasets were of very different means depending on how serious the problematic of reservoir sedimentation is. 3 dams (Mauvoisin, Turtmann and Gebidem) are well-documented due to their high rate of sediment infilling representing a crucial issue to their long-term utility. 4 others reservoirs could provide two bathymetric surveys over their entire impounding surface. Remaining 2 other big dams (Emosson and Mattmark) less concerned about the issue of reservoir sedimentation and therefore containing only sampling measurement of sediment deposits at specific site, such as water intakes and bottomset watergates. Where data were missing or not available, an attempt of estimating the degree of sedimentation in the reservoir was performed based on purges and reservoir draining out performed during security checks. An extrapolation over the whole impounding area is difficult, mainly due to the turbidity current that transport sediment deposits close to the dam, or due to the presence of an older dam inundated at present.

Bathymetric surveys

Bathymetric surveys consist of measuring the depth by means of echo-sounding device over the whole impounding water surface. Points of depth elevation are then interpolated and compared by differencing two maps of the reservoir floor elevation. Usually, detailed maps of the predam valley bottom topography were made up during the construction of the dam.

Sediment trap efficiency of the reservoir

Estimated volumes are corrected according to the sediment trap efficiency (***TE***) of the reservoir, which can be defined as the proportion of the sediment quantity deposed (S_{dep}) in the reservoir over the entire sediment load (S_{in}). The *TE* [%] of a reservoir is not static, but varies depending on its characteristics (size, style of water management) and processes controlling sedimentation (sediment volume already deposed in the reservoir, turbidity current). In this study, TE was estimated based on an empirical relationship developed by Brown (1943) and adapted by Avendaño Salas et al. (1995) for large reservoirs, such as hydropower lakes:

$$TE = \frac{S_{dep}}{S_{in}}\cdot 100 = \left(1-\frac{1}{1+ITE\cdot\frac{C}{W}}\right)\cdot 100 \qquad \text{(Brown, 1943)}$$

where
ITE : index for the style of hydraulic regime
C : reservoir storage capacity [10^3 m^3]
W : catchment area [km^2]

Reservoir	Sediment yield V_s [m^3 $year^{-1}$]	Sediment load V_{ps} [m^3 $year^{-1}$]	Trap efficiency TE [%]	index for the hydraulic regime ITE [-]	Reservoir storage capacity [10^3 m^3]* V_e	catchment area S [km^2]
Les Toules	1750	1750	100	1.43	20.15	39
La Fouly	37037	20000	54	1.43	0.02	48.8
Grande Dixence	50000	50000	100	1.43	401	44.6
Mattmark	26700	26700	100	1.43	101	38
Mattsand	445044	200270	45	1.43	0.21	324
Gebidem	463918	450000	97	0.76	9.2	197.6
Ferden	21978	20000	91	0.76	1.89	132.6
Mauvoisin	348000	348000	100	1.43	211.5	114.6
Moiry	35102	35102	100	1.43	77	29.4
Moiry desilting lake	9765	9082	93	2.1	~ 0.46	14
Turtmann	12680	12300	97	1.43	0.78	28.1
Turtmann desilting lake	5893	4950	84	2.1	~ 0.15	21.93
Emosson	22414	22414	100	1.43	227	25.52
Sénin	3385	3385	100	1.43	2.8	11.35

* most recent construction

Table 1. *Input for the calculation of the effective mean sediment yield since the time of commissioning.*

Reservoir	Coefficient K	Gravel [%]	Sand [%]	Silt [%]	Clay [%]	Dry bulk density ρ_s [kg m^{-3}]		mean solid bedrock density ρ_b [kg m^{-3}]
						Initially T = 0	after compaction (Miller equation)	
La Fouly	216	56.7	36.2	7.2	<1	1532	1769	2700
Mattsand	78	0	26	58	16	1193	1276	2700
Gebidem	166		85	15	>1	1444	1626	2700
Mauvoisin	136	20	33	47	-	1369	1518	2700
Turtmann	77		20	80	-	1246	1331	2700
Turtmann desilting lake	228	-	60	40	-	1556	1806	2700
Moiry	98	10	20	70	-	1287	1395	2700
Moiry desilting lake	203	60	25	5	-	1392	1614	2700
Sénin	90	-	30	55	15	1225	1350	2500
Emosson	77		20	80		1246	1331	2500
Toules	116	-	47	53	-	1327	1453	2700

Table 2. *Input for the calculation of the compacted dry bulk density.*

Conversion of sediment volume into denudation rate

The conversion of sediment volume into denudation rate (DR_m), which is supposed to indicate the erosion and weathering processes intensity encountered in the catchment area for the time period since deposition, was obtained according to the ratio of dry bulk density (ρ_s) of the deposed material to solid bedrock density (ρ_b):

$$DR_m = \frac{V_s}{S\cdot T}\cdot\frac{\rho_s}{\rho_b} \qquad [m^3\ km^{-2}\ y^{-1}]$$

V_s : Averaged sediment volume in the reservoir [m^3 km^{-2}]
S : Contributive catchment area [km^2]
T : Time period of sedimentation [y^{-1}]

Dry bulk density (ρ_s) of the impounded sediment were estimated according to empirical relationship established between grain size distribution, degree of compaction and time (Koelzer & Lara, 1958)

$$\rho_s = \rho_{s_0} + 0.4343\cdot K\cdot\left\{\frac{T}{T-1}\cdot\ln(T)-1\right\}$$

where
T : time of commissioning [y]
ρ_{s_0} : initial mean dry bulk density [kg m^{-3}]
K : coefficient expressing a factor of consolidation related to an average speed of compaction in the reservoir

$$K = \frac{K_{(clay)}\cdot\%clay + K_{(silt)}\cdot\%silt + K_{(sand)}\cdot\%Sand + K_{(gravel)}\cdot\%Gravel}{100}$$

Coarse-textured sediments, such as gravel and sand, settle down almost instantanelly (on a yearly scale), because of the very low velocity of water in the reservoir. Therefore, their κ coefficient can be set to 0. κ coefficient for fine-textured sediments range between 16 to 256 according to the type of reservoir (Koelzer & Lane, 1958).

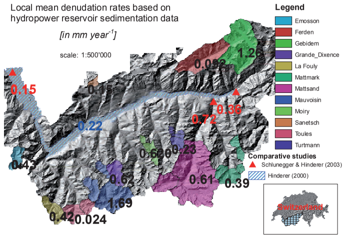

Figure 1. *Local mean denudation rates in [mm year^{-1}] obtained according to the sediment yield deposed in hydropower reservoirs.*

Data analysis

After having reconstructed the recent short-term trend order of magnitude of the sediment load in the lake, DR_m were compared and discussed according to the geomorphology of the watershed, its recent glacial retreat and the fluvial network connectivity. As no distinctive correlation could be established through a single parameter, all considered parameters are now getting to combine to set an erosional relationship (***ER***):

ER = fct(slope, distance glacier-reservoir, max. elevation, normalised Δ elevation, cliffs area, area of connected subwatershed)

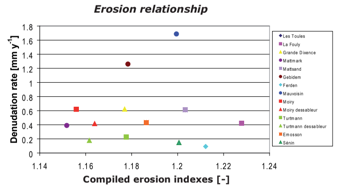

Figure 2. *Results of the erosion relationship set by combining some geomorphic indexes, glacial retreat and sub-catchment connectivity.*

Discussion and overview

- DR_m of the investigated watershed vary between 1.68 to 0.024 mm y^{-1}. 7 watersheds over 12 show a DR_m ranging from 0.39 to 0.62 mm y^{-1}. The overall mean DR per unit area is 0.72 mm y^{-1}.
- Comparison with Hinderer (2000) (0.62 mm y^{-1}) is interesting due to the fact that most of the investigated watersheds are in a post-glacial state since the end of the XIX century.
- The analysis of the results with some simple geomorphometric indexes doesn't allow to draw any distinctive positive correlation within the different watersheds.
- The recent glacial retreat seems to be the most influential input for reservoir sedimentation, although a large discrepency can be showed (cf. Figure 3). Sediments are not transported at the same speed (e.g. topographic reasons). A watershed tends to create sediment deposits, when another watershed undergoes a fluvial regime that easily removes sediments downward the reservoir.

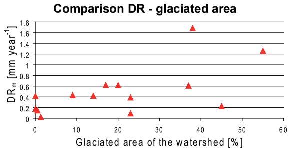

Figure 3. *Comparison between the mean denudation rate DR_m of each watershed with their glaciated area.*

Conclusion

Hydropower reservoir sedimentation assessment are a complementary approach to existing methods of watershed sediment budget, which are fundamental data to classify and understand erosion slope processes.

In this study, sediment budgets of half of the watersheds are strongly restricted due to fragmentary information, so that interpretation is limited to a general overview.

Generally, sediment transport are mostly influenced by single events, such as flooding, avalanches and glacial outburs flow, which can represent an important contribution of sediments in the reservoir. Erosion transport is complex and reservoir sedimentation over a short time period (<60 y) may not reflect at all time the actual state of erosion rates, but contains a time lag due to transport capacities.

References

Hinderer, M. 2000. Late quaternary denudation of the Alps, valley and lake fillings and modern river loads. Geodynamica Acta 14.

Koelzer & Lara, 1958. Densities and compaction rates of deposited sediment. Journal of Hydraulic Division, ASCE 84(HY2). Proceedings Paper 1603.

Avendaño Salas, C. Cobo Rayán, J. L. Gómez Montaña y Sanz Montero, M. E. (1995). Procedimiento para evaluar la degradación especifica (erosion) de cuencas de embaises. Applicación al estudio de embaises españoles. Ingniaria Civil 99, 51-58.

Appendix C

Erosion process monitoring in the Roubine elementary gully of the ERS Draix using TLS devices

Abstract A monitoring of the topographic changes of the Roubine catchment has been performed since 2007 with terrestrial laser scanner (LiDAR), in order to quantify through time the volumes of eroded sediment at the scale of an elementary gully. The Roubine catchment (0.13 ha) is located at the experimental research station of Draix (South French Alps), in the black marl of the Oxfordian age, a lithologic formation particularly prone to weathering processes. These badlands feature high sediment supplies and heavily-loaded flash floods. LiDAR data have been acquired alternatively with an Optech ILRIS-3D and a Leica ScanStation 2, ensuring an accuracy of less than 1 cm upon both distance and position. Topographic changes over a period of 2 years are quantified at centimeter scale by comparing the different series of point cloud data. The Roubine catchment has been monitored since 1983 with different measuring devices (meteorologic station, water and sediment discharge, solid transport). Sequences of erosion rates derived from topographic changes can be compared with volumetric measurements performed on a sediment trap and a gauging station located at the outlet of the basin. They also inform on bedload/suspension solid transport and catchment hydrogeomorphic response to low and high intensity rainfalls. The topographic analysis reflects the mechanical and structural features of the hillslope controlling sediment supplies and transport through the development of small gullies. The analysis of these series of high resolution point clouds enables to observe slope erosion processes at the scale of the elementary gully, especially the seasonal channel network development and collapse, the sediment supply through erosion, the transient deposition and the shallow mass movement. This study completes a period of 25 years of erosion process analysis in this catchment by combining long-term observation of this elementary hillslope with seasonal high resolution topographic data.

UNIL | Université de Lausanne

Erosion process monitoring in the Roubine elementary gully of the ERS Draix using terrestrial laser scanning

Photograph: A. Loye

Technical report

Faculté des Géosciences et de l'Environnement
Institut de Géomatique et d'Analyse du Risque
Loye Alexandre, assistant, PhD student
Jaboyedoff Michel, Professor

With the collaboration of
Josh Theule, PhD student, CEMAGREF - division ETNA, Grenoble
Julien Travelletti, PhD student, IPGS, Strasbourg

Rapport: IGAR – AL – R003

Faculté des géosciences et de l'environnement
Institut de géomatique et d'analyse du risque

Tél.+41 21 692 35 47 | Fax.+41 21 692 35 35 | Alexandre.loye@unil.ch

Contents

0.1 Introduction 1
    0.1.1 Hillslope erosion processes on black marl 1
    0.1.2 The elementary gully experimental site of the Roubine Catchment 1
    0.1.3 Regolith covering and erosion process activity 2
0.2 Lidar survey data 2
0.3 Lidar data processing 4
0.4 Point clouds and sequential data accuracy 4
0.5 quantifying erosion 4
0.6 Results and analysis 5
0.7 Conclusion and Perspectives 9

Bibliography **11**

0.1 Introduction

0.1.1 Hillslope erosion processes on black marl

The *terres noires* (black marl) formation in the Alpes de Hautes Provence (France) are known to be highly sensitive to erosion. Their fast desintegration causes considerable amount of loose material to accumulate in rills and gullies. When the rain comes, the transported solids can be so important, that small debris flows occur. Beside the fact that this phenomenon can be very dangerous, a main issue is also the contribution to man-made dam alluviation.

Figure 1: *(Inset) Location of the Roubine catchment in the ERS of Draix and the extent of the Terres Noires. (Outset) View of the Roubine catchment featuring an elementary gully instrumented since the 1980s with gauging station, sediment trap, a pluviometer and a limnograph.*

0.1.2 The elementary gully experimental site of the Roubine Catchment

The Roubine catchment (0.13 ha), located in the experimental Research Station (ERS) of Draix, displays a morphology similar to badlands (Fig. 1). The geology consists of highly stratified black marl deposited during the Jurassic (Oxfordiens) in an extensive bassin.

The marl are cut into platelets with carbonated nodules. Depending on the carbonate content, they are rather clayey limestone that form occasionnally more competent calcified layers (Antoine et al., 1998).

The Roubine catchment was chosen to observe and quantify erosion processes because it can be considered as an elementary gully since the hillslope is steep enough (35% at the outlet) to avoid transient stream deposit in the gullies (Mathys, 2006).

0.1.3 Regolith covering and erosion process activity

According to weathering intensity (mainly wet/dry and freeze/thaw cycles), a soft and disorganized few 10 cm thick layer of regolith forms continuously and accumulates in rills and gullies through solifluction and splash effect (Fig. 3). Consequently, a voluminous amount of material is provided each year for stream flows (Oostwood and Ergenzinger, 1998). The regolith layer available is rather permeable.

Survey information			Point cloud information			
Surveys Period	Date	Number of viewpoints	Instrument	Number [x 10^6]	Spacing [mm]	Distance [m]
April 2009	14.04.09	6	ILRIS-3D	15	11	50
June 2009	31.05.09	4	ILRIS-3D	4.2	7.5	50
August 2009	11.08.09	6	ILRIS-3D	5.4	8	50
Nov. 2009	03.11.09	4	ScanStation II	7.3	8	30
Mars 2010	19.03.10	4	ScanStation II	7.5	6.5	30

Figure 2: *Time series of Lidar data surveys collected between 2009 and 2010 in the Roubine catchment. TLS data exist since 2006 at the Roubine catchment for monitoring erosion processes.*

0.2 Lidar survey data

A monitoring of the topographic changes of the Roubine catchment through the seasons using terrestrial laser scanner (TLS) was performed during the year 2009, in order to detail volumes of eroded sediments in space and time (Fig. 2). The topography was acquired with two TLS devices alternatively, ensuring an accuracy of less than 1 cm upon both distance and position :

- an Ilris-3D laser scanner of Optech company (Optech, 2008).
- a LiDAR ScanStation II of Leica company.

The catchment was surveyed 5 times during that year from the same multiple viewpoints, in order to limit zones of shadow.

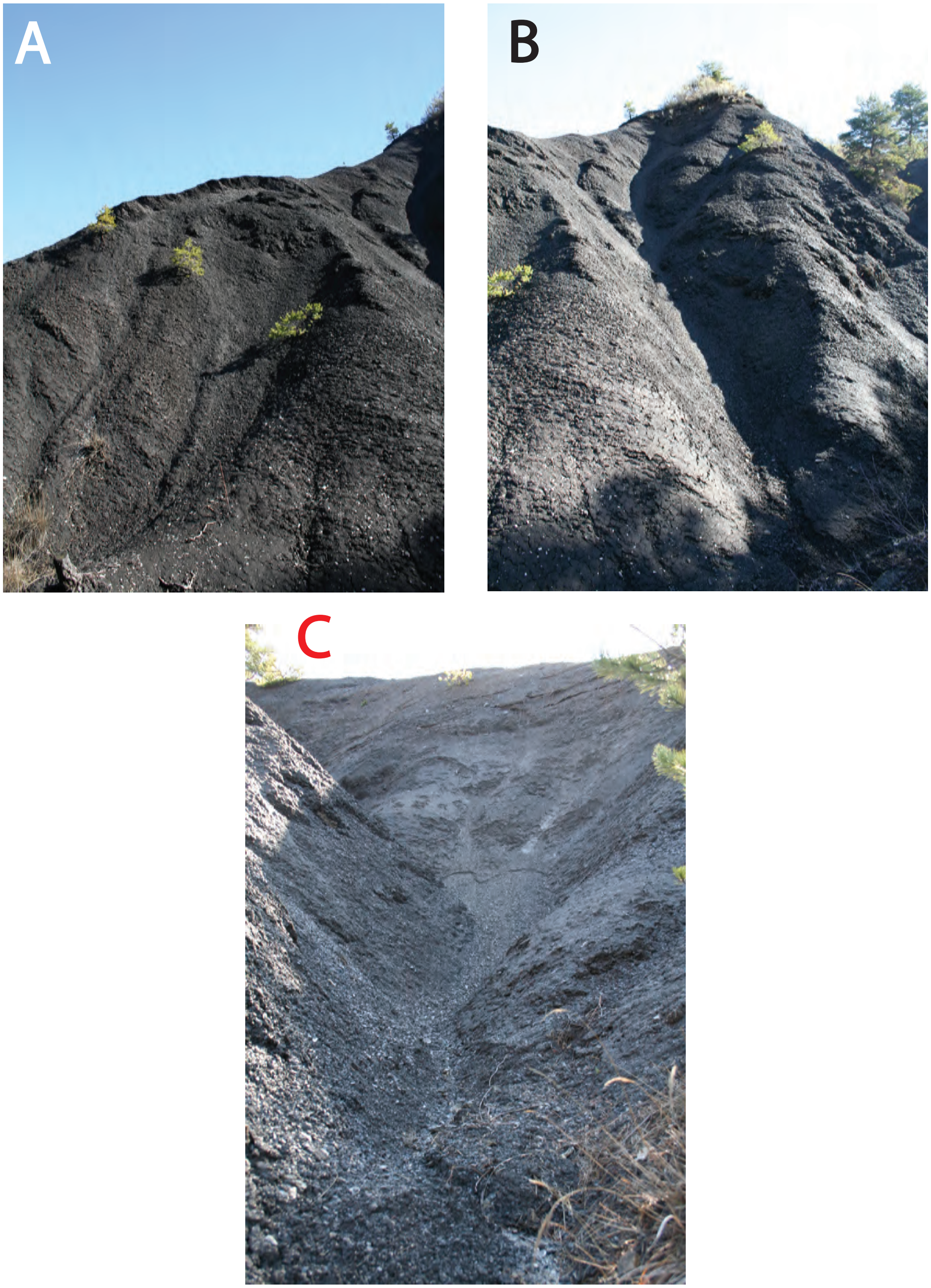

Figure 3: *(A) Regolith layer after that the snow was gone and (B) tributary gully full of loose regolith at the end of the winter. (C) View of the main reach fully recharged with regolith material in mid-mars 2010.*

0.3 Lidar data processing

The sequential point clouds of each scan were processed with the software Polyworks V. 10 (InnovMetric Software Inc., 2009) :

- Erroneous points and vegetation were manually removed and data that fell ouside the area of interest were trimmed.
- The scans of each survey were aligned together using the ICP (Iterative closest point) procedure (Besl and McKay, 1992). This enables to minimize the distance between the sequential point clouds.
- Georeferencing each time serie was performed relative to 8 fixed targets disseminated around the crone of the catchment and using the ICP algorithm on the point cloud of the targets only. This enables to align the sequential sets of point cloud to each other in the same coordinate system.

0.4 Point clouds and sequential data accuracy

The error of alignment and georeferencing can be resumed as :

$$\Delta_{measure} = \varepsilon_{alignment} + \varepsilon_{instrumental} + \varepsilon_{georeferencing} \quad (1)$$

In our case, the very high density of points coupled to the short range and a large overlapping between scans of a time serie could generate a point cloud estimated to 1.3 cm accuracy.

0.5 quantifying erosion

The topographic changes were quantified according to the shortest distance between points of two time series, producing a *map of differences* representing the difference in position between sequential data. This was processed in this way :

- Projection of the *point cloud of differences* into the xy-plane and gridding of this point cloud into a 2 cm cell size DEM. Surface corrections were performed according to the slope angle.
- Filtering of the noise using a principle of adjacency : if the mean value of a group of 16 adjacent *cells of the map of differences* are below the limit of accuracy (Eq. 1), they were then considered as displaying no topographic changes.
- Removal of the outliners using boundary values and of the isolated noisy values with morphological operations. This was performed in a common GIS environment.

0.6 Results and analysis

The sediment budgets deduced from the seasonal topographic changes in the Roubine catchment are displayed in Fig. 4 and Fig. 5 and summarized in Tab. 6 and Tab. 7. The volumetric budgets correspond to the sum of all cell values (negative = erosion ; positive = deposition) detected with the LIDAR surveys. The balance displays the net sediment budget between both time series in regards to the surface covered by the Lidar survey. Occlusion are mostly encountered below the catchment head, behind the curve made by the main gully, providing a source of error.

According that $\sim 30\%$ of the transported material is not deposited in the sediment trap, but exits the catchment as suspended (hyperconcentrated) load with the flow, the net volume of sediment leaving the catchment can be estimated to reach 6 m^3, depending on the rate of desintegration of the fine marl particles during tranport. This corresponds to a sediment yield of 110 t/ha for the period 2009.

Hence, the volumetric sequences of eroded sediment surveyed with LiDAR were very similar to the volume of solid material deposited in the sediment trap for the same periods (cf. tables Fig. 6).

As can be expected, transport of eroded material is related to discharge. This is achieved, however, in a way where small flash floods in spring can already transport a high amount of solid material. This invert relationship seems to reajust to a more positive one during the year. One reason is not only the high quantity of material available after the winter, but rather that this material concentrates in gullies and rills. Especially in the main reach, a conjunction of flow accumulation and concentration of loose material occur during the 1^{st} rainfall of the year.

In 2009, the regolith layer accumulated in the steep lateral impermanent gullies and rills was removed during late summer only, forming transient deposit in the main reach downward. So what can be infered in term of sediment regime: transport-limited or supply-limited regime ?

During the warm season, almost no generalized mark of erosion on the catchment hillslope (beside in gullies and in the main reach) was observed with LiDAR data. Either large slope erosion did not occur or erosion occurred below the detection limit of the LiDAR data ($\sim$1.5 cm in average on multiple grid cells).

During winter, regolith formation and spreading seems to be active, when no runoff occurs. Freeze/thaw cycle distroys the marl surficially and snow melting/light rainfall saturates the regolith layer, recharging rills and gullies through solifluction. Specific spots of regolith production (sources) remain unclear with LiDAR data. Is it a sign of random behavior ?

The heavy rainstorm observed in octobre 2009 may have reactivated erosion in gullies in a remarkable way, which may presuppose some kind of draining or purge effect (?).

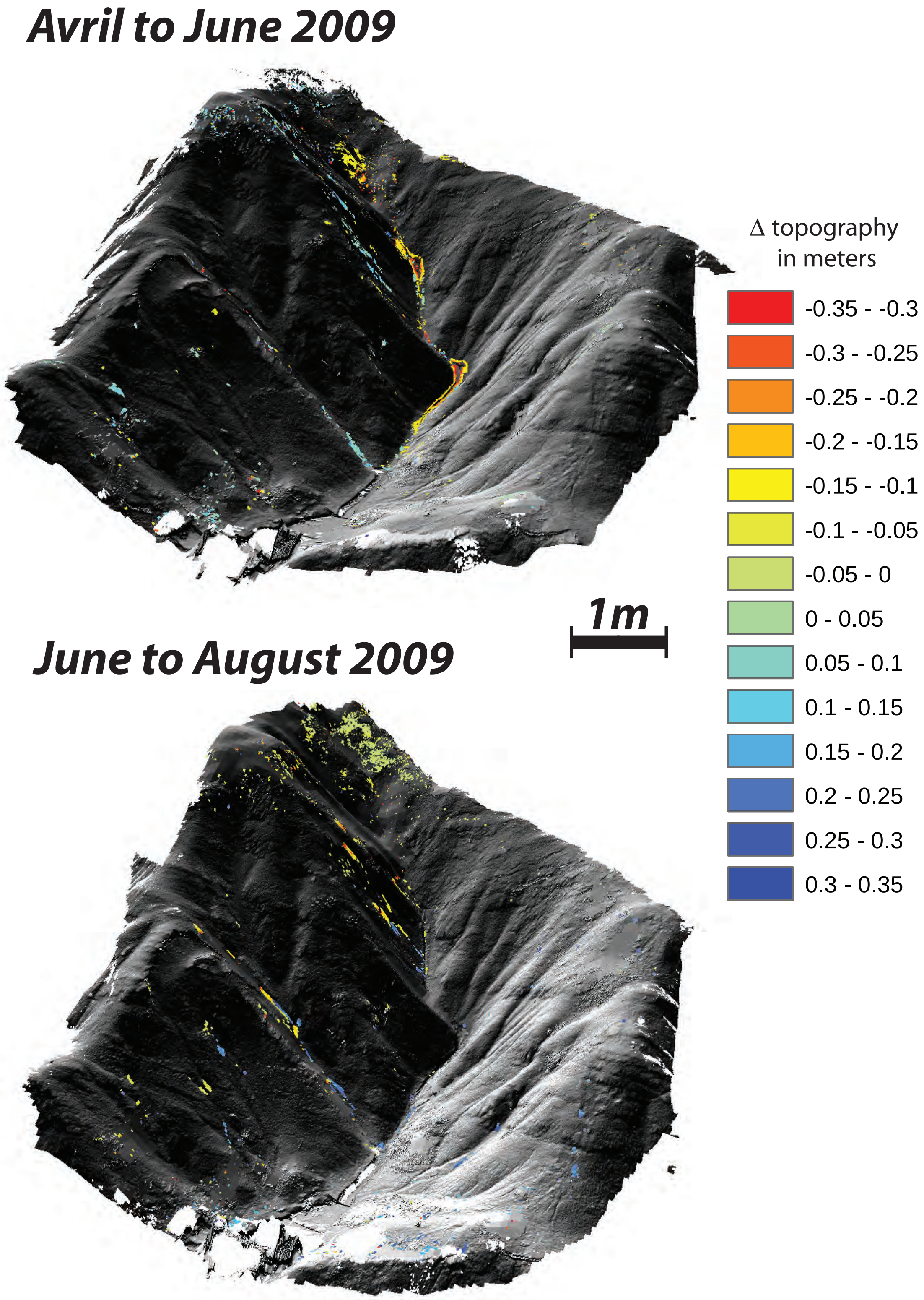

Figure 4: *Comparison od the LIDAR data for the time series between April to August 2009. EROSION is displayed in negative values (warm colors) and the DEPOSITION in positive values (cold colors).*

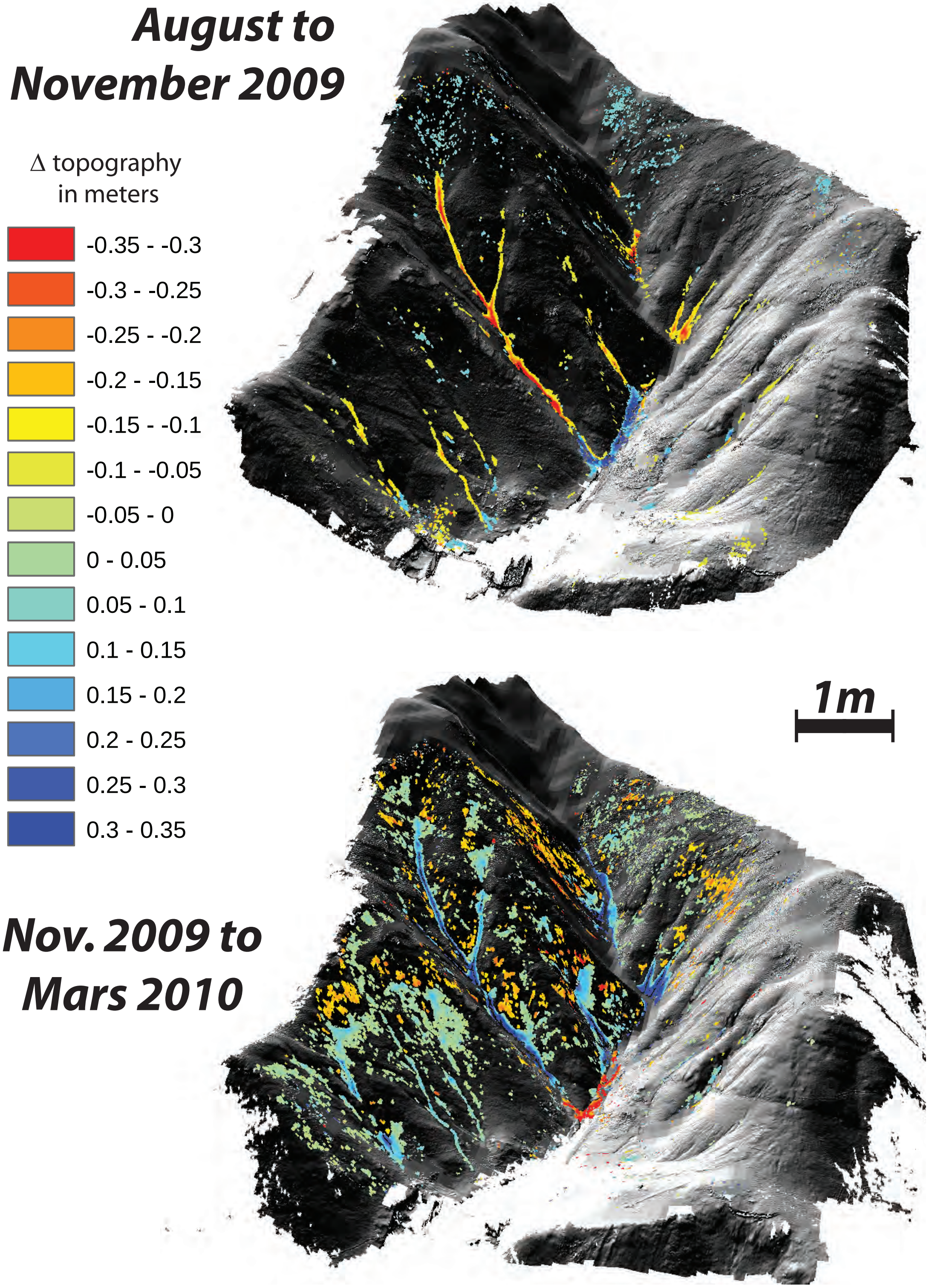

Figure 5: *Comparison of the LIDAR data for the time series from August 2009 over the winter to Mars 2010. EROSION is displayed in negative values (warm colors) and the DEPOSITION in positive values (cold colors).*

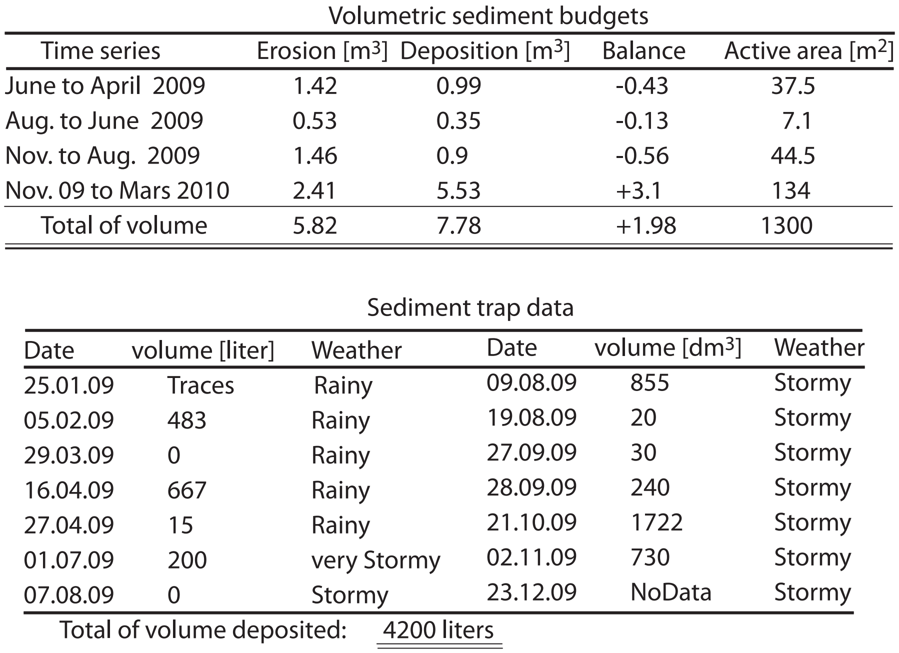

Volumetric sediment budgets

Time series	Erosion [m³]	Deposition [m³]	Balance	Active area [m²]
June to April 2009	1.42	0.99	-0.43	37.5
Aug. to June 2009	0.53	0.35	-0.13	7.1
Nov. to Aug. 2009	1.46	0.9	-0.56	44.5
Nov. 09 to Mars 2010	2.41	5.53	+3.1	134
Total of volume	5.82	7.78	+1.98	1300

Sediment trap data

Date	volume [liter]	Weather	Date	volume [dm³]	Weather
25.01.09	Traces	Rainy	09.08.09	855	Stormy
05.02.09	483	Rainy	19.08.09	20	Stormy
29.03.09	0	Rainy	27.09.09	30	Stormy
16.04.09	667	Rainy	28.09.09	240	Stormy
27.04.09	15	Rainy	21.10.09	1722	Stormy
01.07.09	200	very Stormy	02.11.09	730	Stormy
07.08.09	0	Stormy	23.12.09	NoData	Stormy

Total of volume deposited: 4200 liters

Figure 6: *(Table above) Overall sediment volumes monitored with LIDAR surveys from April 2009 to Mars 2010. The active area corresponds to the surface where erosion or deposition were detected. (Table below) Sediment volumes deposited in the sediment trap at the basin outlet during the year 2009. The volumes are displayed graphically in Fig. 7.*

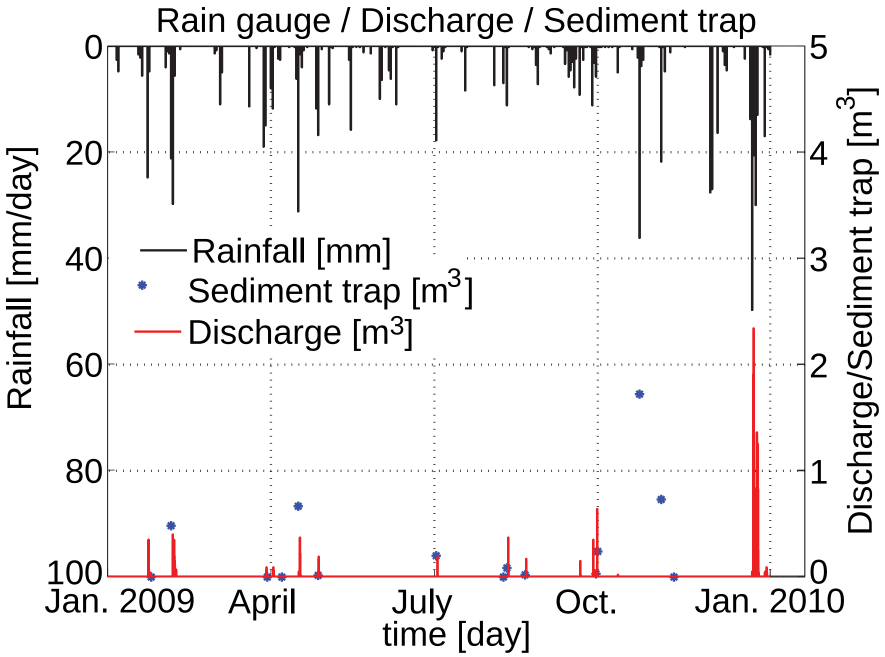

Figure 7: *Hydrological data recorded at the outlet of the Roubine catchment for the year 2009. The rainfall data display the effective amount of rain accumulated per day and the discharge data give the runoff per second at the basin outlet. Don't forget that the catchment is only 1300 m² big.*

0.7 Conclusion and Perspectives

The analysis of topographic changes through erosion processes has shown that:

- The tendency of *transport-limited* regime at the beginning of the warm season seems to evolve to a more *supply-limited* one during the rest of the year;
- The regolith production and gully infilling occur during winter time;
- A progressive upgoing removal of accumulated material follows during the warm season.
- Erosion reactivation (through rain drop splash effect ?) or purge effect in gullies depending on rainfall intensity in autumn.

Previous studies on erosion and transport processes in the *Terres Noires* can be confirmed with LiDAR data survey. LiDAR data can supply a spatially distributed erosion/deposition map through time at centimeter scale, which may improve knowledge significantly. LiDAR data can also provide input volumes and rates of activity for solid transport modeling.

Bibliography

Antoine, P., Giraud, A., Meunier, M., and VanAsch, T. (1998). Properties of the Terres Noires in southeastern France: Wheatering Erosion, solide transport and instability. *Engineering Geology*, 40:223–234.

Besl, P. and McKay, N. (1992). A method for registration of 3-D shapes. *IEEE Transactions on Pattern Analysis and Machine Intelligence*, 14(2):239–256.

InnovMetric Software Inc. (2009). *PolyWorks – 3D scanner and 3D digitizer software*. InnovMetric Inc., 2014 Rue Cyrille – Duquet, Quebec City, QC G1N 4N6, Canada.

Mathys, N. (2006). *Analyse et modélisation à différentes échelles des mécanismes d'érosion et de transport de matériaux solides. Cas des petits bassins versants de montagne sur marne (Draix – Alpes de Haute Provence)*. PhD thesis, CEMAGREF – National Polytechnical Institut of Grenoble.

Oostwood, D. and Ergenzinger, P. (1998). Erosion and sediment transport on steep marly hillslope, Draix, Haute-Provence. *Catena*, 33:179–200.

Optech, I. (2008). *ILRIS 3D, Intelligent Laser Ranging and Imaging System*. Advanced Visual Systems Inc., 300 Interchange Way, Vaughan, ON L4K 5Z8, Canada, summary specification sheet – ILRIS enhanced range mode edition.

Appendix D

Identification of potential rockfall source areas at a regional scale using a DEM-based geomorphometric analysis

published in ***Natural Hazards and Earth System Sciences 9:1643–1653 (2009)***

Nat. Hazards Earth Syst. Sci., 9, 1643–1653, 2009
www.nat-hazards-earth-syst-sci.net/9/1643/2009/

Natural Hazards
and Earth
System Sciences

Identification of potential rockfall source areas at a regional scale using a DEM-based geomorphometric analysis

A. Loye, M. Jaboyedoff, and A. Pedrazzini

Institute of Geomatics and Risk Analysis, University of Lausanne, Lausanne, Switzerland

Received: 30 January 2009 – Revised: 19 August 2009 – Accepted: 25 August 2009 – Published: 8 October 2009

Abstract. The availability of high resolution Digital Elevation Models (DEM) at a regional scale enables the analysis of topography with high levels of detail. Hence, a DEM-based geomorphometric approach becomes more accurate for detecting potential rockfall sources. Potential rockfall source areas are identified according to the slope angle distribution deduced from high resolution DEM crossed with other information extracted from geological and topographic maps in GIS format. The slope angle distribution can be decomposed in several Gaussian distributions that can be considered as characteristic of morphological units: rock cliffs, steep slopes, footslopes and plains. A terrain is considered as potential rockfall sources when their slope angles lie over an angle threshold, which is defined where the Gaussian distribution of the morphological unit "Rock cliffs" become dominant over the one of "Steep slopes". In addition to this analysis, the cliff outcrops indicated by the topographic maps were added. They contain however "flat areas", so that only the slope angles values above the mode of the Gaussian distribution of the morphological unit "Steep slopes" were considered. An application of this method is presented over the entire Canton of Vaud (3200 km^2), Switzerland. The results were compared with rockfall sources observed on the field and orthophotos analysis in order to validate the method. Finally, the influence of the cell size of the DEM is inspected by applying the methodology over six different DEM resolutions.

1 Introduction

Rockfall is defined as individual rocks removed from a slope by sliding, toppling or falling and proceeding downslope (Varnes, 1978). The size of the blocks ranges from small cobbles to large boulders of 100 m^3 (Whalley, 1984). Rockfall risk in mountainous areas is increasing as the population and economic activity increase (Baillifard et al., 2004; Leroi et al., 2005). As a consequence, the identification of rockfall hazard prone areas is of primary importance for producing hazard maps. Several approaches at local and regional scale have been developed to identify rockfall source areas and to assess the resulting hazard or susceptibility (Mazzoccola and Hudson, 1996; Bunce et al., 1997; Guzzetti et al., 1999; Gokceoglu et al., 2000; Jaboyedoff et al., 2005a). During the last two decades, the increasing availability of digital elevation models (DEMs) and GIS data have given rise to a variety of very convenient rockfall models at various scales (Guzzetti et al., 2002; Günther, 2003; Baillifard et al., 2003; Jaboyedoff et al., 2004a; Derron et al., 2005).

However, one of the main difficulties in mapping rockfall hazard at a regional scale is the identification of potential rockfall sources. Those source areas, which correspond to the detachment zones of the blocks, are usually taken from distinctive evidence such as talus slope and scree deposits below cliff faces (Frattini et al., 2008), field and historical inventory of rockfall (Hantz, 2003). Whether these datasets are available, they are often fragmentary in space and time. A variety of empirical, statistical and process-based methods for detecting source areas exists, but only few of them were tested for identifying source zones at a regional scale ($>$500 km^2) (Crosta and Agliardi, 2003). The simplest morphometric approach consists of defining a thresholds angles above which the slope, especially the rock cliffs, may be considered as unstable (Toppe, 1987) (e.g. $>60°$ in Guzzetti et al., 2003; $>45°$ in Jaboyedoff and Labiouse, 2003; $>37°$ in Frattini et al., 2008). Similar attempts were limited to cliff faces (Krummenacher, 1995; Meissl, 1998) or active rockfall slopes only (van Dijke and van Westen, 1990). More evolved methods were developed by combining the slope geometry extracted from a DEM with datasets such as rock type, exposition, slope curvature and land cover for instance in an heuristic or probabilistic way (Marquinez et al., 2003; Aksoy and Ercanoglu, 2006; Acosta et al., 2007). Besides, high resolution DEMs (HRDEMs) have made possible the detection

---

Correspondence to: A. Loye
(alexandre.loye@unil.ch)

of discontinuities sets (Jaboyedoff et al., 2007). Considering the spatial arrangement of discontinuities with the topography, a kinematic analysis can then be performed to detect potential failure mechanisms (planar sliding, wedge failure and toppling) (Wagner et al., 1988; Rouiller et al, 1998; Gokceoglu et al., 2000; Jaboyedoff et al., 2004b, 2005b; Günther et al., 2004; Derron et al., 2005). Those geometrical and geomechanical-based approaches are especially suitable for slope stability analyses in well-known regions where rockfall cause problems. They require however local information on the discontinuity sets that can only be partly obtained with automatic procedures on DEM. Therefore, field work is usually required.

According to Heim's studies (Heim, 1932), one of the main factors necessary for rockfall initiation is a steep slope angle. Gravity-driven surface processes in mountainous regions are closely related to the steepness of the topography and the morphology of the relief, which therefore reflects these instabilities (Montgomery and Brandon, 2002). The slope angles of stability depend on the rock type and the geometrical and mechanical properties of the discontinuity sets (Hoek and Bray, 1981; Selby, 1993). This fact includes frictional angle and cohesion when assuming a Mohr-coulomb failure criterion (Locat et al., 2000). Therefore, it can be considered that the slope angle distribution reflects the type of relief (e.g. glacial, alluvial, plains, etc.) and the mechanical properties of the rocks. As a consequence, different morphologies and rock types induce a range of slope angle values that are characteristic for a given morphotectonic setting (Strahler, 1954) and expressed in a slope angle distribution (SAD). As an example (Fig. 1), the SAD of an Alpine valley profile represented by two morphological units varies randomly around their mean slope angles (20° for the footslopes and 60° for the cliffs), implying a Gaussian distribution of the slope angles around these means. As zones with high curvature are less represented, the morphological units (MU) can be extracted according to their slope angle frequency distribution and assuming a Gaussian-shape curve.

Currently, modern acquisition techniques (Airborne Laser Scanning, Photogrammetry) enable to obtain a regional scale DEM with a resolution as high as 1 m making the topographical analysis more and more relevant since the modelled slope angles are very close to reality. For instance (Fig. 2), for a cliff of 20 m high, a 25 m cell size grid gives an apparent slope angle significantly smaller (60°) compared to a HR-DEM grid of 2 m resolution (∼90°). This study introduces a methodology that enables detecting rockfall sources at a regional scale, based on a geomorphometric analysis performed on such HRDEMs (1 m cell size).

2 Methodology

The study area is divided in homogeneous morphometric areas (HMA) following identical characteristics such as uniform lithology, geologic and morphotectonic history. Potential rockfall initiation areas are determined by analysing the SAD of the main HMA. The SAD is decomposed into several Gaussian slope angle distribution characteristics of a specific morphological unit (Strahler, 1950) such as the cliffs, steep slopes, footslopes and plains for an Alpine valley. The Gaussian distribution "cliffs" enables to extract cliff faces, outcropping areas and bare rock surfaces that can be considered as potential rockfall sources. In addition, the detection of rockfall based on the distribution of the slope angle can be improved by using other documents like geological maps, topographic maps and orthophotos.

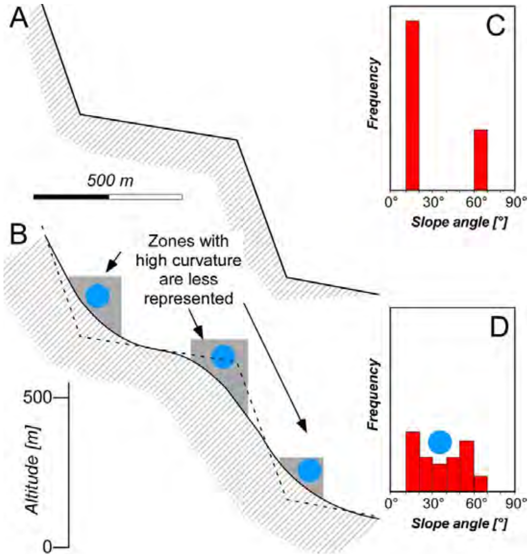

Fig. 1. Ideal sketch profile (A) and realistic profile (B) of an Alpine valley representing two cliffs and two steep slopes; (C/D) their slope angle distribution (SAD) (modified after Rouiller et al., 1998).

2.1 Slope angle distributions (SAD) and its decomposition

The study area is grouped into HMA having similar structural style and morphology as well as close geomechanical behaviour. The underlying assumption states that the slope profiles are different varying HMA. The effective surface area of each grid cell of a DEM depends on its inclination (slope angle), the surface areas of the steep slopes are underestimated in comparison to flat zones (planimetric). In order to consider an effective surface of the topography for the SAD analysis, the 1 m^2 surface of the DEM cells are weighted according to the slope angle β of the HRDEM. The frequency (w_β) of the SAD is then calculated using:

$$w_\beta = \frac{A_{h\beta}}{A_{\text{HMA}} \cos\beta} \qquad (1)$$

where $A_{h\beta}$ is the sum total horizontal area of the DEM cells with the same slope angle β and A_{HMA} is the total area

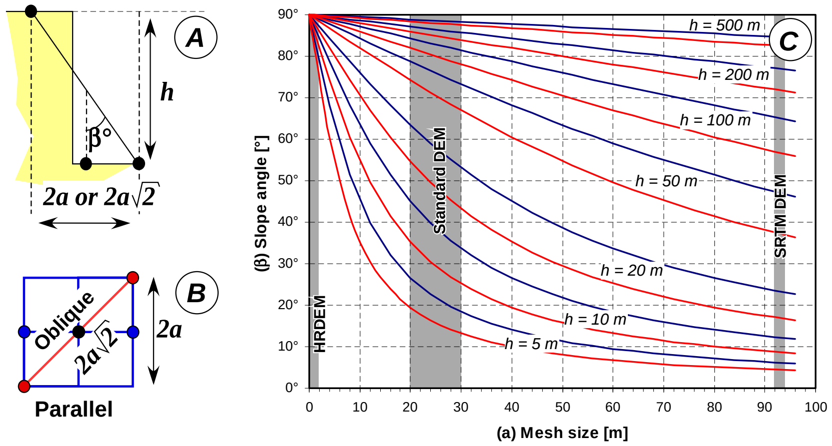

Fig. 2. (A) Relationship between slope angle and cliff height. (B) Computation of the slope angle depending on the orientation of the cliff. (C) Slope angle β computed from a DEM grid of size a for a vertical cliff face of height h. The difference between the red and blue line in (C) indicates the difference between a cliff parallel and oblique (45°) to the DEM grid cells.

of the HMA considered. Then, the obtained SAD can be modelled by Gaussian distributions that can be related to the main morphological units of the topography (Strahler, 1950). Hence, the method consists in decomposing the SAD into several Gaussian (slope angle) distributions characteristic of the main morphological units (GDMU) of a given topography (Fig. 3). The decomposition of the SAD into GDMU is performed by minimizing standard error of the estimated SAD (the sum of the GDMUs) versus computed SAD. In the present study, four main morphological units (MU) can be identified:

1. Plains: low slope angles corresponding to the fluvial and fluvio-glacial deposits.
2. Foot-slopes: gentle slope angles featuring the lower part of the hillslope characterized by colluvial fans, debris flow and landslide deposits.
3. Steep slopes: containing till deposits and rocky outcrops covered with vegetation.
4. Cliffs: very steep slopes, which correspond to rocky outcrops.

The two last morphological units may contain rockfall source areas. They are the units to focus on, in order to define the threshold slope angles above which rockfall sources can be found. The comparison between these MU extracted with Gaussian distribution and the ones on the hillshade shows that they are accurately superimposed (Fig. 4). The above assumptions are however not always verified. As a consequence, a part of interpretation of the GDMU is necessary.

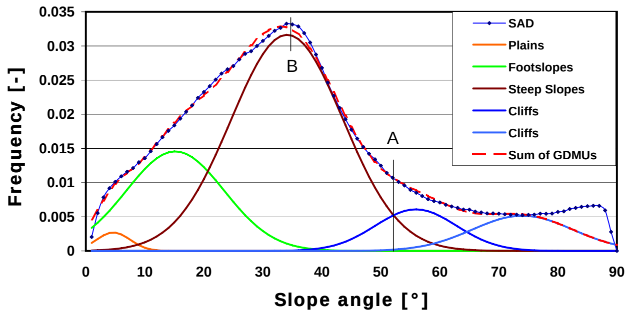

Fig. 3. Slope angle distribution (SAD) of 1° bin size from *Les Diablerets* Alpine Valley test zone featuring the GDMU of the topography. This test site is entirely situated in the Helvetic HMA. A indicates the threshold slope angle above which the slopes belong dominantly to the cliffs and are therefore considered as potential rockfall source area. B indicates the mode of the GDMU steep slopes. The two cliffs units represent two families of bare rock cliff faces lithologically distinct (for explanations refer to Sect. 2.3).

2.2 Method adaptation for non-Alpine topography

This morphological classification can be applied on less rugged landscapes as well. Where large flat zones with small slope angles are dominant, the frequency of slope angles above 30° is very low. This is due to the fact that rugged landscapes are too sparse throughout such a foreland or hilly landscape. The topography is not mirrored in a homogeneous way. Consequently, GDMU extraction is too difficult. Therefore, the GDMU can be calculated based on a SAD coming from a serie of cross-sections along the rugged areas only, without considering any large flat zones in between. Thus, the SAD analysis focuses only on the steep terrain, where rockfall activity is likely to occur. After comparison with the specific test zones, 30 profiles have shown to render the overall slope angle distribution in an accurate way.

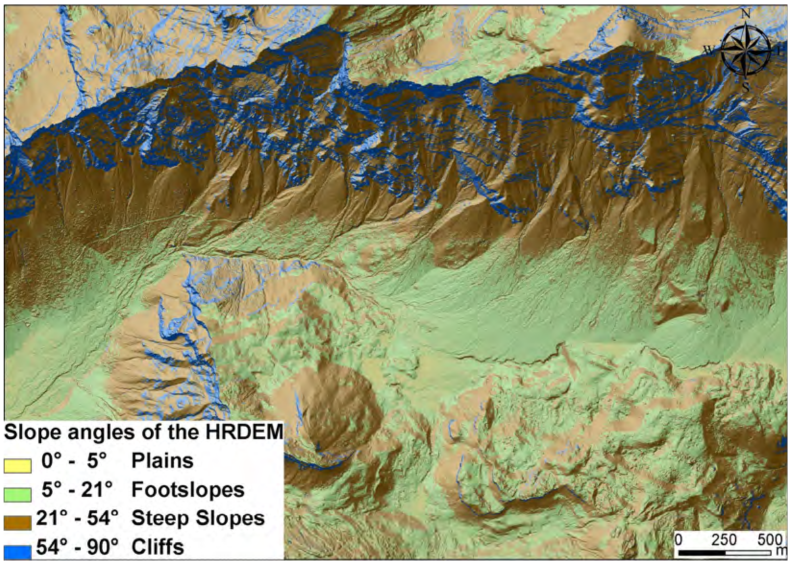

Fig. 4. Hillshade of *Les Diablerets* region displaying with distinct colours the dominant MU extracted from the intersections between GDMU plotted in Fig. 3. Comparison shows that GDMU are accurately superimposed with the morphological units observed on the hillshade (MNT-MO, © 2005 SIT).

2.3 GDMU interpretations

Each Gaussian slope angle distribution can be considered as typical of landscape. The mode of the distribution can be assumed as the average apparent slope angle of stability of a given MU. Consequently in a given landscape, the slope angle of a MU varies around an average as this is for instance the case for scree slopes, which possess an average slope angle close to 35°. As an example, the SAD of the two undisturbed scree deposits illustrated in Fig. 5 accepts the Kolmogorov-Smirnov test (p-value >0.05 and KS-STAT $>$ CV) performed over the SAD sample [31.5°–39.5°]. This means that the slope angle values come from a standard normal distribution. For each HMA, the decomposition of the SAD in GDMU can be interpreted as follow (Fig. 3):

1. A threshold slope angle is defined at the intersection (noted A) between the two steepest MU: the GDMU cliffs and the GDMU steep slopes (Rouiller et al., 1998). All DEM cells with slopes steeper than this threshold angle are considered as potential rockfall source areas, independently of the local lithology and the land cover, because they are cliffs or rocky slope surfaces lightly covered with vegetation.

2. In some cases, there are no GDMU cliffs within the decomposition of the SAD. Thus, the highest GDMU is referred to the rocky steep slopes MU.

3. In very steep topography the SAD can contain two GDMU cliffs. In that case the lower GDMU cliffs is considered and used to estimate the above threshold (1).

4. In the present study the 1:25 000 Swiss topographic vector map (©Swisstopo: DV012716) was used, which contains geo-thematic information among others the cliff outcrops as polygons. However, they can display slope angles down to 0° where rockfall are very unlikely. As a consequence, only the cliff outcrops areas with slope angle value above the mode of the GDMU steep slopes (noted B) are assumed to be potential rockfall sources.

Finally, all these criterions were used to identify potential rockfall source areas within a standard GIS environment for each considered HMA.

3 Data processing

The present study was performed over the entire Canton of Vaud (Switzerland) that represents an area of about 3200 km^2. The method was applied using HRDEM of 1 m cell size (MNT-MO, ©2005 SIT). The results were compared and analysed using orthophotos by inspecting talus screes and blocks deposits over the entire study area. Field observations were performed in specific test zones of each HMA in order to evaluate the quality of the model.

3.1 Homogeneous morphometric areas (HMA)

The Canton of Vaud consists of three main tectonic units (Trümpy, 1980; Escher et al., 1997): the Jura, the Prealps and the Swiss Molasse Plateau (Fig. 6). The western part, the Jura Mountains, is formed by a folded and thrusted Mesozoic to Tertiary carbonates platform series, in a thin skin

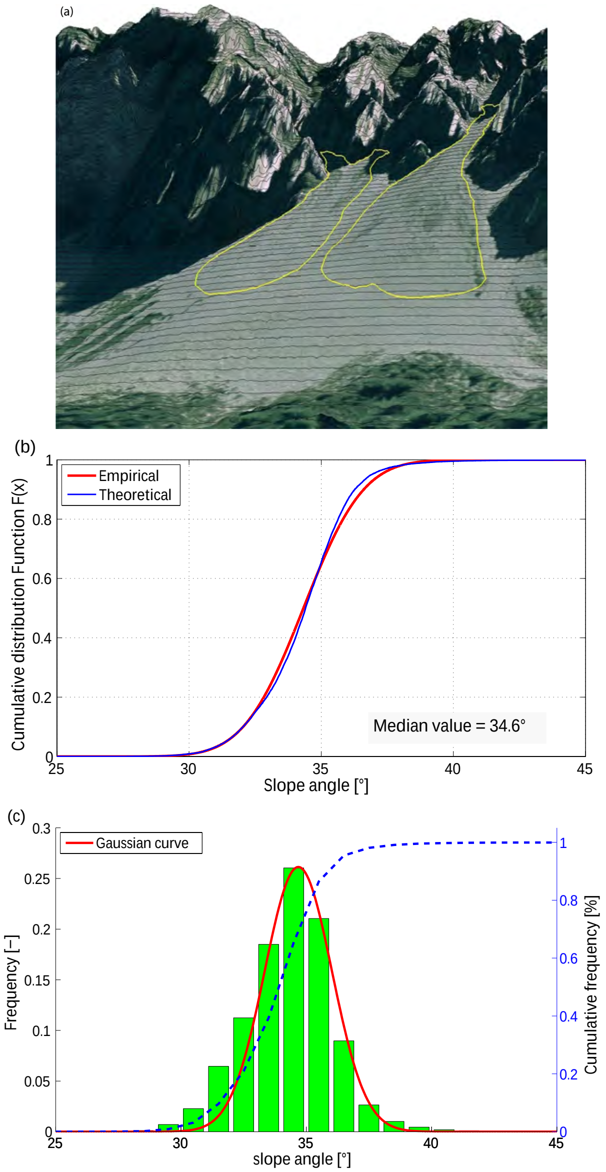

Fig. 5. **(a)** Scree slopes at Mt D'Or, near *Les Diablerets* region. The undisturbed scree deposits are delineated in yellow. **(b)** Scree deposits CDF of the slope angles. Results of the Kolmogorov-Smirnov test statistic: p-value = 0.0679, CV = 0.056 and KSSTAT = 0.058. **(c)** SAD of the two scree deposits with its mode = 34.5°.

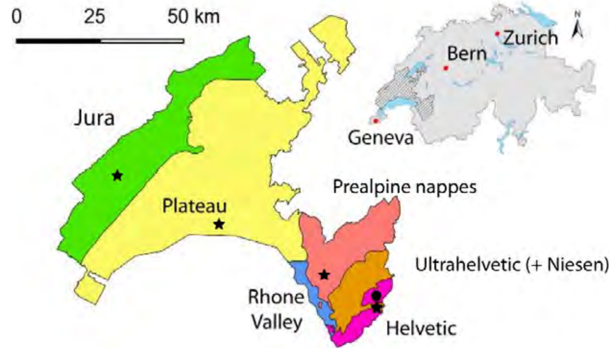

Fig. 6. Geographical location of the Canton of Vaud (Switzerland) with the main HMA. The black dot indicates the test site location of *Les Diablerets* and the black stars the test site of the other HMA.

tectonic style. The elevation of the Jura mountain chain ranges between 400 m a.s.l. to 1700 m a.s.l. The southeast part of the study area belongs to the Alps. They inherited a glacial landscape, which was reworked by fluvial erosion processes and mass movements. Its rugged topography range from 400 m a.s.l. to more than 3000 m a.s.l. The main lithologies are limestones, dolomites, marls, evaporites and shales, which were deposited in several different Mesozoic and Cenozoic basins. Those lithologies control strongly the type of slope movements. This area is divided in three main structural units: the Prealpine nappes deriving mainly from the Briançonnais domain, the Helvetic nappes and the Ultrahelvetic nappes (including the Niesen nappe). Between the Jura and the Alps lies the molassic Plateau. This is a sedimentary foreland basin formed in Oligocene to Miocene, during the Alpine orogeny. Its topography is mostly flat with small hills. The rocks are mainly terrigeneous sediments deposited in marine or continental environments.

3.2 Processing HRDEM and SAD analysis

The HRDEM was processed within the GIS environment ArcGIS®. The SAD analysis is obtained from standard DEM slope angle computation (Burrough and McDonnell, 1997). The slope angles are computed using a 3×3 matrix (Horn, 1981) implemented in the ArcGIS® spatial analyst extension and corrected according to Eq. (1). The slope angle β was classified in bins size of 1°. Five distinct HMA were defined based on the above structural units: Helvetic, Ultrahelvetic (+Niesen) and Prealpine nappes belonging to the Alps, the Plateau and Jura. For the three HMA of the Alps, the SAD was modelled integrally over the considered area. For the Jura and the Plateau, however, the slope angles were computed according to 30 cross-sections evenly distributed along the rugged areas only, as described in Sect. 2.2.

The SAD decomposition in GDMU was performed using the Solver of Excel (©Microsoft) to perform the minimization. Initial parameters that are set manually are the number of GDMU, their estimated mean slope value and standard deviation. These initial values were defined according to the shape of the SAD, where some changes along the curvature of the distribution can be observed. Each GDMU was compared with observations on the hillshade of the HRDEM, orthophotos and the geological and topographical maps. If required, the process started over again with new initial values to increase the matching with the observed morphology. This approach is summarized in the Fig. 7.

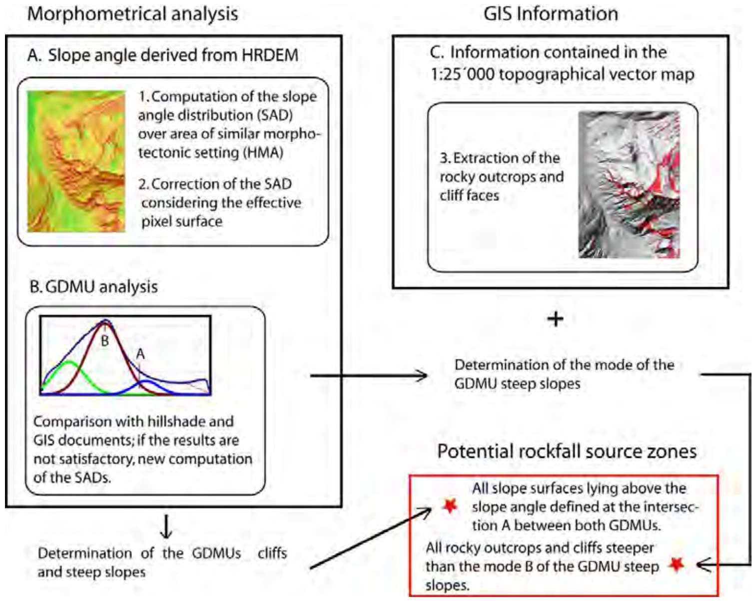

Fig. 7. Flow chart describing the methodology.

4 Results

The threshold slope angles resulting from the computation of the SAD and the extraction of their relative GDMU were interpreted separately for each HMA. The results are analysed according to their specific geology and morphology respectively, since their SAD are strongly influenced by the dominant lithologies. Threshold values obtained for each HMA are summarized in Table 1 and the map of potential rockfall source zones for the entire Canton of Vaud is shown in Fig. 11.

Table 1. Threshold slope angles above which rockfall source areas are potentially considered.

		Threshold angles for	
Location	HMA	A. Slopes belonging to the GDMU cliffs	B. Cliffs and rocky outcrops taken from the topographic vector map (mode of the GDMU steep slopes)
Alps	Helvetic	54°	36°
	Préalpes Médianes	53°	34°
	Ultrahelvetic	49°	33°
Plateau	Molassic Plateau	46°	30°
Jura	Jura Mountains	46°	32°

4.1 Alpine HMA

In the three Alpine HMA, the decomposition of the SAD into four GDMU can be clearly achieved (Fig. 8). The sum of these Gaussian distributions reproduces the SAD with a coefficient of determination close to 1, meaning that the morphologies can be described by the SAD decomposition. The analysis of the hillshade derived from HRDEM and the orthophotos show that the modelled cliffs are delineated accurately. The comparison of the results with field observations and the geological maps show that the modelled potential rockfall sources are mainly located in the limestone and dolomites. In these HMA, the lower slope angle intersection of the GDMU cliffs seems to depend on the percentage of limestone and dolomites per HMA outcropping: the Helvetic containing the greatest area, the Ultrahelvetic (+Niesen) the lowest and the Prealpine nappes in between. These lithologies are very competent and form in great majority the very steep slopes and cliffs. Hence, the morphometric analysis performed in the Alpine units seems to extract the geological constraints as well.

According to SAD analysis, the threshold slope angle for the cliffs ranges in the Alps between 49° for the Ultrahelvetic to 54° for the Helvetic, with an angle of 53° for the Prealpine nappes (Table 1). This simply underlines the fact that Ultrahelvetic nappes are mostly composed of flysch-type deposits creating rock outcrops with lower slope angles than the carbonates belonging to the Helvetic and Prealpine nappes. In addition, it is interesting to notice that most of the mode values of the GDMU steep slopes are close to 35°, the slope angle of sand pile.

The illustration in Fig. 12 shows how all potentially unstable cliffs and rock slopes contained in the 1:25 000 topographic vector map are well constrained by the cliffs modelled with the GDMU approach. In Fig. 13,

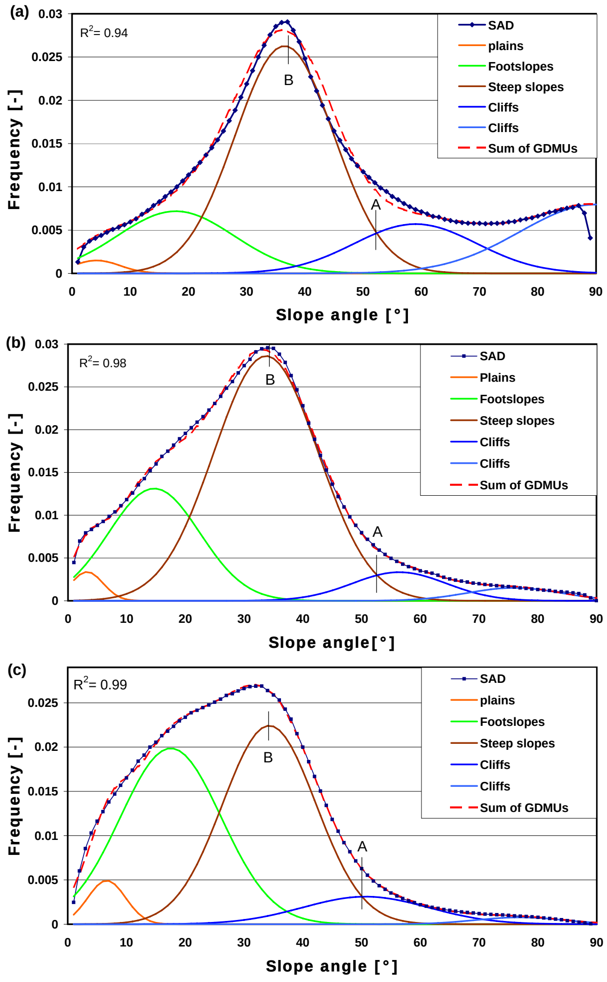

Fig. 8. Results of the SAD decomposition for the Alpine HMA (**(a)** Helvetic HMA, **(b)** Préalpes Médianes HMA, and **(c)** Ultrahelvetic HMA). The numerical values are given in Table 1.

comparison with orthophotos analysis and field observations shows that including all cliffs and rocky outcrops contained in the Swiss topographical vector map steeper than this angle of stability improves the delineation of potential rockfall source zones.

4.2 Molasse Plateau HMA

In the contrary of the Alps, the Plateau was shaped differently. Its morphology results mainly from glacial and fluvial erosion processes. In this hilly topography with large flat terrain, the MU of the cliffs is lacking, even though small cliff faces can be encountered in some parts, but they are seldom. The methodology was then adapted and slope angle profiles were used. According to its specific geomorphological environment, the SAD was decomposed into three GDMU (Fig. 9):

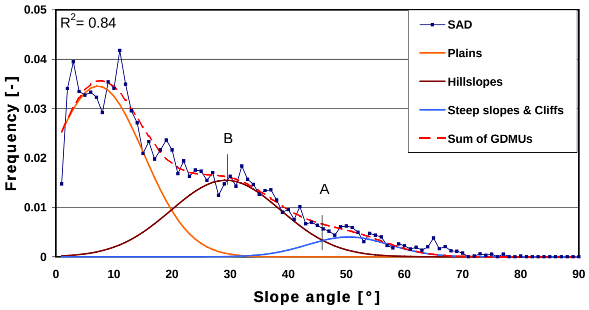

Fig. 9. Results of the SAD analysis for the HMA of the Plateau. According to its morphological environment, the SAD was decomposed into three GDMU only (see text for details). The numerical values are given in Table 1.

1. The plains corresponding to the large flat terrain or areas of low steepness.
2. The hillslopes corresponding to the sides of the small hills.
3. Steep slopes and cliffs corresponding to areas of rugged topography.

The three GDMU could reproduce the SAD in an accurate way. The slope angle intersection of the GDMU steep slopes and cliffs with the GDMU hillslopes is modelled at 46°. And the mode of the GDMU hillslope is at 30°. By analysing orthophotos and shaded reliefs, the modelled potential rockfall source areas show that steep rocky slopes arise predominantly along rivers and impermanent watercourses, as well as at the limits of fluvio-glacial terraces. These small cliffs resulting from fluvial erosion are made of marls and competent sandstones. Comparison with orthophotos analysis and field observations is very satisfactory and allows considering the modelled slopes as potential rockfall source areas.

4.3 Jura Mountains HMA

Although the morphology is different than in the Alps, four main GDMU were used. The Jura morphology is constrained by a thin skin tectonic style. Plains are situated in the synforms and gentle slope angles correspond to the box folds. Erosion of folds limbs and faults create cliffs in the limestone and marls and scree deposits corresponding to the steep slopes. The sum of the GDMU reproduces the SAD accurately (Fig. 10). The GDMU cliffs become dominant upon the GDMU steep slopes above a slope angle of 46°. The mode of the GDMU steep slopes yields to 32°. The analysis of the results with the hillshade shows that the potential rockfall source areas follow the steep parts of the folds where limestone outcrop on the surface or are covered under a thin layer of soil, or they correspond to some very steep slopes

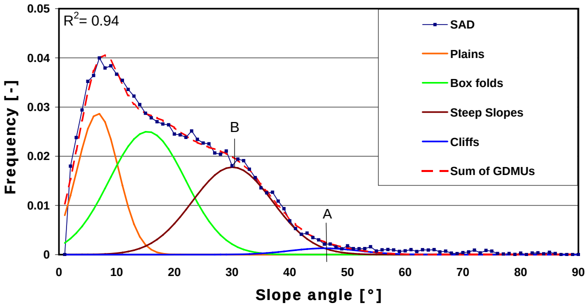

Fig. 10. Results of the SAD analysis for the HMA of the Jura. The numerical values are given in Table 1.

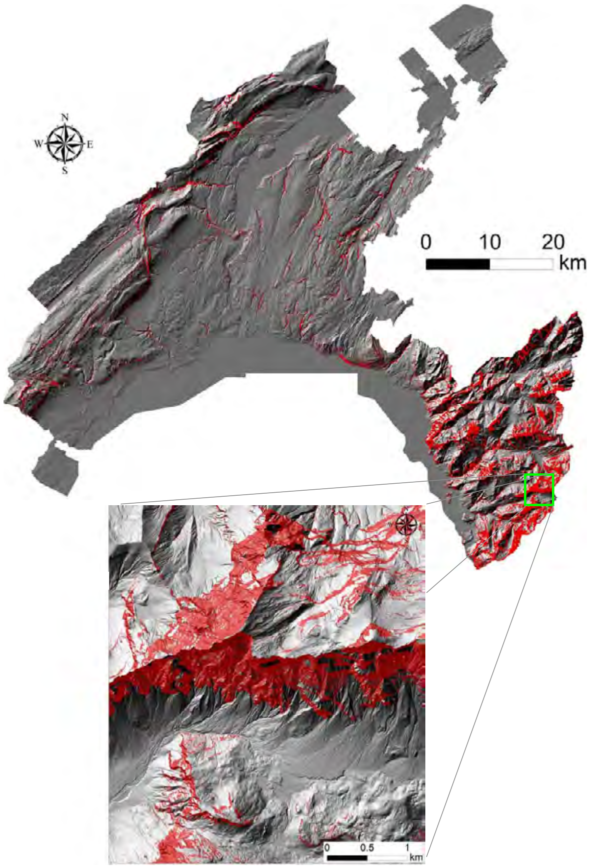

Fig. 11. Potential rockfall sources (in red) map for the entire Canton of Vaud with an original resolution at 1 m reduced 25 m cell size. The enlargement shows *Les Diablerets* test area (MNT-MO, ©2005 SIT).

formed by strike-slip faults (Trümpy, 1980). Historical registers of event and scree deposits observed on orthophotos show that rockfall sources are mostly encountered in those zones. By including all rocky outcrops of the topographic map steeper than the mode of the GDMU Steep slopes (32°), potential rockfall source areas coming from fluvial erosion could also be delineated.

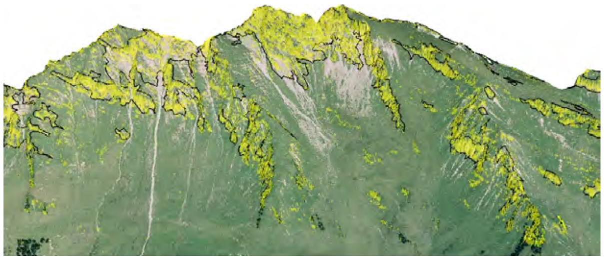

Fig. 12. Section of the test site situated in the Niesen nappe merged with Ultrahelvetic nappes, showing all slopes lying above the threshold slope angle of 49° (delineated in yellow). The cliffs and rocky outcrops taken from the Swiss topographical vector map are surrounded by a black line (SWISSIMAGE ©2004 swisstopo (DV012716)).

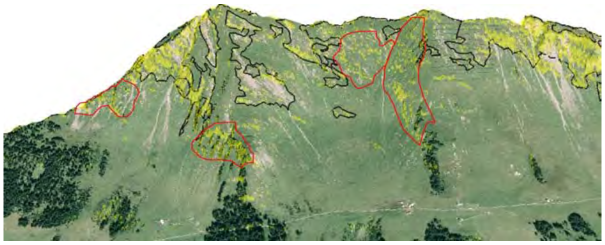

Fig. 13. Same test site as Fig. 12. All slopes lying above the threshold slope angle of 49° are delineated in yellow. The surrounding red lines show the additional rocky slopes detected by the SAD decomposition. This corresponds to the modelled cliffs zones that are not contained in the topographical vector map. Those areas lie above recent talus scree or freshly detached blocks and can therefore be described as potential rockfall sources. Such zones, sometimes lightly covered with vegetation, are not obviously included in hazard assessment (SWISSIMAGE ©2004 swisstopo (DV012716)).

5 Influence of the DEM resolution

According to the resolution of the DEM and the vertical size of the terrain elements, the SAD can vary as described in Fig. 2. The SAD analysis was thus performed on DEMs of *Les Diablerets* test zones with lower resolutions in order to study the changes in slope angle distribution of the four main MU. The SAD decompositions in GDMU were computed for each SAD according to their own initial parameters (e.g. Fig. 14). Then, the mode value of the GDMU steep slopes and the intersection of the GDMU cliffs with the GDMU steep slopes were compared between DEMs of 1 m to 25 m cell size, with a 5 m resolution step. Coarser DEMs were generated from the fine 1 m HRDEM using standard GIS tools, except for the 25 m that is a standard Swiss DEM (©Swisstopo (DV08371)).

The slope angle intersection value between the GDMU cliffs and steep slopes and its distribution mode show a progressive linear decrease when increasing the cell size of the DEM (Fig. 15). Notice that the linear decrease is more important for the intersection of the GDMU than for the mode

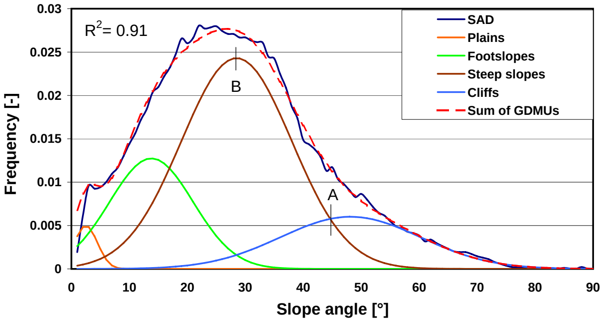

Fig. 14. SAD of *Les Diablerets* test site (same spatial extent as Fig. 3) decomposed using the standard Swiss DEM of 25 m cell size resolution. Note the decrease of the threshold slope angles (A = 45°; mode B = 28°) resulting from the smoothing effect of the coarser DEM resolution in comparison with the HRDEM thresholds angles of the Fig. 3.

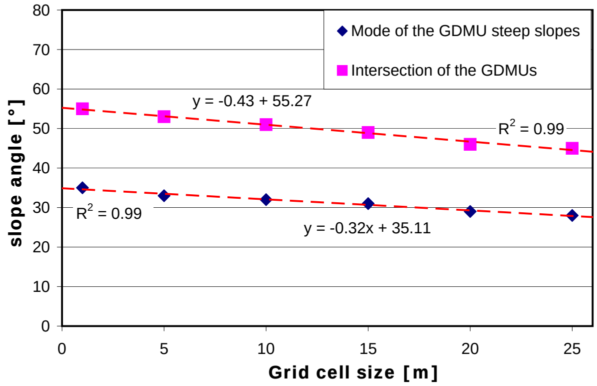

Fig. 15. Results of the SAD analysis performed over input DEM of 6 different resolutions on *Les Diablerets* test site.

of GDMU steep slopes. Observation of the HRDEM shows that cliff faces above a certain size can be delineated (Fig. 2). The comparison displayed in Fig. 16 for instance shows that the cliffs are much more roughly delimited with the 25 m DEM, but surround well the ones detected by the present methodology performed on the HRDEM. In the case where cliffs or steep slopes are too small however, they are not constrained by the model. In the contrary, MU (e.g. footslopes) lying below a certain slope angle are only slightly influenced by the enhanced accuracy of the HRDEM. This analysis shows that even though the computed slope angle of coarser DEM resolution is an approximation, steep zones can be correctly extracted from DEM with large cell size using the SAD decomposition. Threshold slope angles are thus lower and therefore less in accordance with the "reality". Nevertheless, a majority of cliffs above a certain size are detected (Fig. 16), where potential rockfall source areas can be located. This can be used as an indicative overview for large scale rockfall hazard assessment. In addition, HRDEM highlights the small cliff faces and steep slopes from which a rockfall might initiate.

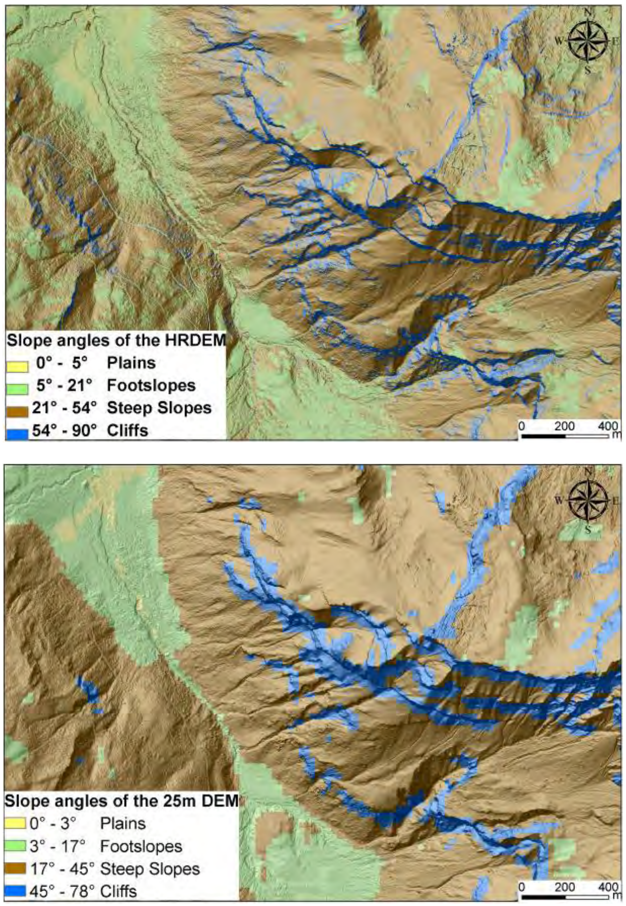

Fig. 16. Display of the main MU according to the SAD analysis performed on a DEM of 1 m and 25 m cell size (see Figs. 3 and 14) (MNT-MO, ©2005 SIT).

6 Conclusions

The present method based on slope angles statistics describes a systematic global approach to identify potential rockfall initiation areas at a regional scale. This is a rather conservative way to consider cliff faces and slope surfaces steeper than a threshold slope angle to be potentially unstable. The results show that estimated potential rockfall source zones correspond well to field observation performed on test zones and extracted from orthophotos analysis. The present study demonstrates that the SAD analysis works on rugged landscapes like in the Alps. This is due to the fact that major distinctive variations of the relief can be reflected more predominantly in the SAD decomposition. The SAD decomposition is very accurate for HMA with an important slope angle variation, like in the glacial-shape valley of the Alps. However, it can be applied elsewhere when considering the inhomogeneity of the topography. For large flat areas or hilly topography, the computation of the Gaussian curves is more ambiguous due to the low frequency difference in steep slopes. This can be adjusted to the GDMU method by taking into account the zones where the topography is only rugged, using series of cross-sections. Comparisons with known rockfall events give evidences that it is possible to assess potential rockfall sources over large areas from DEM-based slope angle parameters, topographical elements and geological maps.

One of the great advantages of this approach is that it detects potential rockfall source zones located on steep slopes covered with vegetation as well, which are not often taken into account in rockfall source detection (Fig. 13).

Such detection of potential rockfall source areas can provide a fast and cost-effective overview of rockfall prone locations, without considering the structural setting in details. The method is not limited to HRDEM. For a general overview of potential rockfall initiation zones, this approach works with poorer resolution DEM as well. However, the contribution of HRDEM, like airborne laser scanning DEMs, is especially significant in detecting small-sized rock faces and steep slopes. This should be taken into account in the development of susceptibility or hazard maps at a regional scale. Outcomes could be used as groundwork for territory management and as overview to focus on detailed field investigations.

Acknowledgements. The authors would like to thank the authorities of the state of Vaud that supported financially this project and particularly D. Morratel and P. Fouvy for their collaboration. Moreover, they are grateful to M.-H. Derron from the Geological Survey of Norway (NGU) for his precious comments all along the development of this project. They appreciated the help of T. Oppikofer and C. Longchamp during the composition of this paper.

Edited by: K. Schellenberg
Reviewed by: J. Corominas and H. Seijmonsbergen

References

Aksoy, H. and Ercanoglu, M.: Determination of the rockfall source in an urban settlement area by using a rule-based fuzzy evaluation, Nat. Hazards Earth Syst. Sci., 6, 941–954, 2006, http://www.nat-hazards-earth-syst-sci.net/6/941/2006/.

Acosta, E., Agliardi, F., Crosta, G. B., and Rìos Aragués, S.: Regional Rockfall Hazard Assessment in the Benasque Valley (Central Pyrenees) using 3D numerical Approach, Tech. rep., Project DAMOCLES, 2007.

Baillifard, F., Jaboyedoff, M., and Sartori, M.: Rockfall hazard mapping along a mountainous road in Switzerland using a GIS-based parameter rating approach, Nat. Hazards Earth Syst. Sci., 3, 435–442, 2003, http://www.nat-hazards-earth-syst-sci.net/3/435/2003/.

Baillifard, F., Jaboyedoff, M., Rouiller, J. D., Couture, R., Locat, J., Robichaud, G., and Gamel, G.: Towards a GIS-based hazard assessment along the Quebec City Promontory, Quebec, Canada, in: Landslides Evaluation and stabilization, edited by: Lacerda, W., Ehrlich, M., Fontoura, A., and Sayaõ, A. A., Balkema, 207–213, 2004.

Bunce, C. M., Cruden, D. M., and Morgenstern, N. R.: Assessment of the hazard from rock fall on a highway, Can. Geotech. J., 34, 344–356, 1997.

Burrough, P. and McDonnell, R. A.: Principles of Geographical Information Systems, Oxford University, 330 pp., 1997.

Crosta, G. B. and Agliardi, F.: A methodology for physically based rockfall hazard assessment, Nat. Hazards Earth Syst. Sci., 3, 407–422, 2003, http://www.nat-hazards-earth-syst-sci.net/3/407/2003/.

Derron, M.-H., Jaboyedoff, M., and Blikra, L. H.: Preliminary assessment of rockslide and rockfall hazards using a DEM (Oppstadhornet, Norway), Nat. Hazards Earth Syst. Sci., 5, 285–292, 2005, http://www.nat-hazards-earth-syst-sci.net/5/285/2005/.

Escher, A., Hunziker, J. C., Marthaler, M., Masson, H., Sartori, M., and Steck, A.: Geological framework and structural evolution of the Western Swiss-Italian Alps. Deep structure of Switzerland – Results of NFP-20, Birkhäuser Basel, 205–222, 1997.

Frattini, P., Crosta, G., Carrara, A., and Agliardi, F.: Assessment of rockfall susceptibility by integrating statistical and physically-based approaches, Geomorphology, 94, 419–437, 2008.

Gokceoglu, C., Sonmez, H., and Ercanoglu, M.: Discontinuity controlled probabilistic slope failure risk maps of the Altindag (settlement) region in Turkey, Eng. Geol., 55(4), 277–296, 2000.

Günther, A.: SLOPEMAP: programs for automated mapping of geometrical and kinematical properties of hard rock hill slopes, Comput. Geosci., 29(7), 865–875, 2003.

Günther, A., Carstensen, A., and Pohl, W.: Automated sliding susceptibility mapping of rock slopes, Nat. Hazards Earth Syst. Sci., 4, 95–102, 2004, http://www.nat-hazards-earth-syst-sci.net/4/95/2004/.

Guzzetti, F., Carrara, A., Cardinali, M., and Reichenbach, P.: Landslide hazard evaluation: a review of current techniques and their application in a multi-scale study, Central Italy, Geomorphology, 31, 181–216, 1999.

Guzzetti, F., Crosta, G., Detti, R., and Agliardi, F.: STONE: a computer program for the three-dimensional simulation of rock-falls, Comput. Geosci., 28(9), 1079–1093, 2002.

Guzzetti, F., Reichenbach, P., and Wieczorek, G. F.: Rockfall hazard and risk assessment in the Yosemite Valley, California, USA, Nat. Hazards Earth Syst. Sci., 3, 491–503, 2003, http://www.nat-hazards-earth-syst-sci.net/3/491/2003/.

Hantz, D., Vengeon, J. M., and Dussauge-Peisser, C.: An historical, geomechanical and probabilistic approach to rock-fall hazard assessment, Nat. Hazards Earth Syst. Sci., 3, 693–701, 2003, http://www.nat-hazards-earth-syst-sci.net/3/693/2003/.

Heim, A.: Bergsturz und Menschenleben, Fretz and Wasmuth Verlag, Zurich, 218 pp., 1932.

Hoek, E. and Bray, J. W.: Rock Slope Engineering, in: The Institution of Mining and Metallurgy, London, 3rd edn., 358 pp., 1981.

Horn, B. K. P.: Hill shading and the reflectance map, Proceedings of the IEEE, 69(1), 14–47, 1981.

Jaboyedoff, M. and Labiouse, V.: Preliminary assessment of rockfall hazard based on GIS data, in: 10th International Congress on Rock Mechanics ISRM 2003 – Technology roadmap for rock mechanics, South African Institute of Mining and Metallurgy, Johannesburgh, South Africa, 575–578, 2003.

Jaboyedoff, M., Baillifard, F., Couture, R., Locat, J., and Locat, P.: New insight of geomorphology and landslide prone area detection using DEM, in: Landslides: Evaluation and Stabilization, edited by: Lacerda, W., Ehrlich, M., Fontoura, A., and Sayaõ, A., Taylor & Francis, London, 191–198, 2004a.

Jaboyedoff, M., Baillifard, F., Couture, R., Locat, J., and Locat, P.: Toward preliminary hazard assessment using DEM topographic analysis and simple mechanic modeling, in: Landslides: Evaluation and Stabilization, edited by: Lacerda, W., Ehrlich, M., Fontoura, A., and Sayaõ, A., Taylor & Francis, London, 199–205, 2004b.

Jaboyedoff, M., Baillifard, F., Derron, M.-H., Couture, R., Locat, J., and Locat, P.: Switzerland Modular and evolving rock slope hazard assessment methods, in: Landslide and avalanches, edited by: Senneset, K., Flaate, K., and Larsen, J. A., ICFL, 187–194, 2005a.

Jaboyedoff, M., Dudt, J. P., and Labiouse, V.: An attempt to refine rockfall hazard zoning based on the kinetic energy, frequency and fragmentation degree, Nat. Hazards Earth Syst. Sci., 5, 621–632, 2005b,
http://www.nat-hazards-earth-syst-sci.net/5/621/2005/.

Jaboyedoff, M., Metzger, R., Oppikofer, T., Couture, R., Derron, M.-H., Locat, J., and Turmel, D.: New insight techniques to analyze rock-slope relief using DEM and 3D-imaging cloud points: COLTOP-3D, Rock mechanics Vol. 1: Meetings Society's Challenges and demands, chap. 7, 61–68, edited by: Eberhardt, E., Stead, D., and Morrison, T., 2007.

Krummenacher, B.: Modellierung der Wirkungsräume von Erd- und Felsbewegungen mit Hilfe Geographischer Informationssysteme (GIS), Schweizerischen Zeitschrift für Forstwesen, 146, 741–761, 1995.

Leroi, E., Bonnard, C., Fell, R., and Mc Innes, R.: State of the art paper: Risk assessment and management, in: Landslide risk management, edited by: Hungr, O., Fell R., Couture, R., and Eberhardt, E., Balkema, 59–198, 2005.

Locat, J., Leroueil, S., and Picarelli, L.: Some Considerations on the Role of Geological History on Slope Stability and the estimation of the Minimum Apparent Cohesion of a Rock Mass, in: Landslides, in research, theory and practice, edited by: Bromhead, E., Dixon, N., and Ibsen, M.-L., Thomas Telford, London, 2000.

Marquinez, J., Menéndez Duarte, R., Farias, P., and Juménez Sánchez, M.: Predictive GIS-based Model of Rockfall Activity in Mountain Cliffs, Nat. Hazards, 30, 341–360, 2003.

Mazzoccola, D. F. and Hudson, J. A.: A comprehensive method of rock mass characterization for indicating natural slope instability, Q. J. Eng. Geol. Hydroge., 29(1), 37–56, 1996.

Meissl, G.: Modellierung der Reichweite von Felsstürzen. Fallbeispiele zur GIS-gestützten Gefahrenbeurteilung aus dem Beierischen und Tiroler Alpenraum, Innsbrucker geografischen studien 28, Ph.D. thesis, Universität Innsbruck, 1998.

Montgomery, D. R. and Brandon, M. T.: Topographic controls on erosion rates in tectonically active mountain ranges, Earth Planet. Sc. Lett., 201(3–4), 481–489, 2002.

Rouiller, J. D., Jaboyedoff, M., Marro, C., Philippossian, F., and Mamin, M.: Pentes instables dans le Pennique valaisan. Matterock: une méthodologie d'auscultation des falaises et de détection des éboulements majeurs potentiels, Rapport final du PNR31, VDF Hochschulverlag AG, ETH Zürich, Switzerland, 1998.

Selby, M. J.: Hillslope Materials and Processes, 2nd edn., Oxford University Press, 1993.

Strahler, A. N.: Equilibrium theory of erosional slopes approached by frequency distribution analysis, Am. J. Sci., 248, 673–696, 800–814, 1950

Strahler, A. N.: Quantitative geomorphology of erosional landscapes, Compt. Rend, 19th Intern. Geol. Cong., Sec. 13, 341–354, 1954.

Toppe, R.: Terrain models – a tool for natural hazard mapping, IAHS, 162, 629–638, 1987.

Trümpy, R.: Geology of Switzerland, a Guide Book, Part A. An outline of the geology of Switzerland, Wepf & CO., Basel, Switzerland, 1980.

van Dijke, J. J. and van Westen, C. J.: Rockfall hazard, a geomorphological application of neighbourhood analysis with ILWIS, ITC – Publication Number, 1, 40–44, 1990.

Varnes, D. J.: Slope movements: types and processes, in: Landslide analysis and control, Transportation Research Board, Special Report 176, edited by: Schuster, R. L. and Krizek, R. J., Washington, DC, 11–33, 1978.

Wagner, A., Oliver, R., and Leite, E.: Rock and debris slide risk maps applied to low-volume roads in Nepal, Transportation Research Record 1106. TRB, National Research Council, Washington, DC, 255–267, 1988.

Whalley, W. B.: Rockfalls, in: Slope Instability, edited by: Brunsden, D. and Prior, D. B., Wiley, Chichester, 217–256, 1984.

Appendix E

Preliminary regional rockfall hazard mapping using LiDAR-based slope frequency distribution and Conefall modelling

Proceedings – *4th Canadian Conference on Geohazard: From Causes to Management*, 20 – 24 May 2008, Québec city. Presse de l'Université de Laval, Québec, p. 238 – 248.

PRELIMINARY REGIONAL ROCKFALL HAZARD MAPPING USING LIDAR-BASED SLOPE FREQUENCY DISTRIBUTION AND CONEFALL MODELLING

Alexandre Loye
Institute of Geomatics and Risk Analysis, University of Lausanne, Switzerland, alexandre.loye@unil.ch
Andrea Pedrazzini and Michel Jaboyedoff
Institute of Geomatics and Risk Analysis, University of Lausanne, Switzerland

RÉSUMÉ
L'élaboration des cartes de danger à l'échelle régionale est souvent limitée par le manque de connaissance des zones sources potentielles. Grâce aux données numériques de terrain haute-résolutions (LiDAR), l'analyse morphométrique de la topographie est devenue une approche appropriée pour détecter les instabilités rocheuses sur des surfaces relativement étendues. A l'aide du concept des « familles de pentes » tiré du modèle numérique de terrain (MNT) laser et autres documents contenu dans la carte topographique nationale, une carte des dangers potentiels chute du bloc a été établie sur l'ensemble du canton de Vaud, Suisse. Les zones sources potentielles sont définies à partir de seuils de pentes établis par analyse géomorphométrique et leur propagation maximale modélisée à l'aide du logiciel CONEFALL. Une comparaison avec les données de terrain ainsi qu'un modèle trajectographique révèle de grandes concordances, démontrant qu'il est possible d'évaluer le danger chute de bloc à grande échelle à partir de paramètres extraits du MNT et des éléments topographiques.

ABSTRACT
A factor limiting preliminary rockfall hazard mapping at regional scale is often the lack of knowledge of potential source areas. Nowadays, high resolution topographic data (LiDAR) can account for realistic landscape details even at large scale. With such fine-scale morphological variability, quantitative geomorphometric analyses become a relevant approach for delineating potential rockfall instabilities. Using digital elevation model (DEM)-based "slope families" concept over areas of similar lithology and cliffs and screes zones available from the 1:25,000 topographic map, a susceptibility rockfall hazard map was drawn up in the canton of Vaud, Switzerland, in order to provide a relevant hazard overview. Slope surfaces over morphometrically-defined thresholds angles were considered as rockfall source zones. 3D modelling (CONEFALL) was then applied on each of the estimated source zones in order to assess the maximum runout length. Comparison with known events and other rockfall hazard assessments are in good agreement, showing that it is possible to assess rockfall activities over large areas from DEM-based parameters and topographical elements.

1. INTRODUCTION

To assess whether an area is potentially endangered by rockfall, preliminary hazard mapping throughout relatively large mountainous zones provides a fast and cost-effective overview of rockfall prone areas. In the framework of susceptibility mapping, the purpose consists of defining potentially rockfall sources zones and their runout zones for rockfall of small size (Lateltin, 1997). Larger events, such as rock avalanches, cannot be taken into account in this modelling approach, because the runout distance depends on the sliding volume (Scheidegger, 1973). The outcome gives a susceptibility hazard map, which can be used as a scientific reference for regional policies of territory management.

The increasing availability of geographic information system (GIS) data, such as digital elevation models (DEM) and topographic vector maps, makes GIS-based and 3D modelling approach very convenient to predict hazards posed by rockfall at regional scales. One of the great limiting factors, however, in predicting and therefore mapping rockfall prone areas, is the lack of knowledge of the potential rockfall source areas and fall tracks. Rockfall sources areas are usually taken from distinctive evidence, such as talus slope deposits at the foot of steep cliff faces or as information extracted from maps (historical register of observations, field measurements) (Hantz, 2003). But rockfalls also occur on slope surfaces covered with vegetation where evidence is less distinct and their related sources areas are not taken into account in planning rockfall hazard assessment.

A variety of empirical and process-based rockfall models exist (Dorren, 2003), but were developed for specifically known regions where rockfall causes problems. Only a few methods were tested for predicting rockfall runout zones at a regional scale (>500km^2) (Dorren et al, 2000; Crosta et al, 2003). For a preliminary assessment of the runout length, the integration of empirical or process-based methods in GIS has shown very promising results (ie, Meissl, 1998; Van Dijke & Van Westen, 1990; Jaboyedoff & Labiouse, 2003). Those models can be defined as distributed models, since they are process-based and they take into account the spatial variability within a certain region. Terrain properties are represented by multiple rasters derived from GIS data layers (Dorren, 2003). Identification of rockfall source areas has started with simple methods that consist of defining thresholds for mean slope gradients (Toppe, 1987; Van Dijke & Van Westen, 1990) or for steep slopes (e.g. > 45°; Jaboyedoff & Labiouse, 2003). Rockfall source areas have also been derived from cliff faces and rocky outcrops on topographical maps (Krummenacher, 1995; Meissl, 1998) or from areas defined as active rockfall slopes on

In : J. Locat, D. Perret, D. Turmel, D. Demers et S. Leroueil, (2008).
Comptes rendus de la 4e Conférence canadienne sur les géorisques: des causes à la gestion.
Proceedings of the 4th Canadian Conference on Geohazards : From Causes to Management. Presse de l'Université Laval, Québec, 594 p.

geomorphological and geological maps (Van Dijke & Van Westen, 1990). Another more realistic and automatic method is to identify rockfall source areas on the basis of combined dataset in GIS, whose could include rock type, exposition, slope curvature, slope gradient and land cover (Acosta *et al.*, 2007 Marquinez *et al.*, 2003; Frattini *et al.*, 2008).

2. STUDY AREA

The canton of Vaud is located in the southwest part of Switzerland and covers an area of about 3200 km^2 (Figure 1 and 5). Its territory consists of three main tectonic units: the Jura, the Prealps and the Swiss Molasse Plateau.

The western mountains, called Jura, are formed by a foreland fold-and-thrust belt covered by Mesozoic sedimentary rocks, mostly carbonates and marls (Trümpy, 1980). The study area is only moderately deformed with a homogeneous trend of smooth fold and faults. On the other side, the southeast mountain range is called the Prealps and was formed by several allochthonous tectonic klippen resting on the alpine foreland in front of the external crystalline basement of the Alps (Mosar *et al.* 1996). They are formed by limestones, dolomites, marls and shales. These can be divided in three underlying units: the Préalpes Médianes, the Helvetic and the Ultrahelvetic geological unit. Its type of morphology is fluvio-glacial containing steep and rugged mountain sides. Finally, the Swiss molasse Plateau lies in between. This is a sedimentary foreland basin from the Oligo-Miocene (Sommaruga, 1997). Its mostly flat topography alternates marin, fluvial and lacustrine sediments, and the morphological structure is the result of fluvial erosion processes (Trümpy, 1980).

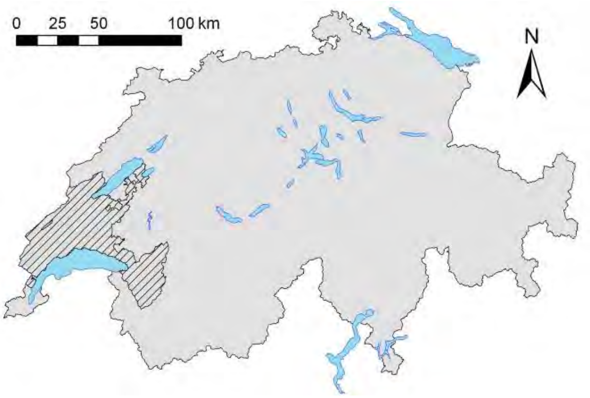

Figure 1 : Geographical location of the canton of Vaud.

3. THEORETICAL METHOD

The delineation of the risk posed by the falling of individual and superficial rocks from a cliff face or rocky outcrops can be broken up into two distinct steps:

a) Identification of potential rockfall sources areas that correspond to the detachment zones of the rocks.

b) Assessment of the maximum runout zones from rockfall source areas discriminated in the first step.

3.1 Data input conditioning factor

Unstable surface processes in mountainous regions are reflected through topography (Montgomery & Brandon, 2002). The identification of potentially unstable cliff faces and rocky outcrops is thus taken from a topographical analysis. This approach appears in many geomorphological studies (ie. Strahler, 1954; Acosta *et al.*, 2002; Dorren, 2003; Glenn *et al.*, 2005). In fact, the most significant contributing factors for rockfall initiation are the slope and the area directly surrounding the potential instability (Dorren, 2003). In the past, terrain characterisation through geomorphological analysis on DEM's produced large inaccuracies in the outcomes of GIS-based distributed rockfalls models, mainly due to the low resolution of the input data. Nowadays, resolution over 1m x 1m compared to 25m x 25m cell size can account for more realistic landscape details such as fine-scale slope variability or inadequate characterisation of the vegetation cover (Figure 2). The use of high resolution topographical data input (e.g. LiDAR) then produces promising results that more accurately characterise fine-scale morphology at a regional scale as well. GIS-based rockfall modelling is therefore not constrained anymore to the input data resolution but can be adapted to the processes scale.

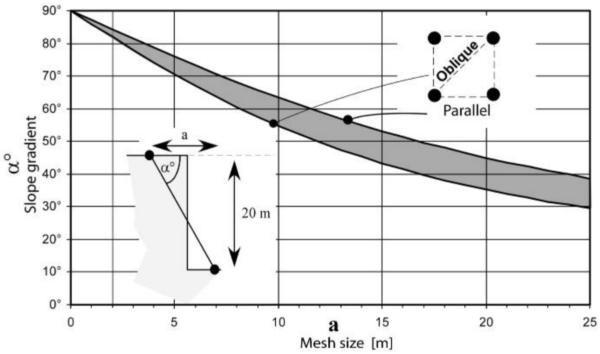

Figure 2 : computed slope gradient α° obtained from a DEM grid of size **a** for a 20m height vertical cliff face. The classical 25m grid gives an apparent slope gradient of about 35°, when a 2m grid DEM shows more than 80° (from Jaboyedoff *et al.* 2005).

3.2 Rockfall source areas delineation

The assessment of model parameter values to highlight rockfall sources zones on a DEM is given by a slope frequency distribution analysis in order to determine a slope angle above which hillslopes become potentially unstable. This was done by the so-called “slope families” concept.

3.2.1 Slope families concept

Rocky outcrops and consequently unstable rockfall source areas are found by definition in steep slopes (Dorren, 2003). Moreover, the angle of internal friction depends on the rock type and some morphological aspects. For that reason, failure susceptibility between a rock and its breaking plane can be characterized through the dynamic frictional angle, which is function of the slope gradient (Wyllie and Mah, 2007).

From that perspective, a slope frequency distribution analysis was carried out by computing the slope histogram over a considered area (Figure 3). Then, the approach consists of reproducing the slope frequency distribution through Gaussian function so that the sum of those normal curves fits the slope histogram (Strahler, 1954). This way to break up the histogram into slope families is called here the “slope families” concept. Indeed, slope gradient frequency of a topographic family varies randomly around its mean slope gradient (Rouiller et al, 1998). Those slope families can therefore be defined by each normal curve, which together fit the histogram. In an alpine topography, at least three families of slope come mostly across (Oppikofer et al, 2007):

a) Low slope gradients corresponding to the plains formed by fluvio-glacial deposits.
b) Mid / gentle slope gradients corresponding to the lower part of the hillslope (Foothills & mountain flanks). They are characterized by alluvial fans (debris flow), landslide mass and till deposits.
c) Steep slopes can be matched to the occurrence of rocky outcrops and cliff faces.

More precisely, the peaks of each fitted curve reflect a distinctive threshold that can be correlated to the major morphological units. Usually, those major topographical features are strongly influenced by the dominant lithologies. In a geomorphologically homogeneous landscape, e.g. in a hillslope concept, the steepest part can be correlated to harder lithologies (Jaboyedoff, 2005).

3.3 Maximum rockfall runout length

In order to complete the rockfall susceptibility mapping, rockfalls are modelled by a simple approach inspired from the shallow angle (Toppe, 1987) method and generalised in a 3D GIS environment.

3.3.1 The so-called cone method

Maximum rockfall runout zones can be estimated following the cone method (Fahrböschung) (Toppe, 1987). This model is based on the idea that an individual falling rock can reach any place in the area situated inside a cone of given aperture (Figure 4). This approach assumes that rockfall over a slope surface can be considered as a sliding process (Evan & Hungr, 1993). The angle of aperture for the length of the runout is then estimated following:

$$\phi_p = \arctan(H_b / x_b) \qquad [1]$$

where H_b is the height difference between the source zone and the furthest monitored boulders and x_b the maximum runout length defined horizontally.

Outcomes of several studies give an angle ϕ_p ranging between 28.5° and 35° (Toppe, 1987). The runout zone is then defined as a straight line between the highest point of the source area and the stopping point of the furthest fallen boulder (Figure 4). This is however important that the line follows the falltrack of the rock.

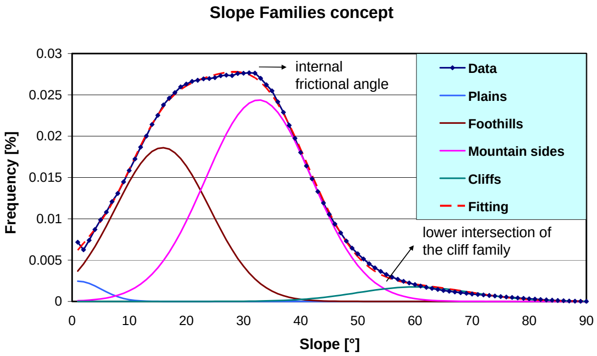

Figure 3 : Plot of a slope frequency distribution featuring the “slope family” concept. The pick of each Gaussian curve represents the mean slope equilibrium of a distinctive morphological unit contained in the considered tectonic unit.

From an energy perspective, a detached boulder falls, bounces and rolls down a slope surface until it stops beyond the intersection point between the topography and a so-called energy line drawn from the source point and making an angle ϕ_p with the horizontal (Scheidegger, 1973).

The cone method is empirical and doesn’t require ambiguous input parameters, such as coefficient of friction and bounding velocity. Its simplicity makes the cone approach very convenient to be applied at regional scale.

3.3.2 The CONEFALL software

Assessment of the runout zones from the potential source areas described above was performed by means of the CONEFALL software (Jaboyedoff, 2003a). CONEFALL simply implements the cone method in a GIS environment by computing on a DEM the following relationship:

$$0 < \Delta x^2 + \Delta y^2 - \tan(\pi/2 - \phi_p)^2 \times (z_0 - z)^2 \qquad [2]$$

and the initial condition z < h (surface height). Δx and Δy are the horizontal distances between the source point and any topographic point and z_0 and z are the elevation of the source point, respectively the topographic point.

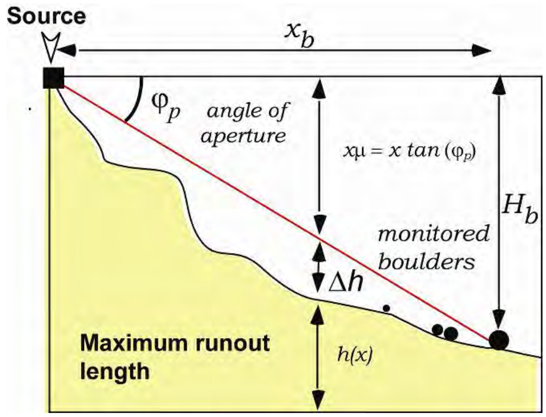

Figure 4 : Longitudinal cross-section of the idealized cone showing the relationship between ϕ_p and the maximum runout length (modified from M. Jaboyedoff, 2003a).

Thus, this GIS-based software allows the estimation of the maximum runout length in 3D by assuming a given aperture angle (90°- ϕ_p) centered on the source point (Figure 5).

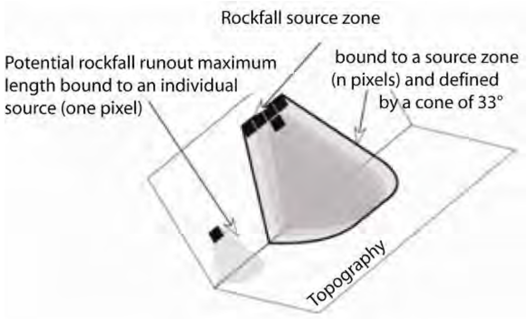

Figure 5 : Scheme of the cone method implemented in the GIS-based software CONEFALL (modified from Jaboyedoff & Labiouse, 2003).

4. DATA PROCESSING

4.1 Identification of the source zones

The slope families method (for delineating potential rockfall sources of instabilities) was performed on high resolution DEM of 1m × 1m cell size over all the state of Vaud (LIDAR DEM, © 2005 SIT, Vaud). The input dataset was handled within the GIS environment ArcGIS®. According to the fact that the occurrence of rockfall instabilities is influenced by geological factors, the slope frequency distribution was performed over similar lithologies. Thus, the geomorphological features of the considered rocks are somehow taken into account. Based on the national tectonic map (swisstopo©), the state of Vaud was therefore divided into five study areas (Figure 6):

- The Helvetic, Ultrahelvetic and median Prealps gave three distinct slope frequency distributions of the alpine topography.
- The Plateau and the Jura gave two other distinct zones of analysis.

For each of those five geologically-based units, a slope frequency distribution was computed and plotted according to each slope angle. But raster projection over a tilted plane shortens the surface area and steep slope gradients are therefore under-estimated over the less steep ones. Their frequency was thus corrected by taking them as they were horizontal, following:

$$A = A_\alpha \times 1/\cos(\alpha) \qquad [3]$$

where A_α is the computed area (number of cell raster) for their respective slope angle α. A is therefore the real area.

In a second step, Gaussian distribution functions, which represent the major geomorphological units, were fitted by means of the software HISTOFIT (Jaboyedoff, 2003b). This Excel-based solver allows computing the most-likely slope distribution curves according to given input parameters in an iterative way. Initial parameters were defined according to the shape of the frequency distribution of the slope, where slope families trends were obvious (unsteadiness in the distribution). Those curves resulting from the computation of the slope frequency distribution and their relative fitted Gaussian curves were interpreted as so (cf. Figure 3):

- On one side, the pick of the slope frequency distribution was taken as the internal frictional angle. Rocky outcrops and cliff faces, available from the 1:25,000 topographic vector map, steeper than this angle were considered as potential rockfall source areas.
- Moreover, threshold angle from steep slopes that are not contained on the above-mentioned topographic map, but potentially rockfall source areas, were defined at the lower intersection of the estimated “Cliff family” with the “Valley flank family”. All surfaces, where the slope gradient is steeper than this threshold angle, are considered as potential rockfall source areas, independently of the lithology and the surface cover (Roullier et al, 1998).

For the tectonic units of the Alpine Prealps, the slope frequency distribution was computed integrally over the considered area, as described above. For the units of the Jura and Plateau, however, weak slope gradients are dominant and rugged landscapes are too sparse over large flat zones. Consequently, the slope frequency contrast from a given steep angle is too low and minor pass point that are supposed to reflect distinct slope families are not perceptible enough on the histogram. Therefore, the slope frequency distribution was performed over the slope gradient of 25 profiles taken along the major zones of interest of the considered unit. After comparison, 25 profiles seem fairly enough to reflect the slope frequency distribution in an accurate way. This doesn't change in any case the validity of the method, but simply allows the rugged landscape to be highlighted on the histogram against a majority of zones where rockfall hazard obviously does not exist.

Figure 6 : Illustration of the tectonic units (cf. study area)

So, potential rockfall source zones of the susceptibility map are made by the sum of the source areas defined on the topographical vector map as well as the ones delimited by the cliff family. Finally, in order to be considered as rockfall source zone, a slope surface must have a critical size of 10m^2. The aim behind that is to filter out the possible artefacts contained in the DEM without removing any essential information.

4.2 Rockfall runout zones

The CONEFALL model was applied to each potential rockfall instability defined previously in order to assess the maximum runout length. For the case of convenience, the source zones were aggregated to a cell size of 25m x 25m and the modelling ran over a DEM of same cell size. For such map anyway, data resolution smaller than 1:25,000 is not required.

Aperture angle of the cones was established empirically by taking into account four aspects:

1. Information contained in the literature (Toppe, 1987; Jaboyedoff & Labiouse, 2003).
2. Comparison with known rockfall run out zones and those that are visible obviously on orthophotos.
3. Fieldwork undertaken on test zones for each tectonic unit.

Finally, no given lateral aperture of the cone was given into the CONEFALL model. The cones are thus restricted laterally by the topography, even though the experience has shown that rockfall trajectories are restricted to 15° from one side to another of the dip direction (Crosta *et al.*, 2003).

4.3 Correction for the Valley-bottom

The cone method performed over mountain sides that overhang alluvial plains (e.g. the Rhone plain) models a rockfall run out maximum length too large compared to the reality. Indeed, boulders reaching flat zones tend to greatly reduce their speed and consequently their energy when the slope goes flat right away. In this study, flat lands were then considered when a surface > 2.5 km^2 has a slope gradient < 11°. Based on orthophotos analyses of scree deposits along flat zones, maximum runout length of cones reaching those plains was limited to 60m. For the Rhone plain, because the steep valley sides are followed directly by a totally flat land, the maximum length was expended to 100 m due to higher falling velocities resulting from this particular configuration (Figure 7).

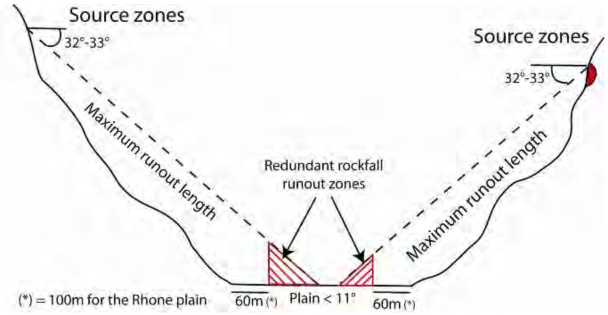

Figure 7 : schematic cross-section of the correction performed on maximum runout length over flat lands.

5. RESULTS & ANALYSIS

Critical angles obtained by the slope families method for each tectonic unit are resumed in Table 1 and plotted below.

5.1 The Prealps

Slope families are clearly represented on the plot and fit the histogram with a coefficient of determination close to 1.

Rockfall source zones modelled by the slope families method are in very good agreement with the geomorphology encountered in the Prealps. The potentially unstable areas are mainly located in the limestones and dolomites. Those lithologies are the hardest ones and form in great majority

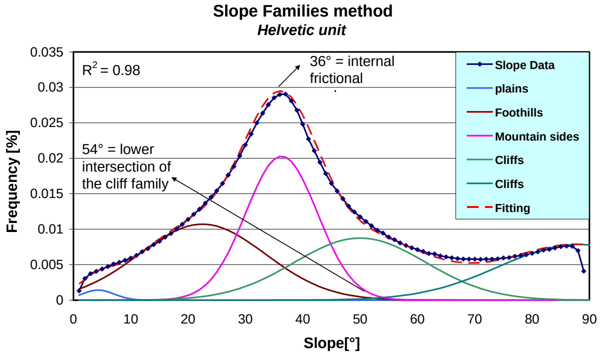

Figure 8 : Slope families population for the Helvetic unit.

the very steep slopes and cliffs zones. As well, all rockfall source areas located on fieldwork and orthophotos analyses can be observed through the modelling.

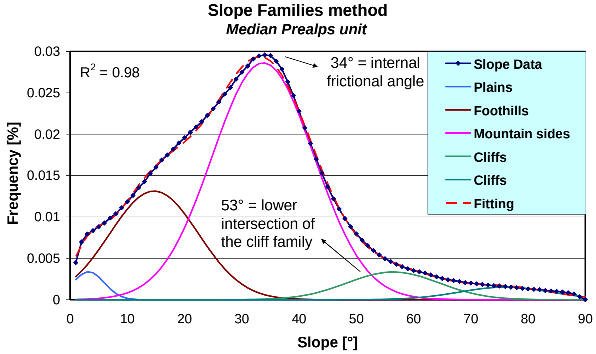

Figure 9 : Slope families population for the Median Prealps.

Table 1 : Threshold angles above which the rockfall source areas are potentially considered

Tectonic unit	Threshold angle	
	Topographic vector map	Intersection Cliff family
Helvetic	36°	54°
Ultrahelvetic	33°	49°
Median Prealps	34°	53°
Molasse Basin (Plateau)	30°	46°
Jura Mountains	32°	46°

5.2 The Plateau

Modelled rockfall source areas over the Plateau are located along rivers and impermanent watercourses as well as fluvio-glacial terraces. These corroborate field observations as in the Swiss molasse basin, where rocky outcrops arise predominantly from fluvial erosion along the marls and sandstones.

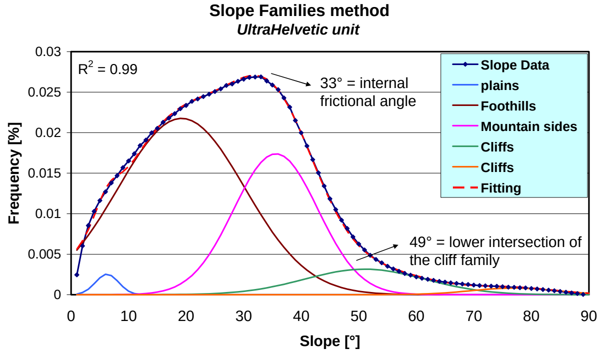

Figure 10 : Slope families population for the Ultrahelvetic unit.

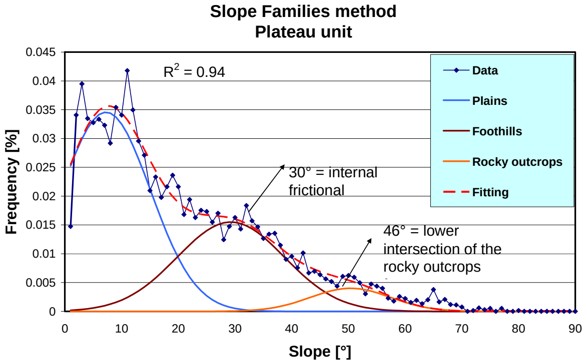

Figure 11 : Slope families population for the Plateau unit performed over 25 slope gradients profiles.

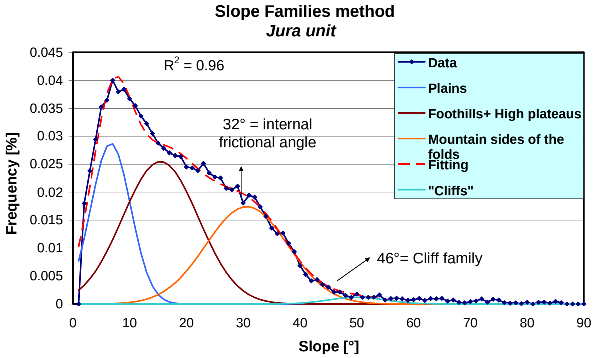

Figure 12 : Slope families population for the Jura unit performed over 25 slope gradients profiles.

5.3 The Jura Mountains

In the Jura, the potentially unstable areas modelled by the slope families method are mostly encountered in steep folds where limestones show up on the surface or nearly close to it, which correspond to what could be observed on study areas. Moreover, the delineation of the rockfall source zones agrees very well with the geomorphology. Rockfall source zones follow the strike-slip fault of the Pontarlier-Vallorbe area as well as the terrain irregularities arising from the fluvial erosion.

5.4 Maximum rockfall runout length

The angle ϕ_p of cone aperture for the length of the runout defined empirically is 33° for all tectonic units. With this angle, the runout surfaces are in great agreement with observation performed on fieldwork and orthophotos analyses. Such an angle, although fairly conservative (usually 35° is admitted), allows the modeling of a maximum runout length. Moreover, it can include a potential remobilization of the screes located beneath the rockfall source areas, which have usually a mean slope of 35° (Van Westen *et al.* 1997). Furthermore, all screes mapped in the topographic vector map where the slope gradient is close to the internal frictional angle of the considered tectonic unit is incorporated in the cone of runout. Finally, the unlimited lateral aperture of the cone seems not to overestimate the lateral propagation of the rockfall runout.

5.5 Comparison with another rockfall hazard assessment

The maximum runout length modeled by CONEFALL was compared with a 3D rockfall trajectography study. This model, called Geotest/Zinggeler, computes rockfall trajectories from given source points by entering physical input parameters like soil features (topography, friction coefficients and coefficients for the strain of the soil) and boulder shape (propensity to rotate). Fallen boulders are simulated through a succession of soil impacts, parabolic rebounds and rolling sequences. The computing then draws up thousands of trajectories that represent potential rockfall prone areas. For similar source areas, rockfall spreadings taken from the SIlVAPROTECT project (Silvaprotect-CH) show a very good adequacy between both models, particularly in very instable zones. In some cases, however, the trajectories go beyond the rockfall perimeter estimated by the cone method. This might involve areas where the terrain morphology is favorable to rebounds and rolls. Such soil features are not taken into account in CONEFALL.

6. CONCLUSION

The present method describes a global approach to develop a rockfall susceptibility hazard map at regional scale and provides a fast and cost-effective way to overview rockfall prone zones over large areas. Rockfall source zones modeled by the slope families concept correspond very well to what can be observed on orthophotos analyses and fieldwork performed on test zones. Moreover, they show some good conformities with the geomorphology by the fact that this method detects rockfall source zones located on steep slopes covered with vegetation as well. This is a rather conservative way to consider cliff faces and slopes surfaces to be potentially instable over a certain slope gradient. Nevertheless, this is reasonable over a long period of time. Likewise, the CONEFALL method shows some very nice results in comparison with a 3D trajectography model, although it doesn't require physically-based parameters.

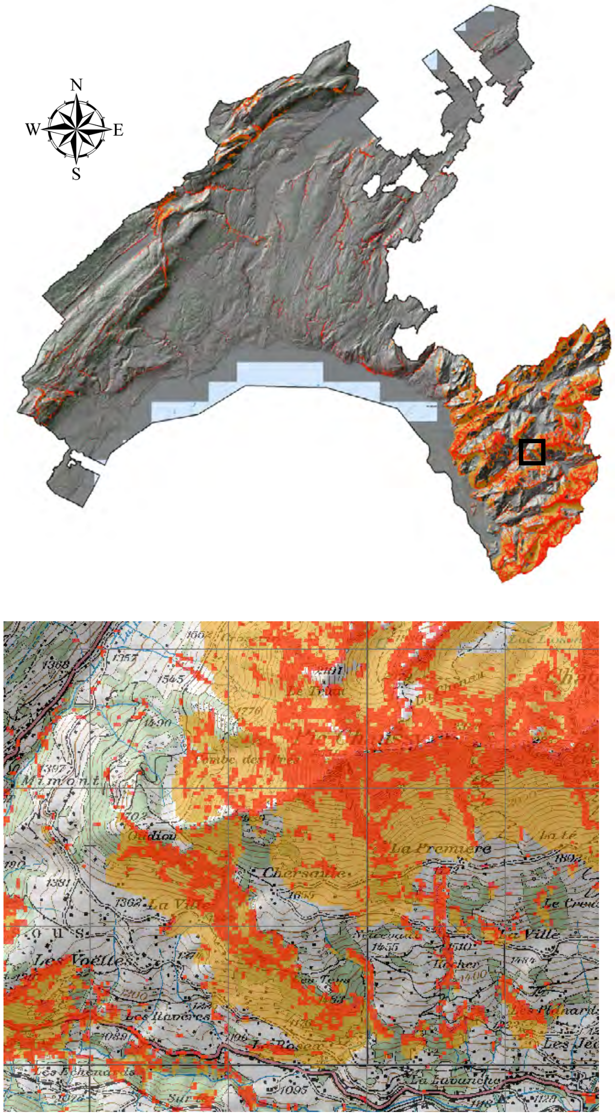

Figure 13 : (Above) The susceptibility rockfall hazard map for the canton of Vaud. Rockfall source zones are drawn in red and the runout perimeter in brown. (Below) Close-up of the map located in the black square.

It allows to quickly but accurately delineating potentially rockfall prone perimeters. Finally, using DEM high resolution (LIDAR), which enables morphological analyses in accordance to the reality, this work tends to show that it is possible to assess potential rockfall prone zones over large areas from DEM-based parameters and slope gradient analysis.

7. AKNOWLEDGMENT

The authors would like to thank the authorities of the state of Vaud for the grant, especially Diane Morattel and Patrik Fouvy from the Forest and Wildlife Service. Moreover, they are grateful to Marc-Henri Derron from Norway Geological Survey (NGU) for his precious comments all along the development of this project. This manuscript benefited from two reviewers: Giovanni Crosta and Corey Froese.

8. REFERENCES

Acosta, E., Agliardi, F., Crosta, G.B. & Rìos Aragués, S. 2007. Regional Rockfall Hazard Assessment in the Benasque Valley (Central Pyrenees) using 3D Numerical Approach. Project DAMOCLES.

Frattini, P., Crosta, G. B., Carrara, A. and Agliardi, F. 2008. Assessment of rockfall susceptibility by integrating statistical and physically-based approaches, Geomorphology. 94: 419-437.

Crosta, G. B. and Agliardi, F. 2003. A methodology for physically-based rockfall hazard assessment. Natural Hazards and Earth System Sciences. 3, 5, 407-422.

Dorren, L.K.A and Seijmonsbergen, A. C. 2000. GIS-based modeling of rockfall on a broad scale using remotely sensed data and detailed geomorphological maps AGIT, GIS-congress, Salzburg, Austria. http://dare.uva.nl/fr/record/180159.

Dorren, L. K. A. 2003. A review of rockfall mechanics and modelling approaches. Progress in Physical Geography 27, 1: pp. 69-87.

Evans, S. and Hungr, O. 1993. The assessment of rockfall hazard at the base of talus slopes. Canadian Geotechnical Journal, 30, pp. 620 - 630.

Glenn, N. F., Steutker, D. R. *et al.* 2005. Analysis of LIDAR-derived topographic information for characterizing and differentiating landslide morphology and activity. Geomorphology. Volume 73, Issues 1-2, January 2006, pp. 131-148.

Hantz, D., Vengeon, J. M. and Dussauge-Peisser, C. 2003. An historical, geomechanical and probabilistic approach to rockfall hazard assessment. Natural Hazards and Eart System Sciences, 3: 1-9.

Jaboyedoff, M. 2003a. CONEFALL 1.0 : A program to estimate propagation zones of rockfall based on cone method. Quanterra, www. quanterra.ch.

Jaboyedoff, M. 2003b. HISTOFIT : modélisation de l'histogramme des pentes par populations gaussiennes. IGAR - Université de Lausanne. Logiciel interne.

Jaboyedoff, M. 2005. Extrait de cours sur les dangers naturels et les destructions des chaînes orogéniques. Document IGAR, Université de Lausanne. Inédit.

Jaboyedoff, M. and Labiouse, V. 2003. Preliminary assessment of rockfall hazard based on GIS data. ISRM 2003 - Technology roadmap for rock mechanics, South African Institute of Mining and Metallurgy.

Jaboyedoff, M., Giorgis, D. and Riedo, M. 2005. Apport des modèles numériques d'altitude pour la géologie et l'étude des mouvements de versant. Bull. Soc. Vaud. Sc. nat. 90.1: 1-21.

Krummenacher, B. 1995: Modellierung der Wirkungsräume von Erd- und Felsbewegungen mit Hilfe Geographischer Informationssysteme (GIS). Schweizerischen Zeitschrift für Forstwesen 146, 741–61.

Lateltin, O. (1997). Recommandations - Prise en compte des dangers dus aux mouvements de terrain dans le cadre des activités de l'aménagement du territoire. Office fédéral de l'Environnement, des forêts et du paysage.

Marquinez, J., Menéndez, R., Farias, P. & Jiménez, M. 2003. Predictive GIS-Based Model of Rockfall Activity in Mountain Cliffs. Natural Hazards 30: 341-360. Kluwer Academic Publishers.

Meissl, G. 1998. Modellierung der Reichweite von Felsstürzen. Fallbeispeile zur GIS-gestützten Gefahrenbeurteilung aus dem Beierischen und Tiroler Alpenraum. Innsbrucker Geografischen Studien 28. Ph.D. Thesis, Universität Innsbruck, Innsbruck, 249 pp.

Montgomery, D. and Brandon, T. 2002. Topographic controls on erosion rates in tectonically active mountain ranges. Earth and Planetary Sciences Letters.

Mosar, J., Stampfli, G.M. & Girod, F. 1996. Western Préalpes Médianes Romandes: timing and structure. A Review. Eclogae geologicae Helvetiae, 89/1: 389-425.

Oppikofer, T., Jaboyedoff, M. et Coe, J., 2007. Rockfall hazard at Little Mill Campgournd, Uinta National Forest: Part 2. DEM analysis. 1st North American Landslide Conference, Vail, Colorado, USA. Association of Environmental & Engineering, pp 1351 - 1361.

Roullier, J.-D., Jaboyedoff, M. *et al.* 1998. MATTEROCK: une méthodologie d'auscultation des falaises et de détection des éboulements majeurs potentiels. Rapport final PRN 31, vdf - ETH Zürich.

Scheidegger, A. E. 1973. On the prediction of the reach and velocity of catastrophic landslides, Rock Mechanics, 5 : 231 - 236.

Silvaprotect-CH, 2006. Schutzwaldhinweiskarte der Schweiz. Giamboni & Wehrli. Office fédéral de l'environnement, des forêts et du paysage (OFEFP).

Sommaruga, A., 1997. Geology of the central Jura and the Molasse Basin. New insights into an evaporite-based foreland fold and thrust belt. Mém. Soc. Neuchâteloise Sci. naturell. 12 176 pp.

Strahler, A. N. 1954. Quantitative geomorphology of erosional landscapes. Compt. Rend. 19th Intern. Geol. Cong., Sec.13: pp. 341-354.

Toppe, R. 1987. Terrain models – a tool for natural hazard mapping. In Salm, B. and Gubler, H., editors, Avalanche formation, movement and effects. IAHS Publication no. 162, 629–38.

Trumpy, R. 1980. Geology of Switzerland, a Guide Book. Part A, an outline of the geology of Switzerland, Wepf & CO., Basel, Swizerland.

van Dijke, J.J. and van Westen, C.J. 1990: Rockfall hazard, a geomorphological application of neighbourhood analysis with ILWIS. ITC Journal 1, 40–44.

Van Westen, C. J., Rengers, N., Terlien, M. & Soeters, R. 1997. Prediction of the occurrence of slope instability phenomena through GIS-based hazard zonation - Geologische Rundschau, 86, 404 - 414.

Wyllie, D. C. and Mah, C. W. 2007. Rock slope engineering. Civil and Mining, 4th edition. Spon press, London.

Appendix F

DEM-based detection of potential rockfall source areas at regional scale using the software COLTOP 3D and susceptibility hazard mapping assessment

Proceedings – ***Interdisciplinary workshop on rock fall protection 2011 (ROCEXS.net)*, 17 – 19 May 2011, Congress Park – Igls, Innsbruck, Austria.**

DEM-based detection of potential rockfall source areas at regional scale using the software COLTOP 3D and susceptibility hazard mapping assessment

Luuk DORREN[1], Alexandre LOYE[2], Michel JABOYEDOFF[2] and Richard METZGER[2,3]

Keywords: Rockfall, susceptibility hazard mapping, COLTOP 3D, morphostructural analysis

INTRO

Susceptibility hazard mapping at regional scale occurs invariably as a prospective tool for developing land planning, risk policy and proper mitigation strategy to protect residential areas and infrastructures. Hence, the requirement for methodology of rockfall hazard mapping at a regional scale (>500 km^2) is prominent. The detection of potential rockfall source areas over an entire region can now be improved by the use of High-Resolution Digital Elevation Model (HRDEM). HRDEM can render accurately the fine-scale morphology of topography over an entire region. This enables taking into consideration the morphostructural aspect of the area under investigation. This study introduces a way of detecting potential rockfall source areas by performing a morphostructural analysis based on the extraction of topographic elements from HRDEM that inform about the local structural setting. The potential instable rock slopes and the failure modes is assessed through kinematic tests performed over the entire slope using the DEM. A susceptibility index to slope failure is inferred according to the number of detected potential instabilities per unit surface combined with a stability parameter. The methodology is illustrated in a rockfall prone area located in the “Oberen Mölltal” (Kärten - Austria).

MORPHOSTRUCTURAL ANALYSIS

Considering that DEMs display surface features that can reflect several structural information, the major discontinuity sets of the study area were identified based on the discontinuity surface of the 3D topographic analysis performed with the software COLTOP 3D (figure 1). COLTOP 3D enables a detailed investigation of the discontinuity sets shaping the rock slope of the study area by representing the dip and dip direction of the slopes of a DEM with a unique color code, the Hue Saturation Intensity system (HIS). The topography is displayed as a 3D shaded relief and the color code is ranged in value of a Schmidt Lambert projection. The confrontation between the structural setting and topography enables to spatially delineating where the slopes in relation with the presence of discontinuities has the configuration of potential rock slopes instabilities. The identified discontinuity sets were compared with the entire topography of the DEM using the software Matterocking. This GIS tool enables to assess potential planar and wedge sliding area on DEM through common kinematic tests and gives the averages number of failure mechanism per DEM cell, according to a given spacing between discontinuities. Toppling was handled in a similar way within a common GIS software. All discontinuities were processed according to their mean dip and dip direction and an arbitrary spacing of 1m (corresponding to the DEM resolution) was assumed for all

---

[1] Luuk Dorren, St. Hilaire du Touvet France, ECORISQ Association, Luuk.dorren@ecorisq.org
[2] Alexandre Loye, Institute of Geomatic and Risk Analysis, Uni Lausanne alexandre.loye@unil.ch
[2] Michel Jaboyedoff, Institute of Geomatic and Risk Analysis, Uni Lausanne michel.jaboyedoff@unil.ch
[3] Richard Metzger, 35bis rue de l’industrie, 1030 Bussigny , TERRANUM S.A.R.L. , richard.metzger@terranum.ch …

discontinuity sets. Wedges with plunge axe < 20° were considered as marginally potential and not considered further.

Figure 1: Discontinuity sets extracted from HRDEM using COLTOP 3D. The geometry of each set is given with its variability of 2σ.

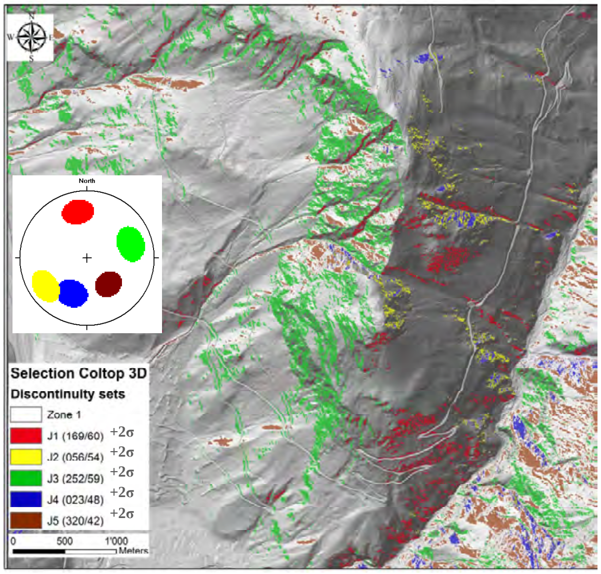

Table 1: Factor of safety computation

Type of failue	FS	Parameters
Planar	$\tan(\Phi) / \tan(\beta)$	Φ = friction angle = 30° β = dip of the sliding plane
Wedge	$k \cdot \tan(\Phi)/\tan(\beta_w)$	Φ = 30°; k = wedge factor β_w = plunge of the wedge axe
Toppling	No weighting through FS, density only!	

A susceptibility to planar, wedge and toppling failures was deduced by weighting the density of potential detected slope failure per unit surface with a factor of safety (FS) based on the equilibrium analysis, considering that the strength of the potential slide plane defined by the discontinuity set is given by the Mohr-Coulomb failure criterion assuming a null cohesive strength of failure surface (Table 1). As the spacing between discontinuities increase when they are not perpendicular to the topography, the number per DEM cell of failure mechanism was first corrected to be based on the apparent spacing of the discontinuities detected by COLTOP 3D. Then, this density of failure was divided by its factor of safety computed for each DEM cell assuming an internal friction angle of 30°. The weighted density value of all three type of failure was then summed up on a DEM cell-by-cell basis. The distribution of the total weighted relative density of failure mechanism of the DEM cells meeting the conditions for potential slope failure can be modelled by a poisson distribution considering the entire study area. This enables to define a degree of susceptibility to potential rockfall zones. In absence of field data to calibrate this weighted density of failure, this was classified in three sets of susceptibility (low - middle - high), whereas the cumulative fitted poisson distribution defines the density at 68-quantile and respectively 95-quantile (figure 3).

CONCLUSION

This methodology suggests a direction to insert local structural data in a GIS based detection and susceptibility mapping of rockfall sources at regional scale. This can provide a fast and cost overview of rockfall prone areas. Depending on the geological conditions, such an approach can easily be improved by quick field surveys or the use of available information such as geological maps, historical registery of events and aerial photo analysis. The statistical classification of the susceptibility index can be refined with field data. In the realistic perspective that HRDEM will be soon available in most densely inhabited places, such a rockfall detection methodology could become a standard in the future for preliminary hazard mapping and quantitative risk assessement.

Figure 2: Cumulative distribution of the weighted density of wedge failure and the fitted Poisson distribution. The colour correspond to the susceptibility classes define at 68-quantile and respectively 95-quantile.

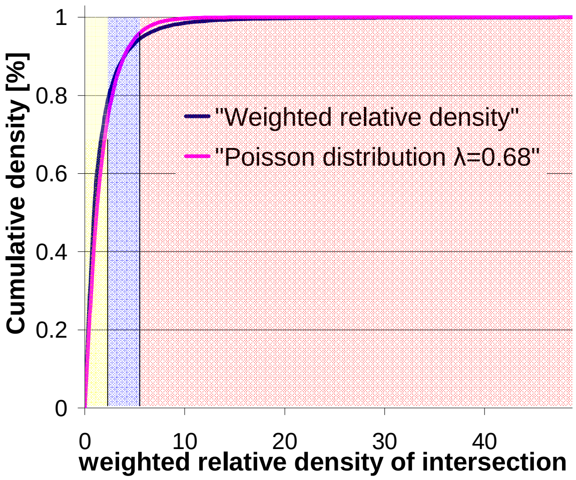

Figure 3: Example of susceptibility index to wedge sliding according to a weighted relative density of failure in the vicinity of Mörtschach (Kärnten - Austria).

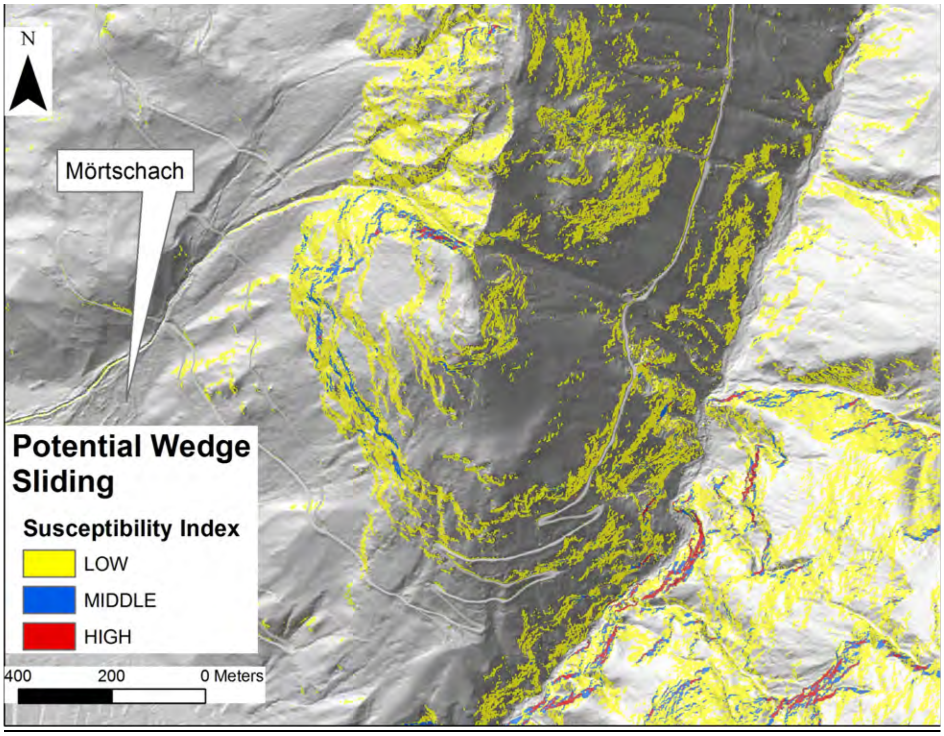

Appendix G

Earth flow in a complex geological environment: the example of Pont Bourquin, Les Diablerets (Western Switzerland)

Proceedings – ***Mountain Risks Research Training –***
Landslide Processes: from geomorphological mapping
to dynamic modelling**, 02 – 07 June 2009, Strasbourg, France.**

Earth flow in a complex geological environment: the example of Pont Bourquin, Les Diablerets (Western Switzerland)

M. Jaboyedoff, A. Pedrazzini, A. Loye, T. Oppikofer, & M. Güell i Pons
Institute of Geomatics and Analysis of Risk, Faculty of Geosciences and Environment, University of Lausanne, Lausanne, Switzerland

J. Locat
Laboratoire d'études sur les risques naturels (LERN) Département de géologie et de génie géologique, Université Laval, Québec, Canada

ABSTRACT: On July 5th 2007, a heavy rainfall event triggered a rapid earth flow of around 11’000 m^3, cutting the road joining les Diablerets to Gstaad. This event was the result of an important reactivation of a landslide active area which had started in 2004. The earth flow involved the upper 5 meters of a “deep” landslide of about 20 m thick. The complex geological setting involves shales, flysch and highly permeable rocks. The dissolution of the cornieule and gypsum located at the toe of the landslide is probably the most important cause of slope destabilization. In this paper, the evolutions of slope stability through time and run-out distance are analyzed. Results are in agreement with observations. This example shows that erosion processes or groundwater changes in such material are responsible for the shallow landslides, even with minor rainfall events.

1 INTRODUCTION

On July 5, 2007 a rapid earth flow was triggered by a heavy rainfall. The landslide cut the road of an important alpine pass between the two famous ski resorts of les Diablerets and Gstaad (Western Switzerland) at the place called “Pont Bourquin”. Fortunately, the event did not cause any causality.

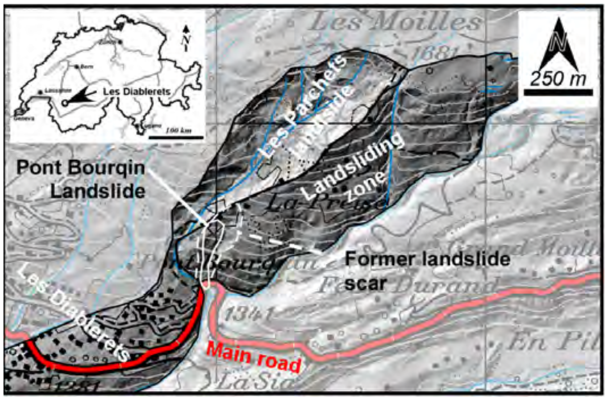

Figure 1. Location of the Pont Bourquin landslide near les Diablerets, surrounded by a large landslide area. Data from Swisstopo (DV335.2; MNT-MO 2008 SIT).

This earth flow occurred in an area that was identified as an active zone since 2004. In September 2006 it was estimated that 3000 to 6000 m^3 of a composite landslide (Cruden and Varnes, 1996) were susceptible to be mobilised in a mud-flow event that would involve the shallow portion of the 40’000 deeper landslide. The mudflow volume is now estimated to be 11’000 m^3 by comparing digital elevation models (DEM). The failure surfaces and volumes were estimated using sloping local base level (SLBL) technique and morphometric considerations. Stability back analysis was performed in order to assess the rock mass conditions for the 2007 event. The analysis confirms that slope was at the limit of stability in saturated conditions. Furthermore, a run-out analysis using BING (Imran et al., 2001) was performed. The results indicate that it is necessary to consider a modification of material properties during downslope flow to explain the run-out distance. This landslide appears very similar to the La Valette landslide (Colas and Locat, 1993; van Asch, et al., 2007) and the observed “slide-flow” at Super-Sauze by Malet et al. (2000). Slope reactivation of this area, close to a tourist resort, is expected to be active and cause further damages to the road. The present example shows that the reactivation of an ancient landslide initiated by erosion probably 15 years ago and not stabilized quickly can lead to risky situations.

2 METHODS

2.1 Field investigations

First field investigations were performed in September 2006 and standard mapping information was collected. In June 2007 and Mai 2008, intense field surveys were performed (Choffet et al., 2008). The geological map was improved and the contours of the landslide were mapped in detail.

2.2 LiDAR and GPS survey

The pre-landslide topographic surface was obtained from the 1 m airborne LIDAR (LIght Detection and Ranging) DEM provided by canton de Vaud. The post event DEM was obtained using a LIDAR ILRIS-3D laser scanning system from Optech Inc. with a wavelength of 1500 nm.

Six scans were used to acquire the topography. For technical reasons, the topography of the top of the landslide was obtained using a DGPS device (TOPCON ® *Hype –Pro*).

The point distance for the Terrestrial Laser Scanner (TLS) DEM is approximately of 7 cm. 386 GPS points were added to complete the top of the DEM. The limits of the landslide were also delineated using 74 DGPS points.

2.3 Failure surface using SLBL

The SLBL is a method to estimate failure surfaces. It uses the limits of the landslide as invariant points. The SLBL can be determined either manually or by using an iterative routine that replaces the elevation of any non-invariant point of a digital elevation model (DEM) by the mean value of the altitude of its neighbors, plus a tolerance up to the moment with no changes in elevation. This leads to a curved surface of second order. In 2D, SLBL can be found numerically by an iterative procedure assuming equidistant z_i altitude data of DEM. All points with an altitude greater (z_i) than the mean of their two neighbors are replaced by the mean value ((zi-1 + z_i+1)/2) or by this value minus a tolerance (Jaboyedoff et al., 2004). This method was applied for the shallow landslide and also for the deeper one, using a 1 m grid DEM.

2.4 Simple geotechnical investigations

We performed vane test (Roctest®) in the field in order to get a rough estimation of the undrained unconfined cohesion (c_{uu}), for the superficial material.

In order to get a characterization of the rock mass conditions, the Geological Strength Index (GSI) (Hoek and Marinos, 1997) was estimated for each lithology inside and outside the unstable area.

In case of lack of geotechnical data the GSI results could be used directly to calculate the factor of safety based on the generalized Hoek and Brown criterion (Hoek and Brown, 1988).

2.5 Modeling

The back analysis of the slope stability was performed using Slide® (Rocscience) software. The safety factor was estimated using different slice methods (Bishop, Spencer, Janbu corrected and Morgestern-Price). The groundwater condition was computed using the finite element analysis implemented in Slide®. A sensitivity analysis of the Ru values was also carried out, in order to confirm this computation. Ru represents a parameter which models the pore water pressure as a fraction of the vertical earth pressure for each slide along the critical slip surface. The deeper landslide was modeled using the GSI values obtained outside the unstable mass. For the earth flow source area, the stability was estimated using the GSI values obtained inside the unstable mass. These values are lower compared to the first ones, due to rock mass damage caused by continuous flexural toppling (Figure 2B) The back analysis of the runout distance is based on the estimation of the mobilized yield strength at the time of failure. Assuming that the final topography reflects the strength of the material involved in the debris flow, a parametric analysis was carried out using Hampton’s (1972) equation:

$$\tau_c = H_c \gamma \sin\beta \qquad (1)$$

Where τ_c is the yield shear strength of the material, H_c the critical thickness, γ the unit weight and β the slope angle. For the run-out modeling we used BING 1D- flow dynamics model software (Imran et al. 2001), with a bilinear rheological model.

3 GEOLOGICAL AND GEOMORPHIC SETTINGS

3.1 Geology

The geology is rather complex; four geological units are encountered within the 300 meters of the landslide (Badoux and Gabus, 1990). The different geological units are delimited by important tectonic thrusts. Starting from the lower part of the slope the following can be observed:

1. Weathered gypsum actively dissolved;
2. Over 50 m of cornieule. This formation is represented by a vacuolar dolomite with high permeability. These two lithologies belong to the Bex Nappe.
3. 150 m of Flysch composed of thin bedded turbidites including shale siltstone and few conglomerate and belonging to the Plaine Morte unit.
4. The next 70 m are thin bedded clayey schists of the Arveyes Nappe;
5. At the top of the slope cornieule from the Meilleret Nappe are outcropping;

6. (4) and (5) are overlaid by moraines; a ground moraine and a terminal moraine on the North-western part.

It is possible that all these lithologies contain folds and others internal thrust. The contacts between units are dipping down to North by 20 to 30°. The bedding of the (3) and (4) lithologies follow the same trend, which allows flexural toppling over at least the first 3 meters.

3.2 *The landslide activity*

In the study area, numerous landslides are still active (Schoeneich, 1996; DUTI, 1985). The Pont Bourquin landslide is located in the western part of a former scar (Fig. 1). West of the Pont Bourquin area, the Parchet landslide is active since year 2000 and moves 5-10 cm.year^{-1} (Schoeneich, 1996). The surrounding zone is certainly active since the last glacial retreat. The Pont Bourquin slope is affected by two landslides which affect mainly the less competent lithologies in the central part of the slope (shale and Flysch) and moranial deposits in the upper part of the slope. The deeper landslide is characterized by an important subsidence at the top, delineating clearly the scar and implying an important rotational component in the upper part. The toe of the landslide is probably located above the cornieule (2).

Figure 2. Views of the gully on September 9, 2006. (A) Western part. (B) Illustration of the flexural-toppling mechanism affecting the first meters of Flysch.

Erosion activity started at least for more than 10 years (Fig. 2). The orthophotos taken in 1995, 1997 and 2004 indicate a constant degradation of slope conditions. In 2006, significant displacements (80 cm) were observed above the erosion area (Jaboyedoff, 2006), indicating that not only the shallow part was moving but also influenced the deeper instability. The 2007 event was triggered after 3 days of heavy rainfall. The rainfall data from the meteorological station of Diablerets village, recorded an accumulated rainfall of 95 mm with a mean rainfall intensity of 2.5mm.h^{-1} the previous 3 days. This value corresponds to a 5 years return period. Even with minor rainfall events, and considering the superficial erosion evolution between 1995 and 2004 (Figure), a major destabilization event is expected in following years.

4 RESULTS

4.1 *Geomorphic interpretation*

The analysis of the morphology and the SLBL method indicate that the mass movement has two differentiated parts: a deep failure with an average thickness of about 15-17 m and a shallow failure with a thickness reaching up to 5 m.

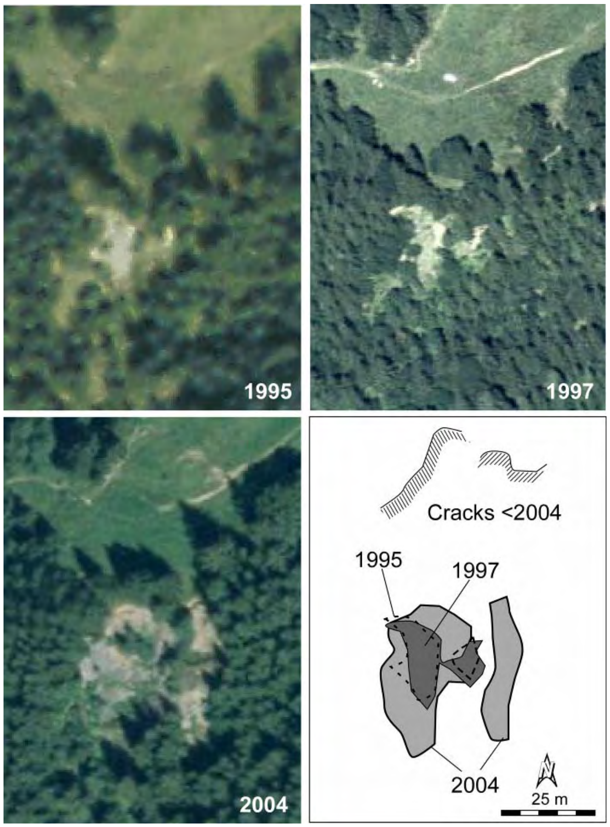

Figure 3. Orthophotos of the upper part of the landslide during the last 13 years. Observe the increase in size of the erosion area especially between 1997 and 2004. Some ortho-rectification problems exist between the photos (data from SWISSIMAGE © 2008 swisstopo (DV012716)).

Figure 4. View of the earth flow at the level of the road on July 8th, 2008.

The total area of the deep landslide is around 8200 m^2. Its width varies from 12 to 60 m. The length is 244 m up to the road. The shallow landslide area is about 5000 m^2. The total volume of the shallow landslide based on the DEM before the event and the SLBL indicate that 11’000 m^3 were mobilized along the slope using only the area that shows significant flows on the topography (Figure 6). Only a few thousand reached the toe and subsequently the road. The estimated volume of the deep landslide is around 40’000 m^3 using the same method, but using as invariant points the external contour of the landslide.

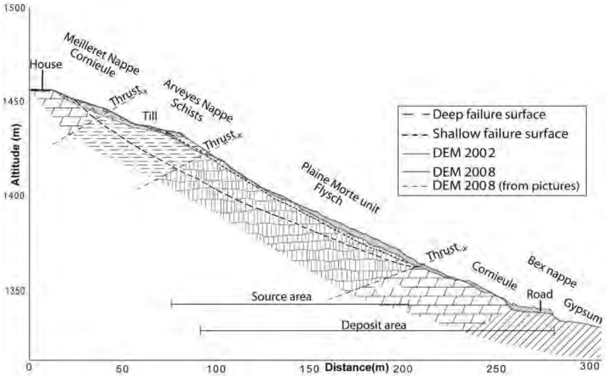

Figure 5. Cross-section along the landslide. Note that in the lower part near the road area the profile of DEM 2008 is extrapolated from pictures just after the 2007 event.

4.2 Geotechnical parameters

The vane tests performed on the top of the landslide vary between 12 to 130 KPa in the superficial formations involved in the earth flow (moraine and schist). The parameters used for the Hoek and Brown failure criterion (1988) are given in Tables 1 and 2. The GSI measurements were performed outside the shallow unstable area to simulate deep landslide and within the landslide for the earth flow initiation zone.

Table 1. Parameters estimated by field investigations outside the main landslide area (deep landslide modeling).

Parameters	Cornieule	Schists	Flysch	Gypsum
Intact UCS (KPa)	35’000	20’000	30’000	15’000
GSI	35-45	25-35	25-35	35-45
Intact Rock Constant m_i	19	6	10	10
Disturbance Factor	0.6	0.7	0.7	0.7
Unit Weight (kN/m^3)	22	23	25	23

Table 2: Parameters estimated by field investigation on the main landslide (shallow landslide modeling).

Parameters	Schists	Flysch
Intact UCS (KPa)	20’000	25’000
GSI	15-25	20-30
Intact Rock Constant m_i	6	10
Disturbance Factor	0.9	0.85
Unit Weight (kN/m^3)	22	23

4.3 Stability back-analysis

Using the parameters obtained in the field we computed the factors of safety for both landslides in fully saturated conditions. Using the undisturbed rock GSI values we obtain a quite deep failure surface with a safety factor varying between 1.3-1.4, depending on the calculation method. This surface corresponds to the deep landslide. This landslide was not directly involved in the 2007 event; nevertheless the FS is relatively low, indicatining a potential unstable situation.

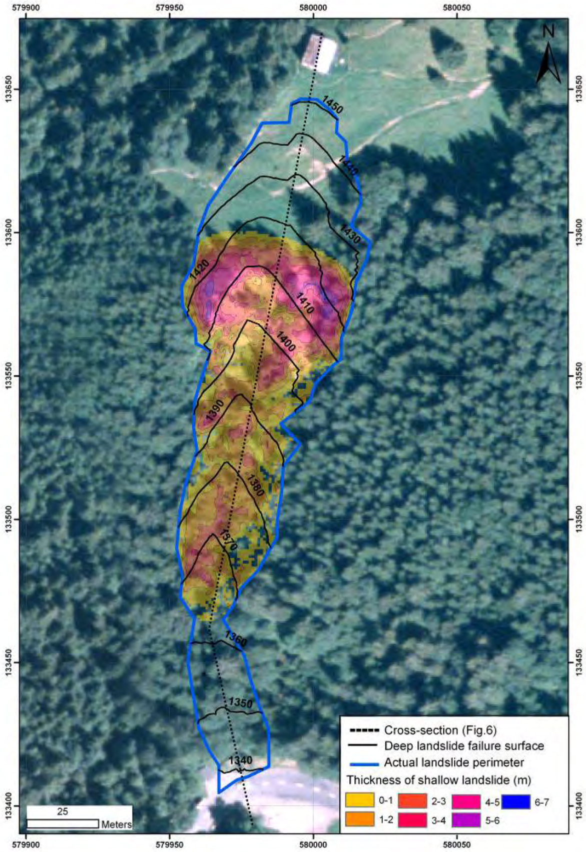

Figure 6. Results of the geomorphic analysis. Colors represents the thickness of he mobilized mass during the 2007 event. Black contours represent the modeled deep failure surface.

Sensitivity analyses for each lithology have been carried out varying Ru values from 0.1 to 0.5. Variations of Ru values in Flysch induce important changes in FS. The FS calculated using the ground water condition based on the finite element method corresponds to a Ru value of 0.2 to 0.3. This represent a realistic range of values compared to the water conditions observed in field. In the second model using the GSI values for the disturbed rock mass we obtained a shallow failure surface with a safety factor close to 1. The failure surface and the calculated volume correspond to the values obtained by the SLBL method. Figure shows that the presence of highly permeable and soluble layers such as cornieule, strongly influences the general slope stability at the toe of the slope. Additionally, during important rainfall we could expect local pore water overpressure due to complex geology. The real influence of the cornieule layer is difficult to model using limit equilibrium model because of time dependent chemical weakening. In addition, an analysis has been carried out varying the anisotropy of the permeability coefficient for the case of the deep slide, obtaining a factor of safety around 1 when vertical infiltration dominates. For the case of shallow slides, a weak layer could exist (flexural buckling) that could promote the development of landslides.

4.4 *Runout back-analysis*

The parametric results using Eq. [1] are shown in Figure . It is interesting to note that field measurements in the shallow zone, provided values of the undrained shear strength ranging from 12 to 130 KPa. Considering that the debris mass had already started to drain these values should be considered as a maximum. As indicated in Figure , using Eq. [1] for a slope corresponding to the starting zone, i.e. about 25° would require a yield strength of about 40 KPa for an average thickness of 5m which is of the same order of magnitude than the in situ strength measured using the vane test.

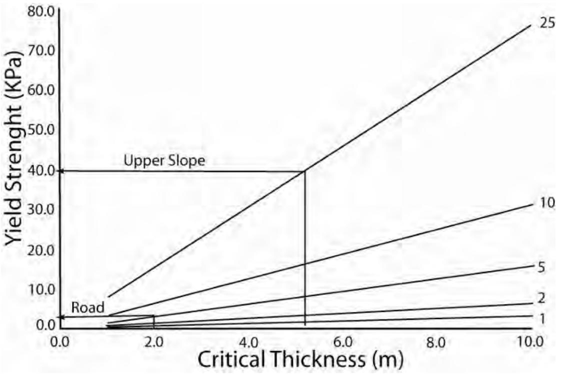

Figure 7. Parametric analysis relating the critical yield strength as a function of the critical thickness for various slope of the debris (using a unit weight of 18 KN/m^3) based on the cross-section in Figure.

The analysis of Pont Bourquin earth flow has been carried assuming that the average unit weight of the debris of 18 KN.m^{-3} and an average strength of 3 KPa, which would correspond to the observations of the material accumulated on the road (2m). This suggests that a significant part of the debris had an increase in the water content and the yield strength was reduced by a factor of 10. Using BING software (Imran et al. 2001) with a set of parameters that enable the flow to stop on the road, that the velocity reached a maximum of 12 m.s^{-1} at the onset of the flow but was moving at velocities less than 5 m/s when approaching the road.

As it has been already shown in La Valette landslide (Colas and Locat, 1993; Malet et al., 2005; van Asch et al., 2007) the landslide in shale-like materiel exhibits a complex behavior. The process starts as a translational slide and transforms progressively to a flow with increasing water content.

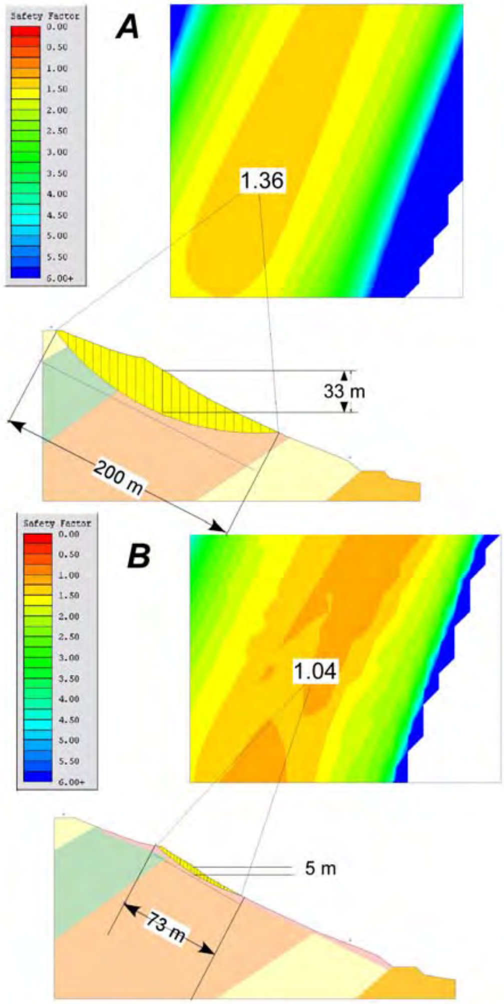

Figure 8. (A) Back analysis of the deep landslide. (B) Back analysis of the shallow landslide stability. See Figure for lithologies.

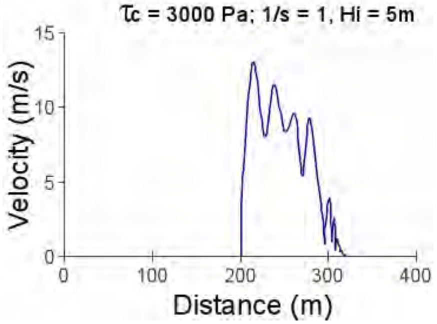

Figure 9. Velocity of the frontal element as a function of distance from its initial position in the slope. The horizontal distance of 300m corresponds to the road location.

The results show that the stability of the mobilized material is close to equilibrium and once it starts to move, the yield strength decreases, increasing the mobility. The preparation factor to weaken the shallow rock can be attributed to flexural toppling.

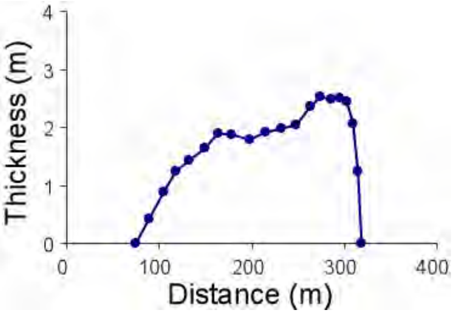

Figure 10. Profile of the deposit at the end showing an average thickness of 2m over a length of about 200m.

This mechanism deforms the rock mass and creates shear bands in the shale layer, that can be transformed to a paste-like material. This weakening is also increased in the first 10 cm by freezing and thaw cycles that fragment the rock up to a paste consistency. Additionally, the till deposits are involved in the earth flow. These factors influence landslides when intense precipitation occurs. As mentioned before, due to the presence of cornieule in this folded complex geology high pore pressure can be suspected inside the slope. It is also clear that gypsum and cornieule at the toe are the source of the deep movements that started the weakening process. Active erosion at the top is certainly one of the main destabilization factors for earth flow processes. The lacks of surface vegetation cover increases surface erosion and can cause bad-lands if the area is not reforested.

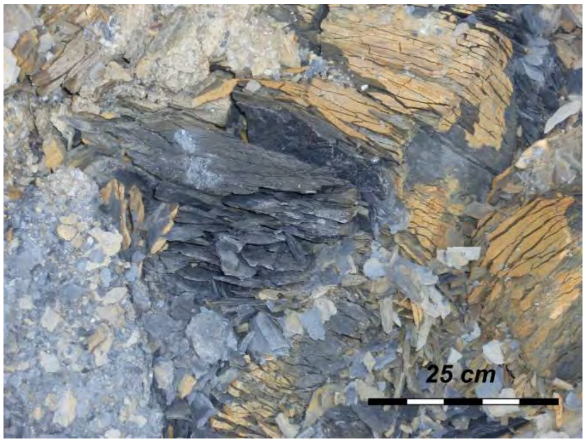

Figure 11. Surface conditions of shale fragmented by mechanical crushing related to freezing and thaw cycles.

5 CONCLUSION

This case study represents an example of the influence of fine grained lithology in the formation of complex mass movements, which start as a slide and evolve into an earth flow, capable to travel down slope at high velocities. The predisposing factors for this phenomenon seem to be related the reduction of the rock mass strength induced by flexural toppling movements, freeze and thaw cycles and continuous surface erosion.

The main triggering factor is an intense rainfall of short return period, inducing a rapid increase of the water pore pressure and influencing the rheology of the material. The complexity and the variability of the geological setting introduce other important variables that very difficult to asses without an intensive geotechnical investigation.

REFERENCES

Badoux, H. and Gabus, J.-H. 1990. Atlas géologique de la Suisse, feuille n° 1285, 1:25’000, Les Diablerets avec notice explicative. Berne 63 pp.

Choffet, M., 2008. Rapport sur le glissement de Pont Bourquin. Université de Lausanne, inédit, 18p.

Colas, G., and Locat, J. 1993. Glissement et coulée de La Valette dans les Alpes de Haute-Provence: présentation générale et modélisation de la coulée. Bulletin de Liaison du Laboratoire des Ponts et Chaussées, 187: 19-28.

Cruden D.M., Varnes D. J. 1996. Landslide types and processes. In: Turner A.K.; Shuster R.L. (eds) Landslides: Investigation and Mitigation. Transp Res Board, Spec Rep 247: 36-75.

DUTI., 1985. Projet d’éccole. Détection et utilisation des terrains instables. Rapport final, rapport général. Ecole polytechnique fédérale de Lausanne. 229 pp.

Hampton, M. A., 1972, The role of subaqueous debris flow in generating turbidity currents: Jour. Sed. Petrology. 42: 775-793.

Hoek, E. and Brown, E.T. (1988). The Hoek-Brown failure criterion – a 1988 update. In Rock Engineering for Undergraound excavations, Proc. 15th Canadian Rock Mech. Symp. (edited be Curran J.C.), 31-38.

Hoek, E., Marinos, P. and Benissi, M., (1998). Applicability of the Geological Strength Index (GSI) classification for very weak and sheared rock masses. The case of the Athens Schist Formation. Bull. Engg. Geol. Env. 57(2), 151-160.

Imran, J., Parker, G., Locat, J., Lee, H., 2001. A1-D numerical model of muddy subaqueous and subaerial debris flows. J. Hydraul. Eng. 127: 958- 969.

Jaboyedoff, M. 2006. Rapport de visite de terrain du 9 septembre 2006 dans le versant au dessus du lieu dit Pont Bourquin (les Diablerets). Institut de Géomatique et Analyse du Risque. 8p.

Jaboyedoff, M., Baillifard, F., Couture, R., Locat, J., and Locat, P. 2004. Toward preliminary hazard assessment using DEM topographic analysis and simple mechanic modeling. In: Lacerda, W.A., Ehrlich. M. Fontoura, A.B. and Sayo. A (eds): Landslides Evaluation and stabilization. Balkema, 191-197.

Malet, J.-P., Laigle, D., Remaître, A., Maquaire, O. 2005. Triggering conditions and mobility of debris flows associated to complex earthflows. Geomorphology, 66 : 215-235.

Schoeneich, P. 1996. Glissment des Parchets, Commune d'Ormont-Dessus. Rapport Inédit pour la Municipalité de des Ormont Dessus.

van Asch, T.W.J., van Beek, L.P.H., Bogaard, T.A. 2007. Problems in predicting the mobility of slow-moving landslides. Engineering Geology, 91, pp 46-55.

Appendix H

Debris flows and Avalanches Susceptibility Hazard Mapping for Pakistan

Technical report – *Earthquake Reduction and Rehabilitation Agency (ERRA)*, Islamabad, Pakistan (in collaboration with the United Nations Development Programme (UNDP)).

Debris Flows and Avalanches Susceptibility Hazard Mapping for Pakistan

Modelling of the two pilot districts Muzaffarabad and Manshera

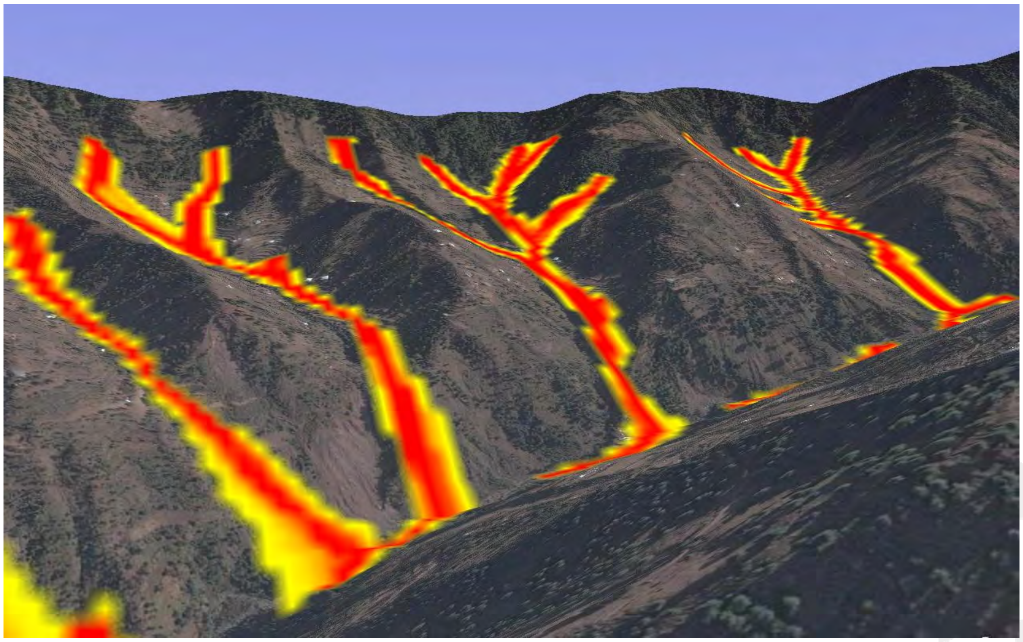

Technical report

06 August 2012

Faculty of Geosciences and Environment
Institute of Geomatics and Risk Analysis

Horton Pascal, Ph.D Student, MSc EPF in Environmental Sciences and Engineering
Loye Alexandre, Ph.D Student, MSc ETH in Earth Sciences

Under the supervision of Dr. Jaboyedoff Michel, Professor

Report: IGAR – R001

Photo on the cover page: Potential debris flows prone area in the Muzaffarabad district, Pakistan, modelled within the methodology described in this report (Image © Google).

Table of Content

1 Introduction *5*
1.1 Mandate description **5**
1.2 Susceptibility hazard mapping **5**
1.3 Natural hazards assessed **6**
1.4 Schedule **6**
2 Methodology *8*
2.1 Choice of the model **8**
2.2 Source areas identification **8**
2.3 Spreading modelling **8**
2.3.1 Flow direction algorithms 8
2.3.2 Runout distance calculation 10
2.3.3 Resulting probabilities 10
2.4 Calibration methodology **10**
2.5 Validation methodology **11**
3 Datasets *12*
3.1 Available datasets **12**
3.2 Datasets selection **12**
3.2.1 Rejected datasets 12
3.2.2 Chosen datasets 13
4 Modelling *14*
4.1 General comments **14**
4.2 Debris flows and major hyperconcentrated flows **14**
4.2.1 Source areas 14
4.2.2 Spreading 15
4.3 Avalanches **16**
4.3.1 Source areas 16
4.3.2 Source areas post treatment 17
4.3.3 Spreading 17
5 Discussion and conclusion *18*
Acknowledgements *20*
References *21*

1 Introduction

The increase of natural risks in mountainous areas is linked to the increase of population and economic activity. One way to reduce the impact on the society and the economy is to lower hazards by mitigation measures, which must be adapted to the socio-economical environment of the considered territory. Therefore, the identification and awareness of the natural hazards susceptibility is of primary importance.

The present mandate consists of giving an overview of the areas potentially endangered by debris flows and snow avalanches at regional scale in the form of indicative “Susceptibility Hazards Maps”. This work will be accomplished on the two pilot districts of Muzaffarabad and Manshera.

1.1 Mandate description

This work is part of the *Disaster Risk Reduction* (DRR) programme coordinated by the *Earthquake Reconstruction and Rehabilitation Authority* (ERRA), which is technically supported by UNDP and funded by World Bank. The required services are the following:

- Assessment of the potential source zones and the potential runout areas in the framework of susceptibility hazard mapping, by implement debris flow and snow avalanche modelling in the two pilot districts
- Provide training to the core staff in use of numeric modelling software for snow avalanche and debris flow hazards

The deliverables at the end of the mandate are listed hereafter.

- Define parameters for debris flow starting zones according to observations and subject to slope stability indications
- Define parameters for snow avalanche starting zones according to observations.
- Calibration of snow avalanche and debris flow modelling parameters within project area and based on mapped events.
- Preparation of snow avalanche and debris flow maps using numeric modelling software
- Train mapping team in use of modelling software
- Modelling software
- Submission of end of the mission report

1.2 Susceptibility hazard mapping

Susceptibility hazard mapping at regional scale consists of delineating the potential occurrence of hazards over a large territory. The goal is to assess whether an area is potentially endangered or not by slope movements like landslide, rockfall, debris flows, avalanches and floods. The maps of susceptibility are of primary order “indicative”, showing only the hazard location at 1:25’000 to 1:50’000 map resolution. Hence, they do not contain any information neither on the frequency of occurrence nor on the intensity of the slope movement. They simply enable to provide a quick overview (screening) of potential hazards over a large territory. Those kinds of maps belong to the first step of the working process leading toward local hazard maps at more detail resolution (Lateltin, 1997). As well, natural elements such as the forest or any kind of mitigation work should not be considered in mapping the hazard susceptibility, because they can disappear.

The increasing availability of geographic information system (GIS) data, such as digital elevation models (DEM) and topographic vector maps, makes GIS-based tools and GIS modelling approach very convenient to map the hazards susceptibility at regional scales. Mapping the susceptibility of an event can be now accomplished in a relatively short time, with a limited amount of data and at reduced costs. However, they should be done within an automatic procedure applied homogeneously over the whole area.

1.3 Natural hazards assessed

Two hazards were investigated in the framework of this mandate:

- Hazard related to debris flows and similar events: this consists of very to extremely rapid flow of predominantly coarse debris consisting of soil, wood and/or weathered bedrock (Varnes, 1978) entrained by a substantial increase in water content. Those debris flows propagation are essentially channelized following the topography. They mainly occur in gullies and along permanent as well as temporary rivers. When the concentration of coarse boulders and weathered rock debris are low, the flow hazard is called hyperconcentrated flow. The susceptibility hazard maps produced during this work assess the susceptibility to debris flow hazards and to major hyperconcentrated flow hazards.
- Hazard related to snow avalanches: the susceptibility hazard map of snow avalanches focuses on “wet snow avalanches” only, following the wish of the mandator. The reason is that they represent, according to the ERRA team, the most common type of snow avalanches in Pakistan. This type of avalanches can pose a great danger due to its great force of destruction (SLF, 1991). They imply the presence of water in the snow, increasing the snow density up to 500 kg/m^3 (Hutter, 1992). Those heavy avalanches can be triggered all along the cold season in Pakistan, when the weather turns milder, and during the spring at snow melt. They flow with a relatively low speed ranging between 20 to 80 km/h (Hutter, 1992) and follow the terrain profile. Very often, their runout paths reach the channels or gullies lying underneath the source areas and can be considered as "Bottom valley snow avalanches". Hence, they are the critical scenarios for the extreme avalanches that can affect residential areas and transportation corridors, principally.

For both hazards, the delineation of the possible occurrence of an event has been separated into two distinct steps:

- Identification of the potential source areas. This corresponds in the case of the debris flow hazard to the initial entrainment zones of the debris. For the case of avalanches, this corresponds to the detachment zone of the snow mass.
- Assessment of the maximum runout zones from the event source areas identified in the first step performed with a model applied homogeneously over the whole territory.

1.4 Schedule

The work has been divided into different steps:

- Introduction of the model to the local team
- Data preparation
    - Delimitation of the regions for calibration and validation
    - Introduction of the datasets in the model and preparation of the calibration and validation subsets.
- Calibration
    - Choice of the algorithms and parameters ranges to test
    - Calibration for both hazards on the calibration zone, on the basis of satellite images and the knowledge of ERRA team.
- Validation
    - Modelling for the two validation zones
    - Field trip to compare the model results to field observations
    - Eventually optimization of the algorithms and parameters to better match the field observations
- Mapping
    - Segmentation of the two districts in areas that the model can handle
    - Final modelling on the whole area
- Report

2 Methodology

2.1 Choice of the model

The choice of the model has been done before by the mandator. The model is a GIS-type data processing tool that first identifies the source areas of the event of interest and then spreads the correspondent flow by means of a probabilistic and energetic approach on the basis of a Digital Elevation Model (DEM). It has been developed in the University of Lausanne (Horton *et al.*, 2008). The model can be used for both hazards of interest, as the key algorithms are commonly used for debris flows and avalanches modelling, and the driving parameters can be changed to stand for the correct behaviour.

The objective of the model is to allow a transparent algorithm choice and an easy customization of the method. Thus, every decisive algorithm is an external function that can be easily selected among others in the main graphical user interface.

Both the sources identification and the spreading area assessment are based on a DEM. Each algorithm is then constrained to work on a grid basis. This approach is quite common in models for spreading assessment, and become increasingly interesting as the DEMs resolution increase.

Input data (ASCII files) for sources identification can represent different types of spatial information, as the corresponding parameters are user-defined. Thus, some preliminary work can be undertaken in GIS software.

The source volumes are not taken into account, due to impossible large scale rapid assessments, and due to the significant mass changes occurring through deposition and erosion (Iverson *et al.*, 2001) which is excessively difficult to estimate.

2.2 Source areas identification

The sources are assessed on the basis of datasets that the user wants to consider. These data are reclassified by means of criteria that are linked to the slope angle. For each criterion, a grid is generated containing three possible values for each cell: possible source – excluded – ignored. The possible source option means that according to the selected criterion, the cell is a potential source area. The ignored option means that there is no evidence if the cell is a source or not, so that no decision is fixed. The excluded option means that the cell cannot be a source area. In combining the grids established for the different criteria, a cell is selected as a source area if it was at least once identified as a possible source but never classified as excluded.

2.3 Spreading modelling

The spreading can be mathematically estimated by two types of algorithms: the first ones are called flow direction algorithms and rule the path that the flow will follow; the second ones determine the runout distance.

The spreading area assessment selects each source area, and spreads it on the DEM which is the only data needed.

2.3.1 Flow direction algorithms

Flow direction algorithms apportion the flow from one cell to its eight neighbours.

The final probabilities (Eq. 3) are function of the slope and the persistence, which is a weighting of the directions according to the previous direction, allowing an integration of the notion of inertia. It is, however, not a mathematical probability in a strict sense, but it has to be interpreted in a qualitative way (Huggel *et al.* 2003).

2.3.1.1 Slope-related algorithms

The slope has a leading effect on the flow path. Various flow direction algorithms have been integrated and evaluated in past case studies. The model contains all these algorithms and the choice is entirely open to the user. Only the algorithm of interest is presented hereafter.

Holmgren (1994) introduced an exponent in the multiple flow algorithm from Quinn ***et al***. (1991) (Eq. 1). The higher is the exponent, the more convergent the flow becomes. When x = 1, it turns into the basic multiple flow direction, and when x → ∞, it becomes a single flow direction

$$f_{si} = \frac{(\tan \quad _i)^x}{\sum_{j=1}^{8} (\tan \quad _i)^x} \qquad \text{for all} \quad \tan \quad > 0 \qquad \text{Eq. 1}$$

where i, j = flow directions (1..8), f_{si} = flow proportion (0..1) in direction i, tan i as defined above and x = variable exponent.

2.3.1.2 Persistence

A weighting of the directions is included to take into account the persistence of the flow, representing its inertia. Based on Gamma (2000), the weight is a function of the change in angle from the last flow direction (Eq. 2):

$$\begin{cases} f_{pi} = w_0 & \text{if} \quad \alpha_i = 0° \\ f_{pi} = w_{45} & \text{if} \quad \alpha_i = 45° \\ f_{pi} = w_{90} & \text{if} \quad \alpha_i = 90° \\ f_{pi} = w_{135} & \text{if} \quad \alpha_i = 135° \\ f_{pi} = 0 & \text{if} \quad \alpha_i = 180° \end{cases} \qquad \text{Eq. 2}$$

where i = flow directions (1..8), f_{pi} = flow proportion (0..1) in direction i, $_i$ = angle between the previous direction and the direction from the central cell to cell i, $w_{0,45,90,135}$ = weights for the corresponding change in direction.

2.3.1.3 Resulting probabilities

Resulting probabilities are the combination of the slope-related algorithm and the persistence.

$$f_i = \frac{f_{si} \cdot f_{pi}}{\sum_{j=1}^{8} f_{sj} \cdot f_{pj}} \cdot f_0 \qquad \text{Eq. 3}$$

where i, j = flow directions (1..8), f_i = total flow proportion (0..1) in direction i, f_{si} = flow proportion from the slope-related algorithm, f_{pi} = flow proportion from the persistence, f_0 = previously determined flow proportion of the central cell.

Each cell having a minimal probability is then included in the debris flow path. For the spreading assessment of a source cell, the calculation thus integrates different paths or divergences in one run. There is no need of random multiple runs as the field of all probabilities is covered.

2.3.2 Runout distance calculation

Runout distance algorithms are basic energy-based calculations that define if a part of the flow can potentially reach another cell. Thus, they control the distance reached by the flow and in addition reduce the divergence. In that way, the energy-based algorithms also influence the flow direction, as each cell that cannot be reached has a probability set to zero.

In a first regional assessment, the source mass is unknown. Thus, runout distance calculation is based on a unit energy balance, a loss function and a maximum threshold (Eq. 4). This approach does not aim to represent exact physical processes, but to remain realistic.

$$E^{i}_{kin} = E^{i-1}_{kin} + \Delta E^{i}_{pot} - E^{i}_{loss} \qquad \text{Eq. 4}$$

where i = time step, E_{kin} = kinetic energy, ΔE_{pot} = change in potential energy and E_{loss} = constant loss.

At start, a source has a certain unit potential energy (without considering the volume) regarding its adjacent cells downhill. During propagation, part of this energy is lost in friction according to the selected algorithm. The kinetic energy is increasing and may reach the eventual maximum threshold, leading to an energy line having the same shape as the terrain. The flow stops when the energy becomes null.

2.3.3 Resulting probabilities

The spreading areas of all sources are combined by keeping the maximum probability values. The result is the total area exposed to the hazard spreading, with an associated qualitative probability qualifying the susceptibility potential. However, the susceptibility mapping approach aims to consider the total area exposed to the hazard, regardless any probability notion.

2.4 Calibration methodology

Neither historical records of damaged residential areas or destroyed forests nor maps of inventory exist. Some information gathered from local people having filled forms with their observations were available and could complete the few investigation conducted during anterior field trips. Unfortunately, these kinds of information were too sparse in number and were not integrated in a GIS platform, making them hard to use in the calibration process.

The calibration process was then mainly based on the field knowledge of the ERRA team. For debris flows, some satellite photographs helped in indentifying visible scarps, especially a visual analysis of the aerial photos available on Google Earth^{TM}.

The calibration has been processed on the Muzaffarabad region. The spreading and the runout distance was discussed and fixed in accordance with the ERRA team.

2.5 Validation methodology

The validation process aimed to compare the first modelling maps with visible occurred events on the field. Three regions were chosen for this control: Muzaffarabad, Balakot and the Kaghan valley.

The visible scarps and snow deposits were compared with the model outputs in terms of occurrence, spreading and runout distance. The susceptible zones identified by the model with no correspondence on the field were assessed as potential or inaccurate. Those observations were then used to choose the best modelling results and to adjust the parameters to insure coverage of the worst cases.

3 Datasets

3.1 Available datasets

The available datasets are the following:

- DEM: The Digital Elevation Model is the SPOT DEM that has been furnished with a resolution of 20 meters.
- Land cover: The Landsat image has been previously processed by ERRA team to extract land cover information. Six classes were extracted:
    1. Unclassified
    2. Forest
    3. Water body
    4. Snow and Ice
    5. Vegetation
    6. Urban barren
- Geology: The geological map is available at a scale of 1: 50,000 for the whole regions. Some parts are mapped at 1:1,000,000.

3.2 Datasets selection

3.2.1 Rejected datasets

For both avalanches and debris flows, the land cover and the geology layers were not considered.

The land cover information derived from the Landsat image has many inconsistencies in regards to the forested areas, which would have been the most interesting type. The first issue is that the automatic classification does not interpret correctly the satellite photo in some regions, leading to an overestimation in forested surfaces, which leads to an underestimation in avalanches source areas. The second issue is the density of the forest, which was observed to be an important factor, and that is not taken into account into the classification process. If the forest is not dense enough, there is much less mitigation on avalanches triggering. A third issue is the image resolution. Relatively large clearings are hardly seen as they may be only few pixels wide. However, at this resolution, these may be large enough to be snow avalanches source areas. Thus, some snow avalanches were observed in the forested area mainly due to the density issue and the missed clearings. It is therefore not wise to exclude the forested areas from the potential source areas. And at this step anyway, the forest represents a mitigation element and should by definition not be considered in the susceptibility hazard map (cf. 1.2).

The geological information, which would has been relevant for the debris flow source areas, are not taken into account due to the fact that no geology type can be excluded. Indeed, there is no geology type on the map that is not susceptible to debris flows. This has been confirmed by field observations.

3.2.2 Chosen datasets

The chosen datasets for the sources identification of the two hazards are the following products derivated from the DEM:

- Slope
- Height (only for avalanches)
- Curvature
- Flow accumulation (only for debris flows)

4 Modelling

4.1 General comments

Some choices made for the spreading modelling of both hazards are the same. These are presented hereafter.

The resulting probabilities were combined by keeping the maximum probability. The calculation mode was set to quick, meaning it enables an energy based discrimination to stop processing small events where a larger has already spread. As in the case of the susceptibility hazard mapping, only the spreading surface is taken into consideration, there is no need to take all trajectories into account, when they are redundant.

The spreading algorithm considered is the one proposed by Holmgren (1994) (Section 2.3.1.1). With its exponent, it can reproduce the behaviour of all others.

The inertia algorithm was found not to play a significant role in the spreading area. Thus, the weight approach with the default parameters set is systematically chosen. The weights values are shown in Table 1.

Table 1 : Weights of the default inertia parameters set for the changes in direction angle.

	w_x
0°	1
45°	0.8
90°	0.4
135°	0
180°	0

4.2 Debris flows and major hyper concentrated flows

4.2.1 Source areas

4.2.1.1 Slope

The slope angle is a determining factor in triggering of debris flows (Takahashi, 1981). Most debris flows occur from terrain with a slope higher than 15° (Rickenmann and Zimmermann, 1993; Takahashi, 1981). Therefore, the minimum slope of 15° has been chosen as a threshold for sources area identification. Some initiation threshold of other factors can be expressed as a relation with the slope angle, as for the contributive area.

The major hyperconcentrated flow source areas were identified for sources between 5 to 10°. Those events occur in riverbeds that are relatively flat, as the water input is higher than for debris flows.

4.2.1.2 Curvature

Another potential morphological characteristic is the curvature, as debris flows are found where curvature is concave (Delmonaco et al., 2003; Wieczorek et al., 1997). To allow an identification of gullies, the plan curvature, which is perpendicular to the steepest slope, was considered. Although this characteristic is often used to recognize the gullies, there is no admitted threshold. A limit had to be established on the basis of previous research work and aerial photographs analysis.

On our study area, a curvature of $-1/100\ m^{-1}$ was found as optimal on the basis of the analysis of aerial photos. It succeeded in identifying the gullies prone to debris flows. A curvature of $-2/100\ m^{-1}$ failed in identifying most sources.

The curvature was not taken into account for the hyperconcentrated flow source areas. Those happen in relatively large riverbeds that are best identified by the contributing area.

4.2.1.3 Hydrology

Debris flows are found along waterways, where the morphology is concave and where water converges (Delmonaco ***et al***. 2003). The upslope contributing area, as a characteristic of water input, is used widely in distributed hydrological models (Erskine ***et al***. 2006). The upslope contributing area is taken into account by means of the calculated flow accumulation, by use of the D8 algorithm.

During the calibration process, we found optimal to limit the contributing area to 2 ha. New sources found below that limit are not relevant, and introduce new channels where no accurate debris flow was found. Above that limit, some noticeable source areas are missing. A buffer of 20m has been considered around the previously identified channels.

The next step for the detection of the sources areas is done through a relationship with the slope. The chosen relationship is based on the work of Rickenmann and Zimmermann (1993) for the 1987 observations of debris flows in Switzerland. This one is an extraordinary rainfall event. According to the high rainfall intensity during monsoon in Pakistan, this threshold for extreme events is accurate. Every point above that limit is considered as critical. The equation is the following:

$$\tan\ _{lim} = 0.31 \cdot S_{UA}^{-0.15} \qquad \text{Eq. 5}$$

where $\tan\ _{lim}$ = slope gradient, S_{UA} = surface of the upslope contributing area.

For the major hyperconcentrated flows, the upslope contributing area taken into account is between 500 ha to 5000 ha. During calibration, lower contributing area were found to be too small to produce major hyperconcentrated flows, and higher values added sources in the main rivers that were not relevant.

4.2.2 Spreading

4.2.2.1 Debris flows

The Holmgren algorithm with an exponent of 6 was found as optimal based on observed events from field observation and satellite photo analysis.

The runout distance was found best represented by means of the 2 parameters friction model. The resulting energy loss show a good correspondence with the topography and the runout distance is coherent. The best values of the two parameters are the following: M/D = 30 and mu = 0.08. There is no velocity limitation, as the friction model with those parameters doesn't reach absurd values.

4.2.2.2 Hyperconcentrated flows

The hyperconcentrated flows are found in large riverbeds already completely channelized. Thus, the dispersion can be important. The Holmgren algorithm with an exponent of 1 was considered in this case, meaning it corresponds to the multiple flow direction model. The dispersion is thus maximal.

The runout distance was found best represented by means of the constant loss function with an energy loss angle of 2°. This model is closer to water behaviour than to an earth mass flow behaviour, which makes sense due to the high content of water in large hyperconcentrated flows. There is no velocity limitation.

4.3 Avalanches

4.3.1 Source areas

After considering the lack of inventory and the great uncertainty in the localisation of the observed sources, the identification of the potential source areas where defined according the topography only. The chosen criteria are thus restricted to the height, the slope angle, the slope curvature and a minimum unstable snow area.

The potential sources areas were introduced in the model as a raster layer according to the following parameters:

4.3.1.1 Height

The altitude threshold was defined as above which snow precipitation is important enough to trigger a snow avalanche. According to ERRA team, elevations under 1900 m.a.s.l. are very unlikely to encounter snow precipitation important enough to trigger an avalanche. All slopes lying above 1900 m.a.s.l were then considered as potential sources.

4.3.1.2 Slope

Large snow avalanche can be triggered only below a threshold slope angle that enable to accumulate a sufficient snow thickness, and its propagation occur only above a given slope angle (Amman, 2003).

The slope angles ranging between 30° to 42° have been chosen as thresholds for large wet snow avalanches. The minimum is a common feature of many mountainous regions, even though wet snow avalanches have already occur at a lower slope angle. The maximum limit corresponds to the type of snow avalanches considered here. Above 42° to 45°, sluffs and small avalanches are common, but snow seldom accumulates to sufficient thickness to generate large wet snow avalanches. Similar criteria were used in similar works, the maximum threshold being higher according to the type of avalanches considered (i.e. 55° in Norway (Derron et al, 2008)).

4.3.1.3 Curvature

On this study area, all cells of the DEM having a total curvature ranging between -2 to 2 m^{-1} were considered as potential source areas. A too large convexity excludes an important accumulation of snow on the slope. And a too large concavity prevents the mobilisation of a snow mass big enough to flow down the slope. The melting or rain water infiltration tend to accumulate in the gentle concave parts of the sloping surfaces and convex parts of the sloping surfaces are often areas of enhanced risk due to increased tensional stresses in the snow pack (Amman, 2003).

4.3.2 Source areas post treatment

The potential sources zones for snow avalanches have been extracted for the entire pilot area according to the procedure defined above. Then, the identified source areas have been subject to a post treatment in order to exclude isolated small cells and to optimize the spreading processing.

Considering a minimum surface of unstable snow mass, all potential source areas (connected cells) having a surface less than 800 m^2 were excluded. This had the advantage as well to eliminate possible artefacts inherent to the DEM.

As a second step, because of the important amount of source cells, only the outer edges of the source areas were considered. Hence, it considers only the source cells situated the most upslope and the most downslope of a source area, the runout area of the inner sources cells being included anyway in both extremes. This procedure decreases the time of computation by a factor of about 7 in the pilot area.

In order to keep the edge of the source zones only (the connected cells) a morphology-based operation (closing) was done first in order to fill the small holes that would create an edge of eight cells around the hole. Then, the inner cells were removed from the source areas by applying a convolution whose eight direct neighbouring cells are “sources” as well.

4.3.3 Spreading

The Holmgren algorithm with an exponent of 4 has shown to render the best lateral spreading, when the snow avalanches are not channelized by the terrain. In the case they are embanked at the bottom of a valley, this parameter does not matter. This has been tested and calibrated according to field observation, shaded-relief DEM and satellite photo analysis.

According to the high density of those kinds of snow avalanches (up to 500 kg/m3) and a relatively low velocity (up to 60 km/h), the persistence of the direction show the best results when they are weighted with 0.8 at 45° and 0.4 at 90° (default parameters set).

The runout distance was found best represented by means of the 2 parameters friction model, which was originally designed for this purpose (Perla, 1980). The best values of the two parameters are the following: M/D = 1500 and mu = 0.25. A velocity limitation to 25 ms^{-1} was introduced.

5 Discussion and conclusion

The dataset derived from the DEM allowed us to identify susceptible debris flows and avalanches. Due to data limitations, the approach has been purely morphologic. The results must be analysed at 1:25'000 scale. All interpretation of the model at a finer scale makes no sense.

The results showed a satisfying correspondence with field observations. Thus, for the purpose of susceptibility mapping, the outputs can be considered as accurate. In the framework of susceptibility mapping, the identified areas are often larger than the observed events on the field. This is on purpose, as the map should be representative of the worst cases, so always rather conservative.

The sources and especially the spreading area are deeply linked to the DEM. Thus, in case of misrepresentation of the reality, the spreading area will contain nonsense results. This has been observed in some places, like illustrated on Figure 1, where a DEM artefact blocks the debris flow to go further down, like it happened in a past event. Furthermore, the 20 m resolution is relatively coarse to represent small gullies and topographic variations that influence the real flow path.

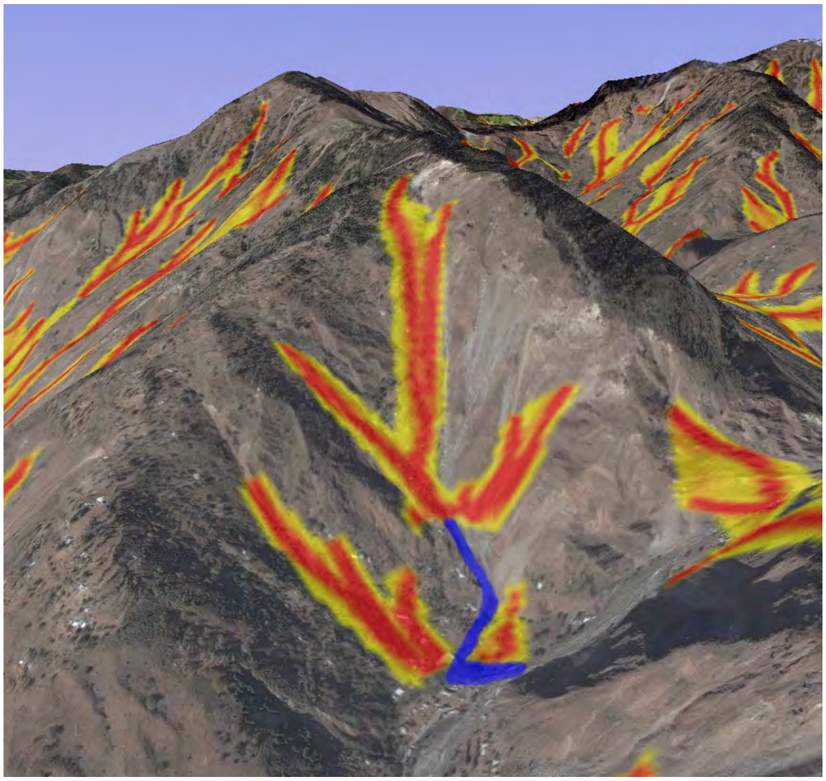

Figure 1 : Effect of a DEM error above Nardajian (Muzaffarabad). The model stops due to misrepresentation of the gully in the DEM. Thus, the model misses a past event (depicted in blue).

Forested surfaces from the land cover map were not removed from the potential sources, denying the protective effect of vegetation. This condition increases considerably the number of probable location of debris flows and avalanches, but we must remember the underlying dangers of some tree cuts and forest fires. And as it has been said previously, the indicative map should not consider it anyway. However, the forest cover may be taken into account in a further step consisting of more detailed local hazard maps.

The indicative map framework implies also to remove the probability information from the outputs and to only consider the potentially endangered area of the modeled events without any classification in the susceptibility. This map is not a hazard map as it does consider neither the magnitude, nor the frequency. Moreover, it cannot be exact as it doesn't take into account the local controlling factors. Further field investigations are necessary to take a decision on the exposure to danger of a specific area. Susceptibility hazard maps provide an excellent overview to indicate where detailed field investigation should be conducted to create a hazard map.

Debris flow and snow avalanche susceptibility maps can first help identifying built-up areas that are exposed to hazard susceptibility in order to assess the effective danger. They should help defining the priorities for local mitigation studies and help planning field investigations in order to be able to better assess the actual danger in a reasonable time.

For unbuilt areas, the process is quite the same. The susceptibility map helps identifying safer areas that are a priority for urban planning and those that may be at risk and need further investigation.

Could you please elaborate a bit more on specific applications of debris flow and snow avalanche susceptibility maps? What are its limitations with reference to development introventions.

Acknowledgements

The authors of this report would like to thank the *Earthquake Reconstruction & Rehabilitation Authority* (ERRA) team, especially Mujeeb Alam and Ejaz Karim for their precious field knowledge and enjoyable collaboration all along the realisation of these susceptibility hazard maps. A special consideration to Air Cdre (R) Naunehal Shah for his great hospitality during our stay there, as well as Raffi who drove us with a lot of care through the north of Pakistan; without him, the field survey would not have been the same. Moreover, they are very grateful to Mr. Markus Zimmermann, the project initiator, for his noticeable technical advises and his kind help before the trip. This project benefits the financial and logistical support of the UNDP (grant No. PU/SSA/09/149)

References

Amman, W., 2002. Schnee- und Lawinenkunde. Skript zur Vorlesung, SS 2003, unveröffentlich, ETH Zürich.

Delmonaco, G., Leoni, G., Margottini, C., Puglisi, C. and Spizzichino, D., 2003. Large scale debris-flow hazard assessment: a geotechnical approach and GIS modelling. Natural Hazards and Earth System Sciences, 3: 443-455.

Derron, M.-H., 2008. Automatic susceptibility mapping of snow avalanches – Proposition of a method (version 1 : 14/10/08), norvegian geological survey NGU, Trondheim. Internal report.

Erskine, R. and Green, T., 2006. Comparison of grid-based algorithms for computing upslope contributing area. Water Resources Research, 42(9).

Gamma, P., 2000. dfwalk-Ein Murgang-Simulationsprogramm zur Gefahrenzonierung. Geographisches Institut der Universität Bern.

Horton, P., Jaboyedoff, M., Bardou, E., 2008. Debris Flow Susceptibility Mapping at a Regional Scale. 4th Canadian Conference on Geohazards, Québec, Qc, Canada.

Holmgren, P., 1994. Multiple flow direction algorithms for runoff modelling in grid based elevation models: An empirical evaluation. Hydrological Processes, 8(4): 327-334.

Huggel, C., Kääb, A., Haeberli, W. and Krummenacher, B., 2003. Regional-scale GIS-models for assessment of hazards from glacier lake outbursts: evaluation and application in the Swiss Alps. Natural Hazards and Earth System Sciences, 3(6): 647–662.

Hutter K., 1992. Lawinen-Dynamik. In Schweizer Ingenieur und Architekt Nr. 13, 26.

Iverson, R.M., Hydrologist, U., Vancouver, W., Denlinger, R.P., 2001. Mechanics of debris flows and debris-laden flash floods, Seventh Federal Interagency Sedimentation Conference, Reno, Nevada.

Lateltin, O., 1997. Recommandations – Prise en compte des dangers dus aux mouvements de terrain dans le cadre des actibités de l’aménagement du territoire. Office fédéral de l’Environnement, des forêts et du paysage.

Perla, R.I., Cheng, T.T. and McClung, D.M. 1980: A two-parameter model of snow avalanche motion. Journal of Glaciology 26, 197-207.

Quinn, P., Beven, K., Chevallier, P. and Planchon, O., 1991. The prediction of hillslope flow paths for distributed hydrological modelling using digital terrain models. Hydrological Processes, 5(1): 59-79.

Rickenmann, D. and Zimmermann, M., 1993. The 1987 debris flows in Switzerland: documentation and analysis. Geomorphology, 8(2-3): 175-189.

SLF, 1991. Swiss federal institute for snow and avalanches research. Schnee und lawinen in den schweizer Alpen, Winter 1990/1991. Winterberich no. 52, Weissflujoch/Davos.

Takahashi, T., 1981. Estimation of potential debris flows and their hazardous zones: Soft countermeasures for a disaster. Natural Disaster Science, 3(1): 57-89.

Varnes D. J., 1978: Slope movement types and processes. In: Schuster R. L. & Krizek R. J. Ed., Landslides, analysis and control. Transportation Research Board Sp. Rep. No. 176, Nat. Acad. oi Sciences, pp. 11–33.

Wieczorek, G.F., Mandrone, G. and DeCola, L., 1997. The Influence of Hillslope Shape on Debris-Flow Initiation. In: ASCE (Editor), First International Conference Water Resources Engineering Division, San Francisco, CA, pp. 21-31.

Appendix I

Monitoring rock glacier with terrestrial laser scanning

Abstract Following the devastating debris flow that swept away the Martign – Orsière railway, a monitoring with terrestrial laser scanner (TLS) of the up-located rock glacier of the *Liapey de Grône* (Durnant valley, Switzerland) started in 2008. The back analysis showed that the main part of the debris load in the swollen torrent came from there. LiDAR data enabled to create a high resolution DEM of the rock glacier and its surrounding rock walls suppling debris. Compared with older topographic data, the analysis could highlight a clear subsidence of the two main channels crossing at the center of the glacier as well as a real loss of material at its front. Topographic survey with LiDAR enables to follow the evolution (activity) of the rock glacier, to quantify the volumes of debris and ice melting as well as to assess the rate of changes, providing significant data for quantitative hazard assessment.

UNIL | Université de Lausanne
Faculté des Géosciences et de l'Environnement (FGSE)
Institut de Géomatique et d'Analyse du Risque (IGAR)
Amphipôle
CH-1015 Lausanne

Mesures 3D au scanner laser terrestre du glacier rocheux du Liapey de Grône

(Vallée du Durnand de la Jure)

Relevés de terrain effectués le 14 octobre 2008

Photo : Crealp

Faculté des Géosciences et de l'Environnement
Institut de Géomatique et d'Analyse du Risque
Loye Alexandre, assistant, étudiant PhD
Oppikofer Thierry, assistant, étudiant PhD
Jaboyedoff Michel, Professeur.

Avec la collaboration de
Guillaume Favre-Bulle, étudiant Master

Rapport: IGAR – AL – R002

Faculté des géosciences et de l'environnement
Institut de géomatique et d'analyse du risque

Tél.+41 21 692 35 47 | Fax.+41 21 692 35 35 | Alexandre.loye@unil.ch

1. Préambule

L'Institut de Géomatique et d'Analyse de Risque (IGAR) de l'Université de Lausanne a été mandaté par M. le Géologue cantonal Jean-Daniel Rouiller pour effectuer un relevé au scanner laser terrestre du glacier rocheux au lieu dit Liapey de Grône, au sommet du bassin versant du Durnand de la Jure, dans la région de Champex (Valais). Le mandat consiste à fournir un model numérique de terrain haute résolution (MNTHR) de l'entier du glacier rocheux.

2. Introduction

Le 26 juillet 2006, à la suite de violents orages déclenchés en fin d'après midi, le Durnand (affluant de la Dranse) s'est transformé en une lave torrentielle qui emporta la voie de chemin de fer Martigny – Orsières, à l'endroit de sa confluence avec la Dranse. L'étude post-évènementielle démontra qu'une partie des matériaux charriés par le torrent en crue provenait du glacier rocheux du Liapey de Grône (Rouiller, 2006). La fonte de la glace contenue dans la tranche supérieure du glacier rocheux ainsi que l'apport d'eau des névés sommitaux sont venus s'ajouter aux précipitations, lesquels ont pu déstabiliser une grande quantité de débris et de matériaux fins responsables du transport de gros blocs et de l'abrasion importante du lit du torrent en contrebas.

Un relevé au scanner laser terrestre (SLT) a été effectué le 14 octobre 2008 par l'IGAR afin d'acquérir un MNTHR du glacier rocheux. Cette acquisition permettra de comparer les données existantes et à venir. Ainsi, il sera possible de suivre l'évolution du glacier rocheux, d'observer les mouvements de masses et de quantifier les volumes en jeu.

3. Acquisition des données

Lors de la campagne du 14 octobre 2008, 13 scans ont été acquis depuis 4 sites (Figure 1). 5 scans (croix rouge) et 5 scans (croix bleue) ont été effectués depuis la rive gauche, respectivement droite du glacier rocheux. 1 scan (croix verte) et 2 scans (croix violette) ont été effectués plus en aval afin d'acquérir des données sur le front gauche (lobe de flux), ainsi qu'à l'avant du glacier rocheux. Ainsi, l'ensemble du glacier rocheux a pu être scanné. L'espacement moyen entre les points de mesures est de 2 à 6 cm selon la distance d'acquisition. Au total, plus de 48 millions de points ont été mesurés ce jour-là sur la surface du glacier rocheux (Tableau 1).

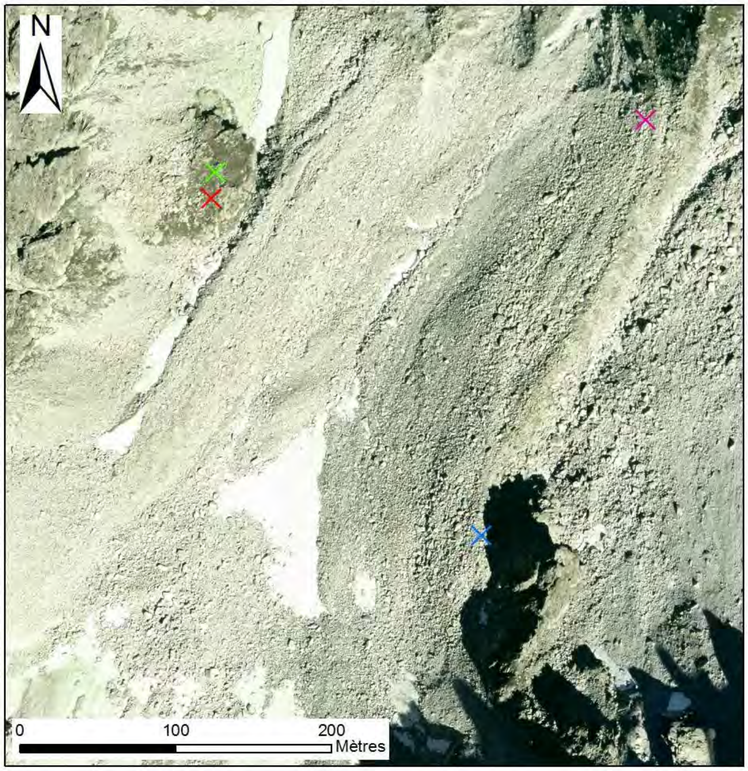

Figure 1: *Orthophoto (© Crealp) du glacier rocheux du Liapey de Grône. Les croix montrent les positionnements successifs du scanner laser terrestre pour l'acquisition des différents scans.*

Tableau 1: *Information sur les 13 scans effectués.*

Information sur le scan		**Tirs**			**Nombre de points de mesures**
Nom	**Date**	**Nombre**	**Espacement Moyen [mm]**	**Distance Moyenne [m]**	
Dur1	14.10.2008	5394370	32.7	122.63	3’952’990
Dur2	14.10.2008	5723874	39.0	146.29	5’354’017
Dur3	14.10.2008	5788836	33.9	127.13	5’727’253
Dur4	14.10.2008	5659641	37.0	138.92	5’490’895
Dur5	14.10.2008	5690568	38.6	144.94	4’820’931
Dur6	14.10.2008	4051437	23.3	87.49	3’124’177
Dur7	14.10.2008	3481524	41.3	129.09	2’923’763
Dur8	14.10.2008	3729132	60.8	190.31	3’567’806
Dur9	14.10.2008	3973910	63.9	199.87	3’949’485
Dur10	14.10.2008	3115770	59.4	185.73	3’101’079
Dur11	14.10.2008	2281690	68.8	215.34	1’799’744
Dur12	14.10.2008	2802141	41.8	120.73	2’788’009
Dur13	14.10.2008	2426512	29.4	73.55	1’924’221
				Total:	48'524’370

4. Assemblage des scans

Les données brutes de chaque scan n'ont pas nécessité de retraitement, la zone étant totalement dépourvues de végétation. Les différents scans ont été assemblés dans un premier temps en les superposant à partir de formes communes (p. ex. des blocs) contenues sur les deux images. Dans un second temps, le programme se charge automatiquement de faire correspondre au mieux les points mesurés à l'aide d'un algorithme itératif d'alignement par moindre carré. Lorsque tous les scans ont été assemblés, un alignement global est effectué. Après analyse, la précision de l'alignement est de l'ordre du cm. Cependant, le scan n°7 (fond du glacier rocheux depuis la rive droite) présente un alignement imparfait (écart de 4 cm en moyenne) et n'a donc pas été pris en compte pour l'alignement global. Il fut aligné individuellement. De plus, entre le scan n°8 et n°9 (partie gauche du glacier rocheux), une ligne de changement nette dans la précision de l'alignement (de 1 cm à 4 cm de moyenne) apparait au milieu du scan. Il peut arriver, que sur des terrains instables comme sur les éboulis du Liapey de Grône, le trépied du scanner subisse un changement de position involontaire lors de l'acquisition. Sur le scan, ceci se traduit soit par des lignes de recouvrement dans les points de mesures, soit des lignes de mesures sans points. L'observation des scans ne révèle cependant rien de semblable. L'origine de ce saut brusque dans la précision de l'alignement est donc inconnue.

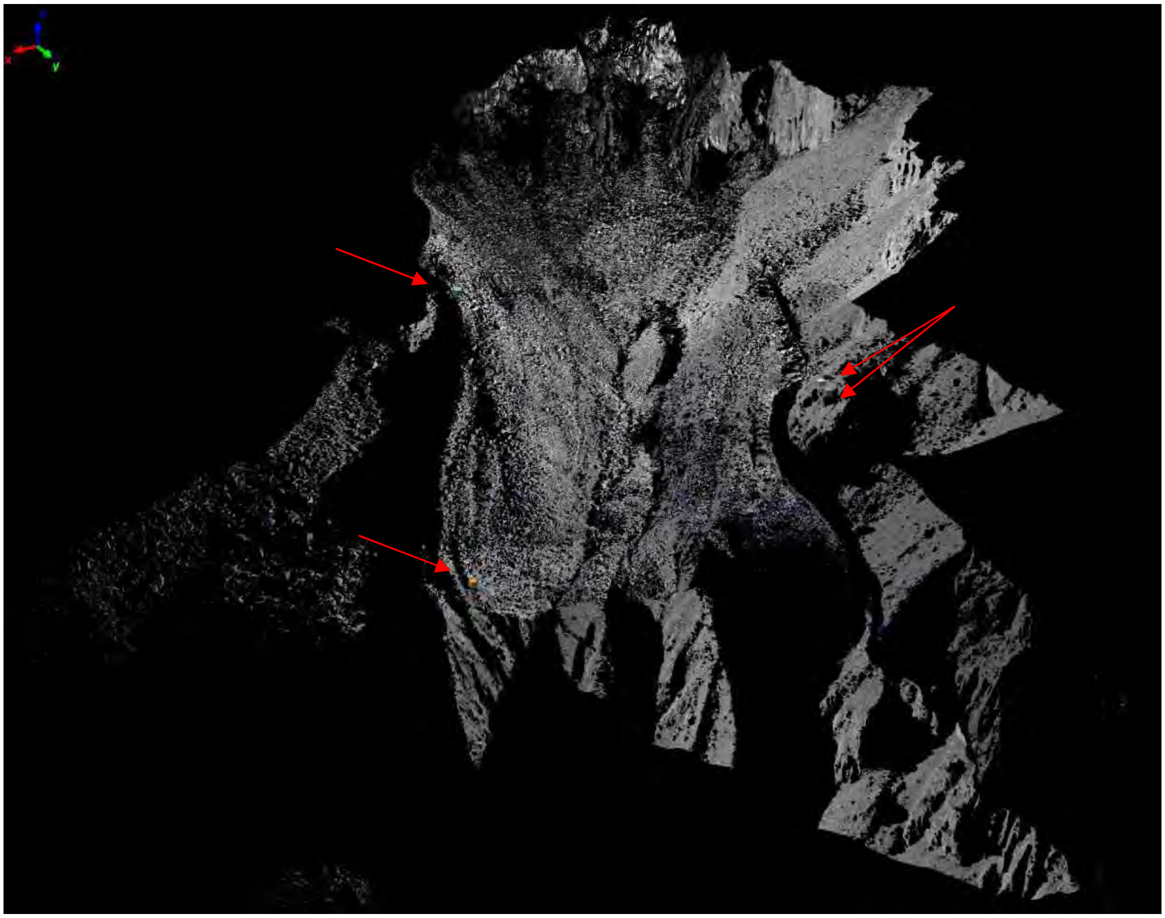

Figure 2: *Vue générale du glacier rockeux du Liapey de Grône après assemblage des scans obtenus par scanner laser terrestre. Les carrés colorés sur l'image représentent la position du scanner lors des différentes acquisitions.*

Une image complète du glacier rocheux et de ces environs est obtenue (Figure 2). La surface du glacier à elle seule est représentée par plus de 30 millions de points de mesures. L'erreur moyenne (écart type) de l'alignement des scans après assemblage est de l'ordre de 2 cm.

5. Création d'un nuage de point géoréférencé

Le nuage de point provenant de l'assemblage des scans a été géoréférencé sur la base du MNT fourni par le Crealp, lequel a été généré par photogrammétrie à partir de données datant du 24.09.2007 et géoréférencé à partir de relevés au sol. La résolution de la maille est de 2 m. Les points de calage fournis avec le MNT 2007 sont pour la plupart situés sur le glacier. Ils ont pu bouger depuis le relevé et ne sont donc pas utilisables. Une autre possibilité consiste à se baser sur les courbes de niveau à intervalle de 1 m qui ont permis de générer le MNT 2007. Cette information étant contenue dans le MNT 2007, le nuage de points a donc été géoréférencé sur la partie inchangée du MNT 2007. Il s'agit des falaises surplombant la rive gauche ainsi que le fond du glacier rocheux (Figure 3).

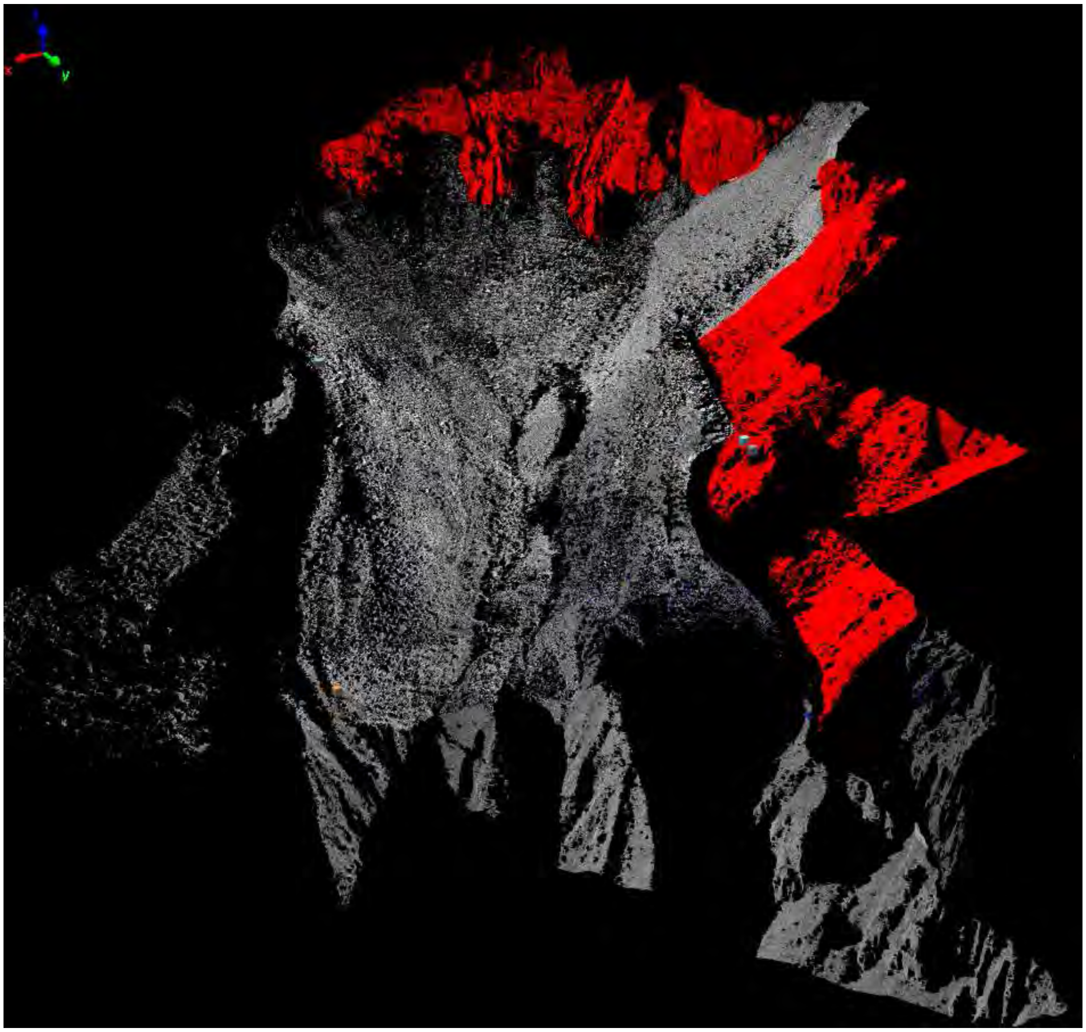

Figure 3: *Image au scanner laser terrestre du glacier rockeux du Liapey de Grône. La partie rouge représente la partie stable sur laquelle a été géoréférencé le nuage de points à partir du MNT 2007.*

Le géoréférencement s’est fait de façon similaire à l’alignement à l’aide d’un ajustement par moindre carré calé sur les parties supposées stables du MNT 2007.

La comparaison des deux images (Figure 4) montre un alignement comportant une erreur moyenne (écart type) de 34 cm. Quelques sections dans la partie supposée stable ont une différence d’alignement de 1 m au maximum, lequel provient de la différence de résolution entre les deux images.

En définitif, le nuage de points assemblé et géoréférencé est exporté en format ASCII contenant les coordonnées X, Y, Z du nuage de points dans le système CH1903_LV03.

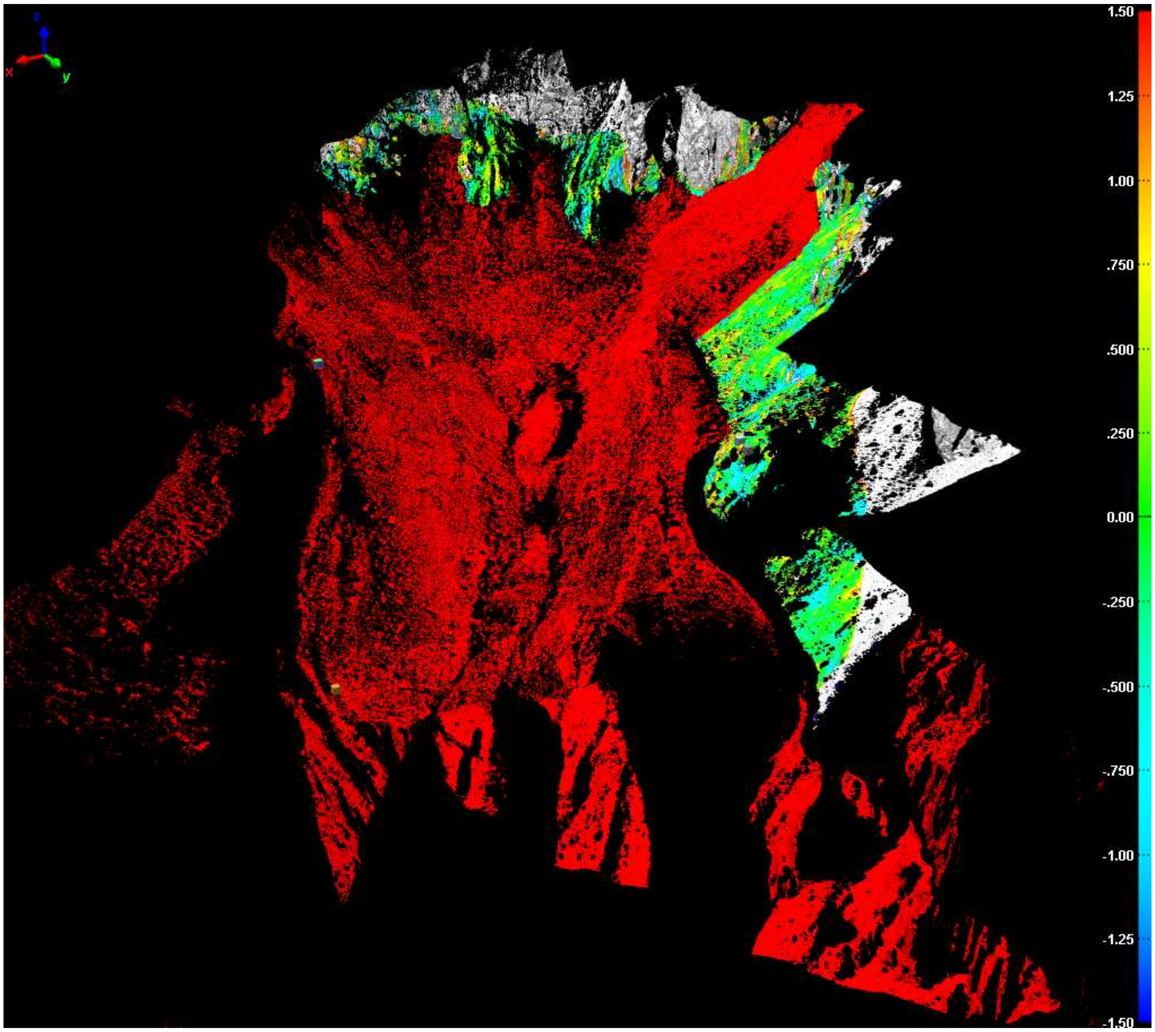

Figure 4: *Comparaison de l’alignement entre le nuage de points et le MNT 2007. La zone en rouge représente le nuage de points supposé instable et n’est donc pas pris en compte lors du géoréférencement. La précision moyenne de l’alignement est de l’ordre de 30 cm.*

6. Création d'un modèle numérique de terrain (MNT) géoréférencé

A partir du nuage de point géoréférencé, une grille régulière de 0.25 m X 0.25 m a été créée à l'aide du programme Surfer 8 (©Golden Software, Inc.). Compte tenu de la grande densité de points, le nuage de point a d'abord été échantillionné pour ne garder qu'un point de mesure tous les 15 cm. Ensuite, une grille régulière est construite par pondération inverse à la distance (Inverse Distance Weighting) avec un exposant au carré et un rayon de recherche de 2 m. La grille du MNT obtenue a une résolution de 25cm (Figure 5).

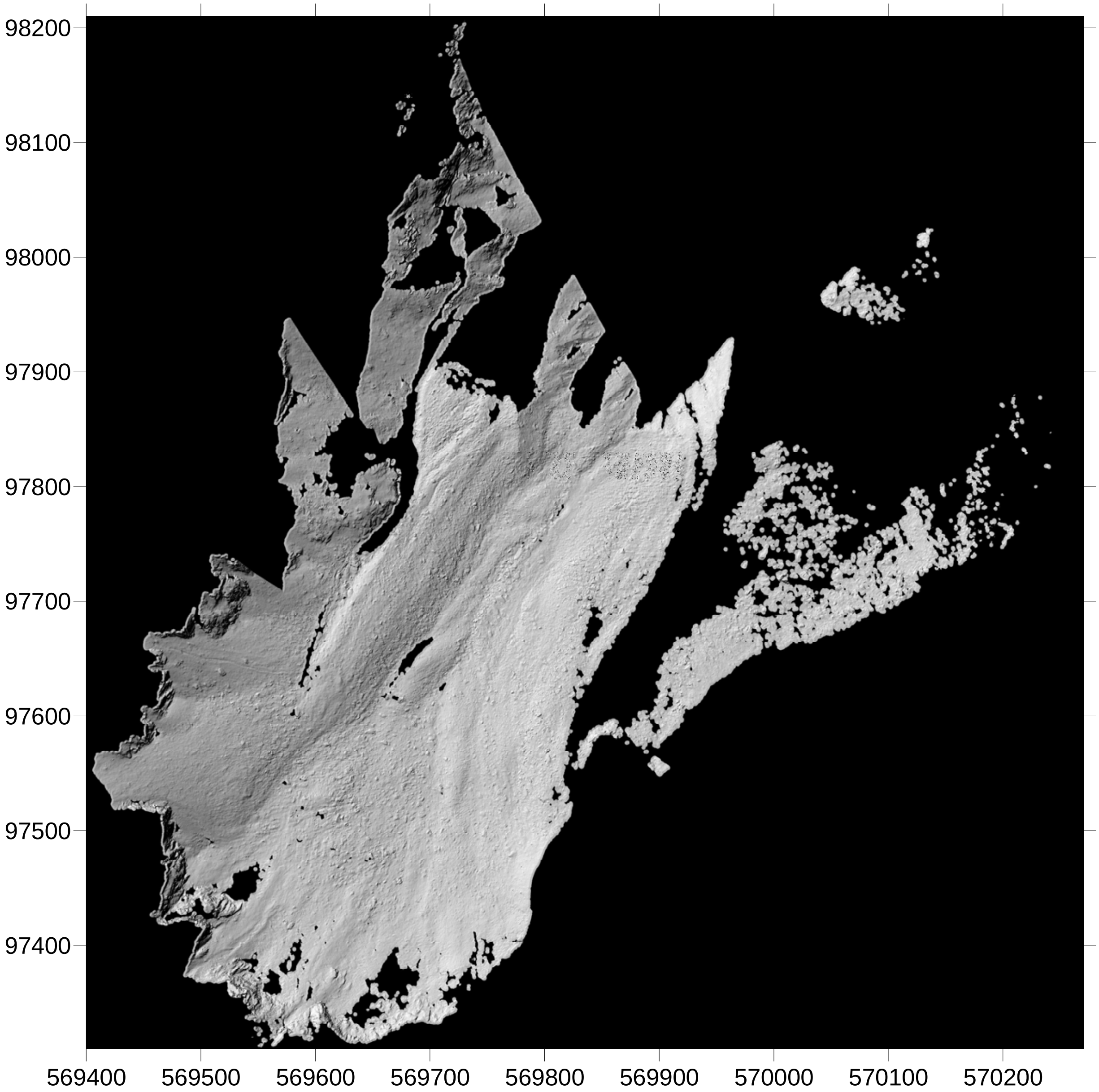

Figure 5 : *Relief ombragé du MNT géoréférencé de* grille régulière de 0.25 m X 0.25 m *obtenu par interpolation du nuage de point. Les coordonnées sont données dans le système CH1903_LV03.*

7. Discussion

L’assemblage des différents scans a pu être effectué avec une précision de l’ordre du cm (écart type = 2 cm). Le nuage de points a pu être géoréférencé sur la base du MNT 2007 avec une précision inférieure à 40 cm en moyenne, ce qui est sensiblement inférieur à la résolution du MNT 2007. L’erreur de géoréférencement du nuage de points est semblable au MNT 2007.

La couverture du glacier rocheux par le nuage de point est très complète et de très haute précision (un point de mesure tous les 2 à 6 cm). Seul 2 petites zones longeant les deux chenaux d’écoulement au milieu du glacier rocheux sont incomplètes. Il s’agit de creux qui se trouvaient en partie dans l’ombre du scanner, mais vraisemblablement aussi recouverts de neige. Par contre, la zone de rupture de pente à l’aval du glacier n’a pu seulement être scannée que depuis la rive droite. Ainsi, une partie des ravines manquent.

L’alignement des zones stables du nuage de points sur le MNT 2007 permet de comparer les deux images avec une erreur totale de 40 cm. Il révèle des différences significatives en l’espace d’une année, particulièrement le long des deux chenaux médians ainsi qu’en son front (Figure 6). Il serait intéressant de poursuivre le monitoring afin de pouvoir quantifier plus précisément ces changements à la surface du glacier, ainsi que d’y inclure les ravines dans les futures relevés au SLT. En outre, pour atteindre une précision encore meilleure dans le géoréférencement du MNTHR, les futurs scans devront être accompagnés d’un relevé adéquat de points de calage à l’aide du GPS différentiel. Il sera ensuite possible de réaligner les données antérieures sur la base de ces nouveaux points de géoréférencement.

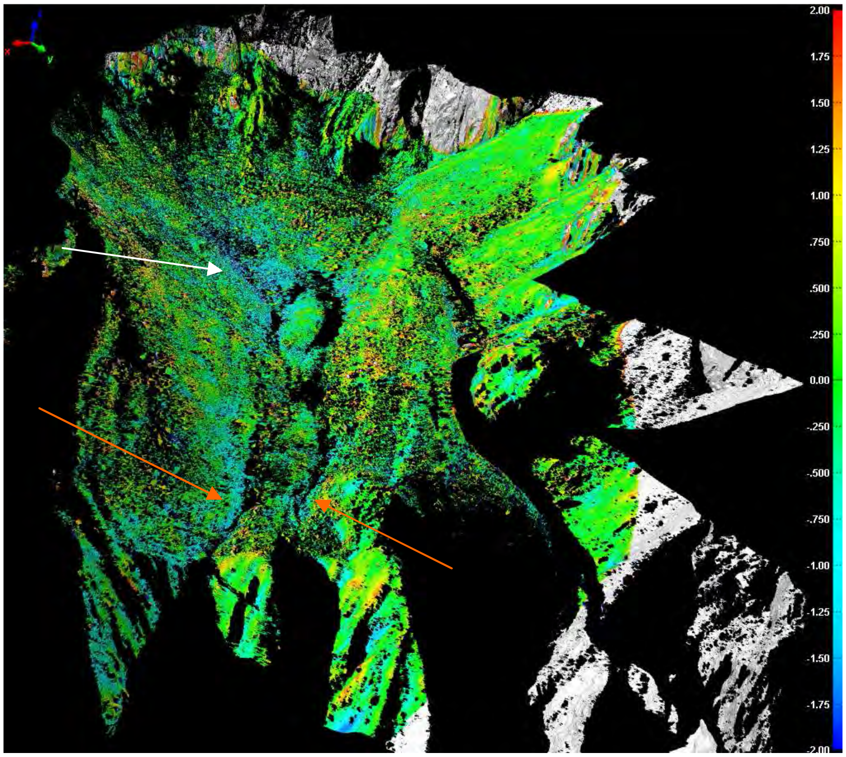

Figure 6 : Comparaison du nuage de points acquis en 2008 avec le MNT 2007. Des différences sont nettement visibles le long des deux chenaux médians, tout particulièrement dans sa partie supérieure (flèche blanche) ainsi qu’au front du glacier rocheux (flèches oranges).

Annexe

8. Contenu du DVD

Le DVD inclus contient les données suivantes:

- Le projet PolyWorks "Durnand2008.pwk" comprenant le nuage de points 3D et les 13 scans assemblés.
- Le dossier « Scans » comportant les données brutes acquises par le SLT et les matrices d'alignement.
- Le Programme "IMView", qui permet d'ouvrir et de consulter le projet PolyWorks en 3D
- Le "IMView Reference Guide"
- Le dossier MNT avec le fichier "PointCloudDurnant14102008.asc" contenant les coordonnées (X,Y,Z) des points de mesure en format ASCII, ainsi que le nuage de point re-échantillionné au 10cm, 15cm et 25 cm.
- Le dossier … MNT\ArcGIS contenant le MNTHR et son relief ombragé compatible ArcGis©.

9. Guide d'utilisation sommaire de "IMView"

- Installer le Software "imview_10-0-32bit.msi" à partir du DVD
- Ouvrir le projet PolyWorks "Durnand2008.pwk" puis le projet IMInspect "Durnand2008"
- A l'aide d'un menu déroulant situé en haut à gauche de la fenêtre, il est possible d'obtenir le projet complet ("Whole Project") qui contient les 13 scans assemblés. Avec cette configuration, il est possible de modifier le type de vues du projet avec le menu "View"→ "Color". Les données peuvent être sélectionnées à partir des organigrammes qui peuvent être activés avec le deuxième bouton en haut à gauche ou à partir du menu "View"→ "Treeview".

- Il est alors possible de tourner, de déplacer et de zoomer sur l'aperçu 3D en procédant comme suit:
  - Rotation: clique gauche + mouvement de rotation
  - Zoom: clique droit + mouvement d'avant en arrière
  - Déplacement: clique du milieu + mouvement dans la direction souhaitée
  - Rotation selon un axe fixe: Shift + clique gauche ou Shift + clique droit
  - Zoom selon un carré de sélection: Shift + clique du milieu
  - Vue depuis en haut: Shift + F5
  - Vue depuis le côté (selon l'axe Y): Shift + F4
- Il est possible d'activer ou de désactiver un ou plusieurs objets du projet à partir de l'organigramme:
  - Pour cacher le(s) objet(s) sélectionné(s): Ctrl + Shift + D
  - Pour rendre visible(s) le(les) objet(s) sélectionné(s): Ctrl + Shift +R
- Un double-clique sur un objet permet d'ouvrir le menu "Object Properties" dans lequel il est, par exemple, possible de changer la couleur de l'objet avec un clique sur le rectangle de couleur.

Pour de plus amples informations sur les fonctionnalités du Software "IMView", consulter le "IMView Reference Guide", que l'on peut trouver en format .pdf sur le DVD sous documentation.

10. Bibliographie :

Rouiller, J.-D. : Situation d'évacuation suite à la crue du torrent Durnand (juillet 2006) - La lave torrentielle du Durnand (25 juillet 2006) : une conséquence directe de la fonte du permafrost. ROUILLER J.-D. Actes de la conférence finale internationale, RISKYDROGEO (24-26 octobre 2006, Aoste), p. 42-45, 2006.)